Multi-Scale Modelling of Monolith Honeycomb Substrates

by

Ivan Cornejo Garcia

A thesis submitted in partial fulfillment of the requirements for the degree of

Doctor of Philosophy
in
Chemical Engineering

Department of Chemical and Materials Engineering
University of Alberta

Abstract

This thesis reports the study of flow inside a honeycomb type substrate. Honeycomb monoliths are extensively used in the automotive industry, as substrates in the exhaust gas aftertreatment system. The flow approaching a honeycomb monolith is usually highly turbulent; However, once entering the channels, turbulence dissipates because of a dramatic reduction of the Reynolds number. The first part of the honeycomb channels can be very active in terms of chemical reactions and can impact the performance of the entire system significantly; Therefore, it is important to study the flow regime transition and other phenomena occurring in that area. The flow regime, pressure drop and convective heat transfer when flow enters, passes through and leaves the substrate are analyzed. Computational models at a channel and a converter scale are used. At a converter scale, the honeycomb is modelled as a continuum, meanwhile, for channels, a discrete model is used. Laminar and turbulent flow approaching the monolith are considered. The cases with turbulent flow are modelled with Reynolds-Average Navier-Stokes (RANS) models and Large Eddy Simulation (LES).

According to the results, the turbulence approaching the honeycomb in fact dissipates inside the channels, but does not lead to a steady flow, instead of that, the flow becomes laminar unsteady. When turbulence effectively enters the channels, it enhances the convective heat transfer in the entrance length; However, in the laminar unsteady region, both the pressure drop and the convective heat transfer coefficient are similar to those for steady laminar flow. Regarding the exit of the substrate, when flow leaves the channels behaves like a jet, and under certain conditions, it generates turbulence, even when the flow inside the

channels is steady. The generation of turbulence is promoted by a higher channel velocity, remaining turbulence inside the substrate and pulsating flow inside the channels, and it is also affected by the channel shape. A new strategy to obtain a realistic decay and generation of turbulence in converter scale simulations using the continuum approach is proposed. The new strategy corrects nonphysical flow regime transitions observed in previous models. A new pressure drop model for flow through a honeycomb is presented. The model accounts for the effects of flow entering, developing and leaving the substrate, and can be applied for circular, square, triangular and hexagonal channel cross-sections. A new correlation for the apparent permeability of a continuum modelling a monolith is reported. The correlation is based on the friction factor inside a monolith channel and accounts for a realistic inlet velocity profile and the hydraulic entrance length.

New correlations for the convective heat transfer coefficient at a constant wall temperature and a constant wall heat flux when laminar flow is entering into a circular cross-section monolith channel are reported. The correlations consider temperature-dependent fluid properties. For the case with a constant wall temperature, when the heating rate is high, the curve of the convective heat transfer coefficient along the channel has a minimum significantly lower than the asymptotic value. Correlations available in the literature are only valid for monotonically decreasing curves; Hence, a new mathematical expression that combines a decreasing function with a sigmoidal one is used. A methodology to calibrate such a model is also presented. A methodology for modelling the effect of the upstream turbulence when it enters the channels on the convective heat transfer coefficient is proposed.

Finally, a wall-flow filter, which is a particular type of honeycomb with porous walls, is analyzed. The developing of the flow inside the filter is investigated. A criterion to consider the flow as fully developed is presented. It is found that the friction factor in the filter channels is different from that of pipes with non-porous walls, as usually assumed. An

improved pressure drop model, based on first principles, is proposed.

Preface

This thesis is presented in the paper format, and is based on eleven papers. To the date of this document, nine papers are accepted and available online, one is submitted and under peer revision, and one more will be submitted shortly.

Chapter 2 has been published as: Cornejo, I., Nikrityuk, P., & Hayes, R. E. (2017). Turbulence decay inside the channels of an automotive catalytic converter monolith. *Emission Control Science and Technology*, 3(4), 302-309. The simulations in this study were performed in the computers provided by Dr. Robert Hayes and Dr. Petr Nikrityuk. They were also the supervisory authors and were involved in discussions of the results and manuscript composition. I performed all of the simulations and post-processing for this work, and also prepared the manuscript.

Chapter 3 has been published as: Cornejo, I., Nikrityuk, P., & Hayes, R. E. (2018). Multiscale RANS-based modeling of the turbulence decay inside of an automotive catalytic converter. *Chemical Engineering Science*, 175, 377-386. The simulations in this study were performed in the computers provided by Dr. Robert Hayes and Dr. Petr Nikrityuk. They were also the supervisory authors and were involved in discussions of the results and manuscript composition. Dr. Nikrityuk provided the computational grid for this paper. I performed all of the simulations and post-processing for this work, and also prepared the manuscript.

Chapter 4 has been published as: Cornejo, I., Nikrityuk, P., & Hayes, R. E. (2018). Turbulence generation after a monolith in automotive catalytic converters. *Chemical Engineering Science*, 187, 107-116. The simulations in this study were performed in the computers provided by Dr. Robert Hayes and Dr. Petr Nikrityuk. They were also the supervisory authors and were involved in discussions of the results and manuscript composition. I performed all of the simulations and post-processing for this work, and also prepared the manuscript.

Chapter 5 has been published as: Cornejo, I., Nikrityuk, P., & Hayes, R. E. (2020). Effect

of substrate geometry and flow condition on the turbulence generation after a monolith. *The Canadian Journal of Chemical Engineering*. DOI: https://doi.org/10.1002/cjce.23687. The simulations in this study were performed in the computers provided by Dr. Robert Hayes and Dr. Petr Nikrityuk. They were also the supervisory authors and were involved in discussions of the results and manuscript composition. I performed all of the simulations and post-processing for this work, and also prepared the manuscript.

Chapter 6 has been published as: Cornejo, I., Hayes, R. E., & Nikrityuk, P. (2018). A new approach for the modeling of turbulent flows in automotive catalytic converters. *Chemical Engineering Research and Design*, 140, 308-319. The simulations in this study were performed in the computers provided by Dr. Robert Hayes and Dr. Petr Nikrityuk. They were also the supervisory authors and were involved in discussions of the results and manuscript composition. I performed all of the simulations and post-processing for this work, and also prepared the manuscript.

Chapter 7 has been published as: Cornejo, I., Nikrityuk, P., Lange, C., & Hayes, R. E. (2019). Influence of upstream turbulence on the pressure drop inside a monolith. *Chemical Engineering and Processing-Process Intensification*. DOI: https://doi.org/10.1016/j.cep.2019.107735. The simulations in this study were performed in the computers provided by Dr. Robert Hayes and Dr. Petr Nikrityuk. Dr. Robert Hayes, Dr. Petr Nikrityuk and Dr. Carlos Lange were the supervisory authors and were involved in discussions of the results and manuscript composition. I performed all of the simulations and post-processing for this work, and also prepared the manuscript.

Chapter 8 has been published as: Cornejo, I., Nikrityuk, P., & Hayes, R. E. (2019). Pressure correction for automotive catalytic converters: A multi-zone permeability approach. *Chemical Engineering Research and Design*, 147, 232-243. The simulations in this study were performed in the computers provided by Dr. Robert Hayes and Dr. Petr Nikrityuk. They were also the supervisory authors and were involved in discussions of the results and manuscript composition. I performed all of the simulations and post-processing for this work, and also prepared the manuscript.

Chapter 9 has been published as: Cornejo, I., Nikrityuk, P., & Hayes, R. E. (2020). The influence of channel geometry on the pressure drop in automotive catalytic converters: Model development and validation. *Chemical Engineering Science*. DOI: https://doi.org/10.1016/j.ces.2019.115317. The simulations in this study were performed

in the computers provided by Dr. Robert Hayes and Dr. Petr Nikrityuk. They were also the supervisory authors and were involved in discussions of the results and manuscript composition. I performed all of the simulations and post-processing for this work, and also prepared the manuscript.

Chapter 10 has been published as: Cornejo, I., Cornejo, G., Nikrityuk, P., & Hayes, R. E. (2019). Entry length convective heat transfer in a monolith: The effect of upstream turbulence. *International Journal of Thermal Sciences*, 138, 235-246. The simulations in this study were performed in the computers provided by Dr. Robert Hayes and Dr. Petr Nikrityuk. They were also the supervisory authors and were involved in discussions of the results and manuscript composition. I performed 90% of the simulations and 90% post-processing for this work, and also prepared the manuscript. Gonzalo Cornejo collaborated with the rest of the simulations and post-processing.

Chapter 11 has been submitted for publication as: Cornejo, I., Nikrityuk, P., & Hayes, R. E. (Submitted). Improved Nu number correlations for gas flow in monolith reactors using temperature-dependent fluid properties *International Journal of Thermal Sciences* and it is currently under peer revision. The simulations in this study were performed in the computers provided by Dr. Robert Hayes and Dr. Petr Nikrityuk. They were also the supervisory authors and were involved in discussions of the results and manuscript composition. I performed all of the simulations and post-processing for this work, and also prepared the manuscript.

Chapter 12 will be submitted for publication as: Vega, I., Cornejo, I., Nikrityuk, P., Votsmeier, M. & Hayes, R. E. Towards a fully predictive multi-scale pressure drop model for a wall-flow filter. This paper was done in collaboration using the computers provided by Dr. Robert Hayes. MSc. Ileana Vega and I performed the computational simulations, data analysis and manuscript preparation in close collaboration (50/50). Dr. Robert Hayes, Dr. Petr Nikrityuk and Dr. Martin Votsmeier were supervisory authors and were involved in discussions of the results and manuscript composition.

"It always seems impossible until it's done."

-Nelson Mandela

Acknowledgements

I want to thank Dr. Robert Hayes and Dr. Petr Nikrityuk for being amazing supervisors. During my entire PhD, I felt totally supported by two committed, wise, rigorous, plenty of knowledge supervisor, with great human quality and high-level professionals. I will never forget your availability for those long hours of enriching discussion. I am also totally grateful for allowing me to meet researchers leading the field around the world and being able to show them my work.

I am grateful to Daniela, for being an amazing partner of life. For joining me on this trip, straight to the other side of the world at expenses of being away from her family. For bearing me when stressed, for always being there and never fail. I also thank my father Ivan Cornejo Clavero, mother Maria Garcia Garrido, my brother Gonzalo Cornejo Garcia, my sister Claudia Cornejo Garcia and Sebastian, for being such an amazing family.

I would like to thank to my friend Dr. Anton Fadic for introducing me to the workgroup, for helping me to adapt to Edmonton and for all those long hours of conversation about how to make this world better. Anton will always find a friend in me. I am also grateful to my friend Msc. Ileana Vega, for her strong commitment when working in collaboration and also for always having a smile, even in the most adverse circumstances, it really made a difference. Her constant, unbeatable and teeming efforts will bring her nothing but success. Last but not least, I want to thank to my friends Dr. Paula Guerra, Dr. Maria Paz Dominguez, Dr. Ricardo Simpson, Dr. Sergio Almonacid, Dr. Juan Yianatos and Dr. Luis Bergh for all their advises and support during this time from Chile.

Finally, I acknowledge the Universidad Tecnica Federico Santa Maria, the receipt of a Becas-Chile (CONICYT) scholarship, other funding provided by the Natural Sciences and Engineering Research Council of Canada, and the support provided by Compute Canada (www.computecanada.ca).

Contents

List of Tables

List of Figures

Nomenclature

Chapter 2

$\overline{x}$	Time-average variable
$\tilde{x}$	Length filtered variable
P	Pressure, Pa
U	Reynolds average velocity, m/s
v	Velocity vector, m/s
I	Identity matrix
D_H	Channel hydraulic diameter, m
t	Time, s
L_s	Sub-grid length scale, m
Re	Channel Reynolds
H_c	Channel height, m
r	Radial position, m
R	Monolith radius, m
α	Permeability, m^2
β_1	Wilcox k-ω model parameter
β^*	Wilcox k-ω model parameter
γ_1	Wilcox k-ω model parameter
ε	Turbulence dissipation rate, m^2/s^3
k	Turbulence kinetic energy, m^2/s^2
μ	Viscosity, Pa-s
μ_t	Turbulence viscosity, Pa-s
ρ	Density, kg/m^3
σ_ω	Turbulence Prandtl number for ω
σ_k	Turbulence Prandtl number for k
ϕ	Monolith void fraction
ω	Specific turbulence dissipation rate, 1/s

Chapter 3

C_ω	Model parameter
D_H	Hydraulic diameter o a monolith channel, m
F_1, F_2	Blending functions
f_β	Model parameter
I	Identity matrix
IC	Inlet conditions
K_α	Permeability tensor, m^2
K_α^{axial}	Axial permeability, m^2
K_α^{radial}	Radial permeability, m^2
L	Characteristic length, m
p	Pressure, Pa
Re	Reynolds number
S_ω	Source or sink of ω, $1/\mathrm{s}^2$
S_κ	Source or sink of turbulence kinetic energy, $\mathrm{m}^2/\mathrm{s}^3$
$S_{\vec{u}}$	Source or sink of momentum, kg-m/s^2
t	Time, s
$\vec{u}$	Time averaged velocity vector, m/s
$\vec{u}'$	Fluctuating component of the velocity, m/s
α_ω	Model parameter
β^*	Model parameter
β_ω	Model parameter
δ	Distance from the inlet of the monolith, mm
ε	Turbulence dissipation rate, $\mathrm{m}^2/\mathrm{s}^3$
κ	Turbulence kinetic energy, $\mathrm{m}^2/\mathrm{s}^2$
μ	Viscosity, Pa·s
μ_t	Turbulence viscosity, Pa·s
ν_t	Kinematic turbulence viscosity, m^2/s
ω	Specific Turbulence dissipation rate, 1/s
ϕ	Void fraction of the monolith
ρ	Density, kg/m^3
σ_κ	Turbulence Prandtl number for κ
σ_ω	Turbulence Prandtl number for ω

Chapter 4

α_ω	Model parameter
β^*	Model parameter
κ	Turbulence kinetic energy, m^2/s^2
κ^*	Dimensionless turbulence kinetic energy
δ	Dimensionless distance starting from the end of the monolith
ε	Turbulence dissipation rate, m^2/s^3
ϕ	Void fraction of the monolith
μ	Viscosity, Pa·s
μ_{SGS}	Sub-grid turbulence viscosity, Pa·s
μ_t	Turbulence viscosity, Pa·s
ν_t	Kinematic turbulence viscosity, m^2/s
ω	Specific turbulence dissipation rate, 1/s
ρ	Density, kg/m^3
σ_κ	Turbulence Prandtl number for κ
σ_ω	Turbulence Prandtl number for ω
C_μ	Model parameter
CFL	Courant-Friedrich-Levy number
F_1, F_2	Blending functions
f_β	Model parameter
L_c	Height of the channels, m
L_w	Wall thickness, m
p	Pressure, Pa
Re	Reynolds number
Re_c	Reynolds number based on the channel size
Re_w	Reynolds number based on the thickness of the wall intersections
s	Standard deviation
t	Time, s
$u_{i(t)}$	Instantaneous velocity, m/s
u_i	Time average velocity vector, m/s
u	Time average velocity magnitude, m/s
u_i'	Velocity fluctuations, m/s
$\overline{u}_i$	Filtered velocity, m/s

Chapter 5

CPSI	Monolith cell density, cells per square inch
D_H	Channel hydraulic diameter, m
k	Turbulence kinetic energy, m^2/s^2
k^*	Dimensionless turbulence kinetic energy
k_{sgs}	Subgrid turbulence kinetic energy, m^2/s^2
$L_{channel}$	Length of the piece of substrate, m
L_{open}	Length of the open section after the substrate, m
L_w	Maximum thickness at the corners of the channels, m
p	Pressure, Pa
Re_c	Channel Reynolds number
Re_w	Reynolds number based on L_w
t	Time, s
u_c	Channel velocity, m/s
u_i	Velocity vector, m/s
w	Substrate wall thickness, w
δ_{ij}	Kronecker delta
δ_w	Dimensionless distance
ν	Kinematic viscosity, m^2/s
ρ	Density, kg/m^3
μ	Molecular viscosity, Pa-s
μ_{sgs}	Subgrid turbulence viscosity, Pa-s

Chapter 6

C_μ, C_ω	RANS model constant
D_H	Channel hydraulic diameter, m
$\vec{K}_\alpha$	Permeability vector, m^2
I	Identity matrix
l_e	Turbulence length scale, m
L_c	Channel side, m
L_w	Monolith wall thickness, m
L_T	Thickness of corners between channels, m
p	Pressure, Pa
Re_c	Channel Reynolds number
Re_w	Corner thickness Reynolds number
u	Velocity magnitude, m/s
$\vec{u}$	Velocity vector, m/s
$u_{(t)}$	Instantaneous velocity, m/s
u_∞	Equilibrium velocity, m/s
$\overline{u}$	Filtered velocity, m/s
β_ω	Model parameter
Δ	Area of the cell, m^2
$\delta_{\kappa/\omega}$	Thickness of the triggering zone, m
ε	Turbulence dissipation rate, m^2/s^3
ϕ	Substrate void fraction
κ	Turbulence kinetic energy, m^2/s^2
μ	Viscosity, Pa-s
μ_t	Turbulence viscosity, Pa-s
ρ	Density, kg/m^3
σ_κ	Turbulence Pr number for κ
σ_ω	Turbulence Pr number for ω
ω	Specific turbulence dissipation rate, 1/s
ω_0	Damping parameter, 1/s

Chapter 7

C_l	Model parameter
p	Pressure, Pa
$\overline{p}$	Filtered pressure, Pa
P_T	Total pressure (static plus dynamic), Pa
Re_c	Channel Reynolds number $=\rho v_c D_H/\mu$
t	Time, s
u_i	Vector of velocity, m/s
$\overline{u_i}$	Vector of filtered velocity, m/s
u	Velocity magnitude, m/s
u'	Standard deviation of velocity magnitude, m/s
U	Time average velocity magnitude, m/s
v_c	Average channel velocity, m/s
w	Substrate wall thickness
k	Turbulence kinetic energy, $\mathrm{m}^2/\mathrm{s}^2$
k_{sgs}	Sub-grid kinetic energy, $\mathrm{m}^2/\mathrm{s}^2$
μ	Molecular viscosity, Pa-s
μ_t	Turbulence viscosity, Pa-s
ρ	Density, $\mathrm{kg/m}^3$
ω	Specific turbulence dissipation rate, 1/s

Chapter 8

A	Flow area, m^2
C	Model constant $= f\mathrm{Re}_{fd}/2$
C_u	Inertial resistance factor
D_H	Hydraulic diameter, m
f	Friction coefficient
Gz_i	Inverse Graetz number
H_c	Cell height, m
L	Channel and monolith length, m
L_H	Hydraulic entrance length, m
Δm	Apparent porous jump thickness, m
P	Pressure, Pa
Pr	Prandtl number
Q	Flow rate, m^3/s
R_1	Radius of the inlet pipe, m
R_2	Radius of the substrate, m
Re	Channel Re number
u_i	Velocity vector, m/s
u_c	Channel velocity, m/s
α_i	Permeability vector, m^2
δ	Kronecker delta
Δ	Cell characteristic length, m
κ	Turbulence kinetic energy, m^2/s^2
ϕ	Monolith void fraction
ρ	Density, kg/m^3
μ	Viscosity, Pa-s
μ_t	Eddy viscosity, Pa-s
μ_{eff}	Effective viscosity, Pa-s
μ_{SGS}	Subgrid turbulence viscosity, Pa-s
ξ	Local friction coefficient
ω	Specific dissipation rate, 1/s
ω_0	Reference specific dissipation rate, 1/s

Chapter 9

c_1, n	Permeability model constants
C_u	Inertial resistance factor
$\mathrm{D_H}$	Channel hydraulic diameter, m
f	Friction coefficient
Gz_i	Inverse Graetz number
L	Channel characteristic length, m
L_H	Channel hydraulic entrance length, m
$\mathrm{L_s}$	Substrate length, m
$\mathrm{L_w}$	Substrate wall thickness, m
P	Pressure, Pa
P_s	Static pressure, Pa
P_d	Dynamic pressure, Pa
Pr	Prandtl number
Re	Channel Re number
R_i	Inlet pipe radius, m
u_i	Velocity vector, m/s
u_c	Channel velocity, m/s
x^+	Dimensionless axial coordinate
α_i	Substrate apparent permeability, $1/\mathrm{m}^2$
α_{afp}	Apparent face permeability, m
δ_{ij}	Kronecker delta
δm	Apparent porous jump thickness, m
ϕ	Monolith void fraction
ρ	Density, $\mathrm{kg/m}^3$
μ	Viscosity,Pa-s
fd	Sub-index standing for fully developed flow

Chapter 10

A, B, C, n	Model parameters
C_p	Specific heat capacity, J/kg·K
CFL	Cell convective Courant number
D	Channel diameter, m
f_B, f_C, f_n	Model sub-functions
Gz	Graetz number
h	Convective heat transfer coefficient, W/m^2·K
k_{eff}	Effective thermal conductivity, W/m·K
l_e	Turbulence length scale, m
Nu	Nusselt number
p	Pressure, Pa
R	Channel radius, m
R^2	Coefficient of determination
Adj-R^2	Adjusted coefficient of determination
Re	Reynolds number
T	Temperature, K
T_s	Surface Temperature, K
T_m	Mixing cup temperature, K
T_i	Turbulence intensity, %
u_i	Velocity vector, m/s
ε	Turbulence dissipation rate, m^2/s^3
κ	Turbulence kinetic energy, m^2/s^2
kl	Laminar kinetic energy, m^2/s^2
ν	Kinematic viscosity, m^2/s
ρ	Density, kg/m^3
μ	Laminar viscosity, Pa-s
μ_t	Turbulence viscosity, Pa-s
μ_{SGS}	Sub-grid turbulence viscosity, Pa-s
ω	Specific turbulence dissipation rate, 1/s

Chapter 11

a,b,B,C,n	Empirical parameters
C_p	Specific heat capacity, J/Kg-K
D	Channel diameter, m
D_1	Cell Hydraulic diameter, m
Gz	Graetz number
k	Thermal conductivity, W/m-K
h	Convective heat transfer coefficient, W/m^2-K
H	Wall heat flux, kW/m^2
L	Substrate or channel length, m
L_1	Reservoir length, m
M_W	Molecular weight, g/mol
Nu	Nusselt number
Nu_H	Nusselt number at a constant wall heat flux
Nu_T	Nusselt number at a constant wall temperature
Nu_∞	Asymptotic Nusselt number
p	Pressure, Pa
Pr	Prandlt number
r	Radial position, m
Re	Channel Reynolds
R_g	Ideal gases constant
Sc	Schmidt number
T	Temperature, K
T_w	Wall temperature, K
T_b	Bulk temperature, K
u_i	Velocity vector, m/s
u_x	Axial velocity, m/s
ρ	Density, kg/m^3
μ	Viscosity, Pa-s
σ_ω	Turbulence Prandlt number for ω
σ_κ	Turbulence Prandlt number for κ
ϕ	Monolith porosity
ω	Specific dissipation rate 1/s

Chapter 12

Δp_f	Pressure drop due to friction, Pa
Δp_i	Pressure drop when entering the filter, Pa
Δp_o	Pressure drop when leaving the filter, Pa
Δp_{kec}	Kinetic energy correction, Pa
Δp_o	Pressure drop when leaving the filter, Pa
F_D	$f \cdot$Re
C_i	Inertial coefficient of the frontal face
C_o	Inertial coefficient of the rear face
D_H	Channel hydraulic diameter, m
f	Darcy friction factor
k_α	kinetic energy correction factor
k_β	Momentum flux correction factor
L'_f	Channel effective length, m
L''_f	Filtrating zone effective length, m
Q	Volumetric flow rate, Nm^3/h
u	Velocity magnitude, m/s
u_c	Channel velocity, m/s
u_inlet	Channel inlet velocity, m/s
u_{max}	Maximum velocity, m/s
Re	Channel local Reynolds number
Re_i	Inlet Reynolds number $=\rho u_c D_H/\mu$
Re_w	Wall Reynolds number $=\rho u_w D_H/\mu$
α	Wall permeability, m^2
α_{afc}	Apparent frontal face permeability, m^2
μ	Viscosity, Pa-s
ρ	Density, kg/m^3
τ_w	Wall shear stress, Pa
ζ	Inertial losses coefficient
ic	Inlet channel
oc	Outlet channel
w	Porous wall

Chapter 1

Introduction

Reducing pollution from industry and human activity has been an important topic in the last and current century. Especial attention has been paid to emissions from cars in cities. Electric vehicles have arised as an alternative, however, their comparatively high cost and large infrastructure requirements make them not yet suitable for many activities, especially in remote locations [1]. Therefore, internal combustion vehicles will continue to play a significant a role in the near and mid future, doubtlessly. For over half a century, the automotive industry has put substantial efforts into the optimization of the exhaust gas after-treatment systems of cars (EGATS) [2]. While a detailed description of an EGATS is beyond the scope of this thesis, it is useful to provide a brief description of its components. The components of the EGATS vary according to the engine and the vehicle. For example, Diesel engines, which are lean burn engines, typically require a direct oxidation catalyst (DOC) to oxidize carbon monoxide and hydrocarbons, a selective catalyst reduction unit (SCR) to eliminate NOx and a particulate filter (DPF) to capture soot. In traditional Port Fuel Injection gasoline engines (PFI), the premixing of the fuel and air produces a very efficient combustion, hence, the only element required is a three-way catalyst (TWC). Recently, Gasoline Direct Injection (GDI) systems have gained popularity, since they yield a higher fuel efficiency compared to PFI. The drawback of GDI systems is the reduction of the mixing inside the cylinders, which leads to a higher generation of soot, making necessary the use of a gasoline particulate filter (GPF), and more recently a catalyst coated filter (cGPF), which combines the functionality of a TWC and a GPF in a single unit. All those component are necessary to meet the environmental regulations. However, they impact the fuel economy and power output of the car significantly. Honeycomb type structures are ideal to be used as a substrate in EGATS. A honeycomb is a solid piece with many channels running in parallel. Usually, the catalyst is attached to the substrates by adding a thin layer of washcoat at the inner walls of the channels. A few of the advantages of honeycombs are their comparatively low back-pressure, high contact area

and excellent structural integrity [3]. Because of that, honeycomb type substrates are used not only in automotive applications, but also in other industrial processes. Monoliths can be found in photo-catalytic reactors [4], hydrogen production reactors [5], ammonia decomposition [6], methanol synthesis reactors [7], full cells [8], steam reforming of hydrocarbons [9] and production of H_2O_2 [10] among others [11]. The objective of this thesis is to improve the understanding and model the flow through monolith honeycomb substrate. It is mainly concerned with EGATS, but, many of the results can be directly applied to other processes involving honeycombs.

There are many phenomena taking place in an EGATS. The chemical reactions in the washcoat are affected by mass transport, and in turn, they have thermal effects on the gas and solid phases. The flow regime of the outflow from the engine is highly turbulent, however, once entering the monolith channels, it laminarizes, becoming turbulent again after leaving the substrate. In addition, given the nature of the operation of an internal combustion engine, its outflow is transient with large variations of the flow rate, chemical composition and temperature [12]. Taking that into account, one can observe that there are many time and length scales involved in the process. From the side of the length, in automotive applications, a pore of the washcoat has a size of the order of the tens or hundreds of nanometers, meanwhile, the channels have a hydraulic diameter of the order of a millimetre. In turn, a whole monolith has a diameter and length of the order of the decimetre. Regarding the time, the fastest scale is the one from the chemical reactions, followed by the time scale of the turbulence, which is of the order of the microseconds. The residence time of the gas inside the monolith is of the order of the centiseconds, the same as the frequency of the pistons of an engine. Finally, the duration of a driving cycle runs from minutes to hours. With the current computational capacity, it is impossible to model every single pore of a converter, as it is impractical to model every single microsecond of operation of an entire driving cycle. This difficulty, named the "Multi-Scale Problem", that affects honeycomb substrates, has received substantial attention in the last decades [13], not only in automotive applications, but also in other industrial processes. Notwithstanding the remarkable advances in the science and engineering of catalytic converters, monolithic substrates have remained relatively simple and literature regarding to the shape optimization is sparse [14, 15]. That is, still being regular cylinders with circular or elliptical cross-sections, flat frontal and rear faces, homogeneous cell density and simple channel shapes. That rises a valid question: "Is there some geometric configuration beyond the shapes currently proposed that improves or optimizes the performance of the reactor significantly?". Certainly, that is hard to answer just proposing some new arbitrary shapes. The underlying hypothesis of this work is that accurate models,

that keep consistency between the multiple scales of the problem will allow further computer aided optimization of catalytic monolith substrates. By mixing extrusion and robocasting (3D printing), the possible combinations of channel cross-sections and monolith shapes are countless [16]. Hence, an additional motivation of this thesis is also to establish and make available a methodology for systematic research of other substrate shapes that can come in the future.

Converter scale data are necessary to optimize the design of the EGATS, but, analytical solutions for the equations governing the flow motion in realistic conditions are not available. On the other hand, experiments are expensive and time consuming. Hence, substantial research in converter optimization has been addressed using numerical models. This thesis uses the Finite Volumes Method (FVM) [17] implemented in the commercial package ANSYS Fluent v17.2 and v18.2 [18, 19]. This method ensured mass, heat and momentum conservation, which is of great importance in chemical engineering. This technique divides the domain in a series of small control volumes, so called elements, meanwhile, the balances are discretized using fully implicit interpolating schemes. A 3D computational model of a channel requires from one to ten million elements, and a single monolith can have of the order of tens of thousands of channels. That makes extremely challenging the direct numerical simulation of a whole converter [20]. A broadly accepted solution is to model the substrate as a continuum, a homogeneous porous medium. That rises a series of questions about how to model a highly heterogeneous piece, with strong interactions between the solid and gas phases by using an utterly homogeneous body. Such a porous medium must be a reliable representation of the substrate and must account for the interaction between the solid and gas phases. That is, producing the same effects on the flow in terms of:

- Pressure drop
- Flow distribution
- Flow regime
- Thermal effects
- Conversion of chemical species

One of the most accepted strategies to overcome the Multi-Scale Problem is to use lumped parameter models. The aforementioned, are typically the aggregate 1D version of a 3D sections of the converter, such as a channel. At a washcoat level, both diffusion and reactions are important. A typical simplification is to neglect the washcoat diffusion, which can be

seen as a sort of 0D washcoat model. Concerning the chemical reactions, either detailed mechanisms or global reactions can be used. The latter are much simpler, but, they force the use of more complex and highly empirical reaction rate expressions. Computational tools, such as DETCHEM$^{\text{MONOLITH}}$ [21], allow the study of the transient behavior of a catalytic monolith with a convenient trade-off between accuracy and complexity. This thesis deals with non-reacting flow, however, interested readers are referred to Pontikakis et al. [22] and Tischer & Deutschmann [23], where the topic has been extensively reviewed.

This work is concerned with the link between the channel and the converter scales in three essential aspects. First, changes in the flow regimen when flow is entering, passing through and leaving the honeycomb. Second, the pressure drop of flow throughout the substrate. Third, the convective heat transfer inside the monolith channels. The contribution of this thesis can be briefly summarized as the improving of the understanding and modelling of the phenomena associated to flow inside a monolith based catalytic converter, paying especial attention to provide with multi-scale consistency whole converter simulations using the continuum approach. More specifically:

i. How the upstream turbulence dissipates inside the monolith channels and how to account for that effect in a converter scale simulation is addressed in Chapter 2 and 3.

ii. The turbulence generated when flow is leaving a substrate with different channel cross-sectn geometries and flow conditions, together with a methodology to implement such an effect in converter scale simulations is investigated in Chapter 4, 5 and 6.

iii. The influence of the upstream turbulence on the flow regime and pressure drop through monolith channels is assessed in Chapter 7.

iv. The pressure drop when laminar flow enters, passes through and leaves a substrate th several channel shapes and open frontal areas, considering realistic inlet velocity profiles and developing flow is modeled in Chapter 8 and 9.

vi. The effect of the upstream turbulence when it effectively enters the channels on the convective heat transfer is studied in Chapter 10.

vii. Convective heat transfer inside monolith channels accounting for a realistic inlet velocity profile, temperature-dependent fluid properties and several heating rates is addressed in Chapter 11.

viii. Chapter 12 uses the methodologies presented in the previous chapters to analyze a wall-flow filter at a channel scale, which is a special type of honeycomb substrate.

A version of Chapters 2 to 12 are currently published or submitted for publication, hence, they can be read somehow independently. However, in addition to this general introduction, the reader is encouraged to read the one in Chapter 7 for the flow regime inside the converter, that in Chapter 6 for the pressure drop throughout the substrate, the one from Chapter 11 for the convective heat transfer inside the monolith channels and Chapter 12 for flow inside a wall-flow filter.

Bibliography

[1] Jun Yang and Hao Sun. Battery swap station location-routing problem with capacitated electric vehicles. *Computers and Operations Research*, 55:2017–232, 2015.

[2] Ameya Joshi and Timothy Johnson. Gasoline particulate filters—a review. *Emission Control Science and Technology*, 4(4):2019–239, 2018.

[3] Michiel T. Kreutzer, Freek Kapteijn, and Jacob Moulijn. Shouldn't catalysts shape up?: Structured reactors in general and gas–liquid monolith reactors in particular. *Catalysis Today*, 111(1-2):111–118, 2006.

[4] Ricardo AR Monteiro, Sandra M Miranda, Caio Rodrigues-Silva, Joaquim L Faria, Adrián MT Silva, Rui AR Boaventura, and Vítor JP Vilar. Gas phase oxidation of n-decane and PCE by photocatalysis using an annular photoreactor packed with a monolithic catalytic bed coated with P25 and PC500. *Applied Catalysis B: Environmental*, 165:306–315, 2015.

[5] Elena Taboada, Inma Angurell, and Jordi Llorca. Dynamic photocatalytic hydrogen production from ethanol–water mixtures in an optical fiber honeycomb reactor loaded with Au/TiO2. *Journal of catalysis*, 309:460–467, 2014.

[6] Ilaria Lucentini, Isabel Serrano, Lluís Soler, Núria J Divins, and Jordi Llorca. Ammonia decomposition over 3d-printed ceo2 structures loaded with ni. *Applied Catalysis A: General*, doi: 10.1016/j.apcata.2019.117382, 2020.

[7] Sofiane Arab, Jean-Marc Commenge, Jean-François Portha, and Laurent Falk. Methanol synthesis from CO2 and H2 in multi-tubular fixed-bed reactor and multi-tubular reactor filled with monoliths. *Chemical Engineering Research and Design*, 92(11):2598–2608, 2014.

[8] Sunil Murthy and Andrei G Fedorov. Radiation heat transfer analysis of the monolith type solid oxide fuel cell. *Journal of Power Sources*, 124(2):453–458, 2003.

[9] Albert Casanovas, Carla de Leitenburg, Alessandro Trovarelli, and Jordi Llorca. Catalytic monoliths for ethanol steam reforming. *Catalysis Today*, 138(3-4):187–192, 2008.

[10] R Edvinsson Albers, M Nyström, M Siverström, A Sellin, A-C Dellve, U Andersson, W Herrmann, and Th Berglin. Development of a monolith-based process for H2O2 production: from idea to large-scale implementation. *Catalysis Today*, 69(1-4):247–252, 2001.

[11] Ronald M Heck, Suresh Gulati, and Robert J Farrauto. The application of monoliths for gas phase catalytic reactions. *Chemical Engineering Journal*, 82(1-3):149–156, 2001.

[12] S. H. Chan and D. L. Hoang. Heat transfer and chemical reactions in exhaust system of a cold-start engine. *International Journal of Heat and Mass Transfer*, 42(22):4165–4183, 1999.

[13] T. Nien, J. Mmbaga, R. Hayes, and M. Votsmeier. Hierarchical multi-scale model reduction in the simulation of catalytic converters. *Chemical Engineering Science*, 93:362–375, 2013.

[14] Anna Holmgren, Thomas Gronstedt, and Bengt Andersson. Improved flow distribution in automotive monolithic converters. *Reaction Kinetics and Catalysis Letters*, 60(2):363–371, 1997.

[15] Tiziano Maffei, Stefano Rebughini, Giancarlo Gentile, Stefan Lipp, Alberto Cuoci, and Maestri Matteo. CFD analysis of the channel shape effect in monolith catalysts for the CH4 partial oxidation on Rh. *Reaction Kinetics and Catalysis Letters*, 86(7):1099–1106, 2014.

[16] Michele Negri, Marius Wilhelm, Christian Hendrich, Niklas Wingborg, Linus Gediminas, Leif Adelöw, Corentin Maleix, Pierre Chabernaud, Rachid Brahmi, Romain Beauchet, et al. New technologies for ammonium dinitramide based monopropellant thrusters–the project rheform. *Acta Astronautica*, 143:105–117, 2018.

[17] W Malalasekera and HK Versteeg. *An introduction to computational fluid dynamics: the finite volume method*. PEARSON Prentice Hall, Upper Saddle River, New Jersey, USA, 2007.

[18] ANSYS Fluent Software Package v17.2, 2016. ANSYS Inc., Canonsburg, PA, USA.

[19] ANSYS Fluent Software Package v18.2, 2017. ANSYS Inc., Canonsburg, PA, USA.

[20] François Bertrand, Christophe Devals, David Vidal, Cyrille Séguineau de Préval, and Robert E Hayes. Towards the simulation of the catalytic monolith converter using discrete channel-scale models. *Catalysis Today*, 188(1):80–86, 2012.

[21] Steffen Tischer, Correa Chrys, and Olaf Deutschmann. Transient three-dimensional simulations of a catalytic combustion monolith using detailed models for heterogeneous and homogeneous reactions and transport phenomena. *Catalysis Today*, 69(1-4):57–62, 2001.

[22] G. N Pontikakis, G. S. Konstantas, and A. M. Stamatelos. Three-way catalytic converter modeling as a modern engineering design tool. *Journal of Engineering for Gas Turbines and Power*, 126(4):906–923, 2004.

[23] Steffen Tischer and Olaf Deutschmann. Recent advances in numerical modeling of catalytic monolith reactors. *Catalysis Today*, 105(3-4):407–413, 2005.

Chapter 2

Turbulence decay inside the channels of an automotive catalytic converter monolith[1]

Abstract

This paper reports a multi-scale study of the turbulence decay inside of a monolith. It is a well known fact that the turbulence at the automotive catalytic converters affects the conversion of chemical species, the composition of the exhaust gas and the performance of the engine significantly. Basically, the flow is highly turbulent before the monolith; nevertheless, it is usually assumed to be fully laminar inside of it. The present work uses numerical simulations at two different scales: A RANS model is used to model gas flow inside of the whole converter and LES model is applied to study the decay of turbulence inside of a single channel. The inflow boundary conditions for LES are taken from the large-scale simulations carried out using RANS. Results of RANS were validated against published experimental data. CFD software ANSYS-Fluent 17.2 was used for RANS and LES simulations. The results for the channels with the highest and the lowest Reynolds number show that the turbulence intensity decays quickly, but, can remain high for a significant distance, depending on its position and the duty of the converter. In some cases, the turbulence intensity can remain high through its entire substrate.

Keywords: Turbulence, monolith, catalytic converter, LES, multi-scale

[1] A version of this article has been published. Cornejo, I., Nikrityuk, P., & Hayes, R. E. (2017). Turbulence decay inside the channels of an automotive catalytic converter monolith. Emission Control Science and Technology, 3(4), 302-309.

2.1 Introduction

The automotive catalytic converter is part of the exhaust gas system of the vehicle, and its function is to treat the outflow from the engine, allowing vehicles to meet the environmental regulations of different countries. The core of the converter is a monolith type substrate made of ceramic or metal, with thousands of small channels running in parallel. A porous thin layer of refractory oxide, called washcoat, covers the walls of the channels and serves as a support for the precious metals catalyst. The converter can have one or more monolith, arranged in series or parallel, depending on its duty.

Since 1980, CFD has been used to study the behavior of the automotive catalytic converter, first in cold flow, then adding the heat transfer and chemical reactions [1, 2]. Basically, the gas flow phenomena in a catalytic converter can be divided into three different length scales: macro-scale ($\approx$cm), mesoscale ($\approx$mm) and micro-scale ($\approx \mu$m). The macro-scale is the analysis of the full catalytic converter, the mesoscale is covered by single channels of monolith and the micro scale involves the phenomenon inside of the washcoat.

CFD simulations of the complete automotive converter can be expensive due to the multi-scale nature of processes inside the converter, which require high computational power to model all scales at once [3, 4]. The global Reynolds number of the inflow of the converter is of the order of 104, it forces to use significantly fine meshes, hence, assumptions must be made to keep the simulation time between reasonable limits [5]. Most published works treat the monolith as a continuous porous medium, and use some form of volume averaging to build the governing conservation equations [6, 7]. This approach sacrifices detail at the micro scale, but, allows the simulation of the complete converter with a reasonable level of accuracy. The installation of sensors inside the converter, to obtain experimental data, presents an additional challenge, because it can modify the value of some of the variables of the process up to 50% [8].

A typical monolith has thousands of channels, and the inlet condition for each one might vary significantly [9]. Most of the reported works at channel scale simulate a representative number of channels and assume that the behavior of the non-simulated channels can be interpolated based on the results of the simulated ones [10, 11]. The focus of the microscale studies is the conversion of chemical species and the heat transfer at the surface of the interstices of the washcoat, where the fluid dynamic at the level of the channel is typically assumed laminar and often fully developed [12].

The different scales and flow regime involved make the simulation of the process non-trivial. The turbulence at channel scale is complex to measure and affects the mixing significantly inside of it, changing the conditions for the washcoat, where most of the chemical reactions occur. Results vary depending on the scale and the analyzed variable, but, in general terms, the inclusion of a realistic representation of the chemical reactions at converter scale remains a major challenge. The influence of turbulence on the pressure drop in a catalytic converter has been experimentally investigated by Ekström and Andersson [13]. They developed a semi-empirical model enabling a prediction of the pressure drop for different inflow conditions. The effects of turbulence have been studied in terms of the Kolmogorov length scale distribution (in the order of magnitude 0.2 – 2.9 mm) inside the monolith. It was shown experimentally that turbulence penetrates the monolith brick. However, exact values of penetration were not given in the text.

To model the problem at converter scale by RANS, representing the monolith as a porous medium, involves setting the porous zone as laminar, to avoid an incorrect generation of turbulence inside of it. As a consequence, the flow is assumed to change from fully turbulent to fully laminar instantaneously, this assumption in the flow pattern have a significant impact on the performance of the converter [14]. To measure how accurate is this assumption it is necessary to compare these converter scale simulations against more detailed channel scale simulations.

The main contribution of this paper is the use of a multi-scale model of an automotive catalytic converter, to illustrate the decay of the turbulence inside of the single channels of the monolith. A large eddy simulation (LES) approach at channel scale was used to understand the damping of the turbulence along two selected channels. The boundary conditions for the LES simulations were taken from a converter-scale simulation using RANS. As a secondary objective, we compared the most usual forms to address the simulation of the monolith at converter level, it means, as a continuous porous medium with laminar flow, against the LES outcome. The results are presented in terms of the turbulence intensity, turbulence kinetic energy and turbulence viscosity ratio along the selected monolith channels and the converter porous medium.

2.2 Problem and Model Formulations

We first consider a cylindrical catalytic converter geometry taken from experiments performed by Clarkson [15]. A schematic of the domain modeled is shown in Figure 1a. The inflow

and outflow tubes have circular cross section of 54.4 mm diameter and with a length of 380 mm to ensure developed flow. The diffuser cone is 54 mm length and has an expansion angle of 30°. The monolith is cylindrical, of 150 mm length and 117.6 mm diameter. The square channels of the monolith are 1.1 mm each side and the wall between the channels is 0.1 mm thick. Figure 2.1a is a cut across the converter scale domain and Figure 2.1b shows a cut of the channel scale. This study assumes that ten centimetres are long enough to study the transition at the beginning of the channel.

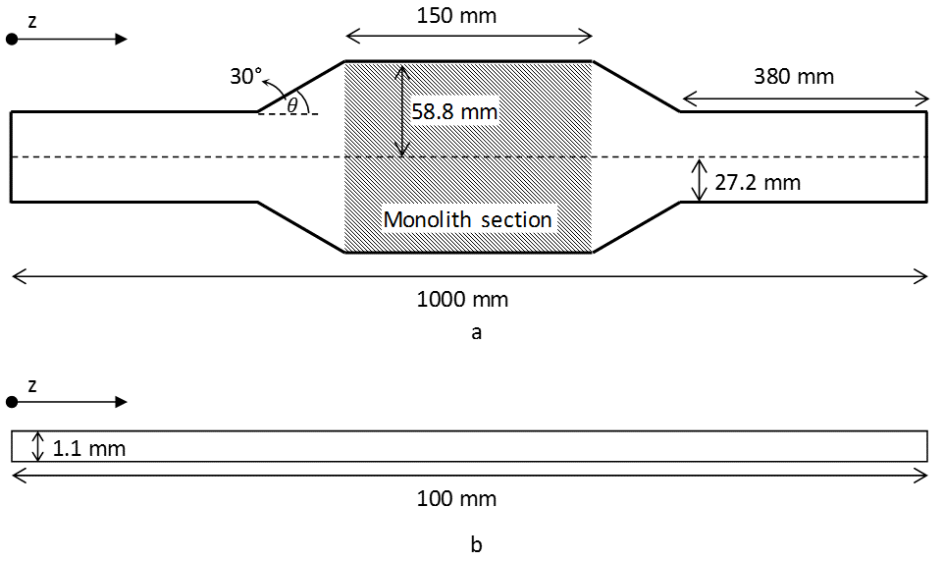

Figure 2.1: a) Cut of the catalytic converter and b) Single channel side view

2.2.1 Modelling the open section of the converter

The open section consists of the sections of the domain before and after the monolith. The scope of this study is the turbulence inside of the catalytic converter and does not consider chemical reactions or thermal effects. Consequently, the momentum and mass conservation equations are sufficient to solve the problem. The changes in pressure over the domain do not cause significant changes in flow density. Hence, the Reynolds-averaged version of the Naiver-Stokes (RANS) equations for the mass conservation equation is [16]:

$$\frac{\partial \rho}{\partial t} + \rho(\nabla \cdot U) = 0 \tag{2.1}$$

The momentum conservation equation, with the closure provided through an eddy vis-

cosity (or turbulence viscosity) model, is:

$$\frac{\partial \rho U}{\partial t} + \rho \nabla \cdot (U^T U) = -\nabla P + 2\mu_t (\nabla \cdot S) + \nabla \cdot (2\mu_t S - 2/3 \rho k I) \tag{2.2}$$

Where:

$$S = \frac{1}{2}(\nabla U + \nabla U^T)$$

The base case of this study considers the Menter Shear Stress Transport (SST) k-ω model [17–19], which uses the standard k-ε model far from the wall, and a transformation of the k-ω model into a k-ε model near the wall. Using the Boussinesq assumption, the eddy viscosity is described by Equation (2.3), meanwhile, k and ω transport equations are taken from the Wilcox k-ω model[20, 21], in Equation (2.4) and Equation (2.5) respectively.

$$\mu_t = \rho \frac{k}{\omega} \tag{2.3}$$

$$\frac{\partial (\rho k)}{\partial t} + \nabla \cdot (\rho k U) = \nabla \cdot \left[\left(\mu + \frac{\mu_t}{\sigma_k} \right) \nabla k \right] + \left(2\mu_t S \cdot S - \frac{2}{3} \rho k \nabla U I \right) - \beta^* \rho k \omega \tag{2.4}$$

$$\frac{\partial (\rho \omega)}{\partial t} + \nabla \cdot (\rho \omega U) = \nabla \cdot \left[\left(\mu + \frac{\mu_t}{\sigma_\omega} \right) \nabla k \right] + \gamma_1 \left(2\mu_t S \cdot S - \frac{2}{3} \rho \omega \nabla U I \right) - \beta^* \rho \omega^2 \tag{2.5}$$

Far from the wall, the ε transport equation is obtained by substituting ε=$k\omega$ into the ω transport equation, leading to a modified ω transport equation, with the addition of a cross diffusion term.

2.2.2 Modeling the Monolith of the Converter

A homogeneous porous medium can represent the monolith, taking into account the presence of solid and air, by a volume-averaged approach. The mass conservation equation in Equation (2.1) is also valid for this section of the domain. Meanwhile, for the VANS momentum conservation equations, a source term derived from Darcy's law is added to the right-hand side of Equation (2.2), resulting in Equation (2.6).

$$\frac{\partial \rho U}{\partial t} + \rho \nabla \cdot (U^T U) = -\nabla P + 2\mu_t (\nabla \cdot S) + \nabla \cdot (2\mu_t S - 2/3 \rho k I) - \frac{\mu}{\alpha} v \tag{2.6}$$

The main parameters of the porous media are the axial and radial permeability. Hayes et al. [6] found that setting a radial permeability at least one hundred times higher than

the axial permeability, the radial velocity is negligible, as in a real monolith. The radial permeability is related to the size of the channels by Equation (2.7) if the Poiseuille flow inside it is assumed [13].

$$\alpha = \frac{\phi D_H^2}{28.4} \tag{2.7}$$

2.2.3 Single channel model

Next we present a 3D model of a single channel inside of the monolith. In this work we use LES model to resolve fluid flow phenomena on the mesoscale of the monolith. The boundary conditions for LES are taken from RANS simulations which predict local values of turbulence quantities and gas flow velocity at the entrance to the monolith channels. Before entering the channel, the flow has a significant amount of turbulence kinetic energy. The decay of the turbulence is expected to be quick, but not instantaneous. The large eddy simulation approach is propitious to study the decay of the major fluctuations in the velocity through the channel. LES uses a spatial filter so separate the large and the small eddies, it resolves in unsteady condition for the large eddies, and the interaction between these and the small eddies through a sub-grid-scale stress (SGS). In the finite volumes method (FVM), the grid acts directly as a spatial filter. Equation (2.8) and Equation (2.9) represent the filtered version of the continuity and momentum equations for LES respectively.

$$\frac{\partial \rho}{\partial t} + \nabla \cdot (\rho \tilde{v}) \tag{2.8}$$

$$\frac{\partial \rho \tilde{v}}{\partial t} + \nabla \cdot (\rho \tilde{v} \tilde{v}) = -\nabla \tilde{p} + \nabla \cdot \left[(\mu_0 + \mu_t)(\nabla \tilde{v} + \nabla \tilde{v}^T) \right] \tag{2.9}$$

FLUENT models the sub-grid scale as RANS, by the Boussinesq hypothesis. This study considered the static version of the Smagorinsky-Lilly SGS model [22], with the sub-grid turbulence viscosity estimated as Equation (2.10).

$$\mu_t = \rho L_s^2 \sqrt{2 \tilde{S} \tilde{S}} \tag{2.10}$$

where L_s is the length of the sub-grid scale (final formula L_s can be found in [23]) and S is the trace-less rate-of strain tensor for the resolved scale, calculated ass:

$$\tilde{S} = \frac{1}{2}(\nabla \tilde{v} + \nabla \tilde{v}^T) \tag{2.11}$$

2.3 Results and discussions

Two simulations at the converter scale were performed, the first setting the porous medium as a laminar zone, and the second without imposing a laminar condition to it. According to Clarkson [15], regarding the geometry, the velocity profile is reasonably axial symmetric. Hence, a two-dimensional axisymmetric geometry can be used to model this converter. At channel scale, two channels were selected, the one with the highest and other with the lowest Reynolds number. The characteristics of the flow from the different scales and conditions were analyzed and compared.

2.3.1 Converter scale

The grid independence is stated measuring the volume-averaged velocity magnitude over the domain. Three grids, with 20 000, 73 000 and 350 000 control volumes, equivalently refined, were used. Figure 2.2 shows the mesh with 20 000 control volumes. After grid test studies the grid with 350 000 CV was chosen.

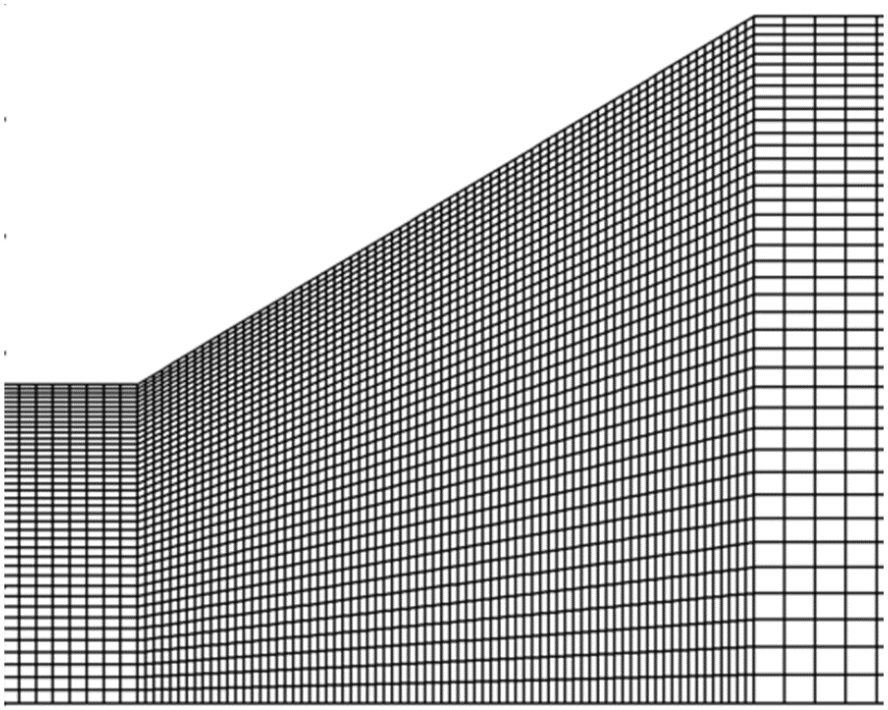

Figure 2.2: Zoomed view of the inlet cone section: 20 000 control volumes mesh

The full-scale simulations were validated against experimental data included in Clarkson [15], where the velocity profile at the outlet of the monolith was measured. The simulation used a monolith with the same characteristics, boundary conditions and operating regime.

Table 2.1 summarize the details of the input parameters and boundary conditions used in the RANS and LES simulations. Both models used the pressure-velocity coupling that was solved using a SIMPLE algorithm [24]. Steady state RANS simulations were carried out using 2^{nd} order Upwind discretization scheme for k, ε and ω equations, momentum conservation equations were discretized utilizing 3^{rd} order Upwind scheme (QUICK). Unsteady LES simulations used a bounded central difference scheme, with a time step of 2×10^{-3} s and 2.0 s as the time span. A comparison between the experimental data and the results of the simulations is shown in Figure 2.3. Results of simulations performed using k-ω RANS were also included.

Table 2.1: Simulation settings and boundary conditions

Material		
Fluid	Air	
Monolith specifications		
Channel section	Square	
Channel size, mm	1.1	
Wall thickness, mm	0.1	
Void fraction, %	76	
Porous medium specifications		
Axial permeability, m^2	3.33×10^{-8}	
Radial permeability, m^2	3.33×10^{-16}	
Converter boundary conditions		
Inlet - Velocity inlet	Re 32 000	
Outlet	Outflow	
Top	No-slip walls	
Bottom	axial-symmetry	
Channel boundary conditions	**Channel 1**	**Channel 9**
Inlet velocity, m/s	2.5	6.4
Inlet turb. generation method	Spectral syn.	Spectral syn.
Inlet turb. intensity, %	35	100
Inlet turb. viscosity ratio	13.1	5.1
Outlet	Outflow	Outflow
Walls	No-slip	No-slip

As a measure of the agreement between the experimental data and the simulations, the total flow was calculated integrating the flow before the porous medium, then compared. The

error of all analyzed models is less than 2%, nevertheless, the SST k-ω was used for the rest of the study. It is noticeable that the disagreement between the velocities near the symmetry axis impacts in a moderate way the estimation of the total flow, because the flow area close to the axis is considerably less than it is near the wall.

Three main variables were analyzed from the converter scale simulations, velocity magnitude, turbulence kinetic energy and turbulence viscosity ratio. Figure 2.4 includes a series of contour plots of these, with and without setting the porous media set as a laminar zone.

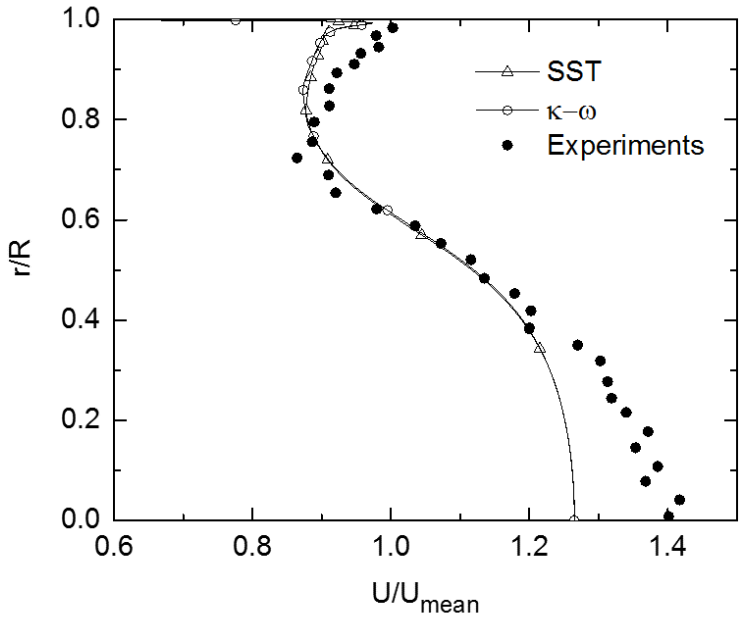

Figure 2.3: Velocity profile at the outlet of the monolith. Experiment points correspond to Clarkson [15]

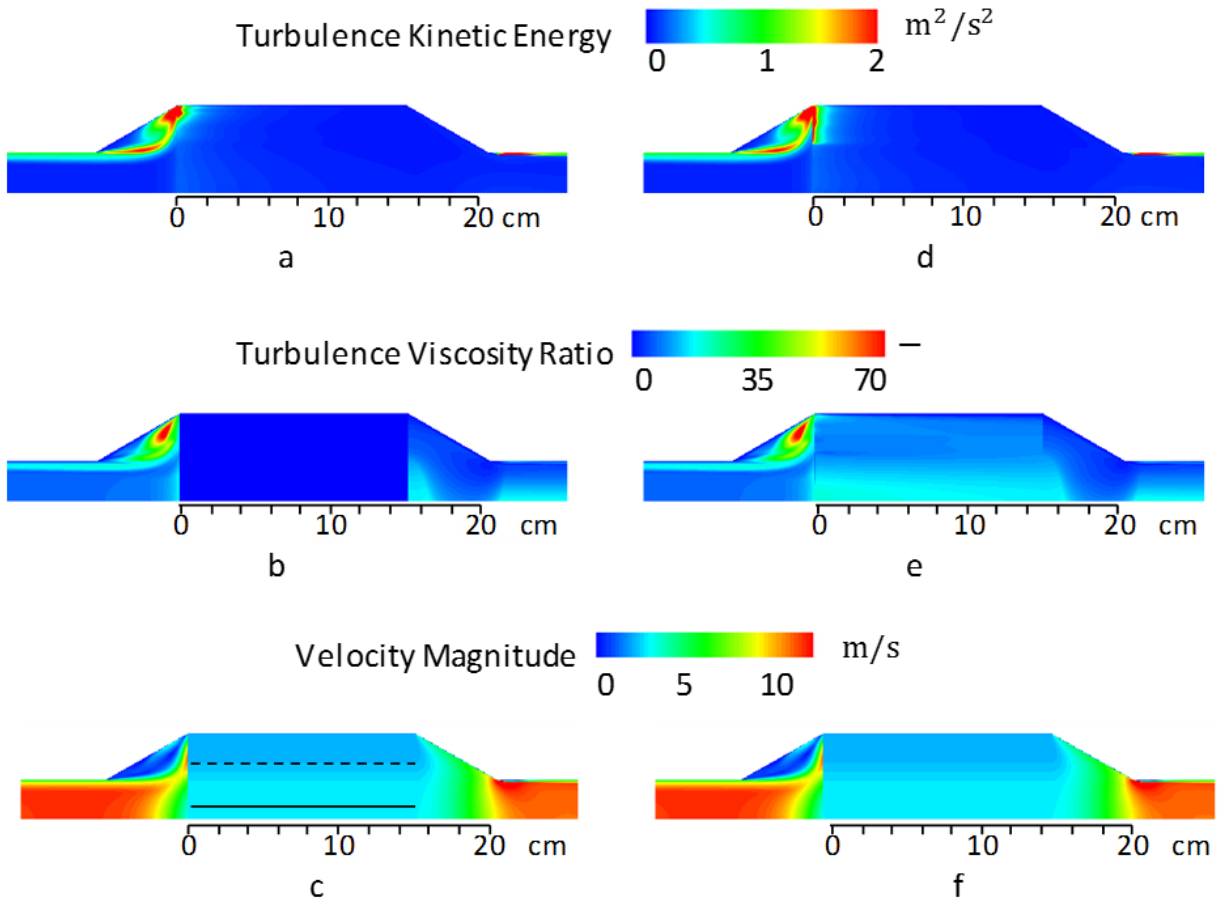

Figure 2.4: Results of RANS simulations of the whole converter: a), b) and c) setting the porous medium as a laminar zone. d), e) and f) without imposing special conditions to the porous medium

The velocity magnitude in both cases, c) and f) is similar and in agreement with the experimental data. The turbulence kinetic energy profiles at a) and d) shows differences at the first part of the porous medium, where d) exhibit a smoother profile across the radius of the converter than a).

As expected, the turbulence viscosity ratio of the flow in b) decreases instantaneously to 0 entering the porous medium, then increases to values from one to twenty after it. This behavior is a consequence of the absence of generation of turbulence in the laminar zone. Quantities as k and ω are still transported through this portion of the domain, consequently, the turbulence viscosity changes exactly to zero inside of the laminar zone, and the turbulence before and after this zone is, in average, of the same order of magnitude. The turbulence viscosity inside of the porous medium in e) is still high and does not represent the expected decay inside of a monolith. The monolith acts as several small parallel channels, with a

relatively low Reynolds number, hence, a quick decay in the turbulence viscosity is expected after entering the channels, and possibly a laminar pattern from some point closer to its inlet than its outlet.

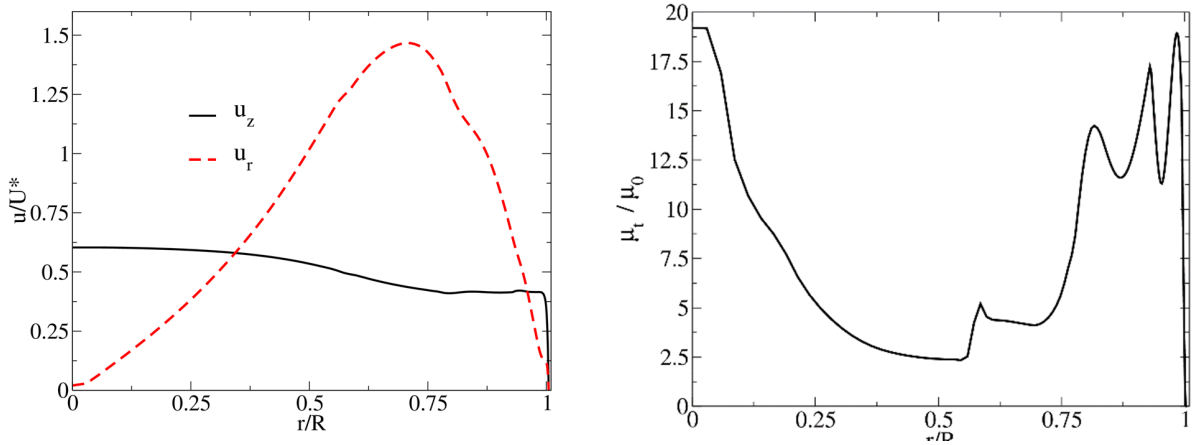

Figure 2.5: Radial profiles of a) non-dimensional velocity and b) turbulence viscosity ratio, at z corresponding to 0.1 mm from the monolith entrance. Porous media was treated without imposing any condition for RANS. Re=32000, μ=1.79 $\times$ 10^{-5} Pa-s, ρ=1.225 kg/m^3, D_H=0.01176 m

2.3.2 Monolith channel scale

A radius of the porous medium was mapped, and the channels with the higher and lower Reynolds number were selected to study the decay of turbulence inside each one. The position of both in the monolith, channel 9 (corresponding to a location of r/R=0.74) with the higher Reynolds, and channel 1 (corresponding to a location of r/R=0.08) with the lower Reynolds are indicated with a dashed and a solid line respectively in Figure 2.4c. The 3D grid used in LES has the dimension 22 x 22 x 2000 CV along x, y and z axis, respectively. The sub-grid-scale turbulence viscosity ratio resulting from simulations is below unity, and the maximum wall y^+ is five, both indicate that most of the flow was resolved by the grid we used for LES.

The Reynolds number inside of the channels is of the order of 10^2; it means that the eddies of a length of 0.1 mm or larger contain most of the energy. Nevertheless, the Reynolds number before the channels is of the order of 10^4, and in a worst-case scenario, where the flow keeps most of its features, even entering the channel, most of the large eddies are in the scale of 0.01 mm or larger. This is in a good agreement with findings provided by Ekstrom

and Andersson [13].

The boundary conditions for LES are given in Table 2.1. The inflow values for the velocity and turbulence quantities such as the turbulence viscosity ratio (see Figure 2.5) are taken from their radial profiles at the entrance to monolith corresponding to the location of channel 1 and channel 9. It can be seen that a strong radial flow exists close to the monolith, however, to simplify boundary conditions for LES we used absolute value of velocity vector, see Table 2.1. The velocity fluctuations at the inlet of the channels were set using a spectral synthesizer built-in the software. It uses the turbulence viscosity ratio, turbulence intensity and velocity specified at this boundary to make a group of one hundred Fourier harmonics, that provides the time varying inlet velocity [23, 25, 26]. As a measure of the fluctuation inside of the channels, transient data of the velocity field from the LES simulations were processed to obtain the turbulence kinetic energy and the turbulence intensity. Figure 2.7 summarizes the behavior of these two quantities in the selected channels.

Results in Figure 2.7 show that channel 9, at r/R =0.74, has a smooth decay of the turbulence, and velocity fluctuations persist a significant distance inside the channel. In the channel 1, at r/R =0.08, the results are different. There is also a smooth decay, but high levels of fluctuation are present even after 20 channel hydraulic diameters. The same tendency can be observed in Figure 2.4e, where the turbulence viscosity ratio is higher in channel 1 than in channel 9. A possible explanation is that close to the symmetry axis of the converter, the turbulence viscosity is higher than near the wall.

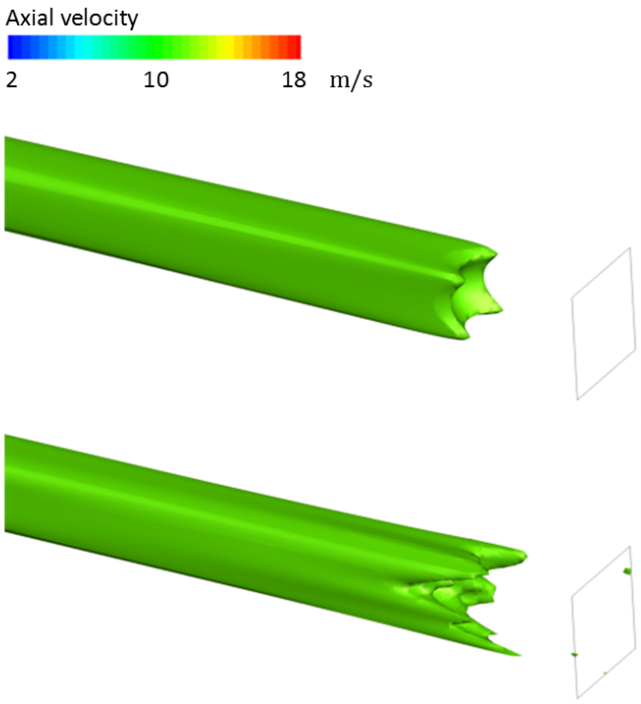

Figure 2.6: LES of a single channel at r/R=0.74: Iso-surface of axial velocity. Top: time-averaged; Bottom: instantaneous

An additional representation of the unsteady behavior of the flow into the channels can be seen in Figure 2.6, which compares the time-averaged and instantaneous axial velocity.

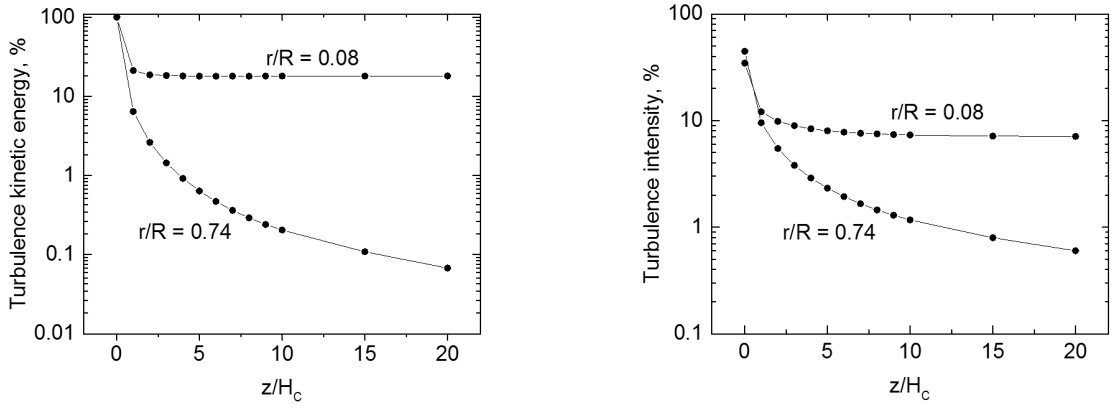

Figure 2.7: Turbulence decay along the centre of two channels. a) Time-averaged turbulence kinetic energy scaled by the inlet value. b) Time-averaged turbulence intensity

Figure 2.7 illustrates a turbulence decay along two channels, based on the velocity at the centre of the channel at two locations in the monolith, r/R=0.08 and r/R=0.74. In

particular, we plot non-dimensional axial profiles of the time-averaged turbulence kinetic energy and time averaged turbulence intensity predicted using LES. It can be seen that for the channel located at r/R=0.74 the time averaged turbulence kinetic energy, k, scaled by the inlet value, decreases from 100% to 1% within 4 heights of the channel. The same behaviour is observed for time averaged value of the turbulence intensity. However, surprisingly, for the channel close to the axis of monolith (r/R=0.08) the turbulence decays rapidly within 2 heights of the channel and then stay almost constant along the channel. Only small decrease in both quantities can be seen for $z > 3D_H$. This effect can be attributed to different inflow conditions used for both channels. Finally, it should be emphasized that more numerical investigations are needed for a complete understanding of the turbulent-laminar transition inside the monolith.

2.4 Conclusions and recommendations

Turbulence decay inside the channels of an automotive catalytic converter has been analyzed numerically using a dual scale model which includes a RANS model for the converter and an LES model for a single channel. Inflow boundary conditions for LES were calculated using RANS model, which was validated against experimental data published in the literature. The results from the LES study indicate that, despite the low Reynolds number (≈100) inside the channel, there are significant velocity fluctuations at the beginning of the channels, as a consequence of the highly turbulent features of the flow before entering it. Depending on the inlet conditions, the velocity fluctuations can persist along the entire channel, apparently depending more on the turbulence viscosity ratio before the channel than on the turbulence intensity at its inlet and the Reynolds number of the channel. The representation of the monolith as a homogeneous porous medium, with or without imposing a laminar condition on it, is effective to predict velocity profiles and agrees on the experimental data. Nevertheless, it does not reproduce the turbulence viscosity accurately inside the monolith and after it. It may affect the heat and mass transfer significantly inside the model of the converter.

2.5 Conflict of interest statement

On behalf of all authors, the corresponding author states that there is no conflict of interest.

Bibliography

[1] Achim Heibel and Michael AA Spaid. A new converter concept providing improved flow distribution and space utilization. *SAE Technical Paper*, No. 1999-01-0768, 1999.

[2] Robert Jahn, Dalimil Snita, Milan Kubíček, and Miloš Marek. 3-D modeling of monolith reactors. *Catalysis Today*, 38(1):39–46, 1997.

[3] François Bertrand, Christophe Devals, David Vidal, Cyrille Séguineau de Préval, and Robert E Hayes. Towards the simulation of the catalytic monolith converter using discrete channel-scale models. *Catalysis Today*, 188(1):80–86, 2012.

[4] Ankan Kumar and Sandip Mazumder. Toward simulation of full-scale monolithic catalytic converters with complex heterogeneous chemistry. *Computers & Chemical Engineering*, 34(2):135–145, 2010.

[5] S Siemund, JP Leclerc, D Schweich, M Prigent, and F Castagna. Three-way monolithic converter: simulations versus experiments. *Chemical Engineering Science*, 51(15):3709–3720, 1996.

[6] RE Hayes, Anton Fadic, Joeseph Mmbaga, and A Najafi. CFD modelling of the automotive catalytic converter. *Catalysis Today*, 188(1):94–105, 2012.

[7] Sophie Porter, Jonathan Saul, Svetlana Aleksandrova, Humberto Medina, and Stephen Benjamin. Hybrid flow modelling approach applied to automotive catalysts. *Applied Mathematical Modelling*, 40(19-20):8435–8445, 2016.

[8] Matthias Hettel, Claudia Diehm, Bentholhoda Torkashvand, and Olaf Deutschmann. Critical evaluation of in situ probe techniques for catalytic honeycomb monoliths. *Catalysis Today*, 216:2–10, 2013.

[9] Kyriacos Zygourakis. Transient operation of monolith catalytic converters: a two-dimensional reactor model and the effects of radially nonuniform flow distributions. *Chemical Engineering Science*, 44(9):2075–2086, 1989.

[10] RE Hayes, ST Kolaczkowski, and WJ Thomas. Finite-element model for a catalytic monolith reactor. *Computers & Chemical Engineering*, 16(7):645–657, 1992.

[11] AK Sharma and Erik Birgersson. Validity and scalability of an asymptotically reduced single-channel model for full-size catalytic monolith converters. *Applied Mathematics and Computation*, 281:186–198, 2016.

[12] RE Hayes, B Liu, R Moxom, and M Votsmeier. The effect of washcoat geometry on mass transfer in monolith reactors. *Chemical Engineering Science*, 59(15):3169–3181, 2004.

[13] Fredrik Ekström and Bengt Andersson. Pressure drop of monolithic catalytic converters experiments and modeling. *SAE Technical paper*, No. 2002-01-1010, 2002.

[14] H Santos and M Costa. Modelling transport phenomena and chemical reactions in automotive three-way catalytic converters. *Chemical Engineering Journal*, 148(1):173–183, 2009.

[15] Rory John Clarkson. *A theoretical and experimental study of automotive catalytic converters*. PhD thesis, Coventry University, 1997.

[16] W Malalasekera and HK Versteeg. *An introduction to computational fluid dynamics: the finite volume method*. PEARSON Prentice Hall, Upper Saddle River, New Jersey, USA, 2007.

[17] F Menter. Improved two-equation k-ω turbulence models for aerodynamic flows. *NASA Technical Memorandum*, ID 19930013620, 1992.

[18] Florian Menter. Two-equation eddy-viscosity turbulence models for engineering applications. *AIAA journal*, 32(8):1598–1605, 1994.

[19] F. Menter. Eddy viscosity transport equations and their relation to the k-ε model. *Journal of Fluids Engineering*, 119(4):876–884, 1997.

[20] David C Wilcox. Reassessment of the scale-determining equation for advanced turbulence models. *AIAA Journal*, 26(11):1299–1310, 1988.

[21] David C Wilcox. *Turbulence modeling for CFD*. DCW Industries, La Canada, California, USA, 1993.

[22] Joseph Smagorinsky. General circulation experiments with the primitive equations: I. The basic experiment. *Monthly Weather Review*, 91(3):99–164, 1963.

[23] ANSYS Fluent Theory Guide v18.2. ANSYS Inc., Canonsburg, PA, USA, 2017.

[24] Suhas Patankar. *Numerical heat transfer and fluid flow*. CRC press, Boca Raton, Florida, USA, 1980.

[25] Robert H Kraichnan. Diffusion by a random velocity field. *The Physics of Fluids*, 13(1):22–31, 1970.

[26] A Smirnov, S Shi, and I Celik. Random flow generation technique for large eddy simulations and particle-dynamics modeling. *Journal of Fluids Engineering*, 123(2):359–371, 2001.

Chapter 3

Multiscale RANS-based modeling of the turbulence decay inside of an automotive catalytic converter[1]

Abstract

This paper presents a multiscale comprehensive study of the turbulence inside of an automotive monolith using a porous medium approach and a representative group of single channels. A series of RANS simulations of an axisymmetric model of the whole converter and a 3D model of a representative group of single channels is combined to study the turbulence at different scales. Results of simulations are validated against experimental data published in the literature. Good agreement is achieved. Results of simulations reveal that although the continuum porous medium model produces good agreement with experimental velocity profiles after the monolith, it does not describe accurately the turbulence inside the monolith. Literature reports that a transition from turbulent to laminar flow regime at the beginning of the monolith channels impacts significantly the performance of the whole converter, but, at the same time, it is usually neglected, due the complexity that it adds to the problem. According to the results from the single channels, there is a smooth decay of the turbulence viscosity inside the monolith, that does not appear using the traditional models of porous zones. This decay can be achieved at the converter scale, via the addition of a damping term for the turbulence to the κ-equation of the RANS model.

[1] A version of this article has been published. Cornejo, I., Nikrityuk, P., & Hayes, R. E. (2018). Multiscale RANS-based modeling of the turbulence decay inside of an automotive catalytic converter. Chemical Engineering Science, 175, 377-386.

Keywords: Catalytic converter, monolith, channels, multiscale, turbulence damping, RANS

3.1 Introduction

Monolith honeycomb reactors are widely used in automotive catalytic converters. As part of the exhaust after treatment system, the monolith is typically a ceramic piece with thousands of channels running in parallel. The surface of the channels is covered by a thin porous layer (washcoat) that supports the metal catalyst. Monolith reactors were initially developed by the automobile industry to control emissions, but now now widely used in other applications, such as catalytic combustion, oxidation, hydrogenation, dehydrogenation to name a few [1–5]. Some of the advantages of monolith reactors compared to a packed bed are lower pressure drop, larger external specific surface area and high selectivity, among others [6].

The modeling of the catalytic converter is a multiscale problem that ranges from the molecular to the converter length scale. The smallest scale is the molecular level, where the mechanism of the chemical reactions between the gases and the metal catalyst occurs. It is followed by the diffusion and reactions in the washcoat, where the objective is to evaluate the performance of the catalyst. A typical washcoat is 10-150 μm thick. At the channel scale, around 1 mm, it is possible to study the effects of the diffusion and convection on the temperature and concentration profiles. To analyze and optimize the performance of the complete reactor, it is necessary simulate the full converter or a significant portion of it, that considers multiple channels [7–9]. All four mentioned scales are related at some level. For example, the inlet conditions for the channels are defined at the converter scale [10], meanwhile, the temperature and concentration of chemical species at the surface of the washcoat is influenced by the convection and diffusion at the channel level. Unfortunately, including all of the scales in a single simulation is beyond the computational capacity available for industrial applications today [11, 12], and a more accurate representation of the chemical reactions and the fluid dynamics, that takes into account the effects of the different lengths, with reasonable computational resources, remains an area of extensive research.

The Reynolds number inside of an automotive catalytic converter is typically of the order of 10^4 before and after the monolith, however, inside of its channels it is about 10^2. Based exclusively on the Reynolds number, a transition at the beginning and end of the monolith is expected. This transition is considered to be critical in modeling the performance of the reactor [13, 14], nevertheless, it is typically neglected, due the complexity that it adds to the problem [15, 16].

Most of the reported works at the converter scale using RANS represent the monolith as a homogeneous porous medium that takes into account the volume averaged behavior of the channels and the solid walls between them [17, 18]. This approach, that emphasizes the macro scale fluid dynamics and sacrifices details at the channel and washcoat level, reduces the computational time required to solve the problem significantly compared to the discrete channel approach [11]. A porous medium is significantly different from a monolith, hence, the addition of special terms or the imposition of special conditions are required to obtain accurate results. As one example, the monolith does not transport momentum between its channels. This effect can be included by setting an adequate permeability for each direction of the porous zone [17]. Other phenomenon, such as the decay of the turbulence in the channels, is typically addressed by setting the porous medium as a laminar zone. This assumption implies a decay of the generation of turbulence to zero instantaneously once the fluid enters the porous zone, however, the turbulence quantities (κ, ω and ε) are still transported through it, giving unrealistic results inside of and after the monolith. Hettel et al. (2013) [19], studied the effect of the placing of probes inside the monolith channels, reporting that the probes might induce up to 50% of error in the measures. This is an additional difficulty for the study of the flow inside the monolith.

Turbulent flows contain a series of vortices that increase the transport of mass, momentum and energy across the flow. Those vortices, also referred as eddies, can decay, split or merge depending on the Reynolds number and the geometry [20–22]. Several authors have discussed the effect of the turbulence entering into a monolith. The smallest eddies in the flow before the monolith might enter into its channels, where they are expected to decay until they disappear based on the Reynolds number [23]. Ekstrom and Andersson (2002) [24] reported experimental evidence of the effect of the turbulence on the pressure drop across the first part of a monolith. Strom (2011) [7] studied the effect of the transition from turbulent to laminar on the aging of a monolith based catalytic converter. Tanno et al. (2013) [25] analyzed the reaction rate in the walls of monolith square channels, specifically, the effect of the transition from laminar to turbulent at the beginning of the channels. Tosun et al. (1988) [23] analyzed the critical Reynolds number inside square ducts, however, they studied the generation of turbulence instead of the decay.

Finally, we emphasize that the problem of turbulence modeling referring to the prediction of turbulence decay in a porous medium received a significant attention in series of works published recently, e.g. see [26–28]. In particular, Mössner and Radespiel [27] developed a

Reynolds stress based model with additional terms taking into account turbulence behavior inside a porous medium to simulate high Reynolds number aerodynamic flows over porous surfaces. Model validation against direct numerical simulations (DNS) computations showed very good agreement. Kuwata et al. [26] developed a multi-scale $k-\varepsilon$ eddy viscosity model for turbulence in porous media. A four equations eddy viscosity model was evaluated against LES for porous wall channel flows and porous rib-mounted channel flows. Satisfactory accuracy of the model was demonstrated. However, in all three works cited above RANS equations require sophisticated source terms and additional closure relations to model turbulence behavior in a porous medium. It should be noted that such models basically can be implemented only in an open-source CFD solver. In this work we develop simple source terms which can be added to any RANS model to predict turbulence decay in an anisotropic porous medium such as automotive catalytic converter. In this view, the objective of this work is the improvement of the monolith representation as a porous medium by adding a turbulence decay term to it. A special source terms for κ and ω equations that damps the turbulence in the porous zone are proposed. The model has been validated against 3D channel resolved simulations where inlet boundary conditions have been taken from converter-scale simulations. In particular, a conventional simulation of the converter was performed, to obtain realistic conditions for a series of representative single channel simulations. Second, the decay of turbulence inside of the channels was analyzed and compared with the results at the converter scale. Acceptable agreement has been demonstrated.

3.2 Model Formulation

3.2.1 Description of the domain

The geometry of the catalytic converter used in this study is similar to that used by Clarkson [29, 30]. It consisted of a cylindrical monolith of 150 mm in length and 117.6 mm diameter, contained in a metal case. The inlet of the case is a tube of 54.4 mm in internal diameter and 380 mm in length, followed by an expansion cone of 54 mm in length with a 35° expansion angle that joins the inlet tube with the monolith. After the monolith there are a reduction cone and outlet tube of the same size as the inlet cone. Figure 3.1 shows the axisymmetric version of the domain used in the 2D simulation of the converter. The inlet and outlet tubes were lengthened intentionally, to ensure fully developed flow. The monolith is unwashcoated and has square cross section channels of 1.1 mm a side and a wall thickness between channels of 0.1 mm.

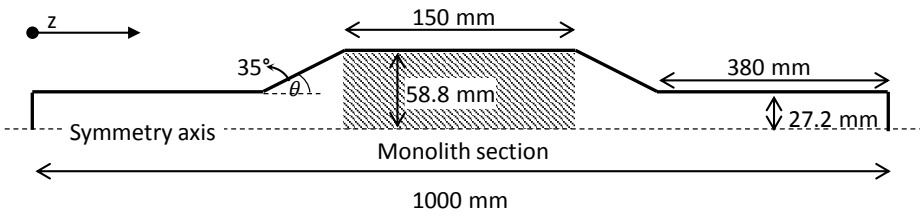

Figure 3.1: Axisymmetric section of the catalytic converter used by Clarkson [29].

The single channel simulations were performed in 3D considering two symmetry planes, parallel to the walls and crossing the centre of the channel. Taking into account this symmetry, the channel was simulated using a quarter of it. Figure 3.2 shows a view of a channel, the symmetry planes and the domain considered for the simulation.

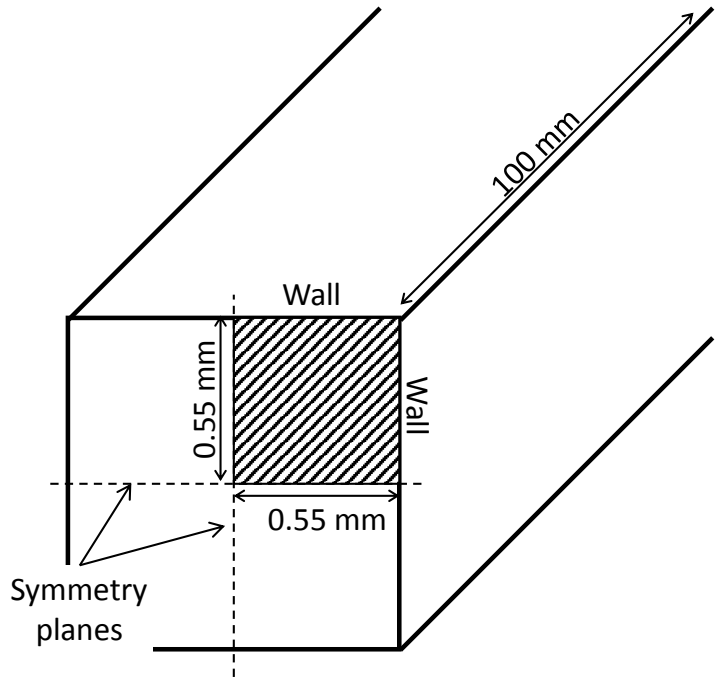

Figure 3.2: Zoom of the inlet of a single channel. Crossed area represents the 3D computational domain used in this work to model a single channel.

3.2.2 Turbulence model

The focus if this work is the study of the fluid dynamics and turbulence inside the converter in cold flow, i.e. without chemical reactions, hence, the mass and momentum conservation

equations are sufficient to describe the problem. The modeling can be separated into three parts. At the converter scale there are the open sections and the monolith, and, at the channel scale, the channel itself. In all cases the flow was assumed to be incompressible and statistically stationary, hence, the steady state RANS approach can be used to describe the turbulence.

- Modeling the open section of the converter

The open section sub-domain represent the zones before and after the monolith at the converter scale. In this part of the domain the Boussinesq approximation was used to close the problem [31–33]. The Reynolds averaged version of the mass and momentum conservation equations for a steady and incompressible flow have the following form [31, 34]:

$$\nabla \cdot \vec{u} = 0 \tag{3.1}$$

$$(\rho \vec{u} \nabla \cdot)\, \vec{u} = -\nabla p + \nabla \cdot \left((\mu + \mu_t) \left[\nabla \vec{u} + \nabla \vec{u}^T \right] \right) - \frac{2}{3} \rho\, \kappa\, I + S_{\vec{u}} \tag{3.2}$$

To model the turbulence viscosity in Equation (3.2), we used the Shear-Stress Transport $\kappa - \omega$ model (SST) [35]. The SST model in ANSYS Fluent 17.2 takes advantages of the $\kappa - \omega$ model [35] close to the wall and the Standard $\kappa - \varepsilon$ model in the free stream zones [33]. It makes the SST model less sensitive to the free stream conditions and, in general, more accurate and reliable for a wider range of problems [33, 35]. The transport equations for κ and ω have the following form [31, 33]:

$$\nabla \cdot (\rho\, \vec{u}\, \kappa) = \nabla \cdot \left[\left(\mu + \frac{\mu_t}{\sigma_\kappa} \right) \nabla \kappa \right] + \mu_t S^2 - \rho \beta^* f_{\beta^*} \kappa \omega + S_\kappa \tag{3.3}$$

and

$$\nabla \cdot (\rho\, \vec{u}\, \omega) = \nabla \cdot \left[\left(\mu + \frac{\mu_t}{\sigma_\omega} \right) \nabla \omega \right] + \alpha_\omega \alpha^* \rho S^2 - \rho \beta \omega^2 + 2(1 - F_1) \rho \frac{1}{\omega \sigma_{\omega,2}} \nabla \kappa \nabla \omega + S_\omega \tag{3.4}$$

where:

$$\mu_t = \rho \frac{\kappa}{\omega} \frac{1}{Max\left(\frac{1}{\alpha^*}, \frac{SF_2}{a_1 \omega} \right)} \tag{3.5}$$

$$S = \frac{1}{2} \left(\nabla \vec{u} + \nabla \vec{u}^T \right) \tag{3.6}$$

The value of μ_t calculated through Equation (3.5) implies a limitation on the turbulence production that prevents an overestimation of the turbulence in low turbulence flows [31].

The values and expressions for F_1, F_2, a_1 β^*, f_β, α_ω, α^* and $\sigma_{\omega,2}$ can be seen in detail in [35] and [33]. The terms S_κ and S_ω in Equation (3.3) and (3.4) include any source term related to κ and ω respectively, and are specific to each problem. This SST $\kappa-\omega$ model was used to model the open section of the converter in 2D and the interior the channels at the channel scale. The two cases differ in the wall treatment, where the converter uses a low Reynolds correction and the channels do not.

- Modeling the monolith

At the converter scale the monolith was represented as an homogeneous porous medium using a volume-averaged Navier-Stokes (VANS) equation. The effect of the solid walls of the monolith channels in the flow can be represented by the addition of a porous inertia term to the momentum conservation equations. To do that, it is necessary to define the permeability of the porous medium in each direction. According to Hayes [17], a realistic representation of the monolith, which does not allow transport of momentum between its channels, is achieved by an anisotropic porous medium with a radial permeability at least two orders of magnitude lower than the axial permeability. Assuming Poiseuille flow inside the monolith, which is expected in the greater portion of the channels, both components of the permeability tensor, axial and radial, can be defined as follows [17, 23]:

$$K_\alpha^{axial} = \frac{\phi D_H^2}{28.4} \tag{3.7}$$

$$K_\alpha^{radial} = 1000 K_\alpha^{axial} \tag{3.8}$$

In Equation (3.7) ϕ is the void fraction of the monolith and D_H is hydraulic diameter of a single channel. Even if there is not a strictly Poiseuille flow into the channels, it provides a good approximation for the axial permeability. The conservation Equation (3.1), (3.3) and (3.4) still apply for this part of the domain, but Equation (3.2) is replaced for Equation (3.9), which includes the source term that models the effect of the porous medium on the momentum conservation.

$$(\rho\vec{u}\nabla\cdot)\,\vec{u} = -\nabla p + \nabla\cdot\left((\mu+\mu_t)\left[\nabla\vec{u}+\nabla\vec{u}^T\right]\right) - \frac{2}{3}\rho\,\kappa\,I - \frac{\mu}{\vec{K}_\alpha}\vec{u} \tag{3.9}$$

Equation (3.9) completes the first analyzed case at the converter scale in 2D. It is the regular case, where the problem is solved without the imposition of special conditions to any part of the domain. The second case, or laminar case, defines the porous medium as a laminar zone. When a laminar zone is set in ANSYS Fluent 17.2, the turbulence viscosity is set to

zero and the turbulence production is disabled in that part of the domain. Nevertheless, the turbulence quantities, κ and ω are still transported through this part of the domain ignoring its effects on the fluid mixing [33]. It is specially useful when there are laminar zones before turbulent zones, but does not represent the phenomenon in the catalytic converter, where the turbulence must decay inside of the monolith channels, instead of being transported from the inlet to the outlet of the channels only. As consequence, the mass, momentum and ω equations are still Equation (3.1), (3.9) and (3.4) respectively, but the transport of κ is calculated as Equation (3.10) in the laminar zone.

$$\nabla \cdot (\rho \vec{u} \kappa) = \nabla \cdot (\mu \nabla \kappa) - \rho \beta^* f_{\beta^*} \kappa \omega \tag{3.10}$$

In this work we considered a third option, adding a damping of the turbulence inside of the porous medium, similar to that used in studying phase change [36], to obtain a decay of the turbulence inside the porous zone in agreement with the decay in the monolith channels. This alternative represents the damped case, and does not require the setting of the laminar zone in the porous medium. The mass, momentum and ω transport equations in the porous zone are still Equation (3.1), (3.9) and (3.4), meanwhile, the transport of κ, including the damping of the turbulence, is shown in Equation (3.11).

$$\nabla \cdot (\rho \vec{u} \kappa) = \nabla \cdot \left[\left(\mu + \frac{\mu_t}{\sigma_\kappa} \right) \nabla \kappa \right] + \mu_t S^2 - \rho \beta^* f_{\beta^*} \kappa \omega - \underbrace{\frac{\mu_t}{K_\alpha^{axial}} \kappa}_{\text{damping } (S_\kappa)} \tag{3.11}$$

It should be noted that the last term in this equation is responsible for the damping of the turbulence inside the monolith. We use this term according to works by Shyy et al. [37, 38] and Prescott and Incropera [36] who modeled the effects of turbulence on the heat transfer inside a porous mushy zone during the solidification of a binary metal alloy. The only difference is that instead of μ we utilize μ_t in the damping term. Even though better agreement was found using the eddy viscosity in the sink of κ, it might lead to an overestimation of the pressure drop, hence, the use of the effective viscosity must be considered too. A source term for ω was considered to be used complementary to the damping in the κ equation. Here, the Equation (3.4) is replaced by Equation(3.12).

$$\nabla \cdot (\rho \vec{u} \omega) = \nabla \cdot \left[\left(\mu + \frac{\mu_t}{\sigma_\omega} \right) \nabla \omega \right] + \alpha_\omega \alpha^* \rho S^2 - \rho \beta \omega^2 + 2(1 - F_1) \rho \frac{1}{\omega \sigma_{\omega,2}} \nabla \kappa \nabla \omega \underbrace{- \frac{\mu}{K_\alpha^{axial}} (\omega - \omega_0)}_{\text{damping } (S_\omega)} \tag{3.12}$$

where:

$$\omega_0 = C_\omega \frac{\mu/\rho}{\beta_\omega L^2/4}$$

Here ω_0 corresponds to the value of ω used as boundary condition the no-slip wall. In this work we use the following values: $\beta_\omega = 3/40$ and $C_\omega = 6$ according to the work [39]. The main idea of a new damping term for ω-equation is to take into account the influence of ω-change coupled with k-damping term on the decay of turbulence. In this view, we use ω_0 as a value of the specific turbulence dissipation rate which should be asymptotically approached by decay of the turbulence at the monolith-entrance region.

- Modeling the single channels

The single channels in 3D are modeled by the SST model, in a similar way as the open section of the converter. It does not have especial zones, and the fluctuations of the turbulence kinetic energy and turbulence viscosity are already considered in the turbulence model. In this case, the mass, momentum, κ and ω equations are Equation (3.1), (3.2), (3.3) and (3.4) respectively.

3.3 Results and discussion

The radial profile of the axial velocity after the monolith is a relevant quantity when simulating the catalytic converter, which is sensitive to the grid and the turbulence model. This study used that profile to examine the grid and modeling requirements. Meanwhile, the turbulence viscosity serves as an indicator of the turbulence pattern in each scale.

3.3.1 Grid study and validation

The maximum axial velocity after the monolith is the most sensitive point of the profile to different grid resolutions, and was used to state the grid independence of the results in the simulation of the converter. For that purpose, we used block structured meshes with refinement close to the wall, and systematically coarse from 640 000 to 20 000 control volumes each. Figure 3.3 shows a zoom of the outlet cone of the 20 000 control volumes grid. According to the results, the peak velocity after the monolith changes less that 0.25% between the 350 000 and 640 000 cv grids, hence, the first one was used for the rest of the experiments.

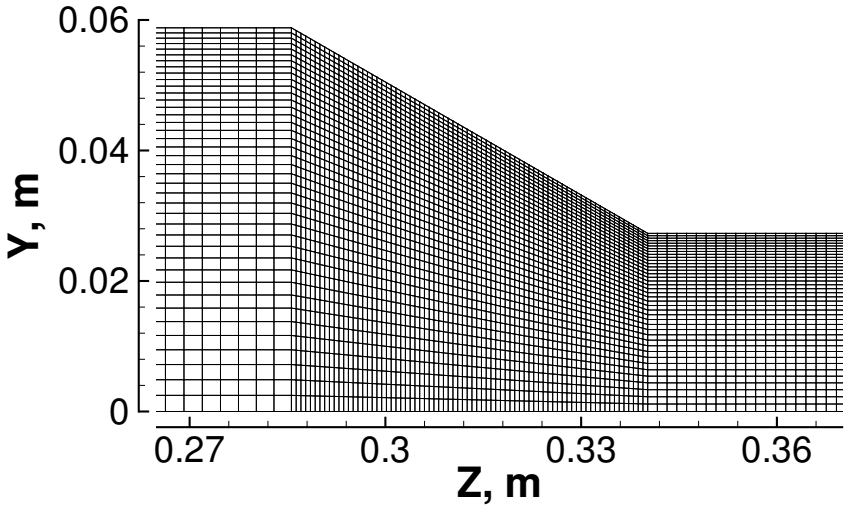

Figure 3.3: Zoom to the outlet cone of the 20 000 control volumes mesh

For the channel scale, we took advantage of its shape, using an orthogonal structured mesh. The volume average of the turbulence viscosity ratio in the first five centimetres of the channel served as a monitor. This average was analyzed for systematically coarse grids from 9 207 000 to 109 000 control volumes, finding differences lower than 0.5% between the two finer grids. Consequently, the study continued using the 9 207 000 control volumes mesh. It is equivalent to an 11μm of mean distance between nodes or approximately 600 000 control volumes per cubic millimetre.

The settings and boundary conditions used in the converter scale simulations are summarized in Table 3.1.

Table 3.1: Boundary conditions and settings for the converter simulations

Material	
Fluid	Air - incompressible
Porous medium specifications	
Axial permeability, m^2	$3.33x10^{-08}$
Radial permeability, m^2	$3.33x10^{-15}$
Converter boundary conditions	
Inlet - Velocity inlet	Re = 32 000
Inlet - Turbulence intensity, %	5
Inlet - Turbulence viscosity ratio	5
Outlet	Outflow
Walls	No-slip wall
Symmetry axis	Axial symmetry
Settings	
Pressure-Velocity coupling	SIMPLE
Momentum scheme	QUICK
Turbulence kinetic energy scheme	QUICK
Specific dissipation rate scheme	QUICK

During the validation with experimental data, other turbulence models were tested, specifically, the Standard $\kappa - \varepsilon$ [40], Standard $\kappa - \omega$ [31] and the SST $\kappa - \omega$ [35] models. Figure 3.4 shows the axial velocity profile at 0.5 mm after the monolith and experimental data from Clarkson [29]. As expected, the differences between models decrease when the mesh is finer, however, the study continued using the SST $\kappa - \omega$ model, which shows the best agreement among the three. The shape of the simulated and experimental profiles are similar, with some lack of fit at the centre of the converter. A possible explanation is the known limitations of the RANS models, describing flows with preferential, or dominant, direction of the turbulence, as well as the representation of the monolith through a homogeneous porous medium.

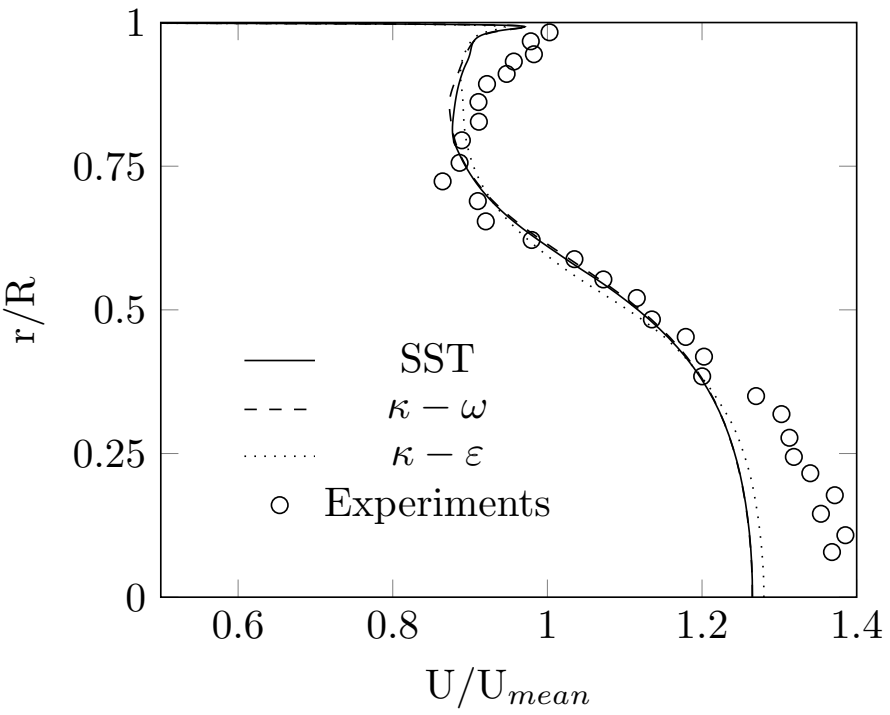

Figure 3.4: Simulated and experimental axial velocity profile [29] after the monolith.

3.3.2 Turbulence in the monolith at converter scale

Figure 3.5a and 3.5b show the turbulence viscosity ratio resulting from the simulations of the converter for the regular and laminar cases. The regular case shows high values of turbulence viscosity ratio inside the porous medium, especially close to the symmetry axis, where it stays over 20 across the complete porous medium. It is not in agreement with the decay of turbulence expected in the channels of the monolith. On the other hand, the laminar case shows a turbulence viscosity ratio decreasing to zero immediately upon entering the porous zone. It is artificial and is a consequence of the imposition of the laminar zone in this part of the domain. Additionally, the turbulence viscosity after the porous medium for the cases with and without the imposition of laminar zone is similar. It does not represent the decay of the turbulence expected in a real monolith. To capture the real turbulence level in the monolith we propose the following: We use the method illustrated in Figure 3.5a so that the turbulence is retained, however, we add a damping as show in Equation (3.11) so that there is a smooth transition to laminar flow to reflect the behaviour of a real monolith. Figure 3.5c shows the turbulence viscosity ratio for the converter simulation using the damping of the turbulence included in Equation (3.11) in the porous medium. It can be seen that the turbulence viscosity decays as we move into the zone, taking into account the turbulence kinetic energy

and turbulence viscosity at each position. This behavior is more in agreement with the decay of the turbulence inside of the channels of an actual monolith than the regular and laminar cases. As a consequence of the damping, the turbulence viscosity decays completely inside the monolith, and the region after it presents practically zero turbulence. The turbulence after the monolith is an important point to be analyzed. The flow abandoning the monolith channels could act as square jets, igniting velocity fluctuations and turbulence [41]. The porous medium approach does not capture the geometric features of an actual honeycomb structure, and the turbulence ignition after the monolith is beyond the scope if this work.

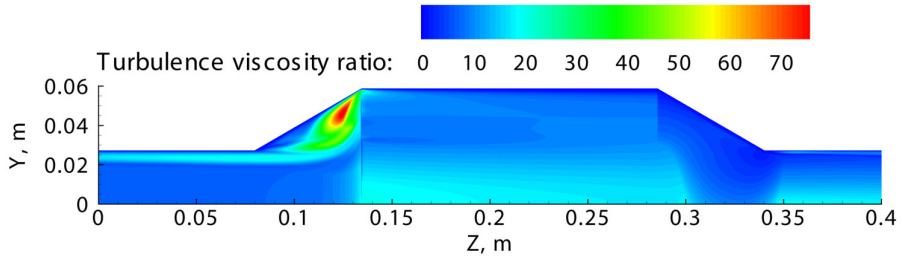

(a)

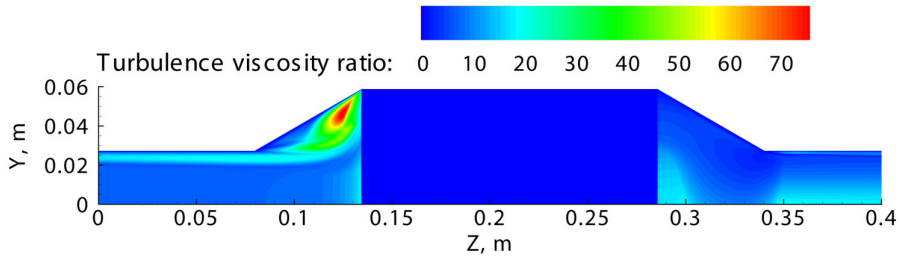

(b)

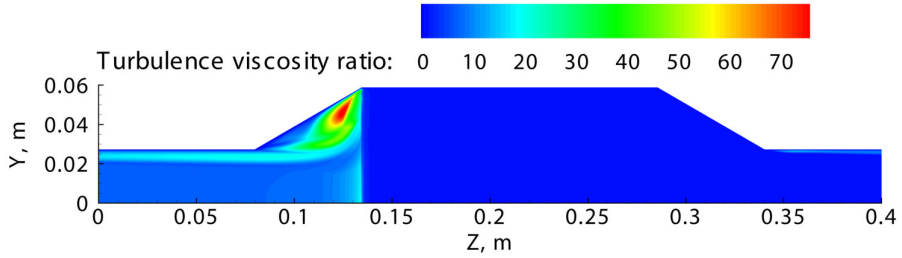

(c)

Figure 3.5: Turbulence viscosity ratio $\frac{\mu_t}{\mu_0}$ of the converter. (a) regular, (b) laminar, (c) damped

Clearly the choice of the damping term is important, and will determ how the turbulence decays. We choose this term based on the results of single channel simulations as described in the section 3.3.

3.3.3 Turbulence in single channels

The settings for the simulations at channel scale are similar to those used for the converter scale (see Table 3.1). Regarding the boundary conditions, the outlet was set as Outflow, the walls as No-Slip wall, and the symmetry planes as symmetry. The inlet values require special attention. There are strong gradients in the zone before the monolith; also, those conditions change if the damping of the turbulence is applied. Figure 3.6 shows the velocity magnitude and the turbulence viscosity ratio at 0.1 mm before the monolith. The profile marked as laminar contains the values when a laminar zone is imposed inside the monolith, the damped profile when the damping of the turbulence in the porous zone is applied and the regular when neither laminar zone nor the damping of the turbulence inside the monolith is used (default in Fluent v17.2).

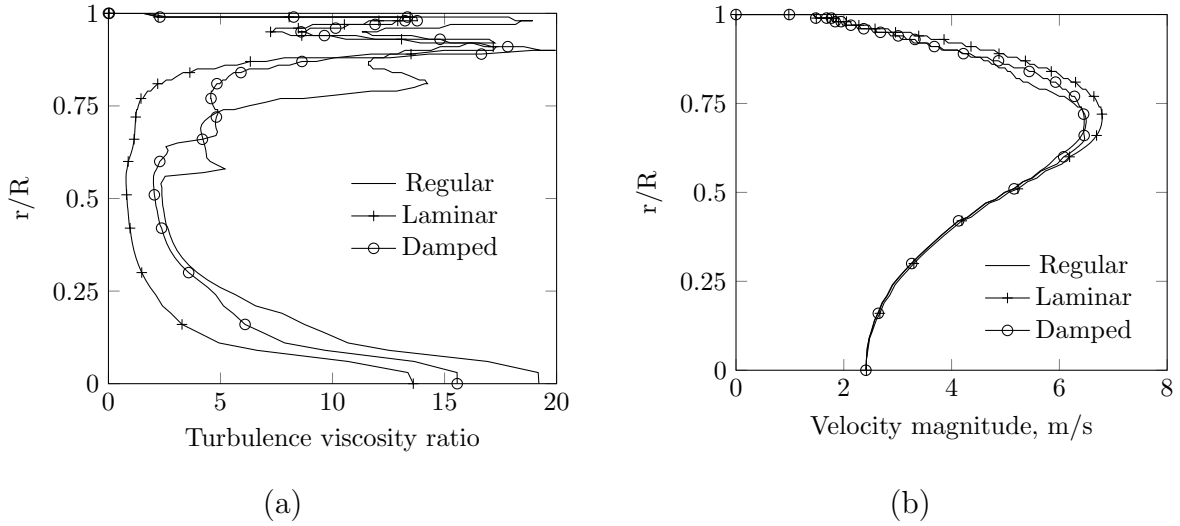

Figure 3.6: Conditions before the monolith, using different models: (a) radial profile of the turbulent viscosity ratio, (b) radial profile of the velocity magnitude.

The values of the velocity, turbulence kinetic energy and specific dissipation ratio for the inlet of the single 3D channel-simulation were taken from 2D simulation of the whole converter, considering the κ-equation in Equation (3.11) at a distance of 0.1 mm before the monolith, it means, including the damping of the turbulence. The exact value of this inlet conditions using the Equation (3.11) are summarized in Table 3.2. It is also noticeable that the velocity profile at the inlet of the channels is not strictly normal to the inlet, nevertheless, we tested this assumption enlarging the single channels domain by the inclusion of the half of the surrounding channels and an open section of 10 mm length before the channel. According the results, a flat profile at the inlet of the channels is a reasonable assumption.

Table 3.2: Boundary conditions a the inlet of the monolith when the damping is applied

Chann.	r/R	ω, 1/s	u, m/s	k, m^2/s^2
1	0.08	2.47	0.15	1 283
2	0.16	2.64	0.16	1 243
3	0.25	2.95	0.16	1 657
4	0.33	3.42	0.16	2 050
5	0.41	4.06	0.16	2 739
6	0.49	4.89	0.17	4 064
7	0.57	5.84	0.21	6 421
8	0.65	6.47	0.47	19 891
9	0.74	6.41	0.69	36 137
10	0.82	5.80	1.20	37 450
11	0.90	3.99	6.81	74 548
12	0.98	1.88	2.56	11 775

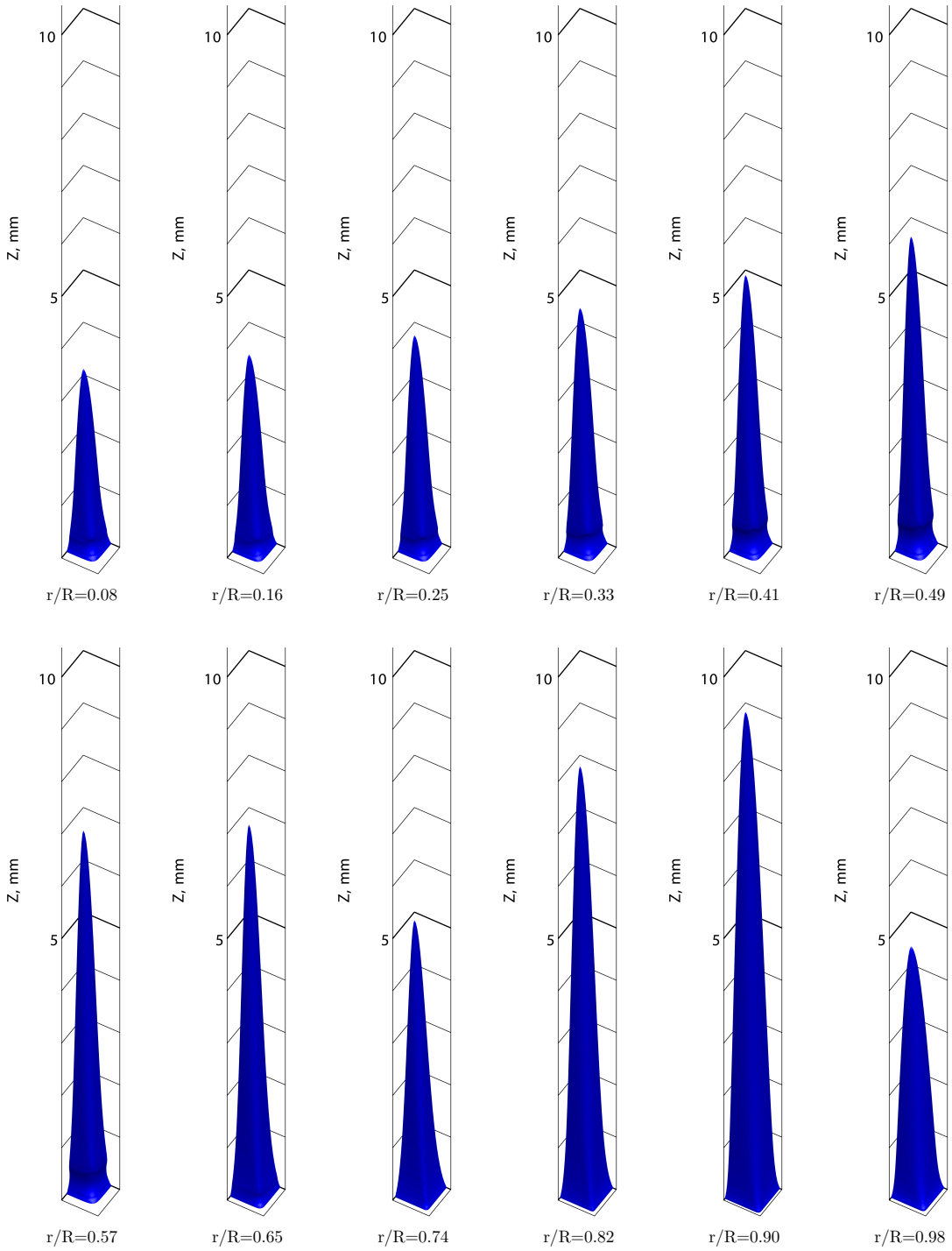

Figure 3.7: Isosurface for turbulence viscosity ratio equals to one ($\frac{\mu_t}{\mu} = 1$) of several channels using inlet conditions from a 2D entire converter simulation which includes the damping of the turbulence

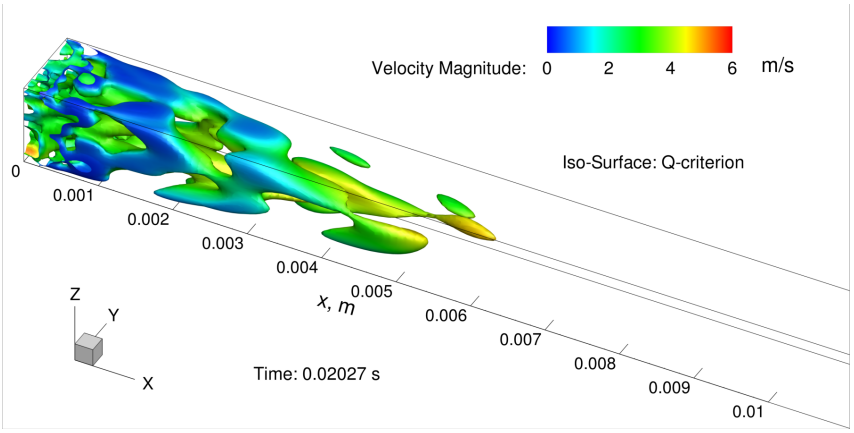

(a)

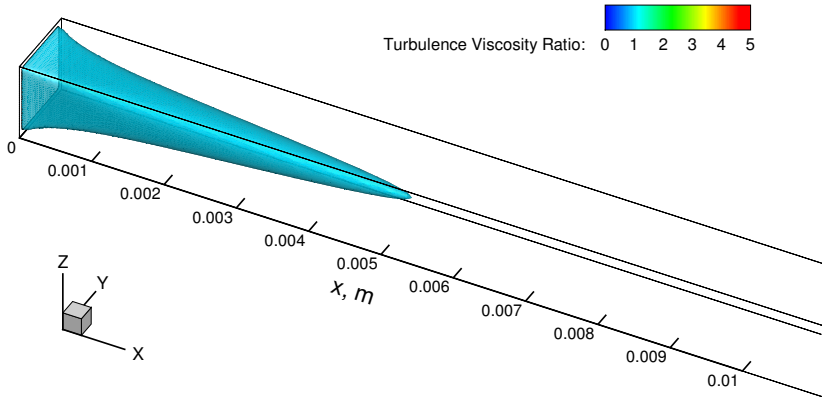

(b)

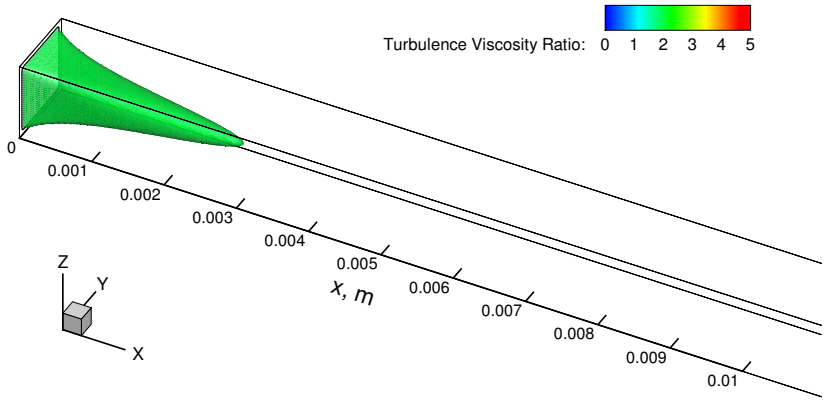

(c)

Figure 3.8: Turbulence decay inside single channels. (a) LES showing Q = 10^5 $1/s^2$, (b) RANS showing μ_t/μ=1 and (c) RANS showing μ_t/μ=2.

The results from the single channels simulation show that there is a decay of the turbulence once the flow enters the channels. Figure 3.7 shows an isosurface where the turbulence viscosity ratio is equal to one for a group of selected channels. Depending on the inlet condition of the channel, the distance from its inlet to where the flow has a turbulence viscosity ratio of one or below, varies from 0 to 10 mm. It is also noticeable that there are two channels with a behavior that is not in the same pattern, the channel 8 (r/R=0.65), which does not show turbulence penetration at all, and the channel 10 (r/R=0.82), which shows turbulence viscosity ratio above the unity up to a distance equivalent of 8 channel hydraulic diameters from its inlet (see Figure 3.9).

The quantity δ is defined as the distance from the inlet of the channel to where the turbulence viscosity ratio decays below one. A comparison between δ, predicted from the converter and channel scales is shown in Figure 3.9. Once the damping of the turbulence is applied to the 2D entire converter, the inlet conditions for the channels change. To be consistent, δ predicted by the entire converter using the damping must be compared against the prediction of the single channels using the inlet conditions taken from a simulation of the entire converter where the damping is applied too. Figure 3.9 includes δ for the single channels using the inlet conditions once the damping described in Equation (3.11) is applied. It can be seen that when the damping of the turbulence is applied, the decay of the turbulence viscosity predicted by the single channels and the whole converter are similar. Meanwhile, using the regular approach, they are not comparable, because the turbulence viscosity ratio remains above one along with the whole monolith if the damping is not applied. For the laminar case, there is no sense into the comparison of δ predicted by the entire converter and the single channels, because the turbulence viscosity is automatically set to zero within the entire laminar zone. In average, the single channels simulations predict a turbulence viscosity ratio below one at 3.8 D_H from the inlet of the channel approximately, meanwhile, from the converter simulation, with the proposed damping of the turbulence, the same condition is predicted at 4.5 D_H in average. There is a decay in the turbulence intensity as well, but it remains above 10% where the turbulence viscosity is equals to one, hence, the fully turbulent flow assumption is still valid, and the final transition to laminar will occur at some point downstream.

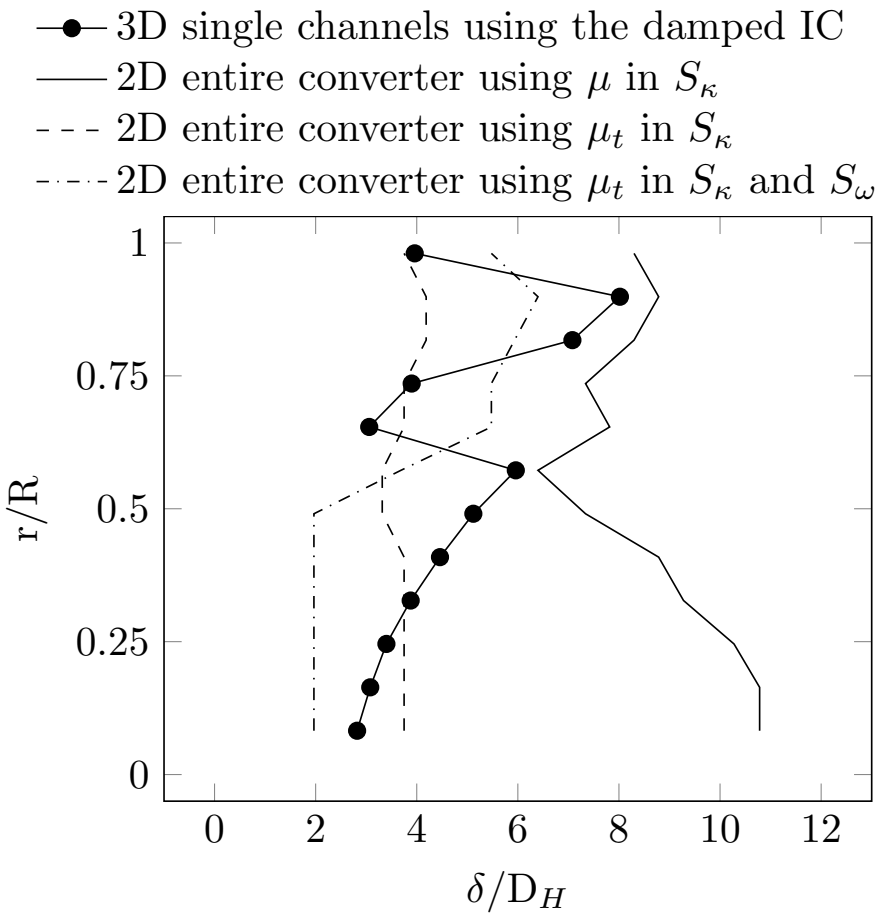

Figure 3.9: Comparison of the distance from the inlet, δ, where the turbulence viscosity ratio decays below one from the 2D entire converter and 3D single channel simulations.

To justify our criterion $\frac{\mu_t}{\mu} = 1$ for the definition of δ we plot in Figure 3.8 results of LES simulations (carried out using setup described in the work [9]) in the form of Q-isosurface and isosurfaces of the turbulent viscosity ratio $\frac{\mu_t}{\mu} = 1$ and $\frac{\mu_t}{\mu} = 2$. It can be seen that the condition $\frac{\mu_t}{\mu} = 1$ predicts acceptably the length in where the major vortices disappear into the channel.

3.4 Conclusions and remarks

A multiscale study, focused in the improvement of the porous medium approach to represent a monolith was performed. Simulations of several single channels of the monolith showed

that a smooth decay of the turbulence occurs from its inlet. The same patter was obtained at the converter scale, through the addition of a source term to the turbulence kinetic energy equation, that effectively damps the turbulence inside of the porous zone. This damping results in a more realistic representation of the turbulence inside of an actual monolith, compared to the imposition of a laminar zone on it.

The decay of the turbulence inside of the channels has a strong dependency on its inlet conditions, and these conditions vary significantly with the position of the target channel, the model of the monolith and the macro structure of the flow. At converter scale, the flow presents high gradients before the monolith, hence, this zone requires especial attention, if experimental or simulated data will be used as inlet conditions for channels.

Given the lack of experimental data inside channels, it is also recommended to perform a deeper study of the turbulence decay inside of the monolith channels, to obtain accurate data of the turbulent to laminar transition, as its consequences in the heat and mass transfer.

Bibliography

[1] Pablo Marín, Miguel AG Hevia, Salvador Ordonez, and Fernando V Díez. Combustion of methane lean mixtures in reverse flow reactors: comparison between packed and structured catalyst beds. *Catalysis Today*, 105(3):701–708, 2005.

[2] Steffen Tischer and Olaf Deutschmann. Recent advances in numerical modeling of catalytic monolith reactors. *Catalysis Today*, 105(3-4):407–413, 2005.

[3] Ronald M Heck, Suresh Gulati, and Robert J Farrauto. The application of monoliths for gas phase catalytic reactions. *Chemical Engineering Journal*, 82(1-3):149–156, 2001.

[4] RE Hayes, LS Mukadi, M Votsmeier, and J Gieshoff. Three-way catalytic converter modelling with detailed kinetics and washcoat diffusion. *Topics in Catalysis*, 30(1):411–415, 2004.

[5] Xiaoding Xu and Jacob A Moulijn. Transformation of a structured carrier into structured catalyst. *Statistics and Operations Research Transactions*, pages 599–616, 1998.

[6] Jinwen Chen, Hong Yang, Neil Wang, Zbigniew Ring, and Tadeusz Dabros. Mathematical modeling of monolith catalysts and reactors for gas phase reactions. *Applied Catalysis A: General*, 345(1):1–11, 2008.

[7] Henrik Strom, Srdjan Sasic, and Bengt Andersson. Effects of the turbulent-to-laminar transition in monolithic reactors for automotive pollution control. *Industrial & Engineering Chemistry Research*, 50(6):3194–3205, 2011.

[8] AK Sharma and Erik Birgersson. Validity and scalability of an asymptotically reduced single-channel model for full-size catalytic monolith converters. *Applied Mathematics and Computation*, 281:186–198, 2016.

[9] I Cornejo, P Nikrityuk, and RE Hayes. Turbulence decay inside the channels of an automotive catalytic converter monolith. *Emission Control Science and Technology*, 3(4):302—309, 2017.

[10] Kyriacos Zygourakis. Transient operation of monolith catalytic converters: a two-dimensional reactor model and the effects of radially nonuniform flow distributions. *Chemical Engineering Science*, 44(9):2075–2086, 1989.

[11] François Bertrand, Christophe Devals, David Vidal, Cyrille Séguineau de Préval, and Robert E Hayes. Towards the simulation of the catalytic monolith converter using discrete channel-scale models. *Catalysis Today*, 188(1):80–86, 2012.

[12] Ankan Kumar and Sandip Mazumder. Toward simulation of full-scale monolithic catalytic converters with complex heterogeneous chemistry. *Computers & Chemical Engineering*, 34(2):135–145, 2010.

[13] Anna Holmgren and Bengt Andersson. Mass transfer in monolith catalysts-CO oxidation experiments and simulations. *Chemical Engineering Science*, 53(13):2285–2298, 1998.

[14] H More, J Mmbaga, RE Hayes, M Votsmeier, and MD Checkel. Heat and mass transfer limitations in pre-turbocharger catalysts. *Topics in Catalysis*, 42(1-4):429–432, 2007.

[15] Evangelos Karvounis and Dennis N Assanis. The effect of inlet flow distribution on catalytic conversion efficiency. *International Journal of Heat and Mass Transfer*, 36(6):1495–1504, 1993.

[16] Gianpiero Groppi, Enrico Tronconi, and Pio Forzatti. Mathematical models of catalytic combustors. *Catalysis Reviews*, 41(2):227–254, 1999.

[17] RE Hayes, Anton Fadic, Joeseph Mmbaga, and A Najafi. CFD modelling of the automotive catalytic converter. *Catalysis Today*, 188(1):94–105, 2012.

[18] Sophie Porter, Jonathan Saul, Svetlana Aleksandrova, Humberto Medina, and Stephen Benjamin. Hybrid flow modelling approach applied to automotive catalysts. *Applied Mathematical Modelling*, 40(19-20):8435–8445, 2016.

[19] Matthias Hettel, Claudia Diehm, Bentholhoda Torkashvand, and Olaf Deutschmann. Critical evaluation of in situ probe techniques for catalytic honeycomb monoliths. *Catalysis Today*, 216:2–10, 2013.

[20] Osborne Reynolds. An experimental investigation of the circumstances which determine whether the motion of water shall be direct or sinuous, and of the law of resistance in parallel channels. *Proceedings of The Royal Society of London*, 35(224-226):84–99, 1883.

[21] Devranjan Samanta, Alberto De Lozar, and Bjoern Hof. Experimental investigation of laminar turbulent intermittency in pipe flow. *Journal of Fluid Mechanics*, 681:193–204, 2011.

[22] Dwight Barkley, Baofang Song, Vasudevan Mukund, Grégoire Lemoult, Marc Avila, and Björn Hof. The rise of fully turbulent flow. *Nature*, 526:550–553, 2015.

[23] Ismail Tosun, Deniz Uner, and Canan Ozgen. Critical reynolds number for newtonian flow in rectangular ducts. *Industrial & Engineering Chemistry Research*, 27(10):1955–1957, 1988.

[24] Fredrik Ekström and Bengt Andersson. Pressure drop of monolithic catalytic converters experiments and modeling. *SAE Technical paper*, No. 2002-01-1010, 2002.

[25] Kenji Tanno, Hisao Makino, Ryoichi Kurose, Satoru Komori, and Takenobu Michioka. Effect of turbulent to laminar flow transition on surface reaction and particle deposition in a square duct. *TSFP Digital Library Online*, 2013.

[26] Y. Kuwata, K. Suga, and Y. Sakurai. Development and application of a multi-scale $k-\varepsilon$ model for turbulent porous medium flows. *International Journal of Heat and Fluid Flow*, 49:135–150, 2014.

[27] M. Mössner and R. Radespiel. Modelling of turbulent flow over porous media using a volume averaging approach and a Reynolds stress model. *Computers and Fluids*, 108:25–42, 2015.

[28] M. Drouin, O. Gregoire, and O. Simonin. A consistent methodology for the derivation and calibration of a macroscopic turbulence model for flows in porous media. *International Journal of Heat and Mass Transfer*, 63:401–413, 2013.

[29] Rory John Clarkson. *A theoretical and experimental study of automotive catalytic converters*. PhD thesis, Coventry University, 1997.

[30] SF Benjamin, RJ Clarkson, Net al Haimad, and NS Girgis. An experimental and predictive study of the flow field in axisymmetric automotive exhaust catalyst systems. *SAE Technical Paper*, No. 961208, 1996.

[31] David C Wilcox. *Turbulence modeling for CFD*. DCW Industries, La Canada, California, USA, 1993.

[32] J Ferziger and M. Peric. *Computational Methods for Fluid Dynamics*. Springer, New York, USA, 2002.

[33] ANSYS Fluent Theory Guide v17.2. ANSYS Inc., Canonsburg, PA, USA, 2016.

[34] W Malalasekera and HK Versteeg. *An introduction to computational fluid dynamics: the finite volume method*. PEARSON Prentice Hall, Upper Saddle River, New Jersey, USA, 2007.

[35] Florian Menter. Two-equation eddy-viscosity turbulence models for engineering applications. *AIAA journal*, 32(8):1598–1605, 1994.

[36] PJ Prescott and FP Incropera. The effect of turbulence on solidification of a binary metal alloy with electromagnetic stirring. *Journal of heat transfer*, 117(3):716–724, 1995.

[37] W. Shyy, Y. Pang, G. Hunter, D. Wei, and M. Chen. Modeling of turbulent transport and solidification during continuous ingot casting. *International Journal of Heat and Mass Transfer*, 35:1229–1245, 1992.

[38] W. Shyy, Y. Pang, G. Hunter, D. Wei, and M. Chen. Effect of turbulent heat transfer on continuous ingot solidification. *Journal of Engineering Materials and Technology*, 115(1):8–16, 1993.

[39] Georgi Kalitzin, Gorazd Medic, Gianluca Iaccarino, and Paul Durbin. Near-wall behavior of RANS turbulence models and implications for wall functions. *Journal of Computational Physics*, 204(1):265–291, 2005.

[40] Brian Edward Launder and Dudley Brian Spalding. *Lectures in mathematical models of turbulence*. Academic Press, New York, USA, 1972.

[41] Minyi Xu, Jianpeng Zhang, Pengfei Li, and Jianchun Mi. On two distinct reynolds number regimes of a turbulent square jet. *Theoretical and Applied Mechanics Letters*, 5(3):117–120, 2015.

Chapter 4

Turbulence generation after a monolith in automotive catalytic converters[1]

Abstract

This work reports theoretical studies of flow behaviour in a monolith outlet zone for different Reynolds numbers covering laminar and transitional/turbulent flow regimes. Monolith type substrate are the core part of automotive catalytic converters. Due to computational limitations, most of the numerical models of converters represent the monolith as a continuum, averaging the effect of the solid and the open space on the flow. This strategy is useful to study the macro-structure of the flow, however, it does not capture the exact behaviour of an actual honeycomb type structure, especially at its entrance and exit. In this work, which is a continuation of the publication by Cornejo et al. [1], a series of 3D LES and RANS simulations are performed using different discrete channel geometry to study and quantify the velocity fluctuations of flow leaving a monolith. The results show that above a certain Reynolds number the instability of the flow after the monolith is significant, leading to turbulence generation. The velocity fluctuations are mainly explained by the flow past the outlet of the monolith, and their magnitude is related to the Reynolds number based on the thickness of the walls between channels. An expression for this critical Reynolds number has been designed and verified against numerical simulations. Parametric studies are carried out to illustrate the influence of the Reynolds number on the appearance of flow fluctuations at

[1]A version of this article has been published. Turbulence generation after a monolith in automotive catalytic converters. Cornejo, I., Nikrityuk, P., & Hayes, R. E. (2018). Turbulence generation after a monolith in automotive catalytic converters. Chemical Engineering Science, 187, 107-116

the outlet zone of the monolith.

Keywords: Catalytic converter, monolith, channels, LES, turbulence, transition

4.1 Introduction

Monolith based catalytic converters were initially developed for the automotive industry to reduce the pollutants present in the exhaust gas, however, due to its many advantages over other reactor types, such as a relatively low pressure drop and high external area, they are now used in other industrial applications [2–6]. In recent years, there has been much work on the modeling of monolith reactors, [7–10], phenomena inside micro channels [11–13] and model-based optimization [14]. Given current computational limitations, numerical models of the converter usually represent the monolith as a homogeneous anisotropic porous medium, through a volume average approach [15–19]. This approach often leads to an acceptable agreement with experimental velocity profiles right after the monolith [19–21], but it fails to represent some phenomena existing in an actual honeycomb structure, especially at the beginning and the end of the monolith [22]. In particular, models utilizing the homogeneous porous medium approach, are unable to predict turbulence-monolith-turbulence interaction adequately. The flow entering the converter has a Reynolds number of the order of 10^4, it decreases to a magnitude of 10^2 inside of the monolith channels, and then increases back to 10^4 after leaving the monolith. Those Reynolds numbers imply flow regime transitions from turbulent to laminar and laminar to turbulent along the converter in a driving cycle. To obtain accurate results in modeling experimental data, decoupled from the effect of the turbulence, researchers carefully control the operating conditions to keep the flow in laminar regime [23–26]. If those conditions are not met, the turbulence inside the channels might have a significant impact on the results [27]. Strom et al. [28] studied the flow transition entering a monolith and its effect on the deposition of solid particles in the monolith entrance. Ekstrom and Andersson [29] reported experimental evidence of the effect of the turbulence at the beginning of the monolith on the pressure drop along the substrate. Cornejo et al. [22] analyzed the decay of the turbulence once the flow enters into a single channel under typical operating conditions, then proposed a damping of the turbulence for a two-equations eddy viscosity models that includes this behaviour in the continuum approach [1]. Despite many works aimed at understanding the flow behaviour in the first part of the monolith, the laminar to turbulent transition at its last part, where the flow pass from inside the substrate into an open space, has not received much attention in the literature. It should be emphasized that this phenomenon is not appropriately represented by a homogeneous porous medium,

because the turbulence generation is a consequence of the presence of the solid substrate. The turbulence after the monolith requires attention because it affects the overall pressure drop of the exhaust gas after-treatment system significantly, which results important for the engine operating efficiency and fuel economy. In addition, in close coupled monoliths, the outflow of the first impacts the performance of the second by changing its inlet conditions.

There are three main phenomena that might generate instability and turbulence in the flow leaving the monolith. These are the turbulence from inside the channels, the turbulence caused by the flow leaving a channel acting as a jet, and the instability from the stream around the last part of the solid walls between channels. The channels of the monolith are often approximately square and the turbulence inside rectangular ducts has been studied by Tosun et al. [30]. They reported a critical Reynolds number close to 1600 and a strong effect of the corners in the generation of turbulence. Xu et al. [31] observed turbulence in single square jets with Reynolds numbers above 30 000. The flow around the end of a wall between channels is comparable to the flow around rectangular objects, which depends on the width of the object, which in the case of a monolith, is the wall thickness. For flow around rectangular objects, Bruer et al. [32] reported that for Reynolds numbers above 300, based on the object width, turbulence is generated after the object. Also, between 90 and 300, the flow is unsteady laminar, meanwhile, below Reynolds 90, it is steady. Those studies considered a single jet and the flow around a single rectangular object. A monolith has thousands of channels running in parallel at a short distance from each other, where the flow might interact, increasing the instability and producing turbulence at lower Reynolds numbers. It is also notable that obtaining detailed experimental data inside and close to the monolith channels is non-trivial. Hettel et al. [33] reported that the inclusion of probes inside a monolith channel might introduce up to 50% of error in the measurements. Hence, numerical experiments are preferable to study this phenomenon at a channel scale.

The objective of this work is the study and description of the velocity fluctuations and flow regimes after the monolith of an automotive catalytic converter. Several geometries in 3D commonly found in the literature were analyzed using large eddy simulation (LES) and Reynolds Average Navier-Stokes (RANS) models in a discrete channel geometry. The results were compared in terms of the average and standard deviation of the velocity, flow regime and turbulence kinetic energy. The main novelty of this work is that we confirmed numerically that at some given values of the Reynolds number, defined using the monolith wall thickness, the flow becomes turbulent. To the best of our knowledge, this problem is not addressed in the literature, and it is needed to design new computational models, that

take into account the generation of turbulence after a monolith.

4.2 Computational model

The central point of this work is the characterization of a flow leaving a monolith, therefore, we considered the last part of a series of discrete channels followed by an open space as a domain. Although phenomena such as the heat produced by the chemical reactions and the irregularity of the washcoat might also affect the flow regime and distribution in an operating catalytic converter, we considered only isothermal unwashcoated channels. Under these conditions, it is reasonable to assume that the flow is atmospheric air [20].

4.2.1 Description of the domain

The full domain considered in this study is a section of the outlet of the monolith consisting of four channels and the corresponding portion of the adjacent ones, completing a total of nine equivalent channels (see Figure 4.2 and 4.3a). Each one of the channels has a side of 1.1 mm and 0.1 mm as wall thickness. The entire length of the domain is 40 mm, where the first 20 mm correspond to the last part of the channels and the other 20 mm represent a portion of the open space immediately after the monolith inside the outlet cone of a converter. Although most of the runs considered a channel length of 20 mm, which does not ensure a fully developed velocity profile across the entire flow area, it does it in the zones close to the walls. Despite the center of the channel, the results showed to be dependent on the local velocity close to the corners. Comparisons with channels twice larger were performed for channel Reynolds up to 1500, finding no substantial differences in the results. This is shown in Figure 4.1.

To quantify the additive effect of multiple channels interacting, a reduced domain and a single corner as shown in Figure 4.3b, were also studied and compared against the results of the full domain. The reduced domain is a single central channel with the corresponding part of the adjacent ones, completing a total of four equivalent channels. The single corner consists of the four fourths of a channel around an intersection between a vertical and an horizontal wall, which is one equivalent channel. All versions of the domain were 40 mm in length.

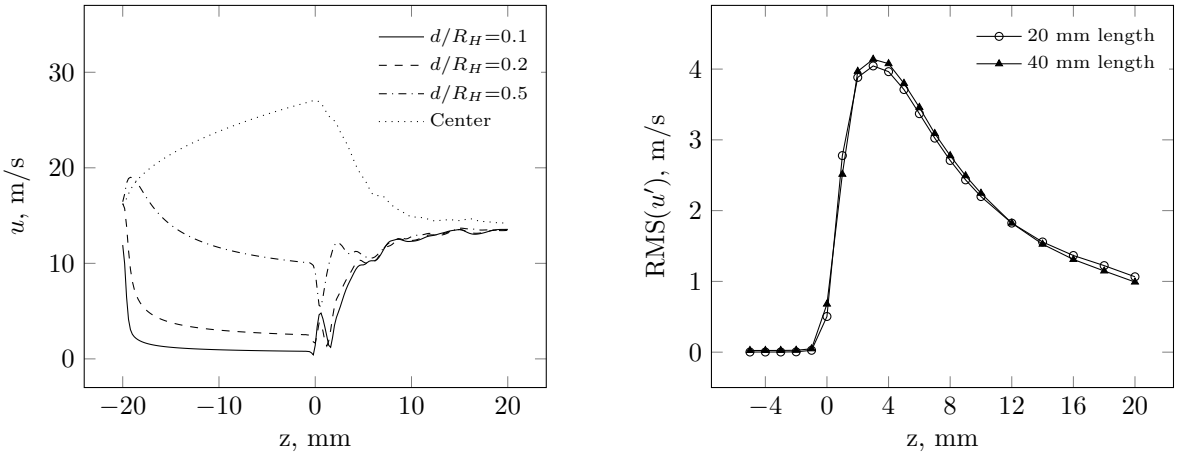

(a) (b)

Figure 4.1: (a) Velocity at several distances from the corner of a 20 mm length channel. (b) Turbulence kinetic energy for two different channel lengths. Channel Reynolds number = 1300

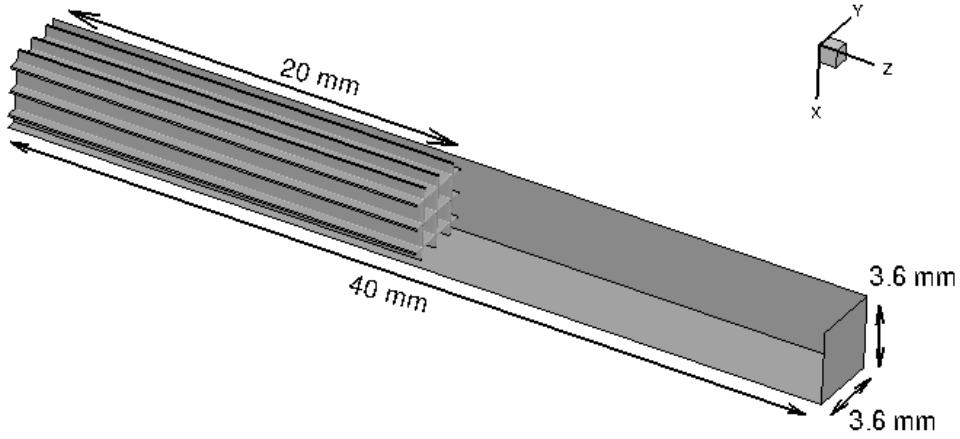

Figure 4.2: Dimensions of the complete domain

4.2.2 Boundary conditions

To define the inlet velocity for the channels we considered the experiments performed by Clarkson et al. [20], the parametric study reported by Hayes et al. [19] and the studies by

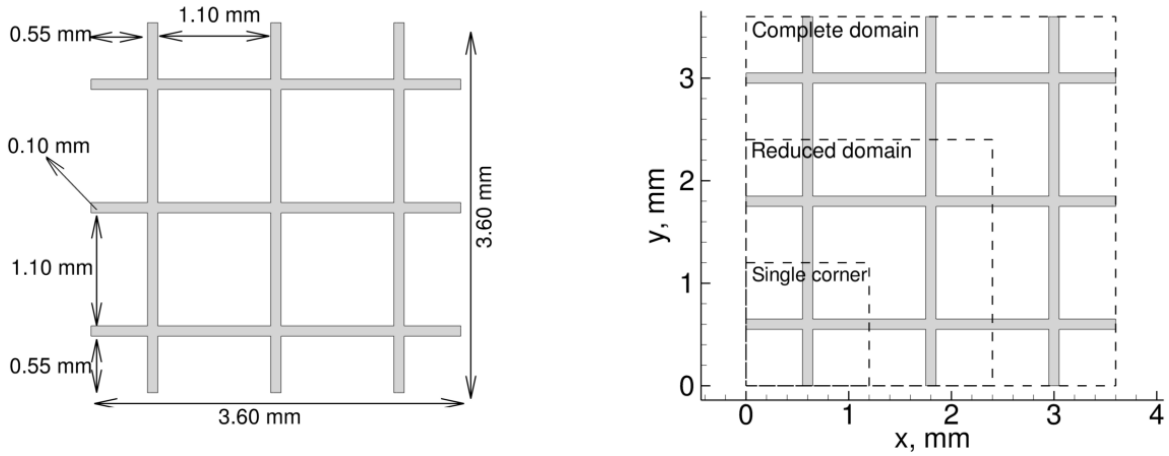

(a) (b)

Figure 4.3: Frontal view showing (a) size of the channels and walls, and (b) limits of the complete, reduced and single corner domains

Cornejo et al. [1, 22]. All of them analyze entire converters, whence the conditions for single channels can be extracted. Additional experiments were carried out to obtain clear trends over a wider range of values. Remains of turbulence and pulsating flow might affect the results; however, the turbulence entering the channels is expected to decay completely in the first part of them. Such decay is still subject of research; hence, in the lack of precise information of the frequency and amplitude of the velocity fluctuations deep inside the channels, this work deals with constant flow only. No slip was assumed in the channel walls and periodic boundary conditions, mirroring the top-bottom and left-right, on the respective sides of the domain. All of the domains have a unique outlet treated as an outflow. Periodicity is potentially more in agreement with the flow leaving the monolith than assuming symmetry, nevertheless, both options were analyzed and the results are reported. The boundary conditions for the RANS simulations were the same as for LES, with the exception of the inlet, where no spectral synthesizer was used, and the periodic boundaries were replaced by symmetry. RANS is statistically steady, hence, symmetry produces the same result as periodic. Table 4.1 summarizes the boundary conditions for all of the cases.

4.2.3 Flow model

The flow is expected to be laminar inside of the channels of the monolith and turbulent in the open sections. Given this transition, the study used LES to describe the velocity field. Equation. (4.1) and (4.2) show the mass and momentum filtered version of the Navier-Stokes

Table 4.1: Boundary conditions

Model type	Boundary	Boundary type	Boundary value
LES (3D)	Inlet	Velocity inlet	4 to 28 m/s
		Spec. synthesizer	Turb. int. 1%
			Hydraulic diameter 1.1 mm
	Outlet	Outflow	-
	Channel walls	No slip wall	-
	Top	Periodic	-
	Bottom	Periodic	-
	Left	Periodic	-
	Right	Periodic	-
RANS (3D)	Inlet	Velocity inlet	4 to 28 m/s
			Turb. Int. 1%
			Hydraulic diameter 1.1 mm
	Outlet	Outflow	-
	Channel walls	No slip wall	-
	Top	Symmetry	-
	Bottom	Symmetry	-
	Left	Symmetry	-
	Right	Symmetry	-

equations for LES [34]. They come from the substitution of $u_{i(t)} = u_i + u'_i$ and $p_{(t)} = p + p'$ and solve the problem up to a cut-off limit, defined by the cell volume, meanwhile, below the cut-off size, a sub-grid scale (SGS) model is employed.

$$\frac{\partial \rho}{\partial t} + \frac{\partial}{\partial x_j}(\rho \overline{u_i}) = 0 \tag{4.1}$$

$$\frac{\partial \overline{u_i}}{\partial t} + \overline{u_j}\frac{\partial \overline{u_i}}{\partial x_j} = -\frac{1}{\rho}\frac{\partial \overline{p}}{\partial x_i} + \frac{\partial}{\partial x_j}\left(\nu \frac{\partial \overline{u_i}}{\partial x_j} + \frac{1}{\rho}\frac{\partial \tau_{ij}}{\partial x_j}\right) \tag{4.2}$$

The term τ_{ij} in Equation (4.2) is the sub-grid-scale-stress and includes the interaction between the resolved flow and the SGS vortices. The problem was closed by the Smagorinsky-Lilly SGS model (SSL) [34, 35]. It defines τ_{ij} as in Equation (4.3). The dynamic version of Smagorinsky-Lilly (DSL) [34, 36] and the Wall-Adapting Local eddy-viscosity (WALE) [34, 37] sub-grid models were also tested and the results reported.

$$\tau_{ij} = -2\mu_{SGS}\frac{1}{2}\left(\frac{\partial \overline{u_i}}{\partial x_j} + \frac{\partial \overline{u_j}}{\partial x_i}\right) + \frac{1}{3}\tau_{kk}\delta_{ij} \tag{4.3}$$

where:

. $\mu_{SGS} = \rho L_s^2 |\overline{S}|$
. $L_s = min(k_v d_w, C_s \Delta)$

In computing the mixing length (L_s), ANSYS Fluent 17.2 assumes Δ as the cubic root of the volume of the cell, d_w as the distance to the closest wall and $|\overline{S}| = \sqrt{2\overline{S}_{ij}\overline{S}_{ij}}$ [34].

As an additional comparison, RANS simulations were also performed. The first model considered was the standard κ-ε model [38], which is relatively simple and present in most of the commercial codes. The transport equations for κ and ε steady state, for incompressible flow, without buoyancy effects and no source terms are shown in Equation. (4.4) to (4.5) [34], meanwhile, the turbulence viscosity is given in Equation (4.6) [34]. For this model $C_{1\varepsilon} = 1.44$, $C_{2\varepsilon} = 1.92$, $C_\mu = 0.09$, $\sigma_\kappa = 1.0$ and σ_ε is 1.3 [34]. Due to the y^+ observed in the results, an enhanced wall treatment (EWT-ε) was applied [34] for this model.

$$\frac{\partial}{\partial x_i}(\rho\kappa u_i) = \frac{\partial}{\partial x_j}\left[\left(\mu + \frac{\mu_t}{\sigma_\kappa}\right)\frac{\partial \kappa}{\partial x_j}\right] + \mu_t S^2 - \rho\varepsilon \tag{4.4}$$

$$\frac{\partial}{\partial x_i}(\rho\varepsilon u_i) = \frac{\partial}{\partial x_j}\left[\left(\mu + \frac{\mu_t}{\sigma_\varepsilon}\right)\frac{\partial \varepsilon}{\partial x_j}\right] + C_{1\varepsilon}\frac{\varepsilon}{\kappa}\mu_t S^2 - C_{2\varepsilon}\rho\frac{\varepsilon^2}{\kappa} \tag{4.5}$$

$$\mu_t = \rho C_\mu \frac{\kappa^2}{\varepsilon} \tag{4.6}$$

The second RANS model tested was the SST κ-ω model [39], because it performs relatively well between the two-equation eddy viscosity models. Its transport equations for κ and ω, assuming steady state, incompressible flow and without source terms are described in Equation. (4.7) and (4.8) respectively [34, 39]. The turbulence viscosity is defined as in Equation (4.9) and includes a limiter to the production of turbulence [34, 39].

$$\frac{\partial}{\partial x_i}(\rho\kappa u_i) = \frac{\partial}{\partial x_j}\left[\left(\mu + \frac{\mu_t}{\sigma_\kappa}\right)\frac{\partial \kappa}{\partial x_j}\right] + \mu_t S^2 - \rho\beta^* f_{\beta^*}\kappa\omega \tag{4.7}$$

$$\frac{\partial}{\partial x_j}(\rho\omega u_j) = \frac{\partial}{\partial x_j}\left[\left(\mu + \frac{\mu_t}{\sigma_\omega}\right)\frac{\partial \omega}{\partial x_j}\right] + \alpha\alpha^*\rho S^2 - \rho\beta f_\beta \omega^2 + 2(1-F_1)\rho\frac{\partial \kappa}{\partial x_j}\frac{\partial \omega}{\partial x_j} \tag{4.8}$$

$$\mu_t = \frac{\rho\kappa}{\omega}\frac{1}{max\left[\frac{1}{\alpha*}, \frac{SF_2}{a_1\omega}\right]} \tag{4.9}$$

Given its complexity and extension, the constants and blending functions of the SST transport equations are not described in this paper. They are extensively discussed in Menter et al. [39] and in the ANSYS Fluent Theory Guide v17.2 [34].

4.3 Discretization and grid independence

The complete domain was discretized into a fully orthogonal and uniform grid, composed of four million hexaedra with 50 μm as characteristic length. The time step was set to obtain a maximum Courant number (CFL) of around 0.5, which is equivalent to time steps of the order of 10^{-6} s. Both, the characteristic size of the control volumes and the CFL set on the simulations are the result of a systematic study described later in this paper. The discretization schemes and solver settings are summarized in Table 4.2. In LES the stop criterion for each time step was the reaching of a maximum value of scaled residuals of the order of 10^{-5}. In RANS, in addition, the volume average turbulence kinetic energy over the entire domain was monitored until it reached a stable value.

Table 4.2: Solver settings (in Fluent v17.2)

	Element	Setting
LES (3D)	Pressure-velocity coupling	SIMPLE
	Pressure	Second order
	Momentum	Bounded central difference
	Transient formulation	Bounded second order implicit
RANS (3D)	Pressure-velocity coupling	SIMPLE
	Pressure	Second order
	Momentum	Second order upwind
	Turbulence kinetic energy	Second order upwind
	ε / ω	Second order upwind

The grid and time step study for the LES considered a temperature of 300 K and an inlet velocity of 16 m/s, which is equivalent to a channel Reynolds number of 1054. This condition is high enough to observe a significant magnitude of the velocity fluctuations in the open section of the domain. Table 4.3 includes the Reynolds number for different channel velocities.

As an indicator, the surface average of the standard deviation of the velocity magnitude (s_u) over different planes normal to z across the domain were observed. They were obtained by Equation (4.10), in which A is the area of an xy plane at a given z. These are relevant quantities for this study, as well as notoriously sensitive to the grid size and time step.

Table 4.3: Equivalence between velocities and Reynolds Numbers

Inlet velocity, m/s	$\mathrm{Re}_c = (\rho u L_c)/\mu$	$\mathrm{Re}_\mathrm{w} = (\rho u 1.41 L_\mathrm{w})/\mu$
4	301	39
10	753	96
12	903	116
13	979	125
14	1054	135
16	1204	154
17	1280	164
18	1355	174
20	1506	193
24	1807	232
28	2108	270

$$RMS(u') = \overline{s_u} = \frac{1}{A}\int_A s_u dA \tag{4.10}$$

The average and standard deviation at each plane were calculated over a moving time window equivalent to the last five residence times of the flow inside the domain. This ensures representative statistically stationary values that are free of the effects of the initialization. Four grids of 823 000, 1 845 000, 3 973 000 and 6 207 000 control volumes were tested, maintaining a maximum CFL of 0.5 in all the simulations. As a result, no appreciable differences were observed in the average velocity magnitude with the different meshes. As it is expected, an increasing value of the standard deviation of the velocity and a decreasing of the sub-grid turbulence viscosity were observed when using finer meshes. Figure 4.4a to 4.4c show those three variables obtained with the four grid sizes. The sensitivity of the problem to the time step was also studied. CFL numbers of 2, 1, 0.5 and 0.25 together with the four million control volumes mesh were analyzed, finding minor differences when using CFL 1 and 0.5, and negligible differences between CFL 0.5 and 0.25. Hence, the study continued ensuring a maximum CFL of 0.5 and the four million cells grid. Figure 4.4d illustrates the effect of the time step on the results.

This study focuses on the velocity fluctuations after the monolith, and it is based on the analysis of the resolved scale, hence, several sub-grid models were tested. Figure 4.5 shows specifically the standard deviation of the velocity using the static Smagorinsky-Lilly (SSL), dynamic Smagorynski-Lilly (DSL) and the Wall-Adapting Local Eddy-viscosity (WALE) sub-grid models, setting 16 m/s as inlet velocity, 300 K as temperature, with the four million cells grid and a maximum CFL of about 0.5. Significant differences explained by the sub-

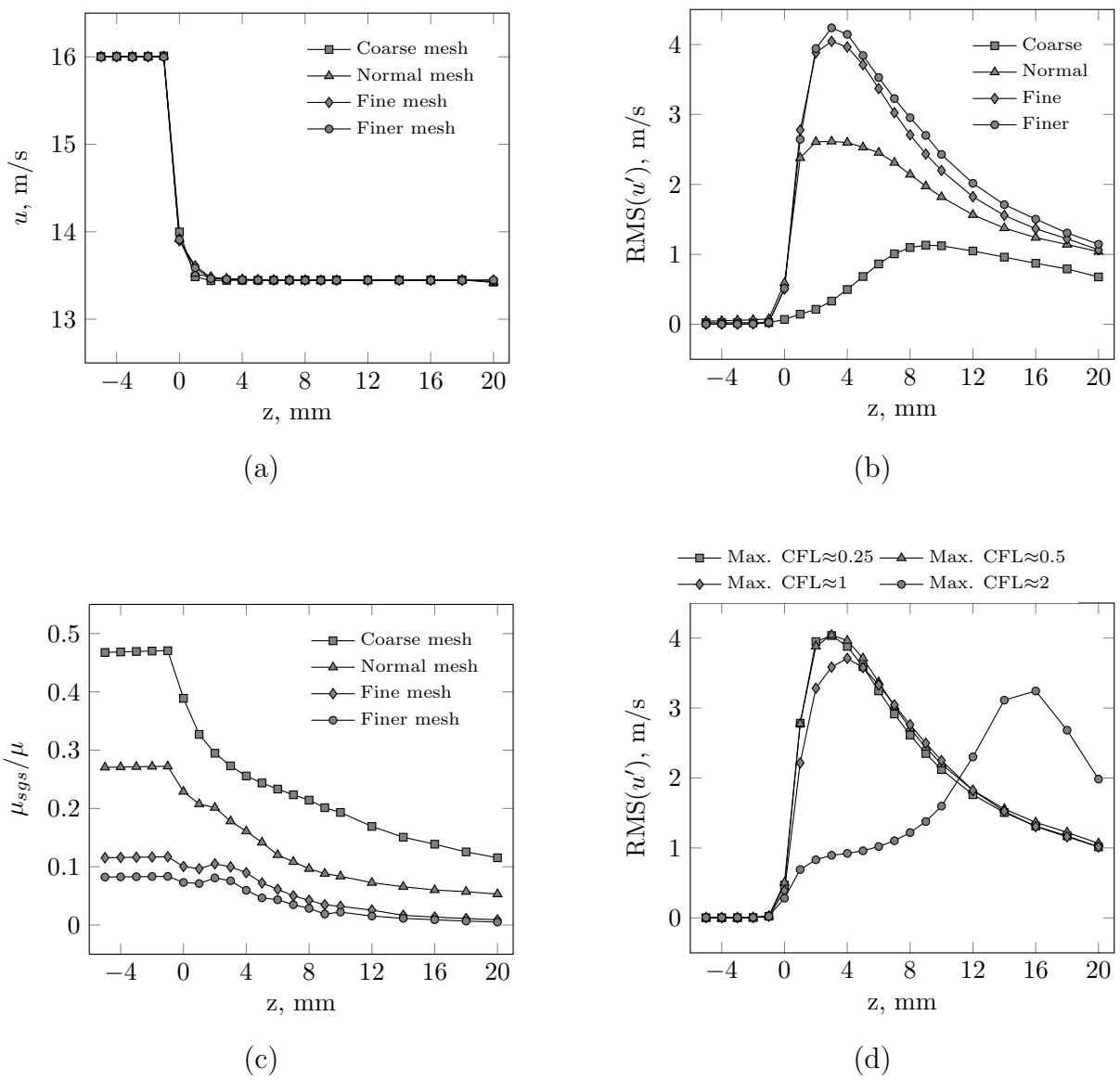

Figure 4.4: Effect of the grid size in (a) the average velocity magnitude, (b) the standard deviation of the velocity magnitude and (c) the sub-grid turbulence viscosity ratio. (d) effect of the CFL in the standard deviation of the velocity magnitude. All using Re_c=1024

grid model were not observed, which can be justified for the relatively small size of the mesh close to the walls and time step in a sufficiently low Reynolds number inside the channels. Substantial local differences were not observed either. The maximum instant μ_{SGS}/μ immediately after the walls was observed to be approximately 0.4, which is of the same magnitude of the surface average μ_{SGS}/μ. Since all of the tested sub-grid models predicted the same relative trend and magnitude for the standard deviation of the velocity, this study continued with the static Smagorinsky-Lilly sub-gid model.

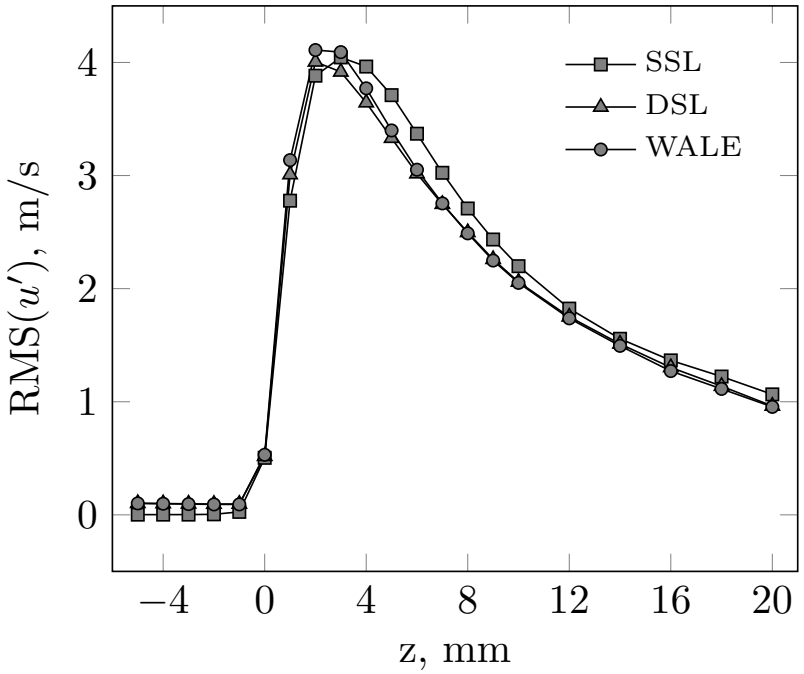

Figure 4.5: Effect of the sub-grid model on the standard deviation of the velocity, using the 3 973 000 cells grid, maximum CFL≈0.5 and Re_c=1024

4.4 Results and discussion

This section discusses the basic flow features occurring at the monolith outlet and their dependence on the Reynolds number. This work uses two different Reynolds numbers to analyze the flow regime, turbulent or laminar, after the monolith. First, the channel Reynolds number, based in the channel size, and second, the wall Reynolds number, referred to the wall thickness of the substrate. Their mathematical expressions are described in Equation (4.11) and (4.12) respectively.

$$\mathrm{Re}_c = \frac{\rho u L_c}{\mu} \tag{4.11}$$

$$\mathrm{Re}_\mathrm{w} = \frac{\rho u \sqrt{2} L_\mathrm{w}}{\mu} \tag{4.12}$$

For both expressions, u is the average velocity magnitude inside the channels and L_w is the wall thickness for an unwashcoated monolith with square section channels.

4.4.1 Flow after the monolith

The standard deviation of the velocity along the last part of the domain was measured with different channel velocities. According to the results shown in Figure 4.6a, there is a critical velocity, below which the flow is stable and steady. As a consequence, velocity fluctuations were not observed neither inside the channels, or in the open section under such operating conditions. If the velocity is sufficiently high, the flow surrounding the last part of the walls between channels plays a key role, being a source of instability, especially after the wall intersections. Figure 4.7a includes an iso-surface of the Q criterion colored by the turbulence kinetic energy using 10 m/s as channel velocity. It is necessary to remark that for LES a pseudo turbulence kinetic energy was calculated by using the Equation (4.13), even in zones where the flow is not strictly fully turbulent. This was done with the purpose to quantify the velocity fluctuations in all directions by a single number, and to compare the results against those obtained by RANS in the same terms. In this study, high values of turbulence kinetic energy in the results from LES cannot be assumed as an indicators of turbulent flow, because it can be high even for regions with laminar unsteady flow. It must be seen simply as an indicator of the magnitude of fluctuations of the velocity.

$$\kappa = \frac{1}{2}\left(u'^2 + v'^2 + w'^2\right) \tag{4.13}$$

As an example, setting 12 m/s as channel velocity, the instability after the corners between walls generates an unsteady laminar flow, with a predominant frequency, however, a value of κ different from zero is obtained if Equation (4.13) is applied. Between 2 mm and 15 mm after the monolith, there is a zone where the flow is transitional, turbulence arises intermittently over the time, but, it is not sustained and decays. Finally, in the last part of the domain, from 15 mm after the monolith, the flow consistently becomes fully turbulent. In addition, Figure 4.7b shows a case where the velocity in channels is 16 m/s. It contains a top view of a Q iso-surface inside two thin layers of 0.2 mm height. The first is around y=1.8 mm, which is the height of a wall between channels. The second, at y=2.4 mm, is at the height of the centre of the channels. As illustrated in this last figure, the instability starts from the corners and propagates from there to the rest of the flow. The magnitude of the fluctuations at a channel velocity of 16 m/s is significantly higher than that observed at 12 m/s, also, the peak of the standard deviation of the velocity is located closer to the end of the monolith.

At constant geometry and fluid properties, the magnitude and tendency of the standard deviation of the velocity is related to the Reynolds number of the channel. The results for several channel velocities are summarized in Figure 4.6a. A first transition is observed with

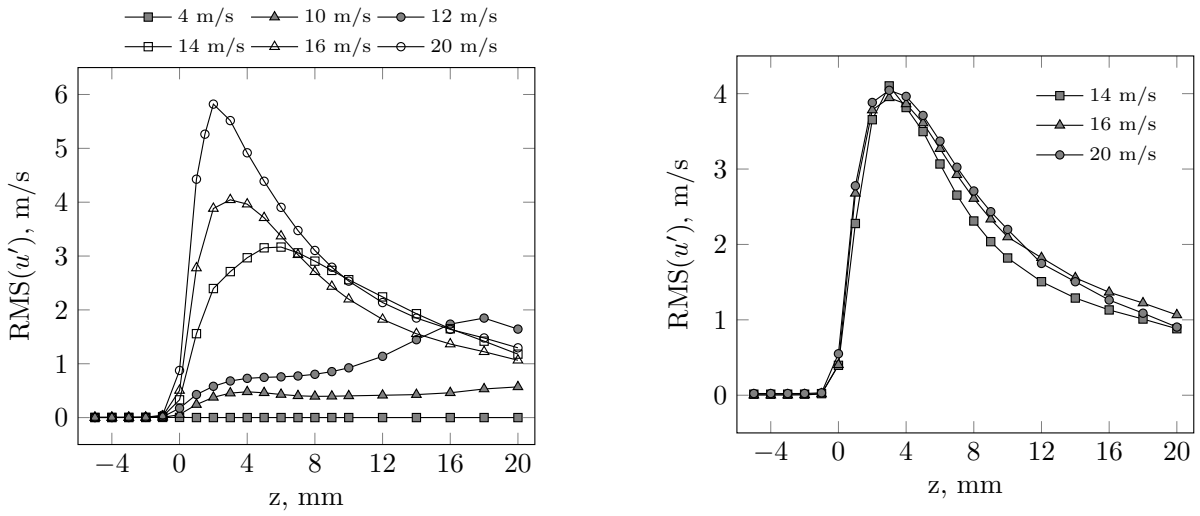

Figure 4.6: Velocity fluctuations after the monolith (a) at different Re_c (b) at different velocities, but manipulating the density to obtain the same Re_c

velocities close to 8 m/s, where the flow becomes unsteady. A second transition is detected for velocities greater than 13 m/s. For them, the peak of the instability moves closer to the end of the monolith, its magnitude increases and the flow becomes fully turbulent earlier in the domain. To confirm that the flow regime depends on the Reynolds number, additional experiments were performed. Figure 4.6b shows three simulations at different channel velocities, but manipulating the density in a form to obtain the same Reynolds number. It can be noticed that the results are approximately the same for the three runs. These results can be compared with those in Figure 4.6a to reinforce the point.

Figure 4.8 shows the instantaneous velocity magnitude over the time on a point at the height of the centre of a channel, at different distances downstream the monolith. There, the channel velocity is 16 m/s (Re_c=1204). At z=0 mm, which is right at the end of the channels, the flow is laminar unsteady, showing oscillations of small magnitude and a clearly predominant frequency. At z=5 mm, the magnitude of the oscillations is larger and other frequencies appear, but there is still a predominating frequency. At 15 mm after the monolith, the frequency content is noticeably more homogeneous. This is in agreement with the results presented in Figure 4.7b.

A consistent pattern can be observed by comparing the dimensionless turbulence kinetic energy and distance from the end of the monolith at different channel velocities (see Figure

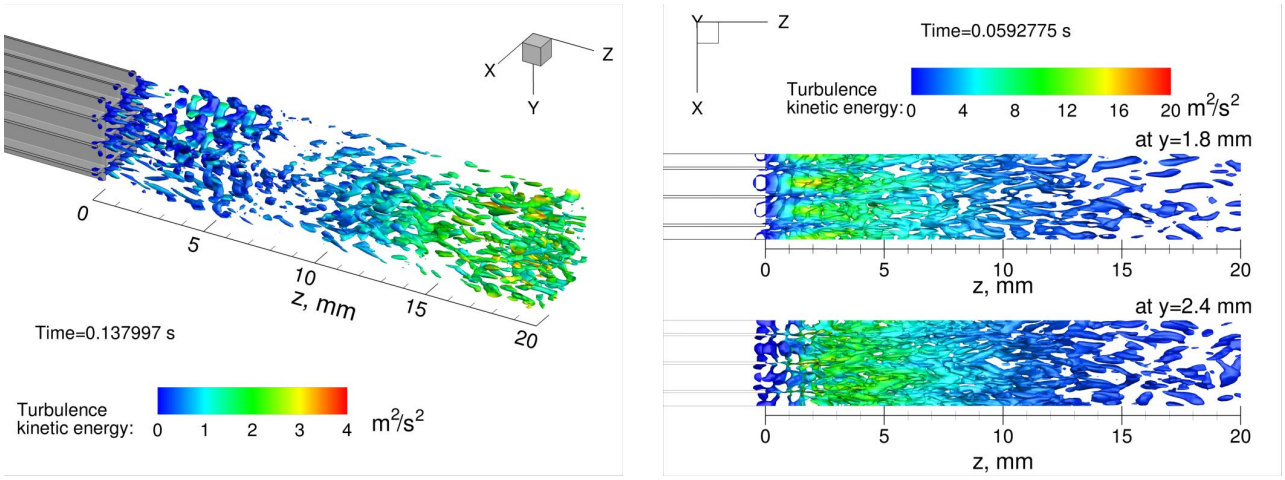

(a) (b)

Figure 4.7: Velocity fluctuations after the monolith setting (a) 12 m/s or Re_c=903 and (b) 16 m/s or Re_c=1204 as channel velocity

4.9). The dimensionless version of the turbulence kinetic energy was defined mathematically by $\kappa^*=\kappa/u_\infty^2$, where u_∞ is the average velocity magnitude once the flow is developed in the open section of the domain. The dimensionless distance was defined as $\delta = z/\sqrt{2}L_w$. Here the denominator is the width of the corners between channels, which is $\sqrt{2}$ times the wall thickness (L_w) for an unwashcoated monolith with square channels. Following the same logic, the flow regime can be related to a Reynolds number based on the same width as $Re_w=\rho u\sqrt{2}L_w/\mu$, where u is the average velocity magnitude inside the channels. Table 4.3 shows the equivalent channel velocity for a series of Re_w.

Analyzing the results in Figure 4.9, for a zone with δ below 70, it can be seen that for Re_w below 100, the flow instability can be neglected and the flow assumed to be steady. For 100 $< Re_w <$ 160, the flow is transitional. It changes intermittently from laminar unsteady to turbulent and vice verse. Finally, when Re_w is greater than 160, the flow becomes turbulent at a short distance after the monolith. In addition, for Re_w above 160, the κ^* profiles are approximately coincident. At any other distance larger than $\delta = 70$, which is about one centimetre for the geometry covered on this study, the influence of other elements, such as the outlet cone, other monoliths, particle filters or piping, might change the flow regime and be the major factor defining the flow regime. It must be emphasized that the information in Figure 4.9 can be used to include the generation of the turbulence after the monolith in RANS and LES models. Since, additional LES experiments, complementary to this work, confirmed that the default use of Darcy's law for flow in porous media does not produce any turbulence after the substrate.

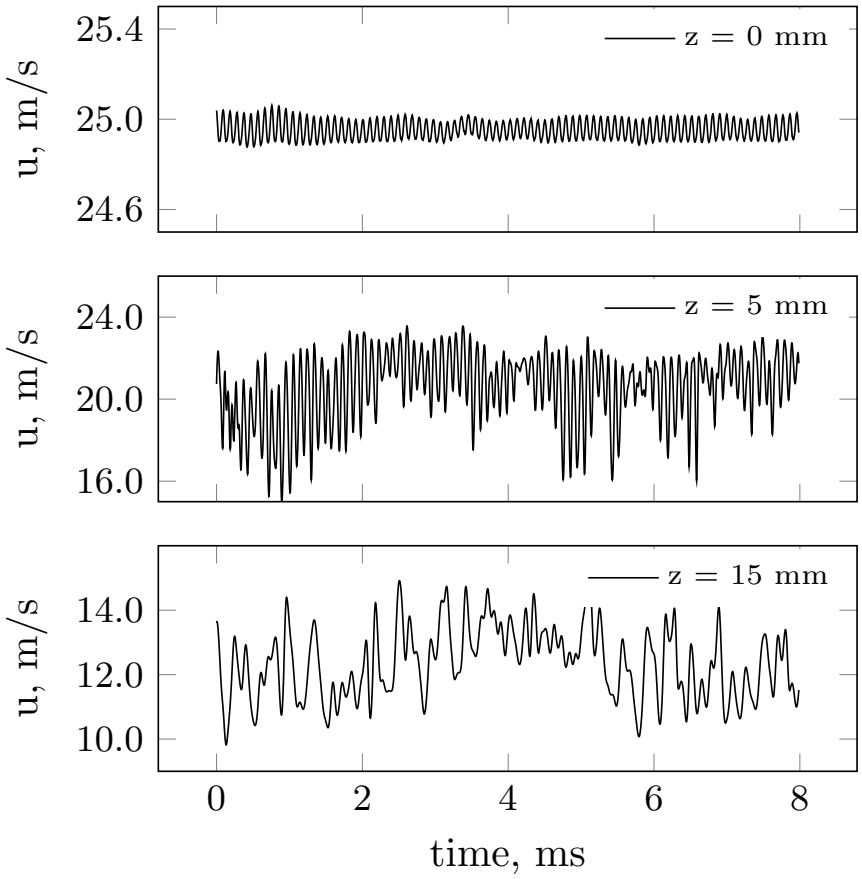

Figure 4.8: Velocity magnitude over the time at three positions downstream the monolith. Here the inlet velocity is 16 m/s (Re_c=1204)

4.4.2 Size of the domain

A typical monolith has thousands of channels running in parallel and it is expected that by including more channels in the domain more instability can be observed and studied. It is also true that at channel scale, the domain can be seen as geometrically periodic or symmetric. Of course, to model the problem as periodic, the flow has to meet that condition too. Given the significant reduction in computational time to analyze the problem in a reduced domain, we compared the results considering from one to nine equivalent channels, as well as setting symmetry and periodicity at the sides of the domain. The resulting standard deviation of the velocity along these domains are included in Figure 4.10. Below the critical condition, where the flow is steady, all the versions of the domain predict the same steady flow. There are differences when the flow is unsteady. In this scenario, all cases predict reasonably well the same statistical parameters if periodic boundary conditions are set. In the case of a

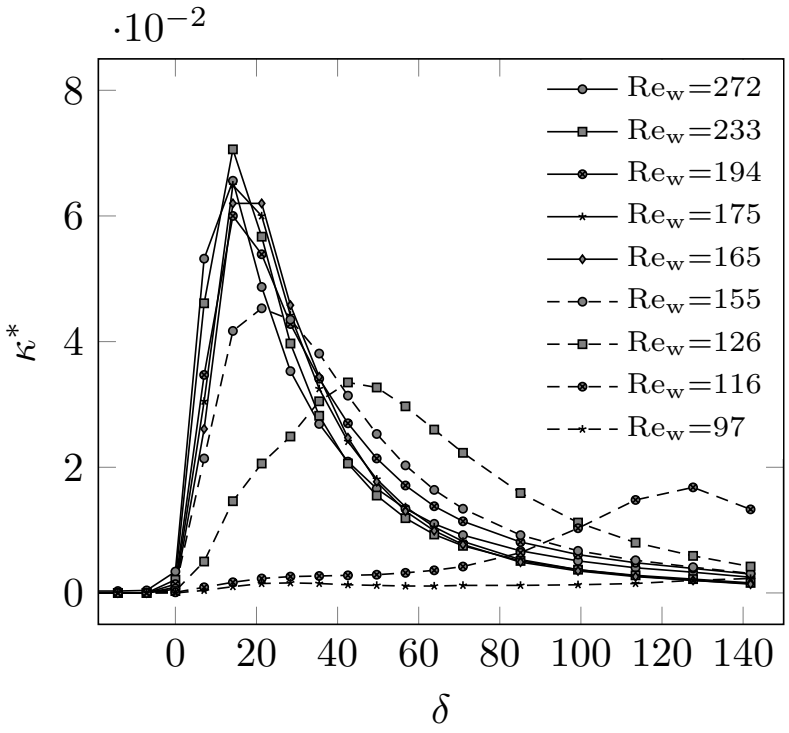

Figure 4.9: Dimensionless turbulence kinetic energy along the domain

single corner and symmetry at the sides, the magnitude of the velocity fluctuations is highly underestimated at the transitional conditions. Increasing the velocity, this underestimation is less pronounced, but still present.

4.4.3 Comparison with RANS models

It is known that RANS models have problems predicting the behaviour of transitional flows like the one after the monolith, however, they are the default option for industrial applications. The results obtained by RANS and LES were compared in terms of the turbulence kinetic energy, and at two conditions. The first using 4 m/s as channel velocity, where LES predicted steady flow, and the second, using 16 m/s as channel velocity, where strong instability was predicted by LES. Results in Figure 4.11 show how the κ-ε largely overestimates the turbulence in all conditions. Setting 16 m/s as channel velocity, the SST model predicts similar levels of turbulence kinetic energy than LES (see Figure 4.7b and 4.11c), but the peak of the fluctuations is displaced downstream. On the other hand, at 4 m/s, where LES predicts steady flow, SST predicts minimum levels of turbulence kinetic energy, which are

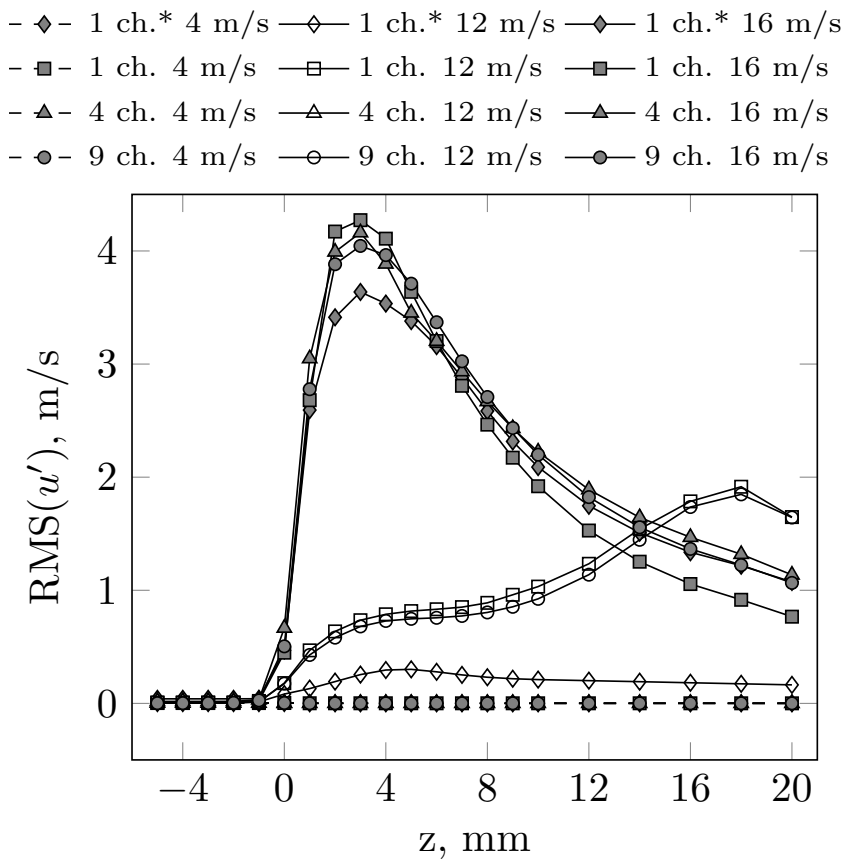

Figure 4.10: Velocity fluctuations after the monolith using different domain sizes. The cases marked with a start considered symmetry instead of periodicity at the boundaries

acceptably accurate. Figure 4.12 shows an additional comparison of LES and RANS. Each point is the surface average turbulence kinetic energy at a series of xy planes at given z values. Results from SST present more diffusion along the domain than LES, nevertheless, the magnitude of the peak predicted by both is comparable. Standard κ-ε predicts a peak in the turbulence kinetic energy times higher than LES and a notably different trend.

Conclusions

The flow after an unwashcoated monolith at different conditions was successfully studied by LES with a discrete channel geometry. The results were analyzed in terms of the flow regime and average and standard deviation of the velocity. Flow instability downstream the monolith was observed and it generates turbulence under certain circumstances. It was found that

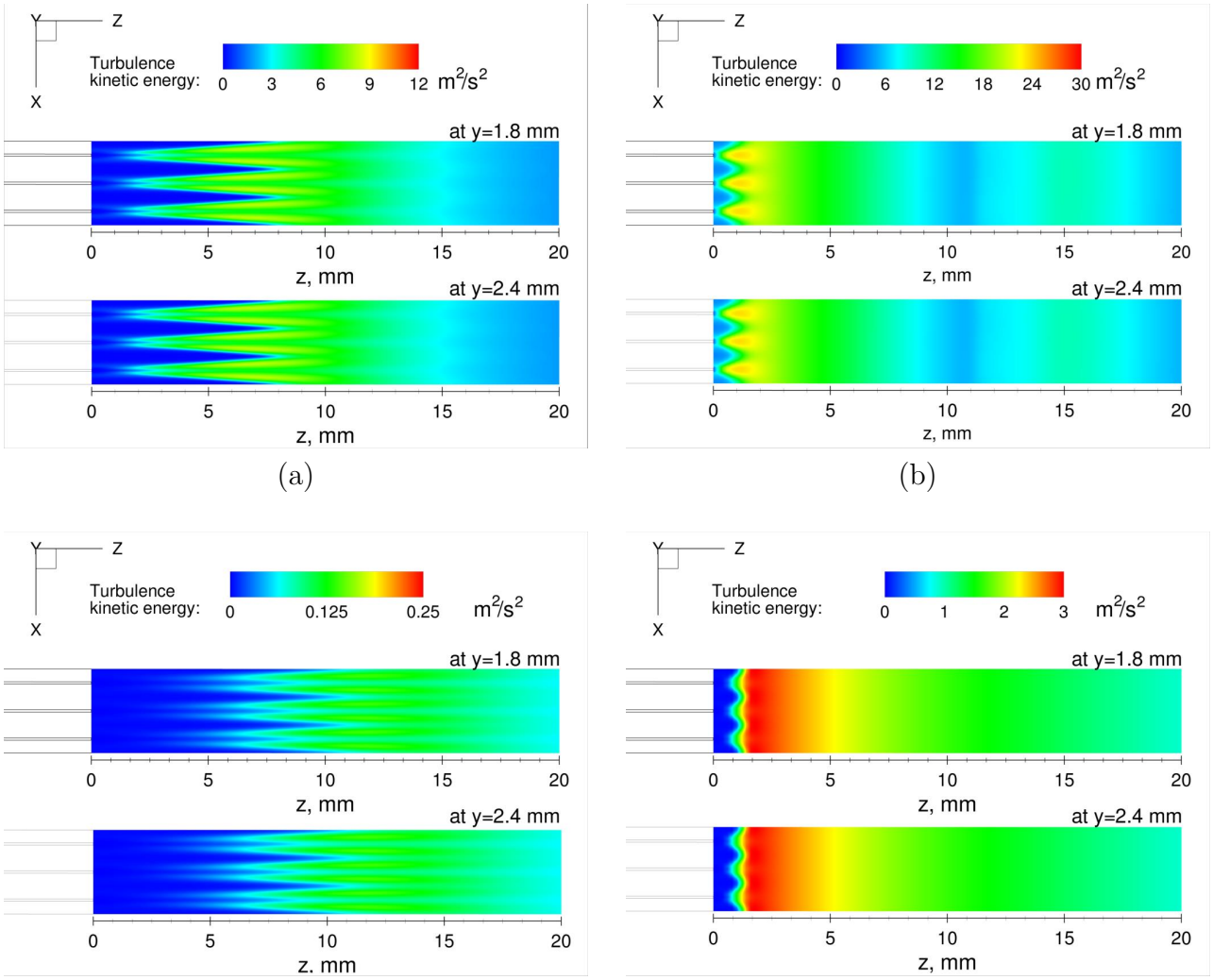

Figure 4.11: Turbulence kinetic energy predicted by (a) SST at 16 m/s, (b) κ-ε at 16 m/s, (c) SST at 4 m/s and (d) κ-ε at 4 m/s

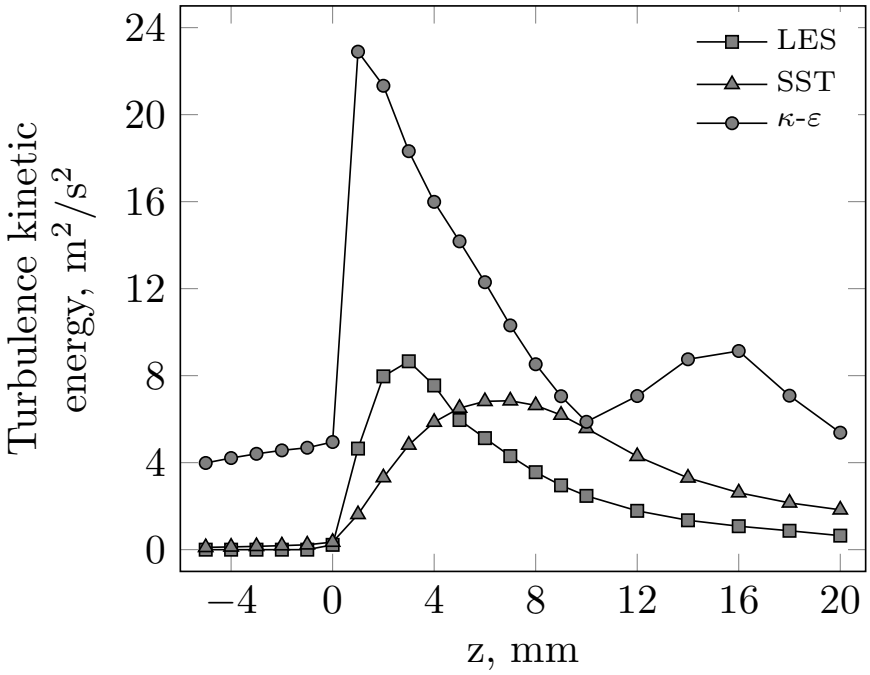

Figure 4.12: Turbulence kinetic energy predicted by different models at 16 m/s as channel velocity (Re_c=1204)

the main source of instability is the flow going around the last part of the substrate and it is focused close to the intersections between walls. For the same reason, this phenomenon is not possible to be observed over 2D domains.

The magnitude of turbulence kinetic energy right after the monolith was observed to be related with the Reynolds number based on the width of the corners of the channels (Re_w). For Re_w below 100 the flow is mainly steady. If Re_w is more than 160 the flow becomes sufficiently unstable to produce turbulence close to the monolith. For the cases in between, turbulence appears sporadically, but, it is not sustained and the regime is transitional. In addition, the dimensionless turbulence kinetic energy lose sensitivity to the Re_w when it is 160 or more, following a reasonably common pattern.

The results of LES were also compared with the predictions obtained by two RANS models in the same geometry. The standard κ-ε predicts magnitudes of turbulence significantly higher than LES. On the other hand, the SST model agrees remarkably more with LES, but there are still notorious differences.

Due to the source of the flow instability is explained by the intersections between walls,

and taking into account the results using nine, four and one equivalent channels, it is conclude that the domain can be considered periodic under the conditions of this study. The modeling of one equivalent channel around an interception between walls, and the setting of periodic boundary conditions at the sides, is sufficient to describe the average velocity and its standard deviation.

Bibliography

[1] Ivan Cornejo, Petr Nikrityuk, and Robert E Hayes. Multiscale RANS-based modeling of the turbulence decay inside of an automotive catalytic converter. *Chemical Engineering Science*, 175:377–386, 2018.

[2] Xiaoding Xu and Jacob A Moulijn. Transformation of a structured carrier into structured catalyst. *Statistics and Operations Research Transactions*, pages 599–616, 1998.

[3] Ronald M Heck, Suresh Gulati, and Robert J Farrauto. The application of monoliths for gas phase catalytic reactions. *Chemical Engineering Journal*, 82(1-3):149–156, 2001.

[4] Pablo Marín, Miguel AG Hevia, Salvador Ordonez, and Fernando V Díez. Combustion of methane lean mixtures in reverse flow reactors: comparison between packed and structured catalyst beds. *Catalysis Today*, 105(3):701–708, 2005.

[5] Steffen Tischer and Olaf Deutschmann. Recent advances in numerical modeling of catalytic monolith reactors. *Catalysis Today*, 105(3-4):407–413, 2005.

[6] Benjamin D Schutt and Martin A Abraham. Evaluation of a monolith reactor for the catalytic wet oxidation of cellulose. *Chemical Engineering Journal*, 103(1):77–88, 2004.

[7] Fatemeh Sadeghi, Behnam Tirandazi, Amirhossein Khalili-Garakani, Simin Nasseri, Ramin Nabizadeh Nodehi, and Navid Mostoufi. Investigating the effect of channel geometry on selective catalytic reduction of NOx in monolith reactors. *Chemical Engineering Research and Design*, 118:21–30, 2017.

[8] Tian Gu and Vemuri Balakotaiah. Analysis of upstream creeping reaction zones in catalytic monolith reactors. *Chemical Engineering Journal*, 317:267–279, 2017.

[9] Audrey Devatine, Hélène Chaumat, Simon Guillaume, Bismath Tati Tchibouanga, Freddy Durán Martínez, Carine Julcour, and Anne-Marie Billet. Hydrodynamic study

of a monolith-type reactor for intensification of gas-liquid applications. *Chemical Engineering and Processing: Process Intensification*, 122:277–287, 2017.

[10] Freddy L Durán Martínez, Carine Julcour, Anne-Marie Billet, and Faïçal Larachi. Modelling and simulations of a monolith reactor for three-phase hydrogenation reactions—rules and recommendations for mass transfer analysis. *Catalysis Today*, 273:121–130, 2016.

[11] M. Iwaniszyn, M. Piatek, A. Gancarczyk, P.J. Jodlowski, J. Lojewska, and A. Kolodziej. "Flow resistance and heat transfer in short channels of metallic monoliths: Experiments versus CFD". *International Journal of Heat and Mass Transfer*, 109:778 – 785, 2017.

[12] AA Avramenko, AI Tyrinov, and IV Shevchuk. Start-up slip flow in a microchannel with a rectangular cross section. *Theoretical and Computational Fluid Dynamics*, 29(5-6):351, 2015.

[13] AA Avramenko, AI Tyrinov, IV Shevchuk, NP Dmitrenko, AV Kravchuk, and VI Shevchuk. Mixed convection in a vertical circular microchannel. *International Journal of Thermal Sciences*, 121:1–12, 2017.

[14] Dimitrios Karamitros and Grigorios Koltsakis. Model-based optimization of catalyst zoning on SCR-coated particulate filters. *Chemical Engineering Science*, 173:514–524, 2017.

[15] G Bella, V Rocco, and M Maggiore. Study of inlet flow distortion effects on automotive catalytic converters. *Journal of Engineering for Gas Turbines and Power. Transactions of the ASME*, 113(3):419–426, 1991.

[16] Anthony J Baxendale. The Role of Computational Fluid Dynamics in Exhaust System Design and Development. *SAE Technical Paper*, No. 931072, 1993.

[17] Ankan Kumar and Sandip Mazumder. Toward simulation of full-scale monolithic catalytic converters with complex heterogeneous chemistry. *Computers & Chemical Engineering*, 34(2):135–145, 2010.

[18] François Bertrand, Christophe Devals, David Vidal, Cyrille Séguineau de Préval, and Robert E Hayes. Towards the simulation of the catalytic monolith converter using discrete channel-scale models. *Catalysis Today*, 188(1):80–86, 2012.

[19] RE Hayes, Anton Fadic, Joeseph Mmbaga, and A Najafi. CFD modelling of the automotive catalytic converter. *Catalysis Today*, 188(1):94–105, 2012.

[20] RJ Clarkson, SF Benjamin, TS Jasper, and NS Girgls. An integrated computational model for the optimisation of monolith catalytic converters. *SAE Technical Paper*, No. 931071, 1993.

[21] Soo-Jin Jeong. A full transient three-dimensional study on the effect of pulsating exhaust flow under real running condition on the thermal and chemical behavior of closed-coupled catalyst. *Chemical Engineering Science*, 117:18–30, 2014.

[22] I Cornejo, P Nikrityuk, and RE Hayes. Turbulence decay inside the channels of an automotive catalytic converter monolith. *Emission Control Science and Technology*, 3(4):302—309, 2017.

[23] Anna Holmgren and Bengt Andersson. Mass transfer in monolith catalysts-CO oxidation experiments and simulations. *Chemical Engineering Science*, 53(13):2285–2298, 1998.

[24] Shi-Jin Shuai and Jian-Xin Wang. Unsteady temperature fields of monoliths in catalytic converters. *Chemical Engineering Journal*, 100(1):95–107, 2004.

[25] Tian Gu and Vemuri Balakotaiah. Impact of heat and mass dispersion and thermal effects on the scale-up of monolith reactors. *Chemical Engineering Journal*, 284:513–535, 2016.

[26] Nicolaas Engelbrecht, Steven Chiuta, Raymond C Everson, Hein WJP Neomagus, and Dmitri G Bessarabov. Experimentation and CFD modelling of a microchannel reactor for carbon dioxide methanation. *Chemical Engineering Journal*, 313:847–857, 2017.

[27] Fatemeh Khodadadian, Merijn W De Boer, Ali Poursaeidesfahani, J Ruud Van Ommen, Andrzej I Stankiewicz, and Richard Lakerveld. Design, characterization and model validation of a LED-based photocatalytic reactor for gas phase applications. *Chemical Engineering Journal*, 333:456–466, 2018.

[28] Henrik Strom, Srdjan Sasic, and Bengt Andersson. Effects of the turbulent-to-laminar transition in monolithic reactors for automotive pollution control. *Industrial & Engineering Chemistry Research*, 50(6):3194–3205, 2011.

[29] Fredrik Ekström and Bengt Andersson. Pressure drop of monolithic catalytic converters experiments and modeling. *SAE Technical paper*, No. 2002-01-1010, 2002.

[30] Ismail Tosun, Deniz Uner, and Canan Ozgen. Critical reynolds number for newtonian flow in rectangular ducts. *Industrial & Engineering Chemistry Research*, 27(10):1955–1957, 1988.

[31] Minyi Xu, Jianpeng Zhang, Pengfei Li, and Jianchun Mi. On two distinct reynolds number regimes of a turbulent square jet. *Theoretical and Applied Mechanics Letters*, 5(3):117–120, 2015.

[32] M Breuer, J Bernsdorf, Durst F Zeiser, and F Durst. Accurate computations of the laminar ow past a square cylinder based on two different methods: lattice-boltzmann and finite-volume. *International Journal of Heat and Fluid Flow*, 21:186–196, 2000.

[33] Matthias Hettel, Claudia Diehm, Bentholhoda Torkashvand, and Olaf Deutschmann. Critical evaluation of in situ probe techniques for catalytic honeycomb monoliths. *Catalysis Today*, 216:2–10, 2013.

[34] ANSYS Fluent Theory Guide v17.2. ANSYS Inc., Canonsburg, PA, USA, 2016.

[35] Joseph Smagorinsky. General circulation experiments with the primitive equations: I. The basic experiment. *Monthly Weather Review*, 91(3):99–164, 1963.

[36] Douglas K Lilly. A proposed modification of the germano subgrid-scale closure method. *Physics of Fluids A: Fluid Dynamics*, 4(3):633–635, 1992.

[37] Franck Nicoud and Frédéric Ducros. Subgrid-scale stress modelling based on the square of the velocity gradient tensor. *Flow, Turbulence and Combustion*, 62(3):183–200, 1999.

[38] Brian Edward Launder and Dudley Brian Spalding. *Lectures in mathematical models of turbulence*. Academic Press, New York, USA, 1972.

[39] Florian Menter. Two-equation eddy-viscosity turbulence models for engineering applications. *AIAA journal*, 32(8):1598–1605, 1994.

Chapter 5

Effect of substrate geometry and flow condition on the turbulence generation after a monolith[1]

Abstract

This paper reports a study of turbulence generation after a monolith honeycomb. Large Eddy Simulation is used to analyze the turbulence generated when steady, turbulent or pulsating flow leaves a monolith channel. Substrates with different cell densities, wall thicknesses, and channel cross-sectional shapes are investigated. According to the results, the magnitude of the turbulence generated depends on the wall thickness and monolith void fraction, but not much on the cell density. For pulsating flow, different pulsating frequencies produced only slightly different results, however, the amplitude of the pulsations is proportional to the magnitude of the turbulence generated. The outflow of the channels can act as a jet and trigger turbulence along a distance from ten to thirty channel diameters after the monolith, significantly affecting the total pressure drop and the inlet conditions for other elements in series downstream, such as particulate filters or other substrates.

Keywords: CFD, monolith, turbulence, channel, catalytic converter

[1] A version of this article has been published. Cornejo, I., Nikrityuk, P., & Hayes, R. E. (2020). Effect of substrate geometry and flow condition on the turbulence generation after a monolith. The Canadian Journal of Chemical Engineering. Url: `https://doi.org/10.1002/cjce.23687`

5.1 Introduction

Honeycomb type substrates have several advantages over other catalyst supports, such as a lower pressure drop and a better flow distribution. They are commonly made of ceramic and are extensively used in automotive catalytic converters and other industrial applications [1–3]. At a macro scale, many important variables, such as the conversion efficiency, ageing, and pressure drop of the reactor, depend on the flow distribution across the substrate. Kreutzer et al. [4] presented an interesting discussion about the advantages of structured reactors and the importance of the study of the extra-particle length on applications where the heat and mass transfer, and pressure drop are important. At a channel scale, the chemical reactions are influenced by the mass and heat transfer, which makes the flow regime, and the shape and size of the channels important subjects of study that can improve significantly the yield of the reactor when manipulated correctly. There is interest in 3D printed substrates, which allows the fabrication of many geometrical configurations [5–7]. That, complemented with the increasing power of computers, opens a wide range of options for designers to optimize substrates and reactors. However, both the shape of the whole substrate and the cross-section of the channels are commonly limited to simple shapes. Reported works on channel shape optimization usually investigate only basic geometries such as square, circular, and triangular cross-sections [8–10]. Also, the entire substrate is typically cylindrical and the literature analyzing its shape optimization is sparse [11]. A deeper understanding of the heat and mass transfer inside honeycomb type substrate is required if complex designs are desired.

As an example, the heat and mass transfer are higher through the entry length of the substrate [12], hence, it appears as a logical solution to use several short substrates instead of a large single one. However, available mathematical models of monoliths are not robust enough for optimization purposes because they include only a few of the many phenomena, such as the effect of the upstream turbulence inside the substrate, variable thermal properties, flow entering at an angle to the channels, and so on [13]. Another important subject in many applications is pulsating flow, because it is common in micro channels [14]. Also, there is evidence that when there is upstream turbulence before the substrate the flow becomes laminar inside it, but it results in pulsating flow downstream [15]. Those phenomena should be studied at a channel scale. There, computational models may be especially useful because having accurate experimental data at a channel scale is challenging [16].

The objective of this paper is to study and quantify the effect of the channel geometry, pulsating flow, and remaining turbulence inside monolith channels on the generation of turbu-

lence after a monolithic substrate. This is especially relevant for applications with monoliths in series and for reverse flow reactors [17–19]. This investigation includes an extensive set of highly resolved computational experiments at a channel scale using Large Eddy Simulations (LES). The remainder of the paper is organized as follows: Section 2 describes the computational model used. Section 3.1 discusses the size of the domain required to capture all of the flow motion. Having defined that, the influence on the kinetic energy downstream the substrate of two groups of variables is analyzed. The first group are geometrical features of the substrate, such as the channel diameter and wall thickness, and its effect is reported in Section 3.2. The second group are the flow features, such as the magnitude of the remaining turbulence intensity, and their influence is reported in Section 3.3. Section 4 finishes with the conclusions.

5.2 Computational model

This section describes the computational domain, inlet conditions, principal assumptions, and the methodology of calculation used in this investigation.

5.2.1 Computational domain

Monolithic honeycomb substrates are commonly specified by their cell density, wall thickness and channel cross-sectional shape. For example, a 400/6.5 square channel substrate has 400 cells per square inch (CPSI), a wall thickness of 6.5 mil (0.1651 mm) and channels with a square cross-section. With that information it is possible to calculate the channel size and void fraction, which are 1.10 mm and 0.74 respectively for this example. The cell density, wall thickness and channel shape are the three geometric variables of this investigation. Channels with circular and square cross-section were considered. Monolith channels can be also triangular and hexagonal, but during the coating process the washcoat tends to accumulate preferentially in the corners of the channels, making their cross-section closer to a circle [20–23]. It should be also considered that when the coating layer is thick, the channel breadth reduces significantly, and the transverse section is almost circular. Such a substrate shape was also investigated. All the substrates considered are listed in Table 5.1.

Table 5.1: List of substrates tested

	Cell density, CPSI	D_H, mm	Wall thickness, mil	Channel shape
Substrate 1	400 (620†)	1.20	2.5 (0.0635 mm)	square
Substrate 2	800 (1240†)	0.84	2.5 (0.0635 mm)	square
Substrate 3	400 (620†)	1.10	6.5 (0.1651 mm)	square
Substrate 4	400 (620†)	1.10	6.5 (0.1651 mm)	circular
Substrate 4	400 (620†)	0.90	6.5 (0.1651 mm)	circular

†Thousands of cells per square metre

The substrates tested were selected to follow an orthogonal experimental design, which means that it is always possible to find a pair of substrates that are different in only one feature. The effect of the cell density can be investigated by comparing substrates 1 and 2, the wall thickness with substrates 1 and 3, and the channel shape with substrates 3 and 4. The length of the domain was composed of the last part of the substrate and the open section downstream of it. According to previous works, the strongest interactions which lead to unsteady and turbulent flow occur at the corners of the channels, hence, the domain must be three-dimensional [24]. Also, the minimum section of the substrate required to capture all of the flow features is one equivalent cell, that is, a whole channel plus the half of the walls around it. That constitutes a fundamental geometrical unit of the substrate. For simulations of fully steady flow only a fourth of such a section is enough if symmetry is applied. However, this investigation deals with flow in transition, hence, the whole section must be considered together with the use of periodic boundary conditions at the top, bottom, left, and right of sides of the open section. The whole domain and the cross-section of the channels are shown in Figure 5.1. The length of the piece of substrate ($L_{channel}$) was kept constant as 10 channel hydraulic diameters, which was long enough to avoid inlet effects because the inlet profile was set to be fully developed in all cases. The extension of the open section after the monolith (L_{open}) was enlarged to 40 channel hydraulic diameters to ensure developed flow for all the conditions analyzed in this study.

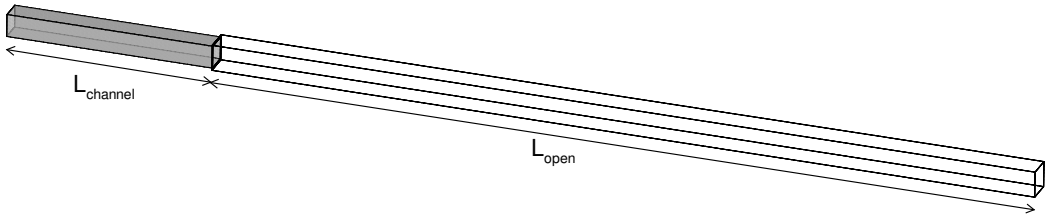

(a) Isometric view of the whole domain

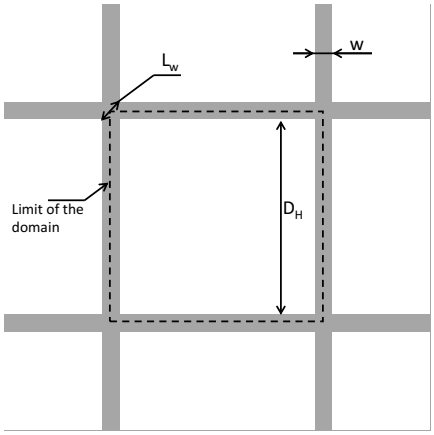

(b) Square channels

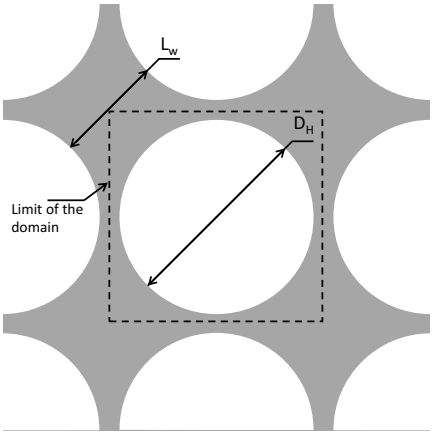

(c) Circular channels

Figure 5.1: (a) Whole computational domain. Cross-section of a substrate with (b) square channels and (c) circular channels. The limits of the computational domain are marked with dashed lines in (b) and (c)

For square channels, the domain was discretized in a series of completely orthogonal hexahedral meshes with a characteristic length of the computational cells of about 50 μm. The number of elements changed according to the cell density and wall thickness of every substrate (the size of the elements was kept constant), however, all meshes contained of the order of the one million three hundred thousand computational cells. For circular channels fully cartesian elements are not possible, but the sacrifice in orthogonality was compensated for with an extra refinement close to walls. Especial care was taken on having a very smooth transition from the size of the elements close to the walls to those at the free stream zone at the centre of the channels, which led to a number of elements of approximately 15% greater than that for square channels.

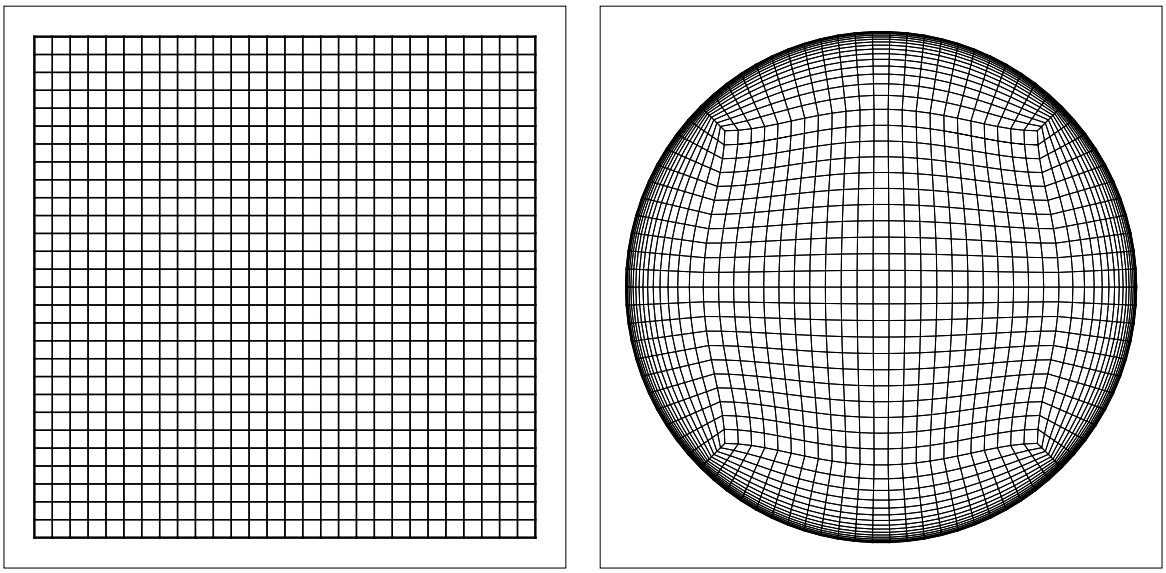

(a) Square channel (b) Circular channel

Figure 5.2: Cross-section of the computational grid inside the channels

The grid independence of the solution was investigated by refining the mesh systematically and monitoring the time average and standard deviation of the velocity field. When refining the mesh, from approximately six hundred thousand to one million three hundred thousand cells the average velocity was exactly the same. The standard deviation of the resolved part of the velocity increased proportionally to the number of elements, however, the total total kinetic energy, which considers the subgrid content, remained constant for the meshes with more than six hundred thousand of cells. It was desired to maintain the largest possible portion of the flow in the resolved scale, hence the meshes used for every substrate were the finest among those tested, despite the computational cost. The maximum wall y^+ observed was 2.46, and the maximum μ_{sgs}/μ was 3.23.

5.2.2 Flow model

The flow was modelled with Large Eddy Simulation (LES) because an accurate description of the flow regime is a central point of this investigation. LES has been validated in many contexts and it is suitable to predict laminar-turbulent transitions. The transport equations for mass and momentum are [25]:

$$\frac{\partial \rho}{\partial t} + \frac{\partial}{\partial x_j}(\rho \overline{u}_i) = 0 \tag{5.1}$$

$$\frac{\partial \overline{u}_i}{\partial t} + \overline{u_j}\frac{\partial \overline{u}_i}{\partial x_j} = -\frac{1}{\rho}\frac{\partial \overline{p}}{\partial x_i} + \frac{\partial}{\partial x_j}\left(\nu\frac{\partial \overline{u}_i}{\partial x_j} + \frac{1}{\rho}\frac{\partial \tau_{ij}}{\partial x_j}\right) \tag{5.2}$$

The overbar in the transport equations indicates a filtered variable as usual for LES. The subgrid-scale stress (τ_{ij}) in Equation (5.2) was modelled with the Dynamic Kinetic Energy Subgrid-Scale (DKE) model proposed by Kim and Menon [26] as follows:

$$\tau_{ij} = \frac{2}{3}\rho k_{sgs}\delta_{ij} - 2C_k k^{1/2}\Delta_f \overline{S}_{ij} \tag{5.3}$$

The DKE model has been successfully validated in several circumstances [27, 28]. No underlying assumption of the equilibrium of the transferred energy between the grid filter and subgrid scales is needed. Instead of that, it uses the following transport equation for k_{sgs}:

$$\rho\frac{\partial k_{sgs}}{\partial t} + \rho\overline{u}_j\frac{\partial k_{sgs}}{\partial x_j} = -\tau_{ij}\frac{\partial \overline{u}_i}{\partial x_j} - C_\varepsilon\rho\frac{k_{sgs}^{3/2}}{\Delta_f} + \frac{\partial}{\partial x_j}\left(\frac{\mu_{sgs}}{\sigma_k}\frac{\partial k_{sgs}}{\partial x_j}\right) \tag{5.4}$$

where

$$\mu_{sgs} = k\rho k_{sgs}^{1/2}\Delta_f$$

The parameters C_k and C_ε are determined dynamically, and Δ_f is the characteristic length of the control volume. Further details about the model and its parameters can be found in Kim and Menon [26].

5.2.3 Solver settings and boundary conditions

The model was implemented in ANSYS Fluent 18.2 [29]. The working fluid was considered atmospheric air at 300 K. The discretization scheme for momentum was set to bounded central differencing, for time it was Bounded Second Order Implicit Euler scheme, and the pressure velocity coupling was solved with the SIMPLE algorithm [30]. The simulations were solved partially in a 40-core work station, consisting of two Intel Xenon E5-2698 v4 @2.2 GHz and partially in the Compute Canada Graham cluster (www.computecanada.ca). The time step was manipulated to ensure a maximum CFL number below one in all the runs. The convergence criterion for time steps was reaching a value of scaled residuals of the order of 10^{-5}. The time averages and standard deviations of the velocity field were calculated with time until stable values along a moving window of four space times of extension were obtained. This ensures representative statistically stationary values free of initialization effects. The walls of the substrate were set as no-slip walls. The boundaries at the left-right and top-

bottom of the open section were set as periodic boundaries. The outlet was treated as outflow and the inlet as a velocity inlet with a fully developed velocity profile. The magnitude of the average inlet velocity changed according the desired channel Re of every case. The list of all the computational experiments covered in this study are listed in Table 5.2.

Table 5.2: List of computational experiments

Subs. geom.	Channel shape	D_H mm	w mm	Inlet flow regime	Re_w	Re_c	Turb. int.	μ_t/μ	Pulse freq.	Pulse ampl.
400/2.5	Square	1.20	0.0635	Steady	105	1642	-	-	-	-
400/2.5	Square	1.20	0.0635	Steady	158	2464	-	-	-	-
400/2.5	Square	1.20	0.0635	Steady	184	2874	-	-	-	-
400/2.5	Square	1.20	0.0635	Steady	211	3285	-	-	-	-
400/6.5	Square	1.10	0.1651	Steady	232	1129	-	-	-	-
400/6.5	Square	1.10	0.1651	Steady	310	1506	-	-	-	-
400/6.5	Square	1.10	0.1651	Steady	542	2635	-	-	-	-
400/6.5	Square	1.10	0.1651	Steady	619	3011	-	-	-	-
800/2.5	Square	0.84	0.0635	Steady	126	1437	-	-	-	-
800/2.5	Square	0.84	0.0635	Steady	152	1725	-	-	-	-
800/2.5	Square	0.84	0.0635	Steady	177	2012	-	-	-	-
800/2.5	Square	0.84	0.0635	Steady	202	2299	-	-	-	-
400/6.5	Circular	0.90	0.1651	Steady	242	616	-	-	-	-
400/6.5	Circular	0.90	0.1651	Steady	484	1232	-	-	-	-
400/6.5	Circular	0.90	0.1651	Steady	726	1848	-	-	-	-
400/6.5	Circular	0.90	0.1651	Steady	967	2464	-	-	-	-
400/6.5	Circular	0.90	0.1651	Steady	362	370	-	-	-	-
400/6.5	Circular	0.90	0.1651	Pulsating	362	370	-	-	10 kHz	±15%
400/6.5	Circular	0.90	0.1651	Pulsating	362	370	-	-	10 kHz	±50%
400/6.5	Circular	0.90	0.1651	Pulsating	362	370	-	-	10 kHz	±100%
400/6.5	Circular	0.90	0.1651	Pulsating	362	370	-	-	5 kHz	±50%
400/6.5	Circular	0.90	0.1651	Pulsating	362	370	-	-	20 kHz	±50%
400/6.5	Circular	0.90	0.1651	Turbulent	362	370	10%	10	-	-
400/6.5	Circular	0.90	0.1651	Turbulent	362	370	20%	20	-	-
400/6.5	Circular	0.90	0.1651	Turbulent	362	370	40%	40	-	-

5.2.4 Analysis methodology

This investigation considered two Re numbers. The first was the channel Re (Re_c) and the other (Re_w) was based on the maximum thickness of solid at the corners of the channels (see Figure 5.1) and were calculated as follows:

$$\mathrm{Re}_c = \frac{\rho u_c D_H}{\mu} \tag{5.5}$$

$$\mathrm{Re}_\mathrm{w} = \frac{\rho u_c \mathrm{w}}{\mu} \tag{5.6}$$

The magnitude of the turbulence was quantified by the dimensionless turbulence kinetic energy (k^*), which was calculated as the turbulence kinetic energy over the square of the channel velocity as in Equation (5.7). The total turbulence kinetic energy (k) was considered the summation of the one at the resolved scale (k_{res}) and the one contained in the subgrid scale (k_{sgs}).

$$k^* = \frac{k}{u_c^2} = \frac{k_{res} + k_{sgs}}{u_c^2} \tag{5.7}$$

where

$$k_{res} = \frac{1}{2}\left(u'^2_1 + u'^2_2 + u'^2_3\right) \tag{5.8}$$

For every simulation, after reaching statistically stationary state, the surface average of u'^2_1, u'^2_2, u'^2_3, and k_{sgs} over a series of planes perpendicular to the stream wise direction were registered and used to calculate k. In this study some regions of the domain show unsteady laminar flow, which return a non-zero k, hence, this value should not be interpreted as an indicator of the presence of turbulence directly.

5.3 Results and discussion

We start by analyzing the visualization of the unsteadiness generated when flow is leaving a substrate. Figures 5.3 (a) and (b) are instantaneous iso-surfaces of Q-criterion and (c) and (d) are contour plots of vorticity magnitude over a centre plane along the domain. For the square channel, the region dominated by the effect of flow around the last part of the walls between channels extends up to approximately 10 channel hydraulic diameters after the substrate. Then, there is a zone with large coherent structures followed by a turbulent zone. In the case with circular channels, the size of the recirculating zones right after the substrate is greater (see Figure 5.3), leading to an earlier development of larger rotating structures in

terms of absolute distance, however, when scaling by the channel diameter, both zones are of a comparable length.

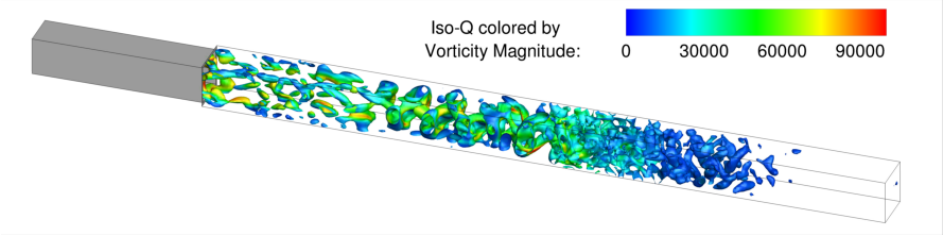

(a) Square channel, Re_w=232, D_H=1.1 mm

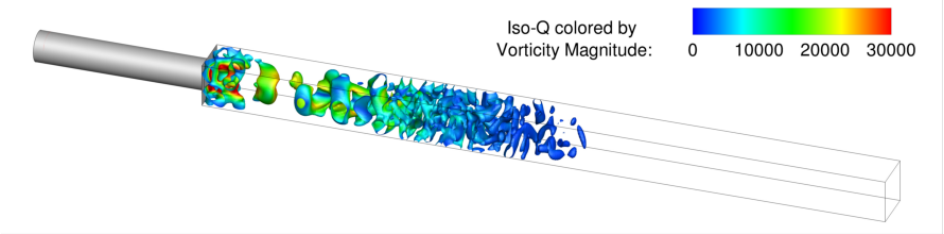

(b) Circular channel, Re_w=362, D_H=0.9 mm

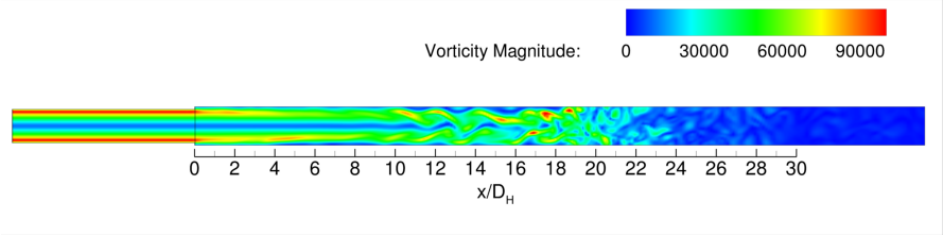

(c) Square channel, Re_w=232, D_H=1.1 mm

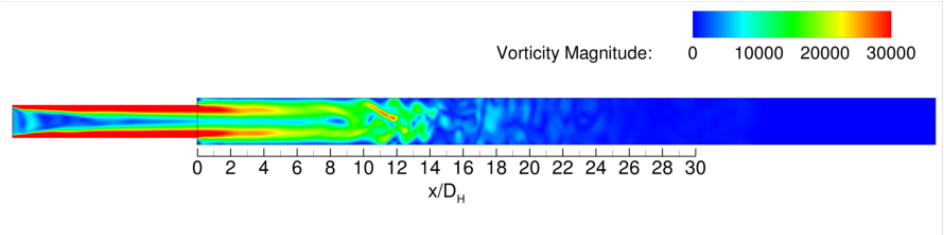

(d) Circular channel, Re_w=362, D_H=0.9 mm

Figure 5.3: Visualization of the unsteady flow after a monolith with square and circular channels. For both cases the inlet flow is steady. Vorticity is in 1/s, and Q is in $1/s^2$

It must be pointed out that for both examples in Figure 5.3 the predominant phenomenon triggering turbulence is the outflow of the honeycomb acting as a jet. Further sections of the paper extend the analysis.

5.3.1 Periodicity of the domain

Flow leaving a honeycomb channel differs from flow leaving a single orifice. The last may behave as a jet, meanwhile, the former is more similar to a series of jets separated by a short distance. Interaction between the outflow of different channels may be strong and it becomes necessary to analyze the size of the domain required to capture every aspect of the flow motion. The periodicity of the domain was previously investigated for a monolith with square cross-section channels [24]. In that paper, the resulting k^* downstream the substrate in a domain containing one, four and nine equivalent-channels was analyzed using LES. As a result, it was found that the k^* profiles was the same for the three domain sizes provided that periodic boundary conditions were used at the top-bottom and left-right boundaries. On the other hand, when symmetry was used, the magnitude of k^* observed was lower than that when using periodic boundaries for the one equivalent-channel domain. In this paper, an homologous study was briefly performed to corroborate if such results are also valid for circular channels. Figure 4a shows a domain containing one and four channels, to which periodic boundary conditions were set for all the cases. According to the results shown in Figure 4b, the two curves that show a peak of k^* ($\mathrm{Re_w}$=512) are essentially the same. Meanwhile, those for $\mathrm{Re_w}$=256 differ, but are still comparable.

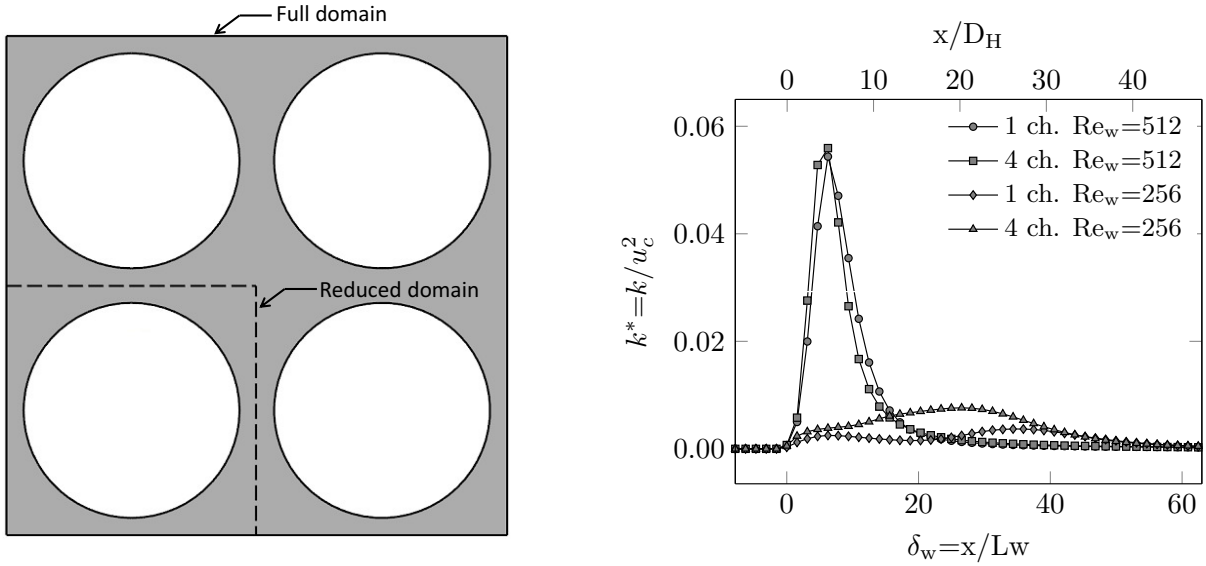

(a) (b)

Figure 5.4: (a) Frontal view of the complete and reduced domains and (b) comparison of k^* profiles for two different domain sizes

In the zone of interest, at a high $\mathrm{Re_w}$ the k^* profile produced by the two domains are almost identical. That allows us to conclude that the periodicity of the solution observed for

square channels is also valid for circular channels, and that modelling a single honeycomb cell is enough provided that periodic boundary conditions are applied.

5.3.2 Effect of the substrate geometry

This section shows the results of the effect of channel size, wall thickness, and channel cross-sectional shape on the turbulence generation after the substrate.

Figure 5.5 summarizes the dimensionless turbulence kinetic energy profiles downstream of the monolith for several substrate configurations. For all the cases, the k^* profiles converge to a unique curve and become insensitive to $\mathrm{Re_w}$ when increasing the channel velocity above a critical value. By comparing Figures 5.5 (a) and (b) it can be seen that at a constant cell density for two different wall thicknesses the turbulence kinetic energy profiles resulted in a different magnitude, but following the same trend. At a low channel velocity, the outflow of the substrate behaves as a jet, but when the channel velocity increases, the flow around the walls dominates and turbulence is triggered almost immediately after the substrate. Also, the peak value of k^* resulted higher for the case with a higher wall thickness. Results shown in Figures 5.5 (a) and (c) used the same wall thickness but a different cell density. The peak values of k^* for both cases are comparable, confirming the observed when comparing Figures 5.5 (a) and (b). That is, the magnitude of the turbulence generated after the substrate is a function of the wall thickness rather than the cell density. However, the tail of the k^* profiles after the peak seems to be much more dissipative. This agrees with the results reported by Cornejo et al. [24], where the length scale of the turbulence generated after the monolith was found to be related to the size of the channels. Smaller channels generate smaller vortices, consequently, are a more dissipate environment for the turbulence.

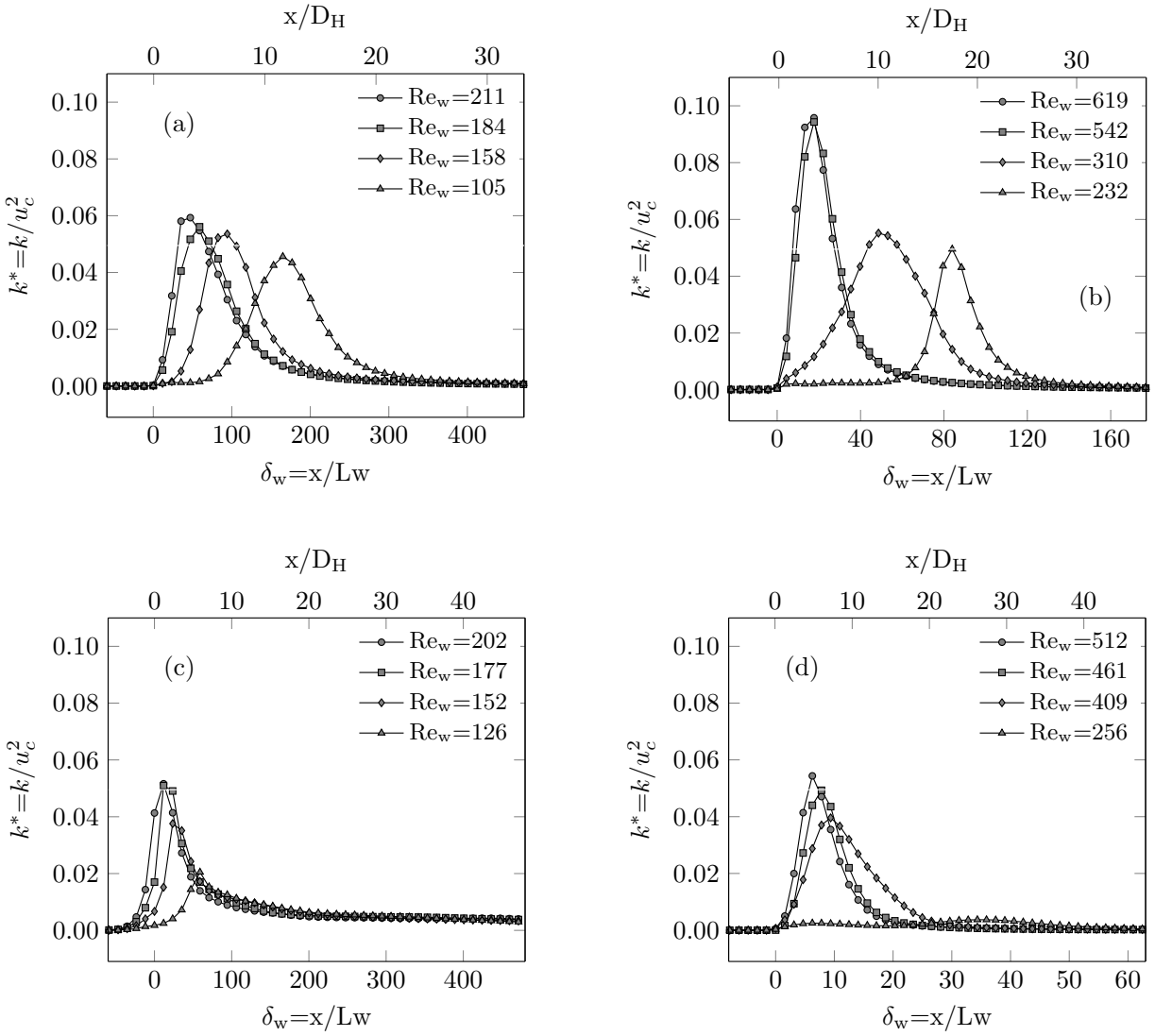

Figure 5.5: Profile $k*$ downstream the substrate for several monolith geometries. The x-axis is scaled by L_w in the bottom and by D_H in the top of every plot. (a) Square 400/2.5, (b) Square 400/6.5, (c) Square 800/2.5 and (d) Circular 400/6.5 D_H=0.9 mm

The effect of the channel geometry can be investigated by comparing Figures 5.5 (b) and (d), which have the same cell density and wall thickness, but a different channel cross-sectional shape. It can be seen that the position of the peak value of k^* expressed in x/D_H was not affected, opposite to that observed when scaling x by L_w. Also, the magnitude of the peak is about 40% lower for circular channels. The square channel substrate has a shorter L_w than that for circular channels, which may promote the interaction between the outflow from different channels and lead to a higher k^*.

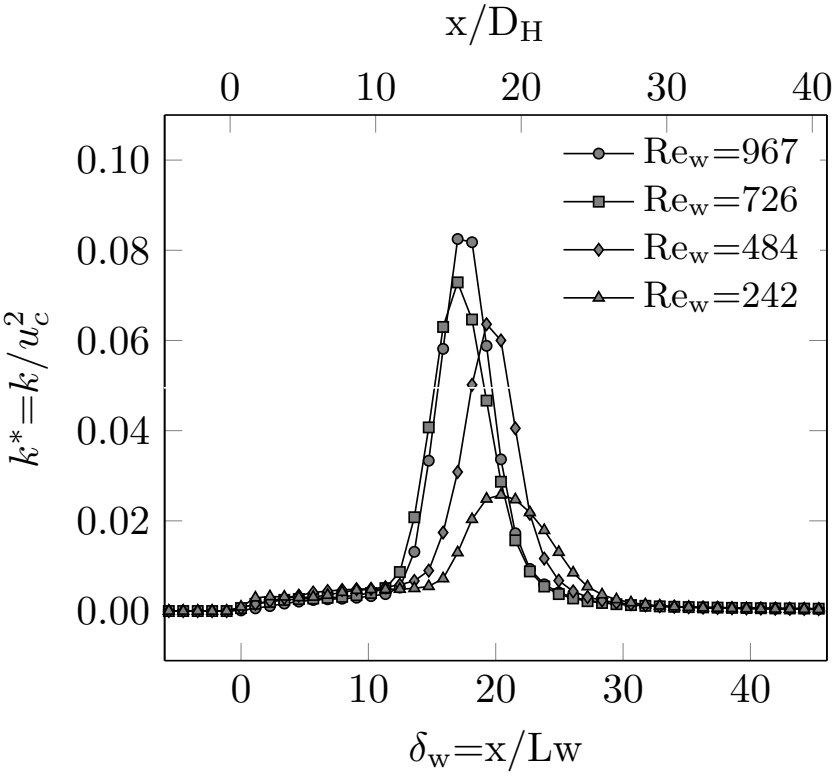

Figure 5.6: k^* profiles for a 400/6.5 substrate with circular channels and D_H=1.1 mm

The void fraction of the substrate also affects the turbulence generation pattern. That can be seen by comparing Figure 5.5 (d) and Figure 5.6. The magnitude of the peak value of k^* is approximately 15% higher for the case with a higher void fraction. However, the largest difference is the shape of the profiles along the open section after the substrate and the location of the peak of k^*. When decreasing the void fraction the phenomenon dominating the unsteadiness of the flow was the outflow of the channels acting as a jet, which happened for relatively low Re_w only in the substrates with a higher void fraction. That also confirms that both the magnitude and especially the location in where turbulence is triggered are highly dependant on the geometry of the substrate.

5.3.3 Effect of pulsating and turbulent flow

This section shows the effect of remaining turbulence and pulsating flow inside the substrate on the turbulence generation after the monolith. All the runs were performed considering a 400/6.5 monolith substrate with circular channels with a breadth of 0.9 mm as D_H.

For many applications, the pulsating flow entering the substrate is approximately si-

nusoidal [31], so pulsations can be characterized by their amplitude and frequency. Both variables were analyzed separately in this paper. Figure 5.7 (a) shows the k^* profiles for several pulsation amplitudes. As expected, the higher the amplitude of the pulsations, the higher the magnitude of k^*. Pulsations contribute to the unsteadiness of the flow in a magnitude significantly higher than that resulting from the turbulence triggered from fully laminar flow (see Figure 5.5), it is sustained at lower $\mathrm{Re_w}$, and it is not captured when assuming steady flow.

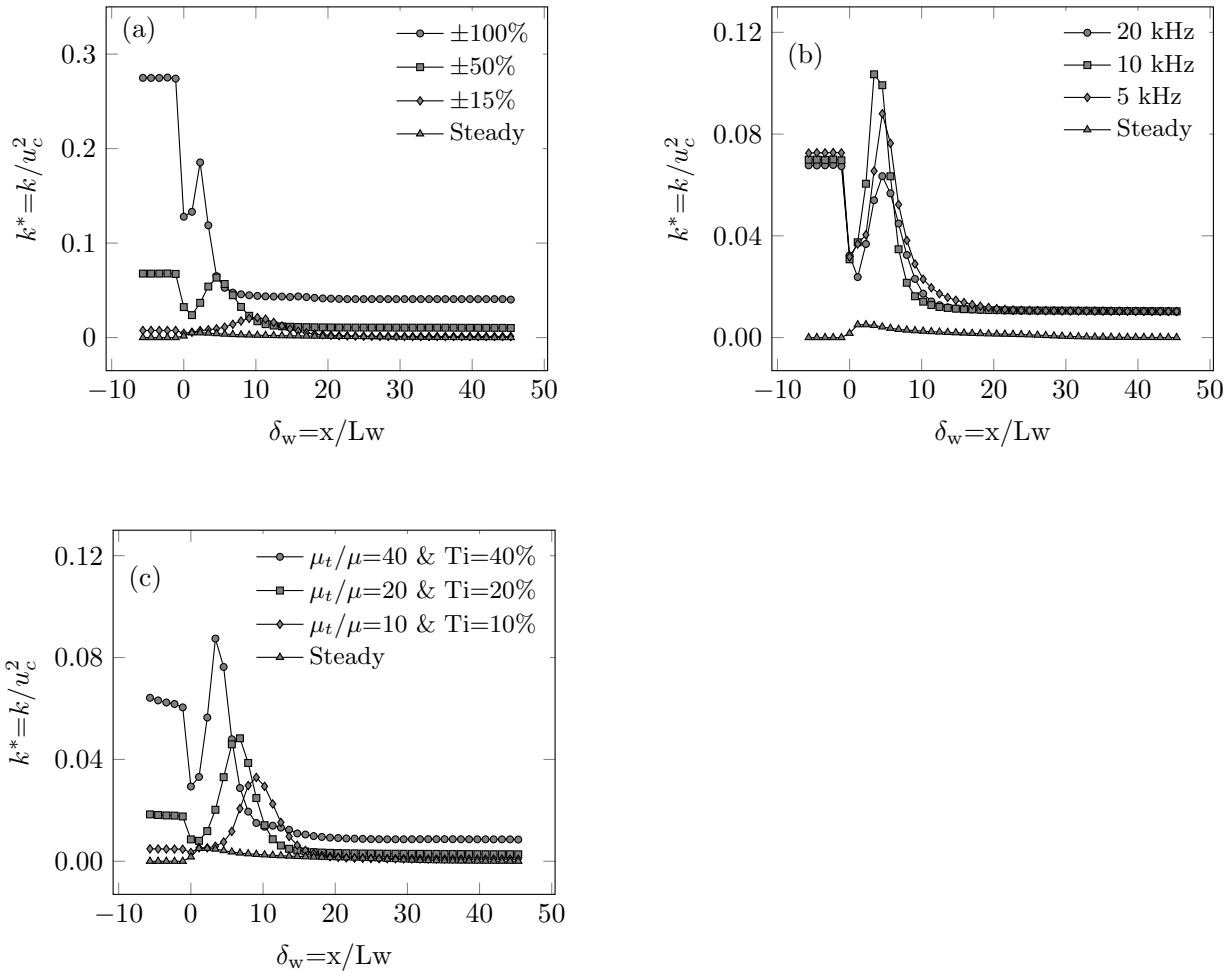

Figure 5.7: k^* profiles after the substrate for (a) pulsating flow at several amplitudes, (b) pulsating flow at several frequencies, and (c) non-pulsating flow with several vales of remaining turbulence. All the runs considered circular channels of a 400/6.5 monolith, with a channel breadth of 0.9 mm and Re_c=370

The effect of the frequency of the pulsations in the flow field after the substrate was analyzed by considering three different frequencies while keeping constant the amplitude of the

fluctuations. Results are shown in Figure 5.7 (b). For the three frequencies the k^* profiles were similar inside and after the channels. The largest difference was found in the peak value of k^*. However, the decay rate of k^* was almost the same. Compared to the amplitude of the pulsations, the frequency affected less the flow regime along and after the substrate.

For the remaining turbulence inside the channels, three scenarios were analyzed. Let us name them low, medium, and high turbulence. The turbulence was quantified by two variables, the turbulence viscosity ratio (μ_t/μ) and the turbulence intensity (Ti). Results are summarized in Figure 5.7 (c). Given the sub-critical Re_c Turbulence decreases along the channels, but, even a small amount of remaining turbulence modifies significantly the k^* profile after the monolith compared to that when the flow is completely steady. The effect of the remaining turbulence is similar to the one when there is pulsating flow inside the channels. This is consistent with the reported previously [15], where the turbulence upstream the substrate decays completely inside the channels, however, the flow becomes laminar unsteady, with a pulsating behavior.

All the $k*$ profiles shown in Figure 5.5 are consistent with those previously reported [24], and they can be implemented in computational models of full scale reactors with available methodologies [13]. Scaling k by u_c^2 made all the k peaks collapse to the same order of magnitude. Unfortunately, finding a scaling factor for the x-axis was much more challenging and was not achieved. It is not obvious what to use as a characteristic length since the object thickness is the standard choice when analyzing flow around objects, that is $\mathrm{L_w}$ in this case. According to the results, the channel hydraulic diameter resulted in a better option for several cases, but not for the all of them; hence further investigation about that is still required. For the particular cases with very high coat loading (see Figure 5.6) the same methodology still can be used, but the turbulence triggering zone should not be placed exactly after the outlet of the substrate to have accurate results. Cases in Figure 5.7, which incorporate pulsating flow, require further investigation because the implementation of the same turbulence triggering model in reactor scale simulations may not apply.

5.4 Conclusions

The effect of the substrate geometry and flow regime on the turbulence generation after a honeycomb type monolith was successfully investigated using Large Eddy Simulation.

The peak of k^* after the substrate was found to be related to the wall thickness rather than to the channel shape and cell density. According to the results, the placement of the peak seems to depend on which phenomenon is dominating between the flow around the solid and the flow as a jet when leaving the substrate. For cases with a void fraction above 50% the triggering of turbulence came from the unsteadiness of flow around the last part of the substrate and there is a significant peak of k^* close to the end of the substrate. All the analyzed cases using a substrate with a void fraction below 50% showed a triggering of turbulence close to 20 channel diameters after the end of the substrate, which was significantly further downstream when compared to the 1 to 4 channel diameters observed for the peak of k^* in the other cases.

The effect of the remaining turbulence on the flow field was found to be comparable to the one of pulsating flow. They both changed the turbulence generation pattern, however, remaining turbulence at the end of the channels is not expected to be high, so pulsating flow requires more attention. The amplitude of the pulsations showed the larges effect on the magnitude of k^*, meanwhile, the effect of the frequency was the smallest. Also it should be remarked that the magnitude of the turbulence generated when having pulsating flow can be several times the one when having steady flow.

In all of the analyzed cases considering steady flow inside the channels, the turbulence generated because of the flow leaving the substrate can be incorporated into reactor scale simulations to provide a multiscale physical consistency with available models. On the other hand, special attention should be given to substrates with low void fraction because the zone of turbulence triggering occurs at a significant distance from the end.

The turbulence generation pattern when considering pulsating flow was quite different in magnitude and trend compared to the case of steady flow inside of the substrate. Hence, further investigation on how to account for that in reactor scale simulations should be carried out, specially considering that the magnitude of the turbulence generated can be several times higher than when pulses are neglected.

Bibliography

[1] Piyanut Inbamrung, Thana Sornchamni, Chaiwat Prapainainar, Sabaithip Tungkamani, Phavanee Narataruksa, and Goran N Jovanovic. Modeling of a square channel monolith reactor for methane steam reforming. *Energy*, 2018.

[2] Nur Izwanne Mahyon, Tao Li, Ricardo Martinez-Botas, Zhentao Wu, and Kang Li. A

new hollow fibre catalytic converter design for sustainable automotive emissions control. *Catalysis Communications*, 120:86–90, 2019.

[3] Audrey Devatine, Hélène Chaumat, Simon Guillaume, Bismath Tati Tchibouanga, Freddy Durán Martínez, Carine Julcour, and Anne-Marie Billet. Hydrodynamic study of a monolith-type reactor for intensification of gas-liquid applications. *Chemical Engineering and Processing: Process Intensification*, 122:277–287, 2017.

[4] Michiel T. Kreutzer, Freek Kapteijn, and Jacob Moulijn. Shouldn't catalysts shape up?: Structured reactors in general and gas–liquid monolith reactors in particular. *Catalysis Today*, 111(1-2):111–118, 2006.

[5] Harshul Thakkar, Stephen Eastman, Amit Hajari, Ali A Rownaghi, James C Knox, and Fateme Rezaei. 3D-printed zeolite monoliths for CO2 removal from enclosed environments. *ACS Applied Materials & Interfaces*, 8(41):27753–27761, 2016.

[6] A Quintanilla, JA Casas, P Miranzo, María Isabel Osendi, and Manuel Belmonte. 3D-Printed Fe-doped silicon carbide monolithic catalysts for wet peroxide oxidation processes. *Applied Catalysis B: Environmental*, 235:246–255, 2018.

[7] Sarah Couck, Julien Cousin-Saint-Remi, Stijn Van der Perre, Gino V Baron, Clara Minas, Patrick Ruch, and Joeri FM Denayer. 3D-printed SAPO-34 monoliths for gas separation. *Microporous and Mesoporous Materials*, 255:185–191, 2018.

[8] Manuel Presti, Lorenzo Pace, Jan Hodgson, Gino Bella, and Alessandro De Maio. A Computational and Experimental Analysis for Optimization of Cell Shape in High Performance Catalytic Converters. *SAE Technical Paper*, No. 2002-01-0355, 2002.

[9] Vemuri Balakotaiah and David H West. Shape normalization and analysis of the mass transfer controlled regime in catalytic monoliths. *Chemical Engineering Science*, 57(8):1269–1286, 2002.

[10] Tiziano Maffei, Stefano Rebughini, Giancarlo Gentile, Stefan Lipp, Alberto Cuoci, and Maestri Matteo. CFD analysis of the channel shape effect in monolith catalysts for the CH4 partial oxidation on Rh. *Reaction Kinetics and Catalysis Letters*, 86(7):1099–1106, 2014.

[11] Anna Holmgren, Thomas Gronstedt, and Bengt Andersson. Improved flow distribution in automotive monolithic converters. *Reaction Kinetics and Catalysis Letters*, 60(2):363–371, 1997.

[12] Theodore L Bergman, Frank P Incropera, David P DeWitt, and Adrienne S Lavine. *Fundamentals of Heat and Mass Transfer*. John Wiley & Sons, New Jersey, NY, USA, 2011.

[13] Ivan Cornejo, Robert E Hayes, and Petr Nikrityuk. A new approach for the modeling of turbulent flows in automotive catalytic converters. *Chemical Engineering Research and Design*, 140:308–319, 2018.

[14] Mukul Tikekar, Shiv Govind Singh, and Amit Agrawal. Measurement and modeling of pulsatile flow in microchannel. *Microfluidics and nanofluidics*, 9(6):1225–1240, 2010.

[15] Ivan Cornejo, Gonzalo Cornejo, Petr Nikrityuk, and Robert E Hayes. Entry length convective heat transfer in a monolith: The effect of upstream turbulence. *International Journal of Thermal Sciences*, 138:235–246, 2019.

[16] Matthias Hettel, Claudia Diehm, Bentholhoda Torkashvand, and Olaf Deutschmann. Critical evaluation of in situ probe techniques for catalytic honeycomb monoliths. *Catalysis Today*, 216:2–10, 2013.

[17] B Liu, RE Hayes, Y Yi, J Mmbaga, MD Checkel, and M Zheng. Three dimensional modelling of methane ignition in a reverse flow catalytic converter. *Computers & Chemical Engineering*, 31(4):292–306, 2007.

[18] Soo-Jin Jeong. A full transient three-dimensional study on the effect of pulsating exhaust flow under real running condition on the thermal and chemical behavior of closed-coupled catalyst. *Chemical Engineering Science*, 117:18–30, 2014.

[19] Ivan Cornejo, Petr Nikrityuk, and Robert E Hayes. Pressure correction for automotive catalytic converters: A multi-zone permeability approach. *Chemical Engineering Research and Design*, 147:232–243, 2019.

[20] F Zhang, RE Hayes, and ST Kolaczkowski. A new technique to measure the effective diffusivity in a catalytic monolith washcoat. *Chemical Engineering Research and Design*, 82(4):481–489, 2004.

[21] Marek Václavík, Petr Kočí, Vladimír Novák, and David Thompsett. NOx conversion and selectivity in multi-layer and sequential DOC-LNT automotive exhaust catalysts: Influence of internal transport. *Chemical Engineering Journal*, 329:128–134, 2017.

[22] RE Hayes, B Liu, R Moxom, and M Votsmeier. The effect of washcoat geometry on mass transfer in monolith reactors. *Chemical Engineering Science*, 59(15):3169–3181, 2004.

[23] Pritpal S Dhillon, Michael Harold, Di Wang, Ashok Kumar, and Saurabh Joshi. Transport and Reaction in Washcoated Monoliths: Cu-SSZ-13 Selective Catalytic Reduction and Dual-Layer Cu-SSZ-13+ Pt/Al2O3 Ammonia Slip Catalyst. *Reaction Chemistry & Engineering*, 2019.

[24] Ivan Cornejo, Petr Nikrityuk, and Robert E Hayes. Turbulence generation after a monolith in automotive catalytic converters. *Chemical Engineering Science*, 187:107–116, 2018.

[25] ANSYS Fluent Theory Guide v18.2. ANSYS Inc., Canonsburg, PA, USA, 2017.

[26] Won-Wook Kim, Suresh Menon, Won-Wook Kim, and Suresh Menon. Application of the localized dynamic subgrid-scale model to turbulent wall-bounded flows. In *35th aerospace sciences meeting and exhibit.*, page 210, Reno, NV, USA, 1997.

[27] Won-Wook Kim and Suresh Menon. A new dynamic one-equation subgrid-scale model for large eddy simulations. In *33rd Aerospace Sciences Meeting and Exhibit*, Reno, NV, USA, 1995.

[28] Suresh Menon and Won-Wook Kim. High Reynolds number flow simulations using the localized dynamic subgrid-scale model. In *34th Aerospace Sciences Meeting and Exhibit*, page 425, Reno, NV, USA, 1996.

[29] ANSYS Fluent Software Package v18.2, 2017. ANSYS Inc., Canonsburg, PA, USA.

[30] Suhas Patankar. *Numerical heat transfer and fluid flow*. CRC press, Boca Raton, Florida, USA, 1980.

[31] SF Benjamin, H Zhao, and A Arias-Garcia. Predicting the flow field inside a close-coupled catalyst—the effect of entrance losses. *Proceedings of the Institution of Mechanical Engineers, Part C: Journal of Mechanical Engineering Science*, 217(3):283–288, 2003.

Chapter 6

A new approach for the modeling of turbulent flows in automotive catalytic converters[1]

Abstract

This work presents a new approach to predict turbulent flows inside of a catalytic converter taking into account a decay and generation of turbulence at the entrance and exit zone of a monolith, respectively. The core part of the converter is a monolith substrate, which is commonly represented as a homogeneous porous medium due to computational limitations. Such a simplification eliminates any interaction with the solid when the flow is entering and leaving the substrate. This work extends the previously addressed decay of the turbulence entering the monolith, with the turbulence generation exiting it. This is achieved by using an immersed boundary condition immediately after the porous medium, whose values are estimated using a local Reynolds, based on observations made in a discrete channel geometry. The results are compared with commonly used converter models, finding substantial differences in the effective viscosity and kinetic energy inside and after the monolith. The proposed model agrees with the one obtained in a discrete geometry, and it also prevents unrealistic changes of the flow regime observed in existing models. The distinguishing feature of the proposed model is the simplicity of its implementation in any commercial or open-source CFD software. The model performance in RANS and LES simulations of the whole automotive converter is illustrated.

[1]A version of this article has been published. Turbulence generation after a monolith in automotive catalytic converters. Cornejo, I., Hayes, R. E., & Nikrityuk, P. (2018). A new approach for the modeling of turbulent flows in automotive catalytic converters. Chemical Engineering Research and Design, 140, 308-319.

Keywords: Catalytic converter, automotive, monolith, CFD, multiscale, turbulence

A monolith is a porous structure containing many parallel channels that form a honeycomb type structure. They are extensively used as a substrate for automotive catalytic converters, although, given their relatively low pressure drop, high open frontal area and flow distribution, they have been used in other industrial processes [1–4]. Figure 6.1 shows an example of a typical catalytic converter, which is composed of a diffuser, a substrate, and an outlet cone. Catalyst metals, such as platinum and palladium, are contained in a thin porous layer of washcoat that adheres to the internal walls of the channels of the substrate.

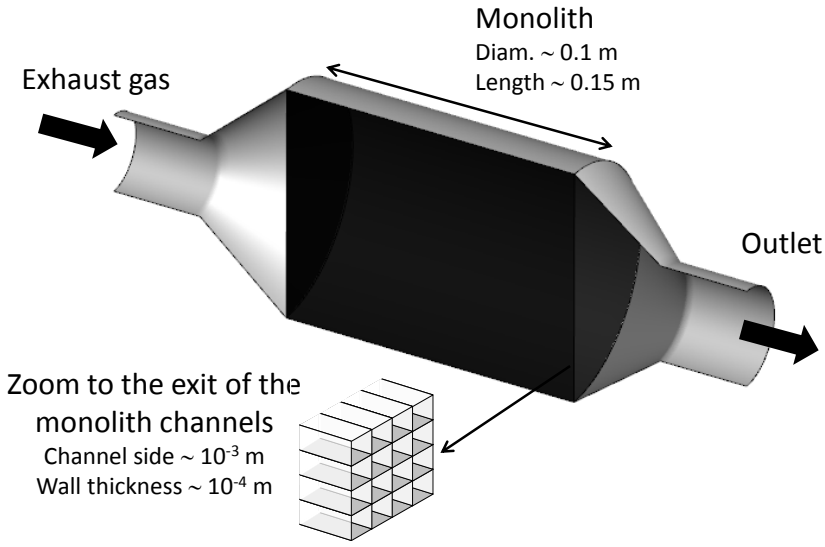

Figure 6.1: Schematic of a catalytic converter

There is a large body of literature on the numerical simulation of monolith reactors, with different computational models used at a converter and channel scale [5–7]. Channel scale refers to the dimension of each channel, and models at this scale are usually reserved for analyzing one channel only. A single channel model in three dimensions can require hundreds of thousands of control volumes. Simulations at the converter scale are necessary to study some of the most relevant variables of the reactor, such as the pressure drop and flow distribution. A single substrate can contain tens of thousands of channels, therefore spatially resolved numerical models of complete monoliths require significant computational power to solve [8], therefore, monoliths are usually modeled as a continuous porous medium for industrial applications [9–11]. A special treatment must be given to the porous medium to obtain results representative of an actual honeycomb. For example, the fluid flow in the radial direction,

which does not happen in a monolith, can be avoided by using an anisotropic porous medium with radial permeability at least two orders of magnitude lower than its axial permeability. Entire converter RANS simulations performed using a continuum model predict high levels of turbulence along with the entire porous zone, which is not expected at the low Reynolds numbers typically observed inside a monolith. In commercial software, such as COMSOL [12] and Fluent [13], this problem is traditionally solved by specifying the continuum as a laminar zone. This option sets the turbulence viscosity to zero immediately once the flow enters the continuum. With this option, the production of new turbulence kinetic energy inside the continuum is prevented, but the turbulence reaching the substrate inlet is transported from the beginning to the end of the laminar zone almost unchanged [14]. Turbulence inside of channels has been studied by several authors. Ekstrom et al. [15] presented experimental evidence of the effect of the flow regime transition on the pressure drop along the monolith, especially the entrance region. They conducted experiments with a short and a long monolith, noticing that above some channel Reynolds number the pressure drop does not have a linear dependence with the length of the monolith, as expected for fully laminar flow. In addition, they noticed a linear dependence on the velocity when subtracting the pressure drop of the shortest monolith to the one of the largest monolith, providing evidence of a change in the flow regime at the beginning of the substrate. Recently, Cornejo et al. [16] analyzed the turbulence decay inside of single channels using LES, and proposed sink terms for a continuum model that damps the turbulence in a similar way to that observed in discrete channels [17]. Using this modified continuum model, the turbulence effectively decays to zero over a short distance after the entrance of the substrate, preventing nonphysical changes in the flow.

In the outlet cone region, there are three potential sources of turbulence after the monolith; first, the turbulence inside the channels [18], second, the outlet of the channels acting as square jets [19] and third, the flow surrounding the last part of the walls between channels [20]. According to a recent study, the predominant source of turbulence at a high channel Reynolds is the flow passing around the last part of the walls between channels, where the magnitude of the turbulence is related to the maximum thickness of the intersection of the walls [21]. Due to the flow instability produced by the interaction with the solid, this phenomenon is not present when the monolith is modeled as a continuum.

Turbulent flow is characterized by the presence of a series of vortices of different sizes, so called eddies [22]. Those vortices can merge, split and decay, increasing significantly the effective transfer of heat, mass and momentum and leading to changes on the reaction rate and pressure drop along the entire converter [23]. In automotive applications, pressure drop

has an impact on the fuel economy of the engine and the compliance with environmental emission regulations.

It should be noted that an adequate prediction of the turbulence generation after the channel outlet plays a significant role in catalytic flow reversal reactors used for the combustion of lean methane in air mixtures [24, 25]. Such reversal reactors consist of a sequence of open, inert and catalyst sections. Inert sections are unwashcoated ceramic or metal monolith, meanwhile catalyst sections are packed beds that can have different shapes [26]. Turbulence in the open sections is responsible for flow mixing and turbulence-chemistry interaction. From that perspective a correct prediction of the turbulence generation at the outlets of monoliths and the exit of the packed beds, which is the focus of this work, allows us to improve the accuracy when modeling homogeneous chemical reactions in the open space between sections, for example, in catalytic flow reversal reactors.

The objective of this paper is to present an integrated computational model of a catalytic converter, which incorporates the effect of the solid substrate in the turbulence when the monolith is modeled as a continuum. The computational model is described in Section 6.1. Section 6.2 analyzes and models the generation of turbulence after the monolith at a channel scale. Section 6.3 illustrates the implementation of the presented model at a converter scale when using the porous medium approach in an eddy-viscosity model, then compares the results with other available models. Section 6.4 is also an application of the proposed model at converter scale but using LES. Emphasis is put in the different necessities of both LES and RANS when modeling a monolith. Section 6.5 summarizes the main conclusions and remarks. The results are analyzed in terms of the turbulence kinetic energy and turbulence viscosity ratio along the converter.

6.1 Computational model

This study compares the flow leaving a monolith using a continuum model against the predictions of LES in a discrete channel geometry. All of the LES data at a channel scale were taken from a previous work, to which the reader is referred for details [21]. In that work, the triggering of turbulence was analyzed by carrying out a series of systematic numerical experiments, where the percentage of kinetic energy resolved is above the 95% in each of them, and the source of such a turbulence was carefully discussed. The data at a channel scale generated in this study are based on a RANS model. It first emulates those performed

with discrete channels, then expands it to a converter scale. At the channel scale, the section of the monolith analyzed had the same size as that used for LES and corresponds to the exit of the monolith (see Figure 6.1). The mentioned portion considers nine equivalent channels, each one with a channel size and a wall thickness of 1.1 mm and 0.1 mm respectively. Since symmetry can be assumed in RANS, the equivalent domain is 2D 3.6 mm high. The total length was kept the same as in LES, being 40 mm in total, where the first 20 mm represents the discrete channels and the last 20 mm are part of the open section after the monolith. Figure 6.2 shows a lateral view of a cut of the 3D discrete channels for LES and the 2D domain for RANS, where the substrate was modeled as a continuum. Data generated with LES at converter scale is shown in Section 6.4, the flow model and simulation conditions are detailed in the same section. The article was organized in such a separated way for more clarity, since LES and RANS differ substantially when modeling a monolith as a porous medium.

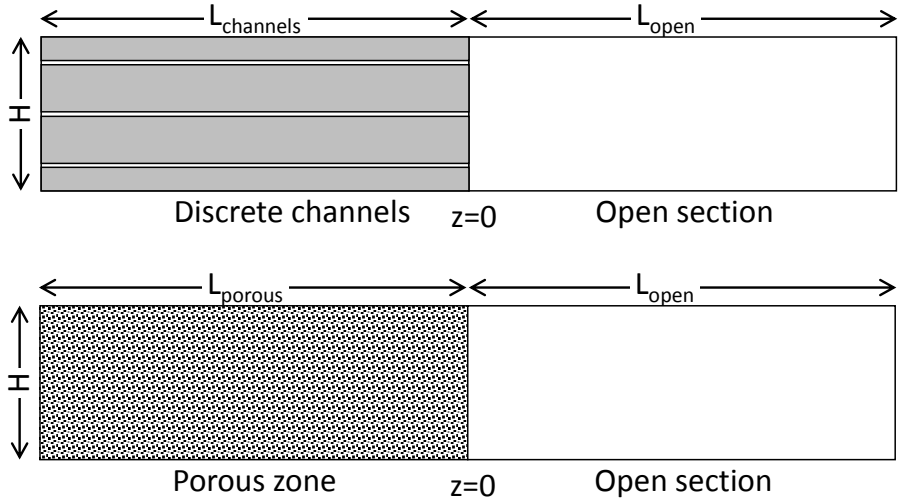

Figure 6.2: Description of the domain at channel scale. Top: Cut of a 3D discrete channel geometry. Bottom: 2D geometry, with a porous medium representing the discrete channels. $L_{channels}$=L_{porous}=L_{open}=20 mm, H=3.6 mm

The flow was modeled with the SST eddy viscosity model. The transport equations for mass and momentum are [14, 27]:

$$\nabla \cdot \vec{u} = 0 \tag{6.1}$$

$$\rho \vec{u} \nabla \cdot \vec{u} = -\nabla p + \nabla \cdot \left[\mu \left(\nabla \vec{u} + \nabla \vec{u}^T - \frac{2}{3} I \nabla \vec{u} \right) \right] - \nabla \cdot \left(\rho \overline{\vec{u}' \vec{u}'} \right) + S_u \tag{6.2}$$

where

$$-\nabla \cdot \left(\rho \overline{\vec{u}'\vec{u}'}\right) = \mu_t \left(\nabla \vec{u} + \nabla \vec{u}^T\right) - \frac{2}{3}\left(\rho\kappa + \mu_t \nabla \vec{u}\right) I \tag{6.3}$$

$$\mu_t = \rho \frac{\kappa}{\omega} \frac{1}{Max\left(\frac{1}{\alpha*}, \frac{SF_2}{a_1 \omega}\right)} \tag{6.4}$$

The turbulence viscosity is computed with a combination of κ and ω, and their transport equations are shown in Equation (6.5) and (6.8). The terms G_κ and G_ω accounts respectively for the generation of κ and ω. The terms Y_κ and Y_ω represent the corresponding dissipation, and D_ω is the cross-diffusion resulting from the blending of the κ-ε and κ-ω equations [27].

$$\nabla \cdot (\rho\kappa\vec{u}) = \nabla \cdot \left[\left(\mu + \frac{\mu_t}{\sigma_\kappa}\right)\nabla\kappa\right] + G_\kappa - Y_\kappa + S_\kappa^{sink} + S_\kappa^{gen} \tag{6.5}$$

where

$$G_\kappa = \mu_t S^2 \tag{6.6}$$

$$Y_\kappa = \rho\beta^*\kappa\omega \tag{6.7}$$

$$\nabla \cdot (\rho\omega\vec{u}) = \nabla \cdot \left[\left(\mu + \frac{\mu_t}{\sigma_\omega}\right)\nabla\omega\right] + G_\omega - Y_\omega + D_\omega + S_\omega^{sink} + S_\omega^{gen} \tag{6.8}$$

where

$$G_\omega = \frac{\alpha\alpha^*}{\nu_t} G_\kappa \tag{6.9}$$

$$Y_\omega = \rho\beta^*\omega^2 \tag{6.10}$$

$$D_\omega = 2\left(1 - F_1\right)\rho \frac{1}{\omega\sigma_{\omega_2}} \nabla\kappa\nabla\omega \tag{6.11}$$

For simplicity, details of the constants and blending functions of the SST model are not given here. They are completely described in Menter et al. [27] and ANSYS Fluent Theory Guide v17.2 [14]. The terms S_u, S_κ and S_ω are source terms for momentum, turbulence kinetic energy and specific dissipation rate respectively, that are specific for each case. In the open section, the three of them are zero. In the porous zone S_κ and S_ω are also zero, meanwhile, the extra pressure drop is taken into account by adding Darcy's law to the momentum equation in the form of a source term, as follows:

$$S_u = -\frac{\mu}{\vec{K_\alpha}}\vec{u} \tag{6.12}$$

The permeability in the axial direction can be obtained from Equation (6.13), where ϕ is

the void fraction of the monolith and D_H is the channel hydraulic diameter [15]. The flow in the radial direction is prevented by setting the radial permeability three orders of magnitude lower than the axial permeability [10].

$$K_{\alpha}^{axial} = \frac{\phi D_H^2}{28.4} \tag{6.13}$$

$$K_{\alpha}^{radial} = \frac{K_{\alpha}^{axial}}{1000} \tag{6.14}$$

The boundary conditions for the top and the bottom are symmetry, the inlet is a velocity inlet with a hydraulic diameter of 1.1 mm and a turbulence intensity of 0.1%. A small amount of turbulence intensity at the inlet is necessary for the RANS model, however, it decays quickly and does not affect the results. The channel velocity was manipulated to obtain channel Reynolds numbers between 300 and 2100, which covers the same range used in the LES performed by Cornejo et al. [21]. The unique outlet was defined as outflow, and the fluid was incompressible air at 300 K. The problem was implemented in ANSYS Fluent 17.2 [13], the solver settings are also shown in Table 6.1.

Table 6.1: Solver settings

Settings	
Fluid	air - incompressible
Porous zone	
Axial viscous resistance, m^2	$3{\cdot}10^7$
radial viscous resistance, m^2	$3{\cdot}10^{10}$
Schemes	
Pressure velocity coupling	SIMPLE
Momentum scheme	second order upwind
Turbulence kinetic energy scheme	second order upwind
specific dissipation rate scheme	second order upwind

The grid independence of the solution was studied by analyzing the average velocity magnitude and the average turbulence kinetic energy over the entire domain. Both of them are the most relevant quantities for this study, as well as being sensitive to the grid resolution. Three regular Cartesian meshes, systematically refined, with cell size from 0.16 mm to 0.01 mm were considered, finding that all of them led to the same result.

6.2 Modeling the turbulence after the monolith

In a discrete channel model, the interaction between the solid and the flow leaving the monolith can trigger turbulence. This is related with a Reynolds $\mathrm{Re_w}=\rho u L_T/\mu$ [21], where u is the channel velocity and L_T is the total width of the corners between channels measured diagonally. For an unwashcoated monolith $L_T = \sqrt{2}L_\mathrm{w}$, where L_w is the thickness of the walls between channels. At $\mathrm{Re_w}$ above the critical, the flow becomes unsteady passing the walls between channels, from where the instability propagates to the rest of the flow. After a certainty distance, rotating structures of the flow interact, merge, and trigger turbulence, a illustrated in Figure 6.3. When the substrate is modeled as a continuum, such a fluid-solid interaction does not exist and turbulence is not generated regardless of the value of $\mathrm{Re_w}$. This section characterizes the turbulence after a monolith, then presents a methodology to emulate such a turbulence generation when modeling the monolith as a homogeneous porous medium.

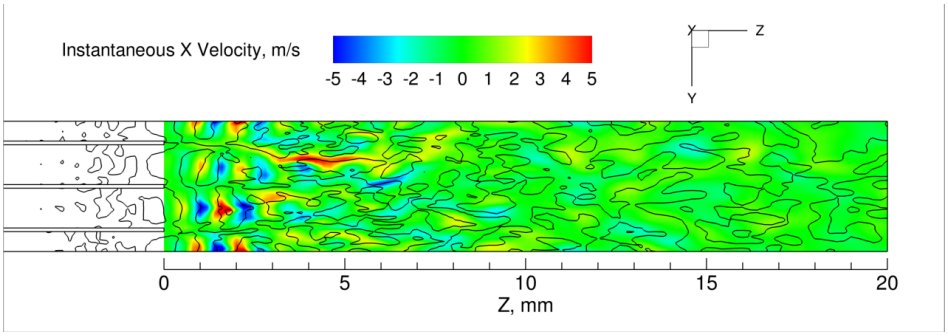

Figure 6.3: Contour of the instantaneous x velocity for flow leaving monolith channels at $\mathrm{Re_w}$=154. The lines correspond to iso-values of the Q criterion. This LES result were adapted from Cornejo et al. [21]

6.2.1 Turbulence generation from a discrete model

The two main features to be defined for the turbulence generation after the monolith are the magnitude of such a turbulence and the place where it appears. As mentioned, when using a continuum, fluid-solid interaction does not exist, hence, a turbulence triggering zone must be added after the porous medium to apply the generation of turbulence and emulate the observed in a discrete model. A schematic of this modified geometry is shown in Figure 6.4.

In RANS models, such as the SST model, the magnitude of the turbulence is defined by two quantities. The turbulence kinetic energy (κ) can be obtained directly from the discrete channel data shown in Figure 6.5. Meanwhile, the specific turbulence dissipation rate (ω) can

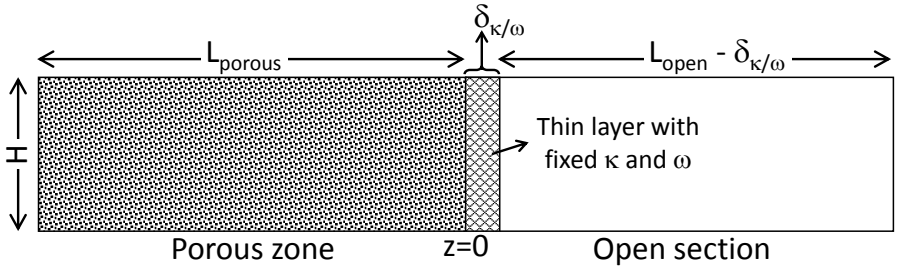

Figure 6.4: Modified domain, showing the adding of a turbulence triggering zone after the porous medium. In the former κ and ω are calculated based on the condition of the flow and fixed. L_{porous}=L_{open}=20 mm, H=3.6 mm

be estimated using Equation (6.15), where the length scale (l_e) is computed by introducing the channel size into the relationship $l_e = 0.07 L_c / C_\mu^{3/4}$ [14]. This leads to a length scale of the same order of magnitude as the value one observed graphically in LES [21].

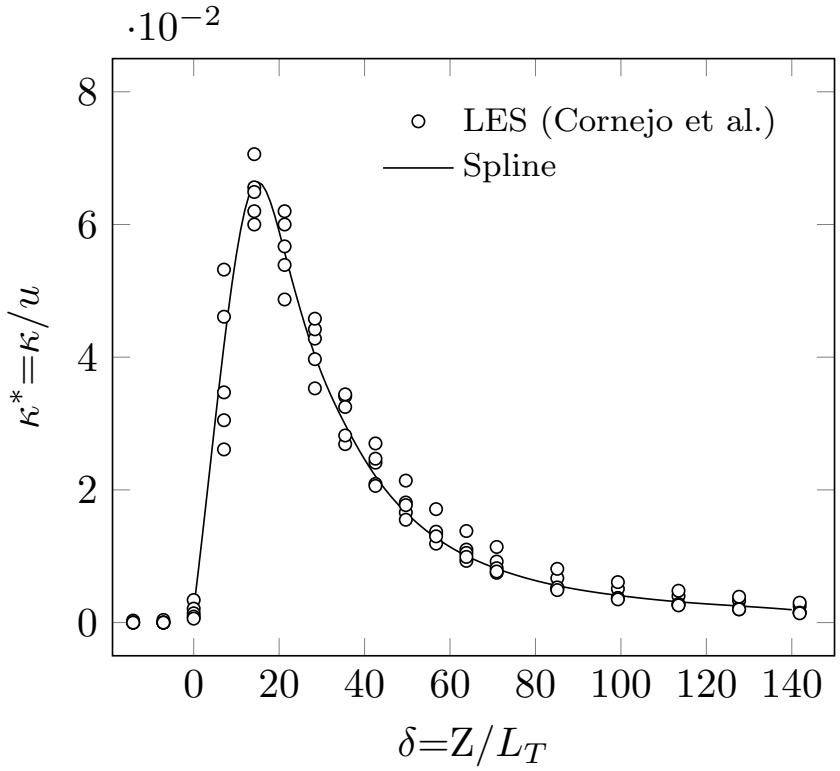

Figure 6.5: Dimensionless turbulence kinetic energy passing the monolith for $150 < \mathrm{Re_w} < 300$ obtained from a discrete channel geometry. Data adapted from Cornejo et al. [21]

$$\omega = \frac{\kappa^{1/2}}{l_e C_\mu} \tag{6.15}$$

The unsteadiness of the flow leaving the monolith starts with a coherent structure and is dominated by a reduced number of frequencies, typical of unsteady laminar flow. Although the largest fluctuations of the velocity are observed in the unsteady laminar region, turbulence does not show up until the interaction of flow from several channels downstream of the end of the monolith. Since the turbulence evolves along the open section, eventually there is a point at which it is sufficiently developed to be described by a RANS model. Such a point, which is precisely the thickness of the triggering zone ($\delta_{\kappa/\omega}$), was investigated by using the following steps:

i. Choose an arbitrary thickness for the triggering zone $\delta_{\kappa/\omega}$ for a RANS simulation (see Figure 6.4)

ii. Estimate κ and ω at a $\delta_{\kappa/\omega}$ distance after the monolith from the discrete channel LES data

iii. Fix the previously estimated κ and ω in the triggering zone in the RANS simulation

iv. Run the RANS simulation and compare the resulting development of the turbulence after the triggering zone to that observed in the discrete channel model

Figure 6.6 shows the turbulence kinetic energy after the triggering zone predicted by the continuum model when choosing several $\delta_{\kappa/\omega}$, and compares it to the discrete channel LES prediction. For the RANS simulations in the figure, the monolith ends at Z/L_T=0 and the triggering zone ends where the solid lines begins. Each line represents a different $\delta_{\kappa/\omega}$ chosen. As expected, LES and SST do not agree when $\delta_{\kappa/\omega}$ is small, because close to the monolith the flow is not sufficiently turbulent to be described with RANS. However, from Z/L_T of approximately 36, both models agree reasonably well with the same curve, establishing the minimum thickness of the zone of transition at such a $\mathrm{Re_w}$.

Figure 6.6b shows the same exercise as Figure 6.6a, carried out systematically for different inlet conditions. The figure shows only the minimum $\delta_{\kappa/\omega}$ that produces agreement between RANS and LES for each $\mathrm{Re_w}$. A pattern can be distinguished, where the thickness of the transition zone decreases as the $\mathrm{Re_w}$ increases. The inverse relationship between $\delta_{\kappa/\omega}$ and $\mathrm{Re_w}$ can be studied by defining a second Reynolds number, based on the distance that the flow has traveled from the outlet of the monolith (l), as shown in Equation (6.16). It was

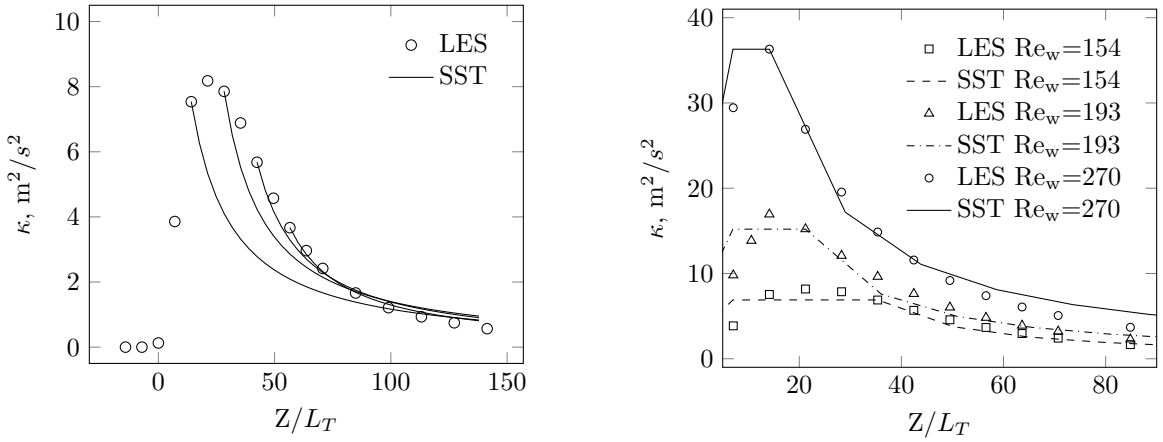

(a) (b)

Figure 6.6: (a) Turbulence kinetic energy predicted by LES and RANS. In RANS κ and ω were fixed at different arbitrary positions after the monolith (Re$_w$=154). (b) Turbulence kinetic energy predicted by LES and RANS at several Re$_w$, where $\delta_{\kappa/\omega}$ is large enough to cover the entire turbulence developing zone

computed with the velocity downstream of the monolith (u_∞), which is ϕ times the channel velocity, where ϕ is the void fraction of the substrate.

$$\mathrm{Re}_l = \frac{\rho u_\infty l}{\mu} \tag{6.16}$$

Reordering Equation (6.16) leads to $\mathrm{Re}_l \mu/\rho = u_\infty l$ = constant. By performing statistical analysis with a set of pairs (u_∞,l), the value of the constant and its 95% confidence interval were found to be 0.051 $\pm$ 0.0047 (R^2=0.94). It led to a critical Re$_l$ of 3800, where l can be assumed an estimation of $\delta_{\kappa/\omega}$.

6.2.2 Adding the turbulence in a continuum model

Having defined the thickness of the triggering zone and the magnitude of the turbulence from a discrete geometry, Figure 6.7 summarizes the steps used to add the turbulence generation after the monolith when using the continuum model. First, determine if the Re$_w$ is above the critical value that triggers turbulence. Second, the distance l in which the flow changes from laminar unsteady to turbulent is estimated according the Equation (6.16) with Re$_l$ = 3800. Third, the magnitude of the turbulence to be added is computed based on, for example, one of the two approaches described in the following.

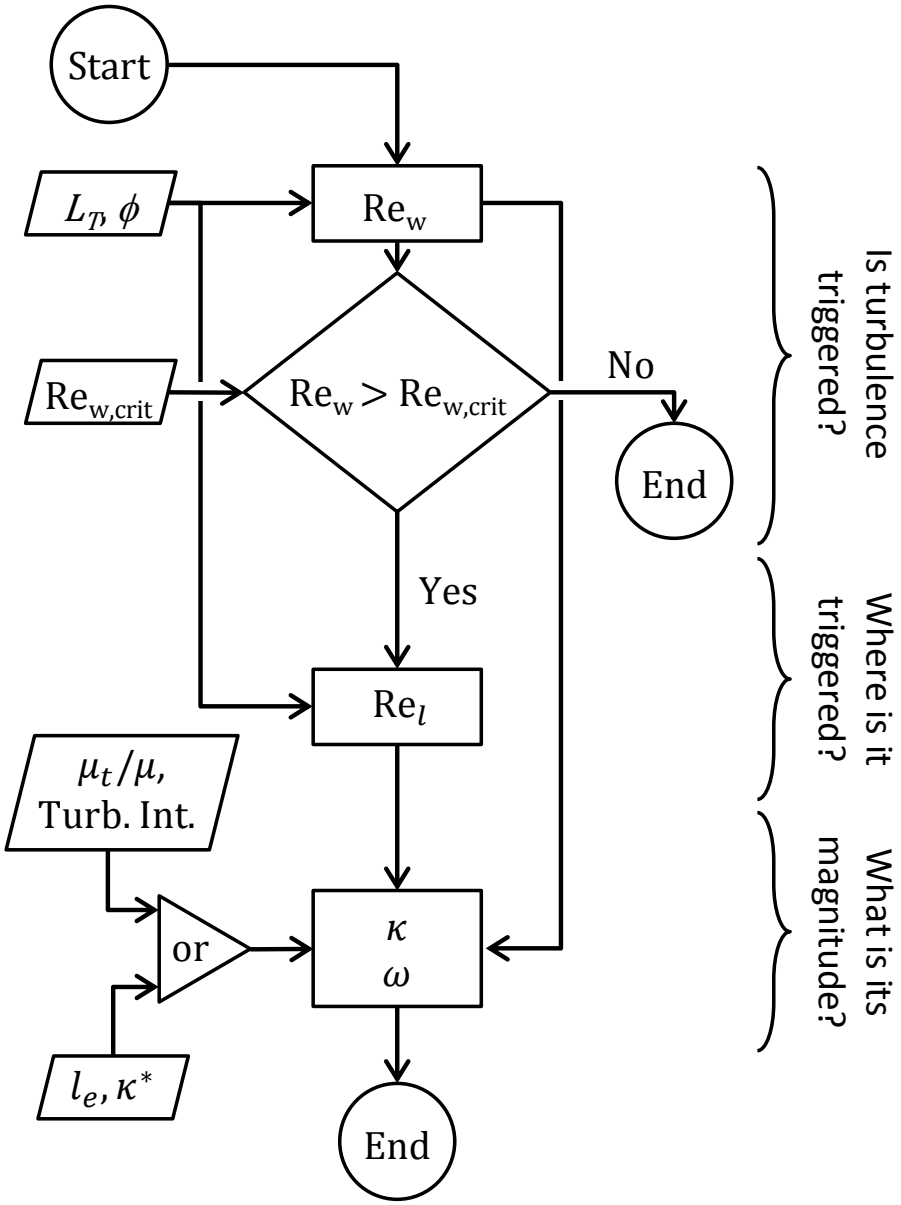

Figure 6.7: Flowchart with the steps to add the generation after a monolith to a continuum model

Turbulence kinetic energy based generation

When fixing κ and ω in Fluent, their transport equations are not solved. Instead of that, their values are replaced by the ones specified by the user. Such values can be linked to a user defined function, in this case, containing the spline in Figure 6.5 and Equation (6.15). The thickness of the zone of transition depends on the Reynolds number after each channel. The flow across a converter is maldistributed [28–30], which leads to a variable $\delta_{\kappa/\omega}$ along with the radius of the converter. Even though open codes are quite customizable, and implementing the model is direct into them, a moving boundary between the triggering zone and the open section imposes additional difficulties for its application in commercial solvers. CFD packages, such as COMSOL and Fluent, are frequent in industrial research, therefore, an assumption that simplifies the implementation of turbulence generation in them is also presented. Since the higher the $\mathrm{Re_w}$ the thinner the transition zone, the worst case scenario is represented by the lowest $\mathrm{Re_w}$ that triggers turbulence. If that worst case is assumed, then the length of the zone of transition will be overestimated for all other higher $\mathrm{Re_w}$, which, in fact, produces a better agreement between RANS and LES. With this, the calculation of $\delta_{\kappa/\omega}$ can be simplified, by assuming it to be constant. Figure 6.8a shows the turbulence kinetic energy predicted by LES and RANS when κ and ω are fixed in a transition zone of $\delta_{\kappa/\omega}$ equivalent to $Z/(\sqrt{2}L_{\mathrm{w}})$=36. By considering $\delta_{\kappa/\omega}$ constant, the prediction of the peak of κ is scarified, however, it does not have significant consequences downstream.

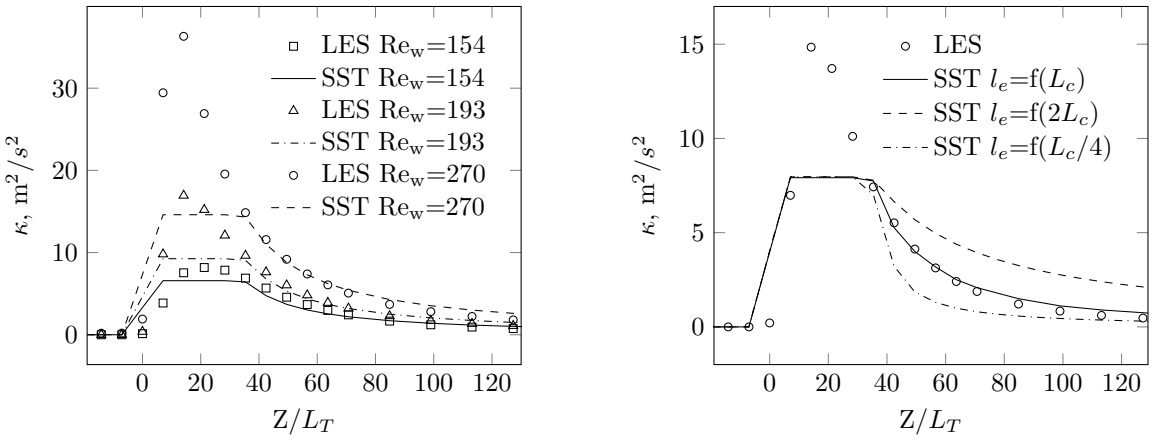

Figure 6.8: (a) Turbulence added at a fixed distance from the monolith for different $\mathrm{Re_w}$. (b) Prediction of the turbulence kinetic energy at $\mathrm{Re_w} = 174$, using different l_e. The values of (μ_t/μ) when using $L_c/4$, L_c and $2L_c$ are 2, 4 and 16 respectively

Turbulence viscosity based generation

Another suggested strategy for adding the generation of turbulence without having the necessity of discrete channel data is to calculate κ and ω based on the length scale and the turbulence viscosity ratio. It follows the same logic given in the turbulence kinetic energy based generation, but the magnitude of the turbulence is estimated differently. It uses two relationships, the first is Equation (6.15), which relates ω and κ, and the second is obtained by manipulating the definition of the eddy viscosity of the RANS model. Due to its simplicity, it is exemplified with the κ-ε model, in which the definition in Equation (6.17) can be changed into Equation (6.18). This was done by multiplying both sides of the equation by μ, and using the relationship $l_e\varepsilon = \kappa^{3/2}$.

$$\mu_t = \rho C_\mu \frac{\kappa^2}{\varepsilon} \tag{6.17}$$

$$\kappa = \left[\left(\frac{\mu_t}{\mu} \right) \frac{\mu}{\rho l_e C_\mu} \right]^2 \tag{6.18}$$

Given the structure of the two-unknowns and two-relations system formed by the Equation (6.15) and (6.18), each pair of turbulence viscosity ratio and length scale leads to a unique pair of κ and ω. By increasing the length scale and the turbulence viscosity ratio in the same factor, it is possible to obtain different values of ω for a fixed κ. It means than if information about the length scale is not available, it is possible to estimate it based on κ information. Figure 6.8b shows the turbulence kinetic energy predicted by assuming several turbulence viscosity ratios and length scales. This approach is specially useful when information about the length scale is not available. Turbulence kinetic energy can be estimated following standard experimental procedures, but the length scale might be complex to obtain. Results in Figure 6.8b confirm that, despite the fact that κ is related to the thickness of the walls, the length scale of the turbulence after the monolith is dominated by the size of the channels.

6.3 Illustration of the model implemented at a converter scale: RANS

This section first briefly review the common methodologies for modeling monoliths, then shows the turbulence predicted by them compared to the model presented in this paper. A fully integrated computational model of the converter involves the modeling of the substrate as well as the associated assembly. Discarding the manifold, three major sections can be

identified in a classic single monolith catalytic converter: The inlet diffuser, the substrate, and the outlet cone (see Figure 6.9). The differences between models are presented in the way that they treat such sections and how they take into account the influence of the solid substrate in the flow when the monolith is modeled as a homogeneous porous medium.

The most basic method, henceforth referred to as the standard model, is the direct application of a RANS model in the three sections of the converter. This work considers the SST model, however, it is possible to find the implementation of other two-equations eddy viscosity models in the literature [11, 31, 32]. The transport of mass and momentum are govern by Equation (6.1), (6.2), (6.5) and (6.8), without any source term other than the S_u in Equation (6.12), which accounts for the extra pressure drop inside the porous zone. The monolith is treated as a homogeneous porous medium, where the flow resistance is determined by the Hagen–Poiseuille equation as the channel Re is generally sub-critical. The main drawback with this model is that the flow inside the monolith is laminar, however, this methodology predicts a turbulence viscosity of about the same magnitude along the entire converter, including the porous zone. This is because the decay of the turbulence caused by the friction with the inner walls of the channels is not represented by a perfectly homogeneous medium model.

To eliminate the effect of the turbulence inside the porous medium, it is often defined as a laminar zone. In practical terms, especially in commercial codes such as ANSYS Fluent, it means fixing the turbulence viscosity to zero in that area [14]. This second methodology makes the effective viscosity equal to the laminar one and prevents the generation of new κ and ω by canceling the terms G_κ and G_ω in the respective transport equations for the porous medium. However, the equations are still being solved, transporting the turbulence from the beginning to the end of the laminar zone with only minor changes. Although this reduces the effect of turbulence drastically, it does not eliminate it entirely. In addition, after the laminar zone, where the turbulence viscosity is not fixed anymore, the effective viscosity suddenly increases rapidly to unrealistic values.

As an alternative that agrees better with the physics inside a monolith, Cornejo et al. [17] proposed a methodology that does not require defining the porous medium as a laminar zone. Instead of that, it uses two damping terms for the turbulence based on results observed in a discrete geometry. Both damping terms are shown in Equation (6.19) and (6.20). When they are implemented in the porous zone an effective and progressive decay of the turbulence kinetic energy entering the porous medium is achieved, emulating the observed in single

channels. This model uses Darcy's law for the extra pressure drop in the momentum transport equation, as well.

$$S_{\kappa}^{sink} = -\frac{\mu_t}{K_{\alpha}^{axial}}\kappa \tag{6.19}$$

$$S_{\omega}^{sink} = -\frac{\mu}{K_{\alpha}^{axial}}(\omega - \omega_0) \tag{6.20}$$

where

$$\omega_0 = C_{\omega}\frac{\mu/\rho}{\beta_{\omega}\Delta^2/4}$$

The parameter ω_0 is the specific turbulence dissipation rate to which ω should approach asymptotically at the monolith-entrance region. According to Ref. [33], this work uses β_{ω}=3/4 and C_{ω}=6, meanwhile Δ is the characteristic length of the control volume.

We now extend the model of Cornejo et al. [21] to incorporate the physics of the flow leaving a monolith. The turbulence in the porous zone is damped with the sink terms in Equation (6.19) and (6.20), and Darcy's law accounts for the pressure drop along the monolith. The novelty of this methodology is the addition of the generation of turbulence when leaving the monolith. Since it is produced by the interaction of the flow with the solid when abandoning the substrate, it does not show up when modeling the monolith as a homogeneous medium. The generation of turbulence is implemented by following the steps in Section 6.2.2 and Figure 6.7, as a Dirichlet immersed condition in the triggering zone (see Figure 6.9). The vlue of $\mathrm{Re_w}$ immediately after the porous zone is calculated and compared to the critical one that triggers turbulence. In this case, $\mathrm{Re_w} > 150$ was assumed as a hard limit to such a triggering. It is important to remark that such a Reynolds number uses the channel velocity. If $\mathrm{Re_w}$ is higher than 150, the corresponding values for κ and ω are estimated with the spline in Figure 6.5 and Equation (6.15) respectively. This immerse boundary condition is evaluated and applied at every cell along the radius of the monolith in the triggering zone (see Figure 6.9).

For comparison purposes, all four approaches were implemented in ANSYS Fluent 17.2, in an axi-symmetric catalytic converter with an unwashcoated monolith 150 mm long and with a radius of 59 mm. The channel size was 1.1 mm, and the wall thickness was 0.16 mm. Both the diffuser and outlet cone were 45 mm long with 30° as the expansion angle. The diameters of the inlet and outlet pipes were 54 mm, both of them were intentionally enlarged up to 380 mm, to avoid boundary effects. A schematic of the converter and its mesh is shown

in Figure 6.9. The triggering zone was used exclusively when implementing the turbulence generation after the monolith. For the other 3 models, that zone was to be considered air, part of the open section inside the outlet cone.

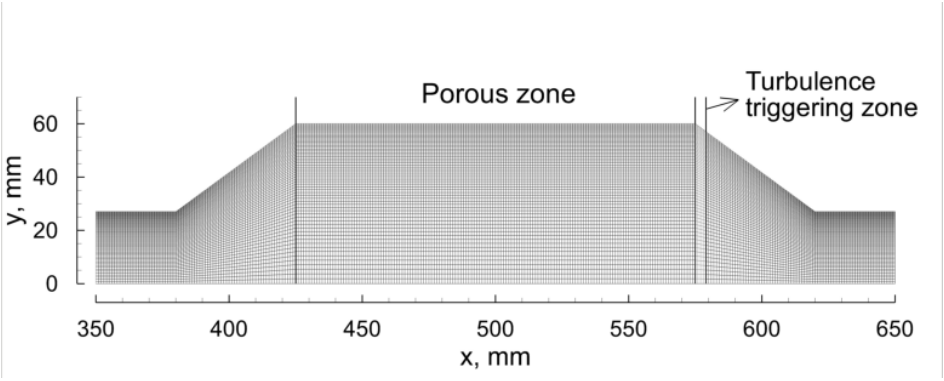

Figure 6.9: Portion of the mesh of the entire converter, including the turbulence triggering zone after the continuum

The grid independence was studied following the same procedure given in Cornejo et al. [17], at inlet Re 30 000 and 60 000. The variables monitored were the peak velocity after the monolith, the volume average velocity magnitude and the volume average effective viscosity. Among them, the first is the most sensitive to the grid, and the last is the core of this study. Since turbulence after the monolith is triggered when the Re_w is above the critical value, simulations at two conditions were carried out, both at an inlet Re equal to 30 000. The first was an unwashcoated monolith, where the Re_w is too low to trigger turbulence. The second emulated a washcoated monolith such as that presented in Vaclavik et al. [34] and in Liu et al. [35]. Both references show multi-layer catalyst, where the high coating load results in a considerable increasing of the width of the corners and a decreasing in the void fraction. Since the lower the void fraction, the higher the channel velocity, both factors contribute to a higher Re_w, which in this case is enough to trigger turbulence after the monolith. based on the mentioned references for dual-layer catalyst, the runs for the coated case considered the same substrate, but adding a maximum washcoat thickness of 300 μm (measured diagonally in the corners), and an effective channel breath of 0.9 mm. It results in a monolith with L_T=826 μm, 40% of void fraction, or an equivalent axial permeability for a porous medium of 1.15×10^{-8} m^{-2}. The converter simulations were implemented in ANSYS Fluent 17.2, using the SIMPLE algorithm and second order upwind scheme for momentum, κ and ω. The convergence criteria was reaching a maximum value of scaled residuals of the order of 10^{-6} and a stable value of the volume average turbulence viscosity ration along the entire domain. The resulting turbulence viscosity ratio along the symmetry axis for each of the four models

is presented in Figure 6.10.

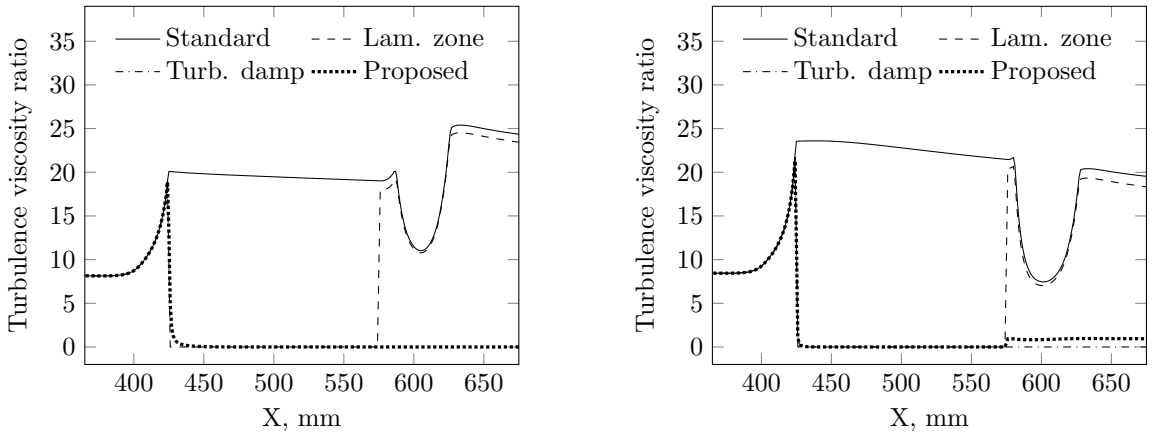

Figure 6.10: Turbulence viscosity ratio along the symmetry axis of the converter for (a) an unwashcoated monolith and (b) a washcoated monolith. Both at inlet Re of 30 000

In the example shown in Figure 6.10a the main differences can be seen from the beginning of the porous zone. The standard model predicts a high value of turbulence viscosity inside the porous medium, which is maintained along the entire monolith. In contrast, when the porous medium is set as a laminar zone, the turbulence viscosity suddenly becomes zero entering the monolith. However, after the laminar zone, the turbulence viscosity ratio is not overwritten anymore, and increases substantially, following almost the same pattern as that seen when using the standard model. On the other hand, when the turbulence is damped, it decreases progressively in the first part of the porous zone. The turbulence viscosity decays to zero as a consequence of the decrease of the turbulence kinetic energy without the necessity of overwriting any variable. This decay is not instantaneous, but rather presents a similar trend as that observed in discrete channels [17]. Finally, using the presented model, that adds the generation of turbulence after the monolith, does not make a difference in this case, because it considers flow conditions that are not sufficient to trigger turbulence. In such a case, damping the turbulence is sufficient. Figure 6.10b shows a different situation, where the conditions to trigger turbulence after the monolith are met. Standard and laminar zone models behave the same as in the previous example, presenting an artificial generation of the turbulence after the monolith. When applying the damping in the porous zone the decay of the turbulence is faster, in agreement with the expected result due to the smaller effective size of the channels. The complete decomposing of the turbulence in the porous zone results

in zero turbulence viscosity ratio even in conditions where generation of turbulence after the monolith is expected. In such conditions the presented model plays a role, effectively producing the triggering of the turbulence. The turbulence viscosity ratio predicted by the presented model is significantly different than that observed using either the standard model or the laminar zone model. The resulting turbulence viscosity ratio in the outlet cone, due to turbulence generation after the monolith, is approximately one. It may seem like a small value, however, it means that the effective viscosity is twice the laminar one, potentially leading to noticeable changes in gas phase reactions or temperature profiles. Figure 6.11 allows us to analyze closely the turbulence kinetic energy along the center of the converter under the same circumstances as those in Figure 6.10b. Looking at the figure it is evident that setting the porous as a laminar zone has a minimum impact on the development of the turbulence kinetic energy. As mentioned, both the standard and the laminar zone models, predict a non-physical increment of the turbulence kinetic energy at the first part of the porous medium, opposite to the expected behaviour for channels at sub-critical Reynolds. Then, κ decreases slowly in the porous medium, to increase again along the outlet cone. The model that damps the turbulence is effectively reaching zero turbulence kinetic energy in the first portion of the monolith, then, when it is complemented with the presented strategy to trigger turbulence, the curve agrees with the physics of a monolith type substrate. Both the decay at the entrance and the peak after the substrate have been observed using LES in discrete channel geometry [17, 21]. The presented model incorporates both phenomena, decay and triggering of turbulence, to a homogeneous porous medium representation of the monolith successfully.

Figure 6.12 shows contour plots of the turbulence viscosity ratio in the second half of the converter predicted by the four analyzed RANS models, under the same circumstances used in Figure 6.10. Comparing Figure 6.12 a and b it can be seen that despite the standard and laminar zone models predicting almost the same the turbulence viscosity along the axis after the porous medium, they differ in the radial direction. However, both still significantly overestimate the turbulence compared to the proposed model in Figure 6.12d. Figure 6.12c predicts zero turbulence inside and after the porous zone, showing that it is effective to model the turbulence inside the substrate, but the physics after it is missing. Figure 6.12d shows that the proposed model predicts about the same turbulence viscosity ratio along the radius of the converter, which is explained by the fact that the washcoated monolith simulated has an equivalent permeability that produces a velocity profile with ratio between the maximum and the minimum velocity close to 1.15. It means that the local $\mathrm{Re_w}$ and the magnitude of the turbulence generated along the radius of the converter is about the same.

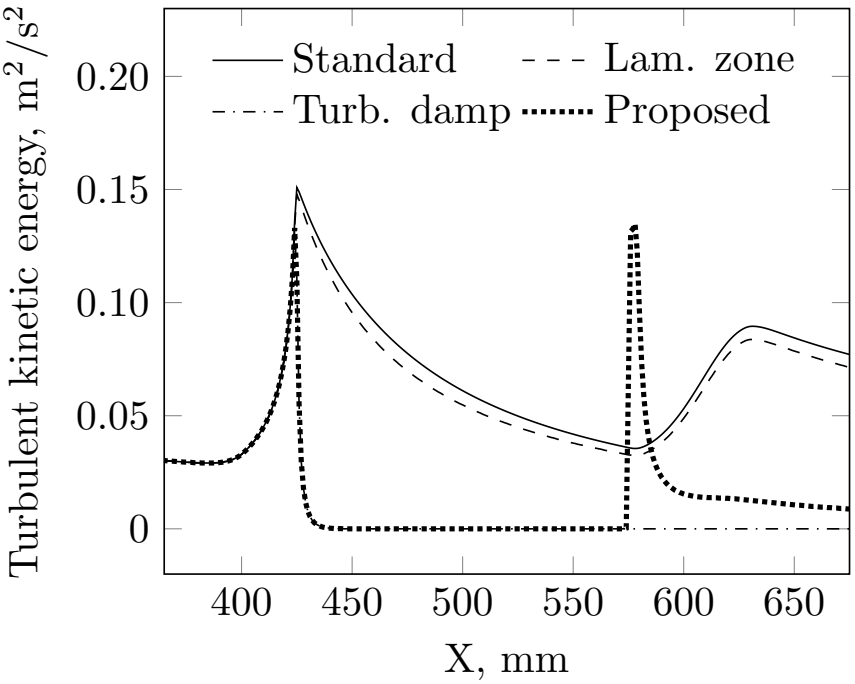

Figure 6.11: Turbulence kinetic energy along the symmetry axis of the converter for a wash-coated monolith, at inlet Re of 30 000 and Re_w high enough to trigger turbulence after the monolith

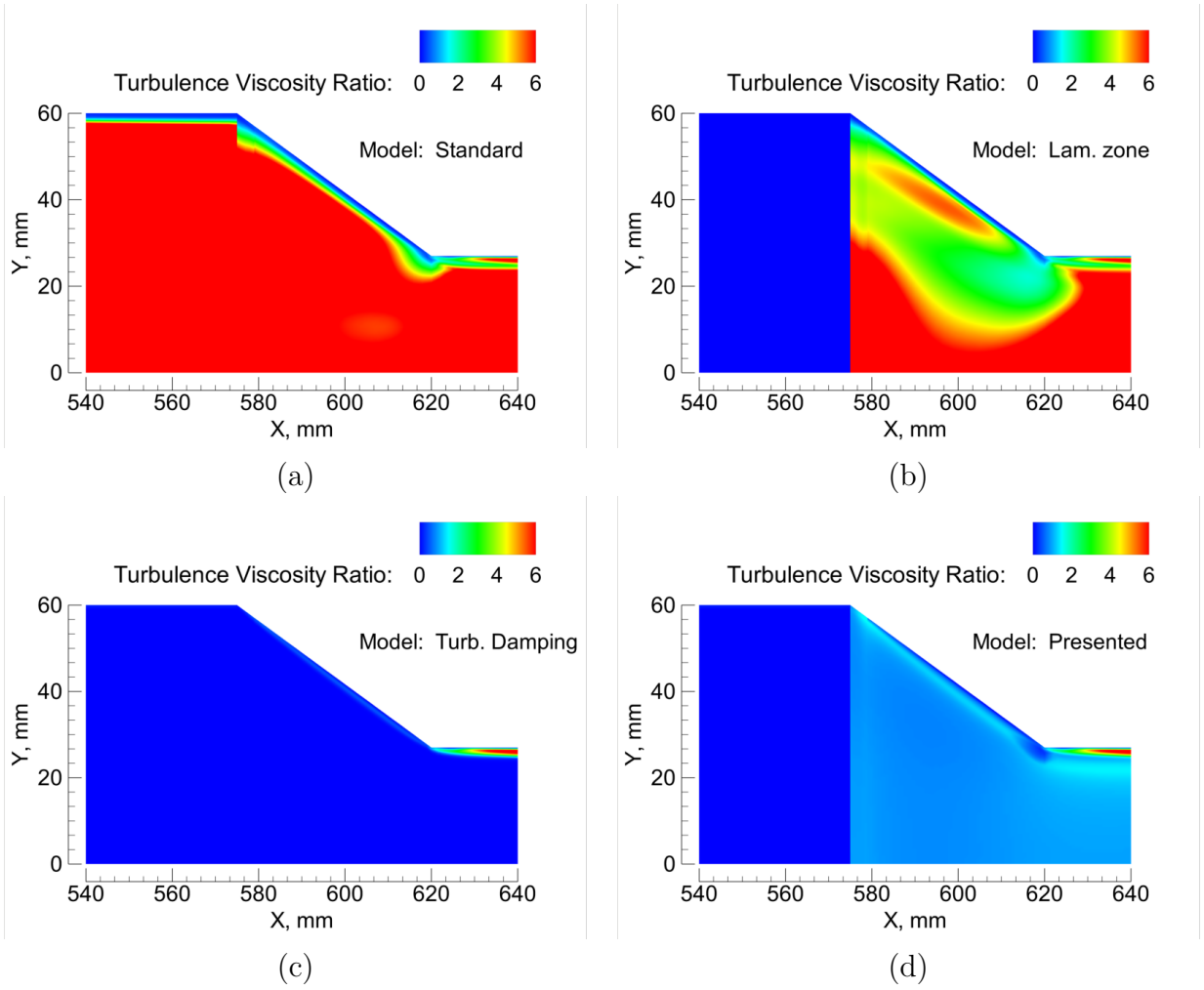

Figure 6.12: Contour plot of turbulence viscosity ratio in the second half of the converter for a washcoated monolith at inlet Re of 30 000. Prediction of (a) the standard model, (b) the laminar zone model, (c) applying the damping of the turbulence, and (d) the presented model (damping and generation).

6.4 Illustration of the model implemented at converter scale: LES

Modeling a monolith by a porous medium in LES has fundamental differences than when using RANS. In an eddy-viscosity model, the turbulence kinetic energy represents the standard deviation of the velocity, which is modeled as a scalar using an additional transport equation. As a result, κ diffuses through the porous zone leading to non-physical results. The sink terms shown in Equation (6.19) and (6.20) are meant to correct such a false diffusion. In LES the phenomenon entering the monolith is different. Inside the porous medium the viscous resistance is so high that automatically damps the turbulence coherently with

that observed in discrete channels without the necessity of any further correction to the flow model. Looking at the outlet of the monolith, both RANS and LES suffer the same problem, which is the missing of the unsteadiness of the flow when leaving the substrate. This is an issue when representing an heterogeneous monolith as a homogeneous porous medium. As mentioned, the turbulence is generated by the interaction between the fluid and the solid, hence, in the absence of the solid, turbulence does not show up. Section 6.3 showed how to add that phenomenon when using a two-equations eddy viscosity model, where it is necessary to define two quantities, κ and ε (or ω). For the cases with LES covered in this section, the only quantity necessary to be specified is the turbulence kinetic energy resulting of the flow leaving the monolith. This is done following the same logic as that for RANS, which is adding the turbulence kinetic energy in a turbulence triggering zone. Transport equations for mass and momentum are the following [14]:

$$\frac{\partial \rho}{\partial t} + \frac{\partial}{\partial x_j}(\rho \overline{u}_i) = 0 \tag{6.21}$$

$$\frac{\partial \overline{u}_i}{\partial t} + \overline{u_j}\frac{\partial \overline{u}_i}{\partial x_j} = -\frac{1}{\rho}\frac{\partial \overline{p}}{\partial x_i} + \frac{\partial}{\partial x_j}\left(\nu \frac{\partial \overline{u}_i}{\partial x_j} + \frac{1}{\rho}\frac{\partial \tau_{ij}}{\partial x_j}\right) - \frac{\mu}{\vec{K}_\alpha}\overline{u} \tag{6.22}$$

The last term at right-hand side of the momentum equation is Darcy's law, which accounts for the extra pressure drop along the porous zone in the same manner as that in Equation (6.12). Variables with an overbar refer to the resolved scale. The sub-grid scale was modeled by the Dynamic Kinetic Energy Sub-grid scale model [36], where τ_{ij} in Equation (6.22) is calculated by using Equation (6.23) and the sub-grid turbulence kinetic energy has the transport equation shown in Equation (6.24).

$$\tau_{ij} = \frac{2}{3}\rho \kappa_{sgs}\delta_{ij} - 2C_\kappa \kappa^{1/2}\Delta_f \overline{S}_{ij} \tag{6.23}$$

$$\rho\frac{\partial \kappa_{sgs}}{\partial t} + \rho\overline{u}_j\frac{\partial \kappa_{sgs}}{\partial x_j} = -\tau_{ij}\frac{\partial \overline{u}_i}{\partial x_j} - C_\varepsilon \rho \frac{\kappa_{sgs}^{3/2}}{\Delta_f} + \frac{\partial}{\partial x_j}\left(\frac{\mu_{sgs}}{\sigma_\kappa}\frac{\partial \kappa_{sgs}}{\partial x_j}\right) \tag{6.24}$$

where

$$\mu_{sgs} = C_\kappa \rho \kappa_{sgs}^{1/2}\Delta_f$$

The converter considered for this section has the same size as that used in Section 6.3, with an inlet pipe of 54 mm as a diameter, a monolith 150 mm long and 118 mm in diameter, and a diffuser of 45 mm in length. Figure 6.13 shows views of two cuts of the mesh used for LES. It contained 2.6 million structured distributed hexahedral control volumes. The grid convergence was investigated comparing a 2.6 millions of cells mesh to one with 5.4 millions of

cells. For both meshes the maximum CFL number was kept below one and the maximum y^+ was about one. Bounded central differencing was used for momentum and bounded second order implicit for time. Both meshes produced the same time-average velocity profile after the monolith, which is a variable sensitive to the grid and relevant for this study.

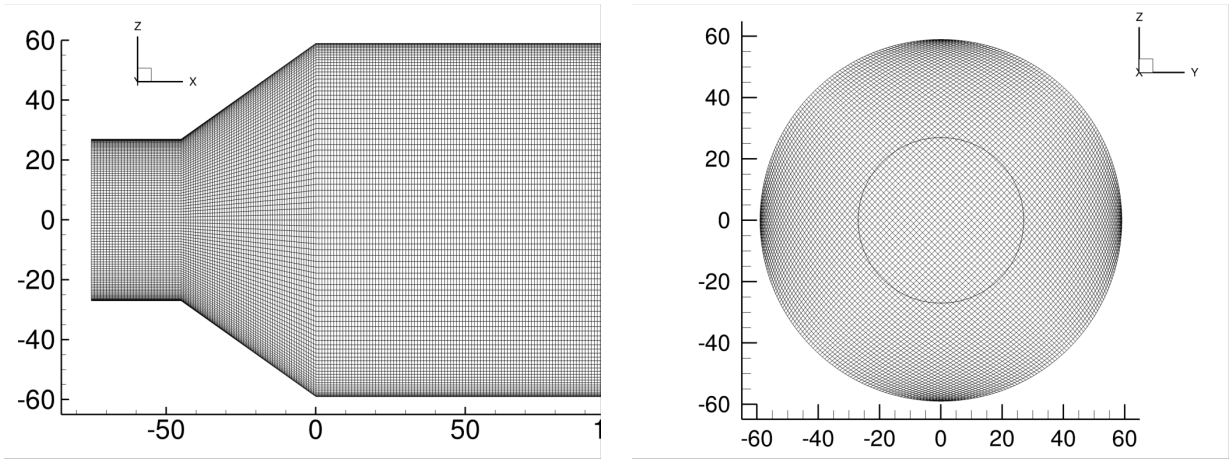

(a) (b)

Figure 6.13: Mesh for LES (axes in millimeters)

The case analyzed was one which produces turbulence after the monolith, to compare results of the simulation when implementing the turbulence generation after the monolith to when it is not implemented. The inlet velocity was 8.7 m/s (or Re 30 000). The axial permeability of the porous medium was 1.15×10^{-8} m^2 and the radial one was two orders of magnitude lower, which emulated a dual-layer catalyst with an effective channel breath of 0.9 mm and maximum washcoat thickness of 300 μm. The results are summarized in Figure 6.14 to 6.16.

Figure 6.14 shows an instantaneous contour plot of the total turbulence kinetic energy inside the converter with and without applying the generation of turbulence after the monolith. It is noted that for both models the magnitude of the turbulence kinetic energy in the recirculation zones after the porous medium is of the same magnitude. Also, it can be seen how the turbulence is damped automatically once the flow enters the porous zone although sink terms for the turbulence were not applied. Figure 6.15 shows a three-dimensional visualization of the turbulence inside the diffuser. An iso-surface of the Q criterion colored by the instantaneous velocity magnitude shows rotating structures close to the wall on its majority, in the recirculation zone, after the detachment of the boundary layer at the beginning of the diffuser. There are many vortices before the monolith, but none persists inside it.

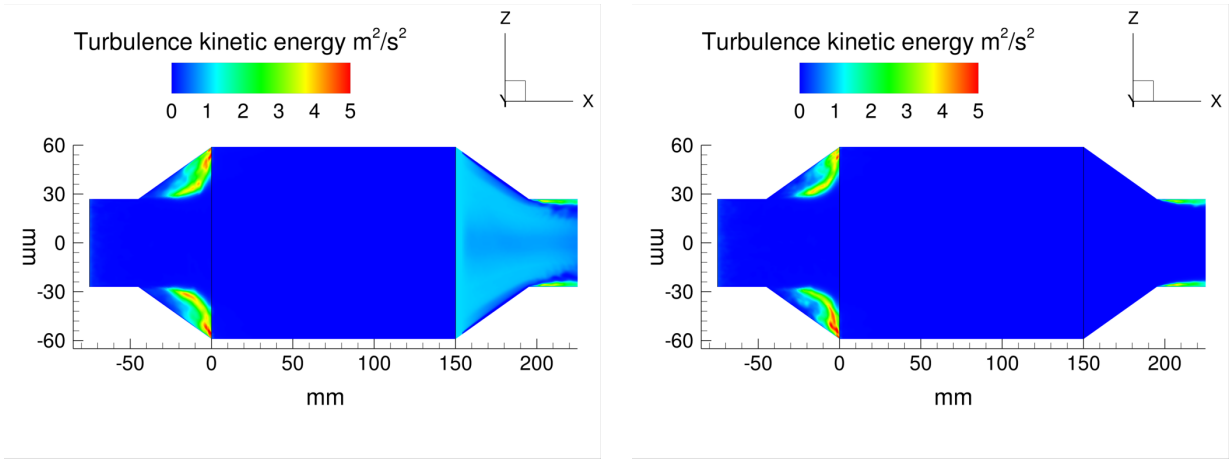

(a) (b)

Figure 6.14: Slice of the turbulence kinetic energy across of the middle of the converter (a) applying and (b) without applying the generation of turbulence after the monolith

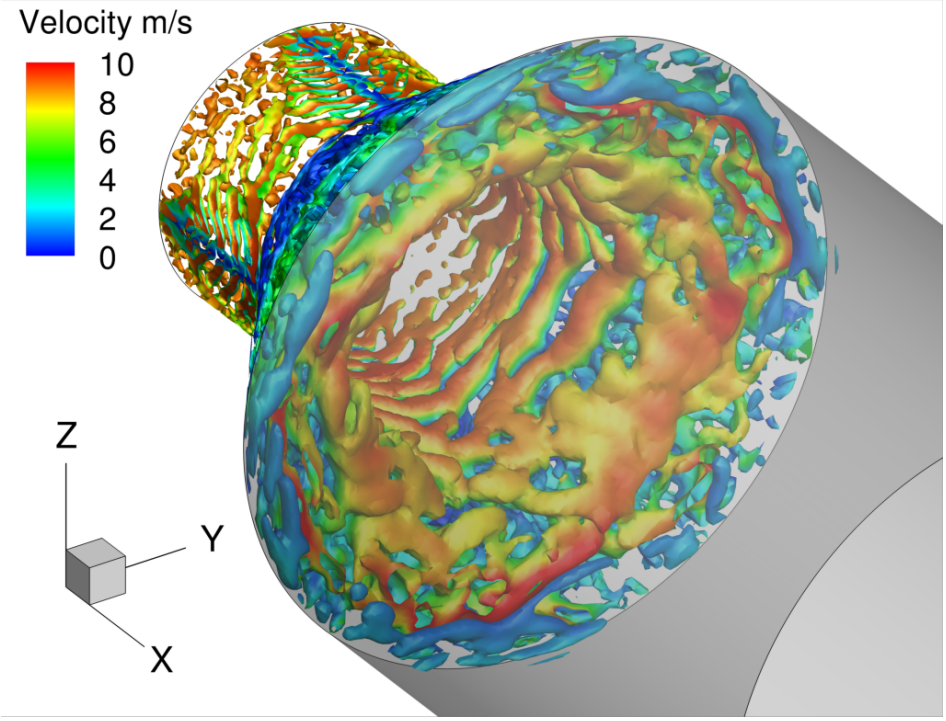

Figure 6.15: Iso-surface of Q colored by the instantaneous velocity magnitude inside the diffuser and porous zone

Figure 6.16 provides a three-dimensional view of the converter with an iso-surface of the instantaneous total turbulence kinetic energy, with emphasis in the regions before and after the porous zone. Both models lead to a similar pattern before the monolith, where the maximum unsteadiness of the flow is located around the main stream that comes from the

inlet pipe. In Figure 6.16a it is noted that if the generation of turbulence is not implemented the flow remains completely steady at the exit of the monolith, which is not consistent with the observed in the discrete channel geometry. This can be corrected by adding the corresponding value of turbulence kinetic energy in a thin triggering zone after the porous zone. The resulting iso-surface is shown in Figure 6.16a.

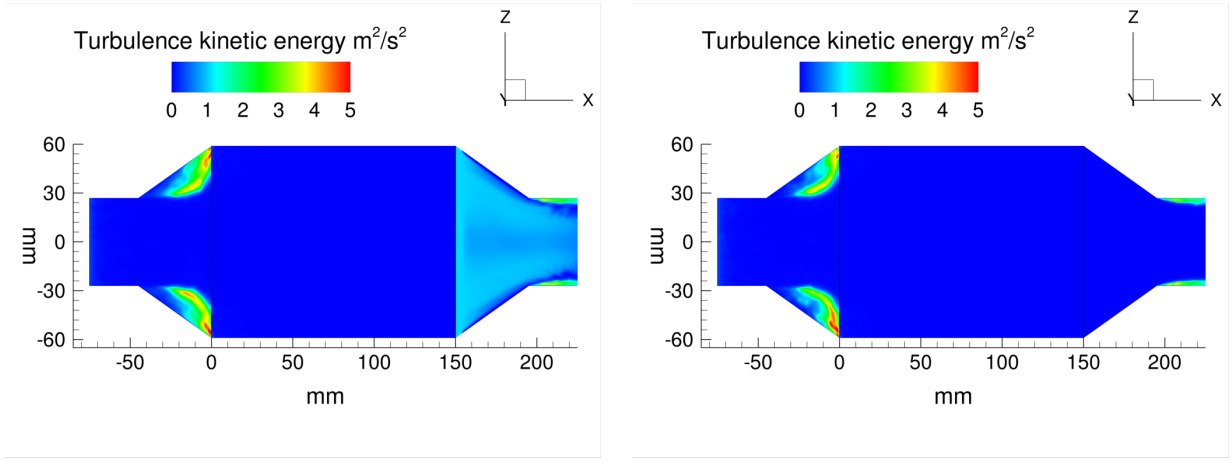

(a) (b)

Figure 6.16: Iso-surface of the turbulence kinetic energy colored by the instantaneous velocity magnitude inside the converter(a) applying and (b) without applying the generation of turbulence after the monolith

6.5 Conclusions

The turbulence generation after a monolith was characterized and added to a continuum model. By establishing a turbulence triggering zone, and using an immersed boundary condition for κ and ω, the same generation of turbulence observed in discrete channels can be obtained using a porous medium model.

The proposed methodology was tested at both channel and converter scales. Since the flow at the converter is not evenly distributed, the thickness of the triggering zone varies along the radius. However, assuming it to be constant appears to be a convenient trade-off between simplicity and accuracy, especially when it is implemented in commercial solvers. The magnitude of the turbulence to be added in the triggering zone can be obtained from discrete channels data. If such data are not available, they can be estimated based on the turbulence viscosity ratio and turbulence intensity.

The proposed model implemented together with the turbulence damping emulates the fluid-flow interaction observed at the beginning and the end of a monolith, despite it being represented as a perfectly homogeneous porous medium. Compared to other available models of the converter, the proposed methodology represents the flow thought an actual honeycomb type substrate better, achieving a realistic behavior along the entire converter. Also, it does not have the nonphysical changes in the turbulence observed in other models, such as the transport of turbulence kinetic energy along the laminar zone and a false turbulence triggering after the continuum. This is especially relevant for coupled monoliths and other reactors that mix open and structured sections.

Bibliography

[1] Pablo Marín, Miguel AG Hevia, Salvador Ordonez, and Fernando V Díez. Combustion of methane lean mixtures in reverse flow reactors: comparison between packed and structured catalyst beds. *Catalysis Today*, 105(3):701–708, 2005.

[2] Yangang Wang, Guanwu Sun, Jiaqi Dai, Guang Chen, Joe Morgenstern, Yanbin Wang, Shifei Kang, Mingwei Zhu, Siddhartha Das, Lifeng Cui, et al. A high-performance, low-tortuosity wood-carbon monolith reactor. *Advanced Materials*, 29(2), 2017.

[3] Zheng Fang, Yongyou Hu, Xueshen Wu, Yanzhe Qin, Jianhua Cheng, Yuancai Chen, Ping Tan, and Huiqin Li. A novel magnesium ascorbyl phosphate graphene-based monolith and its superior adsorption capability for bisphenol A. *Chemical Engineering Journal*, 334:948–956, 2018.

[4] Piyanut Inbamrung, Thana Sornchamni, Chaiwat Prapainainar, Sabaithip Tungkamani, Phavanee Narataruksa, and Goran N Jovanovic. Modeling of a square channel monolith reactor for methane steam reforming. *Energy*, 2018.

[5] Björn Lundberg, Jonas Sjöblom, Åsa Johansson, Björn Westerberg, and Derek Creaser. DOC modeling combining kinetics and mass transfer using inert washcoat layers. *Applied Catalysis B: Environmental*, 191:116–129, 2016.

[6] Sivaram Kannepalli, Andreas Gremminger, Steffen Tischer, and Olaf Deutschmann. Optimization of axial catalyst loading in transient-operated zone-structured monoliths: Reduction of cumulative emissions in automotive oxidation catalysts. *Chemical Engineering Science*, 174:189–202, 2017.

[7] Dimitrios Karamitros and Grigorios Koltsakis. Model-based optimization of catalyst zoning on SCR-coated particulate filters. *Chemical Engineering Science*, 173:514–524, 2017.

[8] François Bertrand, Christophe Devals, David Vidal, Cyrille Séguineau de Préval, and Robert E Hayes. Towards the simulation of the catalytic monolith converter using discrete channel-scale models. *Catalysis Today*, 188(1):80–86, 2012.

[9] SF Benjamin, RJ Clarkson, Net al Haimad, and NS Girgis. An experimental and predictive study of the flow field in axisymmetric automotive exhaust catalyst systems. *SAE Technical Paper*, No. 961208, 1996.

[10] RE Hayes, Anton Fadic, Joeseph Mmbaga, and A Najafi. CFD modelling of the automotive catalytic converter. *Catalysis Today*, 188(1):94–105, 2012.

[11] Soo-Jin Jeong. A full transient three-dimensional study on the effect of pulsating exhaust flow under real running condition on the thermal and chemical behavior of closed-coupled catalyst. *Chemical Engineering Science*, 117:18–30, 2014.

[12] COMSOL Multiphysics Software Package v4.3, 2012. COMSOL AB, Stockholm, Sweden.

[13] ANSYS Fluent Software Package v17.2, 2016. ANSYS Inc., Canonsburg, PA, USA.

[14] ANSYS Fluent Theory Guide v17.2. ANSYS Inc., Canonsburg, PA, USA, 2016.

[15] Fredrik Ekström and Bengt Andersson. Pressure drop of monolithic catalytic converters experiments and modeling. *SAE Technical paper*, No. 2002-01-1010, 2002.

[16] I Cornejo, P Nikrityuk, and RE Hayes. Turbulence decay inside the channels of an automotive catalytic converter monolith. *Emission Control Science and Technology*, 3(4):302—309, 2017.

[17] Ivan Cornejo, Petr Nikrityuk, and Robert E Hayes. Multiscale RANS-based modeling of the turbulence decay inside of an automotive catalytic converter. *Chemical Engineering Science*, 175:377–386, 2018.

[18] Ismail Tosun, Deniz Uner, and Canan Ozgen. Critical reynolds number for newtonian flow in rectangular ducts. *Industrial & Engineering Chemistry Research*, 27(10):1955–1957, 1988.

[19] Minyi Xu, Jianpeng Zhang, Pengfei Li, and Jianchun Mi. On two distinct reynolds number regimes of a turbulent square jet. *Theoretical and Applied Mechanics Letters*, 5(3):117–120, 2015.

[20] M Breuer, J Bernsdorf, Durst F Zeiser, and F Durst. Accurate computations of the laminar ow past a square cylinder based on two different methods: lattice-boltzmann and finite-volume. *International Journal of Heat and Fluid Flow*, 21:186–196, 2000.

[21] Ivan Cornejo, Petr Nikrityuk, and Robert E Hayes. Turbulence generation after a monolith in automotive catalytic converters. *Chemical Engineering Science*, 187:107–116, 2018.

[22] W Malalasekera and HK Versteeg. *An introduction to computational fluid dynamics: the finite volume method*. PEARSON Prentice Hall, Upper Saddle River, New Jersey, USA, 2007.

[23] Ronald M Heck, Suresh Gulati, and Robert J Farrauto. The application of monoliths for gas phase catalytic reactions. *Chemical Engineering Journal*, 82(1-3):149–156, 2001.

[24] R Litto, RE Hayes, H Sapoundjiev, A Fuxman, F Forbes, B Liu, and F Bertrand. Optimization of a flow reversal reactor for the catalytic combustion of lean methane mixtures. *Catalysis Today*, 117(4):536–542, 2006.

[25] B. Liu, R.E. Hayes, Y. Yi, J. Mmbaga, M.D. Checkel, and M. Zheng. Three dimensional modeling of methane ignition in a reverse flow catalytic converter. *Computers and Chemicals Engineering*, 31:292–306, 2007.

[26] A. Kushwaha, , M. Poirier, H. Sapoundjiev, and R.E. Hayes. Effect of reactor internal properties on the performance of a flow reversal catalytic reactor for methane combustion. *Chemical Engineering Science*, 59:4081–4093, 2004.

[27] Florian Menter. Two-equation eddy-viscosity turbulence models for engineering applications. *AIAA journal*, 32(8):1598–1605, 1994.

[28] Kyriacos Zygourakis. Transient operation of monolith catalytic converters: a two-dimensional reactor model and the effects of radially nonuniform flow distributions. *Chemical Engineering Science*, 44(9):2075–2086, 1989.

[29] SJ Porter. *An assessment of CFD applied to a catalytic converter system with planar diffuser*. PhD thesis, Coventry University, 2016.

[30] CP Om Ariara Guhan, G Arthanareeswaran, KN Varadarajan, and S Krishnan. Numerical optimization of flow uniformity inside an under body-oval substrate to improve emissions of IC engines. *Journal of Computational Design and Engineering*, 3(3):198–214, 2016.

[31] Rory John Clarkson. *A theoretical and experimental study of automotive catalytic converters*. PhD thesis, Coventry University, 1997.

[32] Anton Fadic, Teng-Wang Nien, Joseph Mmbaga, Robert E Hayes, and Martin Votsmeier. A case study in multi-scale model reduction: The effect of cell density on catalytic converter performance. *The Canadian Journal of Chemical Engineering*, 92(9):1607–1617, 2014.

[33] Georgi Kalitzin, Gorazd Medic, Gianluca Iaccarino, and Paul Durbin. Near-wall behavior of RANS turbulence models and implications for wall functions. *Journal of Computational Physics*, 204(1):265–291, 2005.

[34] Marek Václavík, Petr Kočí, Vladimír Novák, and David Thompsett. NOx conversion and selectivity in multi-layer and sequential DOC-LNT automotive exhaust catalysts: Influence of internal transport. *Chemical Engineering Journal*, 329:128–134, 2017.

[35] Yi Liu, Michael P Harold, and Dan Luss. Coupled NOx storage and reduction and selective catalytic reduction using dual-layer monolithic catalysts. *Applied Catalysis B: Environmental*, 121:239–251, 2012.

[36] Won-Wook Kim, Suresh Menon, Won-Wook Kim, and Suresh Menon. Application of the localized dynamic subgrid-scale model to turbulent wall-bounded flows. In *35th aerospace sciences meeting and exhibit.*, page 210, Reno, NV, USA, 1997.

Chapter 7

Influence of upstream turbulence on the pressure drop inside a monolith[1]

Abstract

This paper reports the pressure drop through a monolith for turbulent and laminar flow. A computational model of a monolith channel together with the open sections before and after it is used. Simulations at several channel Reynolds numbers, and assuming laminar and turbulent flow approaching the substrate are considered. Reynolds Average Navier Stokes (RANS) and Large Eddy Simulation (LES) are used as flow models for the cases with turbulence. The resulting pressure drop, power spectrum and flow regime are analysed. RANS predicts a decay of the turbulence as the flow approaches the substrate, a small fraction of the turbulence effectively entering the channels to decay rapidly, then steady flow from that point. On the other hand, LES predicts a total dissipation of the turbulence before the flow enters the channels; however, the flow remains unsteady along the entire substrate, in a sort of pulsating regime. Despite the significant differences of the flow regime, both models predict a marginal influence of the upstream turbulence on the total pressure drop. The dominating frequencies of the pulsating flow inside the channels were found to be comparable to the ratio of the channel velocity over the channel diameter, therefore, to the channel Reynolds number.

Keywords: CFD, monolith, turbulence, pressure drop, catalytic converter

[1] A version of this article has been published. 8. Cornejo, I., Nikrityuk, P., Lange, C., & Hayes, R. E. (2019). Influence of upstream turbulence on the pressure drop inside a monolith. Chemical Engineering and Processing-Process Intensification. DOI: `https://doi.org/10.1016/j.cep.2019.107735`.

7.1 Introduction

Structured reactor internals are increasingly being used in practice, both in the chemical process industries and in the catalytic destruction of undesired emissions. Compared to the classical packed bed reactor filled with pellets, structured reactors offer key advantages such as an enhanced structural integrity and a lower pressure drop [1–3]. Possibly the two most common types of structured internals are metallic foams and ceramic monoliths [4]. Monolith substrates became widely used with the introduction of the automotive catalytic converter in the 1970's. In this application, structural integrity and low pressure drop are critical. In particular, the pressure drop affects the fuel economy, which in turn alters the level of carbon dioxide emissions. In automotive applications, the catalyst is contained in a washcoat located on the surface of the parallel channels.

The focus of this paper is on the honeycomb monoliths used in automotive exhaust gas aftertreatment systems (EGATS). In a typical passenger vehicle application, engine exhaust flows in fully developed turbulent flow through the exhaust pipe, typically of the order of 2 to 4 cm in diameter, thence via an inlet expansion cone into the monolith reactor, which is usually 4 to 6 cm in diameter, depending on the vehicle [5]. The channel size in the monolith is smaller than 1 mm, so, not withstanding the large axial velocities of 2 to 10 m/s, the flow therein is laminar [6–8].

Strict government imposed limits on emissions and requirement to maximize fuel efficiency, combined with severe penalties for non-compliance give rise to a challenging optimization problem. A development program based entirely on experimentation would be costly and time consuming, and for this reason much effort has been expended in recent years on the development of advanced computational models to aid the optimization process [9]. Advances over the past few years in both computational hardware and software have made this route a viable option. Computer models for a catalytic converter are mainly divided into single channel models (SCM) and entire converter models (ECM). The former can be very useful for the evaluation of channel scale phenomena, whilst the latter are required to model the actual converter performance, including effects such as the flow mal-distribution and non-isothermal behaviour. Most of the ECM approximate the monolith as a continuum non-isotropic porous medium to reduce computational cost [10, 11].

Superficially, the implementation of a porous medium model appears to be straightforward. However, recent papers [12–14] have illustrated some of the pitfalls encountered when

taking a naive approach in adopting of a porous medium model in commercial software. Some of these errors arise from the situation of having a fully turbulent flow entering a monolith, wherein the flow is laminar, and exiting to a zone where turbulence reestablishes itself. Unless this transition is modelled accurately, the results for flow distribution, velocity profile, pressure drop and internal heat and mass transfer coefficients will not be predicted correctly. Cornejo et al. [15] showed the potential effect of decaying turbulence in the inlet zone of a channel, which was later shown to have an effect on the heat and mass transfer coefficients in that region [16]. Other works reported on an ECM for predicting pressure drop and flow profile using a multi-zone permeability model to account for the turbulence decay inside and generation after the monolith [6, 13].

This paper builds on previous work by showing the results of a detailed investigation using an SCM to model the effect of upstream turbulence on the pressure drop along monolith channels. The main motivation of this paper is to compare the results obtained in the presence and the absence of upstream turbulence, especially in terms of the pressure drop and flow regime trough a monolith channel. In depth Large Eddy Simulations (LES) were performed with a comprehensive analysis of the resulting flow field. Such a study has not previously been reported in the context of the automotive catalytic converter and it is an open discussion among the community.

7.2 Computational model

The computational domain is shown in Figure 7.1. It consisted in a square cross-section monolith channel together with the open scape before and after it. There is evidence in the literature that adding the section before the substrate is important to have a realistic velocity profile at the inlet of the channels [13, 17]. The section after the substrate is relevant, since turbulence can be generated there [14] affecting the total pressure drop.

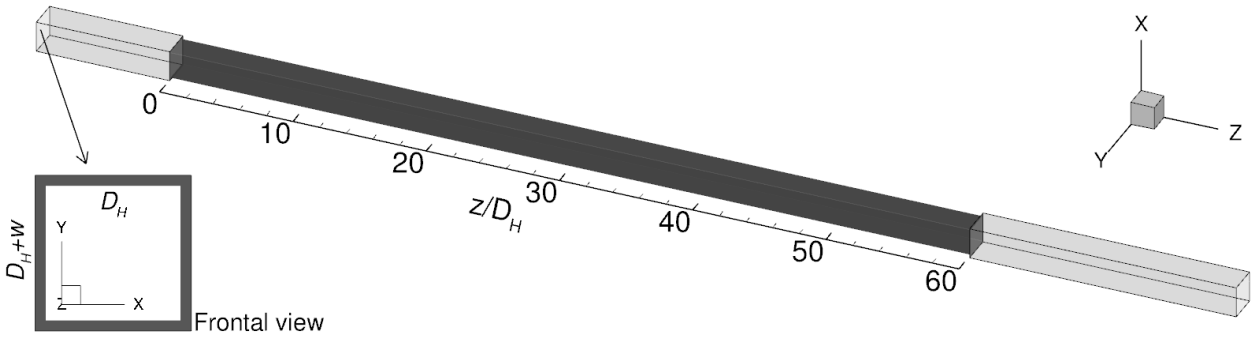

Figure 7.1: Computational domain and boundary conditions. Dark grey: no-slip walls, light grey: periodic boundaries, inlet: prescribed velocity, outlet: prescribed pressure. The frontal view shows the channel hydraulic diameter D_H=1 mm and the wall thickness w=0.16 mm

The channel hydraulic diameter (D_H) and wall thickness (w) were 1 mm and 0.16 mm respectively; that is a substrate void fraction of 0.74 approximately. The channel was 60 D_H long, and the open sections before and after it were 10 and 20 D_H of length respectively, to which size no boundary effects were observed. As shown in Figure 7.1, the boundary conditions for the open sections before and after the substrate were set as periodic, mirroring top-bottom and left-right. For every case, the inlet velocity was set to obtain the desired channel Re. When considering upstream turbulence, a turbulence intensity of 60% and a turbulence viscosity ratio of 20 were specified as inlet condition as well. Finally, in LES, the sub-grid turbulence intensity was assumed to be equal to the resolved one.

7.2.1 Flow model

To quantify the influence of the upstream turbulence on the total pressure drop, cases with and without turbulence were analysed and compared. Special attention should be paid to the turbulence model. In automotive applications, the Reynolds number decreases dramatically when the flow enters the channels from $\sim 10^4$ to $\sim 10^2$ approximately, leading to a transition of the flow regime. RANS models, which are the standard for industrial research, may have difficulties in such situations; hence, in addition, Large Eddy Simulation was also used. LES is much more expensive in terms of computational power, but it is suitable for flow in transition. The flow models used in this investigation are described further in the following sections.

Laminar

For laminar flow, the steady mass and momentum balances were solved directly over the entire domain. Their conservation equations were the following [18]:

$$\frac{\partial(\rho u_i)}{\partial x_i} = 0 \tag{7.1}$$

$$\frac{\partial(\rho u_i u_j)}{\partial x_j} = -\frac{\partial p}{\partial x_i} + \frac{\partial}{\partial x_j}\left[\mu\left(\frac{\partial u_i}{\partial x_j} + \frac{\partial u_j}{\partial x_i} - \frac{2}{3}\frac{\partial u_l}{\partial x_l}\delta_{ij}\right)\right] \tag{7.2}$$

RANS

There are several two-equation RANS models, among them, we selected the k-ω shear stress transport model (SST) This model represents the convection by eddies as additional diffusion through the turbulence viscosity and also accounts for the transport of shear stress. That makes it applicable to a broad range of conditions and it is in general more reliable than other eddy viscosity models [19]. Equation (7.1) is still valid as a mass balance, but for momentum, Equation (7.2) is replaced by (7.3). RANS models solve for the average flow field, so u_i and p represent average rather than instantaneous values when Equation (7.1) and (7.3) are used in RANS.

$$\frac{\partial(\rho u_i u_j)}{\partial x_j} = -\frac{\partial p}{\partial x_i} + \frac{\partial}{\partial x_j}\left[\mu\left(\frac{\partial u_i}{\partial x_j} + \frac{\partial u_j}{\partial x_i} - \frac{2}{3}\frac{\partial u_l}{\partial x_l}\delta_{ij}\right)\right] - \frac{\partial \tau_{ij}}{\partial x_j} \tag{7.3}$$

The term τ_{ij} is the Reynolds stress tensor. In this case, the closure was provided by the Boussinesq assumption, where the eddy viscosity was defined as follows [18, 19]:

$$\mu_t = \frac{a_1 k}{max(a_1\omega, SF_2)} \tag{7.4}$$

The transport equations for k and ω were [18, 19]:

$$\frac{\partial(\rho k u_i)}{\partial x_i} = \frac{\partial}{\partial x_j}\left[\left(\mu + \frac{\mu_t}{\sigma_k}\right)\frac{\partial k}{\partial x_i}\right] + G_k - Y_k \tag{7.5}$$

where

$$G_k = min(\mu_t S, 10\rho\beta^* k\omega)$$

$$Y_k = \rho\beta k\omega$$

and

$$\frac{\partial(\rho\omega u_i)}{\partial x_i} = \frac{\partial}{\partial x_j}\left[\left(\mu + \frac{\mu_t}{\sigma_\omega}\right)\frac{\partial \omega}{\partial x_i}\right] + G_\omega - Y_\omega + D_\omega \tag{7.6}$$

where

$$G_\omega = \frac{\rho\alpha_\omega}{\mu_t}\mu_t S$$

$$Y_\omega = \rho\beta\omega^2$$

$$D_\omega = 2(1 - F_1)\rho 1.168 \frac{1}{\omega}\frac{\partial k}{\partial x_j}\frac{\partial \omega}{\partial x_j}$$

The details of the SST model, its constants and blending functions can be found in Menter [19].

LES

LES has been validated in many contexts and it is suitable to predict laminar to turbulent transitions. LES separates the flow motion into a resolved and a modelled part by using a size filter. The modelled part contains all the flow motion with a characteristic length smaller than the size of the control volumes of the mesh. The finer the mesh, the higher the percentage of the total kinetic energy resolved. The transport equations for mass and momentum for LES were [18]:

$$\frac{\partial \rho}{\partial t} + \frac{\partial(\rho \overline{u}_i)}{\partial x_j} = 0 \tag{7.7}$$

$$\frac{\partial \overline{u}_i}{\partial t} + \overline{u_j}\frac{\partial \overline{u}_i}{\partial x_j} = -\frac{1}{\rho}\frac{\partial \overline{p}}{\partial x_i} + \frac{\partial}{\partial x_j}\left(\nu \frac{\partial \overline{u}_i}{\partial x_j} + \frac{1}{\rho}\frac{\partial \tau_{ij}}{\partial x_j}\right) \tag{7.8}$$

The variables with an overbar are filtered, representing the resolved motion. The rest of the kinetic energy is contained in the subgrid-scale. τ_{ij} in Equation (7.8) was modelled with the Dynamic Kinetic Energy Subgrid-Scale (DKE) model [20] as follows:

$$\tau_{ij} = \frac{2}{3}\rho k_{sgs}\delta_{ij} - 2C_k k^{1/2}\Delta_f \overline{S}_{ij} \tag{7.9}$$

The DKE model, which has been successfully applied in many situations [21, 22], uses the following transport equation for the sub-grid kinetic energy (k_{sgs}):

$$\frac{\partial(\rho k_{sgs})}{\partial t} + \frac{\partial(\rho \overline{u}_j k_{sgs})}{\partial x_j} = -\tau_{ij}\frac{\partial \overline{u}_i}{\partial x_j} - C_\varepsilon \rho \frac{k_{sgs}^{3/2}}{\Delta_f} + \frac{\partial}{\partial x_j}\left(\frac{\mu_{sgs}}{\sigma_k}\frac{\partial k_{sgs}}{\partial x_i}\right) \tag{7.10}$$

where

$$\mu_{sgs} = k\rho k_{sgs}^{1/2}\Delta_f$$

Further details about the model and its parameters can be found in Kim and Menon [20].

7.2.2 Discretization and solver settings

The conservation equations previously presented do not have an analytical solution; hence, they were solved numerically through computational fluid dynamics (CFD). The model was implemented in ANSYS Fluent 18.2 [23], which uses the finite volumes method (FVM). The

domain was discretized in a fully orthogonal homogeneous mesh of 5 018 400 control volumes. To investigate the grid independence with laminar flow and RANS, another mesh of 11 040 480 control volumes was tested, obtaining a total pressure drop that differed in less than the 0.4% from that with the previous mesh for the highest Re_c covered in this study. The working fluid was considered to be atmospheric air at 300 K and the density was calculated using the ideal gas law. For laminar flow and RANS the discretization scheme for momentum was Quadratic Upstream Interpolation for Convective Kinematics (QUICK), which is at least a second order accuracy approximation. A maximum value of scaled residuals of $\sim 10^{-8}$ and reaching a stationary total pressure drop were used as a convergence criterion. The maximum wall y^+ observed in the cases with upstream turbulence was below the unit. In the Finite Volumes Method, y^+ is the scaled distance from a wall to the centre of the closest control volume. A low value of y^+ is necessary to obtain an accurate description of the flow in the near-wall regions.

In LES, a bounded central difference scheme was used for momentum and a bounded second order implicit scheme for the unsteady term [18]. The convergence criterion for every time step was having a maximum value of scaled residuals of $\sim 10^{-6}$. Meanwhile, having a stationary time-average total pressure drop and volume average total kinetic energy over a moving time window four residence time long were considered as the stop criterion for every run. The size of the time step was manipulated to ensure a maximum Courant-Friedrichs-Lewy number below one (CFL=$u\Delta t/\Delta x$ <1), under such a condition the fluid advances a maximum of the length of one cell every time step. The maximum wall y^+ observed was below one and the percentage of kinetic energy resolved was above the 95% percent for all of the Re_c investigated.

7.3 Results and discussion

The influence of the upstream turbulence was analysed in terms of the total pressure drop through the substrate and the flow regime inside the channels. We start comparing the results from RANS and LES, then the total pressure drop with and without upstream turbulence is analysed.

7.3.1 Dissipation of the turbulence and flow regime

Figure 7.2 shows k resulting from using RANS and LES at two different Re_c. For both Re_c, when using RANS, k decreases when the flow is approaching the frontal face of the substrate.

A small amount of k enters the channels and then decays quickly, as the boundary layer develops from the walls of the channels and the inviscid core narrows. k behaves similarly at the highest and lowest Re_c, it decays until the flow becomes steady. The largest difference was that at a Re_c of 300 a slight generation of turbulence is noticeable downstream the channel once the flow leaves the substrate (this is better appreciated in the electronic version of Figure 7.2). It must be recalled that in eddy-viscosity models, k is a conservative quantity transported by diffusion and convection, and that dissipates at a rate according to Y_k in Equation (7.5); hence, such a decay was expected due to the influence of the solid on the flow.

In LES, the resolved and sub-grid kinetic energy were added to obtain the total kinetic energy, as usual (see Equation (7.11)). It must be noted that in the zones with laminar unsteady flow k will be different than zero even if the flow is not turbulent. That is, a value of k non-zero must not be interpreted as an indicator of the presence of turbulence directly, but as an indicator of unsteady flow. Similarly to RANS, in LES k also decays prior to the substrate. However, the flow does not turn into laminar steady. Instead of that, it becomes laminar pulsating inside the channels (more details are provided further in this section). As the flow enters the substrate, the remaining unsteadiness is promoted when the flow enters the channels by the acceleration due to the reduction of the flow area. For Re_c=100, k is higher in the second half of the channel, especially close to the end of the substrate. At a Re_c=300, the peak of k is also placed at the end of the channel, but, there is an additional secondary peak passing the zone of the vena contracta in the first half of the channel. For both Re_c the flow remained unsteady until the end of the domain, including the open space after the channel, where the main difference between the both is a third peak of k downstream the substrate for the case at Re_c=300. Although, the two k profiles are significantly different. It seems that the conjunction of many phenomena, such as the acceleration of the flow passing the frontal face of the substrate, the laminar to turbulent transition and the superposition of many frequencies of pulsation, makes difficult to find a clear pattern of the k profiles inside the channels when increasing Re_c. That involves many variables and significant computational power; hence, it will be addressed in a further paper.

$$k = \frac{1}{2}u_i'^2 + k_{SGS} \tag{7.11}$$

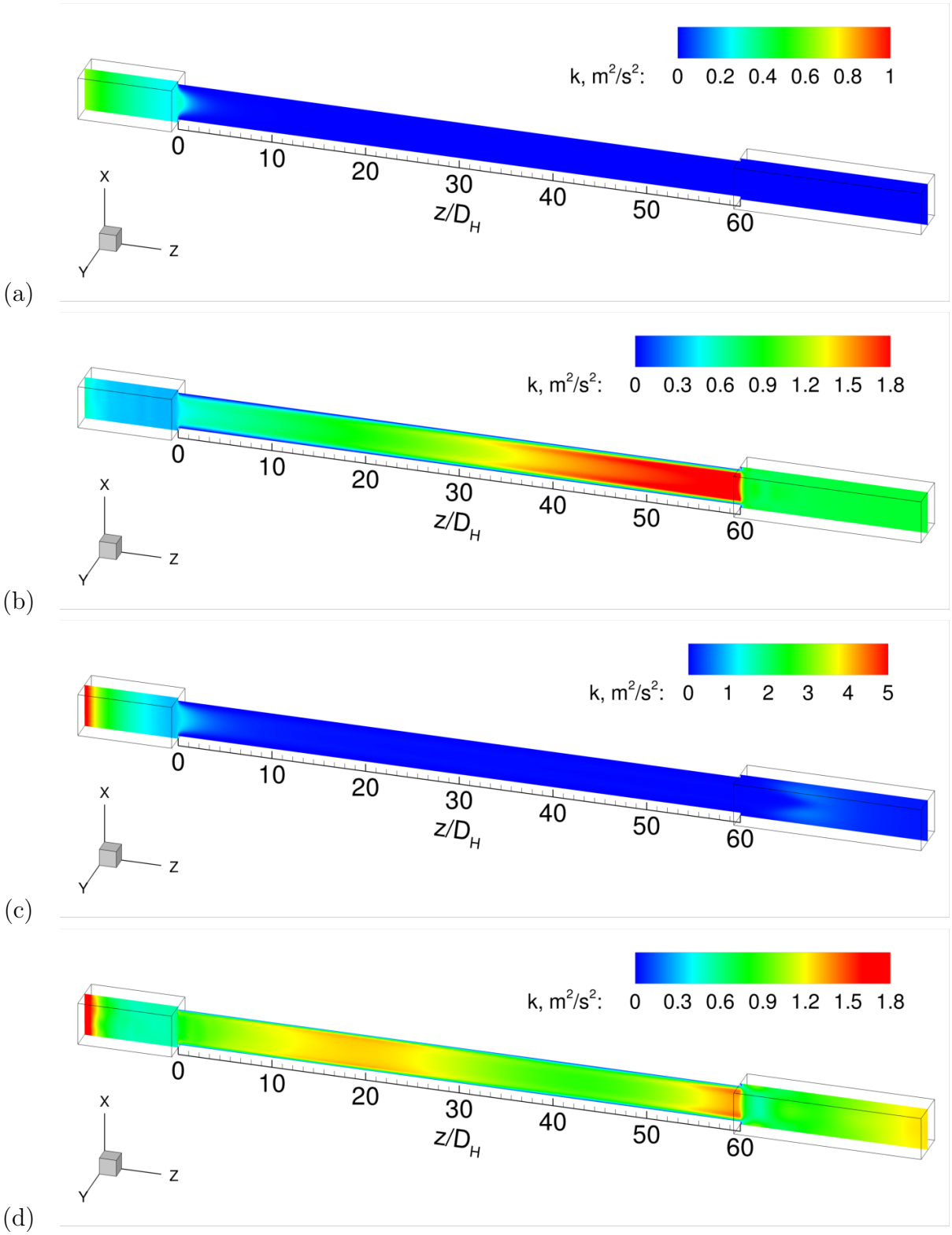

Figure 7.2: Comparison of the turbulence kinetic energy predicted by (a) RANS at Re_c=100, (b) LES at Re_c=100, (c) RANS at Re_c=300 and (d) LES at Re_c=300

Figure 7.3 shows the instantaneous scaled velocity in the centre of the channel at z/D_H=0 (the inlet of the channel) and z/D_H=10. It can be seen that the scaled velocities at the two monitoring points are highly correlated, being both practically the same. This agrees with previously reported data in the literature focused in heat transfer with upstream turbulence [16]. It can be seen in Figure 7.3 that as Re_c increases, the dominating frequency also increases, and that the number of frequencies contained in the velocity signal becomes higher. This also results in a higher number of periods in a same dimensionless time window.

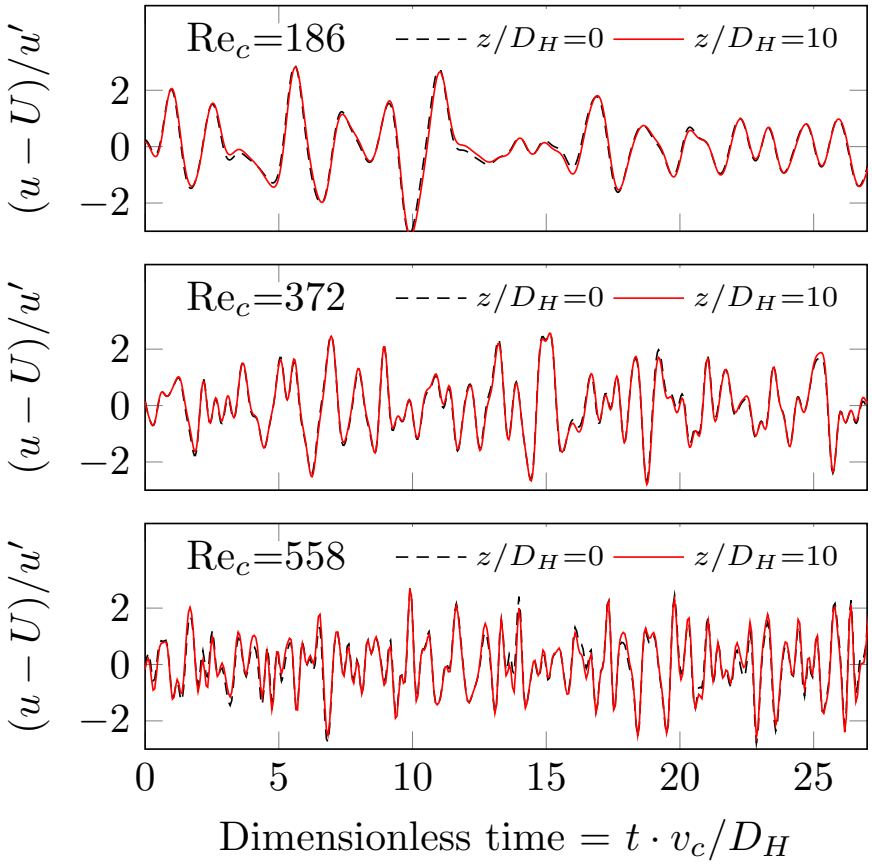

Figure 7.3: Scaled velocity through time at two points in the axis of the channel for several Re_c

A Fourier analysis of the three signals (see Figure 7.4a) confirms that at a higher Re_c there are more frequencies contained in the flow motion, that such frequencies are distributed more homogeneously and also that there is a progressive displacement of the entire distribution to the right. The power spectrum in Figure 7.4b provides additional information about the flow regime. In the three cases, there is a sudden decay of the energy content at a frequency of

about 2×10^3 Hz, 1×10^4 Hz and 2×10^4 Hz for Re_c 186, 372 and 558 respectively. Such gaps are typical of laminar unsteady flow. In contrast, a fully turbulent flow produces a power spectrum with a smooth transition from the inertial to the dissipative scales, as a direct consequence of a series of vortices of many sizes (eddies). The gap in the power spectrum in Figure 7.4b implies that there is not an energy cascade in the flow, and ultimately that the flow regime is laminar unsteady rather than turbulent. This means that convective transport and pressure drop are expected to be similar to those for laminar flow rather than those for fully turbulent flow.

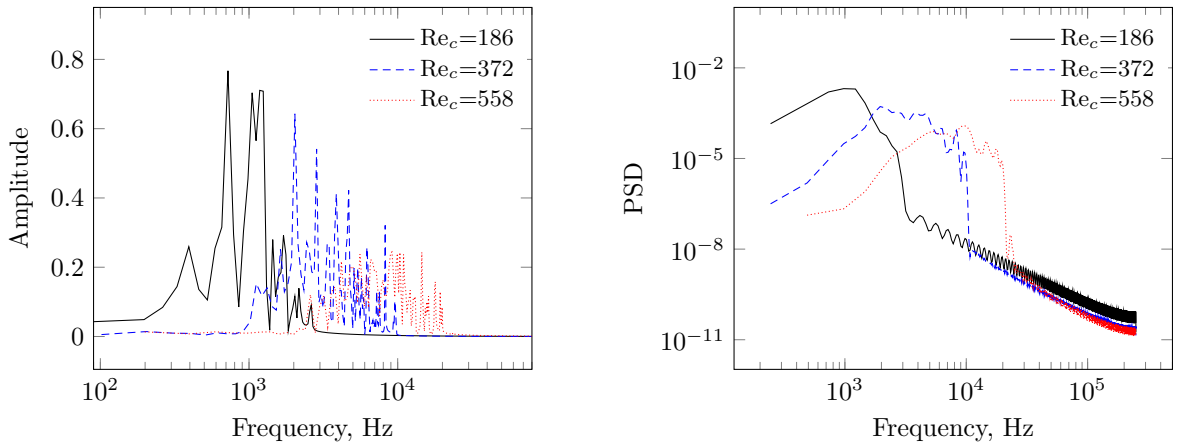

(a) (b)

Figure 7.4: (a) Fourier transform (b) power spectrum for three different Re_c

7.3.2 Total pressure drop

Figure 7.5 shows the total pressure drop through the entire domain and inside the channel for the three flow models analysed. As previously seen in Figure 7.2, RANS predicts a quick decay of the turbulence prior to the substrate and just a small amount of remaining turbulence entering the channels. Consequently, the pressure drop predicted using RANS is almost the same as that obtained assuming laminar flow from the beginning.

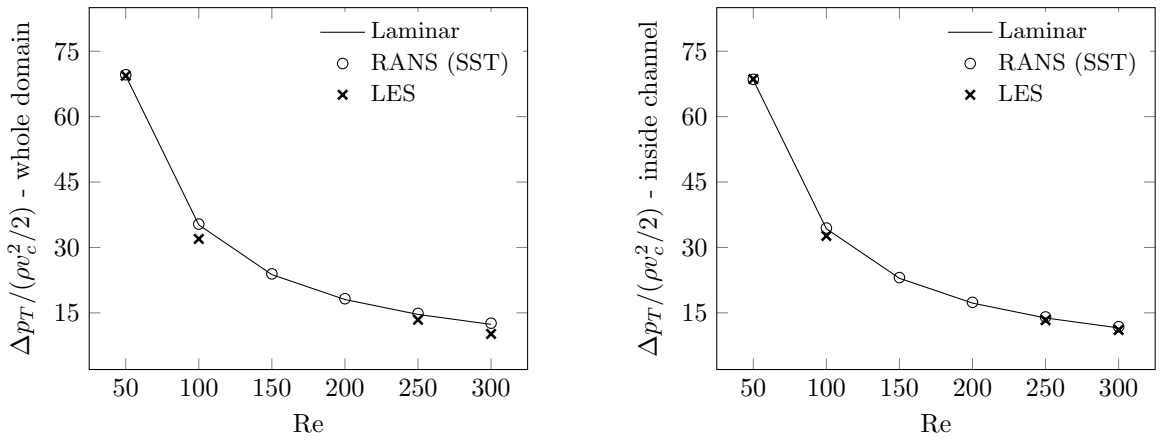

(a) (b)

Figure 7.5: Dimensionless pressure drop (a) along the whole domain and (b) inside the channel

Regarding the flow regime, according to Figures 7.2 to 7.4, results from LES show that once the flow laminarises it becomes laminar pulsating, opposite to RANS, which predicts a transition from turbulent to steady flow. The unsteady regime can be explained because of the upstream turbulence, which is actually changing the mass flow rate that enters the channels through time. According to the power spectrum in Figure 7.4b there are several pulsating frequencies overlapped inside the channels. In fully developed turbulent flow in circular pipes, the dominating frequencies are comparable to $C_l \cdot v_c/D_H$, where C_l is an empirical parameter close to 2 [18]. In this study, C_l was found to be different for every case rather than a unique one, and with a value from 0.5 to 2.5. Pulsating flow is characterised by Womersley number (Wo), defined as [24]:

$$\mathrm{Wo} = \frac{D_H}{2}\sqrt{\frac{\rho 2\pi f}{\mu}} \tag{7.12}$$

but

$$f = C_l \frac{v_c}{D_H} \tag{7.13}$$

then

$$\mathrm{Wo} = \sqrt{C_l \frac{\pi}{2}\mathrm{Re}_c} \tag{7.14}$$

In Wo in Equation (7.13) f is the frequency of a purely sinusoidal wave. For the values of C_l observed in this study and a typical Re_c in automotive applications, Wo moves from 6 to 40 approximately, it means that the flow is between the intermediate and inertial-dominant

regimes from the standpoint of pulsating flow [25]. According to the existing literature, in that condition, the pressure drop differs from that for steady flow [17]. Unfortunately, such a theory applies for Stokes flow only, which is far distant from to be the case in automotive applications. From a general standpoint, the average velocity profile for pulsating flow in channels is flatter than that for steady flow [26], which leads to a lower friction factor, and ultimately, to a lower pressure drop compared to that for a steady case. Hence, regardless the magnitude of the difference, results in Figure 7.5, where LES shows a slightly lower pressure drop instead of an equal or higher one, are feasible, and this paper provides clear evidence of that. However, further investigation is required before adventuring a general conclusion since classical theory of pulsating flow is not valid for the Re_c discussed in this paper, and also because pulsating flow resulting from the decay of upstream turbulence involves many frequencies rather than just a single purely sinusoidal wave. Nonetheless, what can be certainly concluded from this paper is that the influence of the upstream turbulence on the magnitude of the total pressure drop is minor for the conditions analysed. However, it might have other effects in, for example, the convective mass transfer that should be investigated.

7.4 Conclusions

The influence of the upstream turbulence on the pressure drop inside a monolith channel was successfully investigated using a computational model.

According to results from LES, based on a power spectrum analysis, the upstream turbulence decreases as it approaches to the substrate and the flow regime turns into laminar unsteady. This phenomenon was found to not be captured correctly by RANS models, which predict a transition to steady flow once the turbulence dissipates completely. A Fourier analysis of the flow motion once the turbulence dissipates inside the channels showed that the dominating frequencies are of the order of $C_l \cdot v_c/D_H$, by using that, a relationship between Wo and Re was established. That implies Re is the unique dimensionless number necessary to describe and investigate pulsating flow derivative from upstream turbulence. Additionally, the magnitude of the dominating frequency increases faster than Re.

Overall, the total pressure drop in the presence of upstream turbulence is practically the same as that for steady flow. Nonetheless, further investigation of other variables relevant for the design of the reactor, such as the entrance length and critical Re, when upstream turbulence exists is still needed. This paper considered a single channel and setting the boundaries

of the open sections to be periodic. Previous works from the authors showed that such a domain is enough to capture all the features of the flow motion in the section downstream the substrate. However, it should be corroborated that the same equivalence can be applied to the section upstream the channel as well.

Bibliography

[1] Michiel T. Kreutzer, Freek Kapteijn, and Jacob Moulijn. Shouldn't catalysts shape up?: Structured reactors in general and gas–liquid monolith reactors in particular. *Catalysis Today*, 111(1-2):111–118, 2006.

[2] Said Irandoust and Bengt Andersson. Monolithic catalysts for nonautomobile applications. *Catalysis Reviews Science and Engineering*, 30(3):341–392, 1988.

[3] Shaibal Roy, Tobias Bauer, Muthanna Al-Dahhan, Peter Lehner, and Thomas Turek. Monoliths as multiphase reactors: a review. *AIChE journal*, 50(11):2918–2938, 2004.

[4] Pedro Avila, Mario Montes, and Eduardo E Miró. Monolithic reactors for environmental applications: A review on preparation technologies. *Chemical Engineering Journal*, 109(1-3):11–36, 2005.

[5] RE Hayes, Anton Fadic, Joeseph Mmbaga, and A Najafi. CFD modelling of the automotive catalytic converter. *Catalysis Today*, 188(1):94–105, 2012.

[6] Ivan Cornejo, Petr Nikrityuk, and Robert E Hayes. Multiscale RANS-based modeling of the turbulence decay inside of an automotive catalytic converter. *Chemical Engineering Science*, 175:377–386, 2018.

[7] Fredrik Ekström and Bengt Andersson. Pressure drop of monolithic catalytic converters experiments and modeling. *SAE Technical paper*, No. 2002-01-1010, 2002.

[8] Henrik Strom, Srdjan Sasic, and Bengt Andersson. Effects of the turbulent-to-laminar transition in monolithic reactors for automotive pollution control. *Industrial & Engineering Chemistry Research*, 50(6):3194–3205, 2011.

[9] Matthias Hettel, Claudia Diehm, Bentholhoda Torkashvand, and Olaf Deutschmann. Critical evaluation of in situ probe techniques for catalytic honeycomb monoliths. *Catalysis Today*, 216:2–10, 2013.

[10] SF Benjamin, RJ Clarkson, Net al Haimad, and NS Girgis. An experimental and predictive study of the flow field in axisymmetric automotive exhaust catalyst systems. *SAE Technical Paper*, No. 961208, 1996.

[11] François Bertrand, Christophe Devals, David Vidal, Cyrille Séguineau de Préval, and Robert E Hayes. Towards the simulation of the catalytic monolith converter using discrete channel-scale models. *Catalysis Today*, 188(1):80–86, 2012.

[12] Ivan Cornejo, Robert E Hayes, and Petr Nikrityuk. A new approach for the modeling of turbulent flows in automotive catalytic converters. *Chemical Engineering Research and Design*, 140:308–319, 2018.

[13] Ivan Cornejo, Petr Nikrityuk, and Robert E Hayes. Pressure correction for automotive catalytic converters: A multi-zone permeability approach. *Chemical Engineering Research and Design*, 147:232–243, 2019.

[14] Ivan Cornejo, Petr Nikrityuk, and Robert E Hayes. Turbulence generation after a monolith in automotive catalytic converters. *Chemical Engineering Science*, 187:107–116, 2018.

[15] I Cornejo, P Nikrityuk, and RE Hayes. Turbulence decay inside the channels of an automotive catalytic converter monolith. *Emission Control Science and Technology*, 3(4):302—309, 2017.

[16] Ivan Cornejo, Gonzalo Cornejo, Petr Nikrityuk, and Robert E Hayes. Entry length convective heat transfer in a monolith: The effect of upstream turbulence. *International Journal of Thermal Sciences*, 138:235–246, 2019.

[17] Mukul Tikekar, Shiv Govind Singh, and Amit Agrawal. Measurement and modeling of pulsatile flow in microchannel. *Microfluidics and nanofluidics*, 9(6):1225–1240, 2010.

[18] ANSYS Fluent Theory Guide v18.2. ANSYS Inc., Canonsburg, PA, USA, 2017.

[19] Florian Menter. Two-equation eddy-viscosity turbulence models for engineering applications. *AIAA journal*, 32(8):1598–1605, 1994.

[20] Won-Wook Kim, Suresh Menon, Won-Wook Kim, and Suresh Menon. Application of the localized dynamic subgrid-scale model to turbulent wall-bounded flows. In *35th aerospace sciences meeting and exhibit.*, page 210, Reno, NV, USA, 1997.

[21] Won-Wook Kim and Suresh Menon. A new dynamic one-equation subgrid-scale model for large eddy simulations. In *33rd Aerospace Sciences Meeting and Exhibit*, Reno, NV, USA, 1995.

[22] Suresh Menon and Won-Wook Kim. High Reynolds number flow simulations using the localized dynamic subgrid-scale model. In *34th Aerospace Sciences Meeting and Exhibit*, page 425, Reno, NV, USA, 1996.

[23] ANSYS Fluent Software Package v18.2, 2017. ANSYS Inc., Canonsburg, PA, USA.

[24] Mair Zamir and EL Ritman. *The physics of pulsatile flow*. Springer, New York, USA, 2000.

[25] Richard Blythman, Sajad Alimohammadi, Tim Persoons, Nick Jeffers, and Darina B Murray. Parametric analysis of laminar pulsating flow in a rectangular channel. *Heat and Mass Transfer*, 54(8):2177–2186, 2018.

[26] Oswald Jason Lobo and Dhiman Chatterjee. Development of flow in a square mini-channel: Effect of flow oscillation. *Physics of Fluids*, 30(4):042003, 2018.

Chapter 8

Pressure correction for automotive catalytic converters: A multi-zone permeability approach[1]

Abstract

This paper presents an improved model for pressure drop in a honeycomb monolith reactor, which configuration is widely used in automotive exhaust gas after treatment systems. The model is based on pressure drop simulations for single channel models complemented with large eddy simulation. The model has multiple zones, and accounts for the pressure losses for flow entering, passing through, and leaving the substrate. The new multi-zone model is theoretically more consistent than those that use a single permeability for the whole the monolith, and it gives a superior result for pressure drop and hence flow distribution.

Keywords: CFD, monolith, pressure drop, catalytic converter, permeability

8.1 Introduction

Catalytic monolith reactors are comprised of a ceramic or metal substrate consisting of thousands of parallel channels. They are typically favoured for applications that require a low pressure drop and good structural integrity. They are the reactor of choice for automotive exhaust gas aftertreatments systems (EGATS) but have also been used in other industrial

[1]A version of this article has been published. Cornejo, I., Nikrityuk, P., & Hayes, R. E. (2019). Pressure correction for automotive catalytic converters: A multi-zone permeability approach. Chemical Engineering Research and Design, 147, 232-243.

applications [1–3]. In this study we focus on automotive applications, although the results are generally applicable to broader uses such as in Ref. [4, 5]. A typical catalytic converter consists of a metallic container with one or two monoliths in series. The cross section of the channels is most commonly square, but it can also be hexagonal or triangular [6]. A washcoat containing the catalyst is applied as a thin layer to the inner surface of the channels.

The purpose of the converter is to eliminate the pollutants in the exhaust gas from the engine. There are several variables affecting the performance of the reactor, such as the gas temperature, flow rate, washcoat loading, and dimensions of the substrate. In many applications the flow entering a monolith is not evenly distributed, which leads to large differences on the performance of the different channels [7]. The entire converter must be modelled to calculate the global efficiency, because single channel models result in an oversimplification of key results, such as pressure drop, and cannot predict the effect of flow maldistribution inside the converter. A single monolith can have tens of thousands of channels and a computational model may require of the order of the millions of computational cells for each channel, which makes spatially resolved models of the converter prohibitive [8]. To overcome this computational limitation, monoliths are typically modelled as homogeneous media at the converter scale [9]. Such an approximation reduces dramatically the number of required computational cells, allowing the solving of a simulation on a desktop computer within minutes. However, it raises a series of questions about how to obtain an accurate representation of a heterogeneous body with significant interactions between the flow and the solid by using a completely homogeneous medium. This is especially relevant when the flow enters and leaves the substrate. Experimental data about the effect of inlet flow on pressure drop and flow maldistribution for monolith reactors can be seen in Benjamin et al. [10]. Also, a detailed discussion about turbulence passing through homogeneous vs. heterogeneous models of a monolith can be found in Cornejo et al. [11].

Currently, the permeability of the equivalent porous medium representing a monolith is modelled by the Darcy-Frochheimer law where the radial viscous resistance is manipulated to be at least two or three orders of magnitude higher than the axial one. This prevents flow in the radial direction, which would be equivalent to an unrealistic flow between channels [12]. Due to the highly anisotropic permeability, all but the axial component of the velocity are rapidly damped to zero immediately the flow enters the porous zone, changing the flow essentially to 1-D. The underlying problem with that are those phenomena that depend on the local profile inside the channels, such as the pressure drop and heat transfer from the flow to the substrate. 1-D equivalent models for heat and mass transfer in channels have

been proposed in the literature for developed and developing laminar flow, and most recently extended to account for the effect of upstream turbulence [13, 14]. On the other hand, the pressure drop through a monolith has not been addressed properly so far. The simplest and most common models calculate the axial permeability of the equivalent porous medium by equating Darcy's law to Hagen–Poiseuille equation as shown in Equation (8.1). It leads to Equation (8.2), where D_H is the hydraulic diameter of the channel, ϕ is the void fraction of the monolith, and C is a constant that depends on the shape of the channel. The underlying assumption is having fully developed laminar flow along the entire channel (Poiseuille flow), which is reasonable for very large values of L/D_H only, when the hydraulic entrance length is negligible.

$$\frac{\Delta P}{L} = \underbrace{\frac{C\mu Q}{\pi D_H^4}}_{\text{Hagen}} = \underbrace{\frac{\mu Q}{\alpha_{axial} A}}_{\text{Darcy}} \tag{8.1}$$

then

$$\alpha_{axial} = \frac{\phi D_H^2}{C} \tag{8.2}$$

In automotive applications the hydraulic entrance length varies typically from 5 to 55 times the hydraulic diameter of the channels. It can represent an important fraction of the total length of the substrate, which is usually from 45 to 160 times the channel diameter. Similar numbers are also observed in other monolith applications [15]. Benjamin et al. [10] reported that for x^+ smaller than 0.2 the additional pressure drop for the developing region cannot be neglected. They modelled the extra viscous resistance by using the correlation proposed by Shah [16], which is based on an apparent friction factor along a whole channel. That implementation resulted in an improved prediction of the flow distribution and pressure drop for washcoated channels. Later, Ekstrom et al. [17] presented a model for pressure drop along a monolith together with a large set of experimental data. They subtracted the pressure drop from a short monolith to the one from a larger one, finding a quadratic dependency between the mentioned difference and the channel velocity. In that article, the second order dependence was explained by the effect of the upstream turbulence entering the monolith. However, pressure drop produced by the sudden contraction and expansion when the flow enters and leaves the monolith, also shows a quadratic dependence on the channel velocity, so it is not possible to know separately how each of these phenomena contribute to the total pressure drop. Additionally, the energy loss due to the developing velocity profile was not discussed, although that shows a non-linear dependence on the velocity as well. To the best of the knowledge of the authors, the mentioned works are two of the most comprehensive researches on pressure drop through a monolith to date. However, each one of

them is missing the part covered by the other, the way in which the models were developed makes it impossible to use them together, there are still parts missing in both models, and the investigation was done for a limited set of monolith configurations.

Recently, there is an increasing interest on improving the efficiency of monolith reactors by, for example, adding additional layers of catalyst and optimizing the channel geometry [18]. However, a reliable prediction of pressure drop is of great importance and remains unaddressed. This paper was motivated by the necessity of an improved model of a monolith, able to predict the total pressure drop accurately, applicable to a wide range of cases, and useful for further optimization at a reactor scale. The primary objective of this paper is making a comprehensive and detailed analysis of the pressure drop along each part of a monolith to improve CFD-based mixture models, which models the flow through a honeycomb using the continuum approach.

Finally, it should be noted that an adequate prediction of the pressure drop for a porous medium taking into account the inlet and outlet effects is of great importance not only for automotive catalytic converters [19], but also for many different applications in chemical engineering dealing with porous media. Some examples are catalytic flow reversal reactors [20], heat exchangers [21], and many types of filters [22]. A new model introduced in this work is able to predict the total pressure drop accurately using additional source terms in well accepted porous media approach. A distinguishing feature of the new model is its simple implementation into any commercial or open source code.

8.2 Methodology

This section describes the computational models for an entire monolith and a single channel, shows the equivalence between them, and how to move from one scale to the other. It also presents a brief discussion of the single and multiple permeability approaches for models of a whole substrate.

8.2.1 Problem statement

Let us consider a domain equivalent to the experimental setup used by Clarkson et al. [23] shown in Figure 8.1, to illustrate the pressure drop problem.

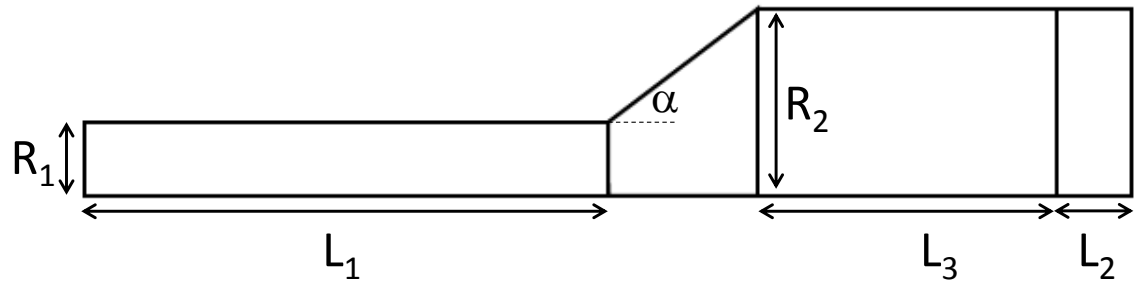

Figure 8.1: Schematic of an axisymmetric converter. L_1=2 m, L_2=30 mm, L_3=152 mm, R_1=27 mm, R_2=59 mm, and α=35°

The domain consisted of an inlet pipe 54 mm in diameter and 2 m long, followed by a diffuser with a 35° angle that connects the inlet pipe to a monolith 152 mm long and 118 mm in diameter. Due to computational limitations at a converter scale, the monolith was modelled as a continuum using a two equations RANS model. The steady state transport equations for mass and momentum at a converter scale, where the flow inside the channels is not resolved, are the following:

$$\rho \frac{\partial(u_i)}{\partial x_i} = 0 \tag{8.3}$$

$$\rho \frac{\partial(u_i u_j)}{\partial x_i} = -\frac{\partial P}{\partial x_i} + \frac{\partial}{\partial x_j}\left[\mu\left(\frac{\partial u_i}{\partial x_j} + \frac{\partial u_j}{\partial x_i} - \frac{2}{3}\frac{\partial u_k}{\partial x_k}\delta_{ij}\right)\right] - \frac{\partial \tau_{ij}}{\partial x_j} + S_{u_i} \tag{8.4}$$

The term τ_{ij} in Equation (8.4) is the Reynolds stress tensor, which depends on the turbulence model used. In this case the SST κ-ω eddy viscosity model [24, 25] was utilized, where:

$$-\tau_{ij} = -\rho\overline{u_i' u_j'} = \mu_t\left(\frac{\partial u_i}{\partial x_j} + \frac{\partial u_j}{\partial x_i}\right) - \frac{2}{3}\left(\rho\kappa + \mu_t\frac{\partial u_l}{x_l}\right)\delta_{ij} \tag{8.5}$$

and

$$\mu_t = \rho\frac{\kappa}{\omega}\frac{1}{Max\left(\frac{1}{\alpha*}, \frac{SF_2}{a_1\omega}\right)} \tag{8.6}$$

The transport equations for κ and ω were:

$$\rho\frac{\partial(\kappa u_i)}{\partial x_j} = \frac{\partial}{\partial x_j}\left[\left(\mu + \frac{\mu_t}{\sigma_\kappa}\right)\frac{\partial \kappa}{\partial x_i}\right] + \mu_t S^2 - \rho\beta^*\kappa\omega - S_\kappa^{sink} + S_\kappa^{gen} \tag{8.7}$$

$$\rho\frac{\partial(\omega u_i)}{\partial x_j} = \frac{\partial}{\partial x_j}\left[\left(\mu + \frac{\mu_t}{\sigma_\omega}\right)\frac{\partial \omega}{\partial x_i}\right] + \alpha\alpha^*\rho S^2 - \rho\beta^*\omega^2 + 2\left(1 - F_1\right)\rho\frac{1}{\omega\sigma_{\omega_2}}\frac{\partial\kappa}{\partial x_j}\frac{\partial\omega}{\partial x_j} + S_\omega^{sink} + S_\omega^{gen} \tag{8.8}$$

For brevity, constants and blending functions for the SST model are not provided. They are completely described in Menter et al. [24] and in the ANSYS Fluent Theory Guide v17.2 [25]. The source term S_{u_i} is the focus of this study. It is applied only inside the continuum and accounts for the extra pressure drop through the substrate. It is computed using the Darcy-Forchheimer law as:

$$S_{u_i} = -\left(\frac{\mu}{\alpha_i}u_i + C_u\frac{1}{2}\rho u_i^2\right) \tag{8.9}$$

Usually, the second term at the right-hand side of Equation (8.9) is neglected and the apparent permeability (α_i) is estimated based on the pressure drop through an ideal channel, as in Equation (8.2). Authors, such as Benjamin et al. [10] and Ekstrom et al. [17], proposed values for C_u based on experimental data or a variable permeability along the channels, assuming developing flow from a flat inlet velocity profile. In any event, using a unique permeability is theoretically inconsistent, because it applies along the entire monolith, however, there are phenomena that occur only at the beginning and entrance of the monolith and those should be independent of the substrate length. In a complete and comprehensive model of pressure drop it is desired to have an expression that accounts for all of the momentum losses and relate them to the typical geometrical features of monoliths. Let us consider Equation (8.10) to summarize all the pressure losses and name ΔP the total pressure drop along the entire substrate, ΔP_i the losses due to flow entering the monolith, ΔP_{el} those along the entrance length, ΔP_{df} for the section of the channel with fully developed flow, and ΔP_o any extra losses when the flow leaves the substrate. The points $A, B, C, D,$ and E are those marked on Figure 8.2.

$$\underbrace{\Delta P}_{P_A - P_E} = \underbrace{\Delta P_i}_{P_A - P_B} + \underbrace{\Delta P_{el}}_{P_B - P_C} + \underbrace{\Delta P_{df}}_{P_C - P_D} + \underbrace{\Delta P_o}_{P_D - P_E} \tag{8.10}$$

8.2.2 Channel scale model

The components of Equation (8.10) can be investigated in a geometry such as that shown in Figure 8.2. The total geometry replicates an actual section of a monolith. It includes a full 3D circular channel with the open sections before and after it (see Figure 8.2a). In automotive applications, bare substrates are most commonly made with square channels. The coating

process makes the channel cross section rounder, therefore, analysing circular channels is a good starting point [6, 26]. However, other channel shapes, especially square channels, should be investigated further. The diameter of the channel was fixed to one millimetre and the size of the inlet and outlet of the domain (H_c) were manipulated to obtain the same rate of contraction and expansion before and after the channel, which represents the void fraction of the monolith. A no-slip condition was set for the walls of the channel and for the frontal and rear faces of the monolith. The boundaries of the open sections looking to the top, bottom, left and right (normal to Z and Y in Figure 8.2a) were set as periodic boundaries. A flat velocity profile was set at the very inlet of the domain, since the scale of the inlet pipe before a monolith is significantly larger than the channel diameter, making the velocity profile of a small section essentially linear. The velocity magnitude at the inlet was manipulated according to the monolith void fraction to obtain channel Re between 100 and 700, which are also typical values for monolith applications. The outlet of the domain was set as outflow. Although, in automotive applications a substrate can be much longer, the length of the channel was fixed to 50 mm, which is sufficient to reach fully developed flow in of all the analysed cases and allows us to model all the relevant phenomena aimed at in this research. The extension of the both open sections were sequentially enlarged up to 20 channel diameters before and 60 diameters after the channel, at which point no boundary effects were observed. It is crucial to consider a section after the substrate large enough to, for example, avoid reverse flow through the outlet. Otherwise, the pressure drop will be in error.

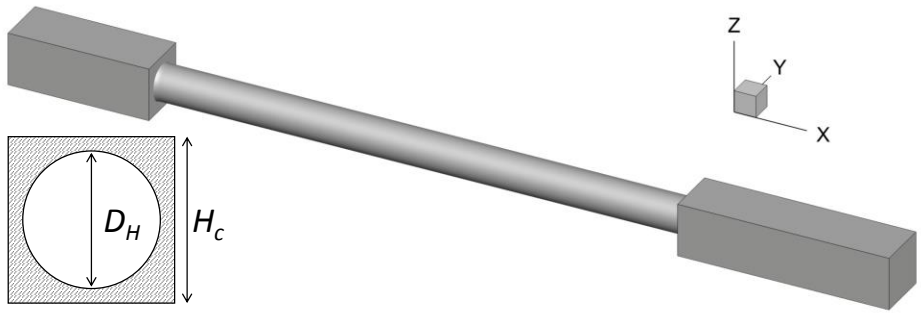

(a)

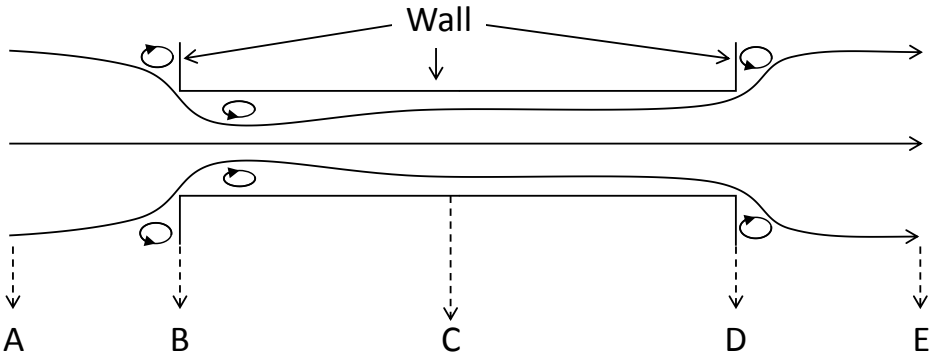

(b)

Figure 8.2: (a) Section of a monolith including a channel, the open space before and after it, and a cut of the inlet of the channel. (b) Lateral view of a cut along of the domain

According to the literature, there is turbulence upstream of the monolith, also, some vortices might enter the substrate to decay quickly along the channels [17, 27–29]. Current models assume fully developed laminar flow along the entire monolith, neglecting any inlet and outlet effect, hence, what was addressed first was extending such an approach to that detailed in Equation (8.10), with laminar flow entering straight to the substrate. Other effects, such as the one of the upstream turbulence when it exists, and thermal effects will be addressed in a further and much broader study, once each component of Equation (8.10) is clearly defined, making it possible to calculate the changes induced by the mentioned variables on the corresponding component of Equation (8.10) separately. The resulting transport equations for a steady laminar isothermal flow are:

$$\rho \frac{\partial(u_i)}{\partial x_j} = 0 \tag{8.11}$$

$$\rho \frac{\partial (u_i u_j)}{\partial x_j} = -\frac{\partial P}{\partial x_i} + \frac{\partial}{\partial x_j}\left[\mu\left(\frac{\partial u_i}{\partial x_j} + \frac{\partial u_j}{\partial x_i}\right) - \frac{2}{3}\frac{\partial u_i}{\partial x_j}\delta_{ij}\right] \tag{8.12}$$

All the simulations were implemented in ANSYS Fluent 18.2 [30], in a 40-core work station, consisting of two Intel Xenon E5-2698 v4 @2.2 GHz. The operating fluid was atmospheric incompressible air at 300 K. The problem is isothermal and the maximum pressure difference observed was 327 Pa, which led to changes in the fluid density below 0.32%. Hence, it was considered constant and set at 1.225 kg/m^{3}3. In models for reacting and non-isotherm flow or with larger pressure changes, which will be addressed in further papers, varying fluid properties should be set accordingly. The momentum scheme was set to QUICK and the SIMPLE algorithm was set to solve the pressure velocity coupling. The convergence criterion was set for a maximum scaled residuals of the order of 10^{-8} and a stable value for the total pressure drop.

8.2.3 Validation

The grid independence of the solution was investigated by refining the mesh systematically until a stable total pressure drop and friction factor along the substrate were observed. Two fully hexahedral meshes of 3.2 and 7.4 millions of control volumes each were compared, giving identical results.The quality of the computational model inside the channels was tested in two ways simultaneously. A flat profile was set to the inlet of the channels, then the hydraulic entrance length was monitored for the developing zone, meanwhile, the friction factor was the variable analyzed in the developed region. A cross section of the mesh inside a channel is shown in Figure 8.3.

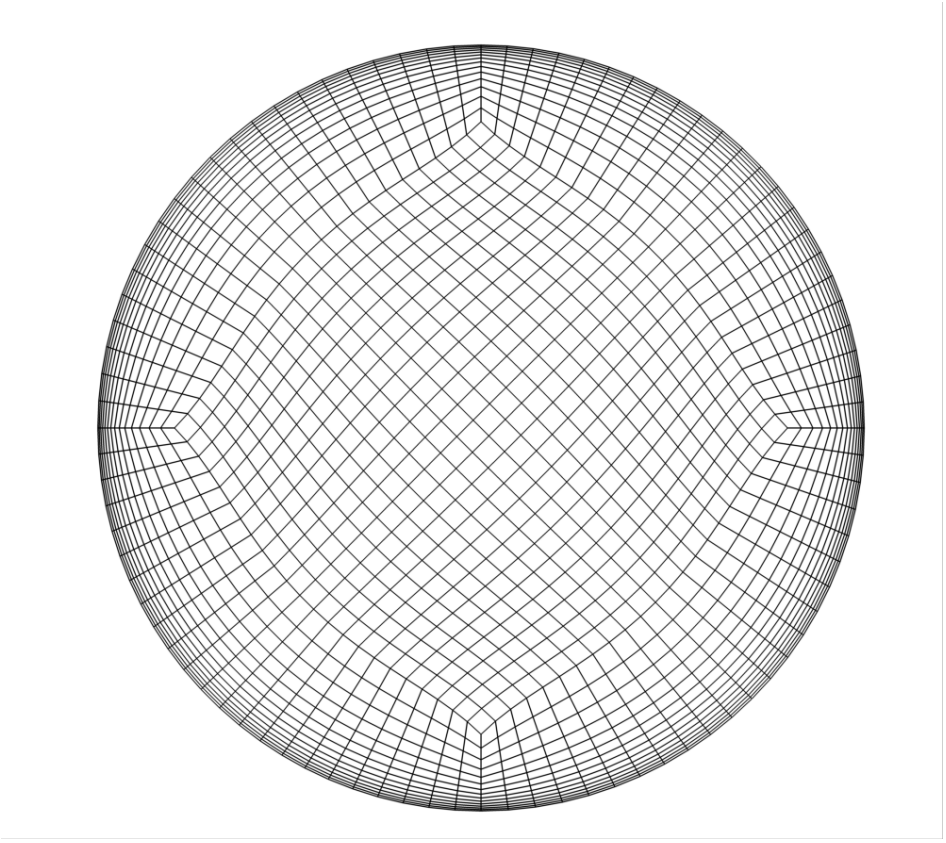

Figure 8.3: Transverse cut of the mesh inside the channel

The use of the friction factor as a monitored variable is ideal because it is sensitive to the flow model and to the quality of the grid. Also, it is a quantity relevant to the pressure drop, which is the focus of this study. Results were compared to data reported in the literature presenting a satisfactory agreement in therms of the hydraulic entrance length and friction factor in the developed zone. Results are shown in Figure 8.4.

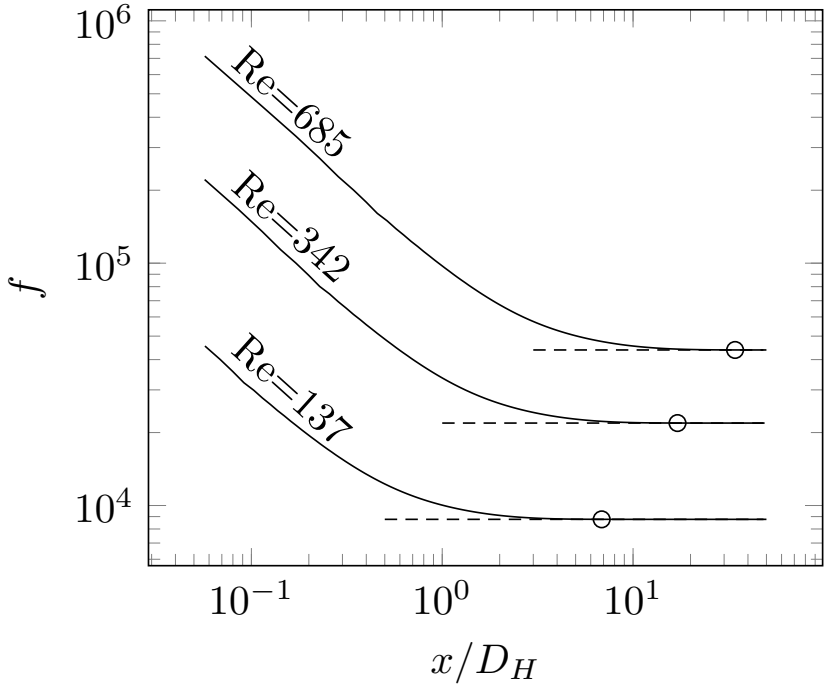

Figure 8.4: Friction factor at three different channel Re. Dashed lines are the analytic friction factors for the developed zone (64/Re) [31]. Circles are showing the hydraulic entrance length for each Re (L_H/D_H=0.05Re) [32]

8.2.4 Confirming the flow regime

A Large Eddy Simulation (LES) using the highest velocity and lowest void fraction among those covered in this study was carried out with the purpose of discarding the triggering of turbulence in the recirculating zones and to confirm the assumption of laminar flow. For that purpose, the inlet was set as steady laminar flow, free of turbulence turbulence (k=0, ω=0). Under such a condition the channel Re was 685 and the monolith void fraction was 30%. The subgrid model was the Wall-Adapting Local-Eddy viscosity model (WALE), which is especially suitable for describing flow close to walls [33]. The mass and momentum equations were [25]:

$$\frac{\partial \rho}{\partial t} + \frac{\partial}{\partial x_j}(\rho \overline{u}_i) = 0 \tag{8.13}$$

$$\frac{\partial \overline{u}_i}{\partial t} + \overline{u_j}\frac{\partial \overline{u}_i}{\partial x_j} = -\frac{1}{\rho}\frac{\partial \overline{P}}{\partial x_i} + \frac{\partial}{\partial x_j}\left(\nu \frac{\partial \overline{u}_i}{\partial x_j} + \frac{1}{\rho}\frac{\partial \tau_{ij}}{\partial x_j}\right) \tag{8.14}$$

where

$$\tau_{ij} = \frac{1}{3}\tau_{kk}\delta_{ij} - 2\mu_{SGS}\frac{1}{2}\left(\frac{\partial \overline{u}_i}{\partial x_j} + \frac{\partial \overline{u}_j}{\partial x_i}\right)$$

$$\mu_{SGS} = \rho L_s^2 \frac{\left(S_{ij}^d S_{ij}^d\right)^{3/2}}{\left(\overline{S}_{ij}\overline{S}_{ij}\right)^{5/2} + \left(S_{ij}^d S_{ij}^d\right)^{5/4}}$$

$$S_{ij}^d = \frac{1}{2}\left[\left(\frac{\partial \overline{u}_i}{\partial x_j}\right)^2 + \left(\frac{\partial \overline{u}_j}{\partial x_i}\right)^2\right] - \frac{1}{3}\delta_{ij}\frac{\partial \overline{u}_i}{\partial x_j} \tag{8.15}$$

The term L_s in the definition of μ_{SGS} was calculated as $min\left(kd, C_W V^{1/3}\right)$, where k is the von Karman's constant, d is the distance to the closest wall, V is the volume of the cell, and C_W is a constant. The LES was implemented in ANSYS Fluent 18.2 [30]. A grid study was conducted refining systematically a full hexahedra grid, monitoring the total pressure drop along the domain. When refining the mesh the time step was manipulated to ensure always a maximum CFL. In each case the solution converged to a steady one and the subgrid content was negligible, with a subgrid turbulence viscosity ratio of the order of 10^{-2} or below.

8.2.5 Experimental design

The computational experiments at a channel scale covered all of the combinations between the channel Re and monolith void fractions listed in Table 8.1. The approaching velocity upstream of the channels was calculated according to each void fraction to obtain the desired set of channel Re. The design was thought to be orthogonal, allowing us to study the degree of dependence of the results on the channel Re at a constant monolith void fraction as well as the results from changing the void fraction at a fixed channel Re. The number of levels of each variable was meant to be sufficient to describe accurately at least a second order dependence, but also to cover a wide range of values among those typically found in monolith applications.

Table 8.1: Parameters and inlet values

Variable	Value						
Re	137	342	479	685			
ϕ	0.31	0.40	0.51	0.65	0.69	0.80	0.91
ρ, kg/m^3	1.225						
μ, kg/m-s	1.789×10^{-5}						
D_H, mm	1						

8.3 Results and discussion

This section presents the results of pressure drop at a channel scale, develops an equivalent permeability model for a whole monolith and implements it at a converter scale.

8.3.1 Single channel

Figure 8.5 shows the pressure and velocity along the centre line of the domain for a channel Re of 342 and a monolith void fraction of 0.65. It is noticeable how the reduction of the flow area when entering the channel causes a rapid increase of the flow velocity at the beginning of the channel (x/D_H=0) together with a sudden decrease of the static pressure due to the combined effects of the losses by friction and the developing velocity profile. After the hydraulic entrance length, the rate of decrease of mechanical energy is the same as that of the static pressure, which is as expected along the fully developed zone. Passing the end of the channel (x/D_H=50), the flow decelerates to reach the same velocity as that in the open section before the monolith, and the static pressure also recovers.

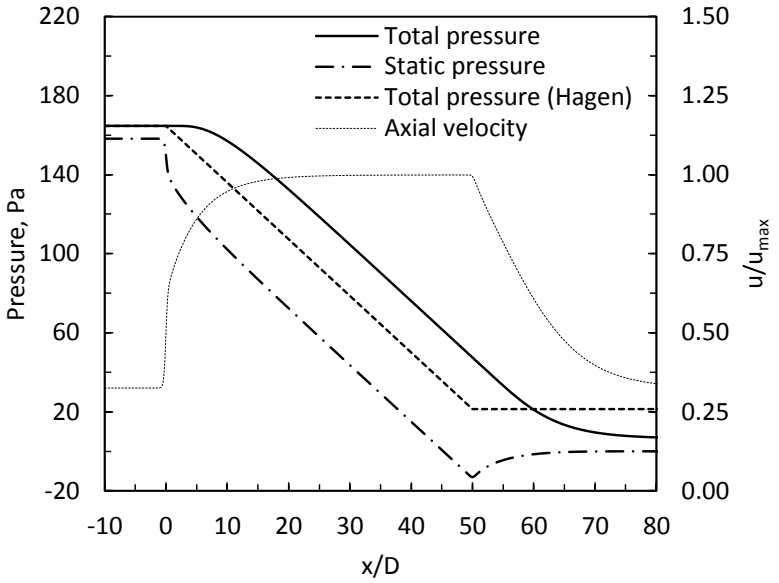

Figure 8.5: Velocity and pressure along the centre line of a monolith channel. Channel Re 342, and void fraction 0.65. The channel runs from x/D_H=0 to x/D_H=50

Additionally to the CFD results, the total pressure along the channel centre line calculated by using the Hagen-Poiseuille equation is also shown in Figure 8.5. This is the theoretical pressure when the inlet and outlet effects are neglected and a fully developed velocity profile is assumed. It can be seen that it describes accurately the energy losses over the developed

zone only. Pressure drop at the inlet, and outlet of the substrate are neglected, meanwhile those at the entrance length are assumed to be the same as those for the developed zone. As a result, the losses are not only underestimated, but also are very insensitive to a main feature of the monolith, namely the void fraction. In the example, for a channel Re of 342 the entrance length is of about 17 channel diameters. However, the Re can be as high as 1000, to which the entrance length is close to 50 channel diameters. Such an extension cannot be neglected, since the friction factor for developing flow is higher than that for developed flow.

A comparison of the error in the estimation of the total pressure drop through a monolith channel when using a discrete model and assuming Poiseuille flow for several channel Re and two void fractions can be seen in Figure 8.6. It is noticeable how the highest percentage of pressure drop is explained by friction along the developed region of the channels, the second in magnitude is the outlet pressure drop, finally, the inlet effect is minor. It is also noticeable how the total error, calculated as the total pressure drop observed in a discrete channel minus the one predicted by the simple use of the Hagen-Poiseuille equation, scales rapidly with the channel Re to be more than 30% in some cases. Also, it must be pointed out that the percentages in the figure are illustrative, since the inlet and outlet effects are independent of the length of the channels, however, their relative weight decreases as the channel length increases. Therefore, the total percentage error for a shorter substrate can be even higher.

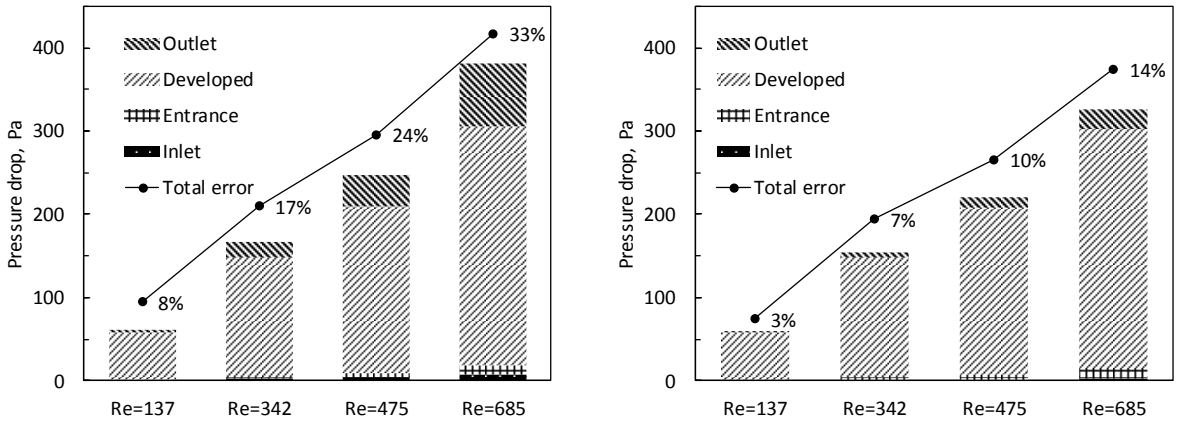

Figure 8.6: Pressure drop at each part of a monolith of (a) 31% and (b) 91% as a void fraction. The total error is referred to the difference when the Hagen-Poiseuille equation is used to calculate the total pressure drop

Detailed results covering all of the values in Table 8.1 are are summarized in Figure 8.7.

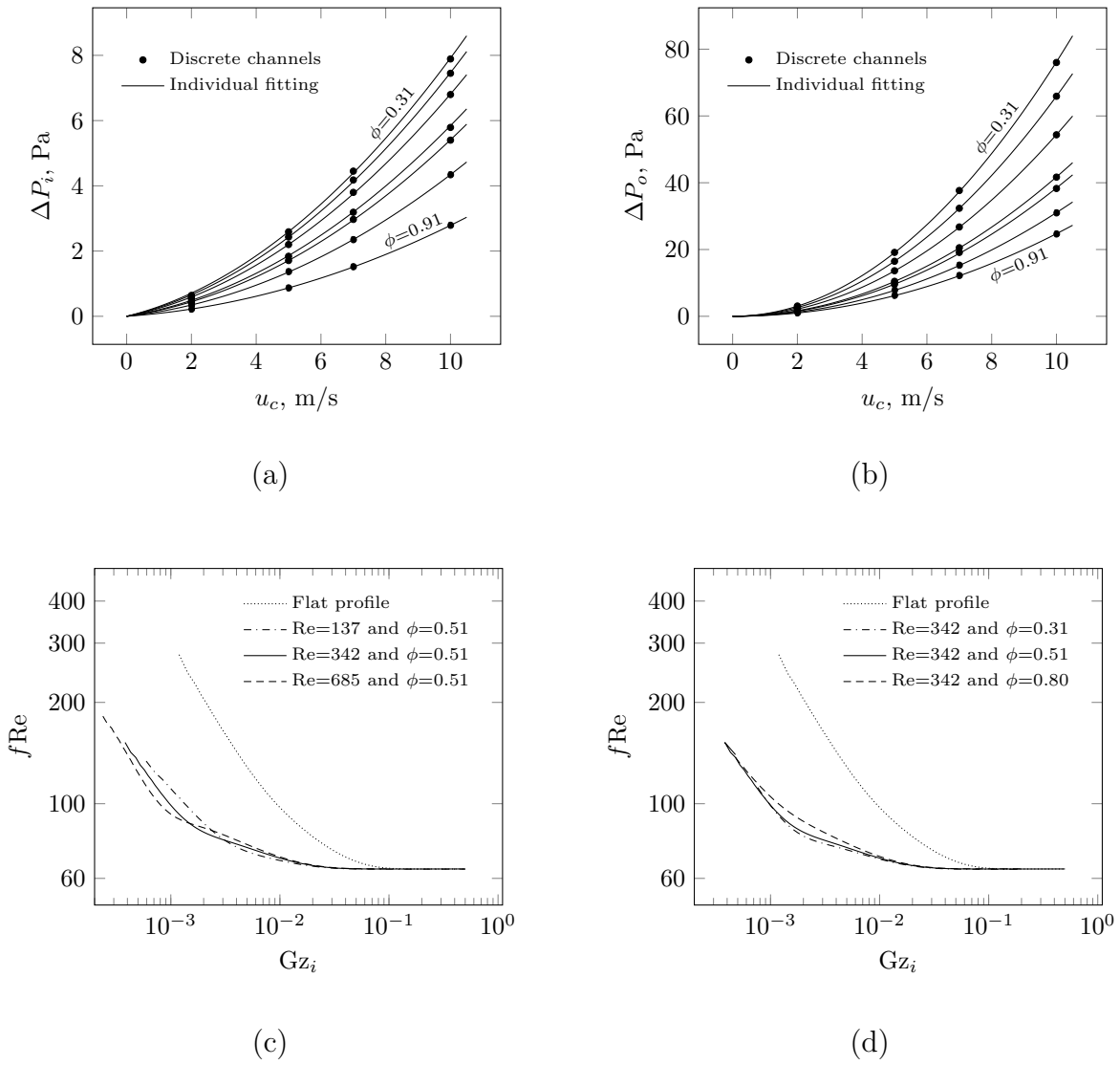

Figure 8.7: Pressure drop when (a) entering and (b) leaving the substrate. (c)-(d) Friction factor inside the substrate. Conditions are listed in Table 8.1

The flow area varies through the domain and the velocity profile changes not only inside the channels, but also when entering and leaving it, hence, the losses were calculated as the differences of the mass weighted average of total mechanical energy, which is the argument of Equation (8.16) integrated across transverse sections of the domain. The inverse of the Graetz number (Gz_i) was used as a dimensionless distance and calculated according to Equation (8.17). The Reynolds number in Equation (8.18) is the channel Re, where D_H is the hydraulic diameter of the channel, and u_c is the channel velocity. The rates of contraction and expansion at the inlet and outlet of the channel were represented by the void fraction of the substrate calculated from Equation (8.19).

$$P = \frac{1}{\int_S \rho u \cdot dS} \int_S \left(P_s + \frac{1}{2}\rho u^2 \right) \rho u \cdot dS \tag{8.16}$$

$$\mathrm{Gz}_i = \frac{x^+}{\mathrm{Pr}} = \frac{x}{\mathrm{RePr}D_H} \tag{8.17}$$

$$\mathrm{Re} = \frac{\rho u_c D_H}{\mu} \tag{8.18}$$

$$\phi = \frac{\text{flow area inside the substrate}}{\text{flow area outside the substrate}} = \frac{\pi D_H^2}{4H_c^2} \tag{8.19}$$

As expected, the pressure drop when entering and leaving the channel increases with the flow velocity and decreases with the monolith void fraction. Inside the channels, the sensitivity of the the group $f\mathrm{Re}$ to the void fraction is minor, however, it describes a curve different from when the inlet velocity profile is flat.

8.3.2 Development of the pressure drop model

The pressure drops for flow entering and leaving the monolith were calculated as $\Delta P_i = P_A - P_B$ and $\Delta P_o = P_D - P_E$ respectively, where the points A, B, D, and E are those in Figure 8.2. Consistent with Borda and Carnot [34], the pressure drops depend on the flow velocity and void fraction, analogously to the pressure drop through a sudden reduction or expansion. When modelling a monolith using a homogeneous medium, the Darcy-Forchheimer law can be used to describe the viscous and inertial losses as the momentum source term shown in Equation (8.9). Alternatively, when the losses occur along a short distance, as in the case of the flow colliding with the frontal face of the monolith, the pressure drop can be assumed to happen through a porous jump as in Equation (8.20) [25]. A porous jump is a 1-D simplification of a thin porous medium, typically used to account for the pressure drop through screens or filters where the pressure-velocity curve is known. It is applied to a face of a computational cell. The thickness of the thin porous layer that the jump is representing is known and finite, but the pressure drop is assumed to occur immediately when the flow passes through the face of the cell, with a magnitude calculated by Equation (8.20). This approach is ideal to model the pressure drop when entering and leaving the monolith.

$$\Delta P = \left(\frac{\mu}{\alpha} u_c + C_u \frac{1}{2} \rho u_c^2 \right) \Delta m \tag{8.20}$$

The data set of each void fraction in Figure 8.7a-b is accompanied by an individual fitting to Equation (8.20), where the linear coefficient is equal to $(\mu/\alpha)\Delta m$ and the quadratic one

to $(C_u \rho u^2/2)\Delta m$. The properties of the fluid are known, therefore, the values for $\Delta m/\alpha$ and $\Delta m C_u$ can be obtain directly for each case.

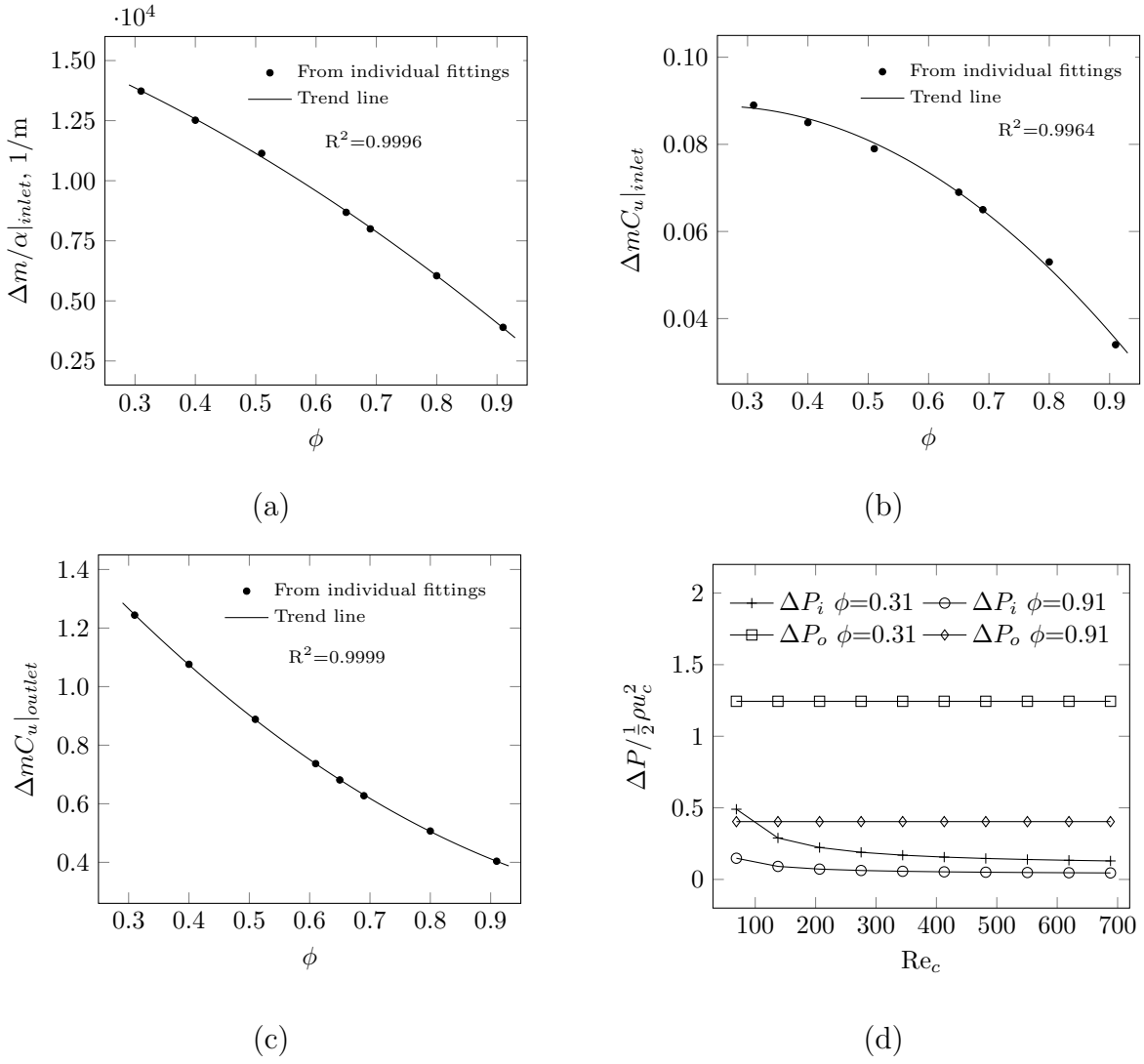

Figure 8.8: (a) Inlet apparent permeability, (b) inlet inertial resistance coefficient, and (c) outlet inertial resistance coefficient as a function of the monolith void fraction. (d) Dimensionless pressure drop at the inlet and outlet of a monolith channel

As shown in Figure 8.8, both coefficients for the inlet have a strong dependency and can be written in terms of the monolith void fraction, leading to Equation (8.21) and (8.22) to describe the pressure drop at the beginning and end of the monolith respectively. All curve fittings show a high R^2 coefficient, however, when testing the parameters individually, the linear term for the outlet proved to be statistically not significant and it was discarded in the final model.

$$\Delta P_i = (f_1|_{inlet})\mu u_c + (f_2|_{inlet})\frac{1}{2}\rho u_c^2 \tag{8.21}$$

where

$$(f_1|_{inlet}) = (\Delta m/\alpha)|_{inlet} = -6678.9\phi^2 - 8294.9\phi + 16956$$

$$(f_2|_{inlet}) = (\Delta m C_u)|_{inlet} = -0.127\phi^2 + 0.0590\phi + 0.0816$$

$$\Delta P_o = (f_2|_{outlet})\frac{1}{2}\rho u_c^2 \tag{8.22}$$

where

$$(f_2|_{outlet}) = (\Delta m C_u)|_{outlet} = 0.9782\phi^2 - 2.5968\phi + 1.9567$$

For the pressure drop inside the substrate, to account for the developing of the velocity profile, it was necessary to study the friction factor along the channel. If the friction factor is known, then Equation (8.23) can be used to estimate the pressure losses [32].

$$\frac{\partial P}{\partial x} = f_{(x)}\frac{1}{D_H}\frac{1}{2}\rho u_c^2 \tag{8.23}$$

For a laminar developed flow, pressure losses can be accurately calculated by the Hagen-Poiseuille law, which is an analytic solution based on the friction between the flow laminae. On the other hand, for developing flow there are several approaches, where an empirical determination of model coefficients is often required. The two main approaches are those similar to the one proposed by Al-Nassari and Unny [35], which uses an apparent friction factor that accounts for the overall losses, and those like the one in Shah [16], where a local friction coefficient that varies along with the pipe is used. Such approaches assume a flat profile at the inlet of the channels. This imposes additional challenges when modelling monolith channels, since the contraction of the flow creates a stagnation zone that separates the main flow stream from the wall close to the inlet of the substrate. As shown in Benjamin et al. [7], the size of the stagnation area in the zone of the *vena contracta* changes significantly when, for example, the flow enters in an oblique angle to the substrate. Figure 8.9a illustrates how different the velocity profiles can be at the inlet of the channels for two channel Re and monolith void fractions.

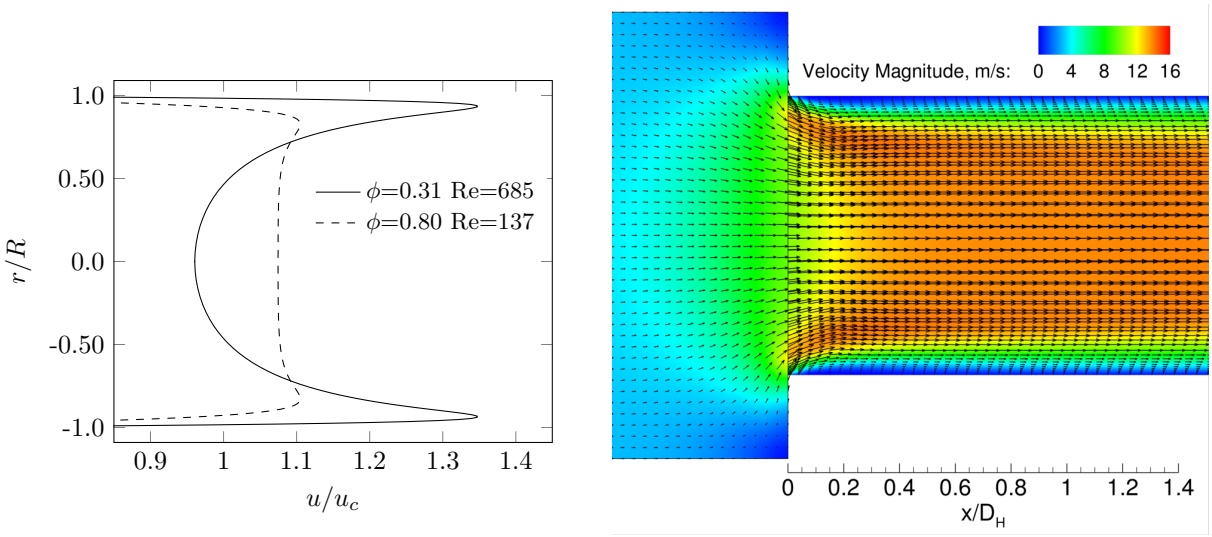

(a) (b)

Figure 8.9: (a) Velocity profile at the inlet of the channel for two channel Re and monolith void fractions. (b) Visualization of flow entering a channel with Re=685 and ϕ=0.31

According to the results in Figure 8.7c-d, modifications on the fRe vs. Gz_i curve produced by the monolith void fraction and channel Re were minor. However, it is also remarkable that all of the curves differed significantly from the one when starting from a flat profile. That is most probably explained because of the presence of a stagnation zone at the area of the *vena contracta*, which size was highly insensitive to the analyzed reduction of the flow area and velocity when the flow approaches straight to the substrate. Figure 8.9b shows the inlet of a channel for a Re of 685 and a reduction rate of 0.31. It can be seen that the development of the boundary layer and the inviscid core are affected by the inlet effect, especially at the corners. However, the size of *vena contraca* does not differ significantly from that in Benjamin et al. [7] for a reduction rate of 0.73. Due to its simplicity and easy implementation, among the expressions for the fRe group, we followed the one with the mathematical shape of Equation (8.24), which has been successfully implemented to describe heat and mass transfer coefficients for developing flow in monolith channels in the past [36, 37].

$$f_{(x)} = \frac{1}{\mathrm{Re}} \left[\left(\frac{c_1}{\sqrt{\mathrm{Gz}_i}} \right)^n + (f_{fd}\mathrm{Re})^n \right]^{1/n} \tag{8.24}$$

The values for c_1 and n in Equation (8.24) were obtained by carrying out a curve fitting on all the curves in Figure 8.7c-d simultaneously (except those for a flat profile), since the difference between them is minor. The result was a value of c_1=2.5855 and n=2.1154, with an overall R^2 of 0.9747. Equations (8.21) to (8.24) complete the pressure drop model. Now,

Equation (8.10) can be recalled and rewritten as:

$$\Delta P = \underbrace{(f_1|_{inlet})\mu u_c + (f_2|_{inlet})\frac{1}{2}\rho u_c^2}_{\Delta P_i} + \underbrace{\int_0^L \frac{\rho u_c^2}{2D_H} f_{(x)} dx}_{\Delta P_{el}+\Delta P_{df}} + \underbrace{(f_2|_{outlet})\frac{1}{2}\rho u_c^2}_{\Delta P_o} \tag{8.25}$$

Finally, an expression for the apparent permeability for an equivalent porous medium was developed for the cases in which it is desired to represent the monolith as a homogeneous medium. That was done by equating the instantaneous pressure drop for Darcy's law to that for flow in pipes. The mathematical formulation is illustrated using the values for a circular pipe as follows:

$$\frac{\partial P}{\partial x} = \underbrace{\frac{u_c \mu}{\alpha_{(x)}}}_{\text{porous}} = \underbrace{f_{(x)} \frac{1}{D_H} \frac{1}{2} \rho u_c^2}_{\text{channel}} \tag{8.26}$$

Solving for $\alpha_{(x)}$ as a function of $f_{(x)}$ and reordering

$$\alpha_{(x)} = \frac{2D_H \mu}{f_{(x)} \rho u_c} \cdot \frac{8D_H}{8D_H} = \frac{64}{\mathrm{Re}} \cdot \frac{1}{f_{(x)}} \cdot \frac{D_H^2}{32} \tag{8.27}$$

By inspecting Equation (8.27), it can be recognized the friction factor (64/Re) and the equivalent permeability ($D_H^2/32$) for a circular pipe with developed laminar flow. Equation (8.28) is a more general expression, where the sub-index fd stands for fully developed zone.

$$\alpha_{(x)} = \alpha_{fd} \frac{f_{fd}}{f_{(x)}} \tag{8.28}$$

Notice that for Equation (8.24) to (8.28) the inlet of the substrate is located at x=0.

8.3.3 Implementation at a converter scale

This section illustrates the implementation of the proposed multi-zone model of pressure drop in Equation (8.25) in a converter scale simulation. Then, the differences in the results when using a single and a multi permeability model are discussed.

Setting up the domain

Figure 8.10 shows the geometry of an axial symmetrical automotive catalytic converter emulating the one used by Clarkson [23]. It contained an unwashcoated monolith 152 mm long and 118 mm as a diameter. The dimensions of the rest of the converter are the same as that in Figure 8.1. That is an inlet pipe 2000 mm long and 54 mm diameter, a diffuser with an

expansion angle of 35°, and a straight section 30 mm long after the substrate. Right after the diffuser there is a porous zone representing the monolith. Also, 1-D layers were added at the beginning and the end of the porous zone, to account for the extra pressure drop when entering and leaving the monolith. As explained later, those layers were set as interior or porous jumps, depending on the permeability model used.

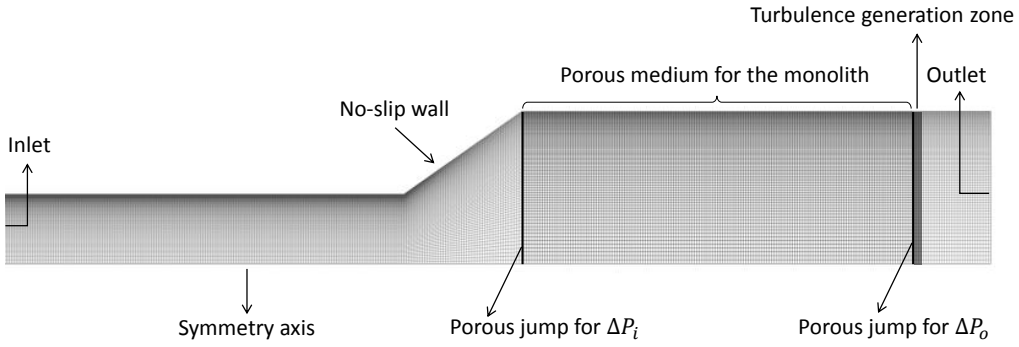

Figure 8.10: Schematic for a whole converter including a 1-D porous jump for ΔP_i followed by the monolith as a continuum, 1-D porous jump for ΔP_o, and a turbulence generation zone. Note: The figure is not showing the whole length of the inlet pipe

Setting up the flow model

The mass and momentum equations were the same than those in Equation (8.3) and (8.4). The turbulence was modelled with the SST eddy viscosity model, where the transport equations for κ and ω are those in Equation (8.7) and (8.8) respectively. A physical decreasing of the turbulence inside the porous zone was achieved by implementing the terms S_κ^{sink} and S_ω^{sink} described in Equation (8.29) and (8.30) into the corresponding transport equations for κ and ω. Both emulate the damping of the turbulence due to the interaction of the flow with the walls of the channels inside the monolith. They were applied exclusively to the porous zone and were implemented as user defined functions [29].

$$S_\kappa^{sink} = -\frac{\mu_{eff}}{\alpha_i}\kappa \tag{8.29}$$

$$S_\omega^{sink} = -\frac{\mu}{\alpha_i}\left(\omega - C_\omega \frac{\mu/\rho}{\beta_\omega \Delta^2/4}\right) \tag{8.30}$$

The terms S_κ^{gen} and S_ω^{gen} account for the turbulence generation terms after the substrate. They were modelled using an immersed boundary condition that evaluates Re based on the channel velocity and wall thickness. If it is higher than the critical vale, it triggers turbulence

right after the substrate, making the flow regime leaving the porous medium consistent with the one leaving a series of channels. The magnitude of the turbulence generated was calculated according to Equation (8.31) and (8.32), and were fixed exclusively to the turbulence generation zone (see Figure 8.10). Further details of the implementation of the turbulence generation after the monolith are extensively described in Cornejo et al. [11].

$$\kappa = \frac{\mu_t}{\rho D_H C_\mu} \tag{8.31}$$

$$\omega = \frac{\kappa^{1/2}}{D_H C_\mu} \tag{8.32}$$

Setting up the permeability model

The apparent permeability of the porous zone accounts for the extra pressure drop of flow through a monolith. Two configurations were tested. The first one assuming Poiseuille flow and estimating the axial apparent permeability of the porous zone representing the monolith as shown in Equation (8.2). The radial permeability was set to be three orders of magnitude lower than the axial one. Porous jumps at the beginning and end of the monolith were not used. It means that they do not produce an additional pressure drop. The second configuration tested was the one composed of multi-zones proposed in this paper. It also uses Darcy law, but with a variable axial permeability, which accounts for the developing and developed flow and is calculated as in Equation (8.28). It was implemented as a user defined function. The radial permeability was kept as 10^{-3} times the axial one, analogously to the previous case. The extra pressure drop at the inlet and outlet of the substrate (ΔP_i and ΔP_o) were each implemented as a porous jump (see Figure 8.10), where the apparent face permeability, pressure jump coefficients, and apparent thickness were estimated by using Equation (8.21) and (8.22).

Solver settings and grid analysis

The pressure-velocity coupling was solved with the SIMPLE algorithm and all the schemes for momentum, k, and ω were set as QUICK. The convergence criterion was reaching a maximum value for the scaled residuals below 10^{-6}, a constant total pressure drop, and a constant volume average velocity magnitude. The grid independence of the solution was investigated by refining the mesh systematically and monitoring the total pressure drop and peak velocity after the monolith, following the same procedure as in previous works [11, 28, 29]. There were no differences on the results when using a mesh with 40 000 and 240 000 control volumes. The maximum wall y^+ observed, 0.93, and the smooth refinement

in radial direction allowed us the use of a low Re correction for the wall treatment [25].

Results at a converter scale

Figure 8.11 shows the velocity profile at the outlet of the substrate of a converter scale simulation. The inlet Re was 30 000, the inlet turbulence intensity was set as 15%, and the turbulence length scale to be 0.4 times the diameter of the inlet pipe as recommended for fully turbulent flow in pipes [25]. Figure 8.11a compares a experimental velocity profile [23] to the one obtained when assuming Poiseuille flow for a substrate with square channels of 1.1 mm of height and a wall thickness of 0.16 mm. Figure 8.11b makes a similar comparison between the Poiseuille model (single and constant permeability) and the one proposed in this work, but for a monolith with circular channels. At the same wall thickness and channel size, that changes the void fraction from 0.76 to 0.60, and the C coefficient from 28.4 to 32 (see Equation (8.2)). It can be seen how simply assuming Poiseuille flow inside the channels underestimates significantly the peak velocity. Additionally, the flow in the section close to the wall ($r/R > 0.6$) the velocity profile is notoriously flatter that the experimental one. It can also be seen in Figure 8.11b that when using the proposed model, both the peak velocity and the section of the profile close to the wall are much more pronounced. The last was also observed for results at an inlet Re of 60 000. Both are important results, since the underestimation of the flow maldistribution across the monolith is a common issue when modelling a converter through the porous medium approach. The same difficulties are present for the secondary velocity peak close to the wall. The total pressure drop through the monolith when using the multi-zone permeability model was 1.3% lower than that obtained when a single and constant permeability was assumed. This is an interesting result, since the simple use of Hagen-Poiseuille law underestimates the pressure drop when a single channel is analyzed, however, at a converter scale it is the opposite. This also agrees with Clarkson [23], who reported that assuming Poiseuille flow overestimates the total pressure drop through the converter. Back pressure affects flow distribution and flow distribution affects back pressure, so the lower pressure drop is consistent with a better flow distribution.

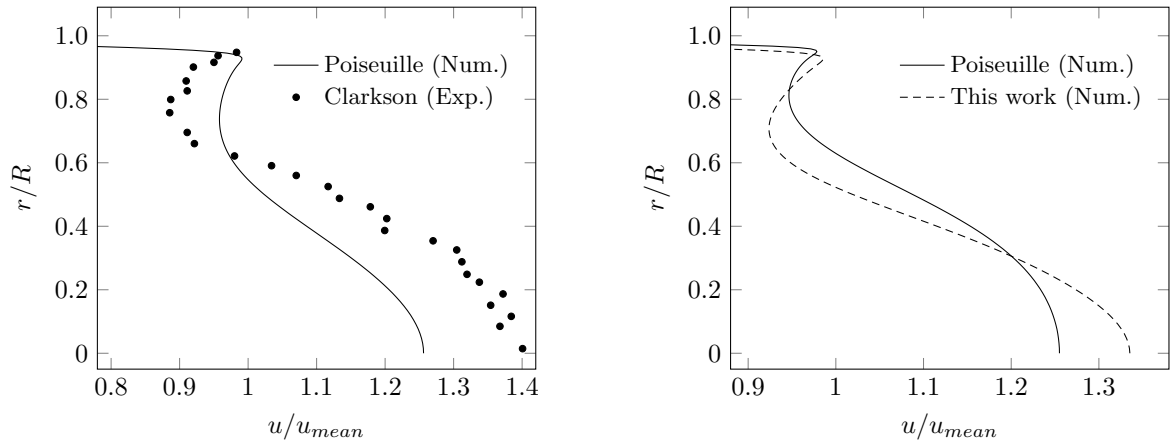

(a) Square channels

(b) Circular channels

Figure 8.11: Axial velocity profile at the outlet of the monolith comparing (a) Poiseuille flow to experimental data for square channels [23], and (b) Poiseuille flow to the results from this work for circular channels

8.4 Conclusions

Pressure drop through a monolith was studied at a channel scale over a range of channel Re and monolith void fractions. A new multi-zone model was presented that improves the accuracy of the prediction of the total pressure drop compared to when a single permeability is assumed. The model makes the continuum approach for modelling a monolith consistent with the results observed in a discrete channel geometry. The multi-zone model is theoretically consistent and applicable to a wide range of cases because it depends on the most relevant geometrical features of a honeycomb.

The presented model proved to be superior to constant permeability models when predicting the peak velocity at the centre of the substrate. In the area close to the wall, the velocity profile is less flat than that predicted by Poiseuille flow and it seems to be more in agreement with the experiments; however, in that area the flow is entering in a oblique angle to the substrate and that effect is not accounted in this paper. Further research covering other channel cross section shapes is also recommended.

Bibliography

[1] Van Nhu Nguyen, Robert Deja, Roland Peters, Ludger Blum, and Detlef Stolten. Study of the catalytic combustion of lean hydrogen-air mixtures in a monolith reactor. *International Journal of Hydrogen Energy*, 43(36):17520–17530, 2018.

[2] Piyanut Inbamrung, Thana Sornchamni, Chaiwat Prapainainar, Sabaithip Tungkamani, Phavanee Narataruksa, and Goran N Jovanovic. Modeling of a square channel monolith reactor for methane steam reforming. *Energy*, 2018.

[3] Young Deok Ahn and Jung Heon Lee. Development of a Polyaniline-coated Monolith Reactor for the Synthesis of Cephalexin Using Penicillin G-Acylase Aggregates. *Biotechnology and Bioprocess Engineering*, 23(3):349–354, 2018.

[4] Sofiane Arab, Jean-Marc Commenge, Jean-François Portha, and Laurent Falk. Methanol synthesis from CO2 and H2 in multi-tubular fixed-bed reactor and multi-tubular reactor filled with monoliths. *Chemical Engineering Research and Design*, 92(11):2598–2608, 2014.

[5] Michele Negri, Marius Wilhelm, Christian Hendrich, Niklas Wingborg, Linus Gediminas, Leif Adelöw, Corentin Maleix, Pierre Chabernaud, Rachid Brahmi, Romain Beauchet, et al. New technologies for ammonium dinitramide based monopropellant thrusters–the project rheform. *Acta Astronautica*, 143:105–117, 2018.

[6] RE Hayes, B Liu, R Moxom, and M Votsmeier. The effect of washcoat geometry on mass transfer in monolith reactors. *Chemical Engineering Science*, 59(15):3169–3181, 2004.

[7] SF Benjamin, N Haimad, CA Roberts, and J Wollin. Modelling the flow distribution through automotive catalytic converters. *Proceedings of the Institution of Mechanical Engineers, Part C: Journal of Mechanical Engineering Science*, 215(4):379–383, 2001.

[8] François Bertrand, Christophe Devals, David Vidal, Cyrille Séguineau de Préval, and Robert E Hayes. Towards the simulation of the catalytic monolith converter using discrete channel-scale models. *Catalysis Today*, 188(1):80–86, 2012.

[9] M.C. Lai, T. Lee, J.Y. Kim, C.Y. Cheng, P. Li, and G. Chui. Numerical and experimental characterizations of automotive catalytic converter internal flows. *Journal of Fluids and Structures*, 6:451–470, 1992.

[10] SF Benjamin, RJ Clarkson, Net al Haimad, and NS Girgis. An experimental and predictive study of the flow field in axisymmetric automotive exhaust catalyst systems. *SAE Technical Paper*, No. 961208, 1996.

[11] Ivan Cornejo, Robert E Hayes, and Petr Nikrityuk. A new approach for the modeling of turbulent flows in automotive catalytic converters. *Chemical Engineering Research and Design*, 140:308–319, 2018.

[12] RE Hayes, Anton Fadic, Joeseph Mmbaga, and A Najafi. CFD modelling of the automotive catalytic converter. *Catalysis Today*, 188(1):94–105, 2012.

[13] RE Hayes and Stan T Kolaczkowski. Mass and heat transfer effects in catalytic monolith reactors. *Chemical Engineering Science*, 49(21):3587–3599, 1994.

[14] Ivan Cornejo, Gonzalo Cornejo, Petr Nikrityuk, and Robert E Hayes. Entry length convective heat transfer in a monolith: The effect of upstream turbulence. *International Journal of Thermal Sciences*, 138:235–246, 2019.

[15] Sarah Couck, Julien Cousin-Saint-Remi, Stijn Van der Perre, Gino V Baron, Clara Minas, Patrick Ruch, and Joeri FM Denayer. 3D-printed SAPO-34 monoliths for gas separation. *Microporous and Mesoporous Materials*, 255:185–191, 2018.

[16] RK Shah. A correlation for laminar hydrodynamic entry length solutions for circular and noncircular ducts. *Journal of Fluids Engineering*, 100(2):177–179, 1978.

[17] Fredrik Ekström and Bengt Andersson. Pressure drop of monolithic catalytic converters experiments and modeling. *SAE Technical paper*, No. 2002-01-1010, 2002.

[18] Rama Krishna Dadi, Keyvan Daneshvar, Dan Luss, Vemuri Balakotaiah, Christos M Kalamaras, and William Epling. Comparison of light-off performance of Pt-Pd/γ-Al2O3 dual layer and dual brick diesel oxidation catalysts. *Chemical Engineering Journal*, 335:1004–1017, 2018.

[19] Qingyun Su, Liang Xie, Shijin Shuai, Jianxin Wang, Jinou Song, and Zhijun Li. Optimization of automotive catalytic converter by numerical modeling and simulation with detailed mechanism. *Catalysis Today*, 216:292–298, 2013.

[20] R Litto, RE Hayes, H Sapoundjiev, A Fuxman, F Forbes, B Liu, and F Bertrand. Optimization of a flow reversal reactor for the catalytic combustion of lean methane mixtures. *Catalysis Today*, 117(4):536–542, 2006.

[21] Marilena Musto, Nicola Bianco, Giuseppe Rotondo, Flavio Toscano, and Giuseppe Pezzella. A simplified methodology to simulate a heat exchanger in an aircraft's oil cooler by means of a porous media model. *Applied Thermal Engineering*, 94:836–845, 2016.

[22] Toni Pujol, Gerard Arbat, Josep Bove, Jaume Puig-Bargues, Miquel Duran-Ros, Joaquim Velayos, and Francisco Ramırez de Cartagena. Effects of the underdrain design on the pressure drop in sand filters. *Biosystems Engineering*, 150:1–9, 2016.

[23] Rory John Clarkson. *A theoretical and experimental study of automotive catalytic converters*. PhD thesis, Coventry University, 1997.

[24] Florian Menter. Two-equation eddy-viscosity turbulence models for engineering applications. *AIAA journal*, 32(8):1598–1605, 1994.

[25] ANSYS Fluent Theory Guide v18.2. ANSYS Inc., Canonsburg, PA, USA, 2017.

[26] Marek Václavík, Petr Kočí, Vladimír Novák, and David Thompsett. NOx conversion and selectivity in multi-layer and sequential DOC-LNT automotive exhaust catalysts: Influence of internal transport. *Chemical Engineering Journal*, 329:128–134, 2017.

[27] Henrik Strom, Srdjan Sasic, and Bengt Andersson. Effects of the turbulent-to-laminar transition in monolithic reactors for automotive pollution control. *Industrial & Engineering Chemistry Research*, 50(6):3194–3205, 2011.

[28] I Cornejo, P Nikrityuk, and RE Hayes. Turbulence decay inside the channels of an automotive catalytic converter monolith. *Emission Control Science and Technology*, 3(4):302—309, 2017.

[29] Ivan Cornejo, Petr Nikrityuk, and Robert E Hayes. Multiscale RANS-based modeling of the turbulence decay inside of an automotive catalytic converter. *Chemical Engineering Science*, 175:377–386, 2018.

[30] ANSYS Fluent Software Package v18.2, 2017. ANSYS Inc., Canonsburg, PA, USA.

[31] Theodore L Bergman, Frank P Incropera, David P DeWitt, and Adrienne S Lavine. *Fundamentals of Heat and Mass Transfer*. John Wiley & Sons, New Jersey, NY, USA, 2011.

[32] Frank M White. *Fluid Mechanics*. McGraw-hill, New York, NY, 2009.

[33] Franck Nicoud and Frédéric Ducros. Subgrid-scale stress modelling based on the square of the velocity gradient tensor. *Flow, Turbulence and Combustion*, 62(3):183–200, 1999.

[34] George Keith Batchelor. *An Introduction to Fluid Dynamics*. Cambridge University Press, Cambridge, UK, 1967.

[35] SA Al-Nassri and T Unny. Developing laminar flow in the inlet length of a smooth pipe. *Applied Scientific Research*, 36(5-6):313–332, 1981.

[36] Nikunj Gupta and Vemuri Balakotaiah. Heat and mass transfer coefficients in catalytic monoliths. *Chemical Engineering Science*, 56(16):4771–4786, 2001.

[37] Robert E Hayes, Andrés Donoso-Bravo, and Joseph P Mmbaga. Entry length effects for momentum, heat and mass transfer in circular ducts with laminar flow. *The Canadian Journal of Chemical Engineering*, 93(5):863–869, 2015.

Chapter 9

The influence of channel geometry on the pressure drop in automotive catalytic converters: Model development and validation[1]

Abstract

This paper presents a detailed physics based model for the pressure drop through a honeycomb substrate for several channel shapes and void fractions. A CFD-based computational model of a single channel is used to study the pressure drop when flow is entering, passing through and leaving the substrate. An extensive set of 3D computational experiments covering square, hexagonal and triangular channel cross-sections, void fractions from 0.39 to 0.84 and channel Re from 95 to 1284 is used. It is shown that altering the void fraction changes the pressure drop at the inlet and outlet of the substrate, however, its effect on the friction factor inside the substrate is minor. The resulting model can be used either as a semi-empirical lumped model for pressure drop and in 3D full-scale simulations with a porous medium representing the substrate. A validation for the velocity profile in a full scale monolith with experimental data available in the literature is carried out and an excellent agreement is observed. The proposed model significantly improves the prediction of the flow distribution across the substrate, which has remained unaddressed historically by existing models and is the most important effect required to make accurate predictions of heat dis-

[1] A version of this article has been published. Cornejo, I., Nikrityuk, P., & Hayes, R. E. (2019). The influence of channel geometry on the pressure drop in automotive catalytic converters: Model development and validation. Chemical Engineering Science. DOI: `https://doi.org/10.1016/j.ces.2019.115317`

tribution, conversion efficiency and others in full-scale simulations.

Keywords: CFD, monolith, permeability, pressure drop, catalytic converter, channel shape

9.1 Introduction

Monolith reactors are extensively used in several industrial systems such as NO_x reduction, H_2 production, CH_4 autothermal reforming and especially as the core part of automotive catalytic converters [1–6]. Typically, monoliths have a honeycomb type structures with many parallel channels. The catalyst is usually contained in a washcoat applied to the surface of the channels. A schematic of a monolithic catalytic converter is shown in Figure 9.1.

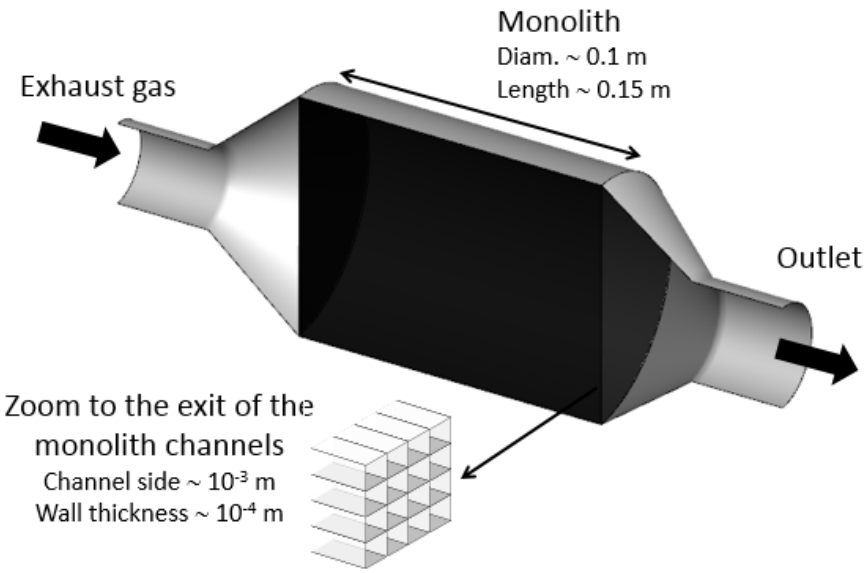

Figure 9.1: Schematic of a catalytic converter. Source Cornejo et al. [7]. *Reprinted with permission of Elsevier*

Modelling a catalytic converter involves many length scales, all related at some level. The smallest scale is the molecular level, where the chemical reactions occur. It is followed by the diffusion inside the washcoat pores that contains the catalysts. At a channel scale, the transport of species from the bulk to the surface of the washcoat is defined. The inlet conditions for the channels are given at a converter scale, also many important variables, such as the heat losses, ageing and pressure drop depend on the flow distribution across the substrate [8–10]. For this reason, reliable models of the whole reactor are necessary for design improvement and process optimisation [11, 12]. At a full scale, honeycomb substrates are modelled as a continuum, because accounting for all the channels individually is computa-

tionally prohibitive [13, 14]. That approach emphasizes the macro scale fluid dynamics at the expense of details at a washcoat and channel level. There are several differences between an actual honeycomb and a homogeneous porous medium, hence models that are physically consistent at a multiscale level are an extensive topic of research. The cornerstone for a reliable converter models is the apparent permeability of the porous medium representing the monolith. The simplest permeability model results when Poiseuille flow is assumed. By matching the Hagen-Poiseuille equation to Darcy's law, a single and constant apparent permeability can be obtained. It neglects any contraction and expansion of the flow at the beginning and end of the substrate, and the flow is assumed fully developed from the very inlet of the channels. That model is easy to implement, however, it fails in predicting the flow distribution and total pressure drop accurately [15]. An apparent permeability model that accounts for the effect of the upstream turbulence was proposed by Ekstrom et al. [16]. In that model an average apparent permeability was obtained by curve fitting a series of experiments of pressure drop through a converter. Separately, Benjamin et al. [17] modelled the extra pressure drop due to the flow entering at an angle to the substrate. According to their results, accounting for that extra resistance affects on the prediction of the flow distribution significantly. Regarding the hydraulic entrance region, the correlation for the friction factor of developing flow in pipes proposed by Shah [18] applied to a honeycomb was also tested, finding that it is not sufficient to predict the flow mal-distribution inside a converter [8]. It should be noted that the velocity profile at the inlet of the honeycomb channel is not flat due to the reduction in the flow area at the frontal face of the substrate. Hence, models for developing flow in pipes starting from a flat profile may not apply directly [19]. In this work, the model proposed by Cornejo et al. [20] was adopted and expanded to several substrate channel shapes. This model was preferred because it accounts for the losses when the flow is entering, developing, developed and exiting the substrate, which is especially important for modelling and control systems using several substrates [21–23]. An exhaust gas system can have several substrates in series and parallel, each one meant to diminish a particular pollutant. Not only the computer aided optimisation of the design, but also synthesising controllers for such a complex system needs reliable, accurate and widely applicable models. The multi-zone model considered in this study requires as an input the values of local friction coefficients, which in turn depend on the geometrical features of the substrate, such as the monolith void fraction and channel cross-section shape. Those coefficients are known for circular channels, but, square, triangular and hexagonal cross-section channels are also commonly used (see Figure 9.2), and the appropriate coefficients need to be determined.

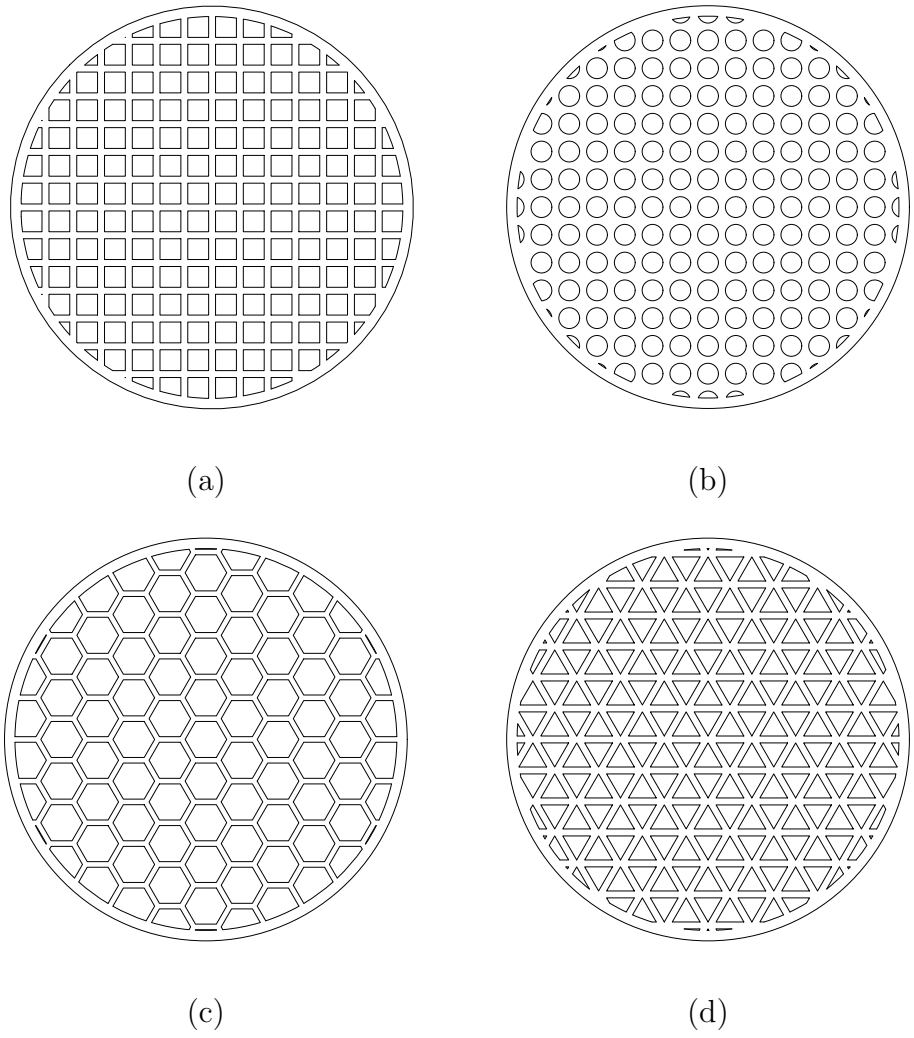

Figure 9.2: Section of an extruded ceramic substrate with (a) square, (b) circular, (c) hexagonal and (d) triangular channels

The purpose of this investigation is to quantify and model the effect of the channel geometry on the pressure drop through a honeycomb type substrate using a single channel model with square, hexagonal and triangular cross-section shape. The novelty of this paper is the detailed modelling of the pressure losses through every part of the substrate, which is important for computer aided optimisation of monolith based catalytic systems. The results at a channel scale are presented in the form of the local loss coefficients for the inlet and outlet of the substrate, together with the friction factor curve along the channels for every cross-section shapes. After the model is presented, it is applied to a whole converter simulation and the results are compared to experimental data.

9.2 Computational models

This section presents the flow model, assumptions and geometrical considerations of a converter scale simulation, then for a series of channel scale numerical experiments that was used to quantify and model the pressure drop along the monolith.

9.2.1 Converter scale model

It is necessary to revisit converter scale flow models to build an understanding of modelling a monolith as a continuum. Figure 9.3 shows a computational domain with the same specifications as the experimental set up in Clarkson [15]. It had an inlet pipe 2000 mm long (Li) and 54 mm in diameter (2Ri), followed by an inlet expansion diffuser with an angle (θ) of 35°, connecting the inlet pipe to a substrate 152 mm long (Lm) and 118 mm in diameter (2Rm). The substrate had square channels 1.1 mm in width with a wall thickness of 0.16 mm. Right after the substrate there was a straight section 30 mm long open to the atmosphere (Lo). The domain is shown in Figure 9.3.

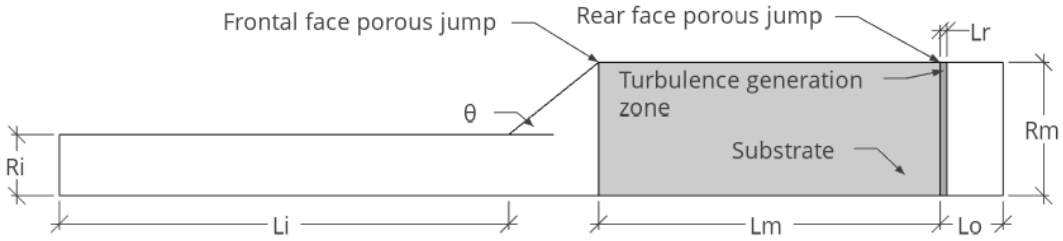

Figure 9.3: Computational domain at a converter scale

Turbulence model

The governing equations for mass and momentum balance are (droping the overline of the velocity average) [24]:

$$\frac{\partial u_i}{\partial x_i} = 0 \tag{9.1}$$

$$\rho \frac{\partial (u_i u_j)}{\partial x_j} = -\frac{\partial P}{\partial x_i} + \frac{\partial}{\partial x_j}\left[\mu\left(\frac{\partial u_i}{\partial x_j} + \frac{\partial u_j}{\partial x_i} - \frac{2}{3}\frac{\partial u_l}{\partial x_l}\delta_{ij}\right)\right] - \frac{\partial \tau_{ij}}{\partial x_j} + S_{u_i} \tag{9.2}$$

The term τ_{ij} is the Reynolds stress tensor and depends on the flow model. In this case, the closure is provided by the Boussinesq assumption, and the SST model is used. In this model, the eddy viscosity is defined as follows [24, 25]:

$$\mu_t = \frac{a_1 k}{max(a_1\omega, SF_2)} \tag{9.3}$$

The transport equations for the turbulence kinetic energy (k) and specific turbulence dissipation rate (ω) are [24, 25]:

$$\rho\frac{\partial k u_i}{\partial x_i} = \frac{\partial}{\partial x_j}\left[\left(\mu + \frac{\mu_t}{\sigma_k}\right)\frac{\partial k}{\partial x_i}\right] + G_k - Y_k - S_k^{sink} + S_k^{gen} \tag{9.4}$$

where

$$G_k = min(\mu_t S, 10\rho\beta^* k\omega)$$

$$Y_k = \rho\beta k\omega$$

and

$$\rho\frac{\partial \omega u_i}{\partial x_i} = \frac{\partial}{\partial x_j}\left[\left(\mu + \frac{\mu_t}{\sigma_\omega}\right)\frac{\partial \omega}{\partial x_i}\right] + G_\omega - Y_\omega + D_\omega - S_\omega^{sink} + S_\omega^{gen} \tag{9.5}$$

where

$$G_\omega = \frac{\rho\alpha_\omega}{\mu_t}\mu_t S$$

$$Y_\omega = \rho\beta\omega^2$$

$$D_\omega = 2(1-F_1)\rho 1.168\frac{1}{\omega}\frac{\partial k}{\partial x_j}\frac{\partial \omega}{\partial x_j}$$

Further details of the blending functions and constants of the SST model can be found in Menter [25]. A realistic decay of the turbulence inside the substrate was obtained by applying the two damping terms in Equation (9.6) and (9.7) to the k and ω equations inside the porous medium [26].

$$-S_k^{sink} = -\frac{\mu_{eff}}{\alpha_i}k \tag{9.6}$$

$$-S_\omega^{sink} = -\frac{\mu}{\alpha_i}(\omega_0 - \omega) \tag{9.7}$$

where

$$\omega_0 = C_\omega\frac{\mu/\rho}{\beta_\omega\delta^2/4}$$

In the previous expression, C_ω is 6, β_ω is 3/4 and Δ^2 is the characteristic cell area.

It is also known that turbulence arises due to the unsteadiness produced by the flow leaving the substrate [27]. That phenomenon was included by adding a turbulence generation zone right after the substrate (see Figure 9.3). The source terms S_k^{gen} and S_ω^{gen} were modelled as immersed boundary conditions, applied to the turbulence generation zone. The length

scale of the turbulence l_e after the substrate was taken from discrete channel data and set as the hydraulic diameter of the channels [7]. Based on the same data, the dimensionless turbulence kinetic energy (k^*) was set to 0.065 [7]. With that, the values for k and ω in the turbulence generation zone can be estimated as:

$$k = k^* u_c^2 \tag{9.8}$$

$$\omega = \frac{k^{1/2}}{l_e C_\mu} \tag{9.9}$$

$\mathrm{Re_w}{=}\rho u_c \sqrt{2} \mathrm{L_w}/\mu$ is evaluated along the radius of the substrate in its rear face. The zones in which it is higher than the critical one ($\mathrm{Re_{w,}}_{crit}$ ≈150), known values for k and ω are imposed. Further details about the implementation of the turbulence generation after the substrate are extensively described in [7].

Permeability model

The sink term S_{u_i} in Equation (9.2) applies only inside the porous zone and accounts for the extra pressure drop through the substrate. For multi-zone permeability models, the total losses of mechanical energy (ΔP_T) can be represented as the summation of the pressure drop at the frontal face of the substrate (ΔP_i), losses inside of the substrate (ΔP_s), and losses when the flow leaves the rear face of the substrate (ΔP_o). The apparent permeability inside the substrate can be accounted for by Darcy's law as [20, 28]:

$$S_{u_i} = -\frac{\mu}{\alpha_{(x_i)}} u_i \tag{9.10}$$

The axial permeability is defined as the apparent permeability in the direction of the channels (i.e. flow direction) and the radial permeability corresponds to the direction perpendicular to the channel axis. For realistic results, the radial permeability should be set to be at least two orders of magnitude lower than the axial one ($\alpha_{axial} \leq 100\alpha_{radial}$) to prevent radial flow across the continuum. The axial permeability, which is referred to as $\alpha_{(x)}$ in the rest of the paper, can be calculated as a function of the friction factor inside a monolith channel [20]:

$$\alpha_{(x)} = \frac{\alpha_{fd} f_{fd}}{f_{(x)}} \tag{9.11}$$

where

$$f_{(x)} = \frac{1}{\mathrm{Re}} \left[\left(\frac{c_1}{\sqrt{\mathrm{Gz}_i}} \right)^n + (f\mathrm{Re}_{fd})^n \right]^{\frac{1}{n}} \tag{9.12}$$

$$\mathrm{Gz}_i = \frac{x^+}{\mathrm{Pr}} = \frac{x}{\mathrm{PrReD_H}} \tag{9.13}$$

The subscript fd stands for the fully developed region, Gz_i is the inverse of the Graetz number, and c_1 and n are model constants that depend on the shape of the channels. The pressure drop due to the sudden contraction and expansion of the flow when entering and leaving the monolith can be modelled as two thin layers, or 1-D porous jumps, one at the frontal and one at the rear face of the monolith. The magnitude of the pressure drop through such a porous jump can be estimated as [24]:

$$\Delta P = \left(\frac{1}{\alpha_{afp}} \mu u_i + C_u \frac{1}{2} \rho u^2 \right) \Delta m \tag{9.14}$$

In Equation (9.14) Δm is the apparent thickness of the jump, which is used together with the apparent face permeability (α_{afp}) and the inertial losses coefficient (C_u). That leads to the following expression for the losses at the front face of the substrate:

$$\Delta P_i = \left(\frac{\Delta m}{\alpha_{afp}} \right) \mu u + (\Delta m C_u) \frac{1}{2} \rho u^2 \tag{9.15}$$

or

$$\Delta P_i = f_1|_{inlet} \mu u + f_2|_{inlet} \frac{1}{2} \rho u^2 \tag{9.16}$$

Note that f_1 accounts for the viscous losses and f_2 for the inertial ones. For the outlet of the substrate, where the inertial losses dominate, the pressure drop is:

$$\Delta P_o = f_2|_{outlet} \frac{1}{2} \rho u^2 \tag{9.17}$$

The factors $f_1|_{inlet}$, $f_2|_{inlet}$ and $f_2|_{outlet}$ in Equation (9.16) and (9.17) can be written as second order polynomials that depend on the monolith void fraction and the channel geometry. The total pressure drop can be summarised by the following expression:

$$\Delta P_T = f_1|_{inlet} \mu u + f_2|_{inlet} \frac{1}{2} \rho u^2 + \int_{x_0}^{x_0 + L_s} \left(f_{(x)} \frac{x}{2\mathrm{D_H}} \rho u^2 \right) dx + f_2|_{outlet} \frac{1}{2} \rho u^2 \tag{9.18}$$

9.2.2 Channel scale model

At a channel scale, it is necessary to include the open sections before and after the substrate to investigate the pressure losses when the flow enters and leaves the substrate. A cut along the domain at a channel scale can be seen in Figure 9.4.

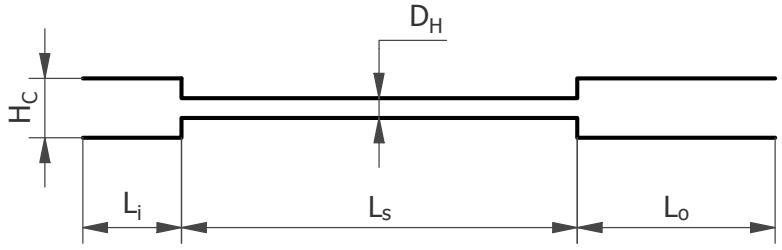

Figure 9.4: Lateral view of a monolith channel with the open sections before and after it. L_i=20 mm, L_o=60 mm, H_C and D_H were set according to the desired channel shape and void fraction

Figure 9.5 shows the frontal view of a section of a monolith for four common channel shapes. Each channel shape is accompanied by a rectangle in dashed line showing the fundamental part of each structure, which includes every feature of the geometry when symmetry is applied to the four sides.

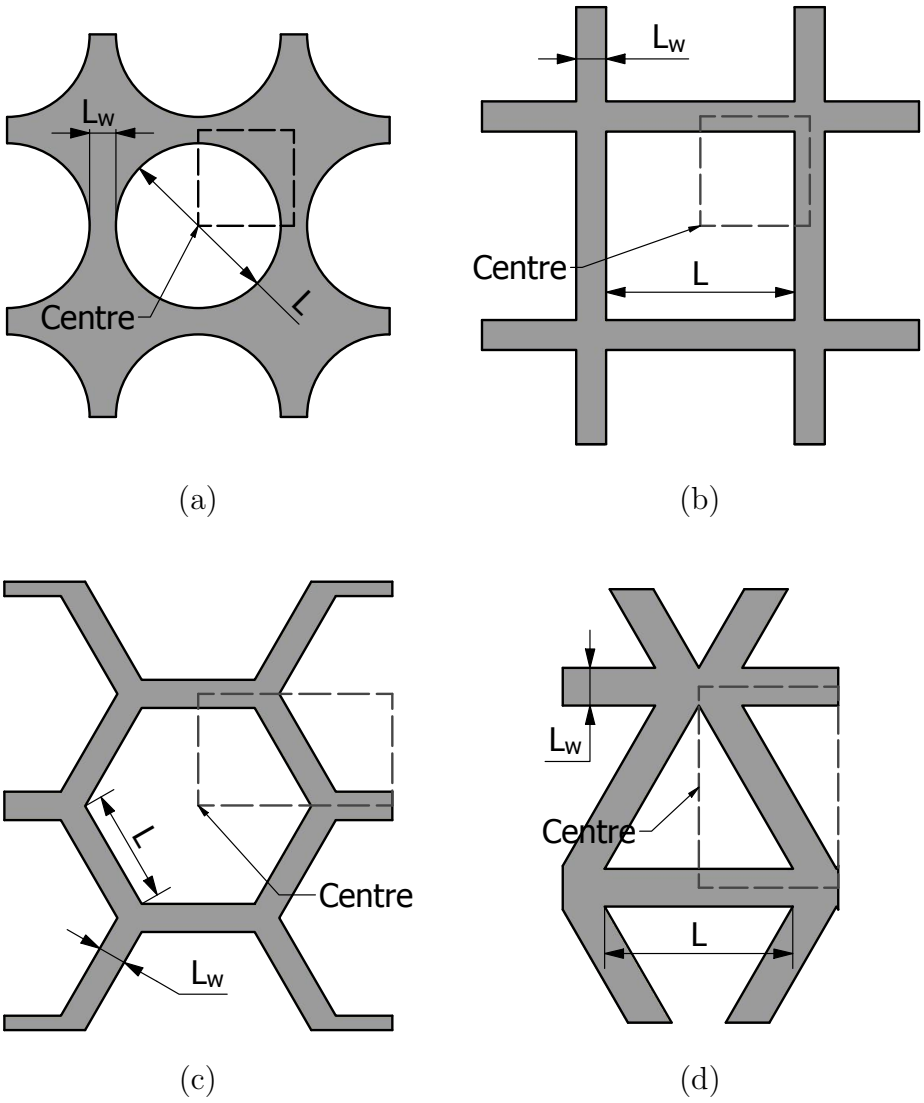

Figure 9.5: Frontal view of a section of a monolith with (a) circular, (b) square, (c) hexagonal and (d) triangular channels. The centre of a channels, wall thickness and characteristic length are marked in every case

The target void fraction for each case was obtained by manipulating the wall thickness (L_w) conveniently while keeping L constant as 1.00 mm, 1.48 mm, and 2.00 mm for the square, hexagonal and triangular channels respectively. The Re number for the channels was calculated based on the channel mean velocity and the respective hydraulic diameter, see Equation (9.19). The length of the open sections before and after the substrate were enlarged systematically until no boundary effects were observed. As can be seen in Figure 9.8, having an open space upstream the substrate from 4 to 10 channel diameters long is sufficient for the flow rates covered in this study. Regarding the space downstream of the channel, that must be long enough to completely cover the recirculating zone after the substrate. That is from

10 to 30 channel diameters according to the literature [27, 29]. In this study, we used L_i=20 mm and L_i=60 mm, after which length, no boundary effects were observed. The length of the substrate (or channel) was kept constant at L_s=40 mm which is long enough to reach fully developed flow for all of the analysed cases.

$$\mathrm{Re} = \frac{\rho u_c \mathrm{D_H}}{\mu} \tag{9.19}$$

The working fluid was atmospheric air at 300 K. The density of the fluid was considered to be constant. This assumption was corroborated with an additional run assuming ideal gas law. The maximum change in density observed was less than the 0.4%, and no significant changes in pressure drop were found also. However, for other scenarios, such as non-isotherm flow, using variable fluid properties is highly recommended. The flow regime was assumed to be laminar, because the channel Re is largely sub-critical in most of the monolith applications. There is evidence of upstream turbulence entering the substrate in automotive applications [16, 26]. There is evidence in the literature that when turbulence enters the substrate, it decays quickly inside the channels, leading to laminar flow [30, 31]. Describing such a transition accurately requires substantial computational efforts and a much more comprehensive analysis, therefore, that will be covered in a dedicated, independent paper in the future. Hence, it was desired to study the effect of the channel geometry in laminar flow first, which is valid for many applications. The resulting steady mass and momentum transport equations were:

$$\frac{\partial u_i}{\partial x_i} = 0 \tag{9.20}$$

$$\rho \frac{\partial (u_i u_j)}{\partial x_i} = -\frac{\partial P}{\partial x_i} + \frac{\partial}{\partial x_j}\left(\mu \frac{\partial u_i}{\partial x_j}\right) \tag{9.21}$$

All of the simulations were implemented in ANSYS Fluent 18.2 [32], which uses the finite volume approach. The inlet of the domain was treated as a velocity inlet, where the flow rate was manipulated according to the monolith void fraction to obtain the desired channel Re. The inner, frontal and rear walls of the section of the substrate were set as no-slip walls. The symmetry planes at the top, bottom, left and right of the domain were considered symmetric boundaries. The outlet of the domain was set as outflow. All the discretization schemes were set as QUICK and the pressure-velocity coupling was solved with the SIMPLE algorithm [33]. The convergence criterion was the reaching of a maximum value of scaled residuals below of 10^{-9} and having a stable total pressure drop along the entire domain. The list of all the numerical experiments covered in this study is shown as Table 9.1. New results

are presented for hexahedral, triangular and square cross-section channels, which were also compared to those for circular channels available in the literature.

Table 9.1: List of numerical experiments

N° Run	Re	ϕ	Channel shape
1	176	0.39	Square
2	353	0.39	Square
3	529	0.39	Square
4	706	0.39	Square
5	117	0.59	Square
6	233	0.59	Square
7	350	0.59	Square
8	467	0.59	Square
9	100	0.69	Square
10	199	0.69	Square
11	299	0.69	Square
12	399	0.69	Square
13	86	0.80	Square
14	172	0.80	Square
15	258	0.80	Square
16	344	0.80	Square
17	321	0.55	Hexagon
18	642	0.55	Hexagon
19	963	0.55	Hexagon
20	1284	0.55	Hexagon
21	272	0.65	Hexagon
22	543	0.65	Hexagon
23	815	0.65	Hexagon
24	1086	0.65	Hexagon
25	232	0.76	Hexagon
26	465	0.76	Hexagon
27	697	0.76	Hexagon
28	929	0.76	Hexagon
29	210	0.84	Hexagon
30	420	0.84	Hexagon

Table 9.1: Cont'd

N° Run	Re	ϕ	Channel shape
31	631	0.84	Hexagon
32	841	0.84	Hexagon
33	132	0.60	Triangle
34	265	0.60	Triangle
35	397	0.60	Triangle
36	530	0.60	Triangle
37	120	0.66	Triangle
38	241	0.66	Triangle
39	361	0.66	Triangle
40	482	0.66	Triangle
41	109	0.73	Triangle
42	218	0.73	Triangle
43	327	0.73	Triangle
44	435	0.73	Triangle
45	95	0.84	Triangle
46	189	0.84	Triangle
47	284	0.84	Triangle
48	378	0.84	Triangle

9.3 Results and discussion

This section describes the validation of the computational model at a channel scale, methodology of calculation, and summarises the results.

Using the outcome of the numerical experiments, the head losses at the inlet and the outlet of the substrate were calculated as the difference of the total pressure between the beginning and end of the respective section. Also, the local friction factor inside the channels was calculated based on the total head losses along them. Following the same notation as that in Figure 9.4 we obtain:

$$\Delta P_i = P|_{x=0} - P|_{x=\mathrm{L_i}} \tag{9.22}$$

$$\Delta P_o = P|_{x=\mathrm{L_i}+\mathrm{L_s}} - P|_{x=\mathrm{L_i}+\mathrm{L_s}+\mathrm{L_o}} \tag{9.23}$$

$$f_{(x)} = \frac{\partial P/\partial x}{\frac{1}{2}\rho u_c^2} \tag{9.24}$$

P was calculated as the mass weighted total pressure across the corresponding transverse section of the domain, which keeps consistency with the momentum balance. Having the results of the computational experiments, they were fitted to Equation (9.12), (9.16) and (9.17) to determine the values for c_1, n, f_1 and f_2. For f_1 and f_2, the void fraction of the substrate, which works as the reduction and expansion rate, was computed as:

$$\phi = \frac{\text{transverse flow area inside the substrate}}{\text{transverse flow area before the substrate}} \tag{9.25}$$

Further details about the final expressions for pressure drop are provided in Section 9.3.2.

9.3.1 Grid independence and model validation

For square channels the domain was spatially discretised into a fully orthogonal hexahedral mesh. For the hexagonal and triangular cross-section channels, polyhedral computational cells were used together with an inflation layer at the walls. Figure 9.6 shows a hexahedral and a polyhedral mesh for the square and hexagonal channels respectively. Since the area of the inlet of the domain was manipulated to obtain the desired set of void fractions, the total volume of the domain slightly changed between cases. However, every mesh had of the order of four million computational cells.

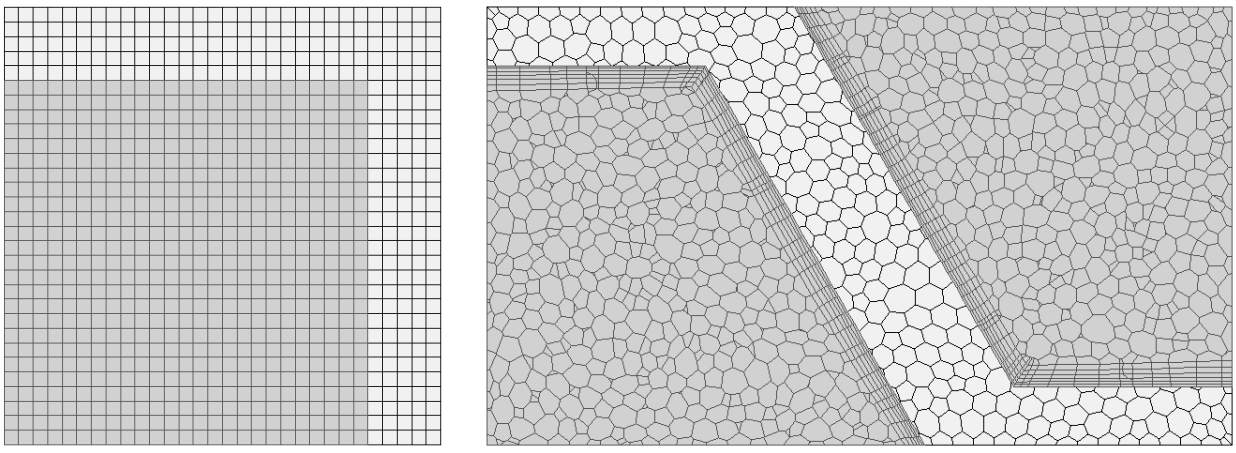

(a) (b)

Figure 9.6: Mesh for a section of a (a) square channel and (b) hexahedral channel. The grey cells represent the mesh inside the channels

The grid independence of the solutions was investigated by refining the mesh systemati-

cally and monitoring the total pressure drop along the domain. In a square channel geometry identical results were obtained for two meshes of 4.2 and 11.9 millions of cells each. The same test was performed for hexagonal and triangular channels leading to equivalent results. In addition, the quality of the solution was analysed in two ways simultaneously, monitoring the hydraulic entrance length (L_H) and the friction factor at the fully developed region ($f\mathrm{Re}_{fd}$).

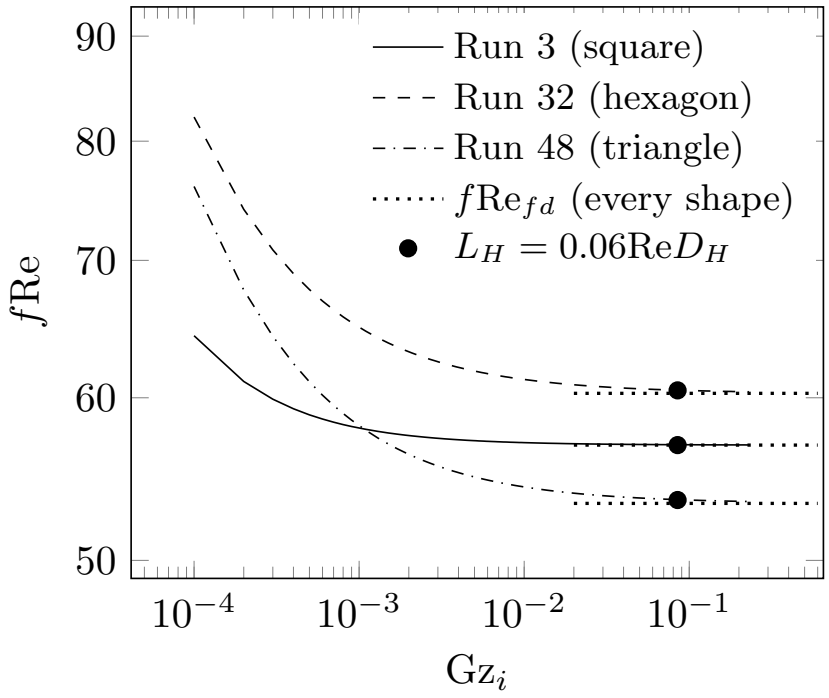

Figure 9.7: Friction factor for three channel cross-section shapes. The expression for L_H was taken from Bergman et al. [34] and the $f\mathrm{Re}_{fd}$ for square, and triangular pipes from White [35]

According to the results in Figure 9.7, the computational model was able to converge exactly to the correct friction factor in the fully developed region for all of the channel Re and channel shapes covered in this study. That constitutes an important validation, because the pressure drop is the main focus of this study and it is a function of the friction factor. In addition, for the hydraulic entrance length, the numerical model showed consistency with the expected, according to literature for the three channel shapes. For honeycomb monoliths, the reduction of the flow area entering the substrate produces a non-flat velocity profile at the inlet of the channels [17, 20]. That has an effect on the extension of the developing region, however, expressions assuming a flat inlet velocity profile still provide a useful approximation to investigate consistency.

9.3.2 Effect of channel geometry on the pressure drop

This section summarises the pressure losses for flow through a substrates. Figure 9.8 provides a first sight to the flow entering and leaving a channel. In this section, the pressure drop in those zones, and also inside the channels, is analysed in detail for several flow rates and channel cross-section shapes.

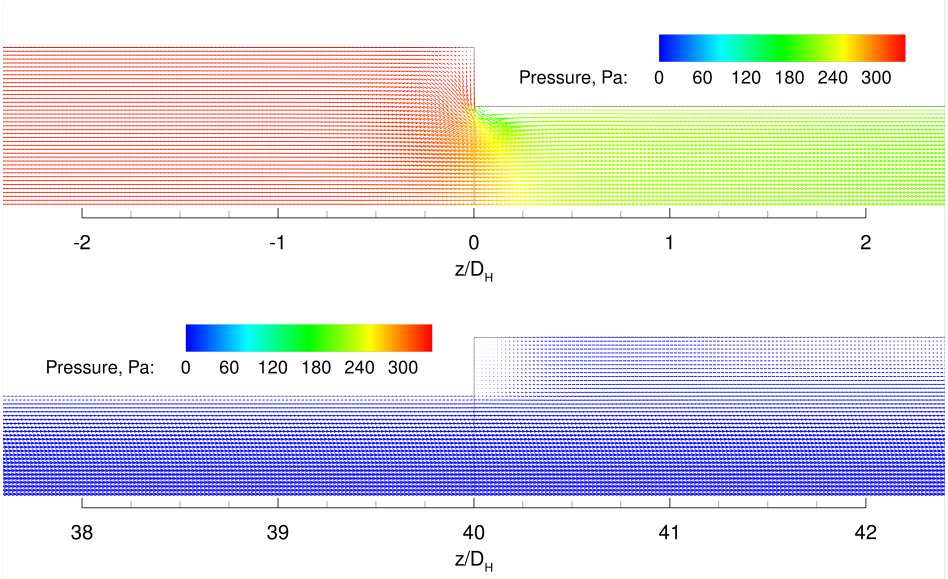

Figure 9.8: Lateral view of velocity vectors on the symmetry plane of a square channel colored by static pressure. Inlet and outlet zones. Re=399 and ϕ=0.69 (Run 12)

Losses when entering and leaving the substrate

Figure 9.9 shows the pressure losses for flow entering and leaving the substrate for several void fractions, channel shapes and channel Re. Consistent with that reported for circular pipes, the head losses have a quadratic dependence on the channel velocity. Also, the magnitude of the losses is inversely proportional to the substrate void fraction (or directly proportional to the reduction rate). When entering the substrate, the magnitude of the losses for hexagonal and triangular channels are comparable and they are significantly lower than those for square channels. Also, the total pressure drop when leaving the substrate was always higher than that when entering the substrate, for a given void fraction and channel velocity.

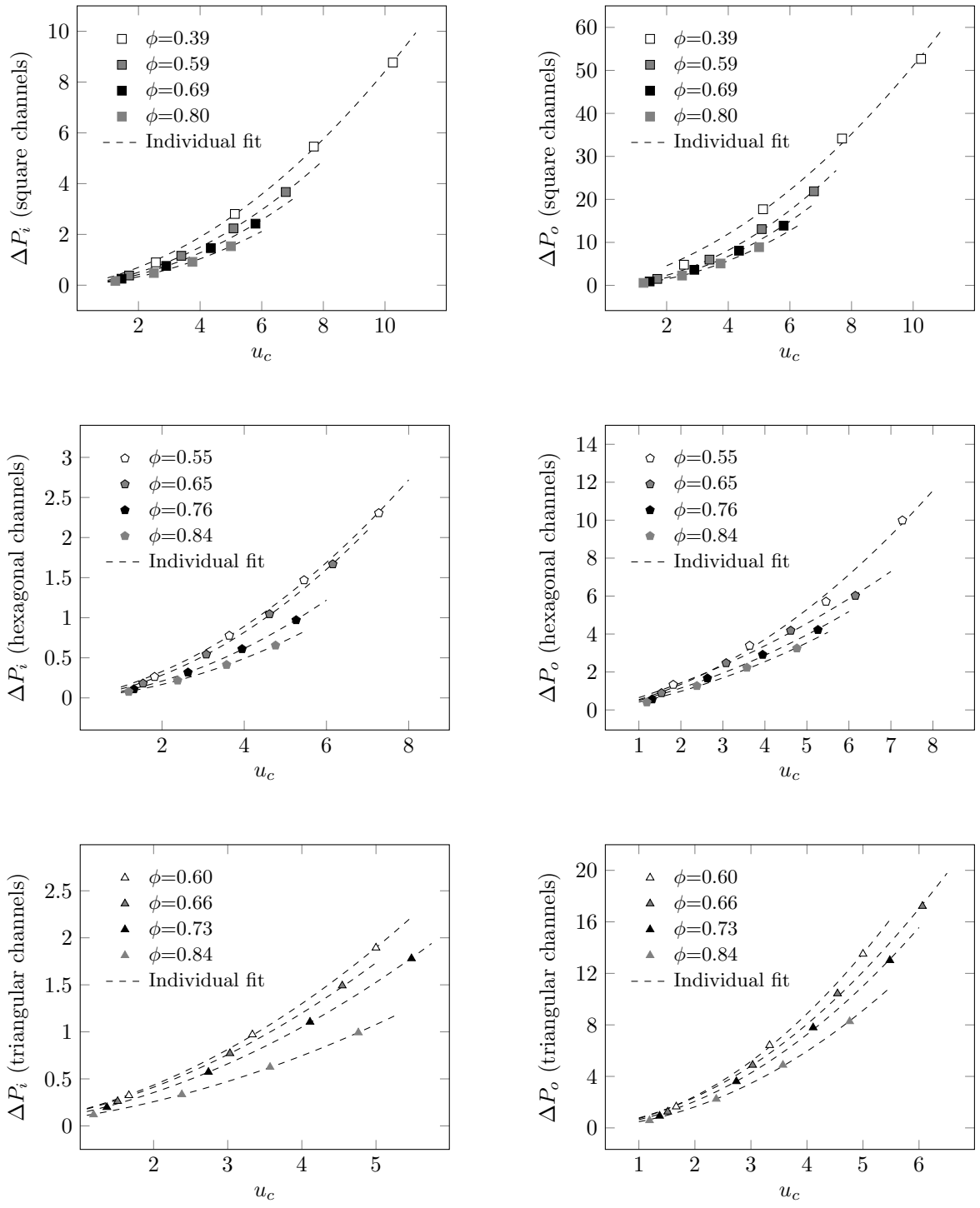

Figure 9.9: Head losses for flow entering (left) and leaving (right) the substrate for several void fractions and channel velocities. ΔP is in Pa and u_c in m/s

Each data set shown in Figure 9.9 is accompanied by an individual fitting to Equation

(9.16) and (9.17) correspondingly. That allowed us to calculate f_1 and f_2 as a function of the monolith void fraction. The resulting expressions are shown in Table 9.2 and they make possible to use Equation (9.16) and (9.17) to describe every curve in Figure 9.9 accurately. The sensitivity of f_1 and f_2 to the channel shape and monolith void fraction can be seen in Figure 9.10. All of the individual fits showed an R^2 above 0.97 and are useful to interpolate f_1 and f_2 for ϕ values between 0.5 and 0.9.

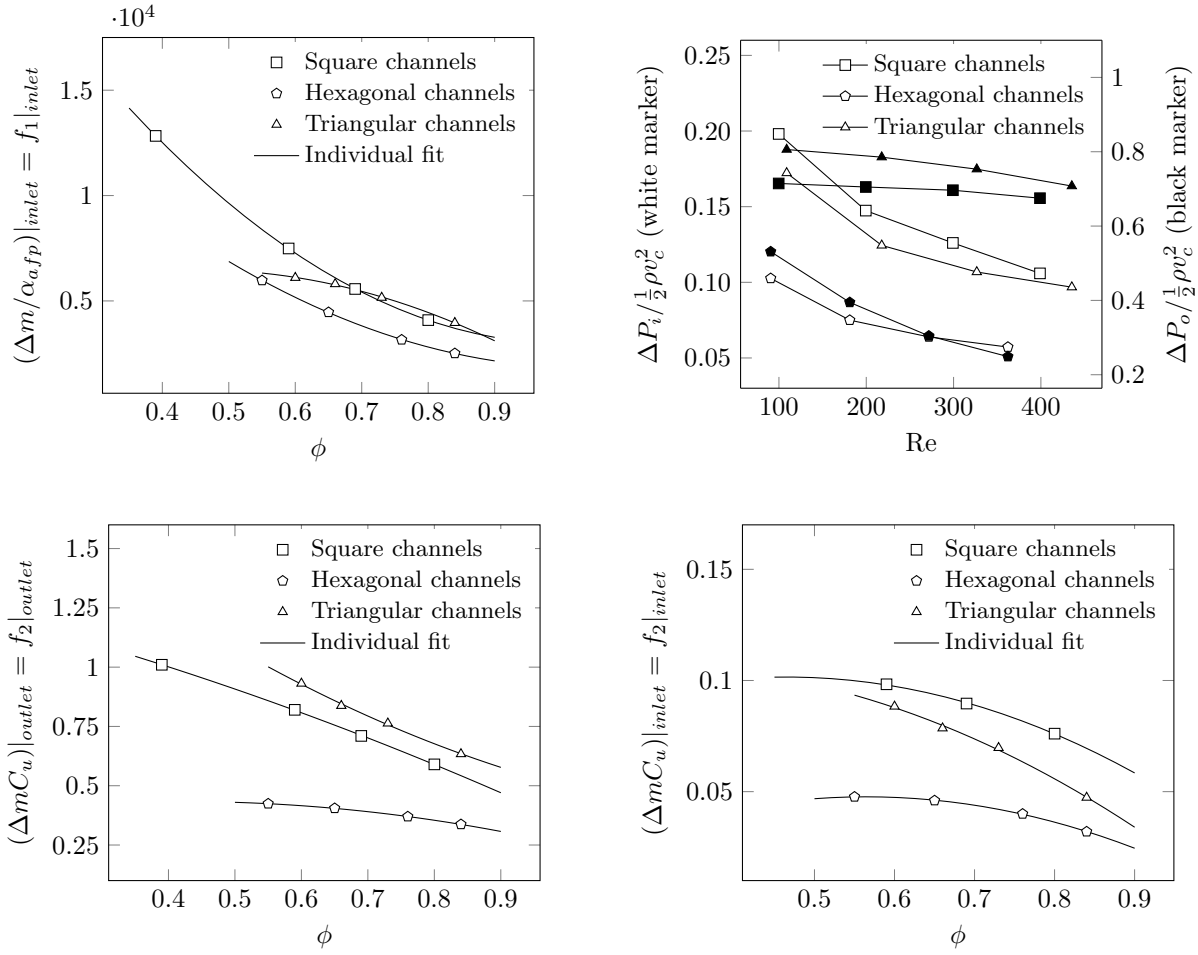

Figure 9.10: Parameters for the local friction coefficient and apparent face permeability for several channel shapes and void fractions. f_1 is in 1/m

Losses inside the substrate

Regarding the pressure drop inside the substrate, the curve fRe-Gz$_i$ was calculated for every case in Table 9.1. The resulting data are shown in Figure 9.11. As observed previously for circular channels [20], the effect of the void fraction and channel Re on the fRe curve is present but moderate in magnitude. Due to the reduction of the flow area, the velocity

profile at the inlet of the substrate changes slightly and the size of the stagnation zone right after the inlet of the channels remains approximately constant. As expected, the $f\mathrm{Re}$ curve for every shape tends asymptotically to the corresponding value at the fully developed zone. However, when the curves are scaled by their respective asymptotic value, all of them follow a similar trajectory. That is shown in Figure 9.11.

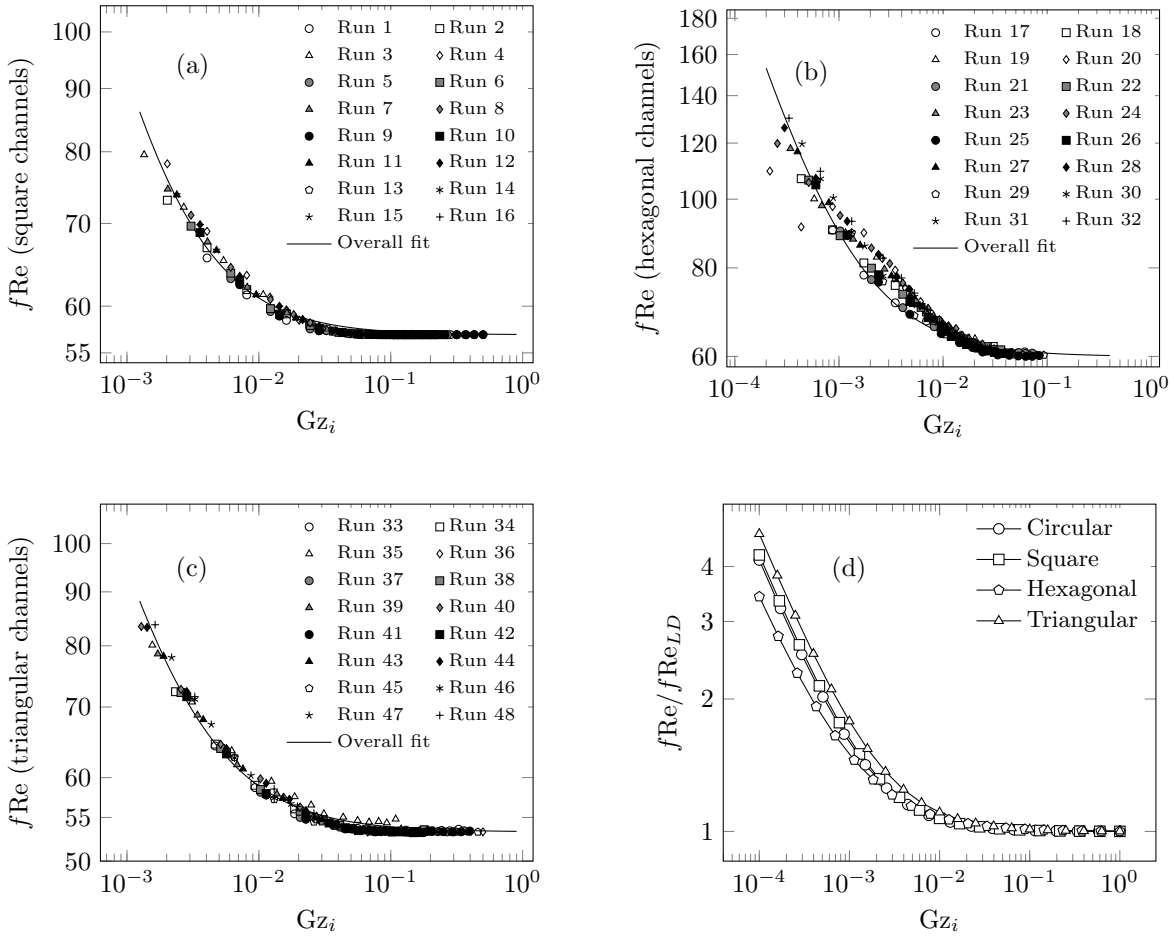

Figure 9.11: Friction factor for (a) square channels, (b) hexahedral channels and (c) triangular channels. (d) shows the scaled friction factor for four channel shapes simultaneously. The run number refer to those in Table 9.1

Summary of the pressure drop model coefficients

Table 9.2 summarises the expressions and parameters to compute the pressure drop of flow entering, within and leaving the substrate for the three channel shapes investigated in this study. Data for circular channels previously reported in the literature were also included.

Table 9.2: Multi-zone permeability parameters for several channel shapes

	Circular [20]	Square
$f_1\|_{inlet}$	-6678.9ϕ^2-8294.9ϕ+16956	25868ϕ^2-52117ϕ+29224
$f_2\|_{inlet}$	-0.127ϕ^2+0.0590ϕ+0.0816	-0.2279ϕ^2+0.2119ϕ+0.0523
$f_2\|_{outlet}$	0.9782ϕ^2-2.5968ϕ+1.9567	-0.3137ϕ^2-0.6540ϕ+1.3131
c_1	2.5855	2.3644
n	2.1154	2.1156
$f\mathrm{Re}_{fd}$	64.0	56.9
	Hexagonal	Triangular
$f_1\|_{inlet}$	17395ϕ^2-36145ϕ+20594	-17021ϕ^2+15493ϕ+2950.3
$f_2\|_{inlet}$	-0.2055ϕ^2+0.2320ϕ-0.0178	-0.1918ϕ^2+0.1084ϕ+0.0918
$f_2\|_{outlet}$	-0.5490ϕ^2+0.4617ϕ+0.3364	0.8620ϕ-2.4613ϕ+2.0943
c_1	1.9048	2.4701
n	1.7270	1.9756
$f\mathrm{Re}_{fd}$	60.3	53.3

9.4 Implementation at a converter scale

Having defined the model parameters for several channel shapes, this section shows the implementation of the permeability model at a converter scale and compares its prediction to experimental data available in the literature for a substrate with square channels.

9.4.1 Flow model

The domain and turbulence model at a converter scale, which included an inlet pipe, a diffuser and a monolith, are described in Section 9.2.1. For the apparent permeability of the substrate, two models for the source term S_{u_i} in the momentum balance in Equation (9.2) were considered. The first one assumed Poiseuille flow, where the apparent permeability of the substrate was assumed constant and estimated as follows:

$$\alpha_{axial} = \frac{\phi \mathrm{D_H^2}}{28.4} \tag{9.26}$$

$$\alpha_{radial} = \frac{\alpha_{axial}}{100} \tag{9.27}$$

The second option was the multi-zone permeability model, with the parameters presented in this work. It accounts for the pressure drop at the inlet, outlet and along the substrate

separately. One porous jump was set at the frontal face of the substrate to account for ΔP_i and another at the rear face to account for ΔP_o. Both porous jumps are 2D surfaces, where the pressure drop occurs immediately once the flow passes through them. The equations for the two jumps are Equation (9.16) and (9.17) respectively. The values for f_1 and f_2 for square channels are given in Table 9.2. One of the main drawbacks of the continuum approach is that, in contrast to a real monolith substrate, there are no channel walls or changes in the flow area, hence, phenomena such as the flow acting as a series of jets leaving the substrate are not represented correctly. Porous jumps are a strategy that allows us to account, at least, for the pressure drop when entering and leaving the substrate. At the frontal face of the substrate, energy losses happen in a thin zone, hence, a porous jump is reasonable. The exit of the substrate requires more attention because of the recirculating flow. Having a detailed model of a progressive pressure drop of the flow moving downstream would be ideal in scenarios in which there is a second element in series, close enough to modify the recirculating zone and pressure drop of the first substrate. A model like that, able to describe jet flow leaving the substrate, requires extensive further research and is beyond the scope of this paper. The permeability inside the substrate was calculated using Equation (9.11) with the parameters for square channels given in Table 9.2.

9.4.2 Solver settings and grid analysis

As previously, the simulations were implemented in ANSYS Fluent 18.2 [32]. The inlet was a velocity inlet, with a velocity magnitude according to the desired inlet Re. The inlet turbulence intensity was set as 15% and the turbulence scale as $0.8\mathrm{R}_i$, which are recommended values for fully developed turbulent flow in pipes [24]. The outlet was treated as a pressure outlet. Advantage was taken from the axial symmetry of the geometry, hence, the centre line of the domain was set as symmetry axis. The outside boundary of the domain was considered a no-slip wall.

The operating fluid was incompressible atmospheric air at 300 K, the same as in Clarkson [15]. The schemes for momentum, k and ω were set as QUICK, and The pressure velocity coupling was solved with the SIMPLE algorithm. The convergence criterion was having scaled residuals with a value below 10^{-6} and a stable total pressure drop and volume average velocity magnitude. The domain was discretized in a fully quadrilateral mesh of 240 000 cells. Another mesh with 480 000 cells was also tested, producing a total pressure drop, volume average velocity magnitude, and velocity profile after the substrate that differ by less than 0.25% from those obtained with the previous mesh.

9.4.3 Results at a converter scale

Figure 9.12 shows the velocity profile after the substrate when assuming Poiseuille flow and when using the permeability model proposed in this work compared to the experiments presented in Clarkson [15].

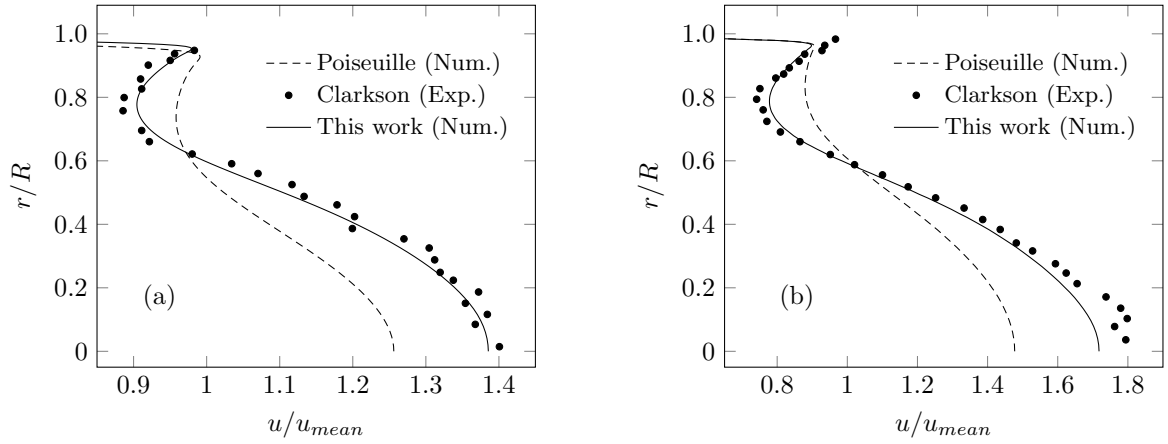

Figure 9.12: Comparison of the predicted and experimental velocity profile after the substrate at (a) inlet Re 30 000 and (b) inlet Re 60 000

Two inlet Re were tested. It can be seen that the new model leads to much better agreement in the velocity profile for both inlet Re. Compared to the case when assuming Poiseuille flow, this work improves the prediction of the main peak velocity and the secondary peak close to r/R=1. Both regions of the velocity profile are a common issue when modelling a converter, because current models tend to predict velocity profiles flatter than those observed experimentally. We emphasize that the improvement in the prediction of the velocity profile achieved in this paper comes from a channel scale model. No parameters were fit using converter scale data, hence, the predicted and experimental velocity profiles are two completely independent data sets; therefore, the model is purely predictive.

It is well established in the literature that a higher pressure drop leads to a comparatively flatter velocity profile. Following that logic, and taking a closer look at the experimental data, it can be seen that the measured velocity profile is more mal-distributed than that from when assuming Poiseuille flow. Consequently, one can conclude that the experimental pressure drop must be smaller than the one when assuming Poiseuille flow. It might be counter-intuitive that after adding extra flow resistance, such as the one from the entering and leaving effects, the flow becomes more mal-distributed. However, contrary to the case for the flow through a unique channel, in a whole monolith, there is an additional degree of freedom, which is

precisely the flow distribution. For the example in Figure 9.12, despite of the significant differences in flow distribution, the total pressure using a variable and a constant pressure drop were comparable (see Table 9.3). This point requires especial attention, together with an extensive and detailed experimental validation, which will be addressed in a further paper.

Table 9.3: Pressure drop through the substrate

Inlet Re	Permeability Model	Pressure drop, Pa
30 000	Pouseuille flow	157.2
30 000	This work	157.4
60 000	Pouseuille flow	344.1
60 000	This work	343.1

It can also be seen that at an inlet Re of 60 000 there is still a small underestimation of the peak velocity. That might be explained by other phenomena not considered in this work, such as the effect of the upstream turbulence on the apparent friction factor inside the channels and the flow entering in a oblique angle to the substrate. Back pressure and flow distribution are interrelated, hence an improvement in the flow distribution due to a better permeability model is expected.

9.5 Conclusions

The effect of the channel geometry on the pressure drop through a monolith honeycomb was investigated by using an extensive set of computational experiments. Local friction coefficients for every investigated channel cross-section shape and monolith void fraction were presented in the form of an apparent permeability model for full monolith scale simulations and also as a semi-empirical lumped model for total pressure drop. A consistent first principles based methodology was proposed for developing pressure drop equations in monolith systems.

Overall, the findings were consistent with those observed previously for circular channels; the monolith void fraction and approach velocity affect the shape of the velocity profile at the inlet of the channels. However, the change in the inlet velocity profile was observed to be relatively small, and had only a minor effect on the $f\mathrm{Re}$ vs. Gz_i curves. Therefore, for each channel shape, a single $f\mathrm{Re}$ vs. Gz_i curve was sufficient to describe the friction factor with an insignificant loss in accuracy. It should be emphasized, however, that use a flat inlet velocity profile leads to significant error. Additionally, the $f\mathrm{Re}$ curves for the different channels

shapes follow a comparable trajectory when they are scaled by their respective asymptotic value.

The new model gives much better agreement with the experimental full-scale velocity profiles than those obtained when assuming Poiseuille flow and a constant apparent permeability. It improves significantly the prediction of the velocity profile across the substrate, especially the main velocity peak at the centre of the substrate and the secondary one, close to the outer boundary. Although the contribution of the so-called minor losses to the total pressure drop is low in percentage, it has been proven that in complex systems, such as a honeycomb substrate, accounting for them improves the accuracy of the model significantly. The channel shapes investigated showed a similar dependence on the substrate void fraction and approach velocity. However, the magnitude of the pressure drop and local friction coefficients were specific for every shape. Since the flow distribution impacts strongly other important variables in catalytic reactors, such as the temperature distribution, conversion efficiency and warm-up time, other channel shapes, for example, those of washcoated channels should be investigated using the same approach. In critical applications, a shape specific correlation should be developed using the reported methodology for the best prediction of the pressure drop and resultant velocity profile.

Bibliography

[1] Jinwen Chen, Hong Yang, Neil Wang, Zbigniew Ring, and Tadeusz Dabros. Mathematical modeling of monolith catalysts and reactors for gas phase reactions. *Applied Catalysis A: General*, 345(1):1–11, 2008.

[2] Chengna Dai, Zhigang Lei, Jie Zhang, Yingxia Li, and Biaohua Chen. Monolith catalysts for the alkylation of benzene with propylene. *Chemical Engineering Science*, 100:342–351, 2013.

[3] A Quintanilla, JA Casas, P Miranzo, María Isabel Osendi, and Manuel Belmonte. 3D-Printed Fe-doped silicon carbide monolithic catalysts for wet peroxide oxidation processes. *Applied Catalysis B: Environmental*, 235:246–255, 2018.

[4] Maria João Regufe, Alexandre FP Ferreira, José Miguel Loureiro, Alírio Rodrigues, and Ana Mafalda Ribeiro. Electrical conductive 3D-printed monolith adsorbent for CO2 capture. *Microporous and Mesoporous Materials*, 2019.

[5] Harshul Thakkar, Shane Lawson, Ali A Rownaghi, and Fateme Rezaei. Development of

3D-printed polymer-zeolite composite monoliths for gas separation. *Chemical Engineering Journal*, 348:109–116, 2018.

[6] Shaibal Roy, Premkumar Kamalanathan, and Muthanna Al-Dahhan. Integration of phase distribution from gamma-ray tomography technique with monolith reactor scale modeling. *Chemical Engineering Science*, 200:27–37, 2019.

[7] Ivan Cornejo, Robert E Hayes, and Petr Nikrityuk. A new approach for the modeling of turbulent flows in automotive catalytic converters. *Chemical Engineering Research and Design*, 140:308–319, 2018.

[8] SF Benjamin, RJ Clarkson, Net al Haimad, and NS Girgis. An experimental and predictive study of the flow field in axisymmetric automotive exhaust catalyst systems. *SAE Technical Paper*, No. 961208, 1996.

[9] Young-Deuk Kim, Soo-Jin Jeong, and Woo-Seung Kim. Influence of spacing on the thermal efficiency of a dual-monolithic catalytic converter during warmup. *Environmental Engineering Science*, 26(7):1171–1187, 2009.

[10] YD Kim and WS Kim. Optimum design of an automotive catalytic converter for minimization of cold-start emissions using a micro genetic algorithm. *International Journal of Automotive Technology*, 8(5):563–573, 2007.

[11] Michael Grimm and Sandip Mazumder. Numerical investigation of wall heat conduction effects on catalytic combustion in split and continuous monolith tubes. *Computers & Chemical Engineering*, 32(3):552–560, 2008.

[12] Margaritis Kostoglou, CP Lekkos, and AG Konstandopoulos. On mathematical modeling of solar hydrogen production in monolithic reactors. *Computers & Chemical Engineering*, 35(9):1915–1922, 2011.

[13] François Bertrand, Christophe Devals, David Vidal, Cyrille Séguineau de Préval, and Robert E Hayes. Towards the simulation of the catalytic monolith converter using discrete channel-scale models. *Catalysis Today*, 188(1):80–86, 2012.

[14] Ankan Kumar and Sandip Mazumder. Toward simulation of full-scale monolithic catalytic converters with complex heterogeneous chemistry. *Computers & Chemical Engineering*, 34(2):135–145, 2010.

[15] Rory John Clarkson. *A theoretical and experimental study of automotive catalytic converters*. PhD thesis, Coventry University, 1997.

[16] Fredrik Ekström and Bengt Andersson. Pressure drop of monolithic catalytic converters experiments and modeling. *SAE Technical paper*, No. 2002-01-1010, 2002.

[17] SF Benjamin, N Haimad, CA Roberts, and J Wollin. Modelling the flow distribution through automotive catalytic converters. *Proceedings of the Institution of Mechanical Engineers, Part C: Journal of Mechanical Engineering Science*, 215(4):379–383, 2001.

[18] RK Shah. A correlation for laminar hydrodynamic entry length solutions for circular and noncircular ducts. *Journal of Fluids Engineering*, 100(2):177–179, 1978.

[19] Oswald Jason Lobo and Dhiman Chatterjee. Development of flow in a square mini-channel: Effect of flow oscillation. *Physics of Fluids*, 30(4):042003, 2018.

[20] Ivan Cornejo, Petr Nikrityuk, and Robert E Hayes. Pressure correction for automotive catalytic converters: A multi-zone permeability approach. *Chemical Engineering Research and Design*, 147:232–243, 2019.

[21] Daniel W Wendland and William R Matthes. Visualization of automotive catalytic converter internal flows. *Fuels and Lubricants*, 95:729–795, 1986.

[22] M-C Lai, J-Y Kim, C-Y Cheng, P Li, G Chui, and JD Pakko. Three-dimensional simulations of automotive catalytic converter internal flow. *Journal of Materials and Manufacturing*, 100(5):241–250, 1991.

[23] Young-Deuk Kim, Soo-Jin Jeong, and Woo-Seung Kim. Optimal design of axial noble metal distribution for improving dual monolithic catalytic converter performance. *Chemical Engineering Science*, 64(7):1373–1383, 2009.

[24] ANSYS Fluent Theory Guide v18.2. ANSYS Inc., Canonsburg, PA, USA, 2017.

[25] Florian Menter. Two-equation eddy-viscosity turbulence models for engineering applications. *AIAA journal*, 32(8):1598–1605, 1994.

[26] Ivan Cornejo, Petr Nikrityuk, and Robert E Hayes. Multiscale RANS-based modeling of the turbulence decay inside of an automotive catalytic converter. *Chemical Engineering Science*, 175:377–386, 2018.

[27] Ivan Cornejo, Petr Nikrityuk, and Robert E Hayes. Turbulence generation after a monolith in automotive catalytic converters. *Chemical Engineering Science*, 187:107–116, 2018.

[28] RE Hayes, Anton Fadic, Joeseph Mmbaga, and A Najafi. CFD modelling of the automotive catalytic converter. *Catalysis Today*, 188(1):94–105, 2012.

[29] Ivan Cornejo, Petr Nikrityuk, and Robert E Hayes. Effect of substrate geometry and flow condition after the turbulence generation after a monolith. *Canadian Journal of Chemical Engineering*, doi: 10.1002/cjce.23687, 2020.

[30] I Cornejo, P Nikrityuk, and RE Hayes. Turbulence decay inside the channels of an automotive catalytic converter monolith. *Emission Control Science and Technology*, 3(4):302—309, 2017.

[31] Ivan Cornejo, Gonzalo Cornejo, Petr Nikrityuk, and Robert E Hayes. Entry length convective heat transfer in a monolith: The effect of upstream turbulence. *International Journal of Thermal Sciences*, 138:235–246, 2019.

[32] ANSYS Fluent Software Package v18.2, 2017. ANSYS Inc., Canonsburg, PA, USA.

[33] Suhas Patankar. *Numerical heat transfer and fluid flow*. CRC press, Boca Raton, Florida, USA, 1980.

[34] Theodore L Bergman, Frank P Incropera, David P DeWitt, and Adrienne S Lavine. *Fundamentals of Heat and Mass Transfer*. John Wiley & Sons, New Jersey, NY, USA, 2011.

[35] Frank M White. *Fluid Mechanics*. McGraw-hill, New York, NY, 2009.

Chapter 10

Entry length convective heat transfer in a monolith: The effect of upstream turbulence[1]

Abstract

In a typical practical monolith reactor implementation, turbulent flow in a large pipe or inlet header enters small monolith channels. After some distance the flow becomes fully developed laminar flow. It has been shown that the distance over which the turbulence transitions to laminar flow is significant. This paper reports results of investigation into the value of the Nusselt number in the entry region of a circular tube under conditions of decaying turbulence. Large Eddy Simulations (LES) are used to model the flow. LES simulations show that the Nusselt number is significantly higher than the classical one for developing laminar flow in the entry region. The entry length Nu number depends not only on the inverse Graetz number, but also on the channel Reynolds number, upstream turbulence length scale and upstream turbulence intensity. A general correlation is developed that relates the Nu number in the entry region to the inverse Graetz number, Reynolds number, inlet turbulence intensity and turbulence length scale.

Keywords: Monolith, channels, turbulence, Nusselt, CFD, catalytic converter

[1]A version of this article has been published. Improved Nu number correlations for monolith reactors. Cornejo, I., Cornejo, G., Nikrityuk, P., & Hayes, R. E. (2019). Entry length convective heat transfer in a monolith: The effect of upstream turbulence. International Journal of Thermal Sciences, 138, 235-246.

10.1 Introduction

Monolith reactors are extensively used in the automotive industry as catalytic converters. A typical converter consists of a metallic carcass containing the monolith, an inlet diffuser, and an outlet cone, as shown in Figure 10.1. To add catalyst metals, such as platinum, palladium or rhodium, a coating process is performed which results in a thin layer of washcoat fixed to the inner walls of the channels of the monolith, where the chemical reactions occur.

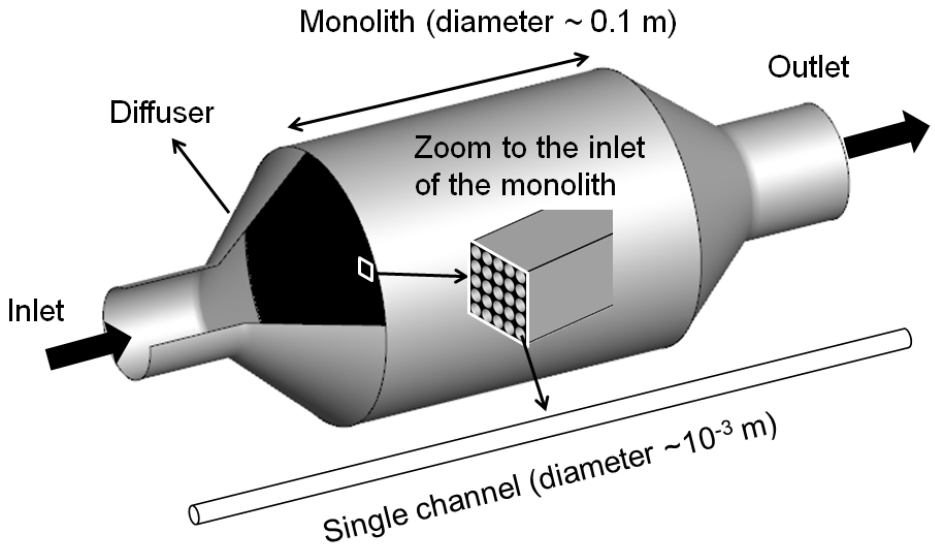

Figure 10.1: Schematic of a catalytic converter

In automotive applications the converter is fed with the exhaust from the engine, which is fully turbulent in the exhaust pipe with a Reynolds number (Re) of the order of 10^4. Due to the size of the monolith channels, the Re decreases by orders of magnitude inside them, down to sub-critical values. Based on that, the flow in the channels is often assumed to be fully laminar along the entire substrate. In reciclity, at the diffuser-monolith interface the turbulence in the diffuser collides with the walls of the monolith and it is forced into the channels, producing an acceleration due to the reduction of the open frontal area [1, 2]. Vortices larger than the cross-section of the channels break into smaller ones and enter the substrate. Despite of the low Re, the turbulence does not disappear spontaneously; it decreases at a rate dominated by the Re, in some cases over a distance that covers a significant portion of the channel. The magnitude of the effect of such a turbulence on the key variables of the converter, such as the pressure drop, and heat and mass transfer inside the substrate, is still a matter of discussion among the community. The performance of the reactor, and the fuel efficiency of the engine, ultimately relies on the design of the substrate and the catalyst, making an accurate description of the phenomena inside of the channels important. The

motivation of this paper is to build an understanding of the effect of the turbulence entering the monolith and to quantify the magnitude of its impact on the effective heat and mass transfer coefficients between the fluid and the channel walls.

In typical catalytic converters, the monolith is made from ceramic and contains thousands of parallel channels. Since the hydraulic diameter of the channels is of the order of one millimetre, it is very difficult to measure local profiles of velocity or temperature inside the substrate without affecting them. Even when it is possible to make measurements, it is done at the expense of the accuracy of the result [3]. Reaction rate constants have an exponential dependence on the temperature, which is often higher close to the entrance of the channels during normal operation. It is precisely there where the turbulence plays a role as well, reinforcing the motivation of this study.

The main focus is the evaluation of the convective heat transfer coefficient along the channels, and to make a comparison of the Nusselt (Nu) with and without turbulence entering the channels. Turbulence is characterised by the presence of a series of vortices of several sizes that improve significantly the transport of momentum, heat and mass. Since the reaction rate can be controlled by either the kinetics or the mass transfer, depending on the conditions of the channels, both the effective diffusion at the wall and in the axis of the channel are relevant [4, 5]. The thermal entry length depends on the Re and the Prandtl (Pr), and the concentration entry length on the Re and the Schmidt (Sc). For typical exhaust gas composition, the ratio of the Pr and Sc is close to unity. In this case the thermal and concentration entry length are similar. Also, changes in the Sherwood (Sh) and Nu are consistent. It means that studying the effect of the turbulence in the convective heat transfer (Nu), provides a good insight into the effect on the mass transfer (Sh) as well.

Apropos convective heat transfer in a channel, the laminar flow entrance length problem has been extensively studied, see for example Shah and London [6] and Kays and Crawford [7]. The Nu for pipes in the presence of fully developed turbulence, as well as in the transition regime has also been carefully discussed in the literature [8, 9]. However, monolith channels present a different scenario. In the literature, flow in circular pipes is separated into three groups [10]: Laminar for Re below 2100, turbulent for Re above 10,000, and transitional for the Re in between. Monolith channels do not fit into any of the former classifications. The channel Re is sub-critical, however, turbulence at the beginning of the channels is sustained by the inflow from the diffuser. Correlations for developed turbulent flow are not meant to work at such a low Re. Also, the flow eventually becomes laminar inside the channel and

developed turbulence is never present. Transitional flow is characterised by turbulence that appears and dissipates sporadically. This could be true at some segment of the channel, but does not describe its beginning or its end. In monolith substrates, turbulence enters the channel; then it is dissipated at a rate that depends on the Re, resulting in laminar flow after some distance. An adequate correlation for the Nu inside a monolithic channel must take into account both the magnitude and rate of dissipation of the turbulence in the entry region. It must also smoothly converge to the correct asymptotic Nu in the fully developed laminar zone. The novelty of this work is that we consider the effect of upstream turbulence on the convective heat transfer in the entry region of a monolith system, which, to the best of our knowledge, has not been studied. When using a one dimensional radially lumped parameter model to simulate the monolith channel, a correct determination of the values of the Nu and Sh numbers may be of significant interest. This will especially be true where the chemical reaction ignites in the entrance region, as higher values of Nu and Sh will result in earlier ignition and potentially significantly different overall reactor performance. In other applications, such as in pre-turbo catalysts, channel Re are much higher than in standard catalytic converters and much of the monolith length will lie within the entry region, therefore it is essential to have accurate knowledge of the Nu and Sh in that region. Furthermore, when the inlet temperature is transient, then a significant amount of heat transfer can occur in the entrance region, increasing the importance of capturing these effects correctly in a one dimensional model. Groppi et al. [11] compared lumped vs. distributed models for heat and mass transfer, finding substantial differences in the wall temperature prediction when gas phase reactions occur to a significant extent of the channels. Later, it was reported that the shape of the transverse section of the channels plays a role also, changing the position of the light-off due to the effect of the corners on the mixing when assuming laminar developed flow along the entire channels [12]. Gundlapally et al. [13] reported an extensive review of correlations for local Nu and Sh for channels with developing flow. That review illustrates the effect of several washcoat and channel shapes on the operating regime of the substrate, either kinetic or mass transfer controlled.

Section 10.2 describes the computational model of the channel, grid, and considerations to calculate the Nusselt and Graetz numbers. Section 10.3 first makes a screening of the effect of the turbulence on the Nu vs. Gz^{-1} relationship, and finishes with a brief comparison of the Nusselt obtained with LES and several RANS models. Section 10.4 shows a systematic experimental design, which results in an extended model that takes into account the effect of the turbulence along the entry, transition, and laminar regions. The limitations of the presented model are reported at the end of this section as well. Finally, Section 10.5 presents

the main conclusions and remarks.

10.2 Computational model

The most commonly used ceramic monoliths have a square cross section, although triangular and hexagonal shape are also used. The starting shape is subsequently altered by the application of the washcoat. The width of the coating tends to be thicker in the corners of the channels, which tends to round the channels. The higher the loading of coating the rounder the shape of the channel, especially for hexagonal or triangular channels and with multi-layer washcoat [4, 14–16]. Since most of practical applications use washcoated monoliths, this study used circular channels. The flow was modeled using Large Eddy Simulation (LES), which is an extensively validated model, suitable for predicting flow in transition, as is expected inside of the monolith channels, and has been successfully implemented to investigate heat transfer in turbulent flow [17–19]. The transport equations for mass, momentum and energy transport are given in Equation (10.1), (10.2) and (10.3) respectively [20].

$$\frac{\partial \rho}{\partial t} + \frac{\partial}{\partial x_j}(\rho \overline{u}_i) = 0 \tag{10.1}$$

$$\frac{\partial \overline{u}_i}{\partial t} + \overline{u}_j \frac{\partial \overline{u}_i}{\partial x_j} = -\frac{1}{\rho}\frac{\partial \overline{p}}{\partial x_i} + \frac{\partial}{\partial x_j}\left(\nu \frac{\partial \overline{u}_i}{\partial x_j} + \frac{1}{\rho}\frac{\partial \tau_{ij}}{\partial x_j}\right) \tag{10.2}$$

$$\frac{\partial}{\partial t}(\rho E) + \frac{\partial}{\partial x_j}(u_i(\rho E + p)) = \frac{\partial}{\partial x_j}\left(k_{eff}\frac{\partial T}{\partial x_i}\right) \tag{10.3}$$

where

$$E = \frac{u^2}{2} - \frac{p}{\rho} + \int_{T_{ref}}^{T} C_p dT$$

Equation (10.3) accounts for the total energy, it means the kinetic and potential energy, and enthalpy. The term τ_{ij} in Equation (10.2) is the sub-grid scale stress, and relates the resolved flow with the sub-grid-scale motion. At sub-grid scale τ_{ij} is modeled as in Equation (10.4). The Wall-Adapting Local Eddy-Viscosity model (WALE) closes the problem [21]. The WALE model was conceived to provide the correct wall asymptotic behavior for wall bounded problems, it also returns zero turbulent viscosity for laminar flows, resulting ideal for the purposes of this study. The WALE model computes μ_{SGS} by using the Equation (10.5) [20, 21].

$$\tau_{ij} = \frac{1}{3}\tau_{kk}\delta_{ij} - 2\mu_{SGS}\overline{S}_{ij} \tag{10.4}$$

$$\mu_{SGS} = \rho L_S^2 \frac{(S_{ij}^d S_{ji}^d)^{3/2}}{(\overline{S}_{ij}\overline{S}_{ji})^{5/2} + (\overline{S}_{ij}^d \overline{S}_{ji}^d)^{5/4}} \tag{10.5}$$

where L_s and S_{ij}^d are defined as:

$$L_S = min(kd, C_w V^{1/3})$$

$$S_{ij}^d = \frac{1}{2}(\overline{g}_{ij}^2 + \overline{g}_{ji}^2) - \frac{1}{3}\delta_{ij}\overline{g}_{kk}^2$$

$$\overline{g}_{ij} = \frac{\partial \overline{u}_i}{\partial x_j}$$

Further details about the model constants and expressions can be found in the ANSYS Fluent Theory Guide [20] and in Nicoud and Ducros [21]. It is necessary to remark that Nicoud and Ducros defined C_w as 0.5, however, intensive subsequent validations reported consistently superior results in Fluent v17.2 with C_w equal to 0.325, which was the value used in this study [20]. The grid convergence was tested by replicating existing results. For laminar flow most of the authors report the Nu vs. Gz^{-1} along the entry region using Equation (10.7), where the Gz^{-1} acts as a dimensionless distance. [22–24]. In Equation (10.7) A is equal to Nu_∞, the asymptotic value of Nu in the fully developed zone, which depends on the channel shape and wall boundary conditions. B, C and n are model constants.

$$\frac{\mathrm{Nu}}{\mathrm{Nu}_\infty} = \frac{\mathrm{Nu}}{A} = 1 + B(\mathrm{Gz})^n \exp\left(-\frac{C}{\mathrm{Gz}}\right) \tag{10.6}$$

or

$$\mathrm{Nu} = A\left[1 + B(\mathrm{Gz})^n \exp\left(-\frac{C}{\mathrm{Gz}}\right)\right] \tag{10.7}$$

where

$$\mathrm{Gz} = \frac{D\mathrm{RePr}}{x}$$

$$\mathrm{Nu} = \frac{hD}{k}$$

As test conditions, air with constant physical properties was used, entering at 300 K with a Re of 300, in a circular pipe of 1.1 mm of diameter, 90 mm in length and with constant wall temperature of 400 K. It is important to point out that for channel Re below 100, variable physical properties might lead to changes in the entry length Nu [25]. The problem was solved by modeling the flow first as laminar and then using LES without fluctuations in the inlet.

In the absence of fluctuations, at such a sub-critical Re, LES must predict steady laminar flow. Comparing both results makes it possible to analyse the performance of the model and discard a possible generation of false turbulence at the sub-grid scale. Two systematically refined meshes were tested for each model. The LES used meshes of 875 700 and 1 751 400 control volumes. For laminar flow the meshes contained 200 100 and 400 500 control volumes. All the simulations, LES and laminar, were done in 3D geometries and as unsteady. Figure 10.2 shows two of the meshes used in the comparison.

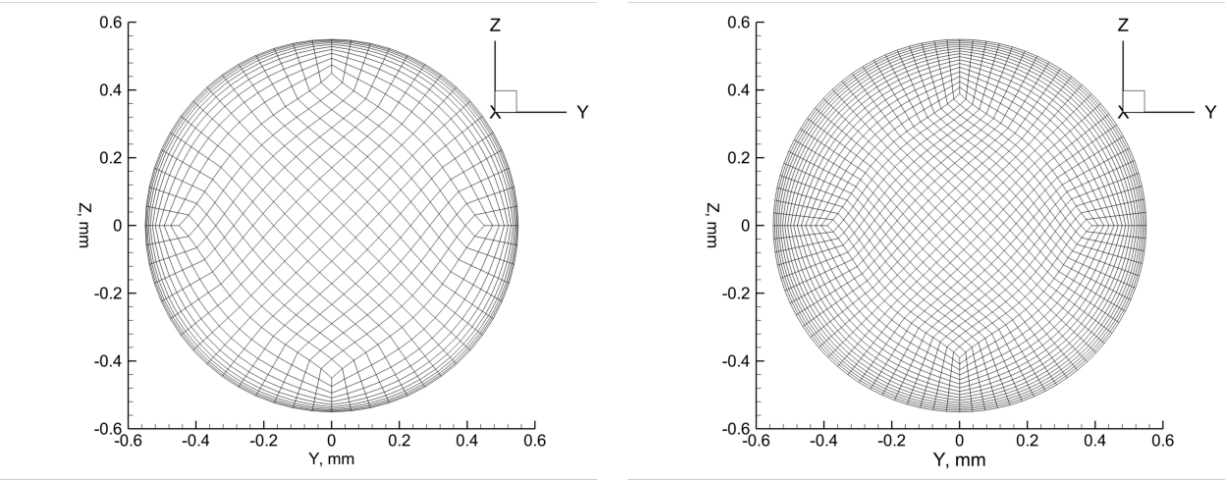

(a) (b)

Figure 10.2: Section of the
meshes of (a) 400 500 control volumes and (b) 1 751 400 control volumes

The problem was implemented in ANSYS Fluent v17.2 [26]. In LES, a bounded central differencing scheme was selected for the momentum and energy equations, a bounded second order implicit scheme for time discretization, and the SIMPLE algorithm for the pressure-velocity coupling. The cell CFL number was monitored to be always 0.75 or lower, which led to time steps of the order of 10^{-6} s. The stop criterion for each time step was the reaching of maximum scaled residuals of the order of 10^{-5}. All further calculations are based on statistically stationary values, obtained by running the simulations until reaching constant mass-weighted velocity magnitude and temperature over the entire domain, along a moving time window of a length of five residence times. The use of a moving window eliminates any initialisation effect. The convective heat transfer coefficient for the Nu was obtained based on the temperature profile, according to Equation (10.8).

$$h(T_s - T_m) = -k\frac{\partial T}{\partial r}\bigg|_{r=R} \tag{10.8}$$

where T_m is the mixing cup temperature defined in the usual way:

$$T_m = \frac{\int_0^R u\rho C_p T r dr}{\int_0^R u\rho C_p r dr}$$

Given that T_s, the wall temperature, is fixed as a boundary condition, especial efforts must be made to obtain smooth profiles close to the wall. The temperature gradient in Equation (10.8) was computed numerically, using a second order accurate backward scheme. Other differencing schemes were tested, finding that first order approximations led to incorrect results and schemes of order three to six did not produce noticeable changes compared to the second order scheme.

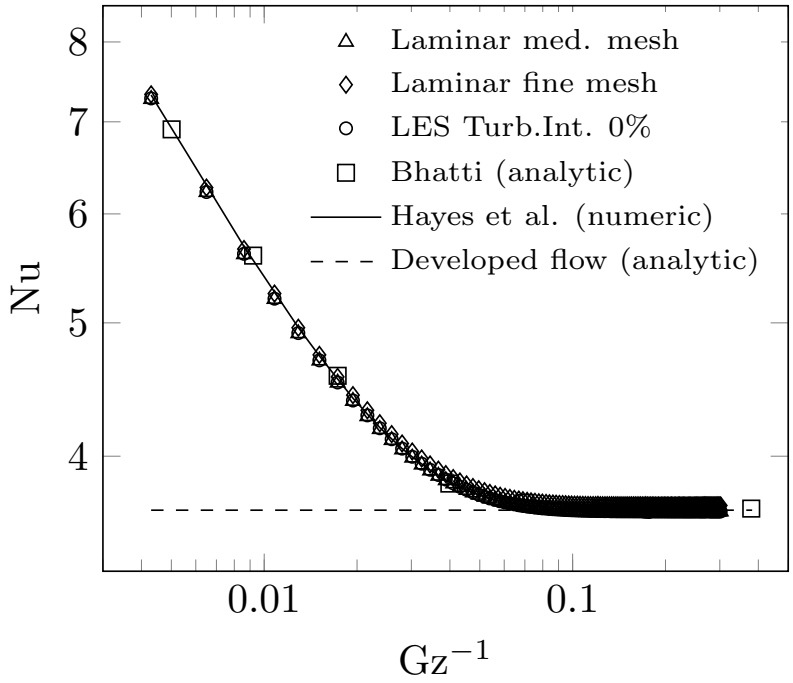

Figure 10.3: Comparison of Nu vs Gz^{-1} curves for developing [25, 27] and developed flow [10]

The results of the LES and laminar models are summarised in Figure 10.3. All of the simulations follow the same curve and converge to the same classical 3.655 Nu in the developed zone for constant wall temperature [10, 25]. An analytic expression for the Nusselt number along a combined thermal and hydraulic entry length with a constant wall temperature and laminar flow was found by Bhatti [27] and reported in the form of an infinite series in Kays and Crawford [28]. A simpler explicit expression for the same curve can be found in Hayes et al. [25]. Both solutions from Bhatti and Hayes et al. were included in the figure.

10.3 Analysing the effect of decomposing turbulence on the convective heat transfer

This section describes how the turbulence decomposes when entering the channel, its effect on the convective heat transfer, and explores the variables which describe that effect.

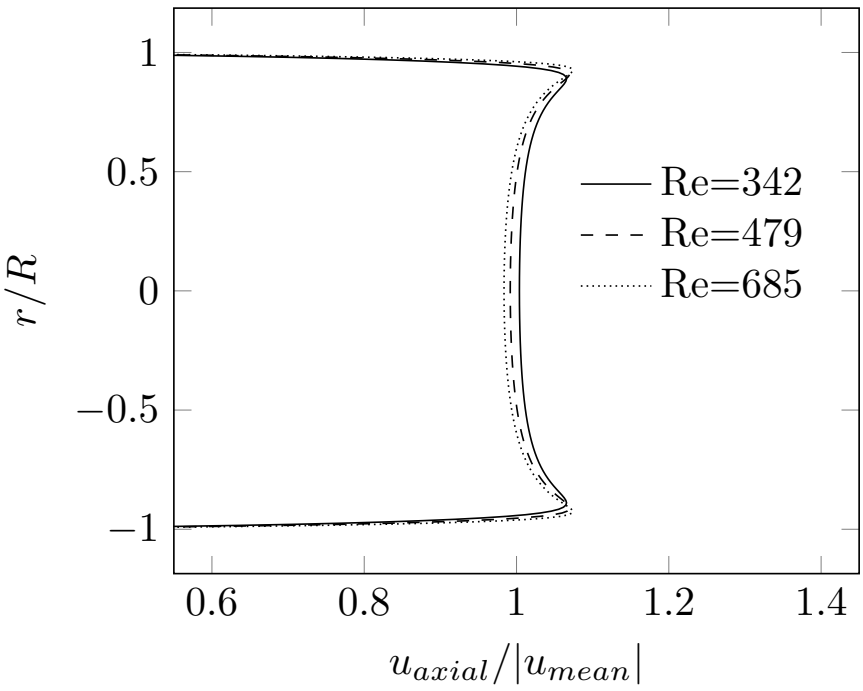

Figure 10.4: Velocity profile at the inlet of a circular channel of a monolith with a void fraction of 65% at three different channel Re

A base testing case was established with Re 300 and turbulence intensity of 40%, such values can be found in the literature [29–31]. The inlet velocity profile of the channel was assumed to be flat, which is reasonable for a typical monolith void fraction of 65% and the channel Re numbers covered in this study. The maximum value observed for the ratio of the peak over the average velocity was 1.06 (see Figure 10.4). Similar results can be found in Benjamin et al. [32]. This assumption may not apply to other applications with a sudden reduction of the flow area or higher channel Re numbers. It is recommended to check this before applying the results reported in this paper. Due to physical constraints, the size of the largest eddies immediately inside the channels is limited to the channel size. Hence, the length scale of the turbulence at the inlet was limited to that size. This described base case was run until reaching a statistically stationary state. During the run the maximum and

average CFL were 0.85 and 0.05 respectively, the same values for the y^+ were 0.36 and 0.01, and for the μ_{SGS} they were 0.43 and 0.03. Figure 10.5 shows instantaneous velocity and temperature values at an arbitrary time after reaching statistically stationary state.

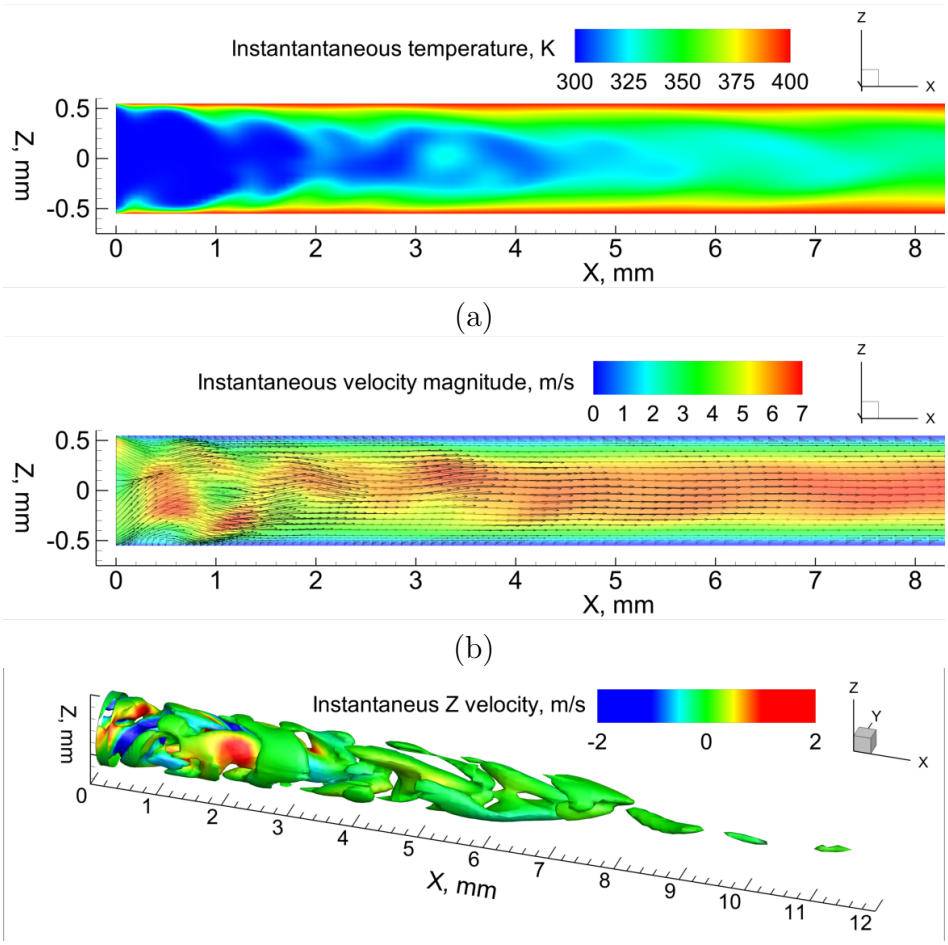

Figure 10.5: Plane along the center of the pipe shwing the instantaneous (a) temperature, (b) velocity magnitude and (c) iso-Q coloured by the instant Z velocity. Inlet conditions: Re 300, turbulence intensity 40% and length scale 2R

Figure 10.5a shows a contour plot of the temperature at an instant over a plane along the centre of the channel. It can be seen that the temperature profile differs significantly from the one produced by a steady laminar flow. There is a development of the thermal boundary layer starting from the channel walls, however, the temperature profile is notoriously irregular at the centre of the channel, at least up to x/D=5. As observed in Figure 10.5b, the velocity fluctuations are considerable in magnitude and direction in the first section of the channel, explaining the mixing observed in the temperature contour. The stabilisation of

the flow is faster than that exhibited by the temperature, with an appreciable diminishing of the resolved portion of the flow fluctuations before x/D=4. Even though the most energetic vortices are effectively resolved, the sub-grid scale make a contribution as well. The iso-Q plot in Figure 10.5c compliments the behavior observed previously for the temperature and allows us to visualise the structure of the flow in more detail. It can be seen how the vortices and rotating structures merge and decay along the channel, to become virtually nonexistent at x/D=10. Such a decay is natural since the Re is sub-critical, and agrees with previously reported data for turbulent flow entering monolith channels [29]. Although those are instantaneous values, they provide first evidence of the effect of the pre-existent turbulence entering the channels on the convective heat transfer.

The low values of μ_{SGS} reported for the simulation indicate that most of the flow was actually resolved. However, to confirm the presence of turbulence in the entry length and its effect, the frequency content and power spectrum were also analysed and reported. Figure 10.6 shows the velocity as a function of time at two axial positions in the center of the channels. It can be seen that close to the inlet the velocity varies in several frequencies. Downstream, the magnitude of the oscillations decreases and the highest frequencies observed close to the inlet are missing.

The complete power spectrum at x/D=1 in Figure 10.7 shows that the low frequency (or large size) vortices are actually in the resolved portion of the flow, which includes a series of length scales in the inertial sub-range as well. At that position, the percentage of turbulence kinetic energy resolved was observed to be superior to 95%, confirming that a minor portion of the total kinetic energy is modeled at sub-grid scale. Since the turbulence decays along the channel, the flow beyond x/D=1 is equally or more resolved.

It is important to remark that the power spectrum at x/D=1 shows a smooth transition from large to small vortices, acting as a vortex cascade typical for turbulent flows, and effectively improving the convective transport. On the other hand, the power spectrum at x/D=20 shows fluctuations at large scale, then an energy gap at approximately $6x10^3$ Hz, that indicates that there is not an actual vortex cascade. All values beyond that frequency are most probably the product of low local CFL numbers. These induced high frequency fluctuations are more noticeable in the laminar unsteady region, however, still with an energy content of about 4 to 5 orders of magnitude below the one at the integral range. Increasing the CFL number sacrifices resolution in the turbulent region, hence, the time step was manipulated to ensure always a maximum CFL of about the unit. Looking at Figure 10.6,

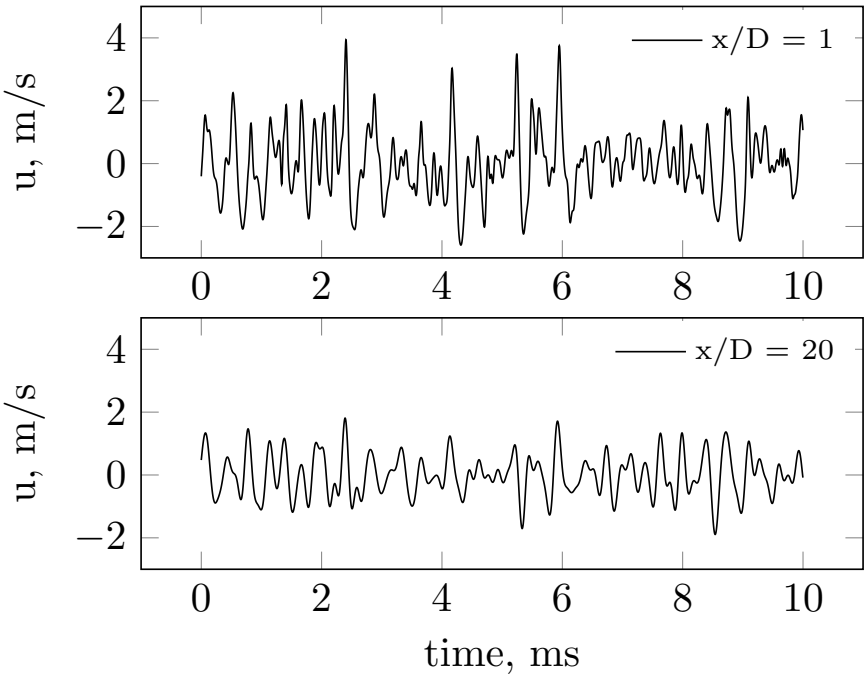

Figure 10.6: History of the x-velocity (axial) at the center the channel. Both velocity trends were centred to zero. Top: at x/D=1, bottom: at x/D=20

a correlation between the peak velocity at the two positions can be distinguished. Due to the unsteadiness of the inlet condition, the actual mass flow rate varies on time, leading to a sort of pulsating flow in the laminar region of the channel. It provides an explanation for the power spectrum at x/D=20, and agrees with the observed behavior in Figure 10.5. Since turbulence remains at the beginning of the channel, an effect on the convective transport in radial direction is expected. Meanwhile, at x/D=20 there is no evidence of remaining turbulence, and the heat transfer is explained mostly by the macro flow and the laminar diffusion.

The average, amplitude and frequency of the fluctuations of flow motion are related to the length scale of the turbulence, the turbulence intensity, and the Reynolds number. Since the diameter of the channel and fluid properties are constant, the Re is a function of the average velocity only, and thus defines it. The turbulence intensity defines the standard deviation of the velocity, that is, the amplitude of the velocity fluctuations, and the length scale dominates the scale and frequency of the largest eddies directly. The three of those quantities were considered independent inlet variables of this study, and to explore the individual contribution of each one of them, the orthogonal numerical experiments in Table 10.1 was proposed. Compared to the base case, Run 1 differs in the Re, Run 2 uses another turbulent intensity,

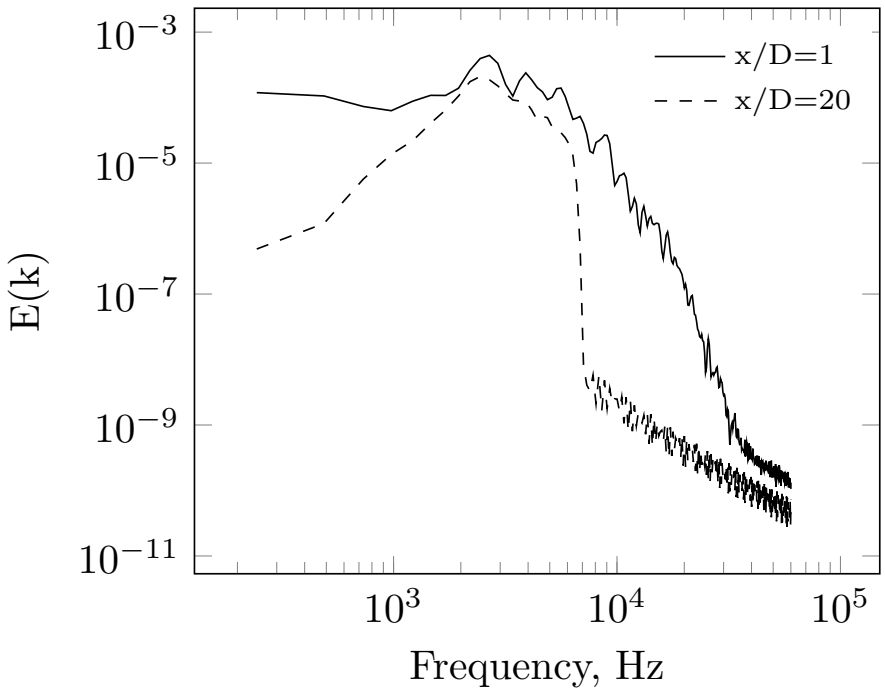

Figure 10.7: Power spectrum of the flow at x/D=1 and x/D=20

and Run 3 changes the length scale of the turbulence. The table includes a fully laminar case as a reference.

Table 10.1: Inlet conditions a series of exploratory runs

Run	Re	Turb. Int.	Length scale	Figure
Laminar	300	-	-	10.8a, 10.8b, 10.8c
Base	300	40%	2R	10.8a, 10.8b, 10.8c
1	100	40%	2R	10.8a
2	300	80%	2R	10.8b
3	300	40%	R	10.8c

According to the results in Figure 10.8, the Re, length scale and turbulence intensity have an individual effect changing the entry region Nu-Gz^{-1} curve. Since the thermal properties and the channel diameter are constant, the alterations of Nu are explained by changes in the convective heat transfer coefficient only. By increasing the turbulence intensity and the length scale, convection is improved, resulting in the higher Nu observed in Figure 10.8a and 10.8b. Following the same logic, at a lower Re the turbulence decreases more rapidly, leading to a lower Nu (see Figure 10.8a). In all the cases, the flow eventually becomes laminar fully developed and the Nu converge to the classical solution for constant wall temperature, 3.655.

The largest effect is induced by the turbulence intensity, followed by that produced by the Re and length scale. The last two displaced the Nu-Gz^{-1} curve in a comparable manner, however, the length scale is limited to the diameter of the channel, hence its maximum individual effect is observed in Figure 10.8c. The Re, meanwhile, can scale up ten times the maximum tested value before reaching the critical value for circular pipes. Since increasing the Re decreases the rate of decay of the turbulence, its individual effect can be larger than that observed in Figure 10.8a making this variable more relevant than the turbulence length scale. This is better appreciated in Figure 10.8b. The figure shows how at the beginning of the channel the turbulence increases the Nu by more than 50%, however, it differs less than 10% compared to the corresponding value for laminar flow at x/D=20 ($Gz^{-1} \approx 0.05$). Although the amplitude of the fluctuations at x/D=1 and x/D=20 are comparable, the lack of a vortex cascade does not improve the convective transport as turbulence does, despite the unsteadiness of the flow.

Although LES is accurate, it is often too computationally expensive for practical applications. RANS models are preferred in an industrial research context because they present a convenient trade-off between cost and accuracy. The most consolidated RANS models are meant to work with fully turbulent flows only, which is not the condition in this work. Since it is a matter of common interest, the accuracy of four RANS models at predicting the correct Nu-Gz^{-1} curve was also investigated. Figure 10.9 shows the Nu-Gz^{-1} predicted by several RANS models, and compares them to the values obtained with LES. All simulations were done under the same conditions: Re of 300, turbulence intensity of 40%, and length scale equal to the channel diameter. For RANS all the schemes were set as QUICK [20] and the same meshes of 8 757 010 and 1 751 400 control volumes than for LES were tested. The convergence criteria were reaching maximum scaled residuals below 10^{-6}, obtaining a stable volume average temperature, and stable volume average velocity magnitude.

Standard κ-ε [33] is the simplest model analysed and it is included in most commercial CFD codes. This model was implemented together with the enhanced wall treatment based on the y^+ observed during the simulations. In Fluent v17.2, it means the application of the Wolfshtein equation [34] to the viscosity-affected near-wall region, which is suitable for $y^+ \approx 1$. As shown in Figure 10.9, it fails converge to the correct Nu in the laminar zone. This is consistent because this model is meant for fully turbulent flows and overestimates the convection when it is implemented in flows with low Reynolds numbers. The second model tested was the SST [35]. It tends to perform better than κ-ε in lower Re scenarios since it takes into account the shear stress transport, limiting the production of turbulence. According to the results, even though it converges to the correct Nu in the laminar zone, it overestimates

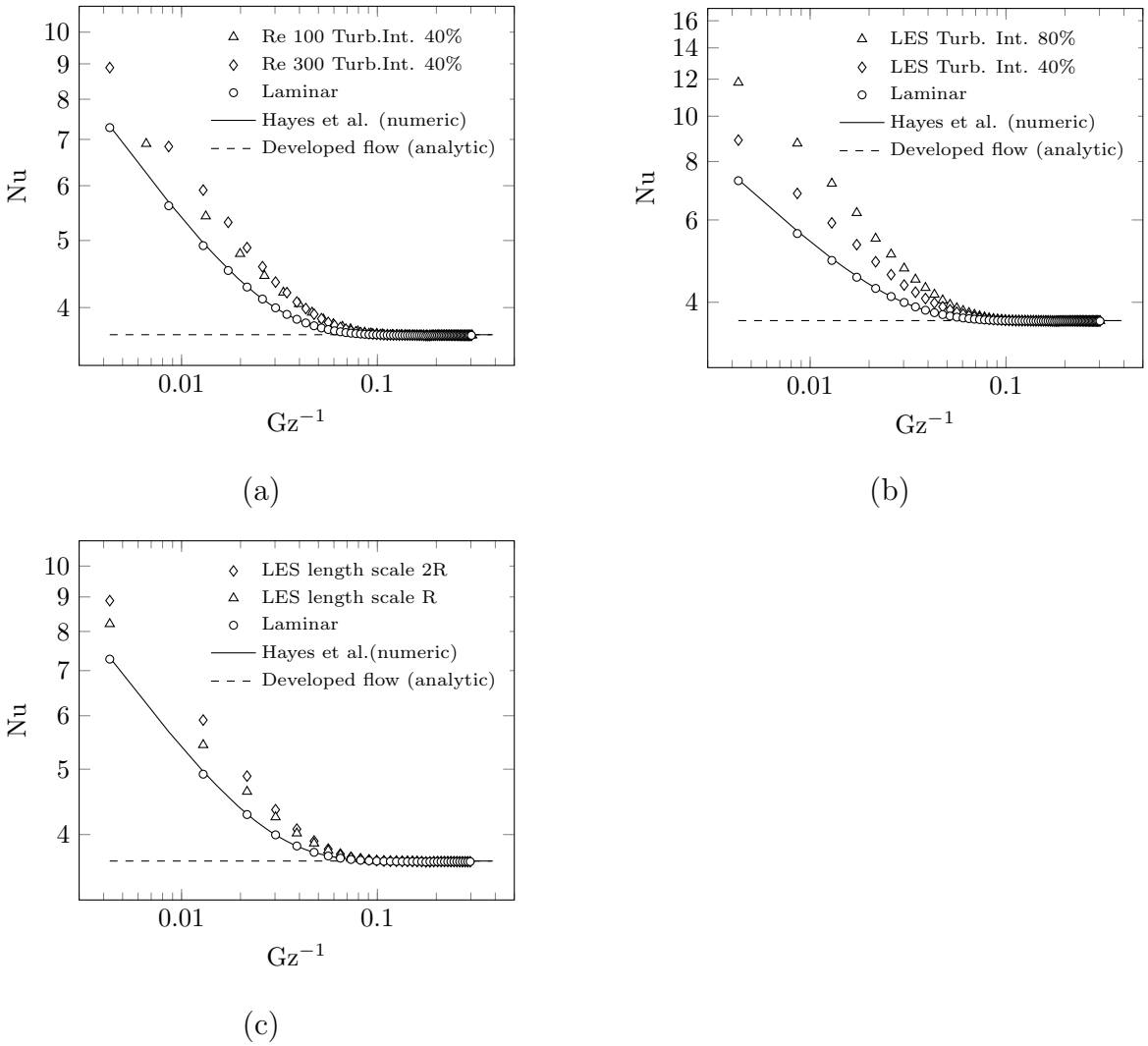

Figure 10.8: Effect of the Re, length scale, and turbulence intensity on the Nu vs Gz^{-1} curve, compared to the laminar developing [25] and developed flow [10]

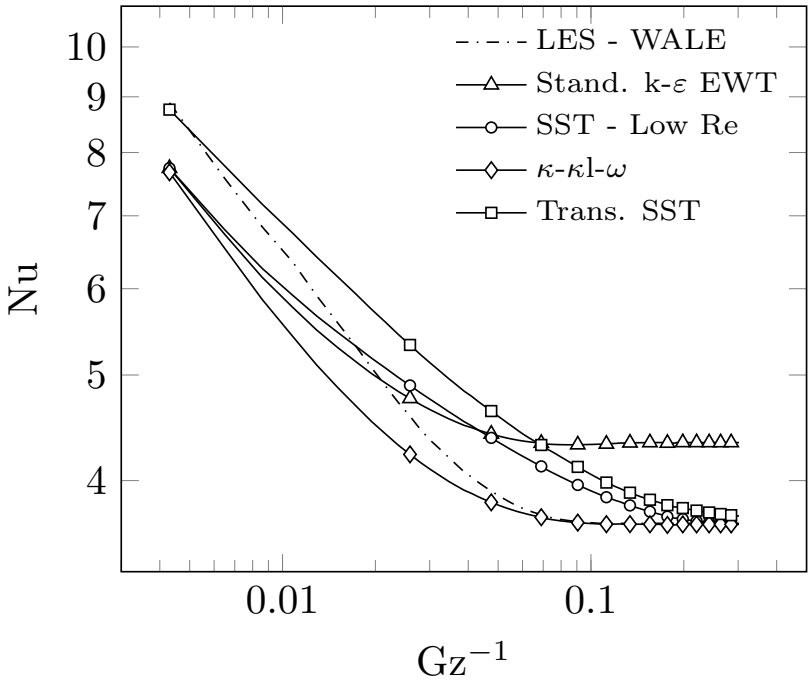

Figure 10.9: Comparison of LES and several RANS models when predicting the Nu vs Gz^{-1} curve

by a significant factor the length of the entry region. In contrast with the two RANS models described above, the next two are transitional models. The transitional SST model introduces the intermittency and momentum thickness Re to model the change of the flow regime [36]. It is a general purpose model, applicable to wall bounded flows. This model predicts the same initial Nu than LES, but it behaves similarly to the SST streamwise, overextending the entry length considerably. It must be mentioned that in the lack of experimental information, the inlet intermittency was set to one. The final transitional model analysed was the κ-κl-ω [37]. It separates the flow motion into two categories according to the frequency of fluctuation. Low frequency fluctuations can be observed in non-turbulent flow, and are modeled by introducing an additional transport equation for the laminar kinetic energy (κl). For the conditions of this study, where the inlet velocity profile is flat, the inlet laminar kinetic is zero. The κ-κl-ω model predicts an initial Nu about 12% lower than LES, and underestimates the convective heat transfer coefficient along the entire entry region. However, it predicts the correct entrance length as well as the correct Nu in the fully developed region. Unlike RANS models, LES is suitable for flow in transition and it has been extensively validated in many contexts [38, 39]. All of the results reported in this paper were obtained with highly resolved LES, where the role of the sub-grid is minor. However, a further experimental validation is highly recommended. This requires the use of accurate non-intrusive techniques, such as PIV or LDA, which are challenging to apply at a channel scale, hence, beyond the scope of this paper.

10.4 Extended model for the Nu vs. Gz^{-1} curve

Having discussed how the turbulence effectively displaces the curve Nu-Gz^{-1} in the entry region, the next step is to determine an extended model that takes into account the turbulence. Looking at Figure 10.8 it is noted that curves with and without turbulence are consistent in their trajectories, hence, the mathematical structure of the extended model was assumed the same as the one for the laminar flow. To find out if this is correct, data for Nu-Gz^{-1} at several inlet turbulence intensities were fitted to Equation (10.7). Results are shown in Figure 10.10. In all cases the channel Re and turbulence length scale were set to 300 and 2R respectively. Each fitted curve was obtained by applying non-linear regression to each data set individually. It means, one fitting for the curve at 20% turbulence intensity, one for the data set at 40% and another for the data at 80% turbulence intensity. All of the regressions and statistical analysis were performed in R, which is a highly specialised programming language, developed for statistical computing [40]. Due to its physical meaning, which is the asymptotic Nu in the laminar developed zone, the parameter A was kept constant at

3.655. Meanwhile, B, C and n were used as regressors. The fitting of each data set led to a different value for the regressors, moving the problem to find an expression for B, C and n as a function of the inlet conditions of the channel.

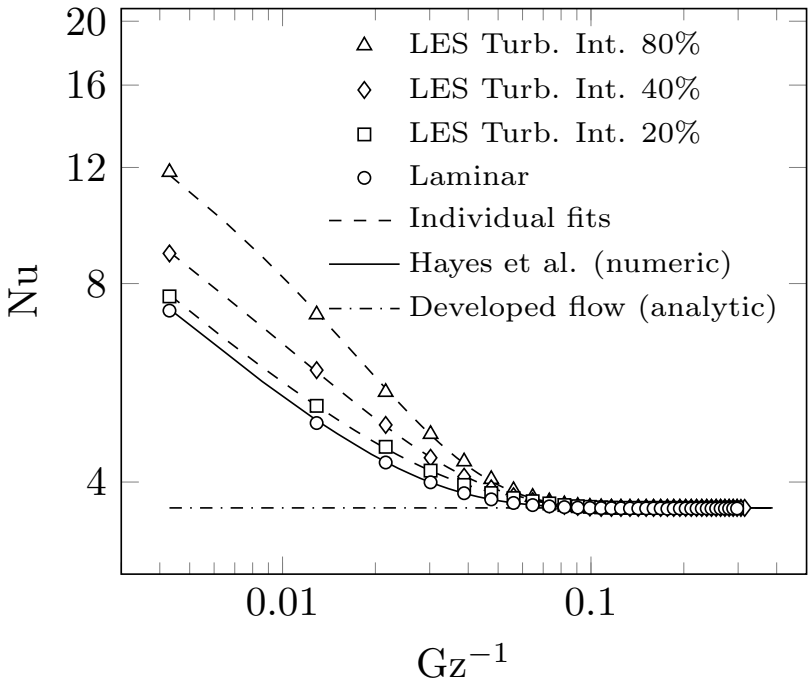

Figure 10.10: Individual fittings of the Nu-Gz^{-1} curve at several inlet turbulence intensities compared with the one for laminar flow [25]

10.4.1 Sub-models for B, C and n

Figure 10.8 provides a screening about how the Re, turbulence length scale (l_e), and turbulence intensity (Ti) modify the Nu-Gz^{-1} curve. In addition, the individual fittings in Figure 10.10 indicate that by changing B, C and n, it is possible to predict such curve for different magnitudes of turbulence entering the channels. Let us consider that B, C and n are not constant, instead of that, they follow the three following functions: $B = f_B(\mathrm{Re}, l_e, Ti)$, $C = f_C(\mathrm{Re}, l_e, Ti)$ and $n = f_n(\mathrm{Re}, l_e, Ti)$, referred to as the sub-models in the rest of the document. Such sub-models can be inserted into Equation (10.7) to extend its capacity to predict the Nu-Gz^{-1} curve when there is turbulence entering the channel. A way to find the sub-models is by using the surface response methodology. It follows a systematic experimental design that quantifies the effect of each input variable, as well as any other possible interaction between variables, separately and free of confusion caused by correlation between

factors [41]. The type of surfaces to be fitted depends in the order of the sub-models. Such information was obtained by performing a series of simulation, changing the inlet variables (Re, l_e and Ti), then registering their effect in B, C and n using the following steps:

i. Choosing arbitrary values for Re, l_e and Ti

ii. Running an LES with the chosen values

iii. Fitting the resulting Nu-Gz^{-1} curve to Equation (10.7)

iv. Registering the B, C, n obtained after the fitting

The results are summarised in Figure 10.11. The column of plots at the left are all results of LES changing Ti, meanwhile, the Re and l_e were fixed at 300 and 2R respectively. In the central column, the only variable changed was the Re, keeping the l_e and Ti constant. Finally, in the column at the right l_e was changed, meanwhile the Re and Ti were kept constant. The plot at the top-left shows the relationship between f_B and Ti, the one at the top-center relates f_B and the Re, and the plot at the top-right shows variations of f_B when changing l_e. The second row follows the same logic, but, applied to f_C instead of f_B. as in the column at the bottom is applied to f_n.

The classical full factorial design considers two levels of each variable. However, this study used three levels for Ti and Re, to investigate possible non-linear relationships related to them. This was not done for l_e, since its range of variation is closely bounded, also the most realistic case is when setting it to be the same as the channel diameter. The plots for f_B-Re and f_n-Ti appear to be the most curved. However, their lack of fit to a line is minor. All linear fittings provide coefficients of determination above 0.95 and explain most of the variance of f_B, f_C and f_n. Due to its resolution and generality, and having discarded non-linear effects, a multi-response full factorial design, with three variables and two levels was proposed to predict f_B, f_C and f_n. Such type of design results in a model with the structure of Equation (10.9).

$$\hat{y}_l = \underbrace{b_0}_{\text{Intercept}} + \underbrace{\sum_{i=1}^{3} b_i x_i}_{\text{Main effects}} + \underbrace{\sum_{i<j}^{3} b_{ij} x_i x_j}_{\substack{\text{Two-factor} \\ \text{interactions}}} + \underbrace{b_{123} x_1 x_2 x_3}_{\substack{\text{Three-factors} \\ \text{interaction}}} \tag{10.9}$$

where the independent variables are:

x_1 : Turbulence intensity

x_2 : Length scale

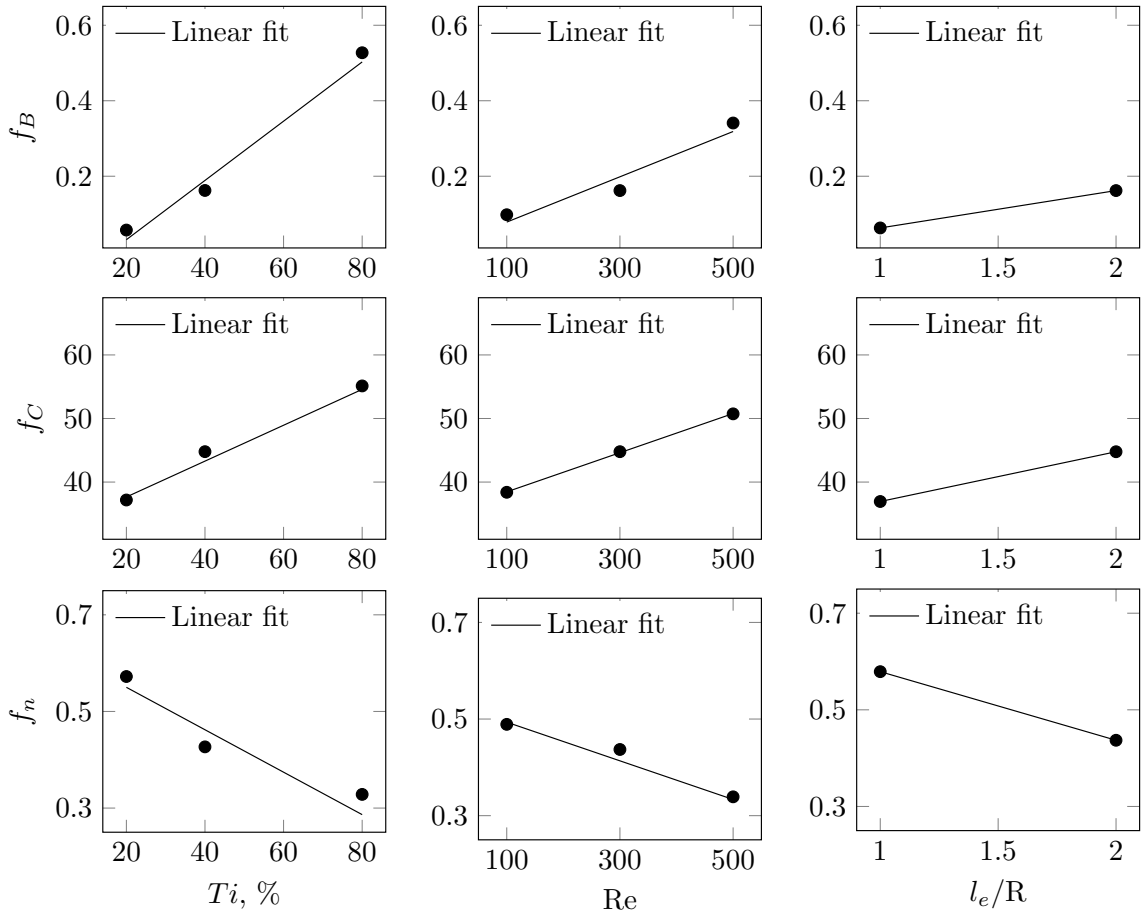

Figure 10.11: Main effects of Re, l_e and Ti in f_B, f_C and f_n. The runs at the left were done with Re=300 and l_e=2R. The runs at the central column used Ti=40% and l_e=2R. The runs at the right considered Re=300 and Ti=40%

x_3 : Reynolds number
and the output variables are:
$\hat{y_1} : f_B$
$\hat{y_2} : f_C$
$\hat{y_3} : f_n$

There are numbers of reports in regard to flow inside a catalytic converter whence ranges for Re, Ti and l_e can be estimated [30, 42–44]. The turbulence intensity after the monolith is typically between 40% and 80%, and common channel Re are from 100 to 400. As discussed, the most reasonable value for the length scale is the diameter of the channel, however, a level at l_e=R was also used to complete the experimental design. Considering these limits, the full factorial design 2^3 shown in Table 10.2 was performed.

Table 10.2: Experimental design containing the levels for Ti, l_e and Re, and the results for B, C and n

Run	Turb. Int.	Length Scale	Re	B	C	n
1	40%	R	100	0.0403	43.9319	0.6609
2	80%	R	100	0.0088	22.7547	0.9624
3	40%	2R	100	0.0975	38.2603	0.4905
4	80%	2R	100	0.3873	50.7066	0.2814
5	40%	R	300	0.0627	36.9369	0.5791
6	80%	R	300	0.0629	45.6911	0.6369
7	40%	2R	300	0.1623	44.7802	0.4367
8	80%	2R	300	0.5272	55.1239	0.3056

The exact values for B, C and n resulting of the fitting of each run are also included in Table 10.2. Interaction plots in Figure 10.12 reveal a strong interaction between Ti and l_e in the determination of f_B and f_n, as well as the interaction between Re-l_e in f_C. It has been reported that vortices entering the channels merge and decompose. This explain in part the role of the l_e interacting with other variables.

The complete surface responses were reduced based in the statistical significance of each predictor. Table 10.3 shows the initial and final value for each coefficient of each sub-model. It is necessary to mention that the reduction for C did not lead to satisfactory results. It might suggest that a different type of surface response describes better the C sub-model. However, performing a higher order design is beyond the scope of this paper.

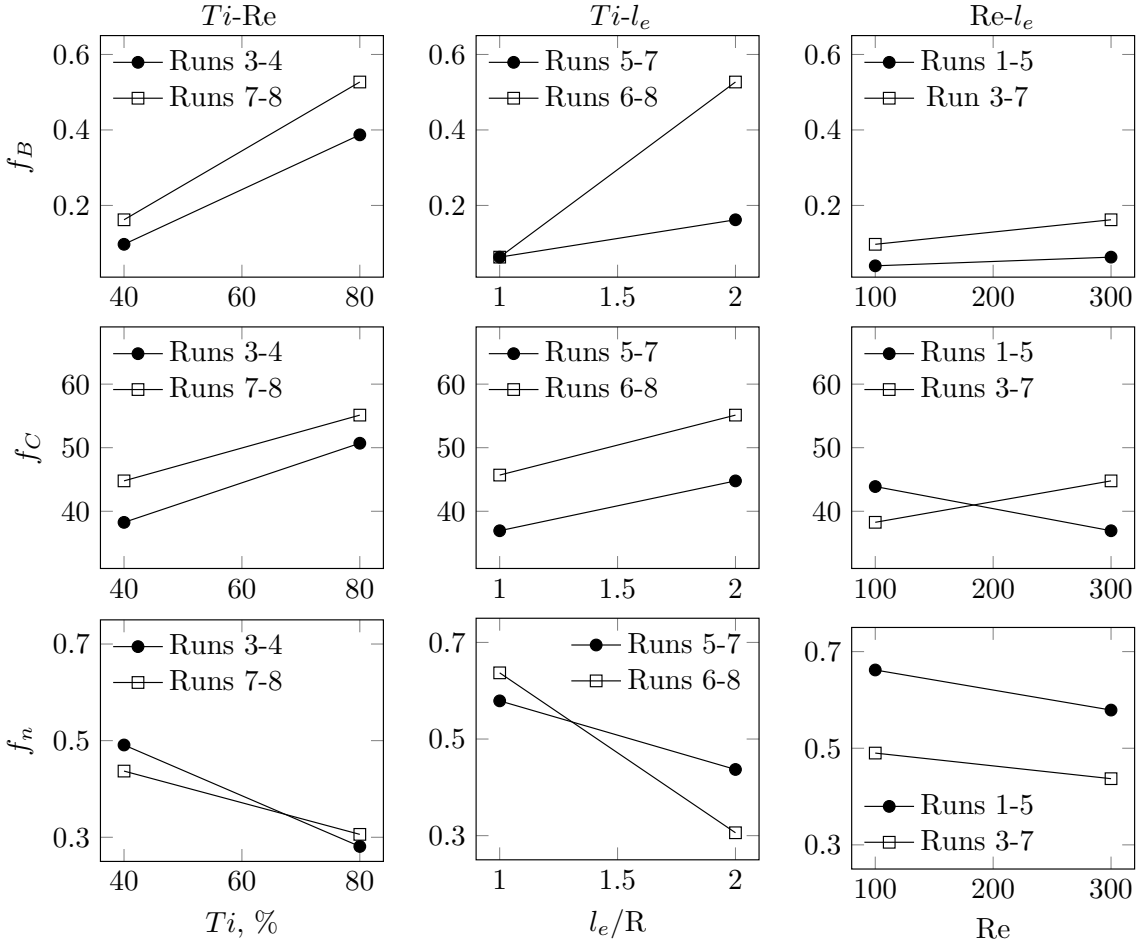

Figure 10.12: Interaction effects resulting from the factorial design. Simulation conditions are in Table 10.2

Table 10.3: Fitting results. To use those parameters, the turbulence intensity must be expressed as a fraction instead of percentage

	f_B			f_C	f_n		
Term	Complete	Reduced	P-value	Complete	Complete	Reduced	P-value
I	0.3401	0.3317	1.002E-03	145.6	-0.2086	0.5370	4.64E-03
Ti	-0.8674	-0.8966	2.030E-04	-214.5	2.737	1.620	9.27E-03
l_e	-0.2636	-0.2646	5.040E-04	-62.07	0.4871	-	-
Re	-4.15E-05	-	-	-0.4124	2.278E-03	-	-
$Ti : l_e$	0.7490	0.7755	8.470E-05	124.1	-1.679	-0.948	9.11E-03
Ti:Re	-1.463E-04	-	-	0.7746	-7.068E-03	-3.65E-03	0.0462
l_e:Re	-5.000E-06	-	-	0.2277	-1.469E-03	-	-
Ti:l_e:Re	5.425E-04	4.10E-04	5.350E-04	-0.4004	4.021E-03	1.82E-03	0.0811
R^2		0.9994		-		0.9651	
Adj-R^2		0.9985		-		0.9185	

According to the goodness of the fit for all of the sub-models, the majority of the variance in f_B, f_C and f_n is satisfactorily explained by the independent variables Re, Ti, l_e. In addition, the R^2 and adjusted R^2 are higher than 0.90, and comparable between then, meeting the suggestion of Box et al. [41]. The final sub-models for each parameter are presented in Equation (10.10) to (10.12). It is necessary to remark that for those equations the turbulence intensity must be expressed as a fraction instead of as a percentage.

$$f_B = 0.3317 - 0.8966Ti - 0.2646\frac{l_e}{R} + Ti\frac{l_e}{R}\left(0.755 + \frac{4.099}{10,000}\text{Re}\right) \tag{10.10}$$

$$f_n = 0.537 + 1.62Ti - \frac{3.65}{1000}Ti\text{Re} - Ti\frac{l_e}{R}\left(0.948 - \frac{1.82}{1000}\text{Re}\right) \tag{10.11}$$

$$f_C = 145.6 - 214.5Ti - 62.07\frac{l_e}{R} - 0.412\text{Re} + 0.7746Ti\text{Re} + 0.2277\frac{l_e}{R}\text{Re} + Ti\frac{l_e}{R}(124.1 - 0.4004\text{Re}) \tag{10.12}$$

10.4.2 Proposed model for Nu vs. Gz^{-1}

The final extended model for Nu-Gz is obtained by Replacing B, C and n in Equation (10.7) for the sub-models f_B, f_C and f_n respectively. It leads to Equation (10.13), where A is still the asymptotic Nu in the laminar fully developed zone.

$$Nu = A\left[1 + f_B(\text{Gz})^{f_n}\exp\left(-\frac{f_C}{\text{Gz}}\right)\right] \tag{10.13}$$

The goodness of the proposed model when predicting the correct Nu was tested in several circumstances. Figure 10.13a compares the proposed model with the Nu predicted by LES. The conditions for Runs 5, 6 and 7 are shown in Table 10.2. There is a good agreement between LES and the model in all the three cases, they start in the same Nu and converge to the correct final value. The different rate of decay of Runs 5 and 6 are correctly predicted, as well as the inflection point in Run 8. Those cases, which belong to the training set, were complimented with the validation cases in Table 10.4. Run 13 in Figure 10.13b has an R^2 of 0.93, the maximum error is located at the inlet of the channel, where the Nu predicted by the model is 11% higher than the obtained with LES. Beyond that point the error decreases quickly, to be less than 2% from x/D=1. It is known that surface responses perform well interpolating, but they must be used carefully when extrapolating. In contrast with the Run 13, the conditions for the Run 10 are outside from the limit of the factorial design, however, the R^2 is 0.96 and the error is similar to the Run 13. The results for Run 9 deserve especial attention, given that the channel Reynolds number is largely outside of the boundaries of the factorial design. Although that the inflection point is not predicted as clearly as in previous cases, the R^2 is a remarkable 0.95, the maximum error in the Nu is 14% at x/D=0, but from x/D=1 it is inferior to 2%.

Table 10.4: Inlet conditions for the validation runs

Run	Re	Turb. Int.	Length scale	Figure
9	500	40%	2R	10.13
10	300	20%	R	10.13
11	1054	40%	2R	10.14b
12	2560	40%	2R	-
13	300	40%	1.5R	10.13
14	300	5%	2R	10.14a
15	200	95%	0.1R	10.14a

10.4.3 Limitations of the proposed model

The main limitation when using the surface response methodology is the capacity of the resulting model to extrapolate values beyond the limits of the experimental design. In this regard, two scenarios were analysed. One when the magnitude of the turbulence is below the value considered in the experiments and the other when such magnitude is above that studied. In the first scenario, with low turbulence, combinations of the inlet conditions can predict negative values for f_B and f_C. This is an issue of the factorial design that might lead to nonphysical solutions. According to the structure of the surface responses, it happens

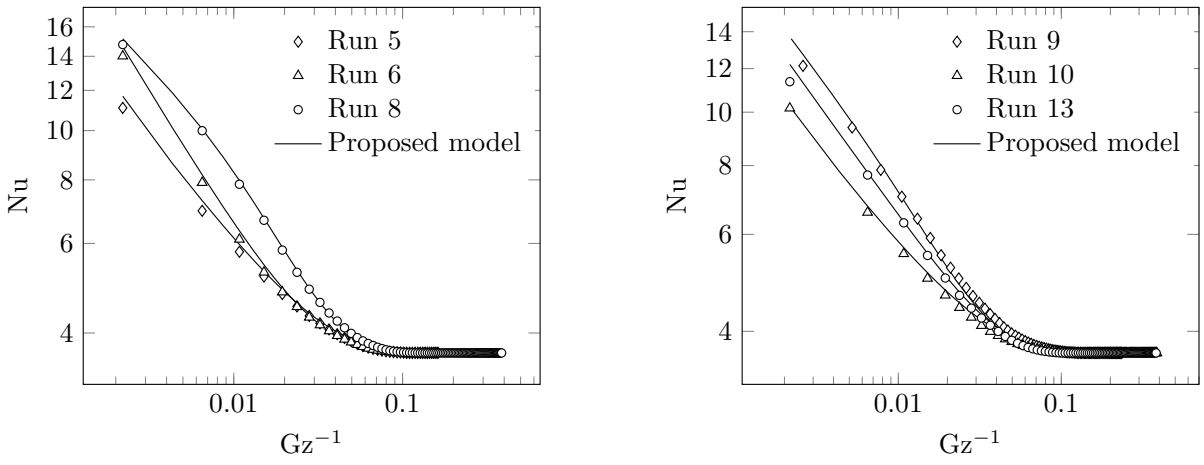

(a) (b)

Figure 10.13: Nu vs. Gz^{-1} curve predicted by the proposed model in several (a) training cases and (b) validation cases

for combinations of a high turbulence intensity and a low turbulence length scale, also for a low turbulence intensity despite the length scale. When anyone of the former variables is low, the effect of the turbulence is minor, especially at a low channel Reynolds number, and the simplest solution is neglecting it. Two examples of this are illustrated in Figure 10.14a. Such situations lead to negative values for f_B and f_C. However, when comparing it with the Nu-Gz curve of a fully laminar case, the difference between them is almost imperceptible.

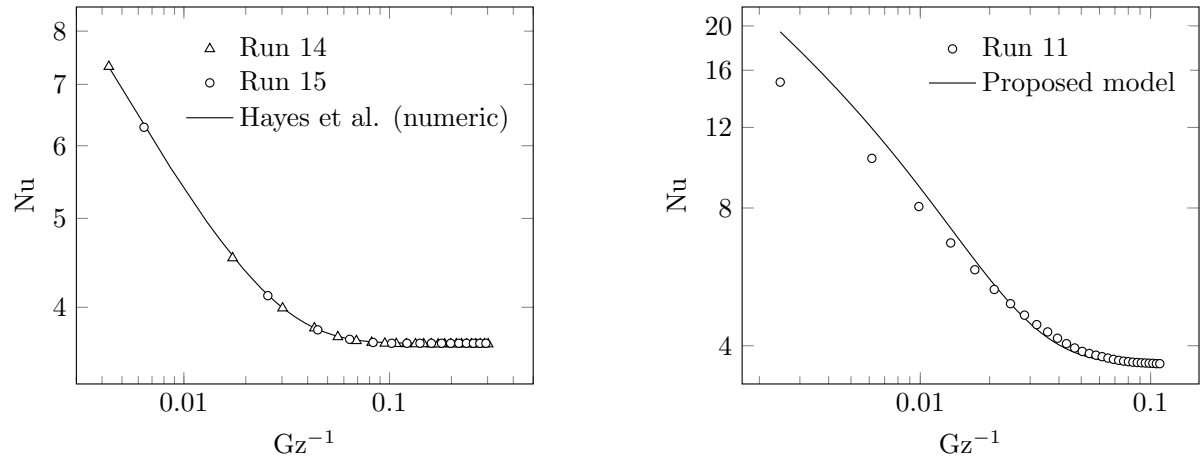

(a) (b)

Figure 10.14: Model limitations. (a) Low turbulence scenarios compared to laminar flow [25] and (b) high Re scenario. Inlet conditions are described in Table 10.4

In the second scenario, when the inlet turbulence is above that covered in this study, due to the length scale and turbulence intensity are physically limited, the most relevant case is when the channel Re is high. The factorial design covered channel Re up to 300 and validation cases with Re 500 resulted in good agreement. Beyond that value, is the especial interest when the channel Re is close to 1000 and when it is 2500. Since the former is uncommon, but possible to be observed in some applications of automotive catalytic converter, and the last is the approximated limit for stable laminar regime reported originally by Gotthilf Hagen [45]. Figure 10.14b compares proposed model with LES when the channel Re is 1054. Both curves are consistent, but it is noted that the presented model overestimates Nu by about 50%. At approximately x/D=4 the error decays to less than 10% and after x/D=6 it is below the 5%. At Reynolds of 2500 (Run 12 in Table 10.4), the error in the Nu is of the order of the 100% along the entire channel. At high Re the lack of fit was observed always an overestimation of the Nu, where the higher the Re, the higher the overestimation.

10.5 Conclusions

The influence of turbulence entering a monolith channel on the convective heat transfer was studied using Large Eddy Simulation. According to the frequency distribution and power spectrum analysis, even though the flow remains unsteady in the major portion of the channel, turbulence is present and has an effect on the convective heat transfer only in the entry region. Once the turbulence decomposes completely, the Nu converges to the classical fully developed laminar value.

The displacement of the Nu-Gz^{-1} curve is dominated by the channel Re and the magnitude of the inlet turbulence. Since the Re is related to the rate of decay of the turbulence, the higher the Re, the higher the effect of the turbulence. An extension of the available correlations for Nu-Gz^{-1}, that takes into account the upstream turbulence was proposed. The new model was obtained by replacing three constants of a Nu-Gz^{-1} correlation with three functions where each one depends on the channel Re and magnitude of the inlet turbulence. Those three functions, referred in the paper as the sub-models, are result of a series of numerical experiments following the surface response methodology.

The proposed model predicts the correct Nu along the entry region, also smoothly converges to the correct value in the laminar developed zone. The proposed model predicts nonphysical values when the magnitude of the turbulence is very low. However, in such conditions, the Nu-Gz^{-1} curve was found indistinguishable to that obtained when assuming

laminar flow. From that standpoint, the model is also useful as a criterion to neglect the effect of the turbulence inside the channels.

This work covered channel Re up to 300. However, good agreement between the proposed model and LES was observed up to channel Re 500. When the Re is 1000, the new model overestimates the Nu up to 25%, however, it predicts the correct entry length. Above that point, the higher the Re the higher the overestimation.

The results obtained with LES were compared to values predicted by several RANS models. Among them, the standard κ-ε did not converge to the correct Nu in the laminar zone, and the SST and Transitional SST largely overestimated the thermal entry length. The κ-κl-ω slightly underestimated the Nu compared to LES, but agreed with it predicting the thermal entry length.

Conflict of interest statement

The authors declare that there is no conflict of interest regarding the publication of this paper.

Bibliography

[1] Fredrik Ekström and Bengt Andersson. Pressure drop of monolithic catalytic converters experiments and modeling. *SAE Technical paper*, No. 2002-01-1010, 2002.

[2] Henrik Strom, Srdjan Sasic, and Bengt Andersson. Effects of the turbulent-to-laminar transition in monolithic reactors for automotive pollution control. *Industrial & Engineering Chemistry Research*, 50(6):3194–3205, 2011.

[3] Matthias Hettel, Claudia Diehm, Bentholhoda Torkashvand, and Olaf Deutschmann. Critical evaluation of in situ probe techniques for catalytic honeycomb monoliths. *Catalysis Today*, 216:2–10, 2013.

[4] RE Hayes and Stan T Kolaczkowski. Mass and heat transfer effects in catalytic monolith reactors. *Chemical Engineering Science*, 49(21):3587–3599, 1994.

[5] Ravi Prasad, Lawrence A Kennedy, and Eli Ruckenstein. Catalytic combustion. *Catalysis Reviews Science and Engineering*, 26(1):1–58, 1984.

[6] Ramesh K Shah and Alexander Louis London. *Laminar flow forced convection in ducts: a source book for compact heat exchanger analytical data*. Academic press, New York, USA, 1978.

[7] WM Kays, ME Crawford, and Bernhard Weigand. *Convective heat and mass transfer*. McGraw-Hill Higher Education, New York, NY, USA, 2004.

[8] Volker Gnielinski. New equations for heat and mass transfer in the turbulent flow in pipes and channels. *NASA STI/recon technical report A*, 75:8–16, 1975.

[9] Sadık Kakaç, Ramesh K Shah, and Win Aung. *Handbook of single-phase convective heat transfer*. John Wiley and Sons, New York, NY, USA, 1987.

[10] Theodore L Bergman and Frank P Incropera. *Introduction to heat transfer*. John Wiley & Sons, New Jersey, NY, USA, 2011.

[11] Gianpiero Groppi, A Belloli, Enrico Tronconi, and Pio Forzatti. A comparison of lumped and distributed models of monolith catalytic combustors. *Chemical Engineering Science*, 50(17):2705–2715, 1995.

[12] Gianpiero Groppi and Enrico Tronconi. Theoretical analysis of mass and heat transfer in monolith catalysts with triangular channels. *Chemical Engineering Science*, 52(20):3521–3526, 1997.

[13] Santhosh R Gundlapally and Vemuri Balakotaiah. Heat and mass transfer correlations and bifurcation analysis of catalytic monoliths with developing flows. *Chemical Engineering Science*, 66(9):1879–1892, 2011.

[14] F Zhang, RE Hayes, and ST Kolaczkowski. A new technique to measure the effective diffusivity in a catalytic monolith washcoat. *Chemical Engineering Research and Design*, 82(4):481–489, 2004.

[15] RE Hayes, B Liu, R Moxom, and M Votsmeier. The effect of washcoat geometry on mass transfer in monolith reactors. *Chemical Engineering Science*, 59(15):3169–3181, 2004.

[16] Marek Václavík, Petr Kočí, Vladimír Novák, and David Thompsett. NOx conversion and selectivity in multi-layer and sequential DOC-LNT automotive exhaust catalysts: Influence of internal transport. *Chemical Engineering Journal*, 329:128–134, 2017.

[17] Xiaosheng Chen and Hao Xia. A hybrid LES-RANS study on square cylinder unsteady heat transfer. *International Journal of Heat and Mass Transfer*, 108:1237–1254, 2017.

[18] Chuangxin He and Yingzheng Liu. Large-eddy simulation of jet impingement heat transfer using a lobed nozzle. *International Journal of Heat and Mass Transfer*, 125:828–844, 2018.

[19] Luteng Zhang, Simin Luo, Yapei Zhang, Wenxi Tian, GH Su, and Suizheng Qiu. Large eddy simulation on turbulent heat transfer in reactor vessel lower head corium pools. *Annals of Nuclear Energy*, 111:293–302, 2018.

[20] ANSYS Fluent Theory Guide v17.2. ANSYS Inc., Canonsburg, PA, USA, 2016.

[21] Franck Nicoud and Frédéric Ducros. Subgrid-scale stress modelling based on the square of the velocity gradient tensor. *Flow, Turbulence and Combustion*, 62(3):183–200, 1999.

[22] U Grigull and H Tratz. Thermischer einlauf in ausgebildeter laminarer rohrströmung. *International Journal of Heat and Mass Transfer*, 8(5):669–678, 1965.

[23] Enrico Tronconi and Pio Forzatti. Adequacy of lumped parameter models for SCR reactors with monolith structure. *AIChE Journal*, 38(2):201–210, 1992.

[24] Robert E Hayes and Stan T Kolaczkowski. *Introduction to catalytic combustion*. CRC Press, Boca Raton, FL, USA, 1998.

[25] Robert E Hayes, Andrés Donoso-Bravo, and Joseph P Mmbaga. Entry length effects for momentum, heat and mass transfer in circular ducts with laminar flow. *The Canadian Journal of Chemical Engineering*, 93(5):863–869, 2015.

[26] ANSYS Fluent Software Package v17.2, 2016. ANSYS Inc., Canonsburg, PA, USA.

[27] MS Bhatti. Fully developed temperature distribution in a circular tube with uniform wall temperature. Unpublished, 7 1985.

[28] W. M. Kays and M. E. Crawford. *Convective heat and mass transfer*. McGraw-Hill, New York, NY, USA, 1993.

[29] I Cornejo, P Nikrityuk, and RE Hayes. Turbulence decay inside the channels of an automotive catalytic converter monolith. *Emission Control Science and Technology*, 3(4):302—309, 2017.

[30] Ivan Cornejo, Petr Nikrityuk, and Robert E Hayes. Multiscale RANS-based modeling of the turbulence decay inside of an automotive catalytic converter. *Chemical Engineering Science*, 175:377–386, 2018.

[31] RE Hayes, Anton Fadic, Joeseph Mmbaga, and A Najafi. CFD modelling of the automotive catalytic converter. *Catalysis Today*, 188(1):94–105, 2012.

[32] SF Benjamin, N Haimad, CA Roberts, and J Wollin. Modelling the flow distribution through automotive catalytic converters. *Proceedings of the Institution of Mechanical Engineers, Part C: Journal of Mechanical Engineering Science*, 215(4):379–383, 2001.

[33] Brian Edward Launder and Dudley Brian Spalding. *Lectures in mathematical models of turbulence*. Academic Press, New York, USA, 1972.

[34] M Wolfshtein. The velocity and temperature distribution in one-dimensional flow with turbulence augmentation and pressure gradient. *International Journal of Heat and Mass Transfer*, 12(3):301–318, 1969.

[35] Florian Menter. Two-equation eddy-viscosity turbulence models for engineering applications. *AIAA journal*, 32(8):1598–1605, 1994.

[36] Florian R Menter, Robin Blair Langtry, SR Likki, YB Suzen, PG Huang, and S Völker. A correlation-based transition model using local variables—Part I: model formulation. *Journal of Turbomachinery*, 128(3):413–422, 2006.

[37] D Keith Walters and Davor Cokljat. A three-equation eddy-viscosity model for Reynolds-averaged Navier–Stokes simulations of transitional flow. *Journal of Fluids Engineering*, 130(12):121401, 2008.

[38] Won-Wook Kim, Suresh Menon, Won-Wook Kim, and Suresh Menon. Application of the localized dynamic subgrid-scale model to turbulent wall-bounded flows. In *35th aerospace sciences meeting and exhibit.*, page 210, Reno, NV, USA, 1997.

[39] Sung-Eun Kim. Large eddy simulation using unstructured meshes and dynamic subgrid-scale turbulence models. In *34th AIAA Fluid Dynamics Conference and Exhibit*, Portland, OR, USA, 2004.

[40] R: A Language and Environment for Statistical Computing, 2008. http://www.R-project.org. Vienna, Austria.

[41] George EP Box, J Stuart Hunter, and William Gordon Hunter. *Statistics for experimenters: design, innovation, and discovery*, volume 2. Wiley-Interscience, New Jersey, NY, USA, 2005.

[42] DN Tsinoglou, GC Koltsakis, DK Missirlis, and KJ Yakinthos. Transient modelling of flow distribution in automotive catalytic converters. *Applied Mathematical Modelling*, 28(9):775–794, 2004.

[43] Gaurav Agrawal, Niket S Kaisare, S Pushpavanam, and Karthik Ramanathan. Modeling the effect of flow mal-distribution on the performance of a catalytic converter. *Chemical Engineering Science*, 71:310–320, 2012.

[44] Cansu Ozhan, Daniel Fuster, and Patrick Da Costa. Multi-scale flow simulation of automotive catalytic converters. *Chemical Engineering Science*, 116:161–171, 2014.

[45] Gotthilf Hagen. Ueber die bewegung des wassers in engen cylindrischen röhren. *Annalen der Physik*, 122(3):423–442, 1839.

Chapter 11

Improved Nu number correlations for gas flow in monolith reactors using temperature-dependent fluid properties[1]

Abstract

This paper reports an investigation of heat and mass transfer coupled with fluid flow inside monolith honeycomb substrates. Many important aspects of multiscale models of a monolith are investigated. Three common geometrical representations of monolith channels are tested, and their advantages and disadvantages are analysed. A detailed computational model and a large set of computational experiments, covering a broad range of substrate void fractions, channel Reynolds numbers and heating rates is used. Results assuming constant and temperature-dependent fluid properties are reported and compared. At a high heating rate, assuming constant fluid properties leads to a significant error in the estimation of Nusselt and Sherwood numbers in the entry region. At a constant wall temperature and a high heating rate, there is a minimum in the Nusselt curve that classical models are not able to describe. Hence, a novel correlation that shows excellent agreement with channel data is presented together with a methodology to calibrate it. Additionally, empirical models to estimate the placement and value of the minimum Nusselt are proposed. These results contribute significantly to the understanding and improvement of lumped parameter multiscale models of

[1] A version of this article is currently submitted to the International Journal of Thermal Sciences and it is currently under peer revision. Cornejo, I., Nikrityuk, P., & Hayes, R. E. (Submitted). Improved Nu number correlations for monolith reactors.

monolith catalytic reactors.

Keywords: CFD, multiscale, monolith, Nusselt, variable properties

11.1 Introduction

Monolith honeycombs are extensively used as a catalytic reactor substrate in industrial applications, and especially in automotive catalytic converters [1–6], which is the application analysed in this paper. Full scale models of such reactors are necessary to investigate important variables such as the flow distribution, heating time, pressure drop and conversion efficiency. A single monolith can have thousands of channels running in parallel and modelling each one of them individually is computationally prohibitive. As an alternative, current reactor scale models use an an-isotropic continuum porous medium to approximate the substrate. When using a continuum porous medium model, channel scale spatial discretization is lost, and the coupling of the fluid and solid phases is achieved using heat and mass transfer coefficients. In effect, the channel level is treated as a lumped parameter model. It is evident that the correct selection of the heat and mass transfer coefficients can be critical in capturing the reactor performance accurately, especially in the entrance region. Appropriate values of Nusselt (Nu) and Sherwood (Sh) numbers can be determined from detailed 2D or 3D simulations of a single channel, provided that the correct operating conditions are used.

Nu correlations are used not only for heat transfer, but also for mass transfer. Using the law of gases and kinetic theory it can be shown that the Lewis number (Le), which is the ratio of the convective heat transfer and convective mass transfer, remains approximately constant over a wide range of temperatures for gases. Hence, the same correlations for Nu apply for Sh. Graetz [7] made the first significant contribution to convective heat transfer in circular ducts. After that, there have been many investigations of heat and mass transfer inside of monolith channels, most of them based on the work of Kays and London [8] for flow in pipes. Several models have been proposed, each of them subject to their own limitations and assumptions. A useful correlation for Nu and Sh must, as a minimum, describe consistently the entrance region, converge asymptotically to the analytic value in the fully developed zone and be applicable over a wide range of conditions. A mathematical expression adopted by many authors has the following form [9–11]:

$$\mathrm{Nu} = \mathrm{Nu}_\infty \left[1 + B(\mathrm{Gz})^n exp(-C/\mathrm{Gz})\right] \tag{11.1}$$

$$\mathrm{Sh} = \mathrm{Sh}_\infty \left[1 + B(\mathrm{Gz}_m)^n exp(-C/\mathrm{Gz}_m)\right] \tag{11.2}$$

where

$$\mathrm{Gz} = \frac{D}{x}\mathrm{RePr} \tag{11.3}$$

$$\mathrm{Gz}_m = \frac{D}{x}\mathrm{ReSc} \tag{11.4}$$

Equations (11.1) and (11.2) can be used either for a constant wall flux or a constant wall temperature (or concentration for Sh) using the appropriate B, C and n, and asymptotic values (Nu_∞ and Sh_∞). Model parameters reported by several authors are summarised in [11]. When temperature gradients are small, constant fluid properties can be assumed without significant loss of accuracy. However, in many engineering situations, from nuclear reactors [12] to automotive catalytic converters [13], changes of temperature in both axial and radial direction are sufficiently large to affect the flow field, especially due to changes in μ and ρ [14]. In such cases, the fluid properties must be considered temperature-dependent, a fully coupled set of transport equations must be solved, mathematical superposition is not allowed and a general solution in the form of Equation (11.1) is not possible. In a monolith the problem is even more complex because of the influence of the reduction of the flow area entering the substrate on the inlet velocity profile of the channels. Shumway and McEligot [15] compared the entrance region Nu for laminar flow of a Newtonian fluid in annuli considering temperature-dependant fluid properties, finding substantial differences when comparing the results to those assuming constant properties. Nobrega et al. [16] reported similar results for a viscoelastic fluid in a circular duct. Hayes et al. [11] also showed that the use of temperature-dependent physical properties give different results from the constant property case, and also demonstrated the effect of adding a reservoir prior to the channel. Unfortunately, the previously mentioned results are not directly applicable to a monolith or cover a limited set of conditions only.

There are many publications concerning convective heat transfer in monoliths, each based on different sets of assumptions, especially regarding the channel geometry and fluid properties. That imposes difficulties when selecting the correct model for every occasion. The motivation of this paper is to provide readers with a deeper understanding of the influence of every assumption on the results when modelling a monolith channel and thus to allow them to make a simpler and better model selection. The main goal of this paper is to contribute substantial new evidence of the influence of using constant or temperature-dependent fluid properties and geometrical simplifications on the convective transport of gas flow through

monolith channels. Those are open questions among the community that, to the best of our knowledge, have not been addressed in sufficient detail in a systematic way. A wide range of conditions is investigated and new correlations are proposed.

11.2 Computational model

11.2.1 Channel models

In this paper we investigate a monolith with circular cross-section channels, which is a commonly assumed geometry for washcoated channels [17]. When modelling monolith channels, three geometrical approaches can be identified, as illustrated in Figure 11.1:

i. Channel alone (or straight) in Figure 11.1a: The simplest approach. The domain runs from the inlet to the outlet of the channel. A flat or fully developed inlet velocity profile is usually assumed.

ii. Channel and a reservoir (or reservoir) in Figure 11.1b: A section with the same diameter as the channel is added prior to it. The outer boundaries of the reservoir are treated as symmetry planes. The purpose of the reservoir is to account for the radial and axial diffusion at the inlet of the channel, looking for a more realistic velocity inlet profile.

iii. Channel with a contraction inlet (or contraction) in Figure 11.1c: An open space is added before the channel. The height of the open space depends on the substrate void fraction. This approach accounts not only for the radial diffusion at the inlet of the channels, but also for a physically consistent velocity of flow entering a monolith.

For simplicity, in the rest of the paper, the three described geometries are called "straight", "reservoir" and "contraction" respectively. Among the three approaches, the channel with the contraction is the most realistic one. It requires more computational effort, however, there is substantial evidence about the effect of such a contraction locally on the inlet velocity profile and globally on the total pressure drop [18, 19]. Although a channel with a contraction is used in this paper, the two other approaches are also investigated to quantify and to illustrate the magnitude of the error in the results when using these simplified shapes. In the three cases, the diameter of the channel (D) was 1 mm and its length (L) was 75 mm. The extension of the reservoir (L_1) was 10 mm and its diameter was the same as that of the channel. For the channel with the contraction, the inlet diameter (D_1) was manipulated to obtain the desired reduction rate for every case and the length of the open section was also 10 mm. The domain was treated as axial symmetrical.

Figure 11.1: (a) channel alone, (b) channel with a reservoir and (c) channel with the inlet contraction. L=75 mm, D=1 mm, L_1=10 mm. D_1 was case-dependent

11.2.2 Flow model

In many monolith applications, the channel Re is sub-critical and the flow is laminar. There is evidence that in some cases, for example, in automotive catalytic converters, upstream turbulence enters the substrate and then decays along it [20–22]. To describe such a flow in transition accurately requires large computational effort; hence, the incremental effect of the upstream turbulence will be addressed in a future investigation [23]. Therefore, in this paper the flow regime was assumed to be laminar. The steady transport equations of mass and momentum are [24]:

$$\frac{\partial(\rho u_i)}{\partial x_i} = 0 \tag{11.5}$$

$$\frac{\partial(\rho u_i u_j)}{\partial x_j} = -\frac{\partial p}{\partial x_i} + \frac{\partial}{\partial x_j}\left[\mu\left(\frac{\partial u_i}{\partial x_j} + \frac{\partial u_j}{\partial x_i}\right) - \frac{2}{3}\frac{\partial u_i}{\partial x_i}\delta_{ij}\right] \tag{11.6}$$

The inlet of the domain was treated as a velocity inlet with a flat velocity profile and a constant fluid temperature. The walls of the channel were set as no-slip walls, with a fixed temperature of fixed wall heat flux, depending on the case analysed. The outlet of the domain was set as a pressure outlet.

11.2.3 Fluid properties

We now compare the use of constant and temperature-dependent transport properties for the convective heat transfer and the selection of a reference temperature in lumped models.

Investigations of the results of varying the properties one at a time have been partially addressed in the literature, establishing that the most important properties that modify Nu are the density and the thermal conductivity [15, 16]. That academic exercise provides useful information, but it is non-physical. In this paper the fluid was considered to be air; therefore, the results are applicable to gases with a Pr close to 0.7. Two main scenarios described below. In both cases the density was temperature-dependent and was calculated using the ideal gas law, meanwhile, for the other properties:

i. Constant properties: μ, k and C_p are constant and are evaluated at the inlet temperature.

ii. Variable properties: μ, k and C_p are all calculated at the local fluid temperature.

The relationship between fluid properties and temperature is often represented by a polynomial. However, to minimise approximation errors, we used fundamental expressions when possible, such as the kinetic theory and the ideal gas law. Both are available in many commercial codes and can be handled with the current computational power. In the two scenarios, the density was calculated with the ideal gas law, to account for local changes in pressure. When using temperature-dependent properties, C_p was estimated by an 8^{th} order piece-wise polynomial, meanwhile, the kinetic theory of gases was used for μ and k. The exact mathematical expressions were:

$$\rho\,(\mathrm{kg/m^2}) = \frac{p}{R_g T/M_W} \tag{11.7}$$

$$C_p\,(\mathrm{J/kg\text{-}K}) = a_0 + a_1 T + a_2 T^2 + a_3 T^3 + a_4 T^4 + a_5 T^5 + a_6 T^6 + a_7 T^7 \tag{11.8}$$

where [24]

Table 11.1: Parameters for C_p in J/kg-K

Parameter	$100 < T, K < 1000$	$1000 < T, K < 3000$
a_0	1.161×10^{3}	-7.069×10^{3}
a_1	-2.3688	3.371×10^{1}
a_2	1.486×10^{-3}	-5.813×10^{-2}
a_3	-5.035×10^{-5}	5.422×10^{-5}
a_4	9.929×10^{-8}	-2.937×10^{-8}
a_5	-1.111×10^{-10}	9.238×10^{-12}
a_6	6.540×10^{-14}	-1.566×10^{-15}
a_7	-1.574×10^{-17}	1.112×10^{-19}

$$k\,(\text{W/m-K}) = \frac{15}{4}\frac{R_g}{M_W}\mu\left[\frac{4}{15}\frac{C_p M_W}{R_g} + \frac{1}{3}\right] \tag{11.9}$$

$$\mu\,\text{Pa-s} = 2.67\cdot 10^{-6}\frac{\sqrt{M_W T}}{\sigma^2\Omega_\mu} \tag{11.10}$$

For μ, the characteristic length (σ) was 3.711 and Ω_μ is a function of the reduced temperature that can be found in [25]. Equation (11.7) to (11.10) are utilised as implemented in Fluent v18.2, which is widely accepted in the literature.

11.2.4 Calculation methodology

Convective heat transfer throughout a monolith channel is analysed either at a constant wall temperature or at a constant wall heat flux. Nu is defined as:

$$\text{Nu} = \frac{hD}{k} \tag{11.11}$$

k was evaluated at the local wall temperature, meanwhile, the other properties of the fluid, where evaluated at the local mixing-cup one, which were the same as those at the inlet when assuming constant properties. The convective coefficient was obtained from the temperature field according to:

$$h(T_w - T_b) = -k\frac{dT}{dr}\bigg|_{y=R} \tag{11.12}$$

The temperature gradient was evaluated at the wall ($y = R$). Especial attention should be paid to the computation of the temperature gradient. At least a second order of accuracy approximation should be used. The mixing-cup, or bulk, temperature (T_b) was defined in the usual way:

$$T_b = \frac{\int_0^R u_x \rho C_p T r dr}{\int_0^R u_x \rho C_p r dr} \tag{11.13}$$

Nu was plotted against a non-dimensional axial position represented by the inverse of the Graetz number (Gz). To compare different options of reference temperature commonly found in the literature, Gz was calculated in two ways. The first one used the fluid properties evaluated at the local temperature and the second evaluated at the inlet one. The two mathematical expressions differ in the subscript i, which stands for inlet, and are the following:

$$1/\mathrm{Gz} = \frac{x^+}{\mathrm{Pr}} = \frac{x}{D}\frac{1}{\mathrm{RePr}} \tag{11.14}$$

$$1/\mathrm{Gz}_i = \frac{x_i^+}{\mathrm{Pr}_i} = \frac{x}{D}\frac{1}{\mathrm{Re}_i\mathrm{Pr}_i} \tag{11.15}$$

When using temperature-dependent properties, the mixing-cup temperature was used to obtain a representative average of all of the radially distributed values of every channel cross-section Another important variable often analysed in heat transfer problems is the loading temperature or heating rate, which for a channel with a constant wall temperature is defined as:

$$\tau = \frac{T_{max}}{T_{min}} \tag{11.16}$$

Table 11.2 shows the list of all of the computational experiments involved in this paper. This investigation covered channel Re from 50 to 600 and heating rates (τ) from 1.1 to 3.0. Those ranges are sufficient to study the effect of the two variables in the Nu vs Gz curves and cover a wide range of applications.

Table 11.2: List of computational experiments

Run	Re	T_i, K	T_w, K	H, W/m^2	Geometry†	ϕ	Flow prop.‡
1	150	300	330	-	Straight	-	Variable
2	150	300	600	-	Straight	-	Variable
3	300	300	330	-	Straight	-	Variable
4	300	300	600	-	Straight	-	Variable
5	50	300	330	-	Straight	-	Variable
6	50	300	330	-	Straight	-	Constant
7	600	300	330	-	Straight	-	Variable
8	600	300	330	-	Straight	-	Constant
9	50	300	600	-	Straight	-	Variable
10	50	300	600	-	Straight	-	Constant
11	300	300	600	-	Straight	-	Variable
12	300	300	600	-	Straight	-	Variable
13	300	300	600	-	Reservoir	-	Variable
14	300	300	600	-	Contraction	0.67	Variable
15	300	300	-	500	Straight	-	Variable
16	300	300	-	500	Reservoir	-	Variable
17	300	300	-	500	Contraction	0.67	Variable
18	300	300	600		Contraction	0.45	Variable
19	300	300	600		Contraction	0.80	Variable
20	300	300	-	500	Contraction	0.45	Variable
21	300	300	-	500	Contraction	0.80	Variable
22	50	300	600	-	Contraction	0.67	Variable
23	150	300	600	-	Contraction	0.67	Variable
24	450	300	600	-	Contraction	0.67	Variable
25	600	300	600	-	Contraction	0.67	Variable
26	150	300	330	-	Contraction	0.67	Variable
27	150	300	400	-	Contraction	0.67	Variable
28	150	300	500	-	Contraction	0.67	Variable
29	150	300	600	-	Contraction	0.67	Variable
30	50	300	-	1000	Contraction	0.67	Variable
31	150	300	-	1000	Contraction	0.67	Variable
32	150	300	-	1000	Contraction	0.67	Variable
33	450	300	-	1000	Contraction	0.67	Variable
34	600	300	-	250	Contraction	0.67	Variable
35	150	300	-	2500	Contraction	0.67	Variable
36	150	300	-	4000	Contraction	0.67	Variable
37	150	300	900	-	Contraction	0.67	Variable
38	150	300	750	-	Contraction	0.67	Variable

† According to Section 11.2.1

‡ According to Section 11.2.3

11.3 Results

11.3.1 Grid independence and validation

The quality of the computational grid was investigated by comparing the numerical results to solutions available in the literature. We started by modelling a channel without a reservoir and with a flat inlet velocity profile. Once having a validated solution, the same element size and refinement were applied to the reservoir and the open space before the channel in the other two geometries; hence, the meshes for the three geometries are homogeneous and have an identical resolution inside the channel. A section of the mesh is shown in Figure 11.2.

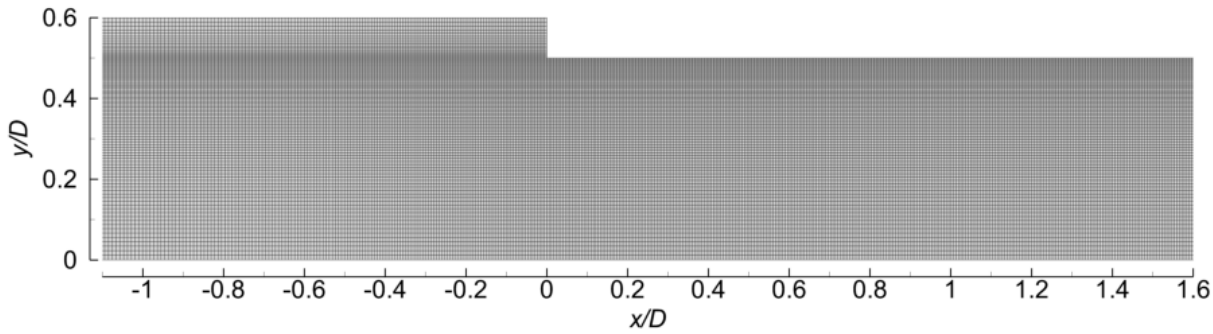

Figure 11.2: Section of the computational grid for a channel with a reduction rate of 0.67. The mesh has 80 radial elements inside the channel

Taking advantage of the cross-section of the channel, axial-symmetry was used. For the channel, two fully orthogonal meshes of 492 164 and 1 968 656 quadrilateral control volumes were tested. The meshes contained 80 and 160 radial elements respectively. The monitored variables were the Nu vs. 1/Gz curve, and particularly Nu in the fully developed region. Results for a constant wall temperature case are shown in Figure 11.3.

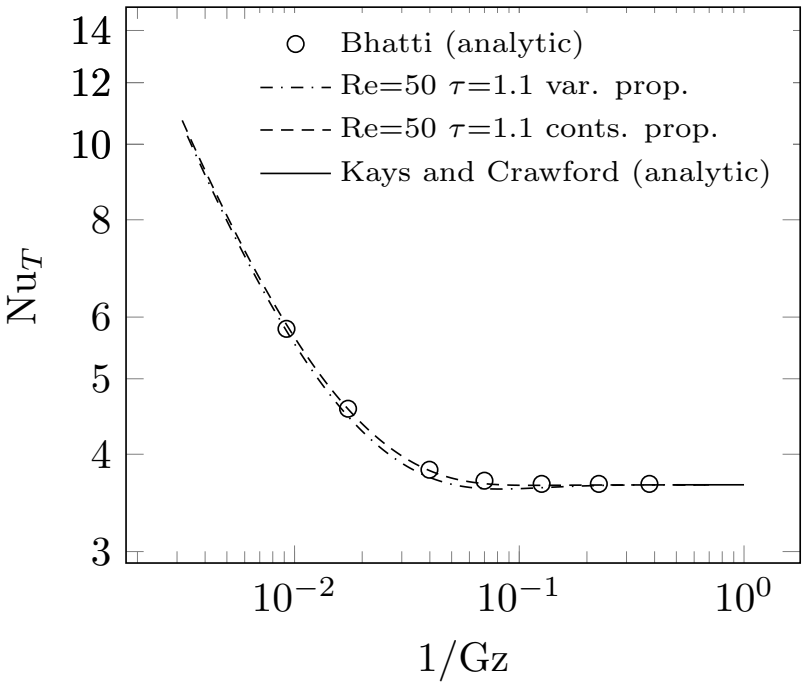

Figure 11.3: Grid investigation. The fully developed Nu for circular pipes from Kays and Crawford [26] is shown as a reference. Bhatti solution, as cited in [26], assumed constant fluid properties [27]

The two meshes gave the same Nu vs. 1/Gz curves in the entrance region and agreed with literature values in the entrance and fully developed zones. Equivalent results were observed for a constant wall heat flux; hence, the mesh with 492 164 control volumes inside the channel was used in the rest of the study. A low heating rate was used in the validation case, to avoid large changes introduced by the variable fluid properties, which is discussed later in this paper.

11.3.2 Selection of a reference temperature

The Nusselt number in the entrance region is usually plotted against a representation of the dimensionless axial distance from the inlet. The most common representation is the inverse Graetz number, which is robust because it accounts for changes in both Re and Pr [28]. When calculating the value of 1/Gz for the case of temperature dependent physical properties, the temperature used when computing Nu, Re and Pr affects the results. Common choices are to use the inlet temperature, a film temperature or the local fluid temperature. The film temperature is an average that can be defined in different ways, but is usually the average of the wall and the mean bulk temperature. Figure 11.4a shows the change in Re and Pr as

a function of distance from the inlet for a straight channel with a constant wall temperature higher than the inlet, with both Re and Pr calculated at the local mixing-cup temperature. Changes in both variables along with the axial coordinate can be noticed, although, the variations in Pr are very low in magnitude and changes in Re vary with the heating rate.

The product of Re and Pr, the Peclet number for heat transfer (Pe_H), changes with the temperature according to the results shown in Figure 11.4b. On this graph the ratio of RePr computed at local temperature to the values computed at inlet temperature is shown as a function of a dimensionless axial distance. Clearly, the error introduced by using the inlet temperature is case specific, depending on both the Re and heating rate, with possible differences as high as 50% or more. The effect of using the inlet temperature to develop the Nu vs. 1/Gz curve is to shift the apparent curve to the right, leading to a different h value. That would also affect the estimation of the thermal and hydraulic entry length. An analysis using a film temperature would also give similar result.

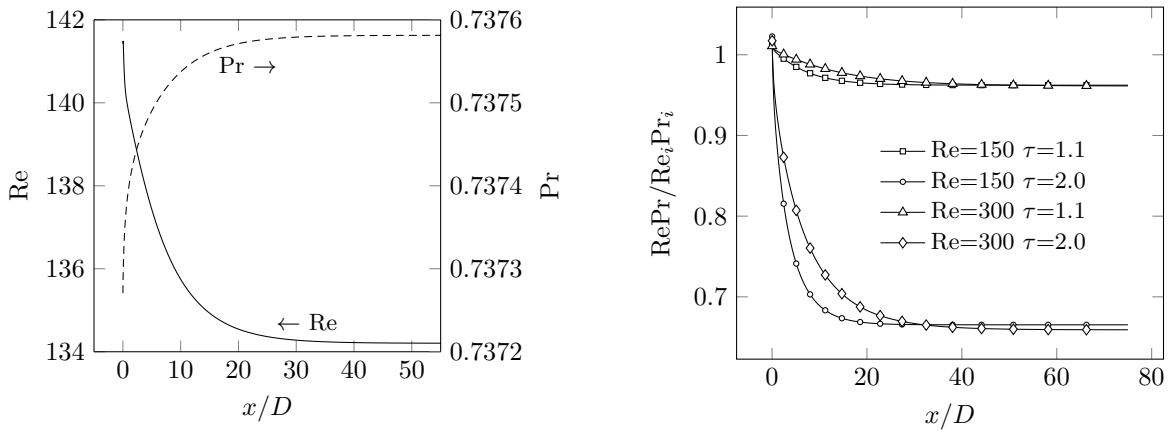

(a) (b)

Figure 11.4: Example of the change in Re and Pr through a straight channel with a flat inlet velocity profile at T_i=300K and a constant wall temperature. All the curves were obtained using temperature-dependent fluid properties and correspond to runs 1 to 4 of Table 11.2

11.3.3 Constant vs. temperature-dependent fluid properties

This section briefly revisits the error in the entrance length Nu when assuming constant fluid properties. This point has been addressed in the literature. However, experiments are commonly carried out over a limited set of conditions and the literature is particularly sparse in terms of the heating rate range. This part of the investigation follows the fashion of a fully

orthogonal 2^2 factorial design to test the influence of the channel Re and heating rate on the displacement of the Nu vs. 1/Gz curve when assuming constant and temperature-dependent fluid properties. Values of 50 and 600 were considered low and high levels for the channel Re and 1.1 and 2.0 for the heating rate. A straight channel with a flat inlet profile and a constant wall temperature was used. Results are shown in Figure 11.5.

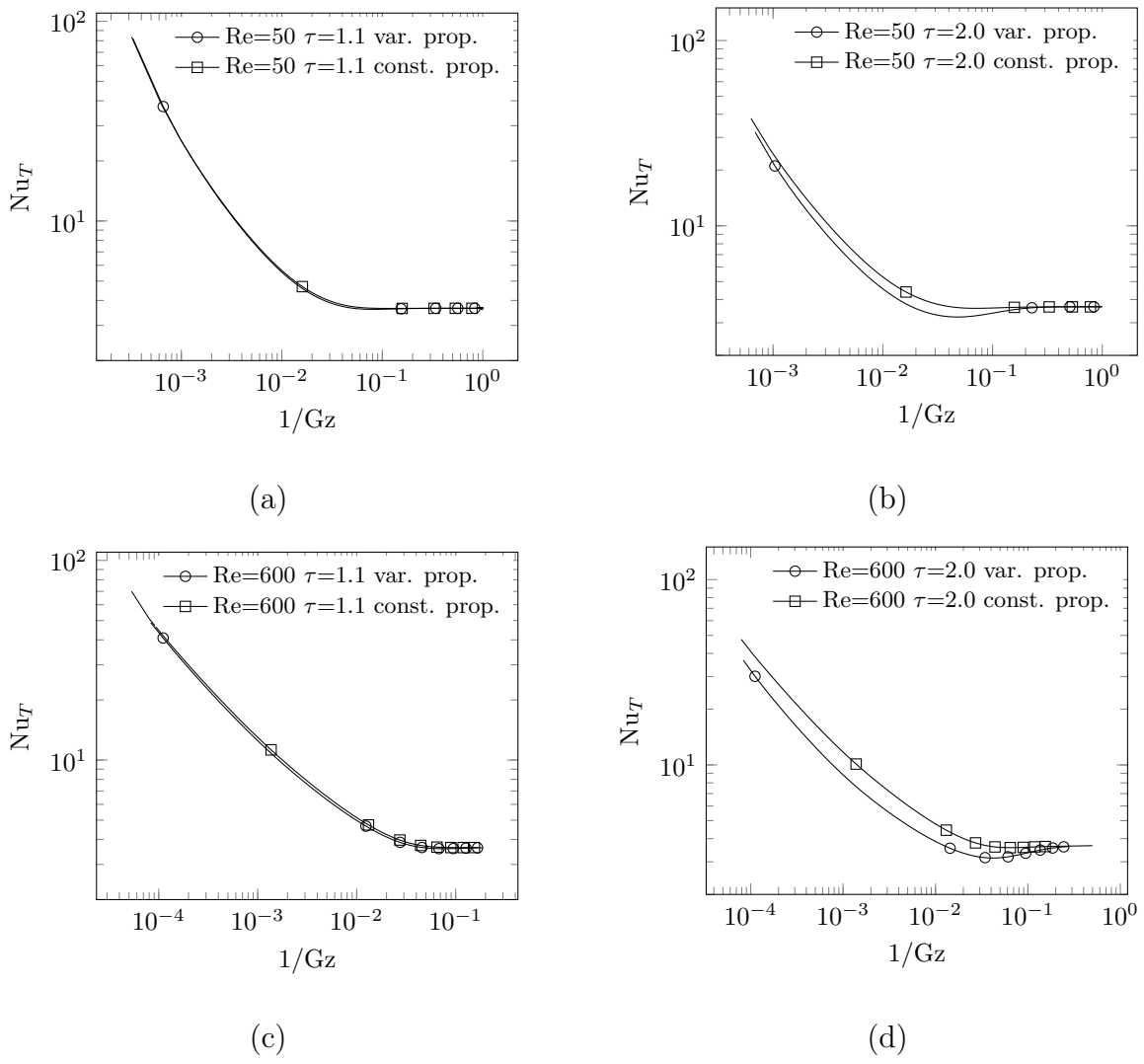

Figure 11.5: Comparison of Nu vs. 1/Gz curves obtained using constant and variable fluid properties at different combinations of Re and τ. Runs 5 to 12 of Table 11.2

Figure 11.5 is organised in a way that shows Nu vs. 1/Gz curves for the following combinations: a low Re and a low τ, a low Re and a high τ, a high Re and a low τ, and a high Re with a high τ. Comparing Figure 11.5 a and c shows that for a low heating rate the entrance Nu is not significantly affected by the assumption of constant properties over a wide range of Re. This effect occurs because at a low heating rate the temperature change

in the inlet region is minor, thus the use of inlet property values does not lead to significant error. It is also intuitive that for an increase of Re, all the other variables being equal, the temperature change in the inlet region is reduced. On the other hand, at a high heating rate, the gap between the curves using constant and variable properties is no longer negligible. Assuming constant fluid properties always overestimates Nu, especially at a high Re. It should be mentioned that the minimum in Figure 11.5b and d has been reported previously in the literature [15, 16, 29]. It is always present, but commonly, its value is comparable to the asymptotic one and it is not appreciable in the curve. That phenomenon, which affects visibly the entrance length, is not captured correctly when constant fluid properties are assumed. As shown in Figure 11.6c, the minimum in the Nu curve is present regardless of having or not a reduction of the ow area entering the substrate. In this paper, similarly to the results in More [29], the minimum in the Nu curve appears as soon as the fluid properties are set to be temperature-dependent. According to More, when setting the fluid properties to be variable one at the time, the one that show the largest influence on the formation of the minimum is the fluid viscosity.

11.3.4 Effect of shape simplifications

This section addresses the differences in Nu vs. 1/Gz curves observed for various inlet geometries. The shapes tested were those described in Section 11.2.1. Variable fluid properties and an inlet temperature of 300 K were used in all the computational experiments of this section. Results for both Nu_T and and Nu_H are shown in Figure 11.6.

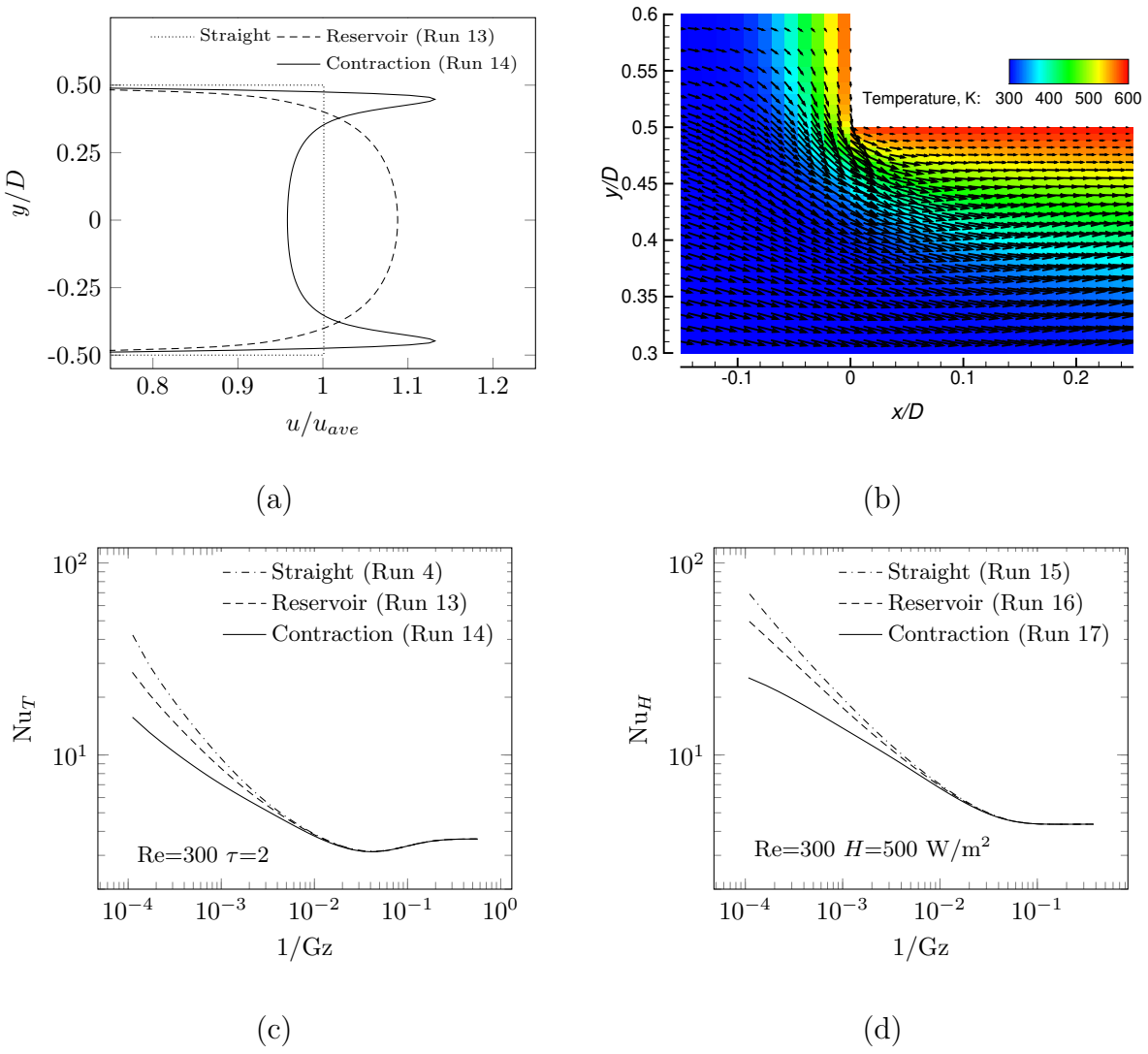

Figure 11.6: (a) Compares the inlet velocity profile of a channel with the contraction and a channel with the reservoir. (b) is a contour plot of the temperature in a channel with the contraction at the inlet. (c) Nu_T and (d) Nu_H for the three channel shapes analysed. The run numbers refer to those in Table 11.2

According to Figure 11.6a, adding a reservoir effectively improves the radial diffusion at the inlet of the channel, because the velocity profile is resolved rather than imposed. However, that is not sufficient to capture the change of the direction of the flow due to the reduction of the open area entering the substrate (see Figure 11.6b). That has been reported for iso-thermal and oscillating flow [18, 19], and now its effect on the convective heat transfer is shown. It can be seen in Figure 11.6c and d, that both the channel alone and when adding a straight reservoir overestimate Nu over a significant part of the entrance length.

11.3.5 Effect of void fraction

Since the reduction of the flow area at the entrance of the substrate affects the development of the boundary layer, the Nu curves produced for different substrate void fractions should be analysed. Three void fractions were selected to cover most cases, including highly loaded dual layer washcoat [30]. The results are shown in Figure 11.7.

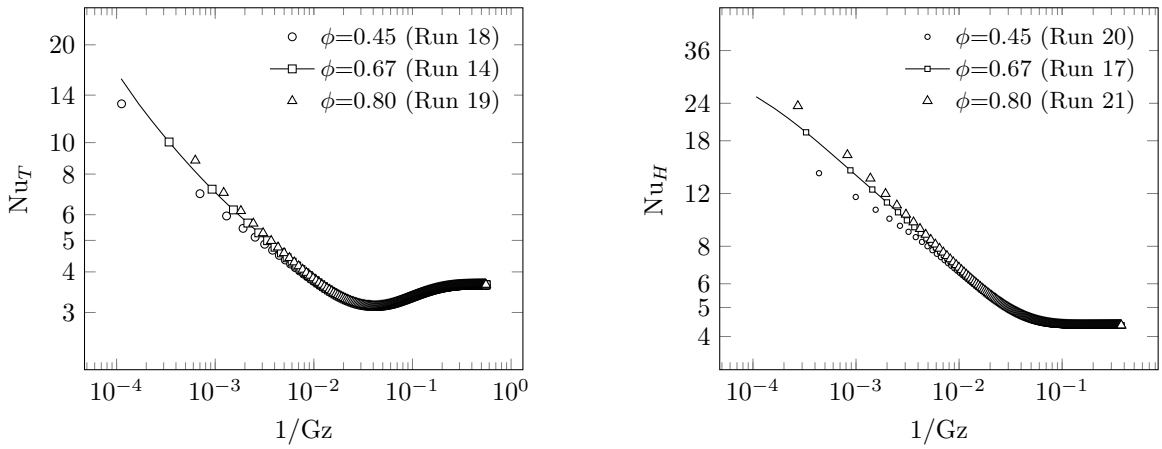

(a) (b)

Figure 11.7: Influence of the substrate void fraction on Nu. For all curves Re is 300 and T_i is 300 K. For Nu_T the wall temperature is 600 K and for Nu_H H is 500 kW/m^2. The run number refers to those in Table 11.2

According to Figure 11.7, for both a constant wall temperature and a constant wall heat flux, changing the void fraction modifies Nu at the entry region. However, the magnitude of the changes is much lower than the one resulting from neglecting the reduction of the flow area. It seems that as long as the contraction exists, its influence depends only slightly on the reduction rate [19, 31], over any realistic range.

11.3.6 Parametric investigation of the effect of Re, τ and H

Having demonstrated the importance of using variable physical properties and the correct inlet geometry, and showing the conceptual relationship between Re and τ or H, we now show the results of a brief parametric study. In all of the cases the channel with a contraction at the inlet was used, along with variable physical properties. Because of the bi-directional coupling between the heat transfer and the flow field, the resulting Nu vs. 1/Gz curves are case dependent, rather than being a unique one. The results of the study are shown in Figure 11.8.

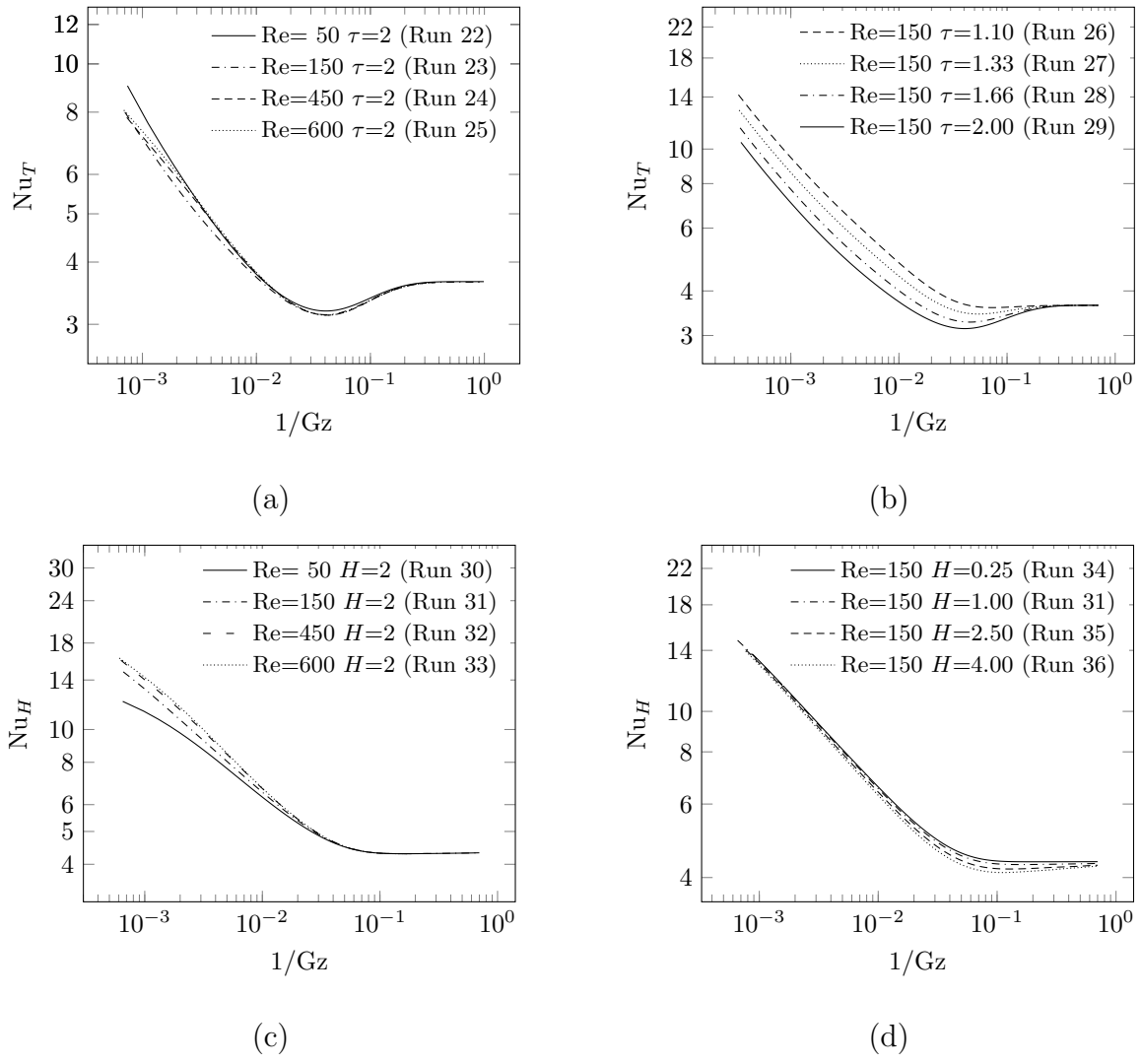

Figure 11.8: Nu_T and Nu_H for several Re, τ and H (in kW/m^2). Effect of (a) Re in Nu_T at a constant τ, (b) τ in Nu_T at a constant Re, (c) Re in Nu_H at a constant H and (d) τ in Nu_H at a constant Re. The run number is referred to those in Table 11.2

It is clear from Figure 11.8 that the effect of changing Re, τ and H is to alter the shape of the curve in the developing region. The first observation is that even for a relatively high heating rate (large τ, Figure 11.8a or large H, Figure 11.8c) the effect of changing Re over a wide range has a relatively minor effect that is concentrated very close to the inlet. This effect is primarily due to the contraction of the flow at the inlet. In cases where the light-off occurs very close to, or at, the inlet this difference might play a role. On the other hand, for a constant wall temperature and a fixed value of Re, the effect of the heating rate is quite significant (Figure 11.8b). Although, the slope of the curve is approximately the same for all values of τ, the curve shifts to the left as τ increases. The value of the minimum observed also

becomes significantly lower as τ increases, reaching a vaule of 16% below the final asymptotic one (Run 29). Interestingly, for the cases of a constant wall heat flux with a fixed Re, an increase in H has a much more minor effect on the curve. The minimum on the Nu vs. 1/Gz plot remains, especially at large value of H, however, it is also less pronounced than for the case of constant wall temperature. The overall conclusion from this short parametric study is that the use of a single Nu vs. 1/Gz curve for all the cases might lead to appreciable error under some circumstances.

11.3.7 Proposed correlations for Nu and Sh vs. 1/Gz in monolith channels

In this section we propose some corrections for the Nu in the entry region for the case with the inlet contraction and variable physical properties.

We consider first the case of a constant wall heat flux. For a constant wall heat flux, Nu_H, a single curve fitted to classical models can be used without much sacrifice of accuracy. Runs 30 to 36, covering Re from 50 to 600 and H from 0.25 kW/m^2 to 4 kW/m^2, were fitted simultaneously to Equation (11.1). The overall R^2 was 0.9901. The data and fitting line can be seen in Figure 11.9a.

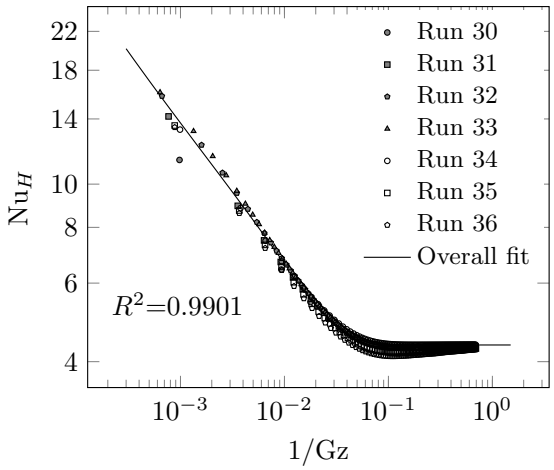

Figure 11.9: Overall fitting curve to model Nu_H for several H and Re. The run number refers to those in Table 11.2

For the situation with a constant wall temperature, Nu_T, at a high heating rate classical models do not apply, because of the presence of the minimum in the curve. A simple solution often found in heat transfer is to use a piece-wise function. The curves with a minimum can

be decomposed into a strictly decreasing section and an S-shaped section. The first part can be fitted to a classic model with the mathematical structure of Equation (11.1), taking the values for B, C and n from Table 11.3. For the second part, we selected a sigmoid function extensively used in machine learning. Figure 11.10a shows an example of the two functions fitted to a dataset.

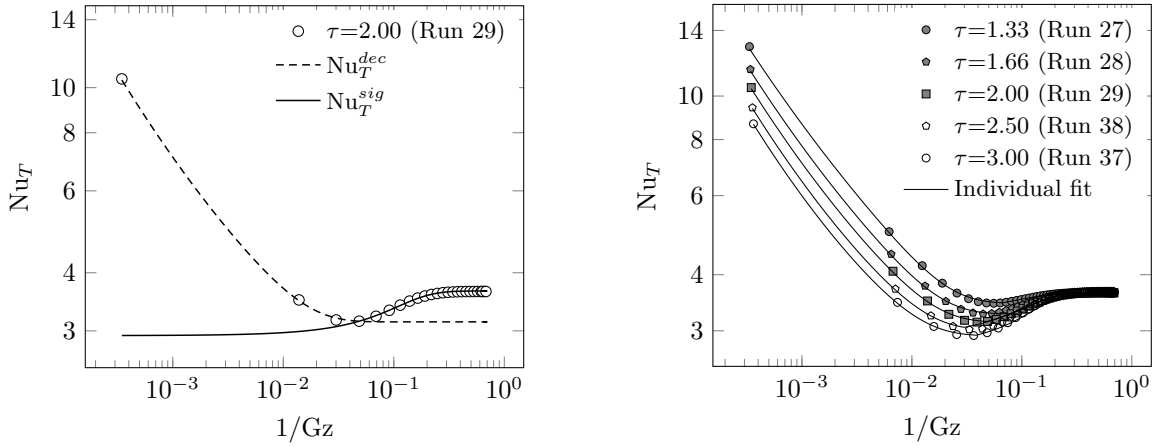

(a) (b)

Figure 11.10: (a) Nu_T^{dec} and Nu_T^{sig} curves fitted to a dataset. (b) Piece-wise function in Equation (11.17) predicting Nu_T at several heating rates. The run number refers to those in Table 11.2

The two parts of the curve can be reasonably described by blending the two functions. Taking advantage of the behaviour of the curves before and after they intercept, a simple way to combine them is to pick the highest between the two predicted values, which leads to the following expression:

$$\mathrm{Nu}_T = \max\left(\mathrm{Nu}_T^{dec}, \mathrm{Nu}_T^{sig}\right) \tag{11.17}$$

where

$$\mathrm{Nu}_T^{dec} = \mathrm{Nu}_{T_{min}}\left[1 + B(\mathrm{Gz})^n exp\left(-\frac{C}{\mathrm{Gz}}\right)\right] \tag{11.18}$$

$$\mathrm{Nu}_T^{sig} = \frac{\mathrm{Nu}_{T_\infty}}{\mathrm{Nu}_{T_{min}}}\left[\left(\frac{1}{1+e^{-\zeta}}\right) + \mathrm{Nu}_{T_{min}} - 1\right] \tag{11.19}$$

$$-\zeta = -a(\mathrm{Gz}^{-1} - \mathrm{Gz}_*^{-1}) + b \tag{11.20}$$

The empirical parameters involved are B, C and n for Equation (11.18), and a and b for Equation (11.19). Gz_*^{-1} in Equation (11.20) is the axial position of the minimum of the

curve. Values for them together with the minimum Nu observed for several heating rates are reported in Table 11.3. Excellent agreement was achieved when the same methodology was applied to different heating rates.

Table 11.3: List of parameters for Nu_T curves at several τ

Run	τ	$\mathrm{Nu}_{T_{min}}$	Gz_*^{-1}	B	C	n	a	b
27	1.33	3.4546	0.05442	0.05613	67.47	0.4860	14.43	1.3360
28	1.66	3.2710	0.04542	0.04489	75.35	0.5053	15.77	0.1363
29	2.00	3.1365	0.03973	0.03750	82.41	0.5207	15.54	0.1205
38	2.50	3.0167	0.03591	0.03049	92.98	0.5376	15.80	0.1100
37	3.00	2.9249	0.03286	0.02610	102.8	0.5497	15.19	0.1353

Unfortunately, a general solution could not be found and remains beyond the scope of this paper. However, the model was completed with empirical functions for $\mathrm{Nu}_{T_{min}}$ and Gz_*^{-1} in Equation (11.21) and (11.22), which can be reasonably assumed to be a function of τ only for the conditions covered in this study (see Figure 11.8). Numerical data and the fitting curve for both variables are shown in Figure 11.11.

$$\mathrm{Nu}_{T_{min}} = 0.144264\tau^2 - 0.933583\tau + 4.433455 \tag{11.21}$$

$$\mathrm{Gz}_*^{-1} = 0.002944\tau^2 - 0.000639\tau + 0.049663 \tag{11.22}$$

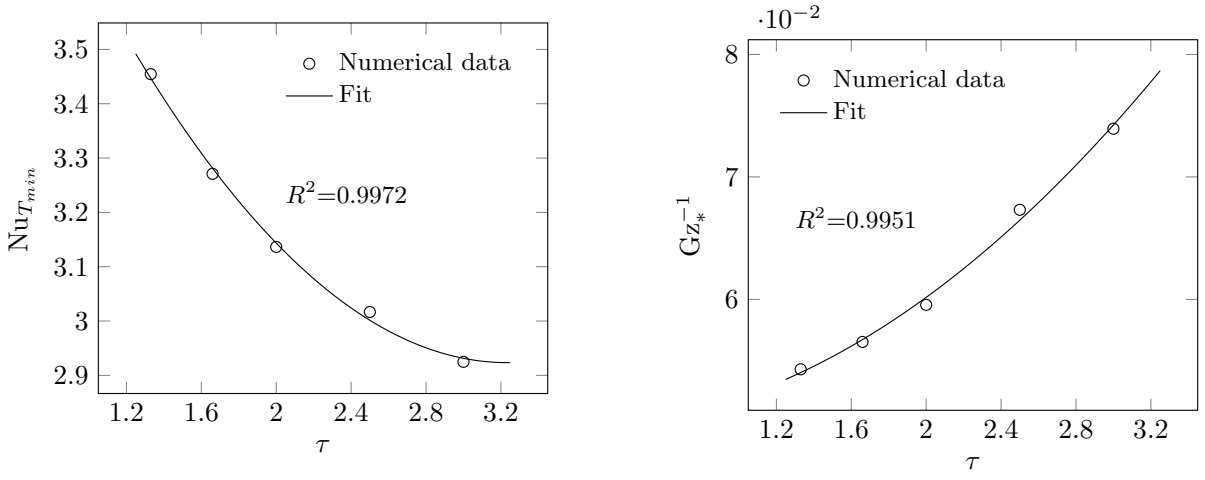

(a) (b)

Figure 11.11: Empirical polynomials for $\mathrm{Nu}_{T_{min}}$ and Gz_*^{-1} as a function of τ

Empirical models for both $\mathrm{Nu}_{T_{min}}$ and Gz_*^{-1} were provided because of their physical

meaning. Mathematical expressions for the rest of the parameters, that is B, C, n, a and b, are also desired. However, because of the high non-linearity of the model and the considerable number of parameters, a comprehensive statistical analysis would be required, and thus a potential model reduction is highly recommended. These aspects will be addressed in a further paper.

11.3.8 Summary of Nu expressions

Table 11.4 summarises the expressions for describing the Nu vs. Gz^{-1} developed in this paper. It can be appreciated that most complex case is that when the loading temperature is higher than 1.33. In such a case, most of the parameters of the functions are no longer constant, but a function of the loading temperature. For completeness and an easier implementation, empirical functions for B, C and n were also included in the table. The three mentioned expressions can be obtained straightforwardly by using the data in Table 11.3, and all the of the show an R^2 of 0.99 or higher. Although, further research should be conducted in order to obtain more fundamental expressions.

Table 11.4: List of Nu expressions

Constant wall heat flux	B	C	n
Nu_H=$\mathrm{Nu}_{H_\infty}(1+B(\mathrm{Gz})^n)\exp(-C/\mathrm{Gz})$	0.141	54.088	0.402
Constant wall temperature τ <1.33	B	C	n
Nu_T=$\mathrm{Nu}_{H_\infty}(1+B(\mathrm{Gz})^n)\exp(-C/\mathrm{Gz})$	0.0729	69.303	0.459
Constant wall temperature $\tau \geq$1.33			
Nu_T=$\max(\mathrm{Nu}_T^{dec}, \mathrm{Nu}_T^{sig})$			
Nu_T^{sig}=$\left(\frac{\mathrm{Nu}_{T_\infty}}{\mathrm{Nu}_{T_{min}}}\right)\left[\left(\frac{1}{1+e^{-\zeta}}\right)+\mathrm{Nu}_{T_{min}}-1\right]$			
$-\zeta = -0.502(\mathrm{Gz}^{-1}-\mathrm{Gz}_*^{-1})+15.575$			
$\mathrm{Nu}_{T_{min}} = 0.144\tau^2 - 0.934\tau + 4.433$			
$\mathrm{Gz}_*^{-1} = 0.00294\tau^2 - 0.000639\tau + 0.0497$			
B=$0.0093\tau^2 - 0.0580\tau + 0.116$			
C=$21.063\tau + 40.012$			
n=$-0.0132\tau^2 + 0.0948\tau + 0.3836$			

11.4 Conclusions

Convective heat and mass transfer in monolith channels was successfully investigated using computational fluid dynamics.

Three geometrical representations of a monolith channel were studied: A straight channel, a channel with a reservoir prior to it and a channel with a contraction of the flow area at its inlet. The three of them led to a significantly different inlet velocity profile, where the channel with the contraction was the most realistic one. The three channel representations also led to a different thermal entrance length values in Nu vs. 1/Gz curve, where the channel with the contraction showed a lower Nu compared to the other two geometries. For the channel with a contraction, several substrate void fractions were analysed. According to the results, the inlet Nu increases together with the void fraction; however, the differences in the Nu vs. 1/Gz curve are small in magnitude and occur very close to the inlet of the channel only.

The use of constant instead of temperature-dependent physical properties affected not only the resulting convective transport coefficient, but also the calculation of the non-dimensional axial coordinate. At a high heating rate, assuming constant fluid properties overestimates Nu over the entry length, and does not capture correctly the minimum that appears in the Nu vs. 1/Gz. Regarding the non-dimensional axial distance, 1/Gz is largely overestimated at a high heating rate, in an error of the order of the 40%. At a τ as low as 1.1, the error in 1/Gz is of about 5%.

Over a certain range of τ a minimum noticeably below the asymptotic value appears in the Nu vs. 1/Gz curve. That is more pronounced at a higher heating rate, being about 16% lower than the asymptotic value for τ=2. The minimum is especially significant at a constant wall temperature and at a high heating rate; however, neither the placement and the value of the minimum seems to be affected significantly by changes in Re. At a constant wall heat flux, the value of the minimum decreases just slightly with an increase of H, being always comparable to the asymptotic value and reasonably negligible under the conditions of this study.

Classical models are not able to describe Nu vs. 1/Gz curves with a minimum. Hence, a new model with a methodology to calibrate it was proposed. The new model mixes classical models with a sigmoid function used in machine learning to describe accurately the Nu vs. 1/Gz curve in all its extension, the decreasing zone, the concave part that contains the

minimum and the asymptotic part showing an excellent agreement in every case. Empirical models for the value and the placement of the minimum Nu were also presented because of their physical meaning and relevance. Such models are a function of τ only because it resulted the most influential parameter for them, and apply for any of the Re covered in this study.

The same methodology presented in this paper can be used to investigate channels with other cross-section shapes commonly found in industry. Models accounting for other incremental effects, such as the one of the upstream turbulence, and flow entering the substrate in an angle can be investigated using the same methodology. A disadvantage of current models for Nu curves is the number of empirical parameters necessary to define to implement the model. A statistical analysis of parameter sensitivity and a potential model reduction are highly recommended to investigate further.

Conflicts of interest

The authors declare that there is no conflict of interest regarding the publication of this paper.

Acknowledgements

I. Cornejo acknowledges the receipt of a Becas-Chile (CONICYT) scholarship. Other funding was provided by the Natural Sciences and Engineering Research Council of Canada. This research was enabled in part by support provided by Calcul Quebec (www.calculquebec.ca) and Compute Canada (www.computecanada.ca).

Bibliography

[1] Kazuhiro Yamamoto, Shingo Satake, and Hiroshi Yamashita. Microstructure and particle-laden flow in diesel particulate filter. *International Journal of Thermal Sciences*, 48(2):303–307, 2009.

[2] Audrey Devatine, Hélène Chaumat, Simon Guillaume, Bismath Tati Tchibouanga, Freddy Durán Martínez, Carine Julcour, and Anne-Marie Billet. Hydrodynamic study of a monolith-type reactor for intensification of gas-liquid applications. *Chemical Engineering and Processing: Process Intensification*, 122:277–287, 2017.

[3] Aldo Javier Guadarrama-Mendoza, Heidi Isabel Villafán-Vidales, Patricio J Valadés-Pelayo, Camilo A Arancibia-Bulnes, David Riveros-Rosas, and Hernando Romero-Paredes. Radiative analysis in a multichanneled monolith solar reactor coated with ZnFe2O4 thin film. *International Journal of Thermal Sciences*, 132:275–284, 2018.

[4] Piyanut Inbamrung, Thana Sornchamni, Chaiwat Prapainainar, Sabaithip Tungkamani, Phavanee Narataruksa, and Goran N Jovanovic. Modeling of a square channel monolith reactor for methane steam reforming. *Energy*, 2018.

[5] Nur Izwanne Mahyon, Tao Li, Ricardo Martinez-Botas, Zhentao Wu, and Kang Li. A new hollow fibre catalytic converter design for sustainable automotive emissions control. *Catalysis Communications*, 120:86–90, 2019.

[6] Selvakumar Kumaresh and Man Young Kim. Numerical investigation of catalytic combustion in a honeycomb monolith with lean methane and air premixtures over the platinum catalyst. *International Journal of Thermal Sciences*, 138:304–313, 2019.

[7] L Graetz. Uber Die Warmeleitungsfahigheit Von Flussingkeiten—Part 1. *Ann. Phys. Chem*, 18:79–94, 1883.

[8] W Kays and M London. *Compact Heat Exchangers*. McGraw-Hill, New York, NY, USA, 1964.

[9] U Grigull and H Tratz. Thermischer einlauf in ausgebildeter laminarer rohrströmung. *International Journal of Heat and Mass Transfer*, 8(5):669–678, 1965.

[10] Enrico Tronconi and Pio Forzatti. Adequacy of lumped parameter models for SCR reactors with monolith structure. *AIChE Journal*, 38(2):201–210, 1992.

[11] Robert E Hayes, Andrés Donoso-Bravo, and Joseph P Mmbaga. Entry length effects for momentum, heat and mass transfer in circular ducts with laminar flow. *The Canadian Journal of Chemical Engineering*, 93(5):863–869, 2015.

[12] CF Bonilla. *Nuclear Engineering Handbook*. McGraw-Hill, New York, NY, USA, 1958.

[13] Renate Schwiedernoch, Steffen Tischer, Chrys Correa, and Olaf Deutschmann. Experimental and numerical study on the transient behavior of partial oxidation of methane in a catalytic monolith. *Chemical Engineering Science*, 58(3-6):633–642, 2003.

[14] Heinz Herwig and Shripad P Mahulikar. Variable property effects in single-phase incompressible flows through microchannels. *International Journal of Thermal Sciences*, 45(10):977–981, 2006.

[15] RW Shumway and DM McEligot. Heated laminar gas flow in annuli with temperature-dependent transport properties. *Nuclear Science and Engineering*, 46(3):394–407, 1971.

[16] JM Nóbrega, Fernando Tavares de Pinho, Paulo J Oliveira, and OS Carneiro. Accounting for temperature-dependent properties in viscoelastic duct flows. *International Journal of Heat and Mass Transfer*, 47(6-7):1141–1158, 2004.

[17] RE Hayes, B Liu, R Moxom, and M Votsmeier. The effect of washcoat geometry on mass transfer in monolith reactors. *Chemical Engineering Science*, 59(15):3169–3181, 2004.

[18] Oswald Jason Lobo and Dhiman Chatterjee. Development of flow in a square mini-channel: Effect of flow oscillation. *Physics of Fluids*, 30(4):042003, 2018.

[19] Ivan Cornejo, Petr Nikrityuk, and Robert E Hayes. Pressure correction for automotive catalytic converters: A multi-zone permeability approach. *Chemical Engineering Research and Design*, 147:232–243, 2019.

[20] I Cornejo, P Nikrityuk, and RE Hayes. Turbulence decay inside the channels of an automotive catalytic converter monolith. *Emission Control Science and Technology*, 3(4):302—309, 2017.

[21] Ivan Cornejo, Petr Nikrityuk, and Robert E Hayes. Multiscale RANS-based modeling of the turbulence decay inside of an automotive catalytic converter. *Chemical Engineering Science*, 175:377–386, 2018.

[22] Ivan Cornejo, Robert E Hayes, and Petr Nikrityuk. A new approach for the modeling of turbulent flows in automotive catalytic converters. *Chemical Engineering Research and Design*, 140:308–319, 2018.

[23] Ivan Cornejo, Gonzalo Cornejo, Petr Nikrityuk, and Robert E Hayes. Entry length convective heat transfer in a monolith: The effect of upstream turbulence. *International Journal of Thermal Sciences*, 138:235–246, 2019.

[24] ANSYS Fluent Theory Guide v18.2. ANSYS Inc., Canonsburg, PA, USA, 2017.

[25] Bruce E Poling, John M Prausnitz, John P O'connell, et al. *The properties of gases and liquids*, volume 5. Mcgraw-hill New York, 2001.

[26] WM Kays, ME Crawford, and Bernhard Weigand. *Convective heat and mass transfer*. McGraw-Hill Higher Education, New York, NY, USA, 2004.

[27] MS Bhatti. Fully developed temperature distribution in a circular tube with uniform wall temperature. Unpublished, 7 1985.

[28] Theodore L Bergman, Frank P Incropera, David P DeWitt, and Adrienne S Lavine. *Fundamentals of Heat and Mass Transfer*. John Wiley & Sons, New Jersey, NY, USA, 2011.

[29] H More, J Mmbaga, RE Hayes, M Votsmeier, and MD Checkel. Heat and mass transfer limitations in pre-turbocharger catalysts. *Topics in Catalysis*, 42(1-4):429–432, 2007.

[30] Yi Liu, Michael P Harold, and Dan Luss. Coupled NOx storage and reduction and selective catalytic reduction using dual-layer monolithic catalysts. *Applied Catalysis B: Environmental*, 121:239–251, 2012.

[31] Ivan Cornejo, Petr Nikrityuk, and Robert E Hayes. The influence of channel geometry on the pressure drop in automotive catalytic converters: Model development and validation. *Chemical Engineering Science*, doi: 10.1016/j.ces.2019.115317, 2020.

Chapter 12

Towards a fully predictive multi-scale pressure drop model for a wall-flow filter[1]

Abstract

This paper presents a detailed study of the fluid dynamics inside a wall-flow filter and a new pressure drop model. A 3D channel scale computational model of a filter validated with experiments is used. A detailed description of the pressure drop for flow entering, passing through and leaving the filter is provided. The computational grid is extensively analyzed, and it is found that wall-flow is very insensitive to the grid quality, opposite to the local pressure, which is very sensitive. Several flow rates and wall permeability are analyzed. The most critical assumptions commonly found in current models are discussed based on the results. It is found that the friction factor of the channels is non-constant, it is different for the inlet and the outlet channels, and both differ from that for pipes with non-porous walls. A new criterion to consider the flow inside the filter as fully developed is also presented. The wall-flow along the perimeter of a cross-section is observed to be non-constant, consistently for many flow rates and wall permeability. The results are also used to develop a comprehensive, physically based, pressure drop model that shows very good agreement with experimental data. It is found that the propagation error when using the model to back-calculate physical parameters is strongly sensitive to the experimental conditions; hence, guidelines to minimize it in further experiments are provided.

[1]A version of this chapter will be submitted to a journal. Vega, I., Cornejo I., Nikrytiuk, P., Votsmeier, M. & Hayes, R. Towards a fully predictive multi-scale pressure drop model for a wall-flow filter.

Keywords: Particle filter, channel, CFD, friction factor, pressure drop

12.1 Introduction

The mitigation of harmful emissions from automotive sources has been of major concern for over 50 years, with Exhaust Gas After-Treatment System (EGATS) being standard equipment on most vehicles in Europe and North America since about 1975, with many other countries following suit later. More recently, global concerns over the potential of Greenhouse gases (GHG) to exacerbate climate change has led to many changes in automotive propulsion systems to achieve a reduction in carbon dioxide emissions, which essentially translates into a need for improved fuel economy. In the automotive market, Electric Vehicles (EV) have drawn attention because they do not produce emissions at the local level. However, the cost competitiveness of EV compared to the Internal Combustion Engine Vehicles (ICEV) remains doubtful, and the electrical generation and distribution systems do not currently have the capacity to meet a massive increase in demand for EV [1]. Therefore, whilst EV will doubtless play a significant role in the longer term, there will remain a major place for ICEV, especially in remote communities, and for many industrial activities [2, 3] for many years to come. Until recently, much emphasis had been placed on Diesel engines, especially in Europe, because they produce fewer GHG than gasoline vehicles, both in the fuel production step as well in having higher combustion efficiency, although EGATS for Diesel are significantly more complex than for gasoline engines with pre-mixed feed. In spite of these advantages, Diesel is now becoming unpopular, and there is renewed interest in improving the efficiency of gasoline engines, thus the Gasoline Direct Injection (GDI) engine has been widely adopted in recent years [4]. Whilst these engines have improved efficiency compared to pre-mixed combustion engines, they have the drawback of producing increased levels of particulate emissions that adversely affect human health. Indeed, particulate emissions from GDI can pose higher risks to human health than those from Diesel engines [5, 6]. For this reason, the car industry has put strong efforts into the development and improvement of wall-flow particle filters for GDI engines, which are simple and efficient, to eliminate particle matter from the car emissions [7–12]. These particulate filters for GDI are similar in concept to those developed earlier for Diesel engines, although they have some significant differences, partly because the particles generated by a GDI engine are quite different from those generated in a Diesel engine [13, 14]. A Particulate Filter (PF) contains a solid substrate made from a porous material with many thousands of channels running in parallel. The substrate is similar to the ceramic monoliths used in other parts of the EGATS, however, in a PF the channels are plugged at alternate ends. As a result, the flow enters the inlet channels at the

frontal face of the filter, passes through the porous walls to the outlet channels and leaves the filter through the rear face. The design of PFs is very important in terms of aiming for the lowest pressure drop possible to maximize fuel efficiency.

There are many variables involved in the design of a PF, which include the wall permeability, wall thickness, channel size and filter length, to name a few. Selection of any or all of these factors depends on the engine type, and each design requires careful optimization to achieve maximum effectiveness. The optimization of a filter design by either experimental or computational means is quite challenging, because it involves the interaction of at least three different spatial scales. The smallest scale is the pore scale within the thin porous walls. The trapping of the particles occurs at this scale, as well as any chemical reactions if it is a catalyzed particulate filter. The second scale is the channel scale, which focuses on the fluid flow inside of the channels and through the walls. The third scale is the filter scale, which is used to study the global performance of the filter, such as the flow distribution, total back-pressure and total particle capture efficiency [15–17].

Computational models for PF have been published in the literature for many years. Computational modeling at the wall structure scale has been published only fairly recently, partly as a result of new tomographic techniques that have revealed the micro-structure of the porous filter wall [11, 12, 18, 19]. More common are channel scale models, with the wall being treated as a porous medium [20–23]. Overall, at this level, models of wall-flow filters extant range from 0D to 3D. A 0D model does not resolve any information at the spatial level, and treats the entire filter as a single entity. 0D models can be useful for the determination of global variables such as total pressure drop, but are not useful for revealing information about local flows or filter efficiency, especially if the filter is catalyzed. In the case where flow information is desired, which would broadly include such things as wall flow distribution, channel flow distribution, particle capture efficiency, effects of non-uniform wall permeability, etc., it is essential to include a minimum level of spatial discretization. In that regard, clearly the preferred and best alternative is to use a full 3D spatially discrete model. Such a model requires few, if any, assumptions and thus will provide the most reliable representation of reality. The main drawback of a 3D computational fluid dynamics (CFD) based model is the high computational cost, especially if performed with rigorous attention to accepted modeling criteria, as is demonstrated later in this paper. For this reason, 1D models are often preferred, especially in industry, where high levels of computational infrastructure and modeling expertise are often unavailable. The accuracy of 1D models depends on the assumptions made in their derivation and lumped parameters used in them. The necessary parameters can in theory be

derived from detailed 3D simulations, although this has not generally been the practice to date. It is evident that much detailed flow information will be lost in moving from a 3D to a 1D model, and there are a number of papers that have used 2D models as a compromise [24, 25]. These models, however, have been shown not to capture correctly velocity patterns, and thus should be avoided [23, 26].

In this work, we describe the development and experimental validation of a comprehensive three dimensional channel scale model for the wall flow particulate filter. The model is used to provide a detailed description of the fluid motion and pressure drop in every part of the PF. These include the flow entering, passing through and leaving the filter. The model is used to investigate the validity of most of the major assumptions that are commonly made my investigators using simpler 1D models of particulate filters. The results report local and global data, together with the most relevant dimensionless numbers and lumped parameters, which are needed to provide with multi-scale consistency to dimensionally reduced models. Finally, modeling guidelines and topics for further research are suggested.

12.2 Theoretical Framework

The velocity patterns and the pressure drop are related through the momentum balance. The overall pressure losses when flow passes throughout a filter can be divided into a number of contributions, typically done as shown in Equation (12.1), or as a disaggregated form reported in Equation (12.2) [27–29].

$$\Delta p = \Delta p_w + \Delta p_f + \Delta p_{in/o} \tag{12.1}$$

$$\Delta p = \Delta p_i + \Delta p_w + \Delta p_{fic} + \Delta p_{foc} + \Delta p_o \tag{12.2}$$

In Equation (12.2), Δp_i and Δp_o are the losses that occur when the flow enters or leaves the substrate, Δp_{fic} and Δp_{foc} are the energy dissipation due to friction inside of the inlet and outlet channels respectively, and Δp_w is the pressure drop because of the flow crossing the porous walls. It has been shown in the literature that Δp_i and Δp_o usually agree very well with values from models for flow passing through a sudden expansion or contraction in flow-through monoliths [30, 31]. In a PF, having a porous wall adds a degree of freedom to the modeling of Δp_i and Δp_o, as shown in Section 12.5.5. The latter terms were not considered in the development of early 1D models. One of the first 1D models generally accepted by the community was published by Bissett [32], upon which most of current PF models were

built [8]. That model uses various assumptions that later have been have reduced to improve the 1D model. For example, the term Δp_w, firstly based on the Darcy-Forchheimer law, was reduced by Konstandopoulos et al. [15] to Darcy's Law. Watling et al. [9] supports the latter statement, although they mention that the contribution of the Forchheimer term to the overall pressure drop increases as the length of the channel decreases. Furthermore, Kinney [33] introduced a momentum flux factor to account for the changes in axial momentum flux in tubes with porous walls. Bissett et al. [34] and Kostoglou et al. [7] added this factor to the convective term in the 1D momentum balance for the inlet and outlet channels. Afterwards, Watling et al. [9] showed the effect of changing the value of the momentum flux correction factor.

An aspect of the pressure drop that requires attention is the pressure drop inside the filter channels (Δp_{fic} and Δp_{foc}). Most of the 1D pressure models approximate this pressure drop by using differential equations for pipes with porous walls. In such a case, Δp can be estimated using classic fluid dynamics, as follows [35]:

$$\Delta p_{f_n} = \int_{L_n} \frac{1}{D_H} f_n \frac{1}{2} \rho u^2 dL_n \tag{12.3}$$

The subscript n corresponds to ic for an inlet and to oc for an outlet channel. The integral in Equation (12.3) is still valid inside the filter, however, it must be emphasized that the velocity along the channel is not constant given the flow passing through the walls. Therefore, to apply it, it is necessary to know the local flow rate in the axial direction. One alternative to calculate Δp_f is to use an average friction factor, the total flow rate and the effective length of the channels, as shown in Equation (12.4):

$$\Delta p_f = \frac{L_{ic}(f_{ic} \cdot \mathrm{Re}_{ic})\mu}{2D_H^2} u_{ic} + \frac{L_{oc}(f_{oc} \cdot \mathrm{Re}_{oc})\mu}{2D_H^2} u_{oc} = \frac{L'_f F_D \mu}{2D_H^2} u_c \tag{12.4}$$

The differential form of the balance can usually be found in 1D lumped parameters filter models, using a sink of momentum, as shown in the last term at the right-hand side of Equation (12.5). Bissett [32] and Konstandopoulos et al. [36] support the use of the latter equation by assuming that only a small amount of flow crosses the porous wall in a given section, which is accurate in many cases.

$$\frac{d\rho u_n^2}{dx} = -\frac{dp_n}{dx} - (f_n \cdot \mathrm{Re}_n)\frac{\mu u_n}{D_H^2} \tag{12.5}$$

The term f_n in Equation (12.3) and (12.5) represents the friction factor for the inlet (f_{ic})

and outlet (f_{oc}) channels respectively. For developing flow, $f{\cdot}\mathrm{Re}$ is a function of a dimensionless distance, typically $x^+ = x/\mathrm{Re}D_H$. In a wall-flow filter, early models assumed that $f{\cdot}\mathrm{Re}$ was a constant value due to the assumption of fully developed flow [27, 32, 36, 37]. That raises an interesting discussion regarding what criterion should be used to state fully developed flow within a PF, since the the flow rate is progressively decreasing in the inlet channel and increasing in the outlet ones. That is discussed in Section 12.5.3 and 12.5.4. Bissett et al. [34] and Kostoglou et al. [7], rather than using a constant value of $f{\cdot}\mathrm{Re}$, aimed for a correlation between $f{\cdot}\mathrm{Re}$ and the wall Re (Re_w) based on previous work from Yuan and Finkelstein [38], Berman [39] and Brady [40], among others. These works derived such a correlation in a special condition, where the wall-flow was constant. The aforementioned works, together with those from Bissett et al. [34] and Kostoglou et al. [7] faced some limitations that showed non-physical flow behavior in a PF, such as a negative friction factor.

In general, a basic 1D model based on first principles has not been reported. Current models are based on various assumptions (see the list below) that have not yet been thoroughly investigated. The majority of models published only work for specific filter configurations or they require experimental data (i.e. curve fitting of key parameters). To the best of the authors' knowledge, there are no generally applicable and predictive pressure models that do not depend on experimental data or on partially validated assumptions. A list of commonly used assumptions in PF models is [41]:

i. The flow is incompressible.

ii. The velocity profile entering an inlet channel is flat.

iii. The flow inside the filter is fully developed.

iv. The friction factor for inlet and outlet channels is equal to the one for a closed square pipe with fully developed flow.

v. The friction factor is a function of the wall Reynolds number.

vi. The radial pressure gradient inside the channels is negligible.

vii. The radial density and velocity gradients are negligible inside the porous wall.

viii. The wall-flow is constant.

ix. No-slip velocity in the surface of the porous wall.

x. The flow that enters and leaves the filter through the porous walls is negligible.

xi. Darcy's law models the porous wall.

xii. Laminar steady flow prevails inside of the channels.

12.3 Experimental setup

The experimental data used to validate the 3D CFD results was obtained using the experimental setup shown in Figure 12.1. Clean atmospheric air was passed through a 300 CPSI cylindrical PF, 127 mm long with 5 in as a diameter. The filter channels were, with 1.26 mm as height. The pressure drop was obtained through DP cell, with the two taps located at 56 mm and 58 mm prior and after the PF respectively. The flow rate was induced by an air compressor. The experiments were run at a pressure and temperature of 1 bar and 21 °C respectively. Twelve flow rates ranging from 0.05 m^3/h to 268 m^3/h were tested.

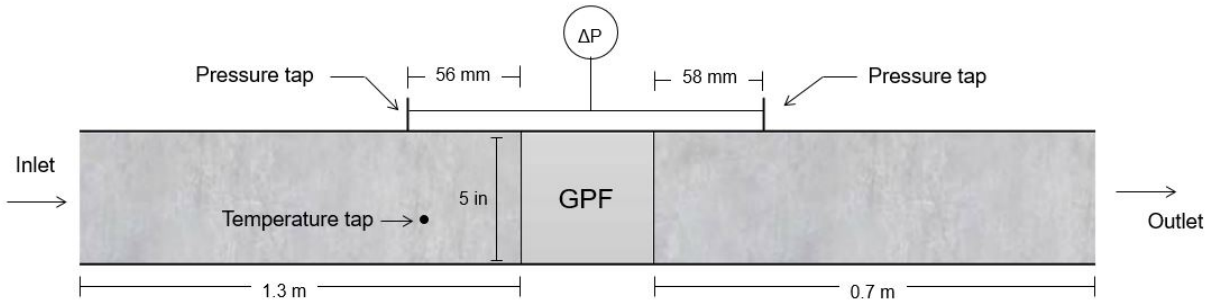

Figure 12.1: Schematic of equipment used to obtain experimental pressure drop in GPF.

12.4 Computational model

This section describes the physical and phenomenological considerations used in the computational model, together with the solver settings and boundary conditions.

12.4.1 Computational domain

The analysis was carried out using a discrete channel model, with the computational domain illustrated in Figure 12.2. It consisted of four fourths of adjacent filter channels, together with an open space before and after the channels. The cross-section of the channels was square and was 1.26 mm in height (D_H). The channels were plugged alternately, two at their inlet and two at their outlet, and separated by porous walls of 0.2 mm in thickness (L_w). The length of the plugs (L_p) was 5 mm, and the length of the upstream and downstream

region were 10 mm and 100 mm respectively. The total length of the filter (L_f) was 127 mm; hence, the effective length of the inlet (L_{ic}) and outlet channels (L_{oc}) was 122 mm (L'_f), meanwhile, the length of the filtrating zone (L''_f) was 117 mm. The origin of the axial coordinate was placed right at the frontal face of the filter; therefore, L_i runs from x=0 mm to x=122 mm, meanwhile, L_o runs from x=5 mm to x=127 mm. It is important to remark that the upstream and downstream zones must be used to account for a realistic inlet velocity profile and to calculate Δp_i and Δp_o. The flow leaving the filter behaves similar to a square jet, producing a large recirculating zone that must not be cut by the end domain, hence, the extension of this zone must be relatively large. In contrast, the upstream zone is not necessarily required to be very large because the velocity profile and Δp_i do not show further change with increasing length beyond five to ten D_H [9, 26, 28, 30, 42–44].

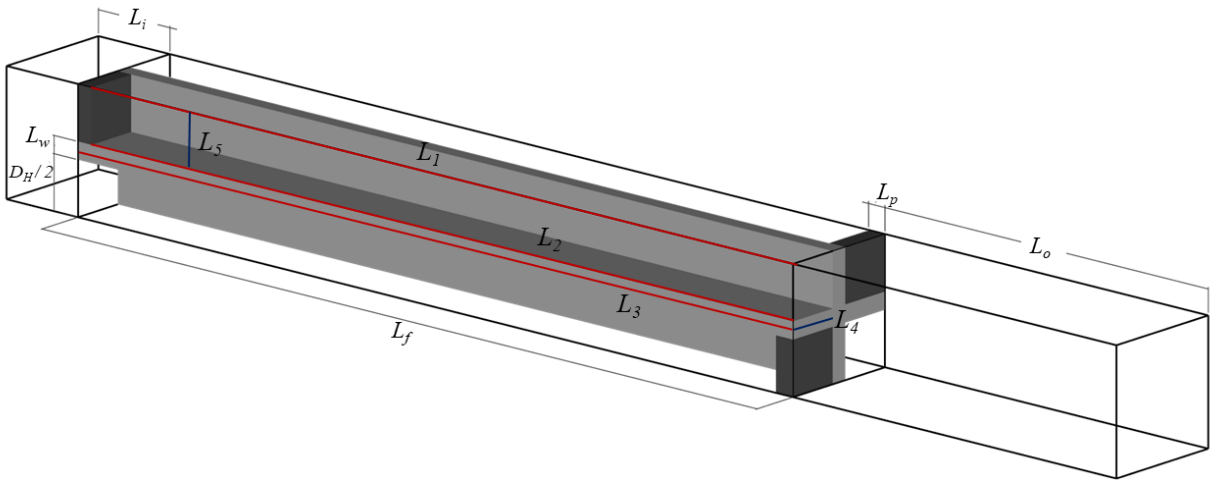

Figure 12.2: Schematic of the domain

12.4.2 Flow model

The fluid was set as clean air at 1 bar, at 303 K for comparing with experiments and at 573 K for analyses at a PF operating temperature. The fluid density (ρ) was calculated using the ideal gas law and the fluid viscosity (μ) by the kinetic theory of gases [45]. The flow regime was assumed to be steady laminar, therefore, the mass and momentum balances were [45]:

$$\frac{\partial \rho u_i}{\partial x_i} = 0 \tag{12.6}$$

$$\frac{\partial(\rho u_i u_j)}{\partial x_j} = -\frac{\partial p}{\partial x_i} + \frac{\partial}{\partial x_j}\left[\mu\left(\frac{\partial u_i}{\partial x_j} + \frac{\partial u_j}{\partial x_i} - \frac{2}{3}\frac{\partial u_l}{\partial x_l}\delta_{ij}\right)\right] + S_u \tag{12.7}$$

The source term S_u in Equation (12.7) was zero in all the domain, except inside the porous walls. The porous walls were modeled as an isotropic continuum, that is, as a porous medium following Darcy's law, where S_u= -$\frac{\mu}{\alpha_i}u_i$ [28]. Three wall permeabilities from 1×10^{-11} m^2 to 1×10^{-13} m^2 were tested. Such a range covers most of the automotive applications, for Diesel and Gasoline engines, and for clean and catalyst coated filters [46, 47].

12.4.3 Solver settings and boundary conditions

The problem was implemented in ANSYS Fluent 18.2 [48], which uses the Finite Volumes Method (FVM), and the post-processing calculations were done in MATLAB R2018a [49]. The inlet of the domain was set as a velocity inlet, with a prescribed velocity according to the desired channel Re of every run. The outlet was specified as pressure outlet with a prescribed pressure of 1 bar. The top, bottom, left and right boundaries of the domain were set as symmetry planes. The pressure-velocity coupling was solved as fully coupled [45, 50] and the discretization scheme for momentum was QUICK [45, 50]. The stop criterion for the simulations was having a maximum value of the scaled residuals of mass and momentum below 10^{-6}, a stationary total pressure drop and volume average velocity magnitude, simultaneously. The computational mesh is extensively described in Section 12.5.1.

12.5 Results

Each component of Equation (12.2), which depend on the flow field, are analyzed in detail and modeled in this section.

12.5.1 Grid analysis

The grid is the discretized version of the domain and it is of critical importance in any computational model. However, this requires special attention when modeling a PF. Usually, in open channel substrates, the emphasis for the grid refinement is in the radial direction to obtain an accurate description of the boundary layer and the velocity profile. In a PF, on the other hand, the resolution of the grid in the axial direction is also vital to obtain the correct wall-flow from the inlet to the outlet channels. Additionally, modeling the porous

walls by Darcy's law results in a homogeneous fluid with a body force rather than a porous solid body. That raises some questions, for example, how necessary is the wall refinement in this kind of problem, where there are not solid walls. This point is discussed further in the paper. For the grid study, local and global variables (pressure and velocity magnitude) obtained from several meshes were analyzed. Given that the downstream section increases significantly the size of the domain, the grid study was carried out considering only the filter and its upstream section. This allows us to emphasize the phenomena inside the filter while avoiding limitations in computational power. After defined the grid size of the grid, the downstream open section was added, using the same element size as that inside the filter.

Two mesh strategies were tested. First, homogeneous Cartesian meshes, then, wall refined meshes (see Figure 12.3a and 12.3b). In all the cases, the size of the elements in the axial direction was manipulated to obtain an aspect ratio of approximately one in the center of the channels and such a size was kept constant along the whole domain. Table 12.1 summarizes the main features of each mesh used in the grid study, together with the total pressure drop predicted in every case. The comparison was done using an approaching velocity of 2.8 m/s, an inlet temperature of 573 K and a wall permeability of 1×10^{-12} m^2.

Table 12.1: Comparison of the computational grids

Mesh	A	B	C	D	E
Structure	Cartesian	Cartesian	Wall ref.	Wall ref.	Wall ref.
Millions of elements[†]	4.2(7.3)	20.9(36.2)	6.7(11.6)	14.6(25.3)	23.0(39.8)
Elements through the wall	4	8	8	10	13
Elements in a cross-section	26x26	52x52	46x46	64x64	80x80
Total pressure drop, Pa	406.12	428.23	439.16	441.45	442.83
Error in pressure drop[††], %	9.04	3.41	0.84	0.31	-

[†] The Number of elements after adding the downstream section is shown in brackets

[††] Referred to the one obtained with the finest mesh

From a global standpoint, it can be seen in Table 12.1 that the results from the Cartesian meshes differ between them, but also are significantly different than those from the wall refined meshes. Mesh B improves with respect to mesh A, however, the error in the total pressure drop is still appreciable, even when a significant number of elements is used. All of the wall refined meshes performed similarly, but it is remarkable that the error in the total pressure drop in mesh C is much lower than the one in mesh B, despite the significantly lower number of elements.

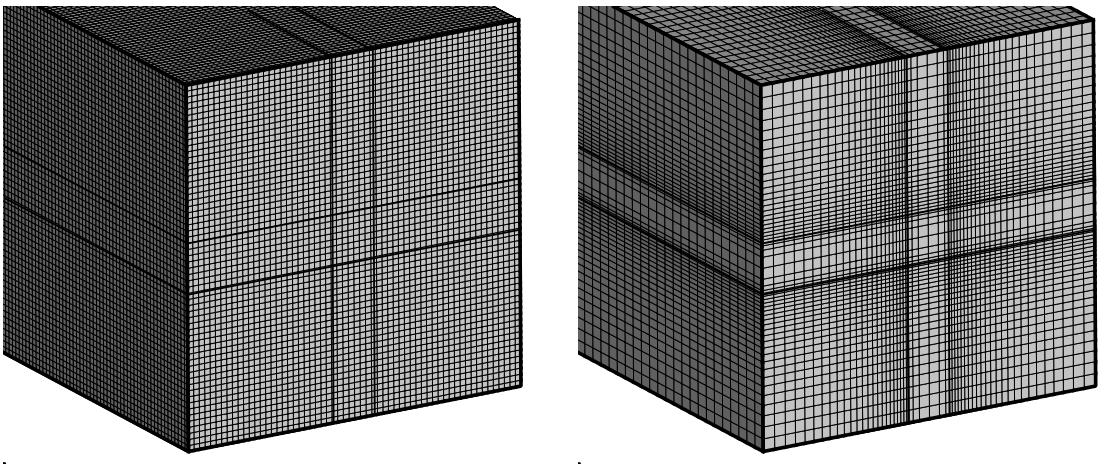

(a) (b)

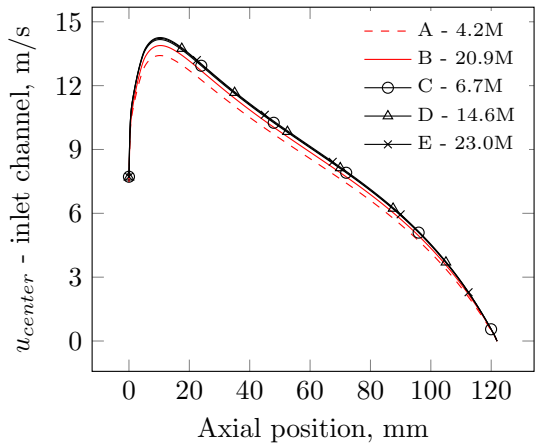

(c)

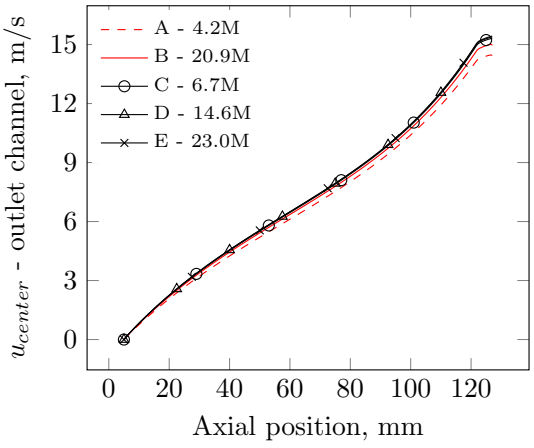

(d)

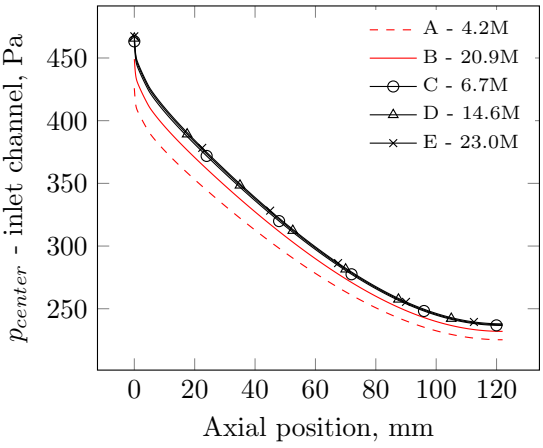

(e)

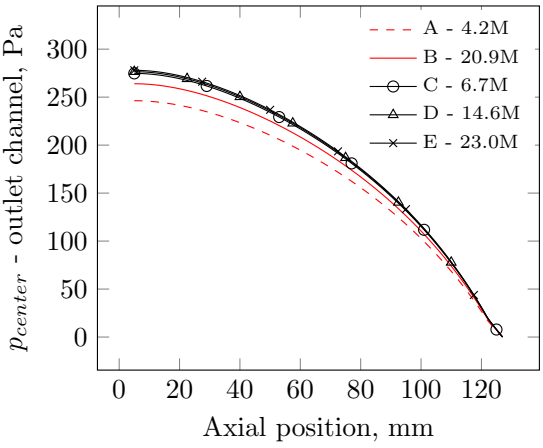

(f)

Figure 12.3: Cross section of the (a) grid B and (b) grid C. The porous walls are marked with solid lines. Velocity magnitude through the center of (c) an inlet channel and (b) an outlet channel. Pressure through the center of (d) an inlet channel and (e) an outlet channel

Figure 12.3 shows a cross-section of the meshes B and C, as well as the velocity magnitude and pressure along the center of an inlet and an outlet channel. Those are local values, that complement the global ones presented in Table 12.1 and that indicate that mesh C is sufficient. A view of the other meshes is included in Section 12.7.1 of the supplementary material. Typically, when modeling PFs, the grid quality is investigated mainly focused on the velocity profiles [21, 36]. That should be reconsidered if the interest is the pressure drop. Figure 12.3c and 12.3e, demonstrate that the grid quality affects the pressure much more than the velocity. It also confirms that in both inlet channel and outlet channel wall refined meshes behave similarly, meanwhile, the Cartesian meshes were insufficient to state the grid independence of the solution. The figure also shows that the pressure of both channels shifts up simultaneously as the mesh is refined, damping the changes in the pressure gradient, and therefore, keeping the wall-flow relatively constant for all of the meshes. Hence, investigating the grid by using the wall-flow is discouraged.

It is striking that the wall-flow velocity profile predicted for all the meshes was about the same, being the least sensitive variable to the grid quality. A possible explanation is the fact that the wall-flow is allowed by Darcy's law, hence, it depends on the pressure gradient rather than on the absolute pressures. That is, if the pressure difference between both the inlet and the outlet channel is correct, then the flow rate transferred from the former to the latter is also correct, despite of the individual error of the pressure of both channels.

This paper focuses mainly on variables derived from the velocity and pressure profiles, to which purpose the mesh C was deemed to be sufficient and was the one used for the rest of the simulations of this paper. Having defined the quality of the grid, the part of the domain representing the open section downstream of the filter was added, using the same element quality and size as that inside the filter, which led to a total number of elements of 11 783 255 for the whole domain. It was corroborated that the pressure drop from the frontal to the rear face of the filter remained the same after adding the downstream section.

12.5.2 Experimental validation

The numerical pressure drop data obtained from the mesh C are seen to have a good agreement with experimental data in Figure 12.4. Nonetheless, it is important to mention that for flow rates above 216 Nm^3/h, convergence was not possible to reach. According to the literature, the flow may become unsteady or even turbulent once it leaves the filter, as shown in similar investigations, even when the flow inside the channels is fully laminar and steady [44, 51, 52]. Under those circumstances, it is necessary to use a substantially different so-

lution methodology. That is, a transient simulation with a flow model suitable to predict laminar to turbulent transition, such as Direct Numerical Simulation (DNS) or Large Eddy Simulation (LES). Nonetheless, a domain composed by only one equivalent channel, such as the one in this study, would be inaccurate in the context of a wall-flow filter. In LES and DNS, periodical instead of symmetrical lateral boundaries are required, forcing the use of a geometrical periodic domain as well. To meet that condition, at least four equivalent channels are needed, therefore, based on the previous grid study, a mesh with of the order of the tens to the hundreds of millions of elements would be necessary. This would also be useful to study unsteadiness inside the filter channels. Typical channels Re for automotive applications are below the critical one for square pipes. However, the flow path through a wall-flow filter is much more tortuous than that for a pipe, which may potentially induce turbulence at a significantly lower channel Re. To the best of the author's knowledge, such analysis is not available in the literature, and therefore, the authors encourage groups with access to the necessary resources to perform such study. It should also be mentioned that at a sufficiently high flow rate and wall permeability, reverse flow can be observed, even when the flow is still steady. For the purposes of this work, the range below 100 Nm^3/h (Re_i=600) is considered as low flow, whereas the range from 100 to 200 Nm^3/h (Re_i=600-900) is considered as high flow. No reverse flow was observed in the low flow region (see Section 12.7.3 of the supplementary material). Figure 12.4 also shows the agreement of the 0D pressure drop model developed in this paper, as well as the results of a widely accepted pressure drop model [27, 53]. A detailed explanation of the differences and similitude of these models are given in Section 12.5.7.

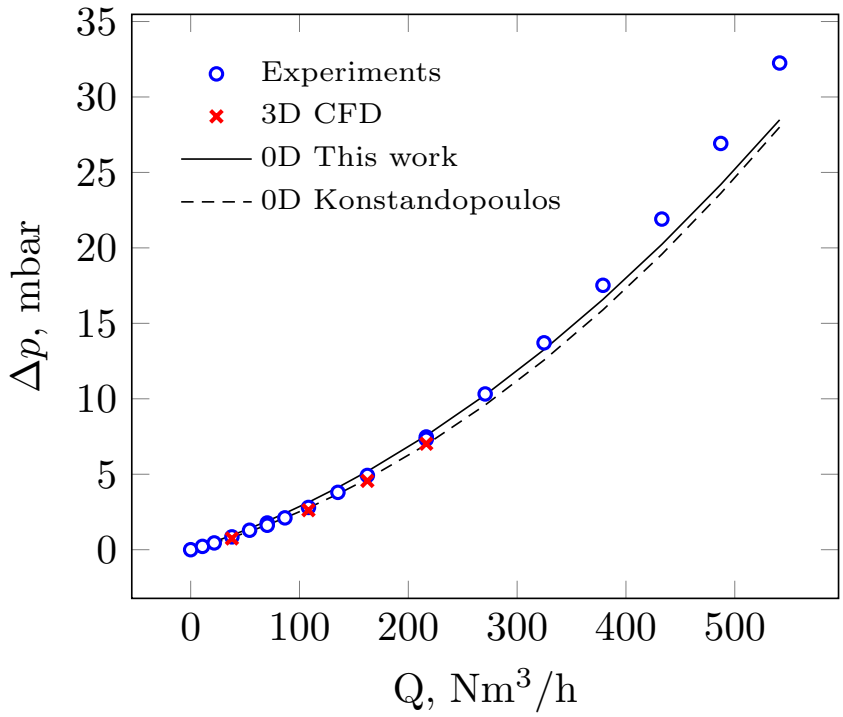

Figure 12.4: Experimental validation of the computational model. The lines represent the predictions from 0D models, discussed in Section 12.5.7

12.5.3 Friction factor analysis ($\Delta p_{f_{ic}}$ and $\Delta p_{f_{oc}}$)

This section analyzes the entrance and developed regions of the inlet and outlet channels in terms of velocity, pressure and friction.

The assumption of a flat velocity profile at the entrance of an inlet channel is used in many of the previous PF models. This assumption is of great significance due to its effect on the velocity profile within the channels. Figure 12.5a shows the cross-section velocity profile at the beginning of an inlet channel. This profile is similar to those observed when flow enters a flow-through monolith or a typical sudden contraction [31, 54–56], it also agrees other results in the literature, such as Vega M. et al. [23] and Watling et al. [9]. Along the inlet channel, the velocity profile develops rapidly from the inlet one to a convex shape, over a distance comparable to the length of the plug (Figure 12.5b). In contrast, Figure 12.5d shows that the flow in the outlet channel develops faster and ends in a convex velocity profile at the exit of the filter (Figure 12.5c).

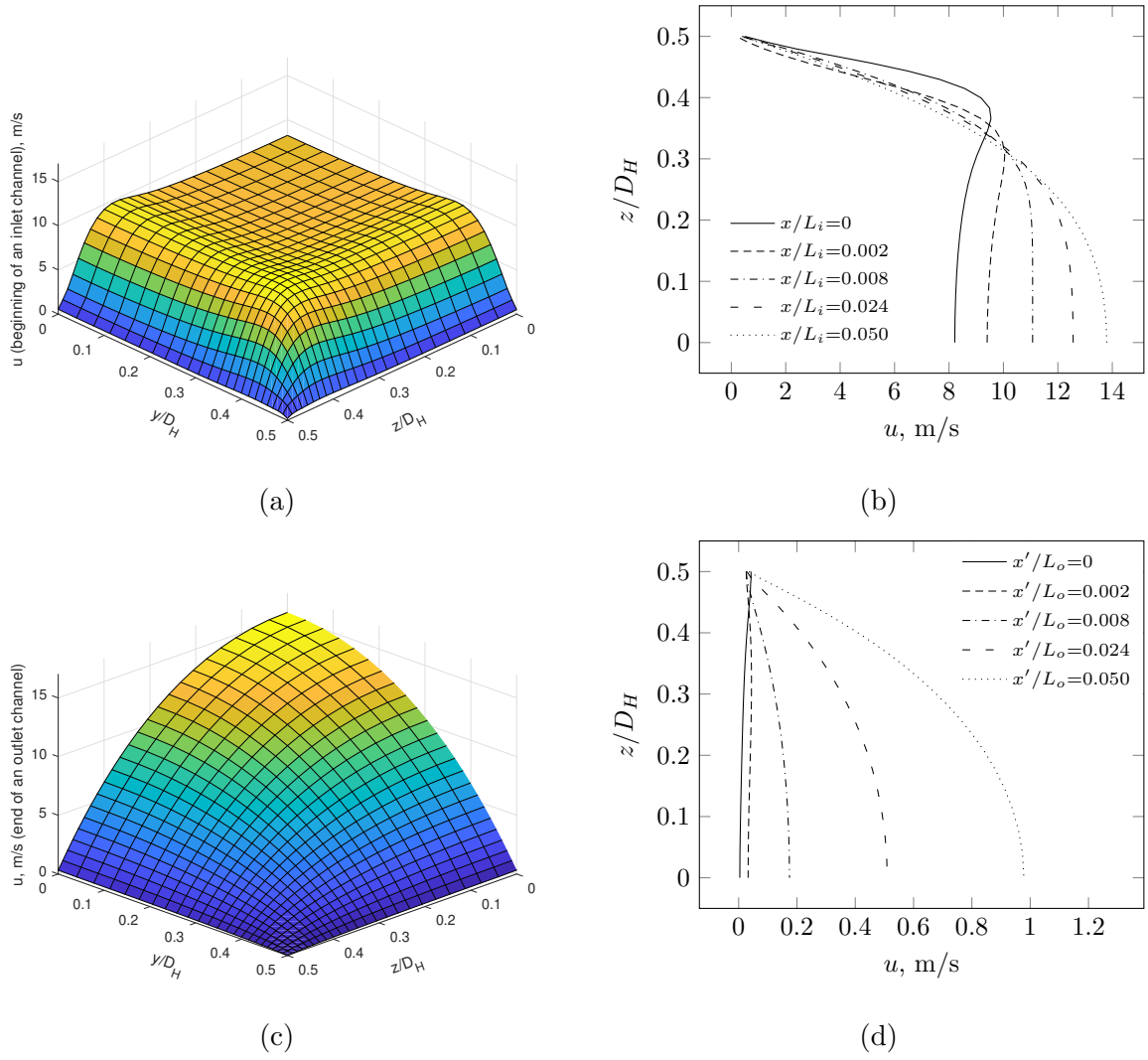

Figure 12.5: Velocity profile at (a) the beginning of an inlet channel and (c) end of an outlet channel. Developing of the velocity profile along the center of (b) an inlet channel and (d) an outlet channel. Inlet Re of 200 and wall permeability of 1×10^{-12} m^2

Fully developed flow is another assumption used in various efforts on modeling PFs. Nonetheless, this raises uncertainties on what criterion to use to state fully developed flow within the channels. Figure 12.6a and 12.6b show cuts of the velocity profile in several positions along an inlet and an outlet channel (see L_5 in Figure 12.2). It can be seen that the curves are not identical in shape, but fairly similar. As expected, the flow decreases in the inlet channel while it increases in the outlet channel. Therefore, the usual criterion of reaching a constant value for u_{max}/u_{inlet} does not apply for this case. However, in Figure 12.6c and 12.6d it can be observed that after scaling the velocity profiles by their maximum in that axial position (u/u_{max}), the curves collapse to a similar one. If the shape of the velocity profile is approximately constant, then the ratio of the maximum over the average

velocity along the channels (see L_1 in Figure 12.2) must also remain approximately constant (see Figure 12.6e and 12.6f). This fact is very important due to the tight relationship between the velocity profile and the friction factor.

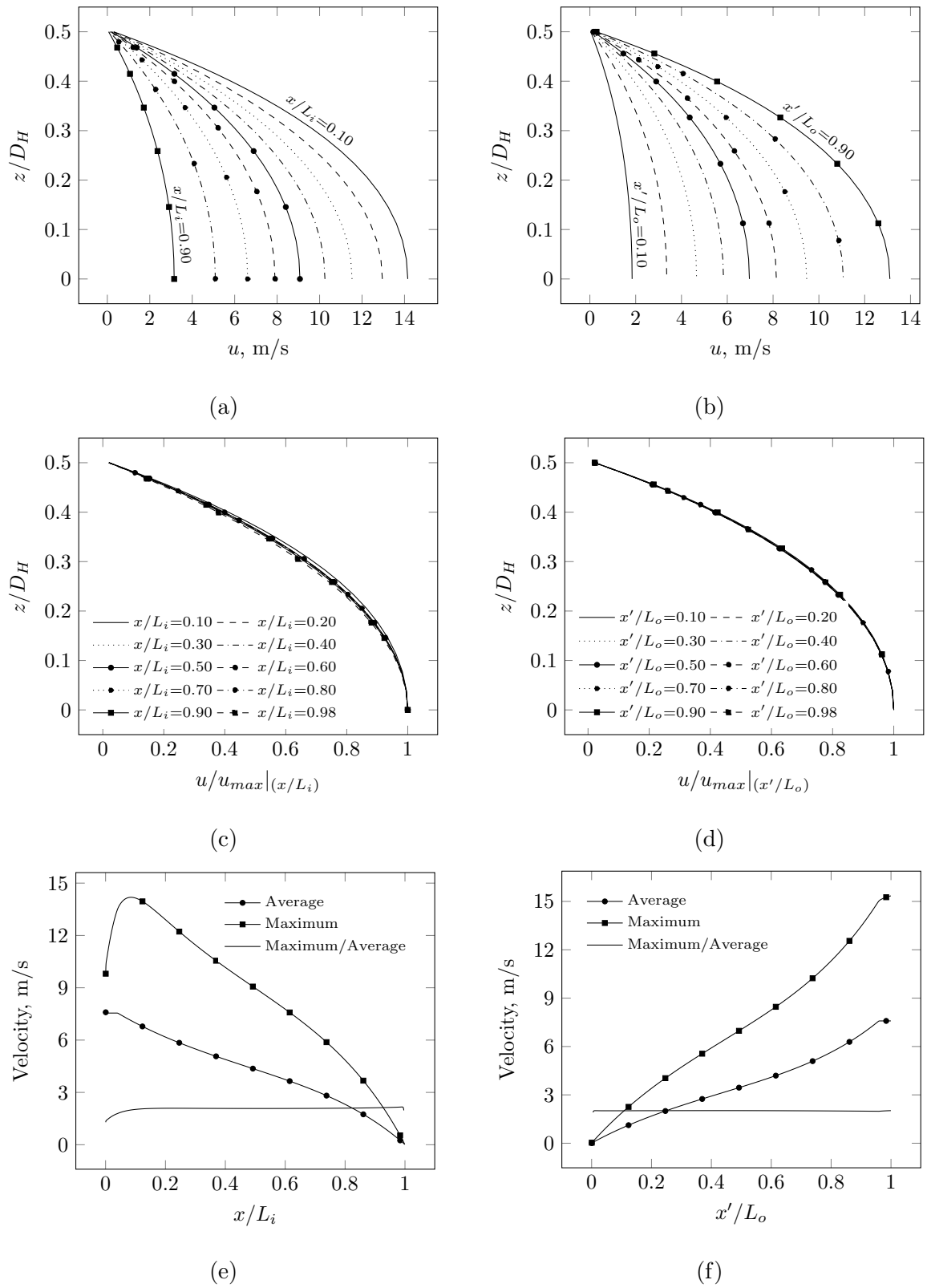

Figure 12.6: (a) and (b) show cuts of the velocity profile for an inlet and an outlet channel respectively. (c) and (d) are the scaled version of the aforementioned profiles, where the scaling factor is the local maximum velocity. (e) and (f) show the average and maximum velocities along an inlet and an outlet channel, together with the ratio between them. Re_i=200, wall permeability= 1×10^{-12} m^2

Having analyzed the velocity profiles, the next step is to calculate the friction factor for each channel. That can computed by using the shear stress (τ_w) on the surface of the porous walls along the filter, as follows [35]:

$$f_n = \frac{\tau_w}{\rho \overline{u}^2} = \frac{\mu}{\rho \overline{u}^2} \frac{\partial u_x}{\partial r}\bigg|_w \tag{12.8}$$

The term $\partial u_x/\partial r$ in Equation (12.8) represents the derivative of the axial velocity in the radial direction. Looking at Figure 12.2, in this work $\partial u_x/\partial r$ refers either to $\partial u_x/\partial y$ or $\partial u_x/\partial z$ depending on the face of the channel analyzed. In both cases, the derivative must be evaluated at the surface of the porous walls. Equation (12.8) was calculated at every axial position, as the area-weighted average from all of the values around the entire perimeter of the respective channel cross-section (see Section 12.7.3 of the supplementary material for more information). The friction factor was computed under several conditions for both inlet and outlet channels. According to the literature, the wall permeability can change significantly when coating a filter [12, 46], hence, three different flow rates and wall permeabilities of three different orders of magnitude were analyzed, following an orthogonal design strategy.

According to Figure 12.7a and 12.7b, $f{\cdot}\mathrm{Re}$ for an inlet channel is variable rather than fixed, especially when moving to a higher flow rate or a higher permeability, where a minimum can be noticed at the end of the channel. Nonetheless, when focusing on the main part of the inlet channel, the values remain in the same order of magnitude, but significantly below the standard 56.9 for the fully developed flow in square pipes[35]. Moreover, the entrance region showed a similar behavior regardless of the flow rate and wall permeability used. The largest deviation was observed in the end section of the inlet channel, where, for the case of highest permeability, a large peak downwards was shown.

Figure 12.7c and 12.7d show f vs. Re in an inlet channel for several wall permeabilities and flow rates. For an inlet channel, the flow is progressively decreasing when advancing through the filter, so, the $f{\cdot}\mathrm{Re}$ curve should be read from right to left. There are mainly three different zones. First, the plug zone, where the velocity profile is moving form the inlet one to a convex shape, in absence of wall-flow. In that zone, $f{\cdot}\mathrm{Re}$ is variable and higher than the $f{\cdot}\mathrm{Re}$ for fully developed flow in pipes. Second, the main part of the channel, where the curve is well approximated by a power law as $f{=}F_D\mathrm{Re}^{-1}$. In this zone, an F_D of 44.3 was found to be a suitable value for all the curves. For example, using $\mathrm{Re}_i{=}200$ and $\alpha{=}1 \times 10^{-12}$ m^2, the F_D is $44.28{\pm}0.004$, with an R^2 of 0.9984. However, for the case with the highest wall permeability, the R^2 decreased to 0.83. Finally, the third zone, which is the last part of the

inlet channel. That region has the lowest Re, and the power law $f{=}c_1\mathrm{Re}^{-c_2} + c_3$ applies. This part of the correlation needs further investigation, however, its contribution should not be significant due to the size of the third zone compared to the total length of the filter.

The same analysis can be done for an outlet channel (see Figures 12.7e and 12.7f). Opposite to the inlet channels, in the outlet ones, the flow rate increases along the filer, and the f vs. Re curve should be read from right to left. In this case, the curves can be split into two main zones. The first zone belongs to the part with low Re, which is limited to 2 to 3 D_H of the channel. Then, the second section where the power law $f{=}F_D\mathrm{Re}^{-1}$ applies. In the case of the outlet channels, the flow reaches the plug zone sufficiently developed, therefore, deviations to the power law in the second section are minimal. A suitable F_D value for the outlet channels was found to be 48.6, where, for example, for Re=200 and $\alpha{=}1 \times 10^{-12}$ m^2, F_D was 48.59$\pm$0.002 with an R^2 of 0.9985. Similarly to the inlet channels, the $f{\cdot}$Re values were below the one for developed flow in square pipes, and the largest deviations were those when using $\alpha{=}1 \times 10^{-11}$ m^2.

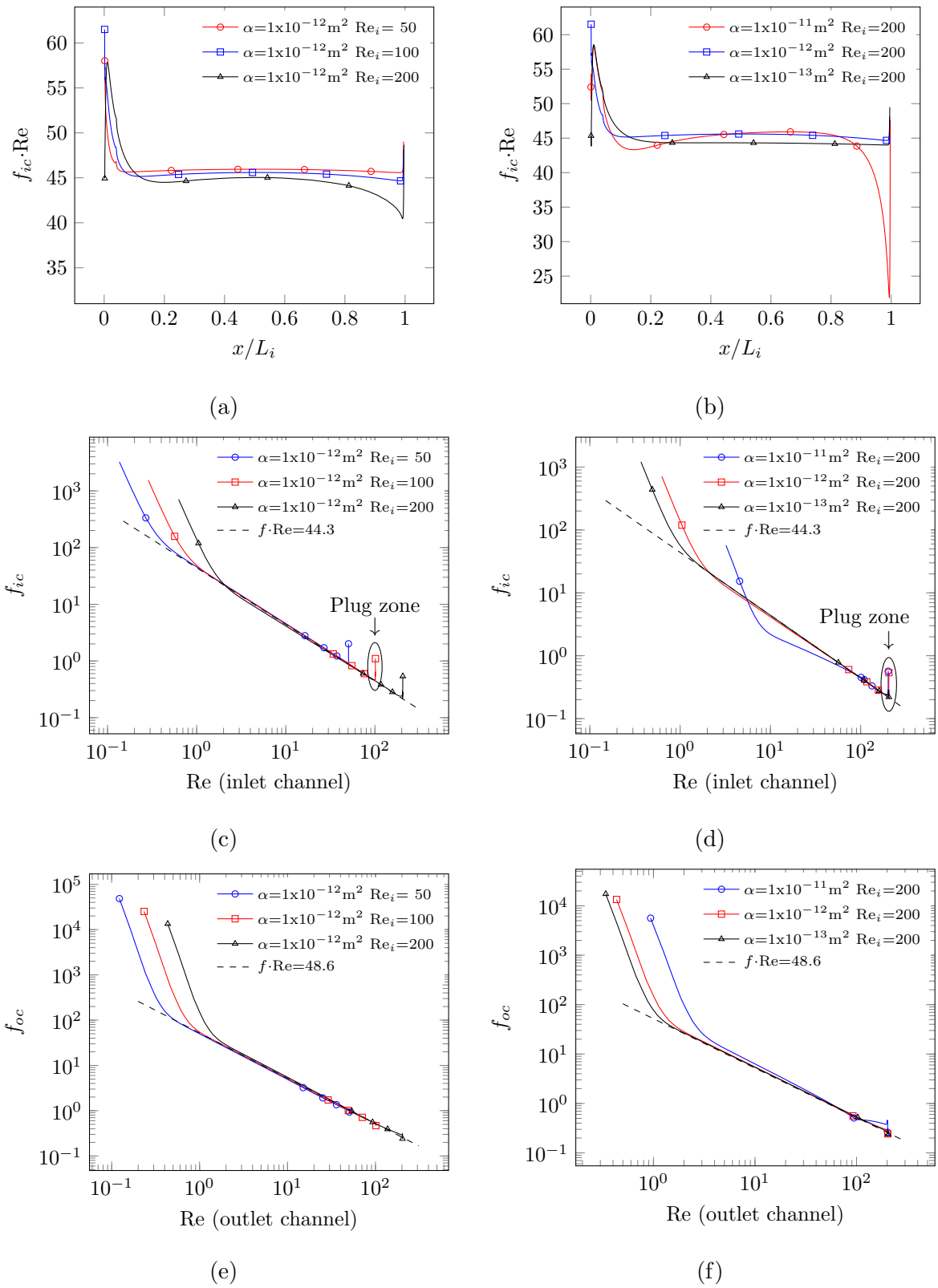

Figure 12.7: Friction factor along an inlet channel for (a) three flow rates and (b) three wall permeabilities. Friction factor as a function of the inlet Re for (c) an inlet channel at three flow rates, (d) an inlet channel at three permeabilities, (e) an outlet channel at three flow rates and (f) an outlet channel for three permeabilities

The error when neglecting the developing zone calculated as $(F_D - \overline{F_D})/\overline{F_D}) \cdot 100\%$ was observed to be below 2% for inlet channel. Nonetheless, this error increases to 10% for outlet channels. The specific values for every case case are shown in Table 12.2. The weight of the developing flow region can be estimated by comparing the friction factor in the developed zone (F_D) and the average friction factor of the entire channel ($\overline{F_D}$).

Table 12.2: Friction factor for an inlet and an outlet channel at several wall permeabilities and flow rates

Channel type	Re_i	α, m^2	F_D	$\overline{F_D}$
Inlet	50	1×10^{-12}	44.3	45.9265
Inlet	100	1×10^{-12}	44.3	45.6082
Inlet	200	1×10^{-12}	44.3	45.0140
Inlet	200	1×10^{-11}	44.3	44.9631
Inlet	200	1×10^{-13}	44.3	44.9546
Outlet	50	1×10^{-12}	48.6	48.7972
Outlet	100	1×10^{-12}	48.6	50.5032
Outlet	200	1×10^{-12}	48.6	53.4094
Outlet	200	1×10^{-11}	48.6	52.8681
Outlet	200	1×10^{-13}	48.6	53.9528

12.5.4 Kinetic energy and momentum flux corrections factors (Δp_{kec})

The mechanical energy redistribution due to the change in the velocity profile is automatically included in 3D models. For 0D and 1D lumped parameter models that do not account for the entrance length in f, it is necessary to add such losses explicitly. In 0D models when gravitational effects are neglected, the energy balance from the front to the rear face of the PF can be written as follows:

$$h_f = \left(p_0 + k_{\alpha_0}\frac{1}{2}\rho_0\overline{u}_0^2\right) - \left(p_L + k_{\alpha_L}\frac{1}{2}\rho_L\overline{u}_L^2\right) \tag{12.9}$$

If the density is almost constant and $\overline{u}_0$ is equal to $\overline{u}_L$, the equation can be reordered as:

$$h_f = (p_0 - p_L) + \frac{1}{2}\rho\overline{u}^2(k_{\alpha_0} - k_{\alpha_L}) \tag{12.10}$$

When the velocity profiles at the inlet and outlet of the analyzed section are identical, then k_{α_0} and k_{α_L} are equal, so, h_f can be calculated as the difference of the static pressure directly. In the case of a PF, the velocity profiles in the inlet and outlet channels are significantly

different; hence, a kinetic energy correction must be considered. The terms k_{α_0} and k_{α_L} in Equation (12.10) account for the extra change in kinetic energy due to the reconfiguration of the flow profile. Typical values for those factors are ≈1 if the velocity profile is flat and ≈2 if it is parabolic. For other shapes, it can be calculated as follows [35, 57]:

$$k_\alpha = \frac{1}{A}\int \left(\frac{u}{\overline{u}}\right)^3 dA \tag{12.11}$$

Figure 12.8 shows the scaled velocity profile at the beginning and end of the filter channels for three wall permeabilities and three flow rates. It can be seen that the influence of both variables on the profile is slight. Table 12.3 shows values of both k_{α_0} and k_{α_L} calculated under several scenarios. According to those values, it is reasonable to assume k_{α_0}=1.35 and k_{α_L}=2.04 as constants.

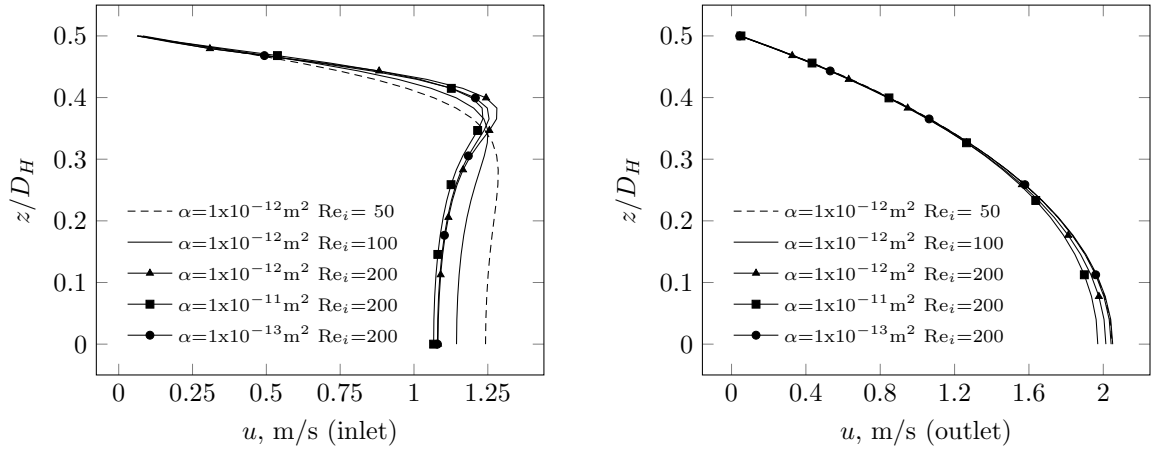

Figure 12.8: Cut of the velocity profiles (a) at the center of the beginning of an inlet channel and (b) at the center of the end of an outlet channel

Table 12.3: Kinetic energy correction factors

Re$_i$	α	k_{α_0}	k_{α_L}
50	1×10^{-12}	1.4041	2.0537
100	1×10^{-12}	1.3526	2.0605
200	1×10^{-12}	1.3433	2.0470
200	1×10^{-11}	1.3262	2.0042
200	1×10^{-13}	1.3456	2.0554

Strictly speaking, the kinetic energy correction is not an energy dissipation; however, it

can represent a significant percentage of the total mechanical energy that is being transferred from the static to the dynamic pressure and must not be neglected. That can be done by adding the term in Equation (12.12) to Δp. It must be pointed out that ρ was not taken as a common factor, because its value can be different at both faces of the filter. k_{α_0} must be multiplied by ρ at the frontal face of the filter, meanwhile, k_{α_L} must be accompanied by ρ at the rear face.

$$\Delta p_{kec} = \frac{1}{2}\overline{u}^2(\rho k_{\alpha_L} - \rho k_{\alpha_0}) \tag{12.12}$$

The previous analysis is a global correction. In axially resolved models, such as in 1D models, this correction can be introduced into the momentum balance directly, by multiplying the convective term by a momentum flux correction factor (k_β). As pointed out by Bissett et al. [34] and Kostoglou et al. [7], this momentum factor should be added because the velocity profile is not uniform inside the channels. Watling et al. [9] provided additional evidence of the effect of such a factor on the estimation of the total pressure drop. They compare the results in both inlet and outlet channel using k_β=1 and k_β=1.377 [9], which correspond to a perfectly flat profile and a fully developed one in a square pipe respectively. In general, k_β can be determined by using Equation (12.13) [57]. In this paper, k_β was computed for several wall permeabilities and flow rates from the 3D CFD results. Table 12.4 shows that the average k_β ($\overline{k_\beta}$) for the inlet channel is slightly higher than that for the outlet channel. Nonetheless, both are only slightly different than that for square pipes with fully developed flow. What should be emphasized is that this correction, which accounts for changes in the velocity profile, is local rather than global, hence, what should be used in the convective term is the local k_β values along the channels. Section S.6 of the supplementary material show curves of k_β along an inlet and outlet channel.

$$k_\beta = \frac{1}{A}\int \left(\frac{u}{\overline{u}}\right)^2 dA \tag{12.13}$$

Table 12.4: Average momentum flux correction terms

Channel	Re_i	α, m^2	$\overline{k_\beta}$
Inlet	50	1×10^{-12}	1.356
Inlet	100	1×10^{-12}	1.357
Inlet	200	1×10^{-12}	1.358
Inlet	200	1×10^{-11}	1.359
Inlet	200	1×10^{-13}	1.362
Outlet	50	1×10^{-12}	1.349
Outlet	100	1×10^{-12}	1.347
Outlet	200	1×10^{-12}	1.341
Outlet	200	1×10^{-11}	1.339
Outlet	200	1×10^{-13}	1.342

12.5.5 Pressure drop when entering and leaving the filter (ΔP_i and ΔP_o)

There are head losses occurring in the frontal and rear faces of the filter. Modeling PFs without including an inlet and an outlet zone can increase the error when it comes to pressure drop. Losses in the frontal face come from friction, the reduction in the flow area and the *vena contracta* effect. According to the results in Figure 12.9a, the *vena contracta* phenomenon is practically nonexistent for the void fraction of typical GPF applications, as in flow-through monoliths [31]. Consequently, most of the entering losses are explained by the flow colliding with the frontal face and the change in flow direction. On the other hand, the head losses at the exit of the PF depend mostly on inertial rather than friction losses, as a jet flow in an open space. Moreover, after the flow leaves the filter, it expands and develops progressively, creating an extensive recirculating zone. Figure 12.9 shows a case with Re_i=300 and α=1×10^{-12} m^2. In this figure, the recirculating zone covers a distance of about 40 D_H from the end of the substrate. A detailed view can be seen in Section 12.7.4 of the supplementary information.

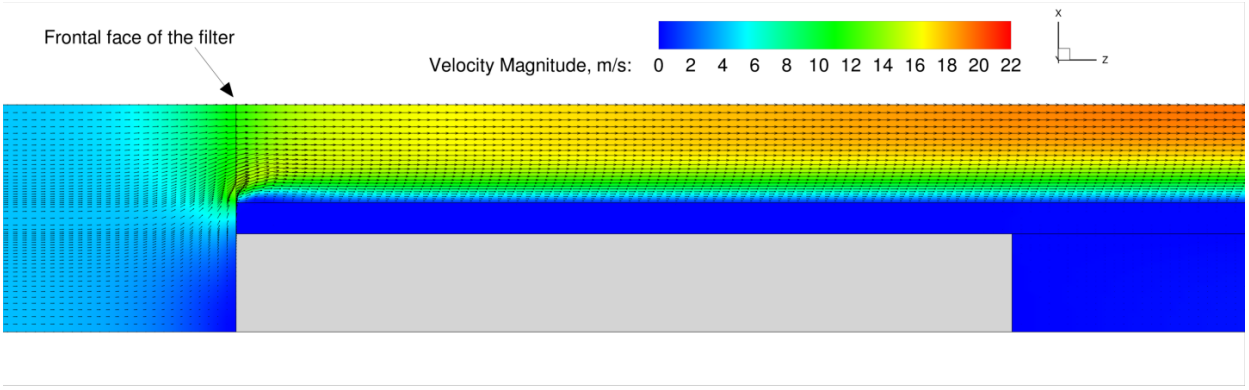

(a)

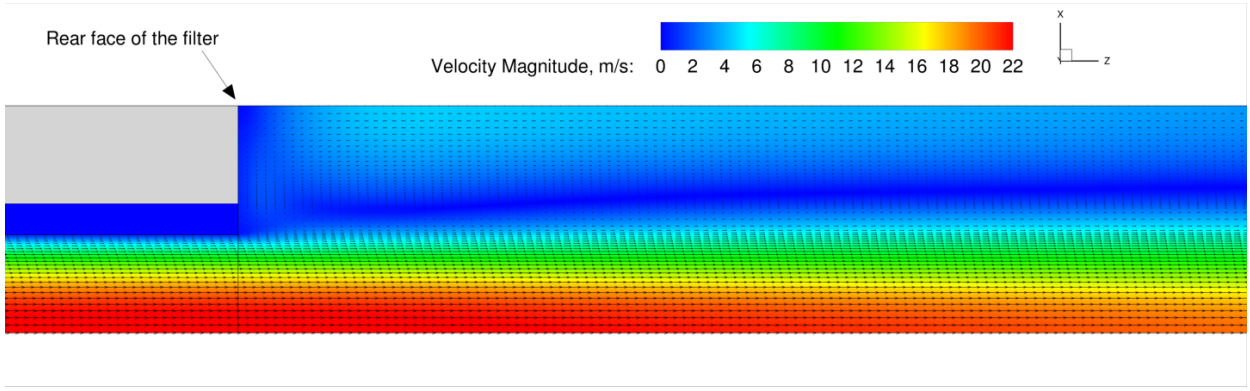

(b)

Figure 12.9: Velocity vectors of flow (a) entering and (b) leaving the filter. Re_i=300, α=1x10^{-12} m^2

Equation (12.14) and (12.15) can be used to model the pressure entering and leaving a PF [31].

$$\Delta p_i = \frac{\mu}{\alpha_{afp}} u_c + \frac{1}{2} C_i \rho u_c^2 \tag{12.14}$$

$$\Delta p_o = \frac{1}{2} C_o \rho u_c^2 \tag{12.15}$$

The term α_{afc} is the apparent face permeability of the frontal face of the filter, meanwhile, C_i and C_o stand for the inertial resistance coefficients at the frontal and rear faces of the filter respectively. In flow-through monoliths the three mentioned coefficients are a function of the open frontal area. However, in a PF, there are at least two additional variables playing a role on their values; Their wall permeability and the wall thickness. The wall permeability is a variable that can vary by orders of magnitude depending on the application; hence, in this paper, what is emphasized is the influence of the wall permeability on Δp_i and Δp_o when both the open frontal area and the wall thickness are fixed.

Figures 12.10a and 12.10b illustrate Δp_i and Δp_o for several flow rates and wall permeabilities. Every data set is accompanied by an individual trend line, which is the result obtained from fitting Equation (12.14) or (12.15) to the corresponding datasets. Δp_i was computed from the 3D CFD data, as the mass-weighted total pressure at the inlet of the domain minus the mass-weighted total pressure at the frontal face of the substrate. It is important to remark that the mass-weighted average is necessary to keep consistence with the momentum balance. Using an area-weighted pressure may lead to a nonphysical negative energy dissipation. Likewise, the total rather than the static pressure drop must be used because of the reduction of the flow area and change in the shape of the velocity profile, as explained in Section 12.5.4.

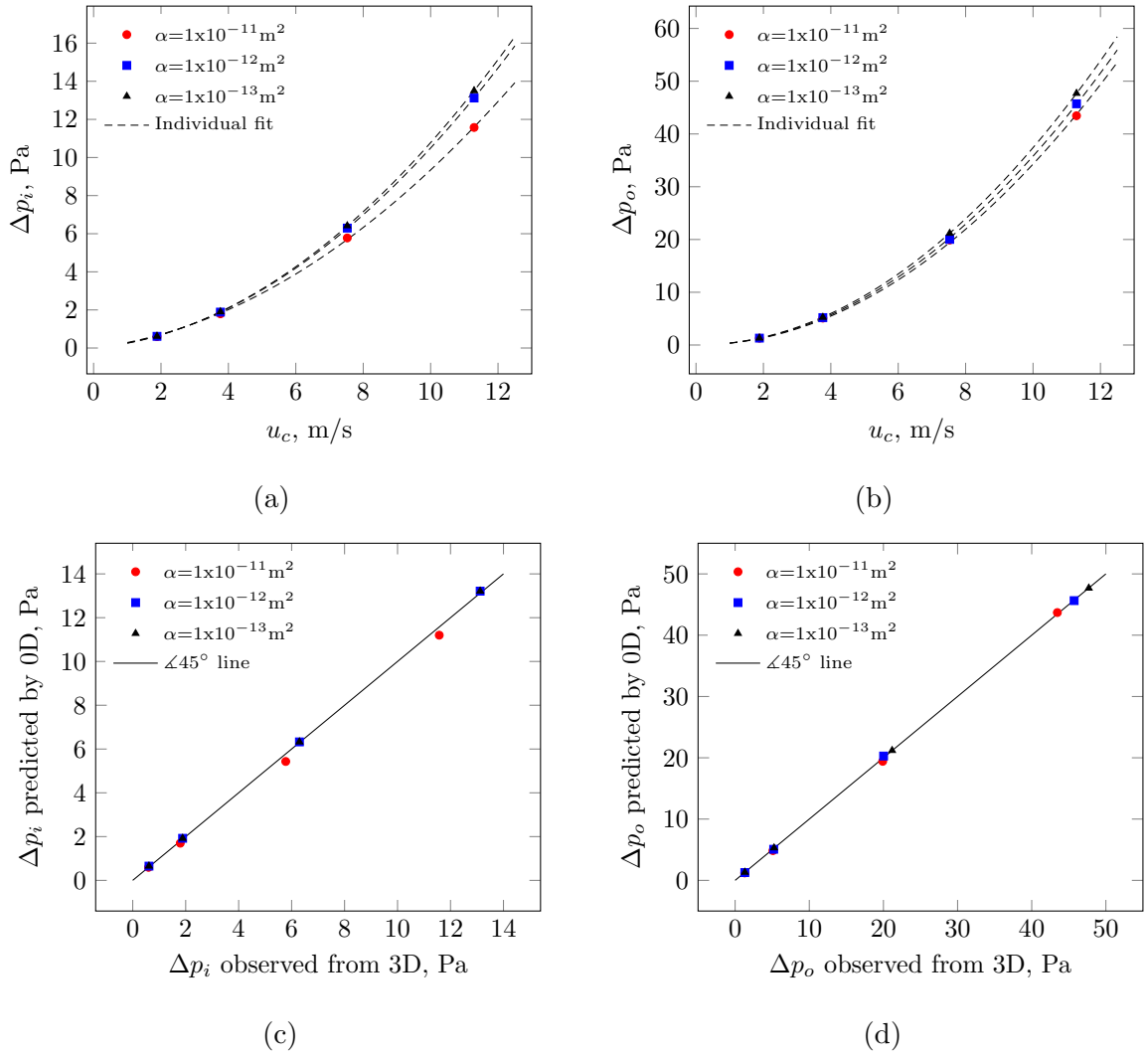

Figure 12.10: Pressure drop for flow (a) entering and (b) leaving a 300/8 filter. Parity plot for flow (a) entering and (d) leaving the filter

It can be seen by comparing Figure 12.10a and 12.10b that Δp_i is significantly lower than Δp_o, similar to what is observed in flow-through monoliths. It can be also seen that the sensitivity of Δp_i to the wall thickness differs from that of Δp_o, hence, lumping the two terms in a single one ($\Delta p_{i/o}$) is discouraged. Δp_i and Δp_o scale differently with the wall permeability and flow rate, hence, grouping them would lead to very specific model parameters for every filter configuration and operating condition.

Three Δp_i curves for three wall permeabilities are shown in Figure 12.10a. Every curve is accompanied by an individual fitting. The three curves follow practically perfectly (R^2=1.000) the mathematical shape of Equation (12.14). That is, a second order equation, with a linear and a quadratic term, and with an intercept in the origin. Equation (12.14) differs from current models in the literature, which are purely quadratic and use only one parameter. Certainly, adding an additional parameter to any model would increase the resulting R^2 and may lead to an over-fitting problem. Hence, in this paper, the statistical significance of both parameters in Equation (12.14) was extensively reviewed, and models with one and two parameters were compared. The details are included in Section 12.7.6 of the supplementary material. From them, it can be strongly concluded that Equation (12.14) is correct and that two parameters are required to model Δp_i. The same analysis was done for Δp_o, concluding that Equation (12.15) is sufficient, and increasing the number of parameters in that case effectively led to over-fitting. Table 12.6 summarizes the coefficients obtained from the individual fittings.

Table 12.5: Model parameters for Equation (12.14) and (12.15)

α, m^2	α_{afc}, m^2	C_i	C_o
1×10^{-11}	1.3303×10^{-4}	0.2363	1.1280
1×10^{-12}	1.6590×10^{-4}	0.2883	1.1777
1×10^{-13}	1.7899×10^{-4}	0.3017	1.2307

It is important to remark that the contribution of the linear term to Δp_i is significant and should not be neglected. That can be corroborated in Table 12.6, which summarizes the contribution of each term of Equation (12.14) to Δp_i. The table also includes the losses that occur when entering and leaving the filter observed from the 3D CFD results and predicted from Equation (12.14) and (12.15). An equivalent analysis was done for Δp_o using the data in Figure 12.10b. A perfect agreement (R^2=1.000) between the data and the Equation (12.15) was reached by using a purely quadratic dependency on the velocity, that is, with only one model parameter, in a similar manner to other models available in the literature, e.g. Cornejo

et al. [31]. Some other comparisons between a flow-through and a wall-flow substrate can be found in Dardiotis et al. [58] and Knoth et al. [59].

Table 12.6: Δp_i and Δp_o for several flow rates and wall permeability

u_c, m/s	α, m^2	$\Delta p_i^{\dagger}$, Pa	$\Delta p_o^{\dagger}$, Pa	μ/α_{afp}, Pa	$1/2\rho C_i v_c^2$, Pa	$\Delta p_i^{\dagger\dagger}$, Pa	$\Delta p_o^{\dagger\dagger\dagger}$, Pa
1.88	1×10^{-11}	0.5965	1.2921	0.3402	0.2544	0.5946	1.2137
3.76	1×10^{-11}	1.7956	5.1002	0.6804	1.0176	1.6980	4.8548
7.53	1×10^{-11}	5.7781	19.9029	1.3607	4.0704	5.4311	19.4193
11.29	1×10^{-11}	11.5748	43.4563	2.0411	9.1584	11.1995	43.6934
1.88	1×10^{-12}	0.6140	1.3061	0.3402	0.3103	0.6505	1.2678
3.76	1×10^{-12}	1.8844	5.1965	0.6804	1.2412	1.9216	5.0711
7.53	1×10^{-12}	6.2952	20.0213	1.3607	4.9648	6.3255	20.2844
11.29	1×10^{-12}	13.1201	45.7213	2.0411	11.1707	13.2118	45.6400
1.88	1×10^{-13}	0.6168	1.3141	0.3402	0.3247	0.6649	1.3243
3.76	1×10^{-13}	1.9012	5.2464	0.6804	1.2988	1.9792	5.2970
7.53	1×10^{-13}	6.4167	21.1701	1.3607	5.1953	6.5560	21.1881
11.29	1×10^{-13}	13.5027	47.6939	2.0411	11.6894	13.7305	47.6733

†From the 3D CFD results. ††From Equation (12.14). †††From Equation (12.15).

There is a specific value of α_{afp} and C_i for every curve in Figure 12.10a, together with a specific value for C_o in Figure 12.10b. That means that those parameters can be written as a function of the wall permeability. Unfortunately, it was not possible to find a suitable model for α_{afp}. Therefore, the average value of α_{afc} of 1.3951×10^{-4} m^2, from fitting the curves with three wall permeabilities, was assumed. Meanwhile, Equation (12.16) and (12.17) were proposed for both inertial losses coefficients. Detailed values of the parameters obtained from every individual fit, together with statistical proofs of the mathematical shape of both models are shown in Section 12.7.6 of the supplementary information. As previously mentioned, α_{afc}, C_i and C_o should also be a function of the filter void fraction and wall thickness, however, those variables were not analyzed in this paper because such an investigation increases by several times the number of computational experiments required. That will be addressed in a further dedicated paper.

$$C_i = -2.098 \times 10^5 \cdot \alpha^{0.5888} + 0.3064 \tag{12.16}$$

$$C_o = 0.6983 \cdot \alpha^{-0.01893} \tag{12.17}$$

The coefficients C_i and C_o together with an α_{afp} of 1.3951×10^{-4} m^2, can be substituted into Equation (12.14) and (12.15) to estimate Δp_i and Δp_o. Using such equations and 3D CFD data, Figure 12.10c and 12.10d compare the predicted pressure drop when entering and leaving a PF. The figures demonstrate that the model has a very good agreement for all of the flows and wall permeabilities analyzed, having a maximum relative error below the 5%.

12.5.6 Wall-flow analysis

The wall-flow velocity (u_w) is one of the most important variables used to describe a particle filter. It determines the capture efficiency and back-pressure. In 0D models, the total pressure drop because of the flow passing through the porous walls is usually estimated using Darcy's law, as follows:

$$\Delta p_w = \frac{Q_f \mu L_w}{\alpha A_f} \tag{12.18}$$

Replacing the volumetric flow rate filtered by Q_f=$u_c D_H^2$, the total filtrating area by A_f=$4L''_f D_H$ and gives:

$$\Delta p_w = \frac{D_H \mu L_w}{4\alpha L''_f} u_c \tag{12.19}$$

In 1D models, the wall velocity can be calculated as u_w=$\alpha(p_{ic}$-$p_{oc})/(\mu L_w)$ [32]. Usually, the wall-flow velocity is non-dimensionlized as Re_w=$\rho u_w D_H/\mu$. It is well established in the literature that the Re_w profile along the channels has a sort of U-shape [20, 26, 29, 60]. Similar results were obtained in this investigation. Figure 12.11a shows Re_w for three permeabilities. Each point of the curve was calculated from a mass balance between two channel cross-sections, separated by 58 μm, which is the size of the mesh elements in the axial direction. It can be seen in the figure that the lower the permeability the flatter the Re_w profile. That effect has been previously reported in the literature, for example, in Haralampous et al. [29], where the wall permeability changes because of soot deposition. The average Re_w remains constant for the three curves, because it is given by the flow rate entering the filter, which is the same for the three curves. What is noticeable is that for the lowest permeability, the Re_w profile is almost flat. Meanwhile, when increasing the permeability, the curve becomes more concave, having progressively higher maxima at both channel ends, together with a lower minimum. Furthermore, Figure 12.11b clearly shows that as the flow rate increases, the average Re_w also increases, being every curve more concave, but, not to the point to overlap the others.

The flow around the perimeter of a cross-section of the channels was also analyzed (see L_4 in Figure 12.2). According to the results, the radial gradient of the static pressure in a channel cross-section is negligible. Nevertheless, the dynamic component and other phenomena such as the secondary flow reduces the wall-flow in the corners of the channels [36]. That can be seen in Figure 12.11c, where u_w=u_y. Each curve represents the velocity profile of the flow through a porous wall moving upwards from an inlet to an outlet channel at several axial positions. First, it is observed that in the axial direction the average u_y decreases and then increases, consistently with the pattern in Figure 12.11a and 12.11b. Second, there is effectively a reduction of the wall-flow at the corners. The magnitude u_y changes consistently along the channel, maintaining a constant shape of the dimensionless velocity profile. That can be seen clearly in Figure 12.11d, where every velocity profile of Figure 12.11c was scaled by their respective maximum, including the very ends of the non-plugged part of the filter. The same phenomenon was observed for all the other cases covered in this study. Figure 12.11e shows the mentioned scaled wall-flow profile for other permeabilities and flow rates. It can be seen that the shape of the scaled velocity profile is insensitive to changes in those variables also.

Another matter of discussion regarding the wall-flow is the axial velocity right at the surface of the porous wall (L_2 in Figure 12.2). Usually, a no-slip condition is assumed when solving a channel model. However, it may impact the solution significantly. According to Beavers et al. [61], flow through parallel coupled porous walls shows a slip-velocity. More information about this phenomenon can be found in Sahraoui and Kaviany [62] and Ochoa-Tapia and Whitaker [63]. In this paper results similar to those from Beavers et al. [61] were obtained. Some other experiments reporter in York et al. [64] provide a very detailed visualization of the axial and through wall flow along a filter, however, due to the degree of resolution required, it is still very challenging to conclude from there an accurate surface velocity. As shown in Figure 12.11f, there is a slip velocity along the channel, that velocity increases together with the flow rate and it is only slightly sensitive to the wall permeability. It should also be mentioned that during the grid analysis a numerical instability of the radial velocity was detected in the near wall. It did not affect the axial velocity profiles, wall-flow or pressure profiles. However, it was included in Section 12.7.2 of the supplementary material, for completeness. Such surface phenomena may not be correctly described by the porous zone model used in this paper. That can be better addressed at a pore scale. There has been substantial research in such topic [11, 12, 18]. Unfortunately, having such a model for a significant length of a channel is still beyond the current computational power for systematical research.

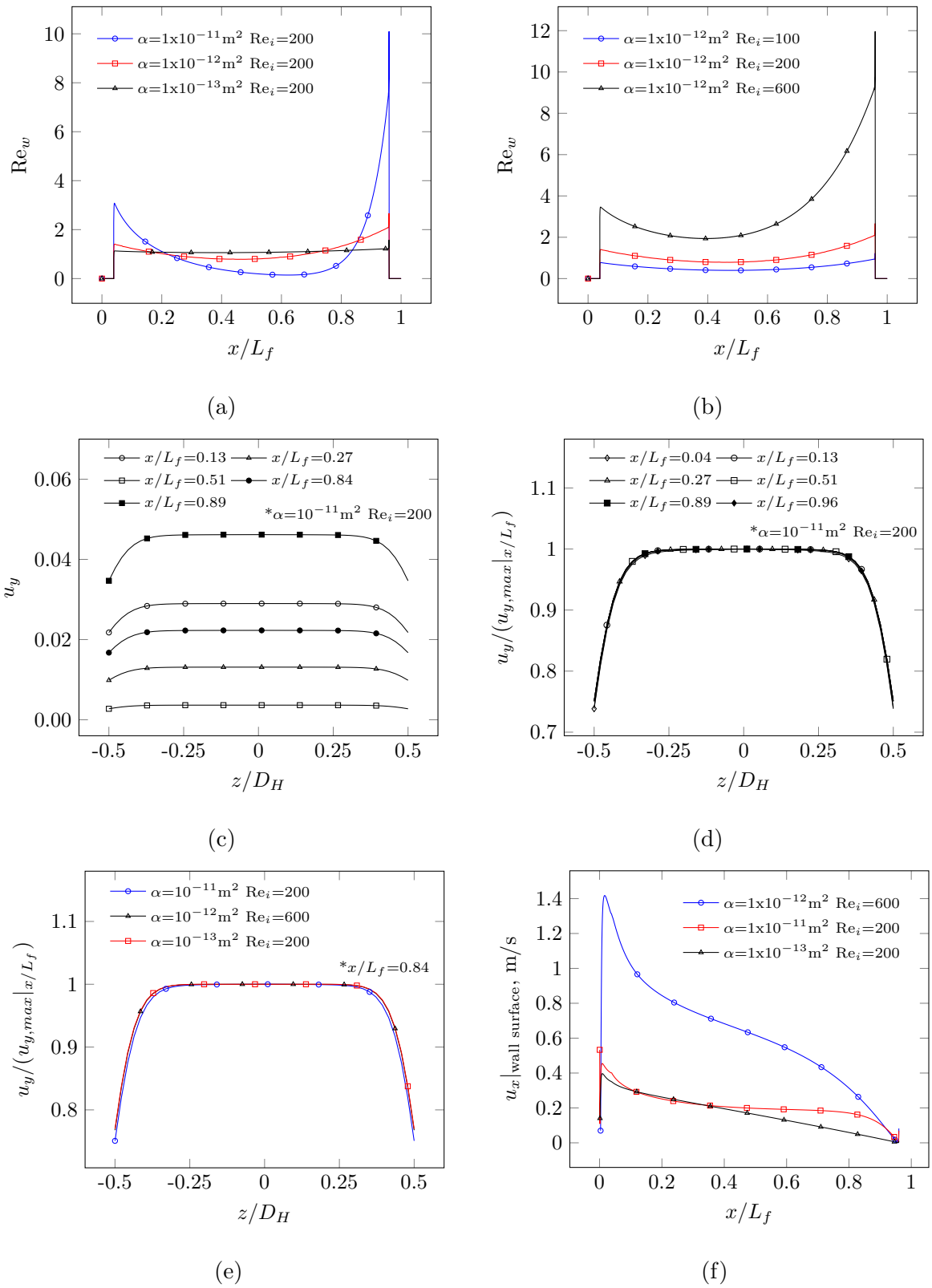

Figure 12.11: Sensitivity of the Wall-flow along the filter to (a) the wall permeability and (b) the flow rate. (c) Wall-flow along the perimeter of several channel cross-sections, (d) scaled wall-flow and (e) scaled wall-flow for several permeabilities and flow rates. (f) slip velocity along an inlet channel

12.5.7 Final pressure drop model

Having defined the expressions for every part of the model and grouping Equation (12.4), (12.12), (12.14), (12.15) and (12.19), Equation (12.2) can be re-called and written in an expanded form as follows:

$$\Delta p = \underbrace{\frac{\mu}{\alpha_{afc}} u_c}_{\Delta p_{i,1}} + \underbrace{\frac{1}{2}\rho C_i u_c^2}_{\Delta p_{i,2}} + \underbrace{\frac{L'_f F_D \mu}{2D_H^2} u_c}_{\Delta p_f} + \underbrace{\frac{D_H \mu L_w}{4\alpha L''_f} u_c}_{\Delta p_w} + \underbrace{\frac{1}{2}\rho C_o u_c^2}_{\Delta p_o} + \underbrace{\frac{1}{2} u_c^2 (\rho k_{\alpha L} - \rho k_{\alpha 0})}_{\Delta p_{kec}} \quad (12.20)$$

The linear and quadratic parts of the term Δp_i in Equation (12.20) were separated into $\Delta p_{i,1}$ and $\Delta p_{i,2}$ respectively for further analysis. The term α_{afc} α_{afc} is assumed to be constant and equals to 1.3951×10^{-4} m^2 because its relationship with the main structural features of a filter has not been found yet. ρ in $\Delta p_{i,2}$ should be the inlet density. C_i comes from Equation (12.16), which is sensitive to the wall permeability, but it still need to be expanded to consider the open frontal area and wall thickness.

The contribution from the inlet and outlet channels were grouped together in the term Δp_f=$\Delta p_{f_{ic}}$ + $\Delta p_{f_{oc}}$, and the friction factor F_D is the average between those from the inlet (44.3) and outlet (48.6) channels. Notwithstanding, for asymmetric channel filters, the contribution of inlet and outlet channels should be calculated separately, using the corresponding D_H and F_D for every case [65–67]. Values of F_D for simple shapes and fully developed flow from the literature can be used. However, further investigation to find more representative values is recommended. Furthermore, the term L'_f represents the effective length of the channels, which is the length of the filter minus the length of the plug.

The term L''_f in Δp_w is the effective length of the filtrating part of the substrate. That is, the length of the filter minus two times the length of the plug. The length of the plugs should not be neglected because it can lead to a significant error in the filtrating area, therefore in Δp.

The value of C_o for Δp_o can be computed from Equation (12.17). Similarly to the case when the flow is entering the filter, an expression for C_o as a function of the open frontal area and wall thickness will be developed in a further paper. ρ in Δp_o should be the one at the exit face of the filter.

For the kinetic energy correction (Δp_{kec}), the terms k_{α_0} and k_{α_L} are 1.35 and 2.04 respectively, and proved to be relatively insensitive to the flow rate. Values for other open frontal

areas should be investigated, however, the largest change, if there is, should be related to $k_{\alpha 0}$. What can change the value of both constants is the shape of the cross-section of the channels, especially for non-symmetric filters, in such a case, the average velocity will also be different at the two faces of the substrate.

Equation (12.20) was derived from data at channel scale, and it demonstrates a remarkably good agreement with the global experimental data (see Figure 12.4). The largest deviation from the 0D pressure drop model developed and the experimental data was observed in the region of high flow, where possible unsteady laminar or turbulent flow is produced. In such condition, fundamental assumptions are no longer valid and average values for F_D are no longer representative. That region should be treated carefully, especially when back-calculating parameters, to avoid introducing error in the parameters of interest, Nonetheless, Equation (12.20) is still highly predictive in high flow region, which speaks well to its utility. Furthermore, Equation (12.20) can be compared to a substantially validated model, such as the one presented in Konstandopoulos et al. [27, 53]:

$$\Delta p = \underbrace{\frac{1}{3}\frac{L'_f F_D \mu}{D_H^2} u_c}_{\Delta p_f} + \underbrace{\frac{D_H \mu L_w}{4\alpha L''_f} u_c}_{\Delta p_w} + \underbrace{\frac{1}{2}\zeta \rho u_c^2}_{\Delta p_{i/o}} \tag{12.21}$$

Usually, Equation (12.21) is written using the Fanning version of the friction factor, in such cases the 1/3 in front of Δp_f have to be replaced by a 2/3. It is also mentioned in Konstandopoulos [27] that the length of the plug must be subtracted to L_f in Δp_f. Hence, for this paper, it was assumed that L''_f should be used instead of L_f in Δp_w in Equation (12.21). Otherwise, a significant error is introduced in the filtration area, therefore, in Δp_w and Δp. Finally, it must be noticed that by grouping together the quadratic terms of Equation (12.20) and comparing them to the $\Delta p_{i/o}$ in Equation (12.21), we obtain:

$$\zeta \frac{1}{2}\rho u_c^2 = \left[C_i + C_o + (k_{\alpha L} - k_{\alpha 0})\right] \frac{1}{2}\rho u_c^2 \tag{12.22}$$

therefore:

$$\zeta = C_i + C_o + (k_{\alpha L} - k_{\alpha 0}) \tag{12.23}$$

Evaluating Equation (12.23) at a void fraction of 0.372; which is the one of the substrate analyzed in this paper; and a wall permeability of 1×10^{-12} m^2, gives ζ=2.12. This value is fairly similar to 2.2, which was obtained experimentally by Konstandopoulos et al. [15], using the same void fraction and a similar wall permeability. This, in turn, explains the good agreement of (12.21) with experimental data as shown in Figure 12.4. Accordingly, the

main difference between Equation (12.20) and (12.21) is that in the latter ζ must be fitted from experimental data or CFD for every case. As shown previously, Δp_i, Δp_o and Δp_{kec} scale differently when changing the flow rate and wall permeability, hence, ζ is to a large extent specific for every case. In Equation (12.20) C_i, C_o and Δp_{kec} were predicted from a channel scale data without requiring experiments. Even if there are still some elements of curve fitting and other minor simplifications in obtaining C_i and C_o, the model in Equation (12.20) can be considered to be a fundamental formulation. Indeed, it is the most physics based and least empirical model for pressure drop in a PF that has appeared in the literature to date.

Summarizing, for a given filter with known geometrical features, what is necessary to find out are the parameters α_{afc}, C_i, C_o, F_D and k_α to be used in Equation (12.20). If explicit functions for them are not available, then, they can be obtained from a channel scale 3D CFD simulation, following the same procedure show in this paper. If the wall permeability is not known, then, it can be back-calculated from global experimental data. In such a case, the experiment must be carefully designed, setting conditions favourable to reduce the error in the back-calculated α, as discussed in Section 12.5.8. Alternatively, experimental data can be used together with Equation (12.21) to back-calculate ζ. That, would compromise the capacity of the model to extrapolate results, but, it is necessary because deriving all the parameters individually from experiments presents several practical unsolved challenges. If the permeability is also unknown, then the two parameters must be fitted simultaneously. Unfortunately, F_D and the wall permeability are statistically correlated, hence, it will not be possible to know with certainty which of them is affected by the estimation error of the other. Experiments have the advantage to come from the actual filter, but the drawback of adding leading to correlated results. In simple words, there will always be a parameter that matches the model with the experiments. On the other hand, CFD channel scale data is blind from the experiments and provides uncorrelated data.

12.5.8 Δp breakdown and back-calculation of α

Table 12.7 shows the individual contribution of every component of Equation (12.20) to Δp for several scenarios.

Table 12.7: Percentage contribution of every component of Equation (12.20) to Δp for flow through a 300/8 filter (D_H=1.26 mm, L_w=0.2 mm, T=573 K)

N	Re_i	α, m^2	L_f, in	Δp, Pa	$\Delta p^{\dagger}_{i,1}$	$\Delta p^{\dagger}_{i,2}$	$\Delta p^{\dagger}_{f}$	$\Delta p^{\dagger}_{w}$	$\Delta p^{\dagger}_{o}$	$\Delta p^{\dagger}_{kec}$	$p^{\dagger,\dagger\dagger}_{L}$
1	10	1×10^{-11}	5	21.1	0.4	0.0	96.5	2.8	0.2	0.1	99.6
2	50	1×10^{-11}	5	107.4	0.4	0.2	94.9	2.7	1.1	0.7	98.0
3	500	1×10^{-11}	5	1269.0	0.3	2.0	80.3	2.3	9.5	5.5	82.9
4	1000	1×10^{-11}	5	2970.9	0.3	3.4	68.6	2.0	16.3	9.4	70.9
5	500	1×10^{-12}	5	1542.4	0.3	2.0	66.1	18.9	8.2	4.5	85.3
6	500	1×10^{-12}	4	1431.5	0.3	2.2	50.6	33.3	8.8	4.9	84.1
7	500	1×10^{-12}	3	1482.7	0.3	2.1	34.4	50.0	8.5	4.7	84.7
8	500	1×10^{-12}	2	2170.7	0.2	1.4	13.8	75.6	5.8	3.2	89.5
9	50	1×10^{-12}	2	196.6	0.2	0.2	15.2	83.4	0.6	0.4	98.8
10	500	1×10^{-13}	5	4173.9	0.1	0.8	24.4	69.9	3.2	1.7	94.4
11	500	1×10^{-14}	5	30423.6	0.0	0.1	3.4	95.8	0.5	0.2	99.2

† Values in %. †† Combined contribution of all the linear terms (p_L=$\Delta p_{i,1}$+Δp_f+Δp_w)

One of the main uses of filter models is to estimate the wall permeability based on measurements of the total filter pressure drop [68]. From a statistical standpoint, it is desirable to use a set of experiments in the region in which the sensitivity of the pressure drop to the wall permeability is as high as possible to minimize the estimation error. That is, looking for the conditions where the contribution of Δp_w is high. In Table 12.7 it seems evident that the more permeable the filter, the harder it to back-calculate the wall permeability accurately. However, other variables can be manipulated in favor of the reliability of the result. One is the filter length, which has a significant impact on the relative contribution of the porous wall (Δp_w). Therefore, when back-calculating the wall permeability based on global results, a short rather than a long filter is highly recommended. Moreover, regarding the flow rate, its increase modifies the contribution of Δp_w only slightly, however, it increases the percentage contribution of Δp_o and the magnitude of Δp_{kec} significantly. Hence, a low flow should me preferred.

There is an easy form to understand the weight of every part of the model on Δp. For instance, it can be seen that the addition of Δp_w and Δp_f in case one and nine of Table 12.7, which uses a very low flow, reaches about 99% of Δp, therefore:

$$\Delta p \approx \Delta p_f + \Delta p_w \tag{12.24}$$

or

$$\lambda_w = \frac{\Delta p_w}{\Delta p_f} = \frac{D_H^3 L_w}{2\alpha L'_f L''_f F_D} \tag{12.25}$$

One can notice immediately that the flow rate does not affect the value of λ_w (it should be emphasized that Equation (12.24) is valid only at a sufficiently low flow). In the meantime, as the flow rate decreases F_D is better estimated by $\overline{F_D}$, decreasing the approximation error. For the case five of Table 12.7, λ_w is 0.286, which means that an error of the 10% in F_D, or in any other parameter, will be translated into an error of about 35% in a back-calculated the α value. This issue can become much more critical in case three of the table, where the same 10% error in F_D translates into 350% error in α. On the other hand, case nine shows a λ_w of 5.48, which damps significantly the propagation of the error in any parameter to the value of a back-calculated α. Other favourable conditions to be considered are using a higher D_H, L_f, and L_w, a shorter plug and having a better estimation of F_D.

12.5.9 Final comments

The flow phenomena within a PF are very complex, which gives difficulty in developing reliable pressure models. Most of the assumptions are mentioned in Section 12.2 were discussed in this paper. The following is a summary of such analysis.

i. The flow is incompressible: First, it should be reminded that incompressible fluid means that ρ is constant, meanwhile, incompressible flow means $\nabla \cdot u_i$=0. An incompressible fluid will lead always to incompressible flow. However, depending on the Mach number (M), a compressible fluid can behave either as a compressible flow (M>0.7) or as an approximately incompressible one (M<0.3). Not surprisingly, in this work the flow is actually incompressible, meanwhile, the density changes with the absolute pressure according to the ideal gas law. Both points are important for the treatment of the balances in, for example, 1D models. While a high M is not common in automotive applications, the density requires more attention. If Δp is lower than 10 mbar, then the error in the density will be lower than 1%. That will affect mainly the quadratic losses ($\Delta p_{i,2}$, Δp_o, Δp_{kec}). This has been previously discussed in Watling et al. [9].

ii. The velocity profile entering an inlet channel is flat: Assuming a flat inlet velocity profile can lead to a significant error, especially at a high flow rate and when the percentage open frontal area is low. In 3D simulations, it is encouraged to include an open zone upstream the frontal face of the filter, to account for a realistic inlet velocity profile. In 0D and 1D models, the corresponding kinetic energy or momentum flux corrections must be applied.

iii. The flow inside the filter is fully developed: It is not trivial to analyze the development of the flow inside a single channel of the filter because of the wall-flow. From an hydrodynamic standpoint, based on the behavior of $f{\cdot}\mathrm{Re}$, the inlet channels have an hydraulic entrance length at, then a zone where $f{\cdot}\mathrm{Re}$ is approximately constant, then, what can be seen as a hydraulic ending length. For the outlet channels, the analysis is more complicated because the inlet is plugged, but there is flow entering by the radial direction, meanwhile, the mainstream is axial. And yet, that is not granted when there is reverse flow inside the channels. Notwithstanding, the flow should not be considered fully developed, an average $f{\cdot}\mathrm{Re}$ can be considered in simulations.

iv. The friction factor is equal to the one for a closed square pipe with fully developed flow: In the same line of the previous point, in the zone of the channel with $f{\cdot}\mathrm{Re}$ approximately constant, it was found to be 44.3 and 48.5 for the inlet and outlet channel respectively. That is a difference of the 24% and 17% when compared to the 56.9 for square pipes.

v. The friction factor is a function of the wall Reynolds number: By analyzing Figure 12.11b it can be seen that as the flow rate increases, the average and local Re_w also increases. On the other hand, Figure 12.7a does not show such an increase in $f{\cdot}\mathrm{Re}$, at least in the fully developed region. Hence, an evident relationship between Re_w and $f{\cdot}\mathrm{Re}$ was not observed in this study.

vi. The radial pressure gradient inside the channels is negligible: According to the results, there is not a significant pressure gradient in the radial direction inside the channels (see Figure S.5 and S.11 of the supplementary material).

vii. The radial density and velocity gradients are negligible inside the porous wall: It was observed from the results that the velocity gradient does not change in radial direction. That has been discussed in the literature at a wall scale in [11]. The density changes according to the pressure, hence, for a very low wall permeability, the gradient of density in the radial direction can be significant inside the wall.

viii. The wall-flow is constant: There is a discussion among the community when defining if this refers to the wall-flow along the perimeter of a channel cross-section or if it is constant in the axial direction. It is well established in the literature that the wall-flow has a U-shape in the axial direction. Regarding the perimeter of a channel cross-section, the results showed that the wall-slow has also a sort of U-shape consistently along the entire channel, being the radial velocity lower in the near-corner regions.

ix. No-slip velocity in the surface of the porous wall: According to the results, the axial velocity in the surface of the porous wall is not zero, and it is related to the remaining flow rate inside the channels. This agrees with the literature. However, this should be corroborated at a wall scale, due to the limitations of the Darcy law approach to represent a non-smooth surface.

x. The flow that enters and leaves the filter through the porous walls is negligible: According to the results, the flow entering and leaving the filter through the frontal and rear faces of the porous walls is less than the 1% of the total one.

xi. Darcy's law models the flow through the porous walls: Konstandopoulos et al. [28] demonstrated that the effects of the Forchheimer term is minimum at the flow rates in typical PFs.

xii. Laminar steady flow prevails inside of the channels: It is widely assumed that the flow inside a filter is laminar steady. However, this should be addressed in a further investigation, since the literature about the influence of the upstream turbulence entering honeycomb type substrates indicates that there might be a transition from a turbulent to laminar regime that leads to unsteady laminar flow in the rest of the channel [69].

12.6 Conclusions

The pressure drop and flow in a wall-flow particulate filter was successfully studied using a channel scale 3D CFD model. The computational model was validated with both experiments and data in the literature. The flow entering passing through and leaving the filter was analyzed in detail and comprehensively. New models for the pressure drop in every part of the filter and for the most relevant dimensionless numbers were presented. The following are the most significant conclusions drawn.

Describing accurately the flow inside the filter requires substantial grid resolution in both axial and radial direction. In radial direction for the developing of the axial velocity profile and in axial direction for the wall-flow profile. Among the variables analyzed, the pressure profile was the most sensitive to the grid quality. Meanwhile, the wall-flow was the least sensitive, therefore, the least recommended to state the grid independence of the solution.

Although the contribution of Δp_i to the total pressure drop is relatively small, the computational domain must include the open area before the filter to account for a realistic

inlet velocity profile and flow development along the filter. On the other end, there were no up-winding effect from the open section after the filter affecting what happens inside it. However, Δp_o can be a significant percentage of the total pressure drop, hence, that area must be also included in the domain, and considered in the experiments.

Although the average fluid velocity charges continuously in both the inlet and outlet channels, the flow can be considered as fully developed using a new criterion. This criterion states that fully developed flow occurs when the dimensionless velocity profile becomes constant. This profile is define by the local velocity at any radial point (at a fixed axial coordinate) divided by the maximum axial velocity at that axial position.

The friction factor coefficient (F_D) for the flow in the filter channels is not constant, but varies with the position and is different for the inlet and the outlet channels. Notwithstanding, the value is reasonable constant over a significant portion of the channel, where the flow can be considered to be fully developed. The average over this fully developed region is less than the commonly used value obtained for fully developed flow in square channels with non-porous walls. The zone with non-developed flow was small compared to the total length of the channels. However, it increased when increasing the flow rate or the wall permeability. There might be a limit from where the flow is never developed, there is reverse flow in a significant part of the filter or the flow becomes unsteady. The friction factor in such conditions can be significantly different and should be investigated.

The wall-flow showed non-homogeneous along the perimeter of a channel cross-section. When scaling the profiles from several axial positions, a consistent shape was observed along the entire filter, for all the wall permeabilities and flow rates analyzed. That profile had a sort of U-shape, with lower radial flow in the corners of the channels and flat in the center.

A new fundamental 0D pressure drop model has been built and validated. This model is useful to back-calculate wall permeability from total pressure drop data and experiments are not necessary. What remains pending, is the corroboration of the model for filters with different geometrical features, such as the open frontal area, channel size and wall thickness. In the proposed model, the total pressure drop is the summation of inlet and outlet effects, losses from flow in the two channels, losses from flow across the porous wall, and losses from profile rearrangement. A new correlation to calculate pressure losses of flow entering the filter is proposed. The new expression allows us to decouple linear and quadratic effects that were statistically confused in other parameters in previous models. The new model also in-

cludes a kinetic energy correction that accounts for the developing of the flow inside the filter.

According to the 3D CFD data and the proposed model, the relative importance of each phenomenon to the total pressure drop depends strongly on both the filter configuration and the operating conditions. That is of great importance when using the model to back-calculate values, such as the wall permeability. By using convenient operating conditions the error in the estimation of the wall permeability from global data can be reduced significantly. Otherwise, experiments can be unintentionally performed in a region that amplifies the estimation error by orders of magnitude.

Acknowledgemets

I. Cornejo acknowledges the receipt of a Becas-Chile (CONICYT) scholarship. Other funding was provided by the Natural Sciences and Engineering Research Council of Canada. This research was enabled in part by support provided by Compute Ontario (www.computeontario.ca) and Compute Canada (www.computecanada.ca).

Conflict of Interest

The authors declare no conflict of interest.

Bibliography

[1] Jun Yang and Hao Sun. Battery swap station location-routing problem with capacitated electric vehicles. *Computers and Operations Research*, 55:2017–232, 2015.

[2] Oscar Van Vliet, Anne Sjoerd Brouwer, Takeshi Kuramochi, Machteld van Den Broek, and André Faaij. Energy use, cost and CO2 emissions of electric cars. *Journal of Power Sources*, 196(4):2298–2310, 2011.

[3] Richard Schmuch, Ralf Wagner, Gerhard Hörpel, Tobias Placke, and Martin Winter. Performance and cost of materials for lithium-based rechargeable automotive batteries. *Nature Energy*, 3(4):267–278, 2018.

[4] Ameya Joshi and Timothy Johnson. Gasoline particulate filters—a review. *Emission Control Science and Technology*, 4(4):2019–239, 2018.

[5] Michael Guarnieri and John R Balmes. Outdoor air pollution and asthma. *The Lancet*, 383(9928):1581–1592, 2014.

[6] Angela Ibald-Mulli, H-Erich Wichmann, Wolfgang Kreyling, and Annette Peters. Epidemiological evidence on health effects of ultrafine particles. *Journal of Aerosol Medicine*, 15(2):189–201, 2002.

[7] Margaritis Kostoglou, Edward J Bissett, and Athanasios G Konstandopoulos. Improved transfer coefficients for wall-flow monolithic catalytic reactors: energy and momentum transport. *Industrial & Engineering Chemistry Research*, 51(40):13062–13072, 2012.

[8] Shichun Yang, Cheng Deng, Yanfei Gao, and Yongling He. Diesel particulate filter design simulation: A review. *Advances in Mechanical Engineering*, 8(3):1–14, 2016.

[9] Timothy C Watling, Maya R Ravenscroft, Jason PE Cleeton, Ian D Rees, and David AR Wilkins. Development of a particulate filter model for the prediction of backpressure: improved momentum balance and entrance and exit effect equations. *SAE International Journal of Engines*, 10(4):1765–1794, 2017.

[10] Olaf Deutschmann and Daniel Chatterjee. Modeling of Exhaust-Gas After-Treatment. *Emission Control Science and Technology*, 3(4):247–248, 2017.

[11] Robert Greiner, Torben Prill, Oleg Iliev, Barry van Setten, and Martin Votsmeier. Tomography based simulation of reactive flow at the microscale: Particulate filters with wall integrated catalyst. *Chemical Engineering Journal*, doi: 10.1016/j.cej.2019.121919, 2019.

[12] Petr Kočí, Martin Isoz, Marie Plachá, Adéla Arvajová, Marek Václavík, Miloš Svoboda, Emily Price, Vladimír Novák, and David Thompsett. 3D reconstruction and pore-scale modeling of coated catalytic filters for automotive exhaust gas aftertreatment. *Catalysis Today*, 320:165–174, 2019.

[13] Bin Guan, Reggie Zhan, He Lin, and Zhen Huang. Review of the state-of-the-art of exhaust particulate filter technology in internal combustion engines. *Journal of Environmental Management*, 154:225–258, 2015.

[14] Panu Karjalainen, Liisa Pirjola, Juha Heikkilä, Tero Lähde, Theodoros Tzamkiozis, Leonidas Ntziachristos, Jorma Keskinen, and Topi Rönkkö. Exhaust particles of modern gasoline vehicles: A laboratory and an on-road study. *Atmospheric Environment*, 97: 262–270, 2014.

[15] Athanasios G Konstandopoulos, Margaritis Kostoglou, Nickolas Vlachos, and Evdoxia Kladopoulou. Progress in diesel particulate filter simulation. *SAE Technical paper*, No. 2005-01-0946, 2005.

[16] AG Konstandopoulos, M Kostoglou, and N Vlachos. The multiscale nature of diesel particulate filter simulation. *International Journal of Vehicle Design*, 41(1-4):256–284, 2006.

[17] Margaritis Kostoglou, Paraskevi Housiada, and Athanasios G Konstandopoulos. Multichannel simulation of regeneration in honeycomb monolithic diesel particulate filters. *Chemical Engineering Science*, 58(14):3273–3283, 2003.

[18] Marek Vaclavik, Marie Placha, Petr Kočí, Miloš Svoboda, Thomas Hotchkiss, Vladimir Novak, and David Thompsett. Structure characterisation of catalytic particulate filters for automotive exhaust gas aftertreatment. *Materials Characterization*, 134:311–318, 2017.

[19] Guillaume Matte-Deschênes, David Vidal, François Bertrand, and Robert E Hayes. Numerical investigation of the impact of thermophoresis on the capture efficiency of diesel particulate filters. *The Canadian Journal of Chemical Engineering*, 94(2):291–303, 2016.

[20] Samir Bensaid, DL Marchisio, D Fino, G Saracco, and V Specchia. Modelling of diesel particulate filtration in wall-flow traps. *Chemical Engineering Journal*, 154(1-3):211–218, 2009.

[21] Chris D Dritselis, Fotini Tzorbatzoglou, Marios Mastrokalos, and Onoufrios Haralampous. Numerical Study of Flow and Particle Deposition in Wall-Flow Filters with Intact or Damaged Exit. *Fluids*, 4(4):201, 2019.

[22] Mengting Yu, Dan Luss, and Vemuri Balakotaiah. Regeneration modes and peak temperatures in a diesel particulate filter. *Chemical Engineering Journal*, 232:541–554, 2013.

[23] Ileana M. Vega M., Nikrityuk Petr Cornejo, Ivan, and Robert E. Hayes. Simulation of flow patterns in particulate filters with various viscous models. *Emission Control Science and Technology*, In press, 2020.

[24] Valeria Di Sarli and Almerinda Di Benedetto. Modeling and simulation of soot combustion dynamics in a catalytic diesel particulate filter. *Chemical Engineering Science*, 137: 69–78, 2015.

[25] Federico Piscaglia, Christopher J Rutland, and David E Foster. Development of a CFD model to study the hydrodynamic characteristics and the soot deposition mechanism on the porous wall of a diesel particulate filter. *SAE Technical Paper*, No. 2005-01-0963, 2005.

[26] Ileana M. Vega Mesquida. Analysis of Flow Pattern in a Gasoline Particulate Filter using CFD. Master's thesis, University of Alberta, 2019.

[27] Athanasios G Konstandopoulos. Flow resistance descriptors for diesel particulate filters: definitions, measurements and testing. *SAE Technical Paper*, No. 2003-01-0846, 2003.

[28] Athanasios G Konstandopoulos, Evangelos Skaperdas, and Mansour Masoudi. Inertial Contributions to the Pressure Drop of Diesel Particulate Filters. *SAE Technical Paper*, No. 2001-01-0909, 2001.

[29] OA Haralampous, IP Kandylas, GC Koltsakis, and ZC Samaras. Diesel particulate filter pressure drop Part 1: Modelling and experimental validation. *International Journal of Engine Research*, 5(2):149–162, 2004.

[30] Ivan Cornejo, Petr Nikrityuk, and Robert E Hayes. The influence of channel geometry on the pressure drop in automotive catalytic converters: Model development and validation. *Chemical Engineering Science*, doi: 10.1016/j.ces.2019.115317, 2020.

[31] Ivan Cornejo, Petr Nikrityuk, and Robert E Hayes. Pressure correction for automotive catalytic converters: A multi-zone permeability approach. *Chemical Engineering Research and Design*, 147:232–243, 2019.

[32] Edward J Bissett. Mathematical model of the thermal regeneration of a wall-flow monolith diesel particulate filter. *Chemical Engineering Science*, 39(7-8):1233–1244, 1984.

[33] Robert B Kinney. Fully developed frictional and heat-transfer characteristics of laminar flow in porous tubes. *International Journal of Heat and Mass Transfer*, 11(9):1393–1401, 1968.

[34] Edward J Bissett, Margaritis Kostoglou, and Athanasios G Konstandopoulos. Frictional and heat transfer characteristics of flow in square porous tubes of wall-flow monoliths. *Chemical Engineering Science*, 84:255–265, 2012.

[35] Frank M White. *Fluid Mechanics*. McGraw-hill, New York, NY, 2009.

[36] Athanasios G Konstandopoulos, Evangelos Skaperdas, James Warren, and Ronny Allansson. Optimized Filter Design and Selection Criteria for Continuously Regenerating Diesel Particulate Traps. *SAE 1999 Transactions - Journal of Fuels and Lubricants*, 104 (4):279–288, 1999.

[37] Athanasios G Konstandopoulos and John H Johnson. Wall-flow diesel particulate filters—their pressure drop and collection efficiency. *SAE Transactions Journal of Engines*, 98(3):625–647, 1989.

[38] SW Yuan and A. Finkelstein. Laminar Pipe Flow with Injection and Suction through a Porous Wall. *Trans. ASME*, 78:719–724, 1956.

[39] Abraham S Berman. Laminar flow in channels with porous walls. *Journal of Applied Physics*, 24(9):1232–1235, 1953.

[40] JF Brady. Flow development in a porous channel and tube. *The Physics of fluids*, 27 (5):1061–1067, 1984.

[41] Grigorios Koltsakis, Onoufrios Haralampous, Christopher Depcik, and J Colter Ragone. Catalyzed diesel particulate filter modeling. *Reviews in Chemical Engineering*, 29(1): 1–61, 2013.

[42] Ivan Cornejo, Robert E Hayes, and Petr Nikrityuk. A new approach for the modeling of turbulent flows in automotive catalytic converters. *Chemical Engineering Research and Design*, 140:308–319, 2018.

[43] Ivan Cornejo, Petr Nikrityuk, and Robert E Hayes. Multiscale RANS-based modeling of the turbulence decay inside of an automotive catalytic converter. *Chemical Engineering Science*, 175:377–386, 2018.

[44] Matthias Hettel, Eric Daymo, Tobias Schmidt, and Olaf Deutschmann. CFD-modeling of fluid domains with embedded monoliths with emphasis on automotive converters. *Chemical Engineering and Processing-Process Intensification*, doi: 10.1016/j.cep.2019.107728, 2019.

[45] ANSYS Fluent Theory Guide v18.2. ANSYS Inc., Canonsburg, PA, USA, 2017.

[46] Svetlana Aleksandrova, Jonathan Saul, Humberto Medina, Oscar Garcia-Afonso, Chunxing Lin, Jose Martin Herreros, Mark Bevan, and Stephen F Benjamin. Gasoline particulate filter wall permeability testing. *SAE Technical Paper*, No. 03-11-05-0039, 2018.

[47] Christine Lambert, Timothy Chanko, Douglas Dobson, Xin Liu, and James Pakko. Gasoline particle filter development. *Emission Control Science and Technology*, 3(1): 105–111, 2017.

[48] ANSYS Fluent Software Package v18.2, 2017. ANSYS Inc., Canonsburg, PA, USA.

[49] MATLAB Software Package R2018a, 2018. The Mathworks Inc., Natick, MA, USA.

[50] Suhas Patankar. *Numerical heat transfer and fluid flow*. CRC press, Boca Raton, Florida, USA, 1980.

[51] Ivan Cornejo, Petr Nikrityuk, and Robert E Hayes. Turbulence generation after a monolith in automotive catalytic converters. *Chemical Engineering Science*, 187:107–116, 2018.

[52] Ivan Cornejo, Petr Nikrityuk, and Robert E Hayes. Effect of substrate geometry and flow condition after the turbulence generation after a monolith. *Canadian Journal of Chemical Engineering*, doi: 10.1002/cjce.23687, 2020.

[53] Athanasios G Konstandopoulos, Margaritis Kostoglou, Evangelos Skaperdas, Eleni Papaioannou, Dimitrios Zarvalis, and Evdoxia Kladopoulou. Fundamental studies of diesel particulate filters: transient loading, regeneration and aging. *SAE 2000 Transactions Journal of Fuels and Lubricants*, 109(4):683–705, 2000.

[54] YL Wang and PA Longwell. Laminar flow in the inlet section of parallel plates. *AIChE Journal*, 10(3):323–329, 1964.

[55] JS Vrentas and JL Duda. Flow of a newtonian fluid through a sudden contraction. *Applied Scientific Research*, 28(1):241–260, 1973.

[56] SF Benjamin, N Haimad, CA Roberts, and J Wollin. Modelling the flow distribution through automotive catalytic converters. *Proceedings of the Institution of Mechanical Engineers, Part C: Journal of Mechanical Engineering Science*, 215(4):379–383, 2001.

[57] Galip Seckin, Hatice Çağatay, Murat Çobaner, and Recep Yurtal. Experimental investigation of kinetic energy and momentum correction coefficients in open channels. *Scientific Research and Essay*, 4(5):473–478, 2009.

[58] Christos K Dardiotis, Onoufrios A Haralampous, and Grigorios C Koltsakis. Catalytic oxidation performance of wall-flow versus flow-through monoliths for diesel emissions control. *Industrial & Engineering Chemistry Research*, 45(10):3520–3530, 2006.

[59] JF Knoth, A Drochner, H Vogel, J Gieshoff, M Kögel, M Pfeifer, and M Votsmeier. Transport and reaction in catalytic wall-flow filters. *Catalysis Today*, 105(3-4):598–604, 2005.

[60] Andrew PE York, Timothy C Watling, Mehrdad Ahmadinejad, David Bergeal, Paul R Phillips, and Daniel Swallow. Modeling the emissions control performance of a catalyzed diesel particulate filter (CDPF) system for light duty diesel applications. *SAE International Journal of Fuels and Lubricants*, 2(1):578–589, 2009.

[61] Gordon S Beavers, Ephraim M Sparrow, and Ronald Allen Magnuson. Experiments on coupled parallel flows in a channel and a bounding porous medium. *Journal of Fluids Engineering*, 30:843–848, 1970.

[62] Melik Sahraoui and Massoud Kaviany. Slip and no-slip velocity boundary conditions at interface of porous, plain media. *International Journal of Heat and Mass Transfer*, 35 (4):927–943, 1992.

[63] J Alberto Ochoa-Tapia and Stephen Whitaker. Momentum transfer at the boundary between a porous medium and a homogeneous fluid—I. Theoretical development. *International Journal of Heat and Mass Transfer*, 38(14):2635–2646, 1995.

[64] Andrew PE York, Timothy C Watling, Nicholas P Ramskill, Lynn F Gladden, Andrew J Sederman, Athanasios Tsolakis, Jose M Herreros, and Isaline Lefort. Visualization of the Gas Flow Field within a Diesel Particulate Filter Using Magnetic Resonance Imaging. *SAE Technical Paper*, No. 2015-01-2009, 2015.

[65] Johann C Wurzenberger and Susanne Kutschi. Advanced Simulation Technologies for Diesel Particulate Filters, A Fundamental Study on Asymmetric Channel Geometries. *SAE Technical Paper*, No. 2007-01-1137, 2007.

[66] Wen Wang and Edward J Bissett. Frictional and Heat Transfer Characteristics of Flow in Triangle and Hexagon Channels of Wall-Flow Monoliths. *Emission Control Science and Technology*, 4(3):198–218, 2018.

[67] Timothy C Watling. A One-Dimensional Model for Square and Octo-Square Asymmetric Particulate Filters with Correct Description of the Channel and Wall Geometry. *SAE Technical Paper*, No. 2018-01-0951, 2018.

[68] Athanasios G Konstandopoulos, Margaritis Kostoglou, Nickolas Vlachos, and Evdoxia Kladopoulou. Advances in the science and technology of diesel particulate filter simulation. *Advances in Chemical Engineering*, 33:213–294, 2007.

[69] Ivan Cornejo, Petr Nikrityuk, Carlos Lange, and Robert E Hayes. Influence of upstream turbulence on the pressure drop inside a monolith. *Chemical Engineering and Processing-Process Intensification*, doi: 10.1016/j.cep.2019.107735, 2019.

12.7 Supplementary material

The supplementary information gives additional details that may improve the understanding of the results, for completeness. This includes preliminary work and additional analyses, complementary to those discussed in the main paper.

12.7.1 Computational grids

The quality of the discretization of the computational domain is of great importance for the reliability of the results. In this work, two meshing strategies were tested: Homogeneous meshes and wall refined meshes. Views of the final mesh used to obtain the results (mesh C) and the finer homogeneous mesh (mesh B) are shown in the article. This section complements that by showing the other meshes tested (Figure 12.12-12.14). All the grids were fully homogeneous in the axial direction, along the entire domain.

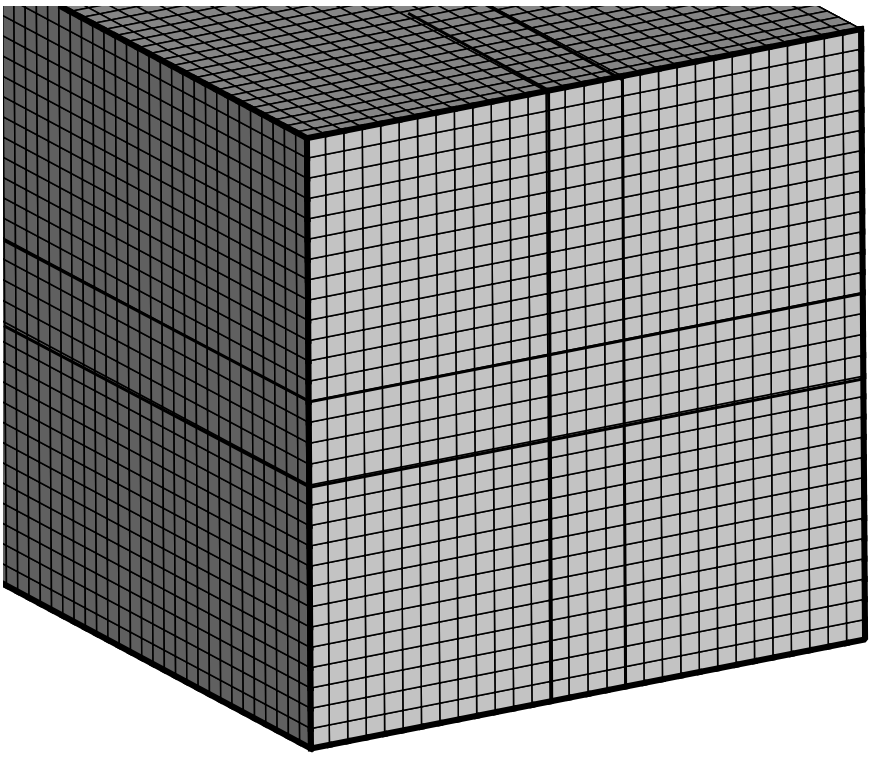

Figure 12.12: Mesh A

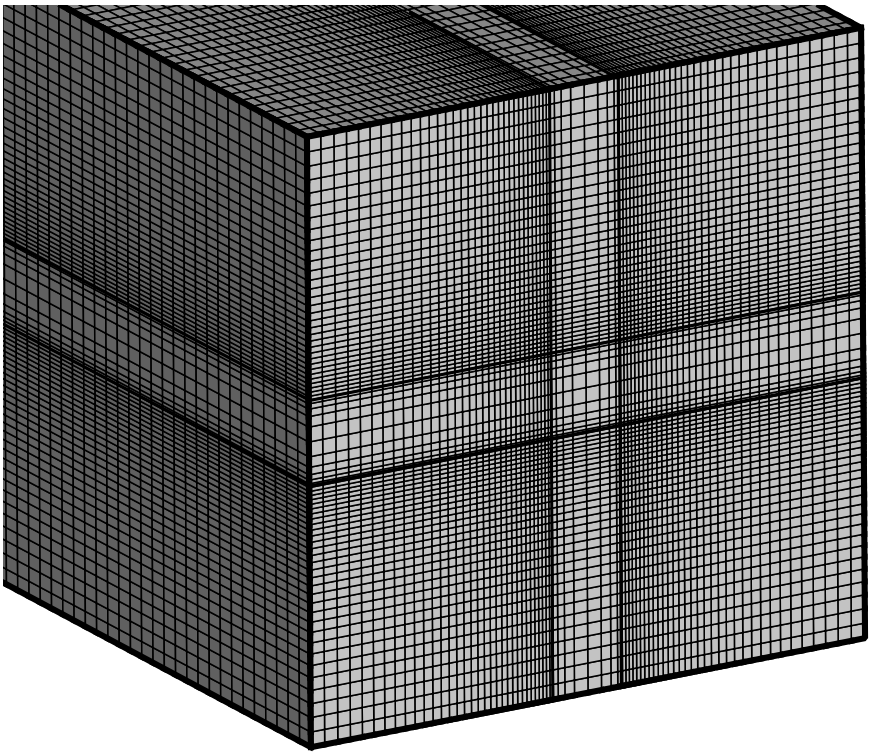

Figure 12.13: Mesh D

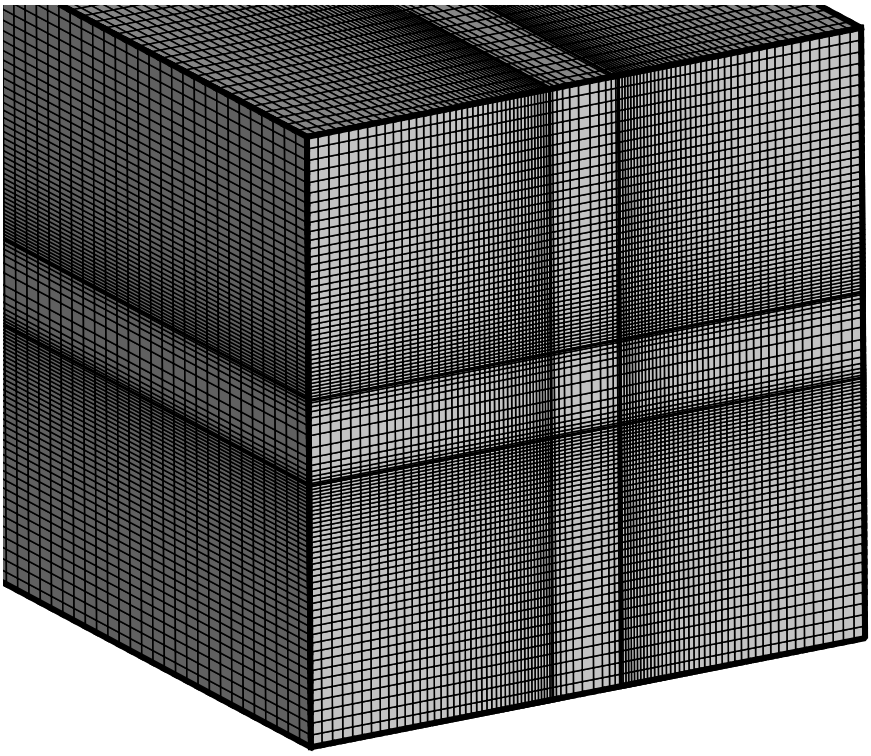

Figure 12.14: Mesh E

12.7.2 Numerical instability in the near-wall area

During the mesh analysis, it was concluded that mesh C was sufficient to obtain a grid independent result in terms of pressure drop, axial velocity profiles and wall-flow. However, an instability of the radial velocity in the near wall region was detected. Such an instability generates an oscillation of the velocity when entering and leaving the porous zone. This phenomenon might be explained by the transition of the flow passing from and to a free flow zone to one with a source term, Darcy's law in this case. An example of the oscillations are shown in Figure 12.15. They were observed in all the meshes tested in this study, despite of the discretization schemes used (LUDS, QUDS, QUICK and MUSCL, as implemented in Fluent v18.2). Different solver strategies for the pressure-velocity coupling were tested also. That is: SIMPLE, coupled and pseudo-transient coupled. Unfortunately, none of the combinations of the aforementioned led to the elimination of the oscillations. Furthermore, the impact of all those changes on the magnitude of the peaks was very small. What was certainly corroborated was that such oscillations did not affect the axial velocity profiles and pressure field (see Figure 12.16).

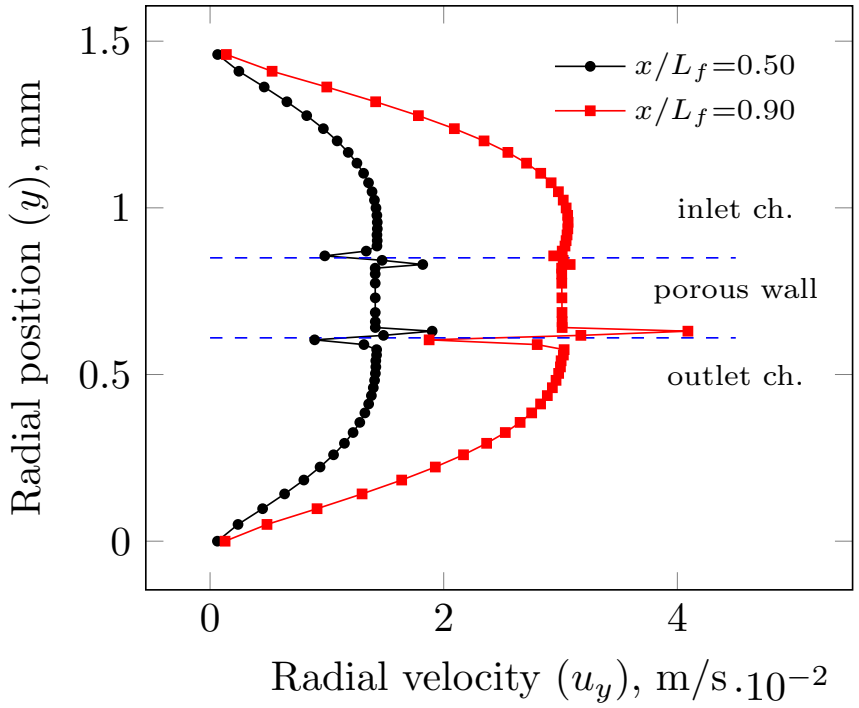

Figure 12.15: Radial velocity profile at two axial positions

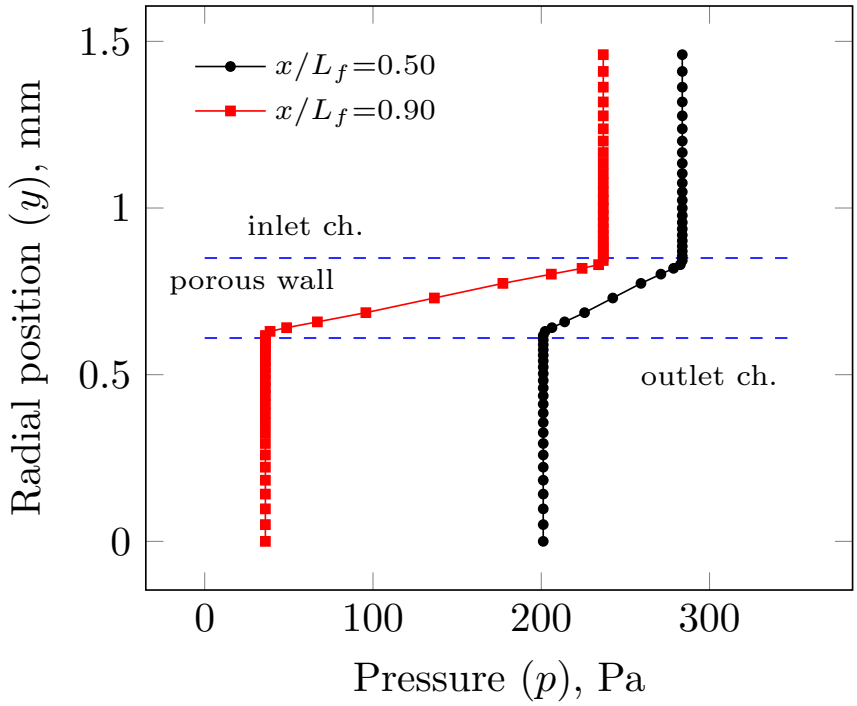

Figure 12.16: Radial pressure profile at two axial positions

It is important to remark that for the reliability of the results, the analysis of the wall-flow was performed with data obtained in two different ways. Firstly, extracting the data from the center of the porous walls (L_4 of Figure 2 of the paper). Secondly, from a mass balance of several cross-sections along the inlet and outlet channels. Both aforementioned methods led to the same wall-flow profile, which provides strong evidence that the effect of the oscillations is limited and does not affect other results. This phenomenon is probably present in other CFD simulations of particle filter reported in the literature; However, to the best of the knowledge of the authors, it has not been highlighted yet. The authors encourage other research groups to find out a methodology to overcome this issue, and also to provide evidence of its potential impact on other results.

12.7.3 Computation of the shear stress (τ_w) and friction factor (f)

Figure 12.17 exemplifies very well why the wall shear stress and the friction factor for non-circular pipes must be calculated as the area-weighted along the entire perimeter of the section. Symmetry can be applied, but, using the center value as a representative one can a introduce significant error. It can be seen that the velocity gradient in the z-direction at y/D_H=0 is significantly higher than that close to the corners of the channels. Therefore, the calculation of the shear stress based on a sample rather than an average velocity gradient leads to a large estimation error of the friction factor.

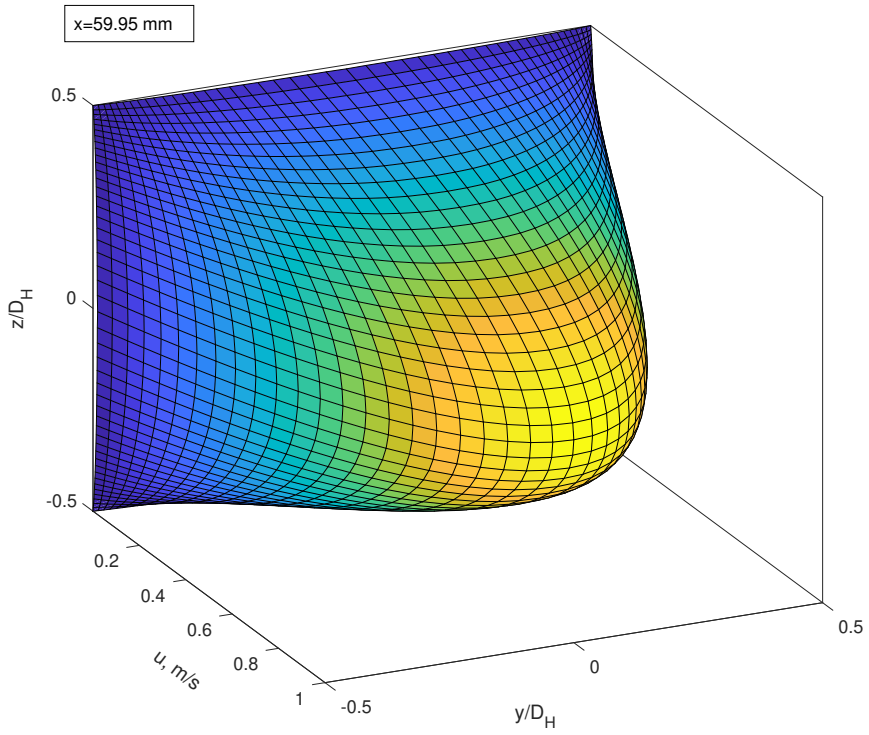

Figure 12.17: Velocity profile of an inlet channel. Re_i=200, D_H=1.26 mm, α=1×10^{-12}, L_f=127 mm

The friction factor can be also obtained from the dissipation of mechanical energy (h_f) between two channel cross-sections, separated by a given axial distance ∂x. Starting from the energy balance:

$$h_f = p|_{(x)} - p|_{(x+\partial x)} + \left(\frac{1}{2} k_\alpha \rho u_c^2\right)\Big|_{(x)} - \left(\frac{1}{2} k_\alpha \rho u_c^2\right)\Big|_{(x+\partial x)} - \left(\frac{1}{2} k_\alpha \rho u_w^2 \frac{4\partial x}{D_H}\right)\Big|_{(x+\partial x/2)} \quad (12.26)$$

The last three terms of Equation 12.26 are the kinetic energy entering from the upstream direction, leaving to the downstream direction and transferred from the inlet channel to the outlet channel respectively. The parameters k_α correspond to the kinetic energy correction factors, which are necessary to account for the changes of the shape of the velocity profile in every case. The multiplier $4\partial x/D_H$ in the last term provides consistency to the momentum balance, which is referred to the channel cross-section area. Having obtained the energy dissipation, the local friction factor can be computed as:

$$f = \frac{2h_f D_H}{\rho u_c^2 \partial x} \tag{12.27}$$

When compared to the τ_w methodology, the two approaches led to a fairly similar relationship between f and Re in the zone of interest. A comparison can be seen in Figure 12.18. In the example, the wall permeability was α=1 $\times$ 10^{-12} m^2, D_H=1.26 mm, Re$_i$=200, T=573 K and the k_α correction factors were computed directly from the 3D CFD results.

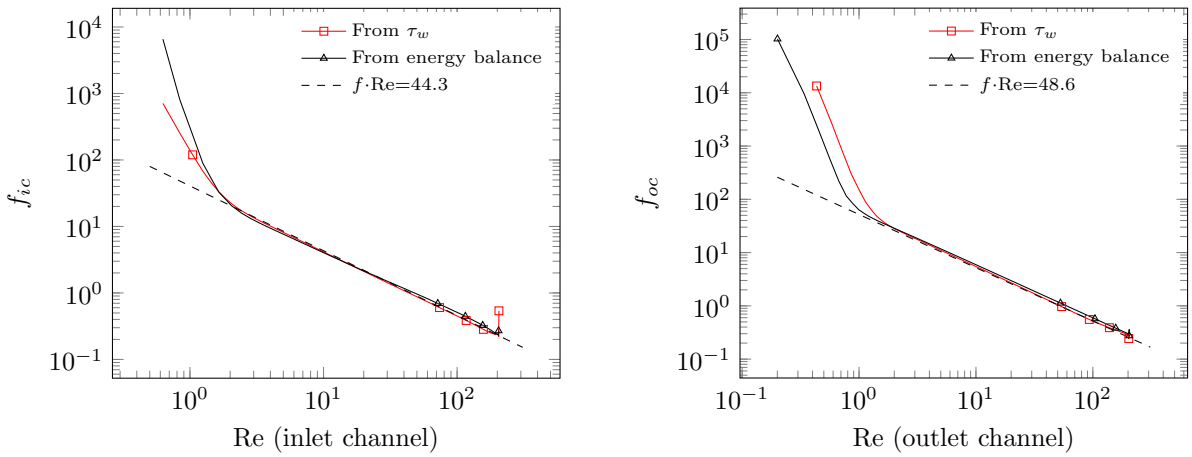

(a) (b)

Figure 12.18: Comparison of f calculated from τ_w and from an energy balance

Both methodologies can an introduce error of a variable magnitude to the friction factor calculation in regions with reverse flow (beginning and end of the channel). It is not possible to state what approach is more accurate in those zones without a detailed investigation. Reverse flow is most likely to appear in an inlet channel, in its first part due to the formation of a *vena contracta*, and in its last part because of the flow colliding with the plug. Between them, the last one has the largest effect. An example of reverse flow is shown in Figure 12.19. Reverse flow is promoted by increasing the flow rate or the wall permeability. In the figure, reverse flow can be seen along the entire perimeter of the channel cross-section, but it is more

pronounced in the corners of the channel.

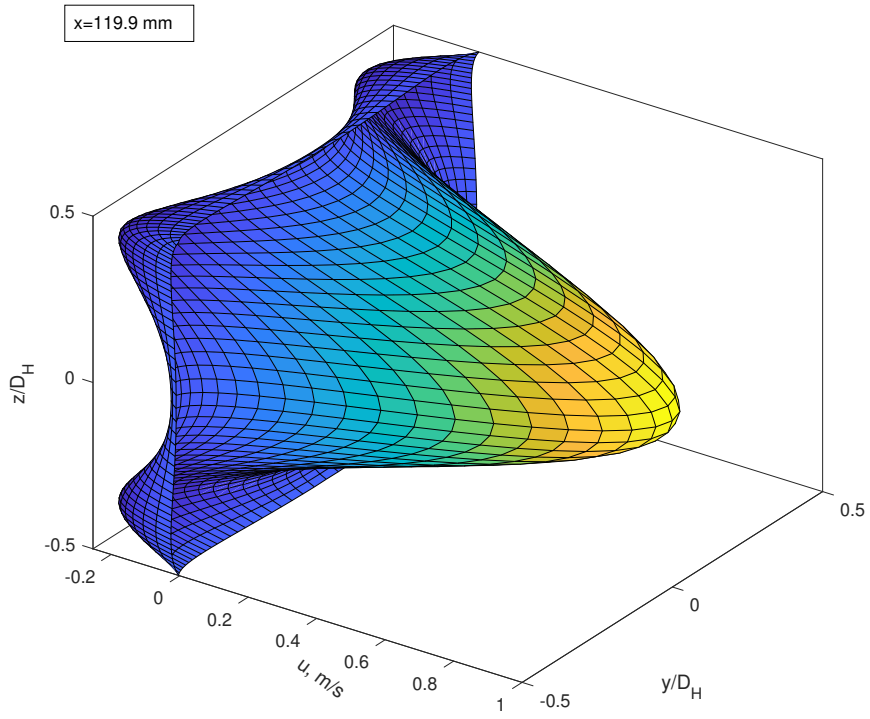

Figure 12.19: Axial velocity profile, showing reverse flow. Re_i=600, L_f=127 mm, α=1×10^{-12} m^2, D_H=1.26 mm and L_w=0.20 mm

12.7.4 Visualization of velocity and pressure inside the filter channels

This section shows an example of the velocity and pressure along a center-plane of the filter (see Figure 12.20-12.22). The main purpose of the figures is to provide a visualization of the flow entering and leaving the filter channels, as well as the axial and radial gradients of pressure and velocity.

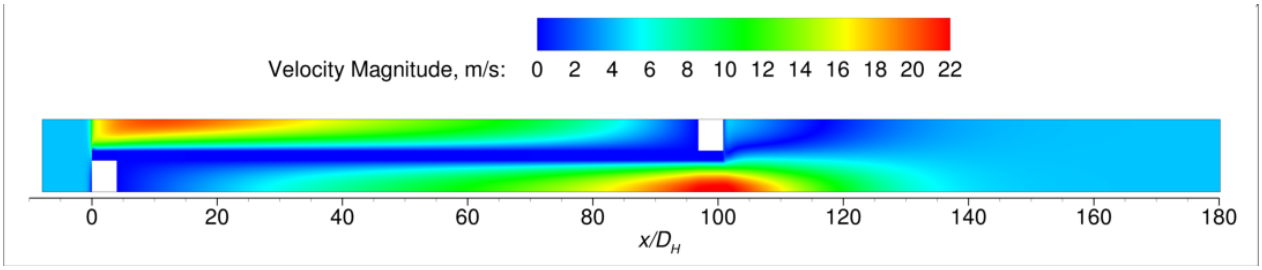

Figure 12.20: Velocity magnitude along the center of an inlet and outlet channel

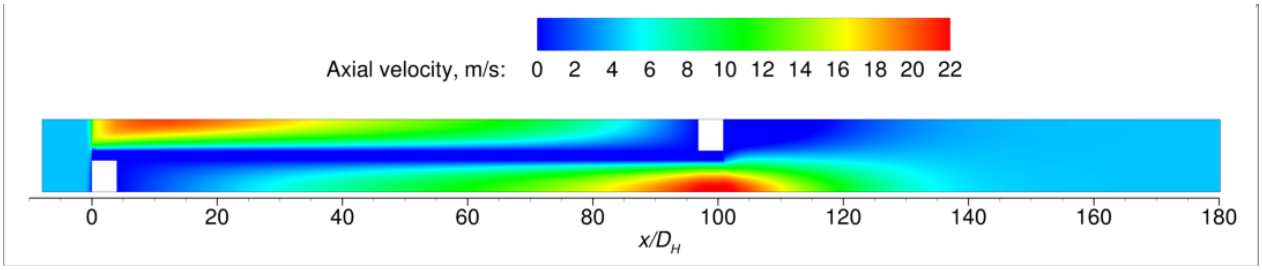

Figure 12.21: Axial velocity along the center of an inlet and outlet channel

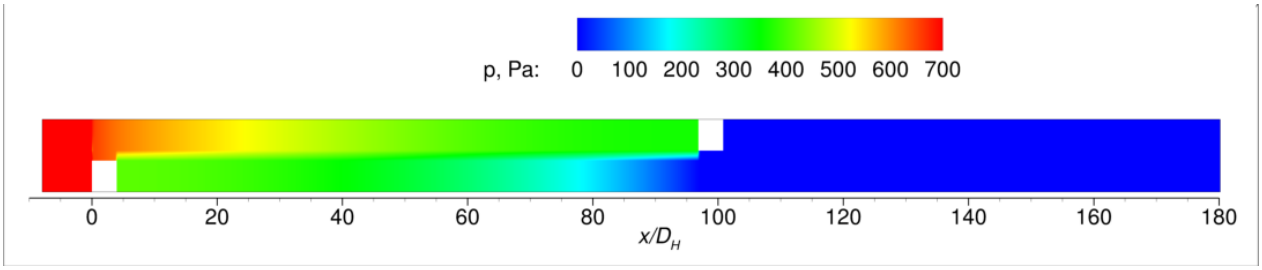

Figure 12.22: Pressure along the center of an inlet and outlet channel

12.7.5 Statistical Analysis of the structure of the models for Δp_i and Δp_o

In the paper, based on previous works, the two terms model in Equation (12.28) is propose for the computation of Δp_i. In the model, $\Delta p_{i,1}$ is the linear contribution and $\Delta p_{i,2}$ is the quadratic contribution to the pressure drop because of entering the filter. In the literature is common to find expressions accounting only for $\Delta p_{i,2}$. In this section, the two model options are compared statistically.

$$\Delta p_i = \underbrace{\frac{\mu}{\alpha_{afc}} u_c}_{\Delta p_{i,1}} + \underbrace{\frac{1}{2}\rho C_i u_c^2}_{\Delta p_{i,2}} \tag{12.28}$$

For simplicity, let us take Equation (12.28) and express it as $\Delta p_i = b_1 u_c + b_2 u_c^2$, where the coefficients α_{afc} and C_i can be derived from b_1 and b_2. For instance, if b_1 and b_2 are statistically significant, then α_{afc} and C_i are also. According to the procedure described in the paper, an individual curve fitting was performed for each one of the three wall permeability; Hence, three sets of b_1 and b_2 were obtained. The values of b_1 and b_2 and their confidence intervals in each case are presented in Table 12.8. It is observed in the confidence intervals that all the coefficients have statistical meaning and there is justification to neglect any of them.

Table 12.8: Statistical analysis of the Δp_i model

Parameter	Value	Confidence interval (95%)
$\alpha = 1 \times 10^{-11}$ m^2		
b_1	0.21840	(0.12630, 0.31050)
b_2	0.07165	(0.06232, 0.08098)
R^2	0.9998	
$\alpha = 1 \times 10^{-12}$ m^2		
b_1	0.17310	(0.13741, 0.20883)
b_2	0.08769	(0.08407, 0.09130)
R^2	1.0000	
$\alpha = 1 \times 10^{-13}$ m^2		
b_1	0.16181	(0.14801, 0.17550)
b_2	0.09162	(0.09022, 0.09301)
R^2	1.0000	

The comparison is enriched by calculating the R^2-adjusted. This indicator is especially suitable to compare models with a different number of parameters. It compensates the

increasing of the flexibility of the model when adding parameters by using a penalty factor.

$$R^2\text{-adjusted} = \frac{(1-R^2)(N_d-1)}{N_d-N_p-1} \tag{12.29}$$

Table 12.9: R^2-adjusted for both Δp_i models

Model	R^2-adjusted
α=1×10^{-11} m^2	
Δp_i=$\Delta p_{i,2}$	0.9912
Δp_i=$\Delta p_{i,1}$+$\Delta p_{i,2}$	0.9997
α=1×10^{-12} m^2	
Δp_i=$\Delta p_{i,2}$	0.9958
Δp_i=$\Delta p_{i,1}$+$\Delta p_{i,2}$	1.0000
α=1×10^{-13} m^2	
Δp_i=$\Delta p_{i,2}$	0.9966
Δp_i=$\Delta p_{i,1}$+$\Delta p_{i,2}$	1.0000

Table 12.9 shows the comparison of the R^2-adjusted for the Δp_i model when using one or two parameters. It can be seen that the R^2-adjusted decreases when removing $\Delta p_{i,1}$ from the Δp_i equation. That means that the two parameter model provides a better fitting even after applying the penalization due to the increment in the number terms. This provides additional statistical evidence and confirms that Δp_i=$\Delta p_{i,1}$+$\Delta p_{i,2}$ is the most meaningful option statistically and phenomenologically.

An equivalent analysis can be performed for the Δp_o model. Similarly to the analysis of Δp_i, let us write Δp_o=$b_3 u_c$+$b_4 u_c^2$ and analyze the statistical significance of b_3 and b_4. Results are summarized in Table 12.9. Based on the confidence intervals, it is clear that in all the cases either b_3 or b_4 fail the null-hypothesis test. That is, using two parameters to describe Δp_o does not have statistical meaning and less parameters should be used; Hence, traditional models with only one parameter are enough to describe Δp_o.

Table 12.10: Statistical analysis of the Δp_o model

Parameter	Value	Confidence interval (95%)
α=1 $\times$ 10^{-11} m^2		
b_3	0.1445	(-0.07859, 0.3675)
b_4	0.3287	(0.30610, 0.3513)
α=1 $\times$ 10^{-12} m^2		
b_3	-0.01872	(-0.2697, 0.2322)
b_4	0.35970	(0.3343, 0.3852)
α=1 $\times$ 10^{-13} m^2		
b_3	-0.01437	(-0.02789, -0.000838)
b_4	0.37540	(0.3741, 0.3768)

12.7.6 Momentum flux correction factor (k_β)

This section briefly shows the momentum flux correction factor along an inlet and an outlet channel. The curves are shown in Figure 12.23.

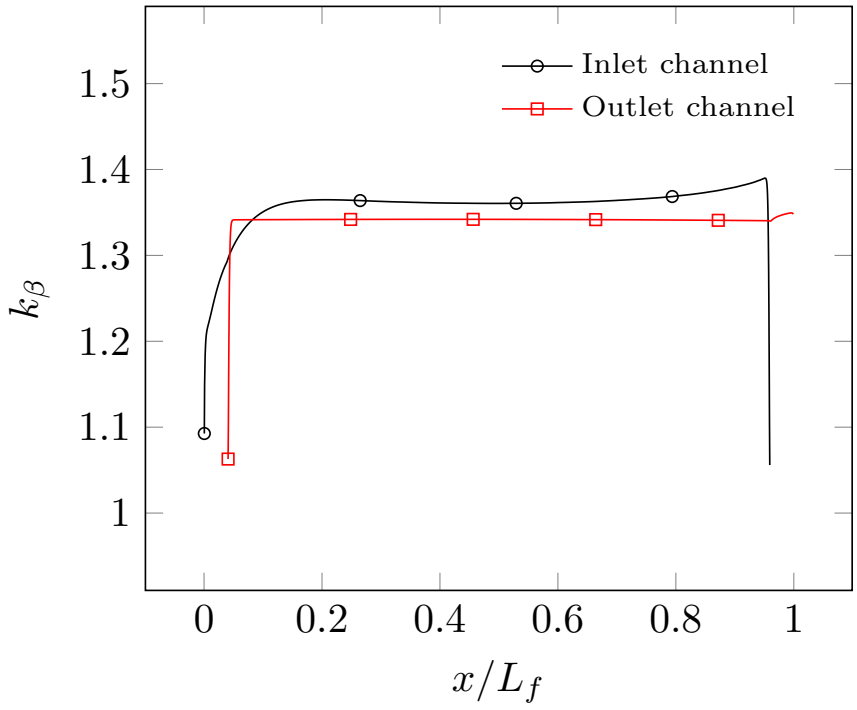

Figure 12.23: Momentum flux correction factor. Re_i=200, D_H=1.26 mm, α=1×10^{-12} m^2, L_f=127 mm

It can be seen in the figure that k_β progressively increases from 1.1, which corresponds to the inlet velocity profile, to approximately 1.36 in the inlet channel. After that, it remains around that value until almost the end of the channel (x=121 mm). The outlet channel behaves differently. k_β suddenly increases from the initial value to 1.34, then remain almost constant until the end of the filtrating zone, where it slightly increases to 1.35.

Chapter 13

Concluding remarks and further work

This chapter gives some general overall conclusions and recommendations for further work. This chapter is complementary to the conclusions given at the end of each chapter.

13.1 Concluding remarks

The flow inside a honeycomb type substrate was successfully investigated in terms of flow regime, pressure drop and convective heat transfer using computational models at a channel and a converter scale.

The influence of the upstream turbulence approaching a honeycomb monolith has been investigated in a channel scale model, using RANS and LES. For the cases analyzed, the approaching Reynolds was of the order of 10^4 and the one inside the channels of the order of 10^2. According to the results from LES, the flow power spectrum shows that the turbulence starts to decay before entering the monolith. For the majority of the cases, the turbulence dissipates completely before entering the substrate, from which point the flow regime turns to unsteady laminar. This phenomenon is not captured correctly when using RANS model, which predicted a transition from turbulent to steady laminar flow. From the analysis of flow leaving a substrate, it is observed that the flow regime remains as laminar until it has passed a distance of several channel diameters before becoming unsteady, and eventually turbulent. Such a distance depends on the flow rate, channel diameter, channel cross-section shape and wall thickness of the substrate. Depending on those variables, the dominating phenomenon triggering the unsteadiness on the flow downstream of the substrate are the flow passing around the last part of the walls between channels and the flow acting as a jet. The former requires a higher flow rate than the latter, and produces turbulence

closer to the exit of the substrate. There are several variables involved in the generation of turbulence at the exit of the substrate; Hence, it was not possible to define a specific and general dimensionless parameter indicating what of the two phenomena is dominating for every case. The understanding of turbulence generation after a substrate has been improved significantly, notwithstanding, the matter still requires further work to develop a general model.

It is concluded that models at a converter scale using the continuum approach do not describe the decay of the turbulence approaching the channels accurately, unless an source term is implemented. The strategy of fixing the turbulence viscosity as zero inside the continuum prevents the generation of turbulence in the zone. However, the pre-existent turbulence kinetic energy is still nonphysically transported from the inlet to the exit of the substrate, creating a fictional generation of turbulence downstream of the substrate. In this thesis, two source terms to be applied in the continuum correct those problems. The first damps the turbulence approaching the substrate emulating the decay observed at a channel scale. The second generates turbulence after the substrate when the conditions for that are met. That eliminates nonphysical results and provide consistency between the converter and the channel scale in whole scale simulations.

According to the Fourier analysis of the turbulence approaching the substrate obtained with LES, once the flow regime turns to unsteady inside the substrate, it is a sort of pulsating flow, with several frequencies overlapped. The dominant frequencies have a magnitude of the order of the ratio of the channel velocity over the channel diameter. Based on that, a relationship between the Womersley number and the channel Reynolds number was derived. For the channel Reynolds investigated (<600), the effect of the upstream turbulence on the pressure drop through the substrate was negligible. However, some other variables, such as the entrance length, should be addressed in a next stage of the research. It was also found that the number of pulsating frequencies inside the channels scales faster that the channel Reynolds, making high channel Reynolds cases particularly interesting for further analysis.

The effect of the turbulence when it effectively enters the channels has been investigated, by removing the open section before the substrate and prescribing turbulence at the inlet of a channel. In such a case, turbulence enhances the convective heat transport in the entrance length. However, after it dissipates and the pulsating regime is established, then the convective heat transfer coefficient is the same as that for steady laminar flow. Since the enhancement of Nusselt depends on the magnitude of the turbulence, the Nusselt curve is not unique. A methodology to expand available models to cover such cases is presented.

The pressure drop of laminar flow through a monolith has been analyzed at a channel scale. The additional head losses because of flow entering and leaving the substrate can be a significant percentage of the total pressure drop through the substrate, therefore, they should not be neglected. The mentioned losses depend on the approaching velocity and substrate open frontal area, being those at the outlet up to one order of magnitude higher that those at the inlet. Inside the channels, the friction factor curve in the entrance length is significantly different from that for pipes with a flat inlet velocity profile; Thence, new correlations, specific for monolith channels are developed. The curves for the friction factor for the different channel cross-section shapes follow a comparable trajectory when they are scaled by their respective asymptotic values. A new pressure drop model is presented. The models account for the losses at the inlet and outlet of the substrate, for the entrance length and for a realistic inlet velocity profile. The new model is also presented in the form of a multi-zone permeability approach, to be used in converter scale computational models, for circular, square, triangular and hexagonal channel cross-sections.

The convective heat transport inside monolith channels when laminar flow enters the substrate has been analyzed. It is important to use temperature-dependent fluid properties to obtain a correct heat transfer coefficient and dimensionless axial position. The open section before the substrate is also essential to obtain a realistic inlet velocity profile and Nusselt curve along the entrance length of the channels. Straight reservoirs do not produce the correct inlet velocity profile. Such a section must be set to represent the correct open frontal area of the substrate. The Nusselt curve is only slightly sensitive to the value of the open frontal area, nonetheless, it is significantly different than that for a flat inlet velocity profile.

Assuming constant fluid properties can introduce a significant error in the calculation of both Nusselt and Graetz numbers. For a heating rate of 3 (maximum over minimum temperature) the error in the Graetz number is of the order of the 50%. For a heating rate of 1.1 the error in the Graetz number is approximately 5%. Although that may be considered low, it displaces the Nusselt vs. Graetz curve significantly and leads to an incorrect heat transfer coefficient.

Between the cases with a constant wall heat flux and a constant wall temperature, the latter is the most affected by the use of temperature-dependent fluid properties. It shows a minimum in the Nusselt curve that is significantly lower than the asymptotic value for certain heating rates. The value of the maximum is very sensitive to the heating rate, for a heating

rate of 2, the minimum is located approximately 16% below the asymptotic Nusselt. The Nusselt curve at a constant wall heat flux also shows a minimum, but, it has approximately the same value than the asymptotic Nusselt, therefore, can be reasonably neglected. Curves with a minimum cannot be described by classical models; Hence, a new modelling strategy is proposed. A combination of an asymptotic and a sigmoid functions can describe the entire curve accurately. The sigmoid function introduced two new parameters: The placement and the value of the minimum Nusselt. The two extra parameters have a clear physical meaning, notwithstanding, they are determined empirically because there are not yet fundamental equations for predicting them available.

13.2 Further work

In this section, further work to be carried out as a continuation or complement of this thesis is described:

Due to computational limitations, the decay of the turbulence approaching the substrate was addressed using a single channel geometry. Using a multiple channel geometry will allow us to elucidate the influence of vortices significantly larger than the cell size entering the channels. Similarly, the decay of turbulence was analyzed only for square cross-section channels. Other channel shapes, such as circular, should be analyzed.

The recirculating zone created when flow leaves the substrate can be even larger much larger than the separation between two substrates in series. That is, the effect of the outflow from one substrate on the inflow of the next one should be analyzed in a next stage of the research.

As mentioned, a general model for turbulence generation after the substrate should be developed, because the current strategy proposed in this thesis requires channel scale data specific of every geometry.

The pressure drop model for monoliths presented in this thesis has been compared with experimental data available in the literature; However, a more extensive experimental validation is recommended. Usually, data available in the literature is limited to a few monolith configurations. Ideally, the model should be tested at a wide range of open frontal areas, monolith lengths and channel cross-section shapes.

Pulsating flow resulting from the dissipation of the upstream turbulence inside the channels should be investigated in more detail. This thesis provides evidence of the effect of such a phenomenon on the pressure drop and heat transfer; However, some other parameters, such as the hydraulic entrance length, critical channel Reynolds, and impact on the light-off should be addressed.

General Bibliography

Agrawal, G., Kaisare, N. S., Pushpavanam, S., and Ramanathan, K. (2012). Modeling the effect of flow mal-distribution on the performance of a catalytic converter. *Chemical Engineering Science*, 71:310–320.

Ahn, Y. D. and Lee, J. H. (2018). Development of a Polyaniline-coated Monolith Reactor for the Synthesis of Cephalexin Using Penicillin G-Acylase Aggregates. *Biotechnology and Bioprocess Engineering*, 23(3):349–354.

Al-Nassri, S. and Unny, T. (1981). Developing laminar flow in the inlet length of a smooth pipe. *Applied Scientific Research*, 36(5-6):313–332.

Albers, R. E., Nyström, M., Siverström, M., Sellin, A., Dellve, A.-C., Andersson, U., Hermann, W., and Berglin, T. (2001). Development of a monolith-based process for H2O2 production: from idea to large-scale implementation. *Catalysis Today*, 69(1-4):247–252.

Aleksandrova, S., Saul, J., Medina, H., Garcia-Afonso, O., Lin, C., Herreros, J. M., Bevan, M., and Benjamin, S. F. (2018). Gasoline particulate filter wall permeability testing. *SAE Technical Paper*, No. 03-11-05-0039.

ANSYS Fluent Software Package v17.2 (2016). ANSYS Inc., Canonsburg, PA, USA.

ANSYS Fluent Software Package v18.2 (2017). ANSYS Inc., Canonsburg, PA, USA.

ANSYS Fluent Theory Guide v17.2 (2016). ANSYS Inc., Canonsburg, PA, USA.

ANSYS Fluent Theory Guide v18.2 (2017). ANSYS Inc., Canonsburg, PA, USA.

Arab, S., Commenge, J.-M., Portha, J.-F., and Falk, L. (2014). Methanol synthesis from CO2 and H2 in multi-tubular fixed-bed reactor and multi-tubular reactor filled with monoliths. *Chemical Engineering Research and Design*, 92(11):2598–2608.

Ashraf, M. A., Sanz, O., Italiano, C., Vita, A., Montes, M., and Specchia, S. (2017). Analysis of Ru/La-Al 2 O 3 catalyst loading on alumina monoliths and controlling regimes in methane steam reforming. *Chemical Engineering Journal*, 334:1792–1807.

Avila, P., Montes, M., and Miró, E. E. (2005). Monolithic reactors for environmental applications: A review on preparation technologies. *Chemical Engineering Journal*, 109(1-3):11–36.

Avramenko, A., Tyrinov, A., and Shevchuk, I. (2015). Start-up slip flow in a microchannel with a rectangular cross section. *Theoretical and Computational Fluid Dynamics*, 29(5-6):351.

Avramenko, A., Tyrinov, A., Shevchuk, I., Dmitrenko, N., Kravchuk, A., and Shevchuk, V. (2017). Mixed convection in a vertical circular microchannel. *International Journal of Thermal Sciences*, 121:1–12.

Balakotaiah, V. and West, D. H. (2002). Shape normalization and analysis of the mass transfer controlled regime in catalytic monoliths. *Chemical Engineering Science*, 57(8):1269–1286.

Barkley, D., Song, B., Mukund, V., Lemoult, G., Avila, M., and Hof, B. (2015). The rise of fully turbulent flow. *Nature*, 526:550–553.

Batchelor, G. K. (1967). *An Introduction to Fluid Dynamics*. Cambridge University Press, Cambridge, UK.

Baxendale, A. J. (1993). The Role of Computational Fluid Dynamics in Exhaust System Design and Development. *SAE Technical Paper*, No. 931072.

Beavers, G. S., Sparrow, E. M., and Magnuson, R. A. (1970). Experiments on coupled parallel flows in a channel and a bounding porous medium. *Journal of Fluids Engineering*, 30:843–848.

Bella, G., Rocco, V., and Maggiore, M. (1991). Study of inlet flow distortion effects on automotive catalytic converters. *Journal of Engineering for Gas Turbines and Power. Transactions of the ASME*, 113(3):419–426.

Benjamin, S., Clarkson, R., Haimad, N. a., and Girgis, N. (1996). An experimental and predictive study of the flow field in axisymmetric automotive exhaust catalyst systems. *SAE Technical Paper*, No. 961208.

Benjamin, S., Haimad, N., Roberts, C., and Wollin, J. (2001). Modelling the flow distribution through automotive catalytic converters. *Proceedings of the Institution of Mechanical Engineers, Part C: Journal of Mechanical Engineering Science*, 215(4):379–383.

Benjamin, S., Zhao, H., and Arias-Garcia, A. (2003). Predicting the flow field inside a close-coupled catalyst—the effect of entrance losses. *Proceedings of the Institution of Mechanical Engineers, Part C: Journal of Mechanical Engineering Science*, 217(3):283–288.

Bensaid, S., Marchisio, D., Fino, D., Saracco, G., and Specchia, V. (2009). Modelling of diesel particulate filtration in wall-flow traps. *Chemical Engineering Journal*, 154(1-3):211–218.

Bergman, T. L. and Incropera, F. P. (2011). *Introduction to heat transfer*. John Wiley & Sons, New Jersey, NY, USA.

Bergman, T. L., Incropera, F. P., DeWitt, D. P., and Lavine, A. S. (2011). *Fundamentals of Heat and Mass Transfer*. John Wiley & Sons, New Jersey, NY, USA.

Berman, A. S. (1953). Laminar flow in channels with porous walls. *Journal of Applied Physics*, 24(9):1232–1235.

Bertrand, F., Devals, C., Vidal, D., de Préval, C. S., and Hayes, R. E. (2012). Towards the simulation of the catalytic monolith converter using discrete channel-scale models. *Catalysis Today*, 188(1):80–86.

Bhatti, M. (1985). Fully developed temperature distribution in a circular tube with uniform wall temperature. Unpublished.

Bissett, E. J. (1984). Mathematical model of the thermal regeneration of a wall-flow monolith diesel particulate filter. *Chemical Engineering Science*, 39(7-8):1233–1244.

Bissett, E. J., Kostoglou, M., and Konstandopoulos, A. G. (2012). Frictional and heat transfer characteristics of flow in square porous tubes of wall-flow monoliths. *Chemical Engineering Science*, 84:255–265.

Blythman, R., Alimohammadi, S., Persoons, T., Jeffers, N., and Murray, D. B. (2018). Parametric analysis of laminar pulsating flow in a rectangular channel. *Heat and Mass Transfer*, 54(8):2177–2186.

Bonilla, C. (1958). *Nuclear Engineering Handbook*. McGraw-Hill, New York, NY, USA.

Box, G. E., Hunter, J. S., and Hunter, W. G. (2005). *Statistics for experimenters: design, innovation, and discovery*, volume 2. Wiley-Interscience, New Jersey, NY, USA.

Brady, J. (1984). Flow development in a porous channel and tube. *The Physics of fluids*, 27(5):1061–1067.

Brauer, H. and Fetting, F. (1966). Stofftransport bei wandreaktion im einlaufgebiet eines strömungsrohres. *Chemie Ingenieur Technik*, 38(1):30–35.

Breuer, M., Bernsdorf, J., Zeiser, D. F., and Durst, F. (2000). Accurate computations of the laminar ow past a square cylinder based on two different methods: lattice-boltzmann and finite-volume. *International Journal of Heat and Fluid Flow*, 21:186–196.

Casanovas, A., de Leitenburg, C., Trovarelli, A., and Llorca, J. (2008). Catalytic monoliths for ethanol steam reforming. *Catalysis Today*, 138(3-4):187–192.

Chan, S. H. and Hoang, D. L. (1999). Heat transfer and chemical reactions in exhaust system of a cold-start engine. *International Journal of Heat and Mass Transfer*, 42(22):4165–4183.

Chen, J., Yang, H., Wang, N., Ring, Z., and Dabros, T. (2008). Mathematical modeling of monolith catalysts and reactors for gas phase reactions. *Applied Catalysis A: General*, 345(1):1–11.

Chen, X. and Xia, H. (2017). A hybrid LES-RANS study on square cylinder unsteady heat transfer. *International Journal of Heat and Mass Transfer*, 108:1237–1254.

Clarkson, R., Benjamin, S., Jasper, T., and Girgls, N. (1993). An integrated computational model for the optimisation of monolith catalytic converters. *SAE Technical Paper*, No. 931071.

Clarkson, R. J. (1997). *A theoretical and experimental study of automotive catalytic converters*. PhD thesis, Coventry University.

COMSOL Multiphysics Software Package v4.3 (2012). COMSOL AB, Stockholm, Sweden.

Cornejo, I., Cornejo, G., Nikrityuk, P., and Hayes, R. E. (2019a). Entry length convective heat transfer in a monolith: The effect of upstream turbulence. *International Journal of Thermal Sciences*, 138:235–246.

Cornejo, I., Hayes, R. E., and Nikrityuk, P. (2018a). A new approach for the modeling of turbulent flows in automotive catalytic converters. *Chemical Engineering Research and Design*, 140:308–319.

Cornejo, I., Nikrityuk, P., and Hayes, R. (2017). Turbulence decay inside the channels of an automotive catalytic converter monolith. *Emission Control Science and Technology*, 3(4):302—309.

Cornejo, I., Nikrityuk, P., and Hayes, R. E. (2018b). Multiscale RANS-based modeling of the turbulence decay inside of an automotive catalytic converter. *Chemical Engineering Science*, 175:377–386.

Cornejo, I., Nikrityuk, P., and Hayes, R. E. (2018c). Turbulence generation after a monolith in automotive catalytic converters. *Chemical Engineering Science*, 187:107–116.

Cornejo, I., Nikrityuk, P., and Hayes, R. E. (2019b). Pressure correction for automotive catalytic converters: A multi-zone permeability approach. *Chemical Engineering Research and Design*, 147:232–243.

Cornejo, I., Nikrityuk, P., and Hayes, R. E. (2020a). Effect of substrate geometry and flow condition after the turbulence generation after a monolith. *Canadian Journal of Chemical Engineering*, doi: 10.1002/cjce.23687.

Cornejo, I., Nikrityuk, P., and Hayes, R. E. (2020b). The influence of channel geometry on the pressure drop in automotive catalytic converters: Model development and validation. *Chemical Engineering Science*, doi: 10.1016/j.ces.2019.115317.

Cornejo, I., Nikrityuk, P., Lange, C., and Hayes, R. E. (2019c). Influence of upstream turbulence on the pressure drop inside a monolith. *Chemical Engineering and Processing-Process Intensification*, doi: 10.1016/j.cep.2019.107735.

Couck, S., Cousin-Saint-Remi, J., Van der Perre, S., Baron, G. V., Minas, C., Ruch, P., and Denayer, J. F. (2018). 3D-printed SAPO-34 monoliths for gas separation. *Microporous and Mesoporous Materials*, 255:185–191.

Dadi, R. K., Daneshvar, K., Luss, D., Balakotaiah, V., Kalamaras, C. M., and Epling, W. (2018). Comparison of light-off performance of Pt-Pd/γ-Al2O3 dual layer and dual brick diesel oxidation catalysts. *Chemical Engineering Journal*, 335:1004–1017.

Dai, C., Lei, Z., Zhang, J., Li, Y., and Chen, B. (2013). Monolith catalysts for the alkylation of benzene with propylene. *Chemical Engineering Science*, 100:342–351.

Dardiotis, C. K., Haralampous, O. A., and Koltsakis, G. C. (2006). Catalytic oxidation performance of wall-flow versus flow-through monoliths for diesel emissions control. *Industrial & Engineering Chemistry Research*, 45(10):3520–3530.

Deng, Y., Zheng, W., Jiaqiang, E., Zhang, B., Zhao, X., Zuo, Q., Zhang, Z., and Han, D. (2017). Influence of geometric characteristics of a diesel particulate filter on its behavior in equilibrium state. *Applied Thermal Engineering*, 123:61–73.

Deuschle, T., Janoske, U., and Piesche, M. (2008). A CFD-model describing filtration, regeneration and deposit rearrangement effects in gas filter systems. *Chemical Engineering Journal*, 135(1-2):49–55.

Deutschmann, O. and Chatterjee, D. (2017). Modeling of Exhaust-Gas After-Treatment. *Emission Control Science and Technology*, 3(4):247–248.

Devatine, A., Chaumat, H., Guillaume, S., Tchibouanga, B. T., Martínez, F. D., Julcour, C., and Billet, A.-M. (2017). Hydrodynamic study of a monolith-type reactor for intensification of gas-liquid applications. *Chemical Engineering and Processing: Process Intensification*, 122:277–287.

Dhillon, P. S., Harold, M., Wang, D., Kumar, A., and Joshi, S. (2019). Transport and Reaction in Washcoated Monoliths: Cu-SSZ-13 Selective Catalytic Reduction and Dual-Layer Cu-SSZ-13+ Pt/Al2O3 Ammonia Slip Catalyst. *Reaction Chemistry & Engineering*.

Di Sarli, V. and Di Benedetto, A. (2015). Modeling and simulation of soot combustion dynamics in a catalytic diesel particulate filter. *Chemical Engineering Science*, 137:69–78.

Dritselis, C. D., Tzorbatzoglou, F., Mastrokalos, M., and Haralampous, O. (2019). Numerical Study of Flow and Particle Deposition in Wall-Flow Filters with Intact or Damaged Exit. *Fluids*, 4(4):201.

Drouin, M., Gregoire, O., and Simonin, O. (2013). A consistent methodology for the derivation and calibration of a macroscopic turbulence model for flows in porous media. *International Journal of Heat and Mass Transfer*, 63:401–413.

Ekström, F. and Andersson, B. (2002). Pressure drop of monolithic catalytic converters experiments and modeling. *SAE Technical paper*, No. 2002-01-1010.

Engelbrecht, N., Chiuta, S., Everson, R. C., Neomagus, H. W., and Bessarabov, D. G. (2017). Experimentation and CFD modelling of a microchannel reactor for carbon dioxide methanation. *Chemical Engineering Journal*, 313:847–857.

Fadic, A., Nien, T.-W., Mmbaga, J., Hayes, R. E., and Votsmeier, M. (2014). A case study in multi-scale model reduction: The effect of cell density on catalytic converter performance. *The Canadian Journal of Chemical Engineering*, 92(9):1607–1617.

Fang, Z., Hu, Y., Wu, X., Qin, Y., Cheng, J., Chen, Y., Tan, P., and Li, H. (2018). A novel magnesium ascorbyl phosphate graphene-based monolith and its superior adsorption capability for bisphenol A. *Chemical Engineering Journal*, 334:948–956.

Ferziger, J. and Peric, M. (2002). *Computational Methods for Fluid Dynamics*. Springer, New York, USA.

Gnielinski, V. (1975). New equations for heat and mass transfer in the turbulent flow in pipes and channels. *NASA STI/recon technical report A*, 75:8–16.

Graetz, L. (1883). Uber Die Warmeleitungsfahigheit Von Flussingkeiten—Part 1. *Ann. Phys. Chem*, 18:79–94.

Greiner, R., Prill, T., Iliev, O., van Setten, B., and Votsmeier, M. (2019). Tomography based simulation of reactive flow at the microscale: Particulate filters with wall integrated catalyst. *Chemical Engineering Journal*, doi: 10.1016/j.cej.2019.121919.

Grigull, U. and Tratz, H. (1965). Thermischer einlauf in ausgebildeter laminarer rohrströmung. *International Journal of Heat and Mass Transfer*, 8(5):669–678.

Grimm, M. and Mazumder, S. (2008). Numerical investigation of wall heat conduction effects on catalytic combustion in split and continuous monolith tubes. *Computers & Chemical Engineering*, 32(3):552–560.

Groppi, G., Belloli, A., Tronconi, E., and Forzatti, P. (1995). A comparison of lumped and distributed models of monolith catalytic combustors. *Chemical Engineering Science*, 50(17):2705–2715.

Groppi, G. and Tronconi, E. (1997). Theoretical analysis of mass and heat transfer in monolith catalysts with triangular channels. *Chemical Engineering Science*, 52(20):3521–3526.

Groppi, G., Tronconi, E., and Forzatti, P. (1999). Mathematical models of catalytic combustors. *Catalysis Reviews*, 41(2):227–254.

Gu, T. and Balakotaiah, V. (2016). Impact of heat and mass dispersion and thermal effects on the scale-up of monolith reactors. *Chemical Engineering Journal*, 284:513–535.

Gu, T. and Balakotaiah, V. (2017). Analysis of upstream creeping reaction zones in catalytic monolith reactors. *Chemical Engineering Journal*, 317:267–279.

Guadarrama-Mendoza, A. J., Villafán-Vidales, H. I., Valadés-Pelayo, P. J., Arancibia-Bulnes, C. A., Riveros-Rosas, D., and Romero-Paredes, H. (2018). Radiative analysis in a multichanneled monolith solar reactor coated with ZnFe2O4 thin film. *International Journal of Thermal Sciences*, 132:275–284.

Guan, B., Zhan, R., Lin, H., and Huang, Z. (2015). Review of the state-of-the-art of exhaust particulate filter technology in internal combustion engines. *Journal of Environmental Management*, 154:225–258.

Guarnieri, M. and Balmes, J. R. (2014). Outdoor air pollution and asthma. *The Lancet*, 383(9928):1581–1592.

Guhan, C. O. A., Arthanareeswaran, G., Varadarajan, K., and Krishnan, S. (2016). Numerical optimization of flow uniformity inside an under body-oval substrate to improve emissions of IC engines. *Journal of Computational Design and Engineering*, 3(3):198–214.

Gundlapally, S. R. and Balakotaiah, V. (2011). Heat and mass transfer correlations and bifurcation analysis of catalytic monoliths with developing flows. *Chemical Engineering Science*, 66(9):1879–1892.

Gupta, N. and Balakotaiah, V. (2001). Heat and mass transfer coefficients in catalytic monoliths. *Chemical Engineering Science*, 56(16):4771–4786.

Hagen, G. (1839). Ueber die bewegung des wassers in engen cylindrischen röhren. *Annalen der Physik*, 122(3):423–442.

Haralampous, O., Kandylas, I., Koltsakis, G., and Samaras, Z. (2004). Diesel particulate filter pressure drop Part 1: Modelling and experimental validation. *International Journal of Engine Research*, 5(2):149–162.

Haralampous, O. and Koltsakis, G. (2004). Oxygen diffusion modeling in diesel particulate filter regeneration. *AIChE Journal*, 50(9):2008–2019.

Hayes, R., Fadic, A., Mmbaga, J., and Najafi, A. (2012). CFD modelling of the automotive catalytic converter. *Catalysis Today*, 188(1):94–105.

Hayes, R., Kolaczkowski, S., and Thomas, W. (1992). Finite-element model for a catalytic monolith reactor. *Computers & Chemical Engineering*, 16(7):645–657.

Hayes, R. and Kolaczkowski, S. T. (1994). Mass and heat transfer effects in catalytic monolith reactors. *Chemical Engineering Science*, 49(21):3587–3599.

Hayes, R., Liu, B., Moxom, R., and Votsmeier, M. (2004a). The effect of washcoat geometry on mass transfer in monolith reactors. *Chemical Engineering Science*, 59(15):3169–3181.

Hayes, R., Mukadi, L., Votsmeier, M., and Gieshoff, J. (2004b). Three-way catalytic converter modelling with detailed kinetics and washcoat diffusion. *Topics in Catalysis*, 30(1):411–415.

Hayes, R. E., Donoso-Bravo, A., and Mmbaga, J. P. (2015). Entry length effects for momentum, heat and mass transfer in circular ducts with laminar flow. *The Canadian Journal of Chemical Engineering*, 93(5):863–869.

Hayes, R. E. and Kolaczkowski, S. T. (1998). *Introduction to catalytic combustion*. CRC Press, Boca Raton, FL, USA.

He, C. and Liu, Y. (2018). Large-eddy simulation of jet impingement heat transfer using a lobed nozzle. *International Journal of Heat and Mass Transfer*, 125:828–844.

Heck, R. M., Gulati, S., and Farrauto, R. J. (2001). The application of monoliths for gas phase catalytic reactions. *Chemical Engineering Journal*, 82(1-3):149–156.

Heibel, A. and Spaid, M. A. (1999). A new converter concept providing improved flow distribution and space utilization. *SAE Technical Paper*, No. 1999-01-0768.

Herwig, H. and Mahulikar, S. P. (2006). Variable property effects in single-phase incompressible flows through microchannels. *International Journal of Thermal Sciences*, 45(10):977–981.

Hettel, M., Daymo, E., and Deutschmann, O. (2018). 3D modeling of a CPOX-reformer including detailed chemistry and radiation effects with duo. *Computers & Chemical Engineering*, 109:166–178.

Hettel, M., Daymo, E., Schmidt, T., and Deutschmann, O. (2019). CFD-modeling of fluid domains with embedded monoliths with emphasis on automotive converters. *Chemical Engineering and Processing-Process Intensification*, doi: 10.1016/j.cep.2019.107728.

Hettel, M., Diehm, C., Torkashvand, B., and Deutschmann, O. (2013). Critical evaluation of in situ probe techniques for catalytic honeycomb monoliths. *Catalysis Today*, 216:2–10.

Holmgren, A. and Andersson, B. (1998). Mass transfer in monolith catalysts-CO oxidation experiments and simulations. *Chemical Engineering Science*, 53(13):2285–2298.

Holmgren, A., Gronstedt, T., and Andersson, B. (1997). Improved flow distribution in automotive monolithic converters. *Reaction Kinetics and Catalysis Letters*, 60(2):363–371.

Ibald-Mulli, A., Wichmann, H.-E., Kreyling, W., and Peters, A. (2002). Epidemiological evidence on health effects of ultrafine particles. *Journal of Aerosol Medicine*, 15(2):189–201.

Inbamrung, P., Sornchamni, T., Prapainainar, C., Tungkamani, S., Narataruksa, P., and Jovanovic, G. N. (2018). Modeling of a square channel monolith reactor for methane steam reforming. *Energy*.

Irandoust, S. and Andersson, B. (1988). Monolithic catalysts for nonautomobile applications. *Catalysis Reviews Science and Engineering*, 30(3):341–392.

Iwaniszyn, M., Piatek, M., Gancarczyk, A., Jodlowski, P., Lojewska, J., and Kolodziej, A. (2017). "Flow resistance and heat transfer in short channels of metallic monoliths: Experiments versus CFD". *International Journal of Heat and Mass Transfer*, 109:778 – 785.

Jahn, R., Snita, D., Kubíček, M., and Marek, M. (1997). 3-D modeling of monolith reactors. *Catalysis Today*, 38(1):39–46.

Jeong, S.-J. (2014). A full transient three-dimensional study on the effect of pulsating exhaust flow under real running condition on the thermal and chemical behavior of closed-coupled catalyst. *Chemical Engineering Science*, 117:18–30.

Joshi, A. and Johnson, T. (2018). Gasoline particulate filters—a review. *Emission Control Science and Technology*, 4(4):2019–239.

Kakaç, S., Shah, R. K., and Aung, W. (1987). *Handbook of single-phase convective heat transfer*. John Wiley and Sons, New York, NY, USA.

Kalitzin, G., Medic, G., Iaccarino, G., and Durbin, P. (2005). Near-wall behavior of RANS turbulence models and implications for wall functions. *Journal of Computational Physics*, 204(1):265–291.

Kannepalli, S., Gremminger, A., Tischer, S., and Deutschmann, O. (2017). Optimization of axial catalyst loading in transient-operated zone-structured monoliths: Reduction of cumulative emissions in automotive oxidation catalysts. *Chemical Engineering Science*, 174:189–202.

Karamitros, D. and Koltsakis, G. (2017). Model-based optimization of catalyst zoning on SCR-coated particulate filters. *Chemical Engineering Science*, 173:514–524.

Karjalainen, P., Pirjola, L., Heikkilä, J., Lähde, T., Tzamkiozis, T., Ntziachristos, L., Keskinen, J., and Rönkkö, T. (2014). Exhaust particles of modern gasoline vehicles: A laboratory and an on-road study. *Atmospheric Environment*, 97:262–270.

Karvounis, E. and Assanis, D. N. (1993). The effect of inlet flow distribution on catalytic conversion efficiency. *International Journal of Heat and Mass Transfer*, 36(6):1495–1504.

Kays, W., Crawford, M., and Weigand, B. (2004). *Convective heat and mass transfer*. McGraw-Hill Higher Education, New York, NY, USA.

Kays, W. and London, M. (1964). *Compact Heat Exchangers*. McGraw-Hill, New York, NY, USA.

Kays, W. M. and Crawford, M. E. (1993). *Convective heat and mass transfer*. McGraw-Hill, New York, NY, USA.

Khodadadian, F., De Boer, M. W., Poursaeidesfahani, A., Van Ommen, J. R., Stankiewicz, A. I., and Lakerveld, R. (2018). Design, characterization and model validation of a LED-based photocatalytic reactor for gas phase applications. *Chemical Engineering Journal*, 333:456–466.

Kim, S. (2004). Large eddy simulation using unstructured meshes and dynamic subgrid-scale turbulence models. In *34th AIAA Fluid Dynamics Conference and Exhibit*, Portland, OR, USA.

Kim, W. and Menon, S. (1995). A new dynamic one-equation subgrid-scale model for large eddy simulations. In *33rd Aerospace Sciences Meeting and Exhibit*, Reno, NV, USA.

Kim, W.-W., Menon, S., Kim, W.-W., and Menon, S. (1997). Application of the localized dynamic subgrid-scale model to turbulent wall-bounded flows. In *35th aerospace sciences meeting and exhibit.*, page 210, Reno, NV, USA.

Kim, Y. and Kim, W. (2007). Optimum design of an automotive catalytic converter for minimization of cold-start emissions using a micro genetic algorithm. *International Journal of Automotive Technology*, 8(5):563–573.

Kim, Y.-D., Jeong, S.-J., and Kim, W.-S. (2009a). Influence of spacing on the thermal efficiency of a dual-monolithic catalytic converter during warmup. *Environmental Engineering Science*, 26(7):1171–1187.

Kim, Y.-D., Jeong, S.-J., and Kim, W.-S. (2009b). Optimal design of axial noble metal distribution for improving dual monolithic catalytic converter performance. *Chemical Engineering Science*, 64(7):1373–1383.

Kinney, R. B. (1968). Fully developed frictional and heat-transfer characteristics of laminar flow in porous tubes. *International Journal of Heat and Mass Transfer*, 11(9):1393–1401.

Knoth, J., Drochner, A., Vogel, H., Gieshoff, J., Kögel, M., Pfeifer, M., and Votsmeier, M. (2005). Transport and reaction in catalytic wall-flow filters. *Catalysis Today*, 105(3-4):598–604.

Kočí, P., Isoz, M., Plachá, M., Arvajová, A., Václavík, M., Svoboda, M., Price, E., Novák, V., and Thompsett, D. (2019). 3D reconstruction and pore-scale modeling of coated catalytic filters for automotive exhaust gas aftertreatment. *Catalysis Today*, 320:165–174.

Koltsakis, G., Haralampous, O., Depcik, C., and Ragone, J. C. (2013). Catalyzed diesel particulate filter modeling. *Reviews in Chemical Engineering*, 29(1):1–61.

Konstandopoulos, A., Kostoglou, M., and Vlachos, N. (2006). The multiscale nature of diesel particulate filter simulation. *International Journal of Vehicle Design*, 41(1-4):256–284.

Konstandopoulos, A. G. (2003). Flow resistance descriptors for diesel particulate filters: definitions, measurements and testing. *SAE Technical Paper*, No. 2003-01-0846.

Konstandopoulos, A. G. and Johnson, J. H. (1989). Wall-flow diesel particulate filters—their pressure drop and collection efficiency. *SAE Transactions Journal of Engines*, 98(3):625–647.

Konstandopoulos, A. G., Kostoglou, M., Skaperdas, E., Papaioannou, E., Zarvalis, D., and Kladopoulou, E. (2000). Fundamental studies of diesel particulate filters: transient loading, regeneration and aging. *SAE 2000 Transactions Journal of Fuels and Lubricants*, 109(4):683–705.

Konstandopoulos, A. G., Kostoglou, M., Vlachos, N., and Kladopoulou, E. (2005). Progress in diesel particulate filter simulation. *SAE Technical paper*, No. 2005-01-0946.

Konstandopoulos, A. G., Kostoglou, M., Vlachos, N., and Kladopoulou, E. (2007). Advances in the science and technology of diesel particulate filter simulation. *Advances in Chemical Engineering*, 33:213–294.

Konstandopoulos, A. G., Skaperdas, E., and Masoudi, M. (2001). Inertial Contributions to the Pressure Drop of Diesel Particulate Filters. *SAE Technical Paper*, No. 2001-01-0909.

Konstandopoulos, A. G., Skaperdas, E., Warren, J., and Allansson, R. (1999). Optimized Filter Design and Selection Criteria for Continuously Regenerating Diesel Particulate Traps. *SAE 1999 Transactions - Journal of Fuels and Lubricants*, 104(4):279–288.

Kostoglou, M., Bissett, E. J., and Konstandopoulos, A. G. (2012). Improved transfer coefficients for wall-flow monolithic catalytic reactors: energy and momentum transport. *Industrial & Engineering Chemistry Research*, 51(40):13062–13072.

Kostoglou, M., Housiada, P., and Konstandopoulos, A. G. (2003). Multi-channel simulation of regeneration in honeycomb monolithic diesel particulate filters. *Chemical Engineering Science*, 58(14):3273–3283.

Kostoglou, M., Lekkos, C., and Konstandopoulos, A. (2011). On mathematical modeling of solar hydrogen production in monolithic reactors. *Computers & Chemical Engineering*, 35(9):1915–1922.

Kraichnan, R. H. (1970). Diffusion by a random velocity field. *The Physics of Fluids*, 13(1):22–31.

Kreutzer, M. T., Kapteijn, F., and Moulijn, J. (2006). Shouldn't catalysts shape up?: Structured reactors in general and gas–liquid monolith reactors in particular. *Catalysis Today*, 111(1-2):111–118.

Kumar, A. and Mazumder, S. (2010). Toward simulation of full-scale monolithic catalytic converters with complex heterogeneous chemistry. *Computers & Chemical Engineering*, 34(2):135–145.

Kumaresh, S. and Kim, M. Y. (2019). Numerical investigation of catalytic combustion in a honeycomb monolith with lean methane and air premixtures over the platinum catalyst. *International Journal of Thermal Sciences*, 138:304–313.

Kushwaha, A., , Poirier, M., Sapoundjiev, H., and Hayes, R. (2004). Effect of reactor internal properties on the performance of a flow reversal catalytic reactor for methane combustion. *Chemical Engineering Science*, 59:4081–4093.

Kuwata, Y., Suga, K., and Sakurai, Y. (2014). Development and application of a multi-scale $k - \varepsilon$ model for turbulent porous medium flows. *International Journal of Heat and Fluid Flow*, 49:135–150.

Lai, M., Lee, T., Kim, J., Cheng, C., Li, P., and Chui, G. (1992). Numerical and experimental characterizations of automotive catalytic converter internal flows. *Journal of Fluids and Structures*, 6:451–470.

Lai, M.-C., Kim, J.-Y., Cheng, C.-Y., Li, P., Chui, G., and Pakko, J. (1991). Three-dimensional simulations of automotive catalytic converter internal flow. *Journal of Materials and Manufacturing*, 100(5):241–250.

Lambert, C., Chanko, T., Dobson, D., Liu, X., and Pakko, J. (2017). Gasoline particle filter development. *Emission Control Science and Technology*, 3(1):105–111.

Launder, B. E. and Spalding, D. B. (1972). *Lectures in mathematical models of turbulence*. Academic Press, New York, USA.

Li, X., Li, W., Rezaei, F., and Rownaghi, A. (2018). Catalytic cracking of n-hexane for producing light olefins on 3D-printed monoliths of MFI and FAU zeolites. *Chemical Engineering Journal*, 333:545–553.

Ligrani, P. M. and Mahmood, G. I. (2003). Variable property Nusselt numbers in a channel with pin fins. *Journal of Thermophysics and Heat Transfer*, 17(1):103–111.

Lilly, D. K. (1992). A proposed modification of the germano subgrid-scale closure method. *Physics of Fluids A: Fluid Dynamics*, 4(3):633–635.

Litto, R., Hayes, R., Sapoundjiev, H., Fuxman, A., Forbes, F., Liu, B., and Bertrand, F. (2006). Optimization of a flow reversal reactor for the catalytic combustion of lean methane mixtures. *Catalysis Today*, 117(4):536–542.

Liu, B., Hayes, R., Yi, Y., Mmbaga, J., Checkel, M., and Zheng, M. (2007a). Three dimensional modeling of methane ignition in a reverse flow catalytic converter. *Computers and Chemicals Engineering*, 31:292–306.

Liu, B., Hayes, R., Yi, Y., Mmbaga, J., Checkel, M., and Zheng, M. (2007b). Three dimensional modelling of methane ignition in a reverse flow catalytic converter. *Computers & Chemical Engineering*, 31(4):292–306.

Liu, Y., Harold, M. P., and Luss, D. (2012). Coupled NOx storage and reduction and selective catalytic reduction using dual-layer monolithic catalysts. *Applied Catalysis B: Environmental*, 121:239–251.

Lobo, O. J. and Chatterjee, D. (2018). Development of flow in a square mini-channel: Effect of flow oscillation. *Physics of Fluids*, 30(4):042003.

Lucentini, I., Serrano, I., Soler, L., Divins, N. J., and Llorca, J. (2020). Ammonia decomposition over 3d-printed ceo2 structures loaded with ni. *Applied Catalysis A: General*, doi: 10.1016/j.apcata.2019.117382.

Lundberg, B., Sjöblom, J., Johansson, Å., Westerberg, B., and Creaser, D. (2016). DOC modeling combining kinetics and mass transfer using inert washcoat layers. *Applied Catalysis B: Environmental*, 191:116–129.

Maffei, T., Rebughini, S., Gentile, G., Lipp, S., Cuoci, A., and Matteo, M. (2014). CFD analysis of the channel shape effect in monolith catalysts for the CH4 partial oxidation on Rh. *Reaction Kinetics and Catalysis Letters*, 86(7):1099–1106.

Mahmood, G., Ligrani, P., and Chen, K. (2003). Variable property and temperature ratio effects on Nusselt numbers in a rectangular channel with 45 deg angled rib turbulators. *Journal of Heat Transfer*, 125(5):769–778.

Mahyon, N. I., Li, T., Martinez-Botas, R., Wu, Z., and Li, K. (2019). A new hollow fibre catalytic converter design for sustainable automotive emissions control. *Catalysis Communications*, 120:86–90.

Malalasekera, W. and Versteeg, H. (2007). *An introduction to computational fluid dynamics: the finite volume method*. PEARSON Prentice Hall, Upper Saddle River, New Jersey, USA.

Marín, P., Hevia, M. A., Ordonez, S., and Díez, F. V. (2005). Combustion of methane lean mixtures in reverse flow reactors: comparison between packed and structured catalyst beds. *Catalysis Today*, 105(3):701–708.

Martínez, F. L. D., Julcour, C., Billet, A.-M., and Larachi, F. (2016). Modelling and simulations of a monolith reactor for three-phase hydrogenation reactions—rules and recommendations for mass transfer analysis. *Catalysis Today*, 273:121–130.

MATLAB Software Package R2018a (2018). The Mathworks Inc., Natick, MA, USA.

Matte-Deschênes, G., Vidal, D., Bertrand, F., and Hayes, R. E. (2016). Numerical investigation of the impact of thermophoresis on the capture efficiency of diesel particulate filters. *The Canadian Journal of Chemical Engineering*, 94(2):291–303.

Menon, S. and Kim, W.-W. (1996). High Reynolds number flow simulations using the localized dynamic subgrid-scale model. In *34th Aerospace Sciences Meeting and Exhibit*, page 425, Reno, NV, USA.

Menter, F. (1992). Improved two-equation k-ω turbulence models for aerodynamic flows. *NASA Technical Memorandum*, ID 19930013620.

Menter, F. (1994). Two-equation eddy-viscosity turbulence models for engineering applications. *AIAA journal*, 32(8):1598–1605.

Menter, F. (1997). Eddy viscosity transport equations and their relation to the k-ε model. *Journal of Fluids Engineering*, 119(4):876–884.

Menter, F. R., Langtry, R. B., Likki, S., Suzen, Y., Huang, P., and Völker, S. (2006). A correlation-based transition model using local variables—Part I: model formulation. *Journal of Turbomachinery*, 128(3):413–422.

Monteiro, R. A., Miranda, S. M., Rodrigues-Silva, C., Faria, J. L., Silva, A. M., Boaventura, R. A., and Vilar, V. J. (2015). Gas phase oxidation of n-decane and PCE by photocatalysis using an annular photoreactor packed with a monolithic catalytic bed coated with P25 and PC500. *Applied Catalysis B: Environmental*, 165:306–315.

Montgomery, D. C. (1996). *Desing and analysis of experiments*. Jonh Wiley & Sons, New Jersey, NY, USA.

More, H., Mmbaga, J., Hayes, R., Votsmeier, M., and Checkel, M. (2007). Heat and mass transfer limitations in pre-turbocharger catalysts. *Topics in Catalysis*, 42(1-4):429–432.

Mössner, M. and Radespiel, R. (2015). Modelling of turbulent flow over porous media using a volume averaging approach and a Reynolds stress model. *Computers and Fluids*, 108:25–42.

Murthy, S. and Fedorov, A. G. (2003). Radiation heat transfer analysis of the monolith type solid oxide fuel cell. *Journal of Power Sources*, 124(2):453–458.

Musto, M., Bianco, N., Rotondo, G., Toscano, F., and Pezzella, G. (2016). A simplified methodology to simulate a heat exchanger in an aircraft's oil cooler by means of a porous media model. *Applied Thermal Engineering*, 94:836–845.

Negri, M., Wilhelm, M., Hendrich, C., Wingborg, N., Gediminas, L., Adelöw, L., Maleix, C., Chabernaud, P., Brahmi, R., Beauchet, R., et al. (2018). New technologies for ammonium dinitramide based monopropellant thrusters–the project rheform. *Acta Astronautica*, 143:105–117.

Nguyen, T. D., Lim, Y.-I., Eom, W.-H., Kim, S.-J., and Yoo, K.-S. (2010). Experiment and CFD simulation of hybrid SNCR–SCR using urea solution in a pilot-scale reactor. *Computers & Chemical Engineering*, 34(10):1580–1589.

Nguyen, V. N., Deja, R., Peters, R., Blum, L., and Stolten, D. (2018). Study of the catalytic combustion of lean hydrogen-air mixtures in a monolith reactor. *International Journal of Hydrogen Energy*, 43(36):17520–17530.

Nicoud, F. and Ducros, F. (1999). Subgrid-scale stress modelling based on the square of the velocity gradient tensor. *Flow, Turbulence and Combustion*, 62(3):183–200.

Nien, T., Mmbaga, J., Hayes, R., and Votsmeier, M. (2013). Hierarchical multi-scale model reduction in the simulation of catalytic converters. *Chemical Engineering Science*, 93:362–375.

Nóbrega, J., Pinho, F. T. d., Oliveira, P. J., and Carneiro, O. (2004). Accounting for temperature-dependent properties in viscoelastic duct flows. *International Journal of Heat and Mass Transfer*, 47(6-7):1141–1158.

Ochoa-Tapia, J. A. and Whitaker, S. (1995). Momentum transfer at the boundary between a porous medium and a homogeneous fluid—I. Theoretical development. *International Journal of Heat and Mass Transfer*, 38(14):2635–2646.

Oxarango, L., Schmitz, P., and Quintard, M. (2004). Laminar flow in channels with wall suction or injection: a new model to study multi-channel filtration systems. *Chemical Engineering Science*, 59(5):1039–1051.

Ozhan, C., Fuster, D., and Da Costa, P. (2014). Multi-scale flow simulation of automotive catalytic converters. *Chemical Engineering Science*, 116:161–171.

Patankar, S. (1980). *Numerical heat transfer and fluid flow*. CRC press, Boca Raton, Florida, USA.

Piscaglia, F., Rutland, C. J., and Foster, D. E. (2005). Development of a CFD model to study the hydrodynamic characteristics and the soot deposition mechanism on the porous wall of a diesel particulate filter. *SAE Technical Paper*, No. 2005-01-0963.

Poling, B. E., Prausnitz, J. M., O'connell, J. P., et al. (2001). *The properties of gases and liquids*, volume 5. Mcgraw-hill New York.

Pontikakis, G. N., Konstantas, G. S., and Stamatelos, A. M. (2004). Three-way catalytic converter modeling as a modern engineering design tool. *Journal of Engineering for Gas Turbines and Power*, 126(4):906–923.

Pope, S. B. (2001). *Turbulent flows*. IOP Publishing, Bristol, UK.

Porter, S. (2016). *An assessment of CFD applied to a catalytic converter system with planar diffuser*. PhD thesis, Coventry University.

Porter, S., Saul, J., Aleksandrova, S., Medina, H., and Benjamin, S. (2016). Hybrid flow modelling approach applied to automotive catalysts. *Applied Mathematical Modelling*, 40(19-20):8435–8445.

Prasad, R., Kennedy, L. A., and Ruckenstein, E. (1984). Catalytic combustion. *Catalysis Reviews Science and Engineering*, 26(1):1–58.

Prescott, P. and Incropera, F. (1995). The effect of turbulence on solidification of a binary metal alloy with electromagnetic stirring. *Journal of heat transfer*, 117(3):716–724.

Presti, M., Pace, L., Hodgson, J., Bella, G., and De Maio, A. (2002). A Computational and Experimental Analysis for Optimization of Cell Shape in High Performance Catalytic Converters. *SAE Technical Paper*, No. 2002-01-0355.

Pujol, T., Arbat, G., Bove, J., Puig-Bargues, J., Duran-Ros, M., Velayos, J., and Ramırez de Cartagena, F. (2016). Effects of the underdrain design on the pressure drop in sand filters. *Biosystems Engineering*, 150:1–9.

Quintanilla, A., Casas, J., Miranzo, P., Osendi, M. I., and Belmonte, M. (2018). 3D-Printed Fe-doped silicon carbide monolithic catalysts for wet peroxide oxidation processes. *Applied Catalysis B: Environmental*, 235:246–255.

R: A Language and Environment for Statistical Computing (2008). http://www.R-project.org. Vienna, Austria.

Raithby, G. (1971). Laminar heat transfer in the thermal entrance region of circular tubes and two-dimensional rectangular ducts with wall suction and injection. *International Journal of Heat and Mass Transfer*, 14(2):223–243.

Regufe, M. J., Ferreira, A. F., Loureiro, J. M., Rodrigues, A., and Ribeiro, A. M. (2019). Electrical conductive 3D-printed monolith adsorbent for CO2 capture. *Microporous and Mesoporous Materials*.

Reynolds, O. (1883). An experimental investigation of the circumstances which determine whether the motion of water shall be direct or sinuous, and of the law of resistance in parallel channels. *Proceedings of The Royal Society of London*, 35(224-226):84–99.

Roy, S., Bauer, T., Al-Dahhan, M., Lehner, P., and Turek, T. (2004). Monoliths as multiphase reactors: a review. *AIChE journal*, 50(11):2918–2938.

Roy, S., Kamalanathan, P., and Al-Dahhan, M. (2019). Integration of phase distribution from gamma-ray tomography technique with monolith reactor scale modeling. *Chemical Engineering Science*, 200:27–37.

Sadeghi, F., Tirandazi, B., Khalili-Garakani, A., Nasseri, S., Nodehi, R. N., and Mostoufi, N. (2017). Investigating the effect of channel geometry on selective catalytic reduction of NOx in monolith reactors. *Chemical Engineering Research and Design*, 118:21–30.

Sahraoui, M. and Kaviany, M. (1992). Slip and no-slip velocity boundary conditions at interface of porous, plain media. *International Journal of Heat and Mass Transfer*, 35(4):927–943.

Samanta, D., De Lozar, A., and Hof, B. (2011). Experimental investigation of laminar turbulent intermittency in pipe flow. *Journal of Fluid Mechanics*, 681:193–204.

Santos, H. and Costa, M. (2009). Modelling transport phenomena and chemical reactions in automotive three-way catalytic converters. *Chemical Engineering Journal*, 148(1):173–183.

Schmuch, R., Wagner, R., Hörpel, G., Placke, T., and Winter, M. (2018). Performance and cost of materials for lithium-based rechargeable automotive batteries. *Nature Energy*, 3(4):267–278.

Schutt, B. D. and Abraham, M. A. (2004). Evaluation of a monolith reactor for the catalytic wet oxidation of cellulose. *Chemical Engineering Journal*, 103(1):77–88.

Schwiedernoch, R., Tischer, S., Correa, C., and Deutschmann, O. (2003). Experimental and numerical study on the transient behavior of partial oxidation of methane in a catalytic monolith. *Chemical Engineering Science*, 58(3-6):633–642.

Seckin, G., Çağatay, H., Çobaner, M., and Yurtal, R. (2009). Experimental investigation of kinetic energy and momentum correction coefficients in open channels. *Scientific Research and Essay*, 4(5):473–478.

Shah, R. (1978). A correlation for laminar hydrodynamic entry length solutions for circular and noncircular ducts. *Journal of Fluids Engineering*, 100(2):177–179.

Shah, R. K. and London, A. L. (1978). *Laminar flow forced convection in ducts: a source book for compact heat exchanger analytical data*. Academic press, New York, USA.

Sharma, A. and Birgersson, E. (2016). Validity and scalability of an asymptotically reduced single-channel model for full-size catalytic monolith converters. *Applied Mathematics and Computation*, 281:186–198.

Shuai, S.-J. and Wang, J.-X. (2004). Unsteady temperature fields of monoliths in catalytic converters. *Chemical Engineering Journal*, 100(1):95–107.

Shumway, R. and McEligot, D. (1971). Heated laminar gas flow in annuli with temperature-dependent transport properties. *Nuclear Science and Engineering*, 46(3):394–407.

Shyy, W., Pang, Y., Hunter, G., Wei, D., and Chen, M. (1992). Modeling of turbulent transport and solidification during continuous ingot casting. *International Journal of Heat and Mass Transfer*, 35:1229–1245.

Shyy, W., Pang, Y., Hunter, G., Wei, D., and Chen, M. (1993). Effect of turbulent heat transfer on continuous ingot solidification. *Journal of Engineering Materials and Technology*, 115(1):8–16.

Siemund, S., Leclerc, J., Schweich, D., Prigent, M., and Castagna, F. (1996). Three-way monolithic converter: simulations versus experiments. *Chemical Engineering Science*, 51(15):3709–3720.

Smagorinsky, J. (1963). General circulation experiments with the primitive equations: I. The basic experiment. *Monthly Weather Review*, 91(3):99–164.

Smirnov, A., Shi, S., and Celik, I. (2001). Random flow generation technique for large eddy simulations and particle-dynamics modeling. *Journal of Fluids Engineering*, 123(2):359–371.

Strom, H., Sasic, S., and Andersson, B. (2011). Effects of the turbulent-to-laminar transition in monolithic reactors for automotive pollution control. *Industrial & Engineering Chemistry Research*, 50(6):3194–3205.

Su, Q., Xie, L., Shuai, S., Wang, J., Song, J., and Li, Z. (2013). Optimization of automotive catalytic converter by numerical modeling and simulation with detailed mechanism. *Catalysis Today*, 216:292–298.

Taboada, E., Angurell, I., and Llorca, J. (2014). Dynamic photocatalytic hydrogen production from ethanol–water mixtures in an optical fiber honeycomb reactor loaded with Au/TiO2. *Journal of catalysis*, 309:460–467.

Tanimu, A., Jaenicke, S., and Alhooshani, K. (2017). Heterogeneous catalysis in continuous flow microreactors: A review of methods and applications. *Chemical Engineering Journal*, 327:792–821.

Tanno, K., Makino, H., Kurose, R., Komori, S., and Michioka, T. (2013). Effect of turbulent to laminar flow transition on surface reaction and particle deposition in a square duct. *TSFP Digital Library Online*.

Thakkar, H., Eastman, S., Hajari, A., Rownaghi, A. A., Knox, J. C., and Rezaei, F. (2016). 3D-printed zeolite monoliths for CO2 removal from enclosed environments. *ACS Applied Materials & Interfaces*, 8(41):27753–27761.

Thakkar, H., Lawson, S., Rownaghi, A. A., and Rezaei, F. (2018). Development of 3D-printed polymer-zeolite composite monoliths for gas separation. *Chemical Engineering Journal*, 348:109–116.

Tikekar, M., Singh, S. G., and Agrawal, A. (2010). Measurement and modeling of pulsatile flow in microchannel. *Microfluidics and nanofluidics*, 9(6):1225–1240.

Tischer, S., Chrys, C., and Deutschmann, O. (2001). Transient three-dimensional simulations of a catalytic combustion monolith using detailed models for heterogeneous and homogeneous reactions and transport phenomena. *Catalysis Today*, 69(1-4):57–62.

Tischer, S. and Deutschmann, O. (2005). Recent advances in numerical modeling of catalytic monolith reactors. *Catalysis Today*, 105(3-4):407–413.

Tosun, I., Uner, D., and Ozgen, C. (1988). Critical reynolds number for newtonian flow in rectangular ducts. *Industrial & Engineering Chemistry Research*, 27(10):1955–1957.

Tronconi, E. and Forzatti, P. (1992). Adequacy of lumped parameter models for SCR reactors with monolith structure. *AIChE Journal*, 38(2):201–210.

Tsinoglou, D., Koltsakis, G., Missirlis, D., and Yakinthos, K. (2004). Transient modelling of flow distribution in automotive catalytic converters. *Applied Mathematical Modelling*, 28(9):775–794.

Václavík, M., Kočí, P., Novák, V., and Thompsett, D. (2017). NOx conversion and selectivity in multi-layer and sequential DOC-LNT automotive exhaust catalysts: Influence of internal transport. *Chemical Engineering Journal*, 329:128–134.

Vaclavik, M., Placha, M., Kočí, P., Svoboda, M., Hotchkiss, T., Novak, V., and Thompsett, D. (2017). Structure characterisation of catalytic particulate filters for automotive exhaust gas aftertreatment. *Materials Characterization*, 134:311–318.

Van Vliet, O., Brouwer, A. S., Kuramochi, T., van Den Broek, M., and Faaij, A. (2011). Energy use, cost and CO2 emissions of electric cars. *Journal of Power Sources*, 196(4):2298–2310.

Vega M., I. M., Cornejo, Ivan, N. P., and Hayes, R. E. (2020). Simulation of flow patterns in particulate filters with various viscous models. *Emission Control Science and Technology*, In press.

Vega Mesquida, I. M. (2019). Analysis of Flow Pattern in a Gasoline Particulate Filter using CFD. Master's thesis, University of Alberta.

Vrentas, J. and Duda, J. (1973). Flow of a newtonian fluid through a sudden contraction. *Applied Scientific Research*, 28(1):241–260.

Walters, D. K. and Cokljat, D. (2008). A three-equation eddy-viscosity model for Reynolds-averaged Navier–Stokes simulations of transitional flow. *Journal of Fluids Engineering*, 130(12):121401.

Wang, W. and Bissett, E. J. (2018). Frictional and Heat Transfer Characteristics of Flow in Triangle and Hexagon Channels of Wall-Flow Monoliths. *Emission Control Science and Technology*, 4(3):198–218.

Wang, Y. and Longwell, P. (1964). Laminar flow in the inlet section of parallel plates. *AIChE Journal*, 10(3):323–329.

Wang, Y., Sun, G., Dai, J., Chen, G., Morgenstern, J., Wang, Y., Kang, S., Zhu, M., Das, S., Cui, L., et al. (2017). A high-performance, low-tortuosity wood-carbon monolith reactor. *Advanced Materials*, 29(2).

Watling, T. C. (2018). A One-Dimensional Model for Square and Octo-Square Asymmetric Particulate Filters with Correct Description of the Channel and Wall Geometry. *SAE Technical Paper*, No. 2018-01-0951.

Watling, T. C., Ravenscroft, M. R., Cleeton, J. P., Rees, I. D., and Wilkins, D. A. (2017). Development of a particulate filter model for the prediction of backpressure: improved momentum balance and entrance and exit effect equations. *SAE International Journal of Engines*, 10(4):1765–1794.

Wendland, D. W. and Matthes, W. R. (1986). Visualization of automotive catalytic converter internal flows. *Fuels and Lubricants*, 95:729–795.

White, F. M. (2009). *Fluid Mechanics*. McGraw-hill, New York, NY.

Wilcox, D. C. (1988). Reassessment of the scale-determining equation for advanced turbulence models. *AIAA Journal*, 26(11):1299–1310.

Wilcox, D. C. (1993). *Turbulence modeling for CFD*. DCW Industries, La Canada, California, USA.

Wolfshtein, M. (1969). The velocity and temperature distribution in one-dimensional flow with turbulence augmentation and pressure gradient. *International Journal of Heat and Mass Transfer*, 12(3):301–318.

Wurzenberger, J. C. and Kutschi, S. (2007). Advanced Simulation Technologies for Diesel Particulate Filters, A Fundamental Study on Asymmetric Channel Geometries. *SAE Technical Paper*, No. 2007-01-1137.

Xu, M., Zhang, J., Li, P., and Mi, J. (2015). On two distinct reynolds number regimes of a turbulent square jet. *Theoretical and Applied Mechanics Letters*, 5(3):117–120.

Xu, X. and Moulijn, J. A. (1998). Transformation of a structured carrier into structured catalyst. *Statistics and Operations Research Transactions*, pages 599–616.

Yamamoto, K., Satake, S., and Yamashita, H. (2009). Microstructure and particle-laden flow in diesel particulate filter. *International Journal of Thermal Sciences*, 48(2):303–307.

Yang, J. and Sun, H. (2015). Battery swap station location-routing problem with capacitated electric vehicles. *Computers and Operations Research*, 55:2017–232.

Yang, S., Deng, C., Gao, Y., and He, Y. (2016). Diesel particulate filter design simulation: A review. *Advances in Mechanical Engineering*, 8(3):1–14.

York, A. P., Watling, T. C., Ahmadinejad, M., Bergeal, D., Phillips, P. R., and Swallow, D. (2009). Modeling the emissions control performance of a catalyzed diesel particulate filter (CDPF) system for light duty diesel applications. *SAE International Journal of Fuels and Lubricants*, 2(1):578–589.

York, A. P., Watling, T. C., Ramskill, N. P., Gladden, L. F., Sederman, A. J., Tsolakis, A., Herreros, J. M., and Lefort, I. (2015). Visualization of the Gas Flow Field within a Diesel Particulate Filter Using Magnetic Resonance Imaging. *SAE Technical Paper*, No. 2015-01-2009.

Yu, M., Luss, D., and Balakotaiah, V. (2013). Regeneration modes and peak temperatures in a diesel particulate filter. *Chemical Engineering Journal*, 232:541–554.

Yuan, S. and Finkelstein, A. (1956). Laminar Pipe Flow with Injection and Suction through a Porous Wall. *Trans. ASME*, 78:719–724.

Zamir, M. and Ritman, E. (2000). *The physics of pulsatile flow*. Springer, New York, USA.

Zhang, F., Hayes, R., and Kolaczkowski, S. (2004). A new technique to measure the effective diffusivity in a catalytic monolith washcoat. *Chemical Engineering Research and Design*, 82(4):481–489.

Zhang, L., Luo, S., Zhang, Y., Tian, W., Su, G., and Qiu, S. (2018). Large eddy simulation on turbulent heat transfer in reactor vessel lower head corium pools. *Annals of Nuclear Energy*, 111:293–302.

Zygourakis, K. (1989). Transient operation of monolith catalytic converters: a two-dimensional reactor model and the effects of radially nonuniform flow distributions. *Chemical Engineering Science*, 44(9):2075–2086.